[redacted]

MISSILE AND SPACE VEHICLE DEPARTMENT

PROJECT APOLLO

A Feasibility Study of an Advanced Manned Spacecraft and System

FINAL REPORT

VOLUME VI. AERODYNAMICS, CONFIGURATIONS, HEATING, STRUCTURES, AND MATERIALS

(NASA-CR-135728) PROJECT APOLLO: A FEASIBILITY STUDY OF AN ADVANCED MANNED SPACECRAFT AND SYSTEM. VOLUME 6: AERODYNAMICS, CONFIGURATIONS, HEATING, STRUCTURES, (General Electric Co.) 363 p 00/99

N73-73970

Unclas 18926

CLASSIFICATION CHANGE

TO = UNCLASSIFIED [redacted]

By authority of [redacted] E.O. 11652

Changed by Lorna J. Hoopman Date 7-18-73

GENERAL ELECTRIC

[redacted]

[redacted]

NOTICE

~~This document contains information affecting the national defense of the United States within the meaning of the Espionage Laws, Title 18, U.S.C. Sections 793 and 794. The transmission or revelation of its contents in any manner to an unauthorized person is prohibited by law.~~

CASE FILE COPY

~~CONFIDENTIAL~~

36p

[redacted]

K63 80885

This Document Contains 380 Numbered Pages
Copy No. 1 of 400 Copies, First Series.

354830

NASA Contract NAS 5-302

~~GROUP 4 Downgraded at 3 year intervals; declassified after 12 years~~

PROJECT APOLLO

A Feasibility Study of an Advanced Manned Spacecraft and System

FINAL REPORT

VOLUME VI. AERODYNAMICS, CONFIGURATIONS, HEATING, STRUCTURES, AND MATERIALS

Program Manager: Dr. G. R. Arthur

Project Engineer: H. L. Bloom

Prepared for:

NATIONAL AERONAUTICS AND SPACE ADMINISTRATION

Contract NAS 5-302

May 15, 1961

GENERAL ELECTRIC

MISSILE AND SPACE VEHICLE DEPARTMENT

A Department Of The Defense Electronics Division

3198 Chestnut Street, Philadelphia 4, Penna.

[redacted]

TABLE OF CONTENTS

CHAPTER I

Section		Page
I.	Aerodynamics, Configurations	I-1
1.0	Re-entry Vehicles	I-1
1.1	Introduction	I-1
1.2	Nomenclature	I-1
1.3	Configurations	I-4
1.3.1	B-2 Configuration	I-4
1.3.2	C-1 Configuration	I-4
1.3.3	D-2 Configuration	I-13
1.4	High L/D Configuration	I-38
1.5	High Attitude Configuration	I-38
1.6	Modified Lenticular Configuration (R-3)	I-41
1.6.1	Aerodynamic Characteristics	I-44
2.0	Spacecraft	I-59
2.1	Configuration	I-59
2.2	Aerodynamic Characteristics of the Spacecraft	I-59
3.0	Effect of Spacecraft Aerodynamics on Booster	I-63
4.0	Landing Retardation and Maneuvering	I-75
4.1	Problem Definition	I-75
4.2	The Conventional Retardation System of the Semi-Ballistic Re-entry Vechicle, D-2	I-76
4.2.1	Normal Re-entry Landing	I-76
4.2.2	Launch Pad Abort Recovery of the Selected Configuration, D-2	I-87
4.3	Maneuver During Landing of Semi-Ballistic Re-entry Vehicle, D-2	I-89
4.3.1	Introduction	I-89
4.3.2	Equations of Motion	I-92
4.3.3	The Equilibrium Glide	I-94
4.3.4	The Spiral Descent	I-98
4.3.5	Parawing Development Problems	I-101

TABLE OF CONTENTS - Continued

Section		Page
4.4	Advanced Retardation and Landing for the Semi-Ballistic Re-entry Vehicle, D-2	I-102
4.4.1	Rotor System	I-102
4.4.2	Parachutes and Other Retardation Devices	I-123
4.4.3	Approach and Landing - R-3 Configuration	I-127

CHAPTER II

1.0	Summary and Conclusions	II-1
2.0	The Selected Configuration, D-2	II-5
2.1	Re-entry Vehicle	II-5
2.1.1	Introduction	II-5
2.2	Re-entry Vehicle Control Surfaces	II-28
2.3	Powered Launch	II-34
2.4	Internal Thermal Protection	II-43
2.5	Advanced Thermal Protection Systems	II-51
2.5.1	Reinforced Plastics	II-51
2.5.2	Refractory Metals (Graphites)	II-51
3.0	Additional Vehicle Configuration Studies	II-59
3.1	D-1 Configuration	II-59
3.2	B-2 and C-1 Configurations	II-59
3.3	R-3 Configuration	II-59
3.3.1	Method of Analysis	II-70
3.3.2	Heat Flux to the Lenticular Vehicle	II-77
4.0	Ablation Materials	II-88
4.1	Introduction	II-88
4.1.1	Refractory Vaporizing Oxides	II-89

TABLE OF CONTENTS - Continued

Section		Page
4.1.2	Refractory Metals	II-89
4.1.3	Reinforced Plastics	II-90
4.1.4	Thermoplastics	II-90
4.2	State-of-the-art of Ablation	II-90
4.2.1	Mass Transfer in Laminar and Turbulent Flow	II-91
4.2.2	The Ablation of a Refractor Vaporizing Oxide - Quartz	II-93
4.2.3	The Ablation of a Refractory Metal - Graphite	II-95
4.2.4	The Ablation of a Thermoplastic - Teflon	II-100
4.2.5	The Ablation of a Reinforced Thermosetting Plastic	II-100
4.2.6	Applied Engineering Techniques for the Prediction of the Ablation of a Reinforced Thermosetting Plastic	II-104
4.2.7	Conclusions	II-117
4.3	Nominal Performance of Ablation Materials in the Superorbital Velocity Regime	II-118
5.0	Recommended Tests for the APOLLO Heat Protection System	II-126

CHAPTER III

1.0	Structural Description	III-1
1.1	Spacecraft Structural Description - D-2 Configuration	III-1
1.1.1	Separation Device	III-2
1.1.2	Radiator	III-2
1.1.3	Solar Collector	III-2
1.1.4	Communication Antenna	III-8
1.2	Mission Module Structural Description - D-2 Configuration	III-8
1.3	Re-entry Vehicle Structure - The Selected System, D-2	III-8
1.3.1	Heat Protection Thermo - Structural Design	III-14
1.3.2	Flap Structure	III-14
1.4	Structural Description - R-3 Vehicle	III-16
1.4.1	Primary Structure and Thermal Protection	III-20
2.0	Structural Design Criteria	III-31
2.1	Environmental Criteria	III-36

TABLE OF CONTENTS - Continued

Section		Page
3.0	Summary of Structural Characteristics	III-37
3.1	Weight Analysis	III-37
3.1.1	Weight Statement - D-2 Configuration (The Selected Configuration)	III-37
3.2	Weight Statement - R-3	III-40
4.0	Structural Optimization	III-61
5.0	Meteroid Impact Evaluation	III-65
6.0	Leakage and Seal Design	III-69
6.1	Friction/Welding	III-69

Appendix

A-A	Analytical Methods	A-1
A-B	Experimental Aerodynamics Related Experience, Present and Proposed Program	A-7

LIST OF ILLUSTRATIONS

CHAPTER I

Figure		Page
I-1-1	Nomenclature and sign convention	I-2
I-1-2	B-2 Configuration	I-6
I-1-3	B-2 Configuration - variation of lift coefficient with angle of attack - newtonian	I-6
I-1-4	B-2 Configuration - variation of drag coefficient with angle of attack - newtonian	I-6
I-1-5	B-2 Configuration - variation of Lift - drag ratio with angle of attack - newtonian	I-6
I-1-6	B-2 Configuration - variation of pitching moment coefficient with angle of attack - newtonian	I-7
I-1-7	B-2 Configuration - variation of pressure ratio with longitudinal length	I-9
I-1-8	B-2 Configuration - cumulative lateral load distribution - hypersonic	I-10
I-1-9	C-1 Configuration	I-12
I-1-10	C-1 Configuration - variation of lift coefficient with angle of attack - hypersonic	I-12
I-1-11	C-1 Configuration - variation of drag coefficient with angle of attack - hypersonic	I-12
I-1-12	C-1 Configuration - variation of lift-drag ratio with angle of attack - hypersonic	I-12
I-1-13	C-1 Configuration - variation of pitching moment coefficient with angle of attack - hypersonic	I-14
I-1-14	C-1 Configuration - variation of pressure ratio with longitudinal length	I-14
I-1-15	C-1 Configuration - cumulative axial load distribution - hypersonic	I-14
I-1-16	D-2 Configuration - lift-drag ratio vs angle of attack for spherical sections - newtonian	I-15
I-1-17	D-2 Configuration - variation of lift-drag ratio with radius - newtonian	I-16
I-1-18	Basic D-2 configuration	I-18

LIST OF ILLUSTRATIONS - Continued

Figure		Page
I-1-19A	D-2 Configuration - variation of drag coefficient with angle of attack body alone	I-18
I-1-19B	D-2 Configuration - variation of drag coefficient with angle of attack - hypersonic	I-19
I-1-19C	D-2 Configuration - drag coefficient with mach number body alone $\alpha = 0^\circ$	I-19
I-1-20A	D-2 Configuration - variation of lift coefficient with angle of attack body alone	I-20
I-1-20B	D-2 Configuration - variation of lift coefficient with angle of attack - hypersonic	I-20
I-1-20C	D-2 Configuration - variation of lift coefficient slope with mach number body alone $\alpha = 0^\circ$	I-22
I-1-21A	D-2 Configuration - variation of lift-drag ratio with angle of attack - hypersonic	I-22
I-1-21B	D-2 Configuration - variation of lift to drag ratio with mach number - trimmed condition	I-23
I-1-22	D-2 Configuration - variation of trim angle of attack with center-of-gravity offset - hypersonic	I-23
I-1-23A	D-2 Configuration - variation of pitching moment coefficient with angle of attack - body alone	I-25
I-1-23B	D-2 Configuration - variation of pitching moment coefficient with angle of attack - hypersonic	I-25
I-1-23C	D-2 Configuration - variation of pitching moment coefficient with angle of attack - hypersonic	I-26
I-1-23D	D-2 Configuration - variation of the pitching moment slope coefficient with mach number - body alone	I-28
I-1-24A	D-2 Configuration - variation of damping - in pitch parameter with angle of attack - body alone	I-28
I-1-24B	D-2 Configuration - variation of dynamic damping parameter with mach number body alone $\alpha = 0^\circ$	I-29
I-1-25	D-2 Configuration - variation of side coefficient with mach number body alone $\alpha = 0^\circ$	I-29
I-1-26A	D-2 Configuration - estimated directional stability characteristics of basic vehicle with and without flap deflections $-5^\circ < \beta < 5^\circ$	I-31

LIST OF ILLUSTRATIONS - Continued

Figure		Page
I-1-26B	D-2 Configuration - estimated variation of directional stability parameter characteristics with mach number body alone $\alpha = 0°$	I-32
I-1-27A	D-2 Configuration - estimated lateral stability characteristics of basic vehicle with and without flap deflections $\beta \leq 5°$	I-33
I-1-27B	D-2 Configuration - estimated variation of lateral stability characteristics with mach number body alone $\alpha = 0°$	I-35
I-1-28	D-2 Configuration - variation of pressure coefficient ratio with axial length - hypersonic	I-35
I-1-29	Variation of pressure ratio for a flat flap - hypersonic	I-36
I-1-30A	D-2 Configuration - accumulative axial design loads - hypersonic $\alpha = 40°$	I-36
I-1-30B	D-2 Configuration - accumulative normal design load hypersonic $\alpha = 40°$	I-37
I-1-30C	D-2 Configuration - accumulative moment hypersonic $\alpha = 40°$	I-37
I-1-31	High L/D glider design	I-39
I-1-32	General arrangement - high attitude re-entry vehicle - APOLLO	I-40
I-1-33	General arrangement - APOLLO recovery vehicle - "R-3" - concept 4	I-43
I-1-34	Modified lenticular general longitudinal stability characteristics	I-46
I-1-35	Modified lenticular general lateral stability characteristics	I-47
I-1-36	Modified lenticular low speed effects of variable geometry on directional stability	I-49
I-1-37	Modified lenticular low speed longitudinal characteristics $\phi = 50°$	I-50
I-1-38	Modified lenticular hypersonic longitudinal stability characteristics M = 20 h = 200,000 ft fins folded	I-52
I-1-39	Modified lenticular hypersonic lateral stability characteristics - fins folded	I-53
I-1-40	APOLLO modified lenticular longitudinal dynamic stability characteristics subsonic short period	I-58
I-1-41	APOLLO modified lenticular lateral directional stability characteristics subsonic	I-58
I-2-1	Spacecraft and launch abort vehicle	I-60
I-2-2	Spacecraft and launch abort vehicle center of pressure location vs mach number $\alpha = 0°$	I-60

LIST OF ILLUSTRATIONS - Continued

Figure		Page
I-2-3	Spacecraft - launch abort configuration variation of drag coefficient with mach number	I-61
I-3-1	Saturn C-2 booster system with spacecraft	I-64
I-4-1	Equilibrium glide for D-2 configuration	I-82
I-4-2	Retardation system weight vs impact velocity	I-82
I-4-3	Impact attenuator system weight vs impact velocity	I-82
I-4-4	Total landing and recovery system weight vs impact velocity	I-84
I-4-5	Impact velocity vs drag area	I-84
I-4-6	System III terminal (retardation) trajectory payload wt. = 5000 pounds	I-85
I-4-7	Altitude vs velocity, dynamic pressure, axial load system VI	I-86
I-4-8	Altitude vs range system VI	I-90
I-4-9	Abort recovery trajectory - abort run no. 30	I-90
I-4-10	Abort recovery trajectory - abort run no. 33	I-91
I-4-11	Abort recovery trajectory - abort run no. 35	I-91
I-4-12	Altitude at apogee vs altitude at V_T = 30 ft/sec	I-93
I-4-13	Diagram for development of equations of motion	I-93
I-4-14	Downrange corrections available utilizing a parawing for lift augmentation	I-95
I-4-15	Typical retardation trajectory utilizing parawing intermediate slage	I-95
I-4-16	Lift/drag required for equilibrium glide	I-96
I-4-17	Parawing area required for equilibrium glide D-2 configuration	I-97
I-4-18	Schematic of spiral descent maneuver	I-99
I-4-19	Spiral radius as a function of velocity	I-99
I-4-20	Lift augmentation required to initiate spiral maneuver - D-2 body	I-100
I-4-21	Parawing area required for initiation of spiral maneuver - D-2 body	I-100
I-4-22	Rotor landing system operating sequence	I-104
I-4-23	Rotor opening characteristics	I-105

LIST OF ILLUSTRATIONS - Continued

Figure		Page
I-4-24	Rotor drag characteristics in cropeller braking and windmilling state	I-107
I-4-25	Variation of airspeed with altitude subsonic opening case	I-108
I-4-26	Variation of airspeed with altitude supersonic opening case	I-109
I-4-27	Comparison of lift drag ratios of fixed and rotating wing aircraft	I-111
I-4-28	Preliminary weight estimates of rotor recovery system vs vehicle landing weight	I-111
I-4-29	Preliminary comparison of rotor recovery system weights using weights or tip rockets	I-112
I-4-30	RRS maximum tip weight (lb) considering blade strength	I-116
I-4-31	RRS rotor length selection	I-117
I-4-32	RRS weight estimation	I-118
I-4-33	APOLLO recovery system with flexirotor recovery system	I-119
I-4-34	Expected rotor performance during flare	I-122
I-4-35	Supersonic spiked parachute configuration illustrative sketch	I-126
I-4-36	Effect of canopy loading on horizontal velocity - per reference 11	I-126
I-4-37	L/D and approach speeds for acceptable landing characteristics	I-128
I-4-38	Modified lenticular vehicle subsonic glide characteristics	I-128

CHAPTER 2

II-2-1	APOLLO - D-2 re-entry configuration	II-6
II-2-2	APOLLO - D-2 configuration, typical shallow re-entry trajectory	II-6
II-2-3	APOLLO - D-2 configuration, typical steep re-entry trajectory	II-10
II-2-4	APOLLO - D-2 configuration, gross heat fluxes during re-entry	II-10
II-2-5	APOLLO - D-2 configuration, gross heat fluxes during re-entry - afterbody	II-11
II-2-6	APOLLO - D-2 configuration, gross heat fluxes during re-entry - forebody	II-11

LIST OF ILLUSTRATIONS - Continued

Figure		Page
II-2-7	APOLLO - D-2 configuration, gross heat fluxes during re-entry - afterbody - most windward meridian	II-13
II-2-8	APOLLO - D-2 configuration, coefficient of pressure ratio distribution	II-13
II-2-9	APOLLO - D-2 configuration, gross heat fluxes during re-entry - afterbody - 90 degree meridian	II-14
II-2-10	APOLLO - D-2 configuration, gross heat fluxes during re-entry afterbody - 90 degrees meridian	II-14
II-2-11	APOLLO - D-2 configuration, gross heat fluxes during re-entry afterbody - leeward	II-15
II-2-12	APOLLO - D-2 configuration, gross heat fluxes during re-entry afterbody - leeward	II-15
II-2-13	Heats of ablation	II-17
II-2-14	APOLLO - D-2 configuration, temperature and front face recession histories during re-entry, afterbody - windward meridian	II-17
II-2-15	APOLLO - D-2 configuration, temperature and front face recession histories during re-entry, forebody	II-18
II-2-16	APOLLO - D-2 configuration, temperature and recession histories during re-entry, afterbody - windward meridian	II-19
II-2-17	APOLLO - D-2 configuration, temperature and recession histories during re-entry, afterbody - 90 degree meridian	II-19
II-2-19	APOLLO - D-2 configuration, temperature and recession histories during re-entry - forebody	II-20
II-2-20	APOLLO - D-2 configuration, temperature and recession histories during re-entry, afterbody - windward meridian	II-20
II-2-21	APOLLO - D-2 configuration, temperature and recession histories during re-entry, afterbody - 90 degree meridian	II-21
II-2-22	APOLLO - D-2 configuration, body locations studied	II-22
II-2-23	Schematic of re-entry vehicle with flap	II-29
II-2-24	APOLLO - D-2 configuration, gross heat flux to flap during re-entry	II-32
II-2-25	APOLLO - D-2 configuration, gross heat fluxes to flap during re-entry	II-32
II-2-26	APOLLO - D-2 configuration, boost configuration	II-35
II-2-27	APOLLO - D-2 configuration, trajectory during powered flight	II-36

LIST OF ILLUSTRATIONS - Continued

Figure		Page
II-2-28	APOLLO - D-2 configuration, coefficient of pressure distribution	II-36
II-2-29	Composite of spacecraft honeycomb structure	II-38
II-2-30	APOLLO - D-2 configuration, net heat fluxes during powered flight	II-39
II-2-31	APOLLO - D-2 configuration, temperature histories powered flight	II-40
II-2-32	APOLLO - D-2 configuration, temperature histories powered flight	II-40
II-2-33	APOLLO - D-2 configuration, temperature histories powered flight	II-41
II-2-34	APOLLO - D-2 configuration, temperature histories powered flight	II-41
II-2-35	Temperature of the char-virgin material interface vs time for a typical point on the D-2 afterbody	II-44
II-2-36	Effect of virgin material thickness on overall system weight and bond temperature, insulation ~ Min K	II-45
II-2-37	Effect on virgin material thickness on overall system weight and bond temperature, insulation ~ multiple layer radiation barrier	II-46
II-2-38	Effect of active cooling system on overall system weight, temperature of bond = 500 F	II-48
II-2-39	Effect of active cooling system on overall system weight, temperature of bond = 800 F	II-48
II-2-40	Effect of active cooling system on overall system weight, temperature of bond = 1100 F	II-49
II-2-41	Comparison of overall system weight vs ablative material bond temperatures for different insulations and cooling systems	II-49
II-2-42	Analog trace of wall and compartment	II-50
II-2-43	Thermal conductivity vs temperature, pyrolytic graphite, across planes "C" direction	II-50
II-2-44	APOLLO - D-2 configuration, temperature vs time during re-entry, re-entry angle = 4.7 degrees	II-53
II-2-45	APOLLO - D-2 configuration, temperature vs time during re-entry, re-entry angle = 8.4 degrees	II-53

LIST OF ILLUSTRATIONS - Continued

Figure		Page
II-2-46	APOLLO - D-2 configuration, mass loss vs time during re-entry, re-entry angle = 4.7 degrees, commercial graphite	II-55
II-2-47	APOLLO - D-2 configuration, mass loss vs time during re-entry, re-entry angle = 4.7 degrees, pyrolytic graphite	II-55
II-2-48	APOLLO - D-2 configuration, mass loss vs time during re-entry, re-entry angle = 8.4 degrees, commercial graphite	II-56
II-2-49	APOLLO - D-2 configuration, mass loss vs time during re-entry, re-entry angle = 8.4 degrees, pyrolytic graphite	II-56
II-3-1	APOLLO - D-2 configuration, body locations studied	II-61
II-3-2	APOLLO - D-1 configuration, re-entry configuration	II-62
II-3-3	APOLLO - B-2 configuration, re-entry configuration	II-62
II-3-4	APOLLO - C-1 configuration, re-entry trajectory	II-63
II-3-5	APOLLO - C-1 configuration, re-entry trajectory	II-63
II-3-6	APOLLO - B-2 configuration, re-entry trajectory	II-64
II-3-7	APOLLO - B-2 configuration, re-entry trajectory	II-64
II-3-8	APOLLO - C-1 configuration, angle of attack vs time	II-65
II-3-9	APOLLO - C-1 configuration, angle of attack vs time	II-65
II-3-10	APOLLO - B-2 configuration, angle of attack vs time	II-66
II-3-11	APOLLO - B-2 configuration, angle of attack vs time	II-66
II-3-12	APOLLO - R-3 configuration, flat face heat flux distribution, laminar flow	II-74
II-3-13	APOLLO - R-3 configuration, flat face heat flux distribution, turbulent flow	II-74
II-3-14	APOLLO - R-3 configuration, average flat face heat flux distribution	II-75
II-3-15	APOLLO - R-3 configuration, heat flux rate to the bottom surface referenced to A 5.5' radius sphere	II-75
II-3-16	APOLLO - R-3 configuration, nose cap radiation intensity and typical entry trajectories	II-78
II-3-17	APOLLO - R-2 configuration, time histories of heat flux and heat flux rate	II-79
II-3-18	APOLLO - R-3 configuration, time histories of heat flux and heat flux rate	II-81

LIST OF ILLUSTRATIONS - Continued

Figure		Page
II-3-19	APOLLO - R-3 configuration, heat flux and heat flux rate to the leading edge	II-82
II-3-20	APOLLO - R-3 configuration, heat flux and heat flux rate to the leading edge	II-82
II-3-21	APOLLO - R-3 configuration, heat flux and heat flux rate to the leading edge	II-83
II-3-22	APOLLO - R-3 configuration, heat flux to the bottom surface of vehicle oriented at 90 degrees to airstream	II-83
II-3-23	APOLLO - R-3 configuration, equilibrium wall temperature	II-85
II-3-24	APOLLO - R-3 configuration, equilibrium wall temperature	II-85
II-3-25	APOLLO - R-3 north - south flight	II-86
II-4-1	Heat of ablation of a refractory vaporizing oxide quartz (stagnation point)	II-94
II-4-2	Mass transfer regimes for ablating graphite	II-97
II-4-3	Theoretical heat of ablation of teflon (stagnation point)	II-101
II-4-4	Heat of ablation of teflon	II-102
II-4-5	Correlation of air arc results with theory (typical thermosetting plastic)	II-108
II-4-6	Observed and predicted ablation and temperature of a typical plastic foil simulated re-entry heating thermosetting	II-110
II-4-7	Observed and predicted ablation and temperature of a typical thermosetting plastic for simulated re-entry heating	II-111
II-4-8	Predicted partition of aerodynamic heating for simulated re-entry	II-112
II-4-9	Predicted partition of aerodynamic heating for simulated re-entry	II-113
II-4-10	Variation of surface temperature with heat rate and char thickness	II-115
II-4-11	Heat of ablation variation of typical thermosetting resin combined with quartz type reinforcement (turbulent flow)	II-116
II-4-12	Heat of ablation, typical heat protection system materials	II-119
II-5-1	Variation of temperature with enthalpy and extent of ionization	II-127
II-5-2	Pressure enthalpy environment of re-entry	II-128

LIST OF ILLUSTRATIONS - Continued

Figure		Page
II-5-3	Comparison of super orbital environment with current facility and flight test	II-129
II-5-4	Hypersonic arc configuration	II-138
	CHAPTER III	
III-1-1	D-2 configuration - structural arrangement, space vehicle	III-3/III-4
III-1-2	Design proposal solar concentrator	III-5/III-6
III-1-3	Solar collector sequence	III-7
III-1-4	Communications antenna arrangement	III-9/III-10
III-1-5	Structural arrangement, recovery vehicle - APOLLO D-2 configuration	III-11/III-12
III-1-6	Control flap structure	III-15
III-1-7	Structure arrangement - APOLLO recovery vehicle R-3, concept #4	III-17/III-18
III-1-8	Structural arrangement - APOLLO recovery vehicle R-3, concept #4	III-23/III-24
III-1-9	Bending moment distribution for various frame configuration	III-28
III-2-1	Spacecraft launch and abort conditions axial load, side shear and bending moment	III-33
III-2-2	Spacecraft axial skin load, side shear flow and external normal pressure for critical conditions	III-34
III-2-3	Limit external pressure distributions re-entry vehicle	III-35
III-4-1	Structural efficiency, external collasping pressure loading	III-62
III-4-2	Weight optimization, conical frustrum sta. 122.6 to 238.6, uniform external collapsing pressure	III-63
III-5-1	Meteoroid population	III-66

LIST OF TABLES

CHAPTER I

Table		Page
I-1-I	APOLLO Configurations Geometric Summary Table	I-42
I-1-II	Stability Derivatives Used In Roots Analysis	I-55
I-4-I	Initial Design Concepts	I-77
1A	D-2 Configuration	A-11
1B	R-3 Configuration	A-15

CHAPTER II

II-2-I	Thermal Properties and Assumptions Used for Re-entry	II-23
II-2-II	APOLLO D-2	II-24
II-2-III	Thermal Properties and Assumptions Used for Powered Flight	II-42
II-2-IV	APOLLO D-2	II-52
II-2-V	Erosion D-2 Configuration	II-54
II-2-VI	Erosion D-2 Configuration	II-57
II-3-I	APOLLO D-1	II-60
II-3-II	Heat Protection for C-1 Configuration	II-67
II-3-III	Heat Protection for B-2' Configuration	II-68
II-5-I	Key Technical Problems of the Super Orbital Velocity Regime	II-130
II-5-II	Phenomena "Unique" to Super Orbital Velocity Regime	II-130
II-5-III	Design Information Needs	II-131
II-5-IV	General Specification for Simulation	II-132
II-5-V	Systems Approach to APOLLO Materials Research	II-134
II-5-VI	Utility of High Enthalpy Ground Facility	II-135
II-5-VII	Required Facility Capability to Obtain Design Information Needs	II-136
II-5-VIII	Required Flexibility of a High Enthalpy (Air Arc) to Obtain Design Information	II-137

LIST OF TABLES - Continued

CHAPTER III

Table		Page
III-2-I	Summary of Design Conditions (Limit Loads)	III-32
III-3-I	Summary of Structural Characteristics	III-38
III-3-II	Weight Summary, D-2 Configuration	III-39
III-3-III	Weight Breakdown, D-2 Configuration	III-39
III-3-IV	APOLLO Mission Weight Profile	III-41
III-3-V	Weight and Balance Summary, D-2 Re-entry Vehicle	III-42
III-3-VI	Weight and Balance Summary, D-2 Spacecraft	III-43
III-3-VII	Detail Weight Breakdown, D-2 Configuration	III-44
III-3-VIII	Weight Summary - R-3 Configuration	III-50
III-3-IX	Summary Weight and Balance - R-3 Spacecraft	III-51
III-3-X	Detail Weight and Balance R-3 Configuration	III-52
III-5-I	Analysis of Meteoroid Population	III-67

CHAPTER I

AERODYNAMICS, CONFIGURATIONS

I. AERODYNAMICS, CONFIGURATIONS

1.0 Re-entry Vehicles

1.1 INTRODUCTION

Descent through the atmosphere is possible along various flight paths-ballistic, semi-ballistic, and glide. Each of these paths requires a different type of vehicle and involves different levels of aerodynamic heating, re-entry deceleration loads, range control and maneuvering capability. These factors, in turn, are largely dependent on the aerodynamic characteristics of the re-entry vehicle. The important consideration of crew survival and comfort, along with structural characteristics of the vehicle, are also prime considerations in the design of a multi-manned re-entry configuration. Considerable improvement over a ballistic trajectory (lift-to-drag ratio $\approx$ 0) can be achieved in the range and cross-range capability, peak "g's", relief in aerodynamic heating and widening of the re-entry corridor by utilizing a vehicle capable of developing lift-to-drag ratios in the order of 0.5.

A variety of aerodynamic shapes encompassing the range from ballistic through lifting vehicles has been studied and their basic aerodynamic characteristics (including trim capabilities) are discussed herein. Results from some of the parametric studies made in selecting the external contour of the lifting re-entry bodies and the associated pressure-load distributions are also presented.

1.2 NOMENCLATURE

The aerodynamic results are generally referred to a stability axis system (Figure I-1-1) except where noted. The reference area for all aerodynamic coefficients is based on the maximum diameter of the specific vehicle (or plan form area in the case of glide vehicles) and all moment data are referred to the center of gravity of the vehicle. The characteristic length used in defining the moment coefficients is, again, the maximum diameter of the configuration, for the semi-ballistic configuration or vehicle length for the glide configurations.

CONFIDENTIAL

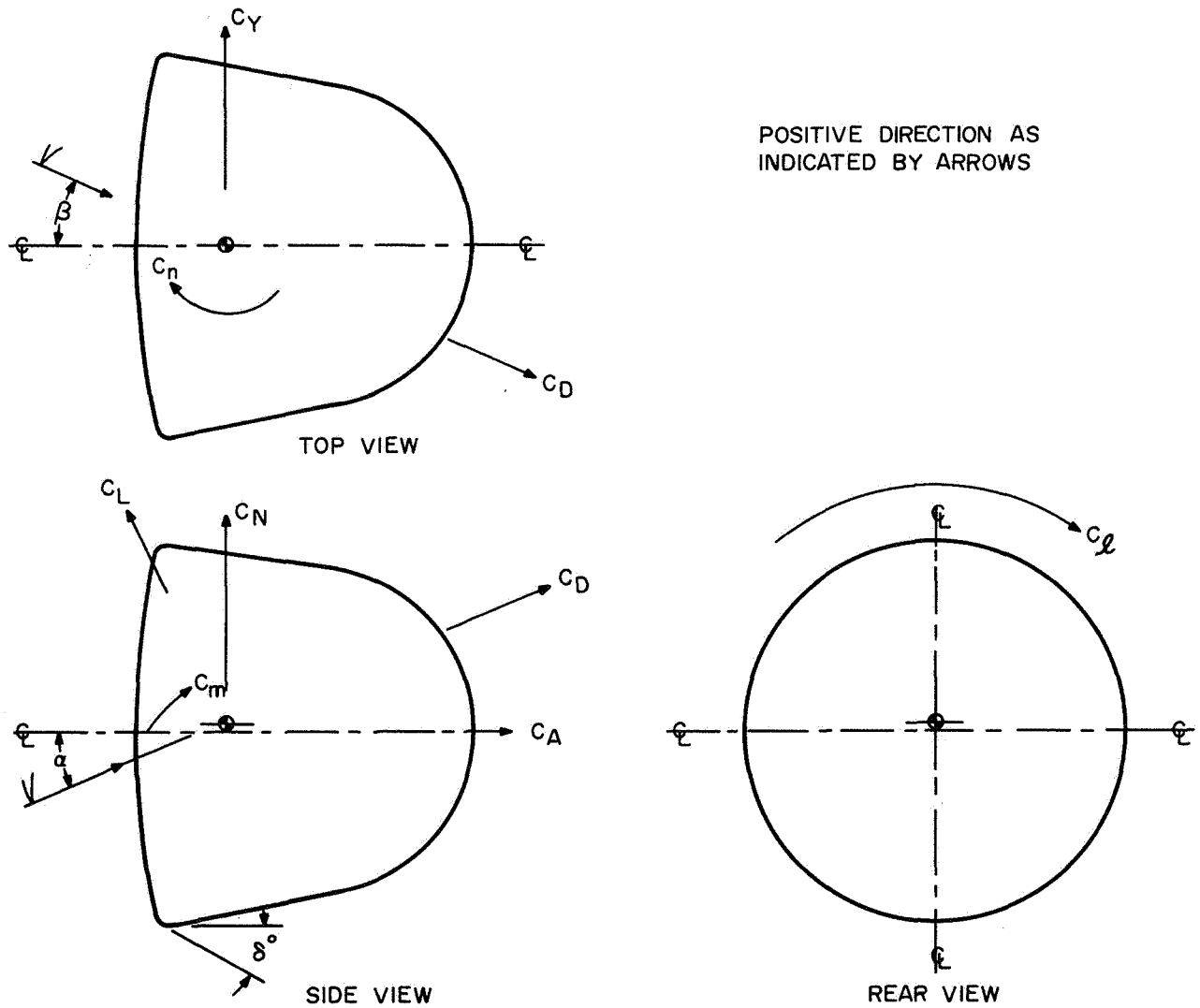

Figure I-1-1. Nomenclature and sign convention

CONFIDENTIAL

NOTATION	DEFINITION	UNITS
C_A	Total axial force coefficient $\left(\frac{\text{Axial force}}{q_\infty S_{Ref}}\right)$	-
C_D	Total drag coefficient $\left(\frac{\text{Drag force}}{q_\infty S_{Ref}}\right)$	-
C_L	Lift coefficient $\left(\frac{\text{Lift force}}{q_\infty S_{Ref}}\right)$	-
C_{L_α}	Slope of the lift curve $(\partial C_L/\partial \alpha)_{\alpha=0°}$	1/Degree
L/D	Lift-to-drag ratio $\left(\frac{C_D}{C_L}\right)$	-
C_ℓ	Rolling moment coefficient $\left(\frac{\text{Rolling moment}}{q_\infty S_{Ref} D_B}\right)$	-
C_{ℓ_β}	Rolling moment due to sideslip $\left(\partial C_1/\partial \beta\right)_{\beta \approx 0°}$	1/Degree
C_m	Pitching moment coefficient $\left(\frac{\text{Pitching moment}}{q_\infty S_{Ref} D_B}\right)$	-
C_{m_α}	Slope of the pitching moment $\left(\partial C_m/\partial \alpha\right)_{\alpha = 0°}$	1/Degree
C_{m_q}	Damping in pitch derivative $\left(\frac{2V}{D_B} \frac{\partial C_m}{\partial \alpha}\right)$	1/Radian
C_n	Yawing moment coefficient $\left(\frac{\text{Yawing moment}}{q_\infty S_{Ref} D_B}\right)$	-
C_{n_β}	Slope of the yawing moment $\left(\frac{\partial C_n}{\partial \beta}\right)_{\beta \approx 0}$	1/Degree
C_p	Pressure coefficient $\left(\frac{p_\ell - p_\infty}{q_\infty}\right)$	-
C_y	Side force coefficient $\left(\frac{\text{Side Force}}{q_\infty S_{Ref}}\right)$	-
C_{y_β}	Slope of the side force coefficient $\left(\frac{\partial C_y}{\partial \beta}\right)$	1/Degree

NOTATION	DEFINITION	UNITS
D_B	Maximum base diameter	Feet
L	Length of vehicle	Feet
M_∞	Free stream Mach number	-
p	Local pressure	Lb/sq ft
p_∞	Free stream static pressure	Lb/sq ft
q_∞	Free stream dynamic pressure	Lb/sq ft
q	Pitching angular velocity	Radians/second
S_F	Flap area	Sq ft
S_{Ref}	Reference area $\left(\frac{\pi D_B^2}{4}\right)$	Sq ft
V	Free stream velocity	Ft/sec
X_{CG}	Longitudinal location of center of gravity	Feet
α	Angle of attack (relative to vehicle centerline-in-pitch plane)	Degrees
$\dot{\alpha}$	Variation of α with respect to time	Radians/Second
β	Angle of sideslip (relative to vehicle centerline-in-yaw plane)	Degrees
δ	Flap deflection angle (relative to line parallel to vehicle centerline and passing through flap hinge line)	Degrees
θ	Half cone angle	Degrees
σ	Radius of gyration	Feet

1.3 CONFIGURATIONS

1.3.1 B-2 Configuration

1.3.1.1 EXTERNAL CONTOUR:

The external shape and general dimensions of the B-2 vehicle are presented in

Figure I-1-2. This re-entry vehicle is a body of revolution having a sphere-cone forebody (Shield), a cylindrical midsection and a rearward tapering afterbody. A possible control flap for trimming this configuration at an angle of attack covering α for $C_{L_{MAX}}$ and $(L/D)_{MAX}$ is also shown. The B-2 shape is the same as that of the General Electric Co. Mark 2, IRBM-ICBM nose cone, which has been extensively tested and successfully "flown".

1.3.1.2 AERODYNAMIC CHARACTERISTICS:

The theoretical (inviscid Newtonian)[1] longitudinal aerodynamic characteristics, lift, drag, lift-drag ratio and pitching moments calculated ofr the B-2 configuration are presented in Figures I-1-3 through I-1-6 as a function of angle of attack for various flap deflection angles. Trimmed lift coefficients in the order of 0.30 and lift-drag ratio of $\approx$ 0.29 are achieved at $\alpha \approx -40$ degrees, using flap deflections up to δ = 90 degrees. Since the lift curve slope for this vehicle is negative, positive (L/D) is achieved by re-entry at negative angles of attack. The negative C_{L_α} curve simply results from the fact that at positive angles of attack a large lift component of the axial force acting on the vehicle is greater than the positive lift component of the normal force. Because of the $-C_{L_\alpha}$ and the favorable position of the center-of-gravity for stable flight; the flap lift will augment the body lift, hence, increasing the (L/D) over that of the basic body.

In order to support the aerodynamic design predictions at high Mach numbers, a limited experimental program [(2)] was undertaken on small scale models of the B-2 configuration in the General Electric Co., (MSVD) 6-Inch Shock Tunjel. Results in the form of lift-drag ratio as a function of angle of attack and flap deflections, were obtained at M-12.4 and Reynolds number (based on model length) of 2.8 $(10)^5$. These results show that the calculated values generally agree well with the experiment (Figure I-1-5).

At hypersonic velocity, the B-2 configuration is shown in Figure I-1-6 to be statically stable in pitch and in the trimmed attitude beyond α for maximum (L/D) for a flap deflection greater than zero and for an on-center line center-of-gravity location of location of $\left(\frac{X_{CG}}{D_B}\right) \approx 0.339$. At supersonic and transonic speeds, the B-2 configuration is statically stable; [(3)] however, a dynamic limit cycle of moderate amplitude is expected to develop below $M_\infty \approx 1.1$. Inasmuch as the B-2 configuration is designed

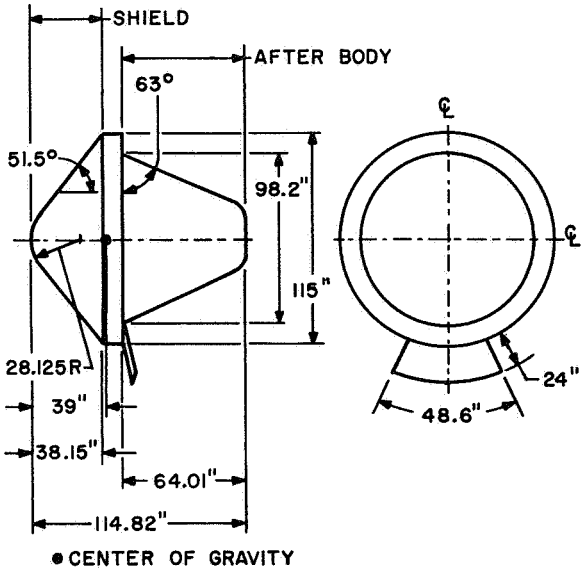

Figure I-1-2. B-2 Configuration

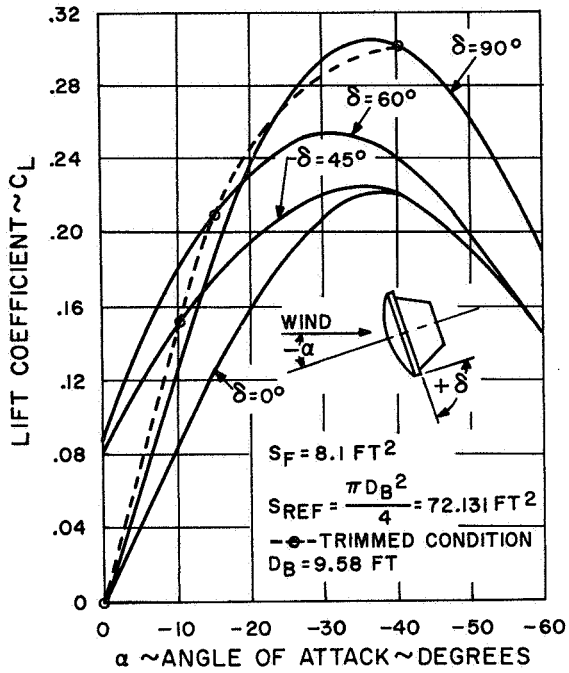

Figure I-1-3. B-2 Configuration - Variation of lift coefficient with angle of attack - Newtonian

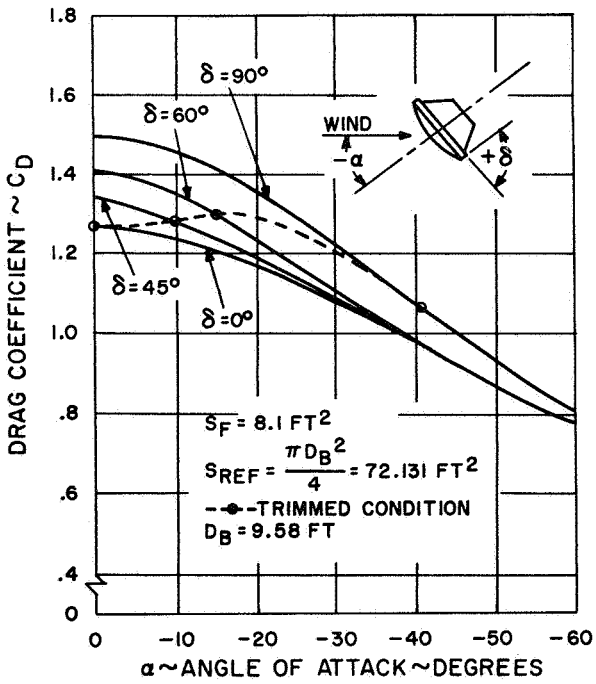

Figure I-1-4. B-2 Configuration - Variation of drag coefficient with angle of attack - Newtonian

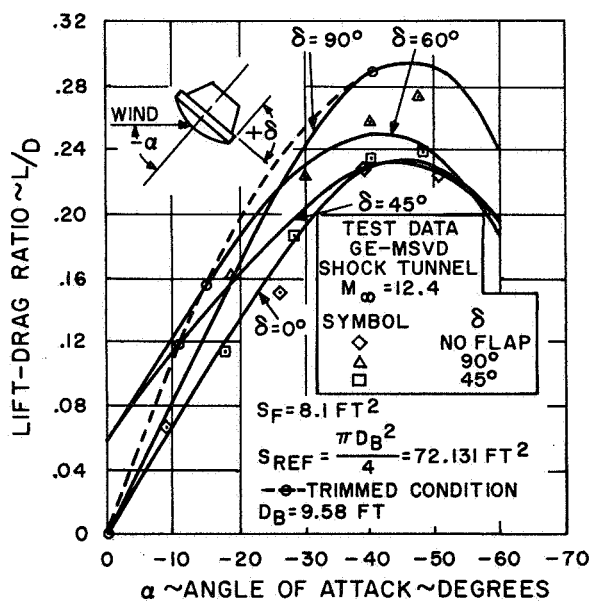

Figure I-1-5. B-2 Configuration - Variation of lift-drag ratio with angle of attack - Newtonian

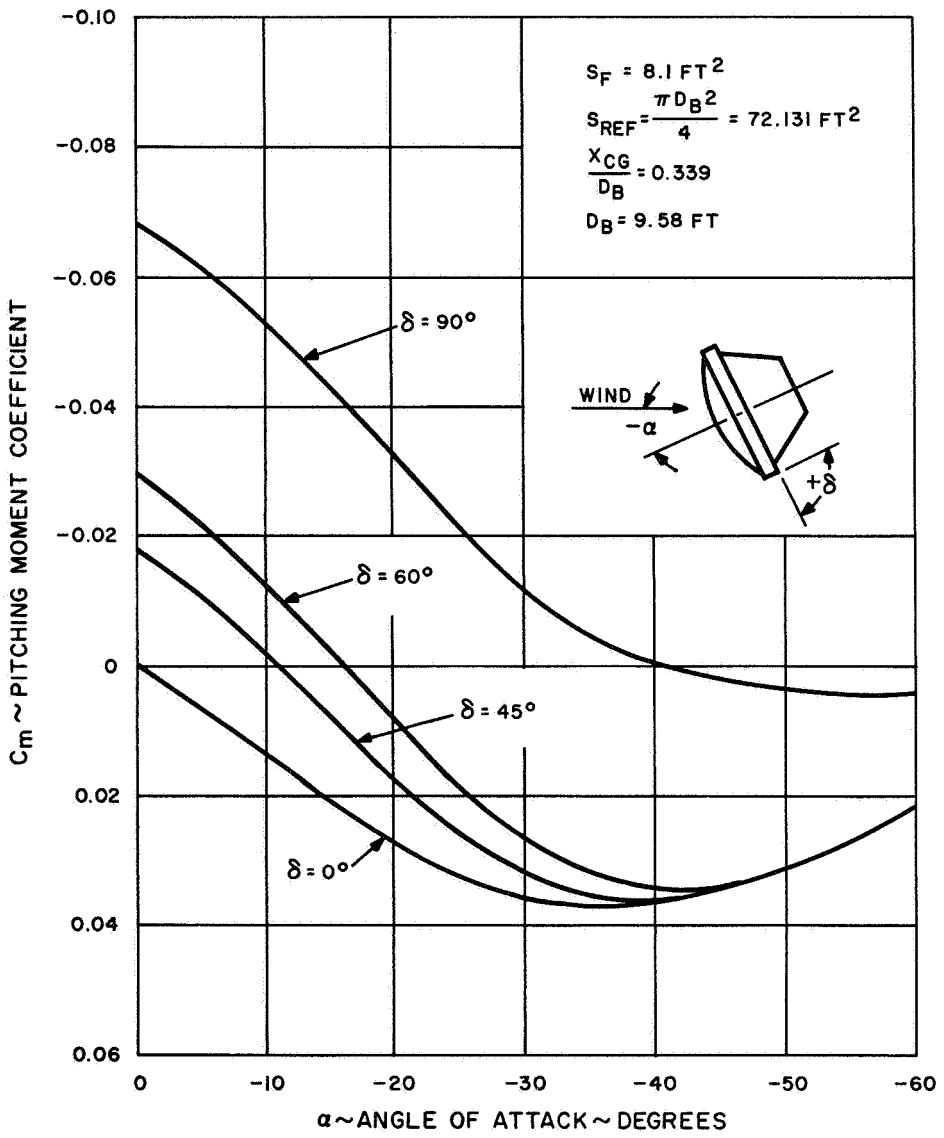

Figure I-1-6. B-2 Configuration - variation of pitching moment coefficient with angle of attack - Newtonian

to be recovered by parachute, which will be deployed at high transonic speeds, the effects of these dynamic oscillations will be minimized.

1.3.1.3 MANEUVER CAPABILITY:

The cross range maneuvering of the B-2 vehicle is accomplished by rolling and pitching the vehicle so that the flight path is displaced in the lateral direction. The rolling motion, which modulates the magnitude and direction of the resultant force, is accomplished by reaction jets and pitch in the yaw plane is achieved by the external chin flap.

1.3.1.4 PRESSURE AND LOAD DISTRIBUTION:

It is well known that the pressure distribution on the spherical portion of a blunt nose vehicle is adequately predicted for hypersonic Mach numbers by Newtonian theory. (4) Also, the relatively high cone angle (θ = 51.5°) on the forebody of the B-2 vehicle allows use of Newtonian theory in predicting the pressure distribution over this portion of the vehicle, as a pure function of ($\theta + \alpha$), independent of distance along the spherical surface. On the cylindrical ring and afterbody section use of full (3) and small scale (5) experimental data and Prandtl-Meyer expansion was made in estimating the pressures on both the leeward and windward surfaces, by decreasing the local Prandtl-Meyer expansion on the windward surfaces by the magnitude of the angle of attack and increasing the expansion angle by a similar amount on the leeward side. Figure I-1-7 presents the variation of pressure coefficient over the surface of the B-2 vehicle at M_∞ = 25 and α = 45°, as obtained by the methods perscribed above. It should be noted that flow separation (6) is expected to occur off of the back edge of the cylindrical center section and some differences between the estimated and actual pressure levels are expected to exist, particularly on the leeward side.

The lateral load distribution for the B-2 configuration at hypersonic conditions are presented in Figure I-1-8 for α = 0°, 15°, 25°, and 30°. These loads were derived for pressure distributions (discussed previously) at peak axial and lateral load conditions and are normalized at each station by the value of the total integrated load. Similar load distributions were made also for axial and pitching moment loads, for use in stress and structural analysis.

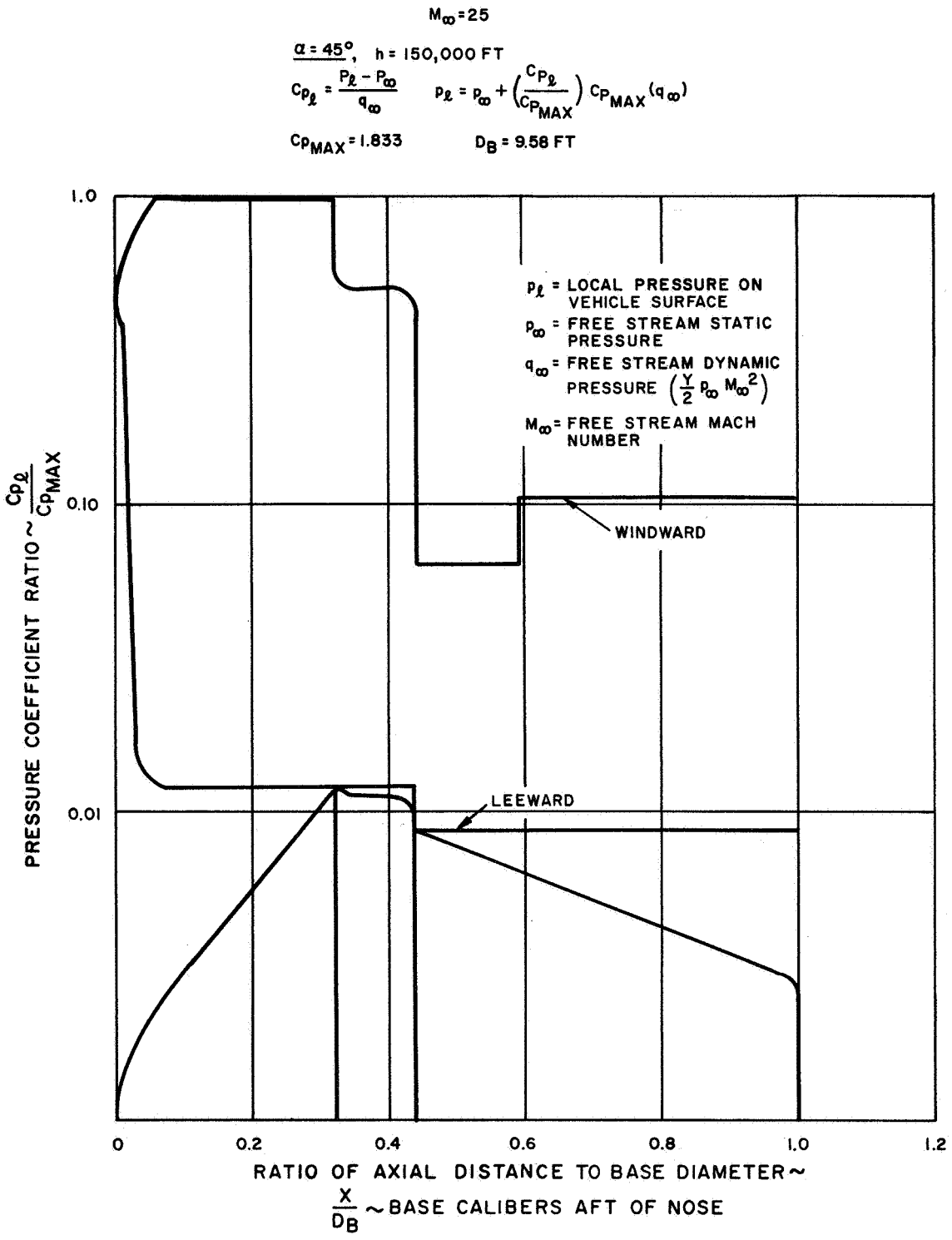

Figure I-1-7. B-2 Configuration - variation of pressure ratio with longitudinal length

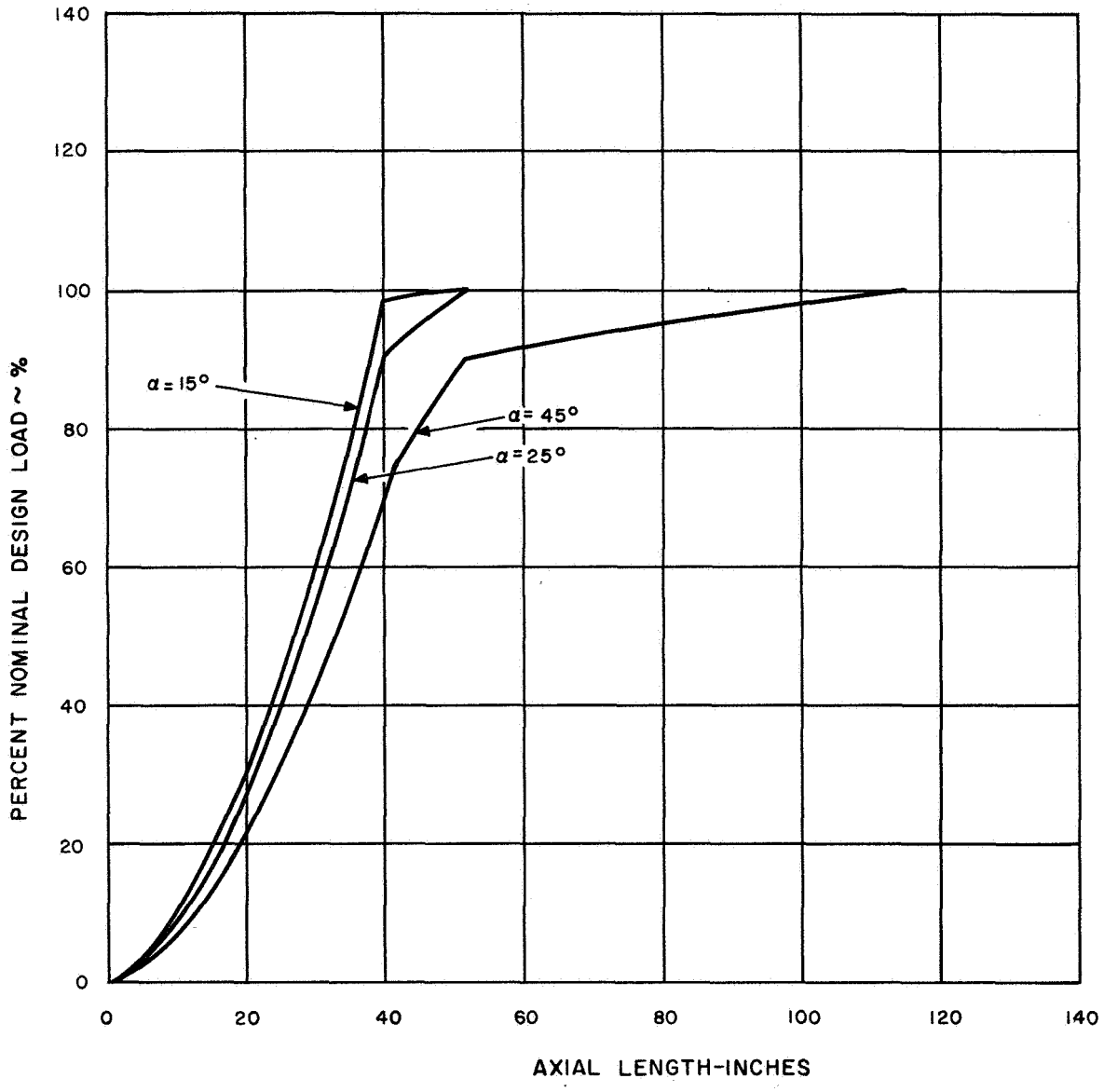

Figure I-1-8. B-2 Configuration - cumulative lateral load distribution - hypersonic

1.3.2 C-1 Configuration

1.3.2.1 EXTERNAL CONTOUR:

The body configuration for the C-1 is a sphere-cone (body of revolution) having a half cone angle of 9 degrees and a bluntness ratio (nose radius/base radius) of 0.314 (Figure I-1-9). Highly swept, all moveable control surfaces having blunted wedge cross sections are used to trim this configuration in order to achieve the $C_{L_{MAX}}$ and $(L/D)_{MAX}$ and to maintain the proper relation between the center-of-gravity and center of pressure of the vehicle. (Depending on this latter relation, the tail surfaces may or may not augment the body lift, which ultimately affect the lift and lift drag ratios attained.)

1.3.2.2 AERODYNAMIC CHARACTERISTICS:

The hypersonic static longitudinal aerodynamic force and moment variation with angle of attack were obtained from small scale experiments performed in the General Electric MSVD 6-Inch Shock Tunnel at Mach number equal to 12.4 and are presented in Figure I-1-10 through I-1-13. Trimmed $C_{L_{MAX}} \approx 0.86$ at $\alpha = 40°$ and $(L/D)_{MAX} \approx 0.73$ at $\alpha = 24°$ is achieved by deflecting the horizontal control surfaces to negative angles relative to the free stream direction. Figure I-1-13 indicates that with $\delta = -30°$ the static pitching moment is such as to promote stable flight up to $\alpha = 45°$ at hypersonic speeds. However, because of inadequate techniques of predicting the mutual interference effects between the fins and the body, additional experimental investigations to better define the effects of the fins are needed.

1.3.2.3 MANEUVER CAPABILITY:

The directional and lateral control for the C-1 vehicle would be respectively achieved by deflecting the vertical surfaces in unison and the horizontal controls differentially. However, considerable theoretical and experimental varification of the cross-coupling effects on the directional lateral and longitudinal characteristics of this vehicle is necessary to verify the feasibility of such an approach to the control problems.

1.3.2.4 PRESSURE AND LOADS DISTRIBUTION:

The pressure distribution (Figure I-1-14) for $\alpha = 0°$, 5°, 10°, 15° and 25° over the surface of the C-1 vehicle at $M_\infty = 20$ was calculated using the General Electric real gas flow field method, [7] which is known to be in excellent agreement with full scale

CONFIDENTIAL

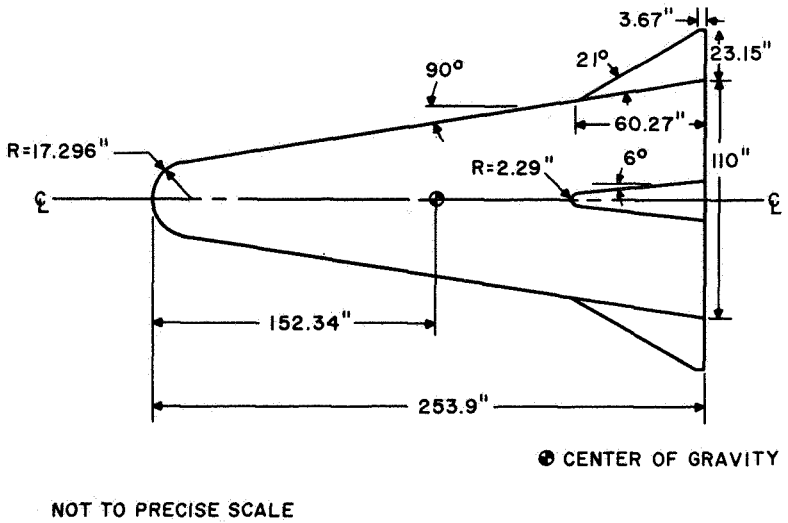

Figure I-1-9. C-1 Configuration

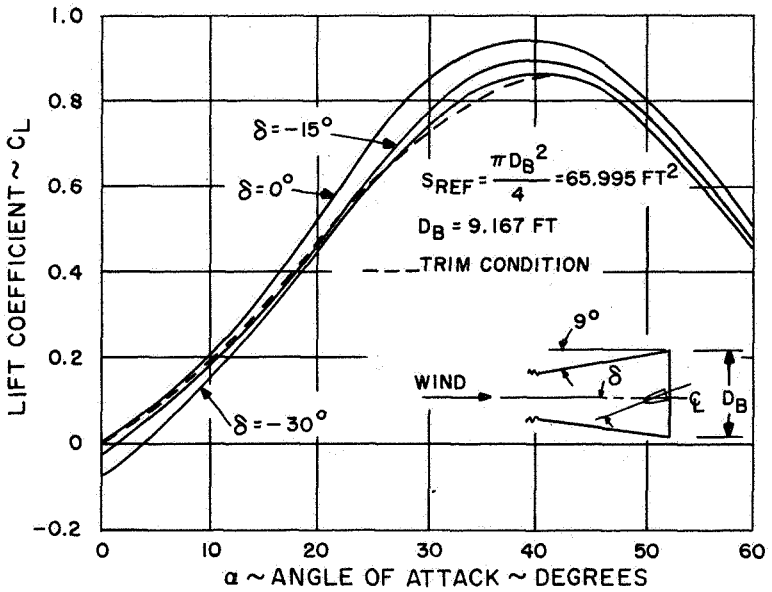

Figure I-1-10. C-1 Configuration - Variation of lift coefficient with angle of attack - hypersonic

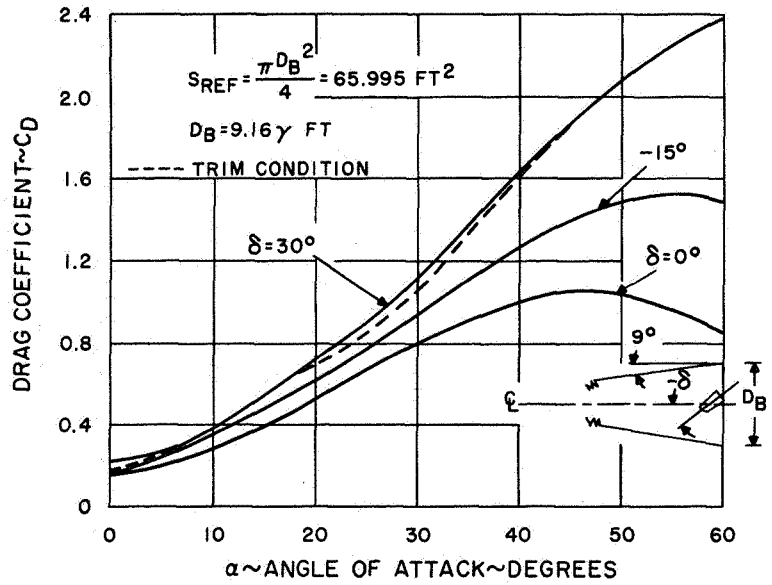

Figure I-1-11. C-1 Configuration - Variation of drag coefficient with angle of attack - hypersonic

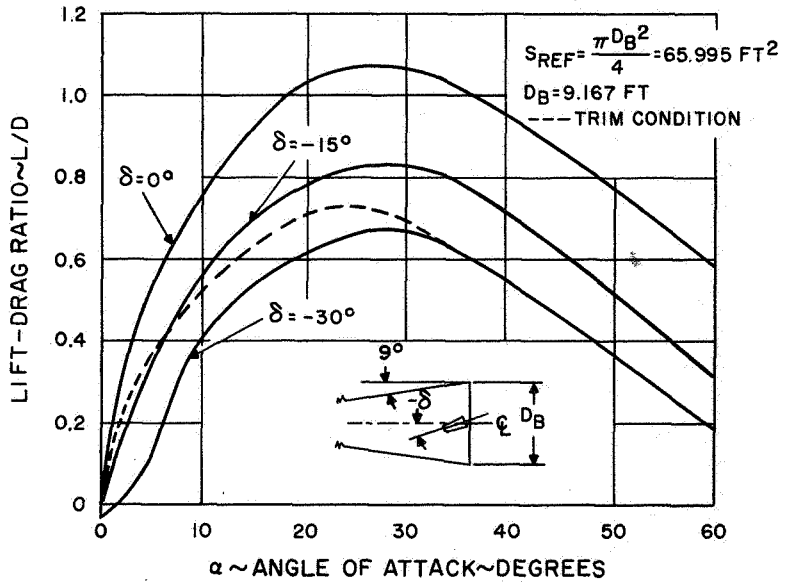

Figure I-1-12. C-1 Configuration - Variation of lift-drag ratio with angle of attack - hypersonic

CONFIDENTIAL

ICBM flight test results. The pressure distributions for angles of attack up to 45° were obtained by using the basic flow field solution with modifications to include the effect of angle of attack by assuming a windward side cone angle of $(\theta + \alpha)$ and a leeward side cone angle of $(\theta - \alpha)$ and Prandtl-Meyer expansion beyond the sonic point.

The variations of cumulative axial loads distribution for hypersonic peak load conditions were computed based on the windward and leeward pressure distributions discussed above. These results are presented in Figure I-1-15 and represent the hypersonic loads distribution which may be used for stress and structural analysis. Such loads analysis were also performed for the normal force and pitching moment.

1.3.3 D-2 Configuration

1.3.3.1 CONFIGURATION SELECTION:

The employment of aerodynamic lift during entry into the earth's atmosphere at orbital or escape speeds will enhance the longitudinal and lateral range of a vehicle, relieve deceleration loads for a given entry grazing angle and maintain total energy transfer approximately the same as that of a nonlifting vehicle. Therefore, in the aerodynamic design of a re-entry vehicle it is beneficial to consider configurations which are capable of developing some lift as well as a high modulation of drag.

Parametric studies of the variation of hypersonic lift-to-drag ratio with angle of attack for various spherical nose sections were made using modified Newtonian theory, which is known to predict the lift and drag of blunt faced bodies reasonably well. The results of this study (Figure I-1-16) indicated that by increasing angle between the tangency point and the local horizontal for a spherical segment, an increase in (L/D), approaching the value developed by the aerodynamically efficient flat plate, is achieved. The heating problem and consequent high heat protection requirements forced a compromise away from the ideal flat plate to a forebody comprised of a 77 degree segment. This makes some allowance for boundary layer buildup, aerodynamic heating relief and provides a better load bearing surface from the structural point of view.

A Newtonian parametric study on the effect of afterbody cone angle and afterbody blunting was performed using several fixed forebodies. The results of this study are presented in Figures I-1-17. From this illustration it is observed that further gains in maximum (L/D) may be realized by increasing the afterbody cone angle for a given

CONFIDENTIAL

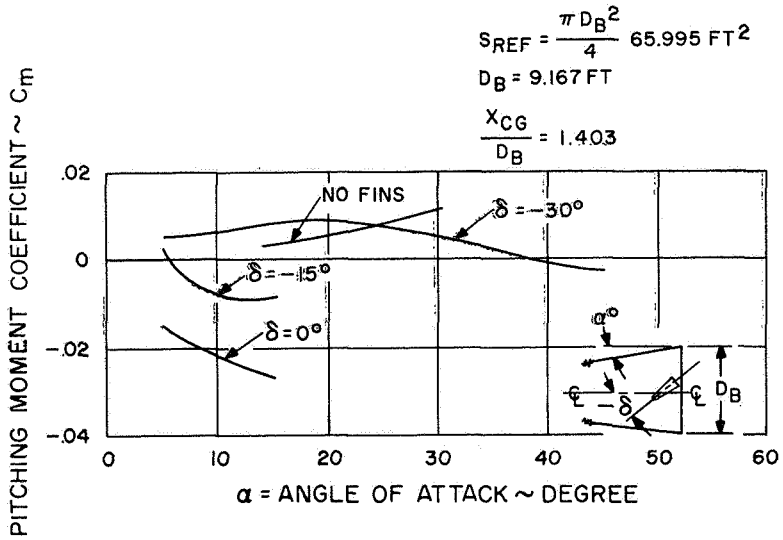

Figure I-1-13. C-1 Configuration - Variation of pitching moment coefficient with angle of attack - hypersonic

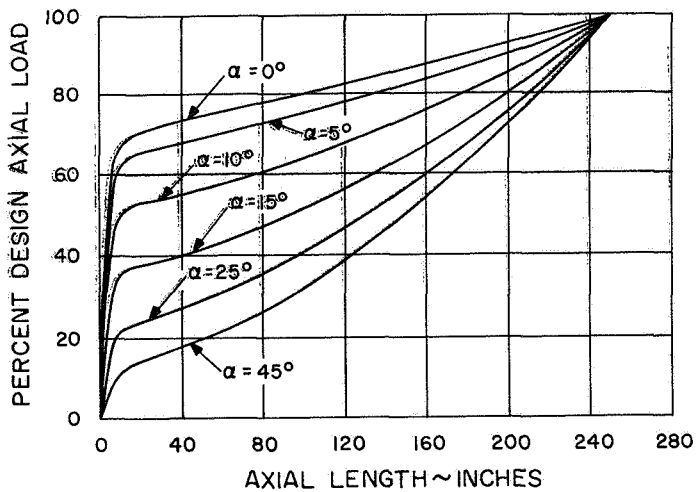

Figure I-1-15. C-1 Configuration - Cumulative axial load distribution - hypersonic

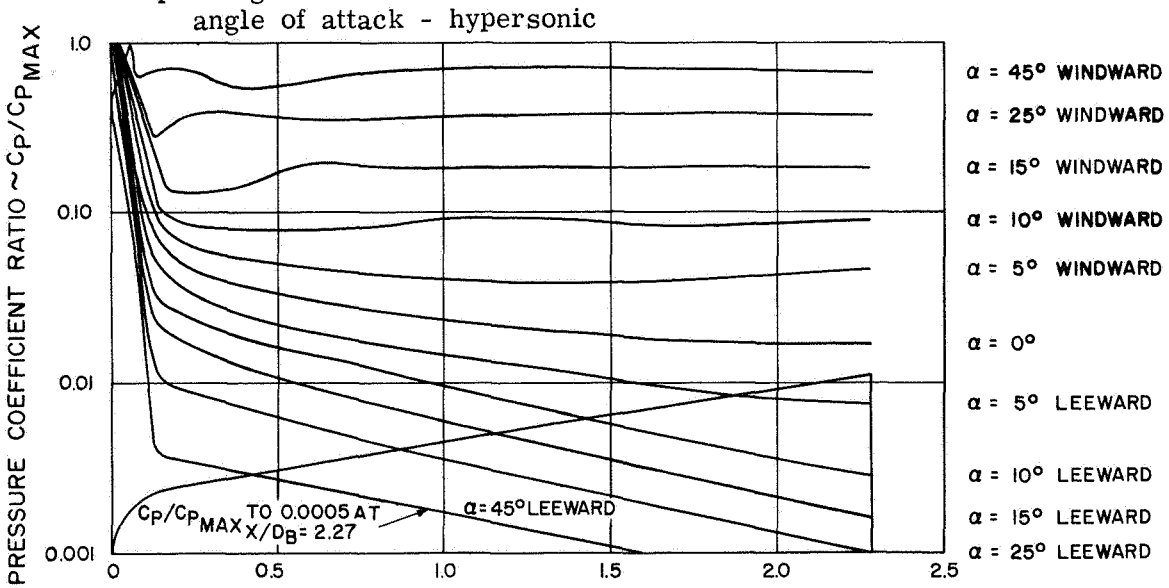

D_B = 110.0 INCHES

M_∞ = 20

$C_{P_{MAX}}$ = 1.838

M_∞ = FREE STREAM MACH NUMBER

P_ℓ = LOCAL PRESSURE ON VEHICLE SURFACE

P_∞ = FREE STREAM STATIC PRESSURE

g_∞ = FREE STREAM DYNAMIC PRESSURE ($\gamma/2\ P_\infty\ M_\infty^2$)

$$C_{P_\ell} = \frac{P_\ell - P_\infty}{g_\infty}$$

$$P_\ell = P_\infty + \left(\frac{C_P}{C_{P_{MAX}}}\right) C_{P_{MAX}}\,(g_\infty)$$

Figure I-1-14. C-1 Configuration - Variation of pressure ratio with longitudinal length

CONFIDENTIAL

CONFIDENTIAL

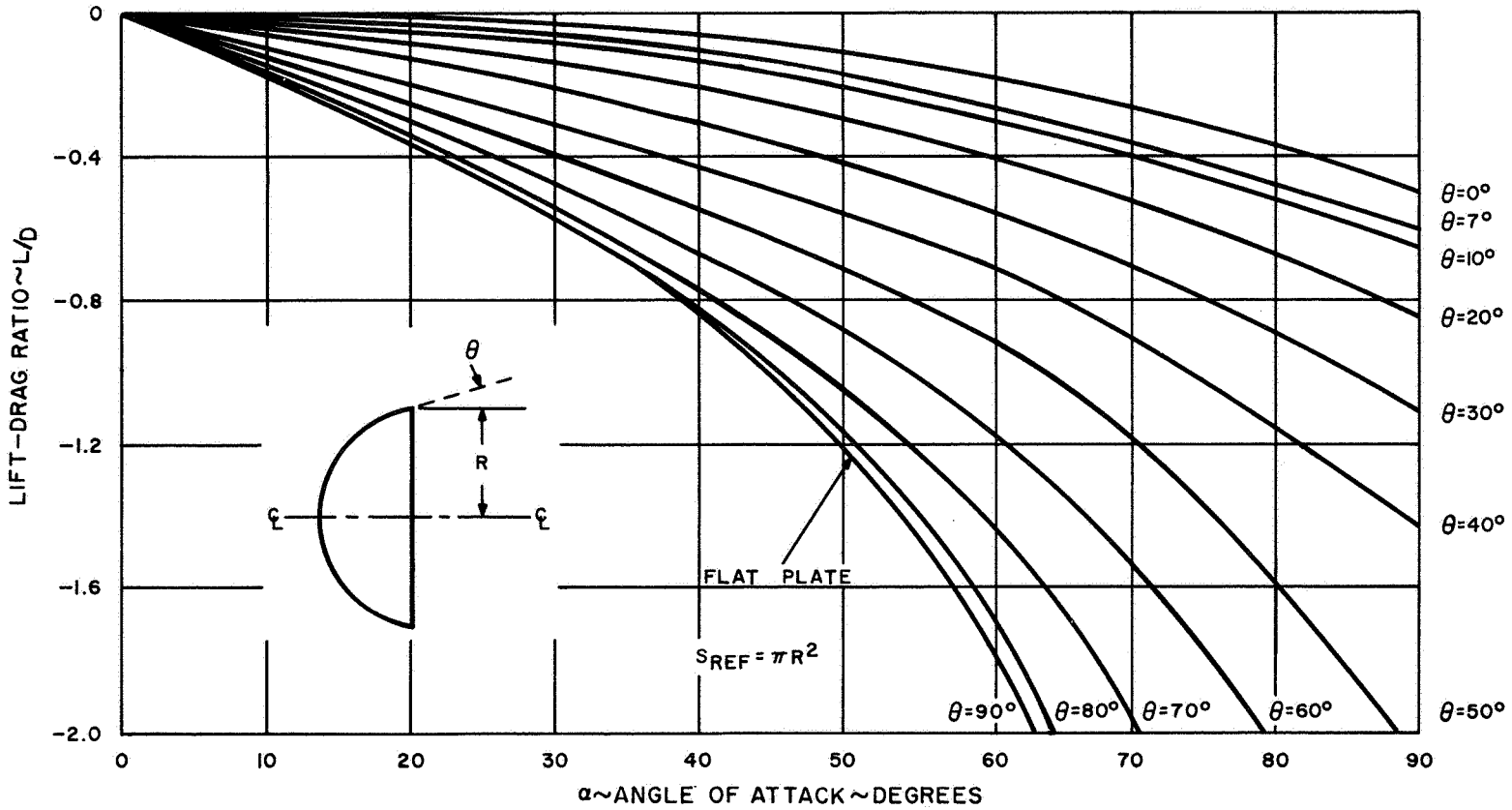

Figure I-1-16. D-2 Configuration - Lift-drag ratio vs angle of attack for spherical sections - Newtonian

CONFIDENTIAL

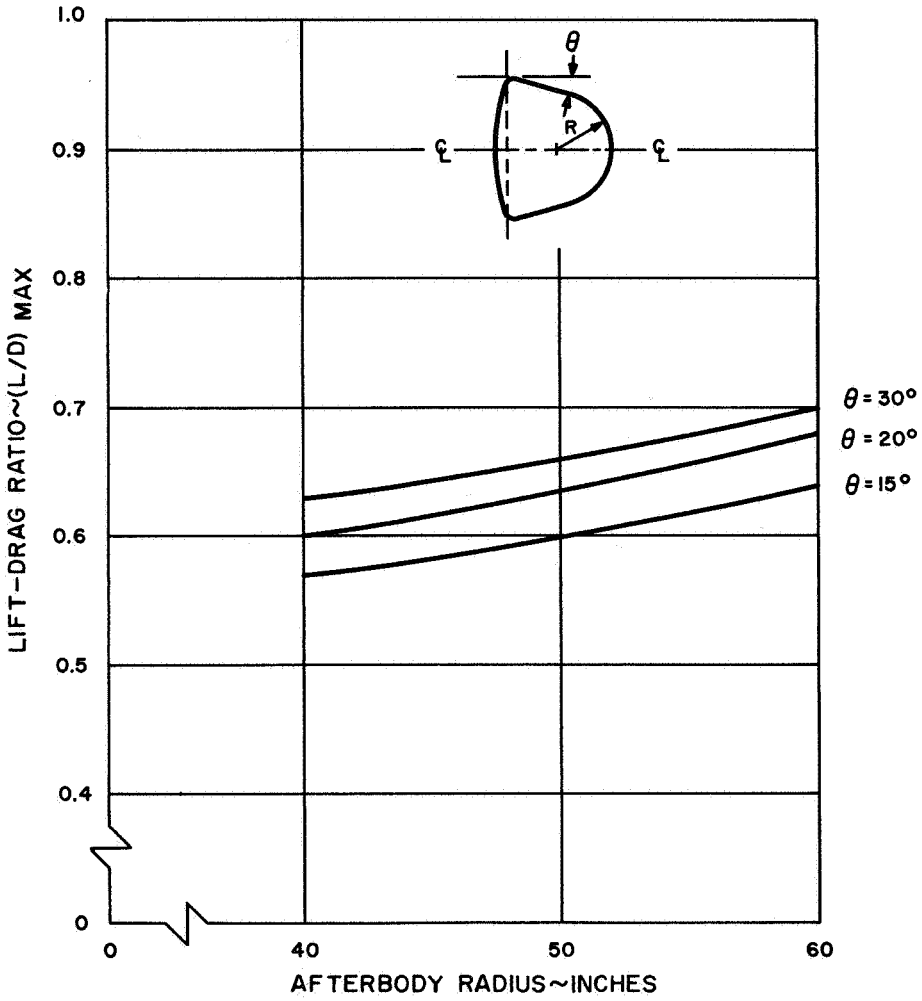

Figure I-1-17. D-2 Configuration - Variation of lift-drag ratio with radius - Newtonian

afterbody radius. However, trade-offs between volumetric, packaging, afterbody heating, and aerodynamic stability led to the selection of a 15 degree rearward tapering afterbody (Figure I-1-18).

The center of gravity location for this vehicle (hereafter referred to as the D-2 configuration) was selected at $\left(X_{CG}/D_B\right) = 0.272$ and offset vertically at $\left(\frac{Y_{CG}}{D_B}\right) = 0.020$, which makes the vehicle self-trimming and statically stable over the entire flight Mach number range. An auxiliary chin flap is also provided, which is capable of augmenting the lift and increasing the trim angle of attack in the normal re-entry attitude or can nullify the trim effects of the off-set center of gravity when the vehicle is rolled by 90 degrees, as discussed later.

1.3.3.2 AERODYNAMIC CHARACTERISTICS:

1.3.3.2.1 Drag.

The estimated variation of drag coefficient for the basic D-2 body as various Mach numbers (1.0, 2.0, 5.0 and 20.0) is presented in Figure I-1-19A as a function of angle of attack. These predictions are based on Newtonian impact theory for hypersonic speeds, along with extrapolation and interpolation of small scale experimental data on similar blunt faced vehicles (9-28).

The trimmed and untrimmed variation of drag coefficient with angle of attack of the D-2 configuration in hypersonic Newtonian flow are presented in Figure I-1-19B, as a function of angle of attack and flap deflection. The variation of the zero lift drag with Mach number for the D-2 vehicle shown in Figure I-1-19C, was calculated based on the method of References 19 and 20, which is known to calculate $C_{D_{\alpha = 0°}}$ for blunt nose vehicles reasonably well. The values of the drag coefficient shown represent the cumulative effects of forebody pressure, base pressure and skin friction.

1.3.3.2.2 Lift.

The variation of lift coefficient with angle of attack (Figure I-1-20A) for various Mach numbers was estimated using References 9-28 and Newtonian theory. The effect of flap deflection on lift coefficient for various angles of attack at hypersonic speeds is shown in Figure I-1-20B. Also presented is the predicted trimmed lift curve for the D-2 configuration. Figure I-1-20C presents the variation of lift curve slope with Mach

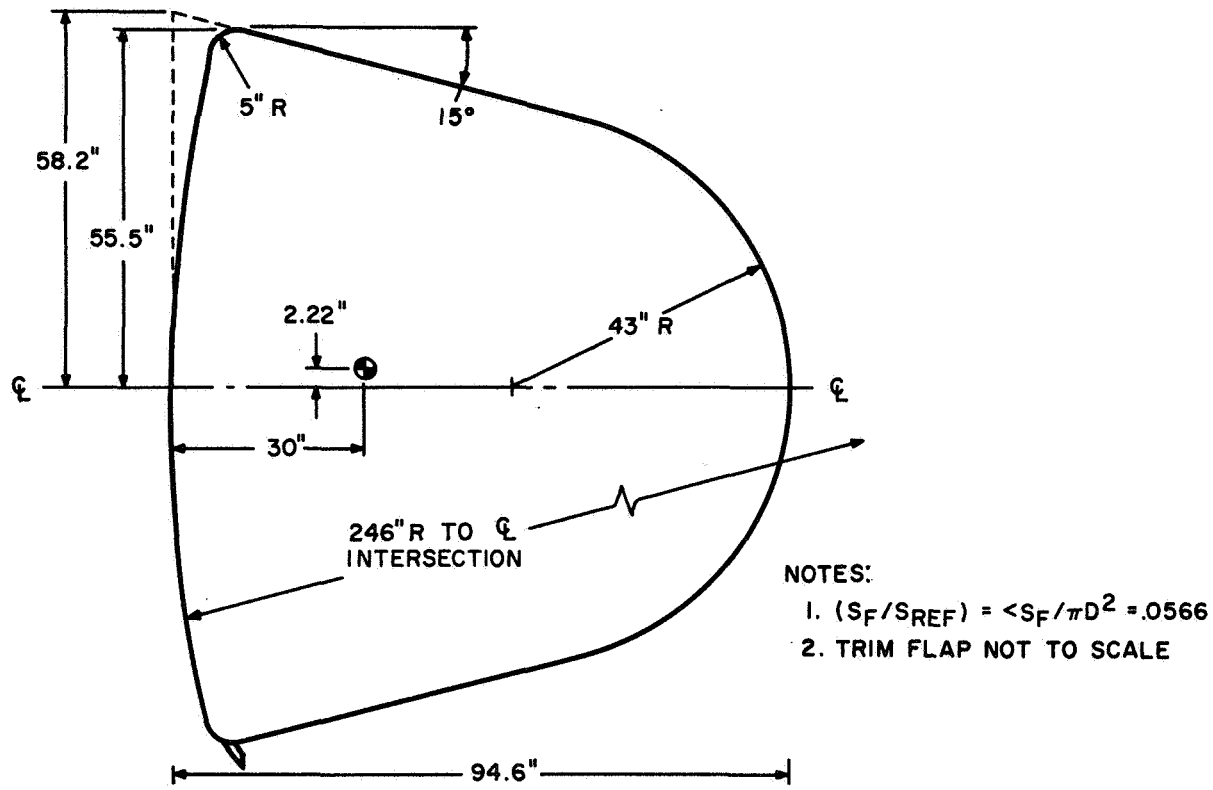

Figure I-1-18. Basic D-2 Configuration

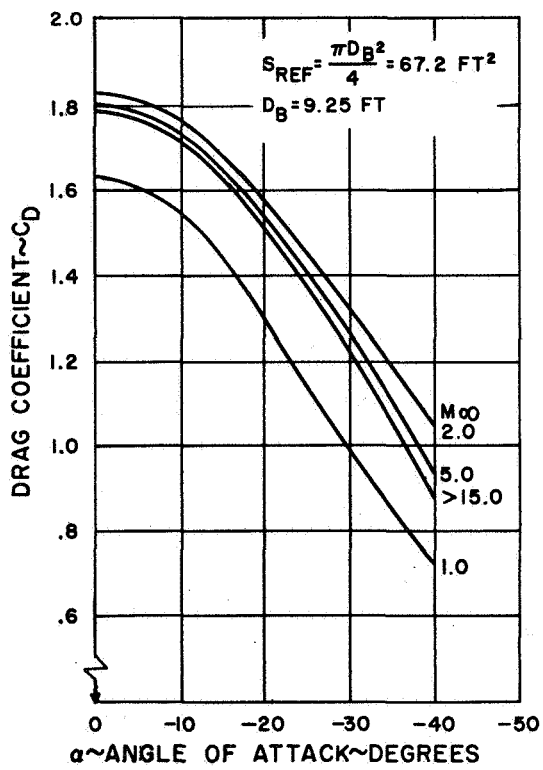

Figure I-1-19A. D-2 Configuration - Variation of drag coefficient with angle of attack - body alone

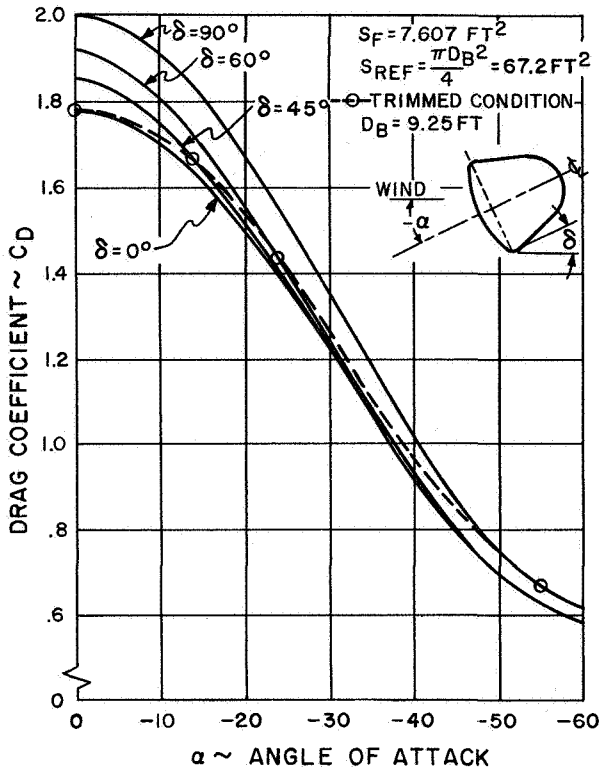

Figure I-1-19B. D-2 Configuration - Variation of drag coefficient with angle of attack - hypersonic

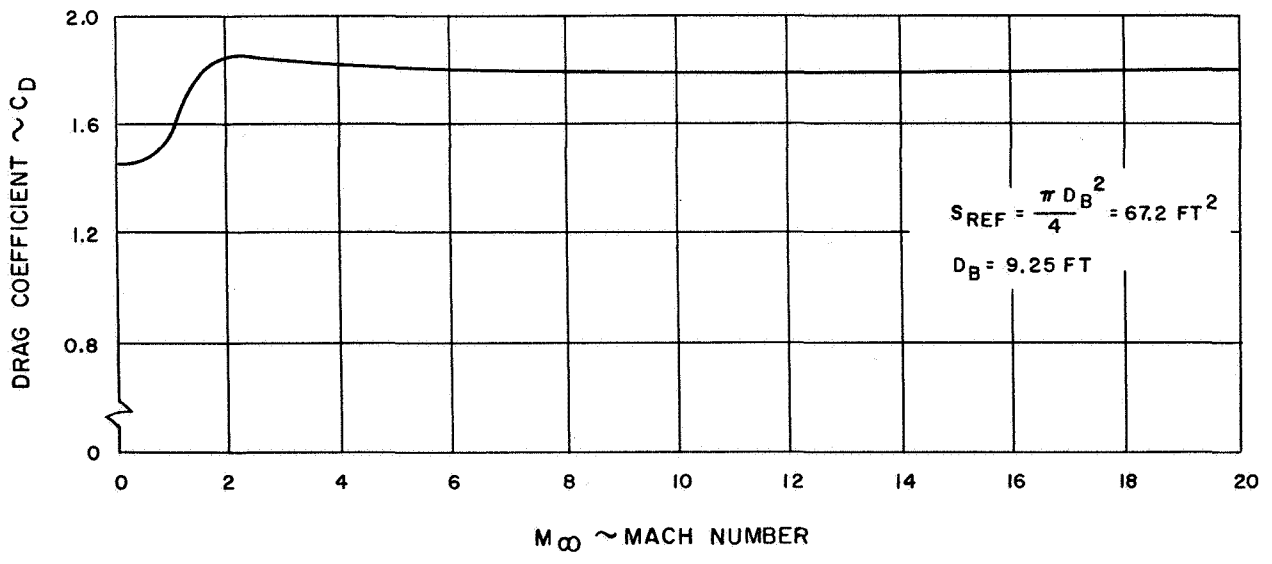

Figure I-1-19C. D-2 Configuration - Drag coefficient with mach number - body alone $\alpha = 0°$

CONFIDENTIAL

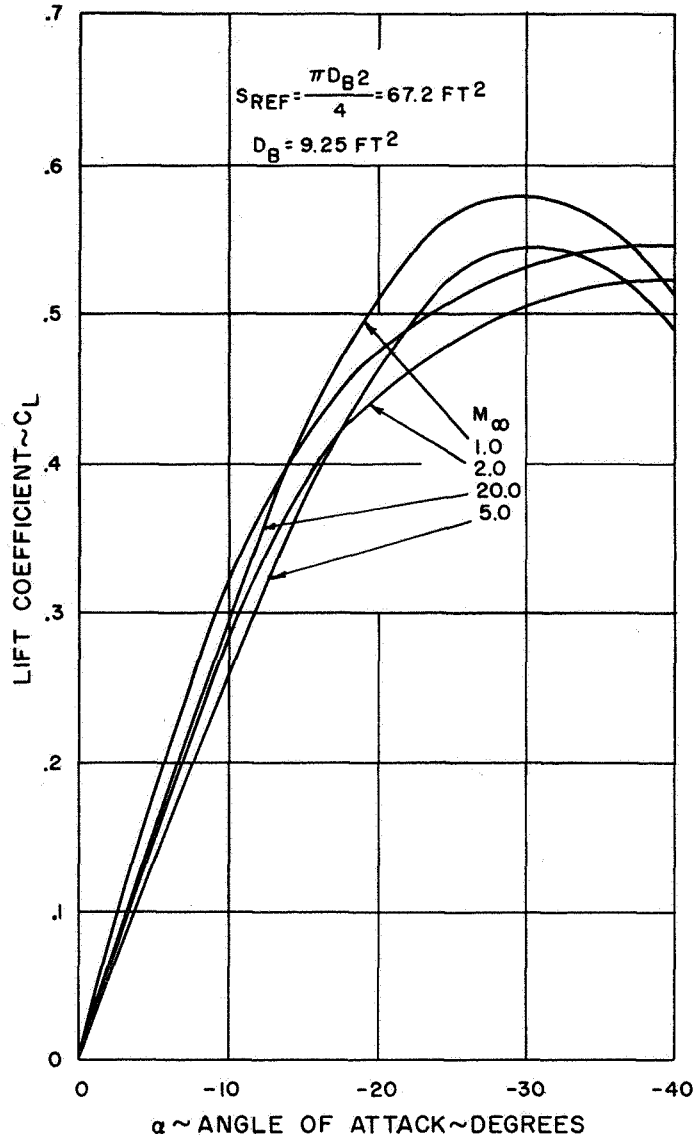

Figure I-1-20A. D-2 Configuration - Variation of lift coefficient with angle of attack - body alone

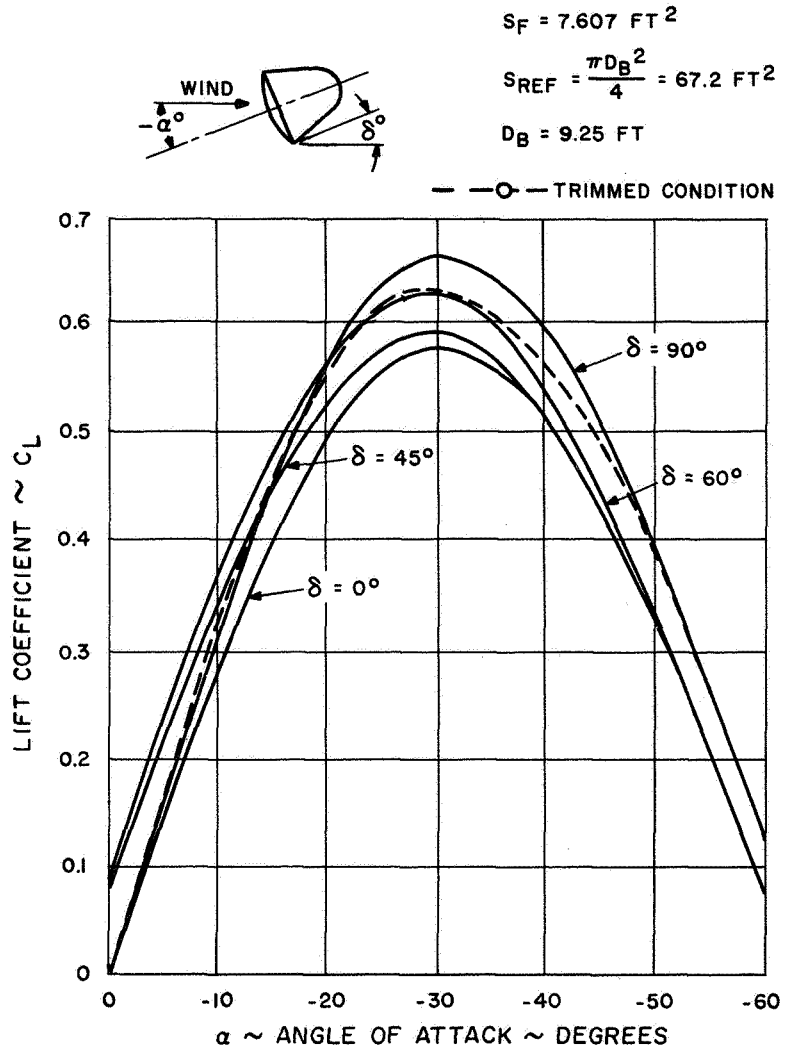

Figure I-1-20B. D-2 Configuration - Variation of lift coefficient with angle of attack - hypersonic

CONFIDENTIAL

number. It is of interest to note that the values of C_{L_α} are negative due to the fact that the negative component of the axial force is larger than the positive component of the axial force is larger than the positive component of the normal force. The $-C_{L_\alpha}$ is characterisitc of the high drag shapes which have considerable nose blunting, necessitated by aerodynamic heating effects. Therefore; the D-2 vehicle will re-enter at negative angles of attack in order to develop positive (L/D) and any flap positions up to $(\delta + \alpha) = 90°$, necessary for trim will aid in increasing the lift and lift-drag ratio in the normal re-entry mode.

1.3.3.2.3 Lift-to-Drag Ratio

Reasonably good agreement in the hypersonic lift-to-drag ratio variation with angle of attack for various flap deflections on the B-2 configuration were obtained between Newtonian theory and small scale experimental findings [(2)] performed at $M_\infty = 12.4$ in the GE MSVD 6-Inch Shock Tunnel. Figure I-1-21A shows the trimmed and untrimmed L/D variation with α for the D-2 configuration. Trimmed $(L/D)_{MAX}$ in the order of 0.59 at $\alpha = -40°$ and flap deflection of 90° (the mechanical capability of the chin flap is 135°) are achieved for the D-2 vehicle, and are believed to be reasonable data, based on the B-2 Shock Tunnel results mentioned.

The variation of trimmed maximum lift-to-drag ratio with Mach number is given in Figure I-1-21B. These curves generally follow the results of the maximum values of (L/D) obtained from the lift and drag variations with angle of attack presented previously.

1.3.3.2.4 Effect of Offset Center of Gravity.

An additional advantage in increased trim angle of attack is obtained by resorting to an off-set center of gravity. Figure I-1-22 shows that a center of gravity (c.g.) offset of 0.02 base calibers is capable of trimming the D-2 vehicle at angles of attack up to -29 degrees. The auxiliary chin flap, however, will augment the lift of the basic body and increase the trim angle in a normal entry attitude or can nullify the trim effect of the offset center-of-gravity when the vehicle is rolled 90 degrees. However, in this latter case, a second flap would be necessary to trim at angles of attack less than -30 degrees, with a consequent increase in weight and a loss in lift/drag ratio of approximately 10 percent. A third method in trimming the D-2 vehicle would be to use an offset center of gravity of only $\left(\frac{Y}{D_B}\right) = 0.01$, to trim the basic D-2 vehicle

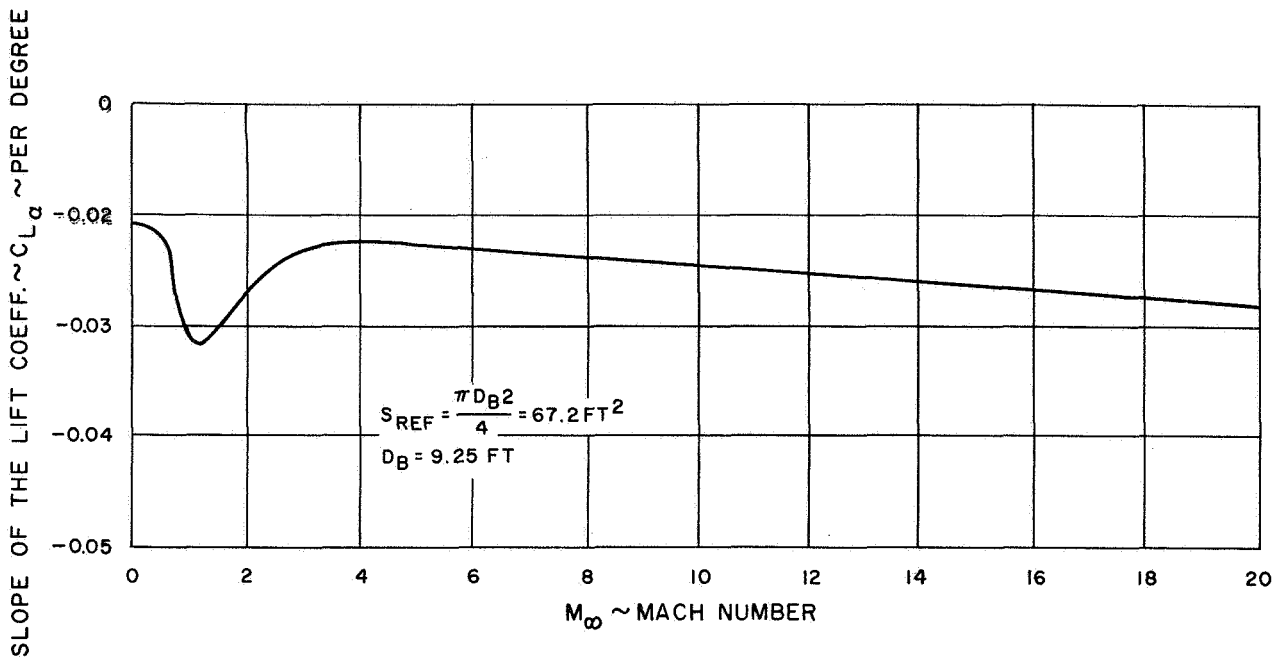

Figure I-1-20C. D-2 Configuration - Variation of lift coefficient slope with mach number - body alone $\alpha = 0°$

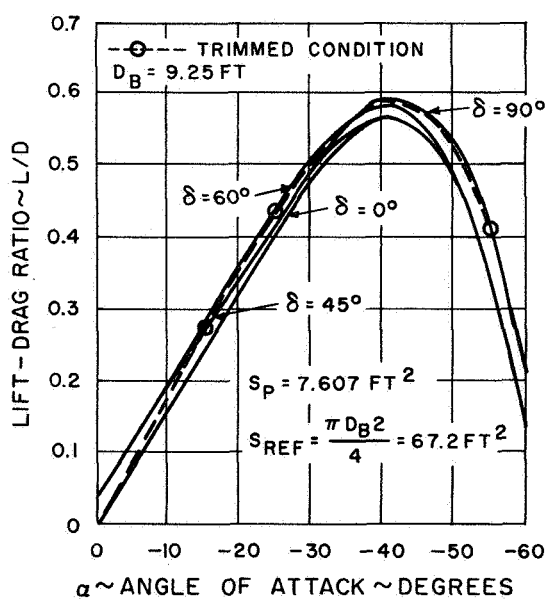

Figure I-1-21A. D-2 Configuration - Variation of lift-drag ratio with angle of attack - hypersonic

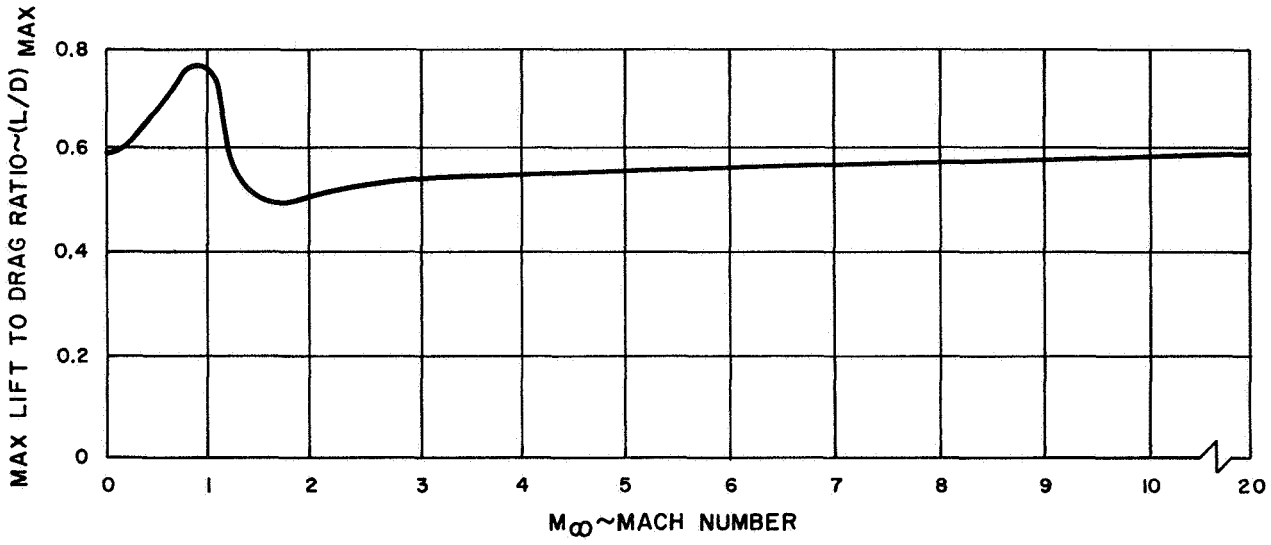

Figure I-1-21B. D-2 Configuration - Variation of lift-drag ratio with mach number - trimmed condition

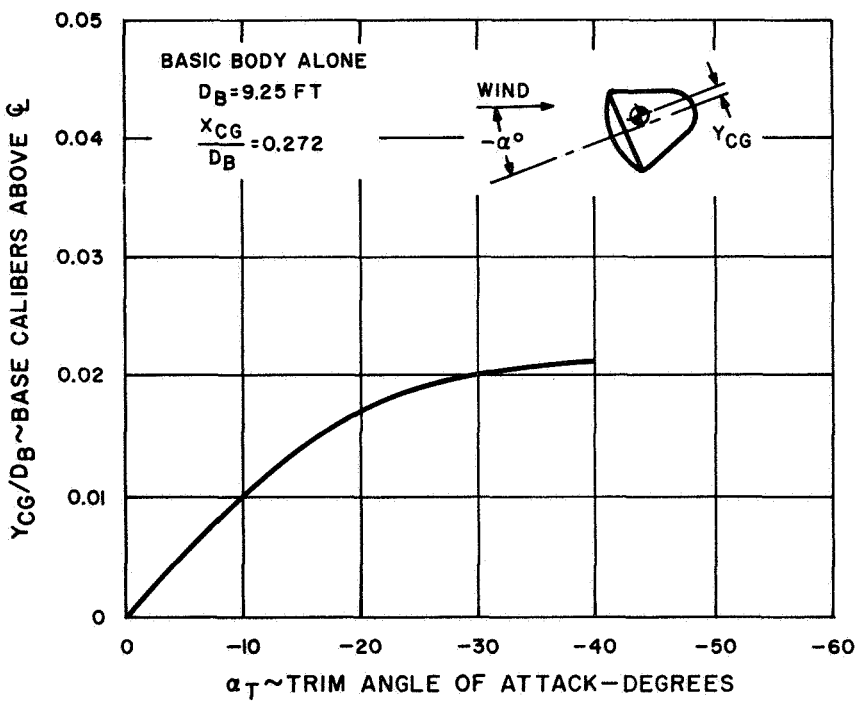

Figure I-1-22. D-2 Configuration - Variation of trim angle of attack with center-of-gravity offset - hypersonic

at $\alpha = 10°$ and use the trim flap to modulate C_L, C_D and L/D between $-10° = \alpha > -45°$.

Recent unpublished information on the effect of control geometry in achieving trim at high angles of attack on a blunt faced vehicle, as the D-2, indicate that a conical flap is slightly superior to the flat plate type of flap at supersonic speeds. Such a flap could be incorporated to trim the D-2 vehicle without a weight penalty. (This same reference indicates that the conical chin flap had a stabilizing effect on the dynamic stability of a configuration similar to the D-2 at hypersonic speeds).

1.3.3.2.5 Pitching Moment.

The estimated variation in pitching moment with angle of attack for various Mach numbers and offset center of gravity, is presented in Figure I-1-23A. Small scale experimental data (9-28) on similar configurations, as the D-2, along with Newtonian theory was used in obtaining these results. With no center of gravity offset the pitching moment characteristics (Figure I-1-23B) up to trim at $\alpha \approx -45°$ would dictate the use of a relatively large flap (effective flap area = 11.3 percent of body reference area) with a consequent penalty in weight.

The pitching moment characteristics at hypersonic speeds (Figure I-1-23C) were computed using Newtonian theory for the D-2 configuration with various chin flap deflections and an offset center of gravity of $(Y/D_B) = 0.02$. Note in Figure I-1-23C that for the high drag shape D-2, the center of gravity offset is an important factor in promoting trim to high angles of attack.

Figure I-1-23D presents the variation of C_{m_α} with Mach number at zero lift conditions, which indicates the D-2 vehicle is statically stable for this condition over the entire Mach number range. These data are based on the large amounts of aerodynamic stability data available for the configurations having a likeness to the D-2 vehicle. Although the center of pressure for the D-2 is expected to move forward of the center of gravity at transonic and supersonic speeds, the vehicle remains statically stable over the entire Mach number range, through virtue of a change in direction of the resulting normal force. Although not shown, the effect of flap deflection on the static stability of the D-2 vehicle is expected to be a stabilizing one and the total configuration is statically stable in the trimmed condition.

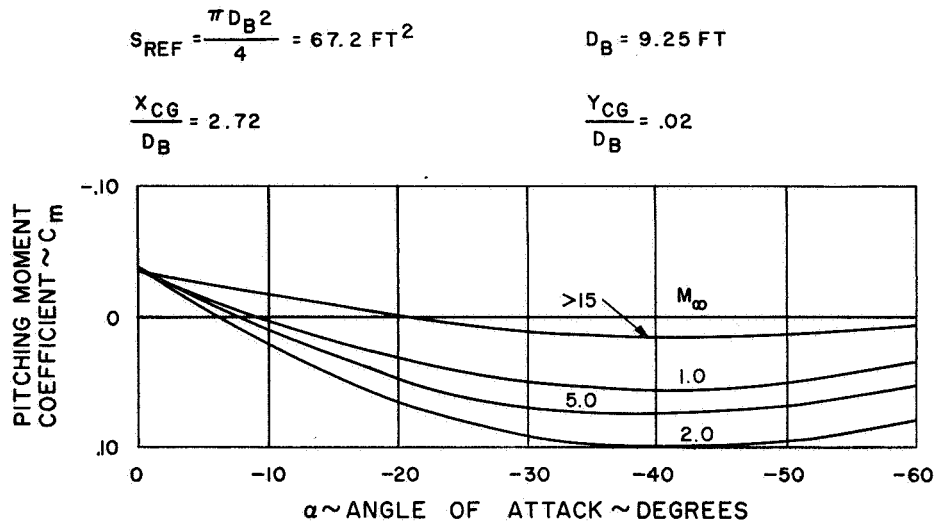

Figure I-1-23A. D-2 Configuration - Variation of pitching moment coefficient with angle of attack - body alone

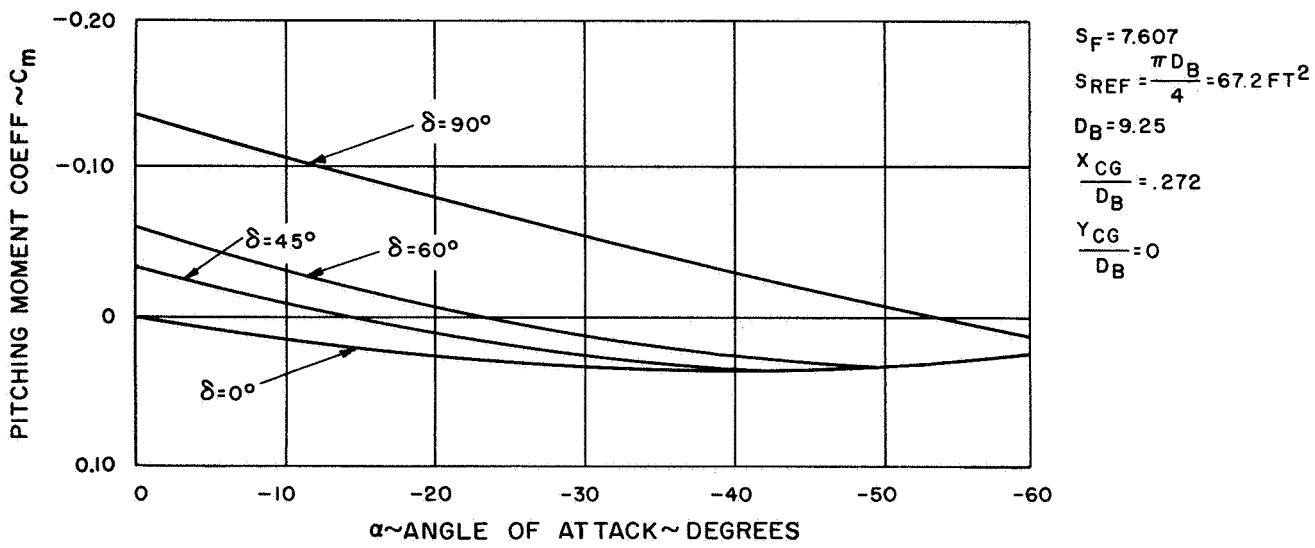

Figure I-1-23B. D-2 Configuration - Variation of pitching moment coefficient with angle of attack - hypersonic

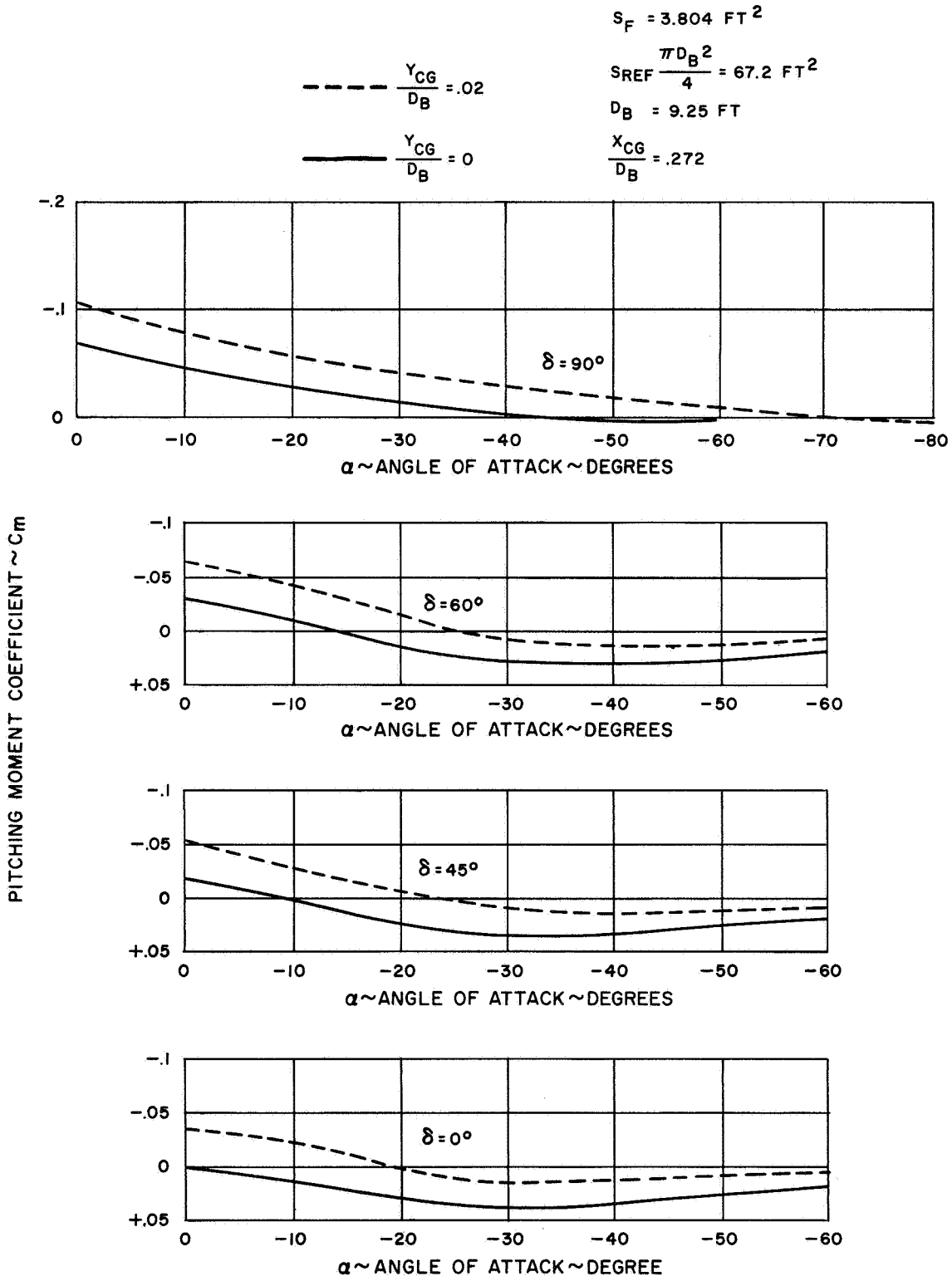

Figure I-1-23C. D-2 Configuration - Variation of pitching moment coefficient with angle of attack - hypersonic

1.3.3.2.6 Dynamic Stability.

For short, blunt faced bodies of revolution, with a contracting afterbody section, such as the D-2 configuration, the sign of the dynamic damping-in-pitch parameter, $C_{m_q} + C_{m_{\dot{\alpha}}}$, is positive at $\alpha = 0°$ (Figures I-1-24(A-B) indicating that dynamic divergence may be encountered. On inspection of the Allen [29] damping factor $C_D - C_{L_\alpha} + (C_{mq} + C_{m_{\dot{\alpha}}}) \left(\frac{L}{\delta}\right)^2$, it is observed that because of the high drag and negative lift curve slope this factor is positive throughout the re-entry trajectory. Moderate amplitude oscillations are expected to be experienced but because of the inherent static stability of the vehicle and the inclusion of a closed loop rate damping system, the effect of these dynamic oscillations may be kept small and within engineering and human limits. At transonic speeds, the recovery system is deployed after which the oscillations will become of little or no consequence. Theoretical and experimental dynamic stability studies such as the effect of afterbody length angle, forebody-afterbody junction radius, and use of fins or flare, etc. may offer some insight to the solution of dynamic stability problems associated with extremely blunt faced vehicles like the D-2.

At trim conditions, near $\alpha = -40°$ the damping-in-pitch parameter, $C_{m_q} + C_{m_{\dot{\alpha}}}$, as shown in Figure I-1-24A is negative. However, the overwhelming effect of high drag and $-C_{L_\alpha}$ will make the Allen damping factor positive. It is noteworthy to mention that except for the dynamic damping data obtained for Project Mercury [30], very little experimental aerodynamic information is available on blunt faced bodies with converging afterbodies, particularly at hypersonic speeds. The variations of damping-in-pitch coefficient with angle of attack (Figure I-1-24A) was, therefore, obtained by displacing the value of the damping parameter at zero angle of attack and then following the trends of Mercury data. The variation of $C_{m_q} + C_{m_{\dot{\alpha}}}$ with Mach number (Figure I-1-24B) was obtained through summary [29-35] and correlation of dynamic damping data. Newtonian theory is shown to predict the hypersonic damping in pitch parameter quite poorly, even to the extent of being opposite in sign.

1.3.3.2.7 Side Force Due to Sideslip:

The slope of the side force coefficient for small angles of sideslip ($\beta \leq 5°$ and $\alpha = 0°$) with Mach number for the basic D-2 configuration is presented in Figure I-1-25. This curve is basically the same as the slope of the normal force variation with angle of

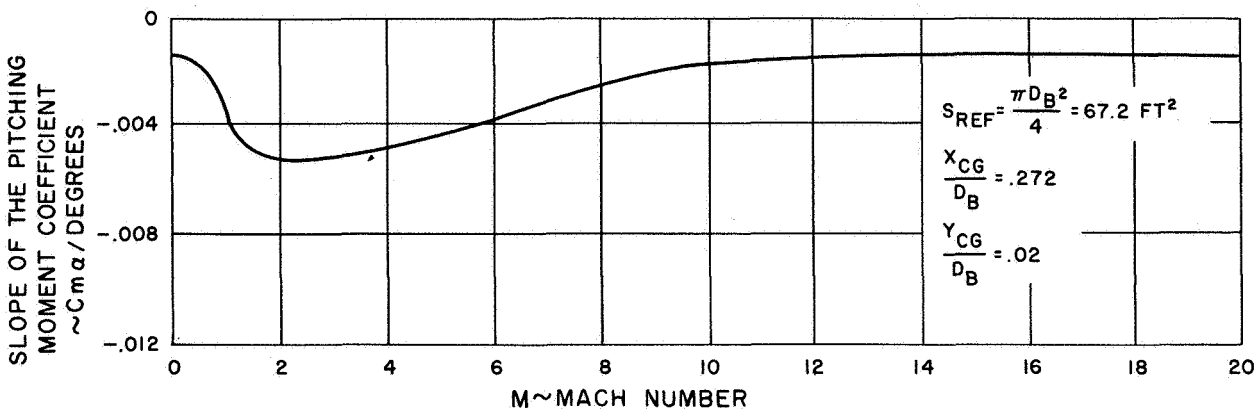

Figure I-1-23D. D-2 Configuration - Variation of the pitching moment slope coefficient with mach number - body alone

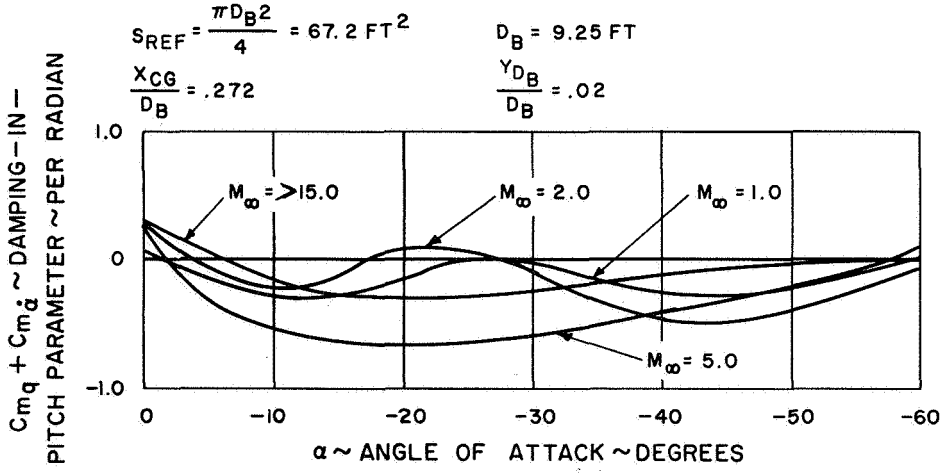

Figure I-1-24A. D-2 Configuration - Variation of damping-in-pitch parameter with angle of attack - body alone

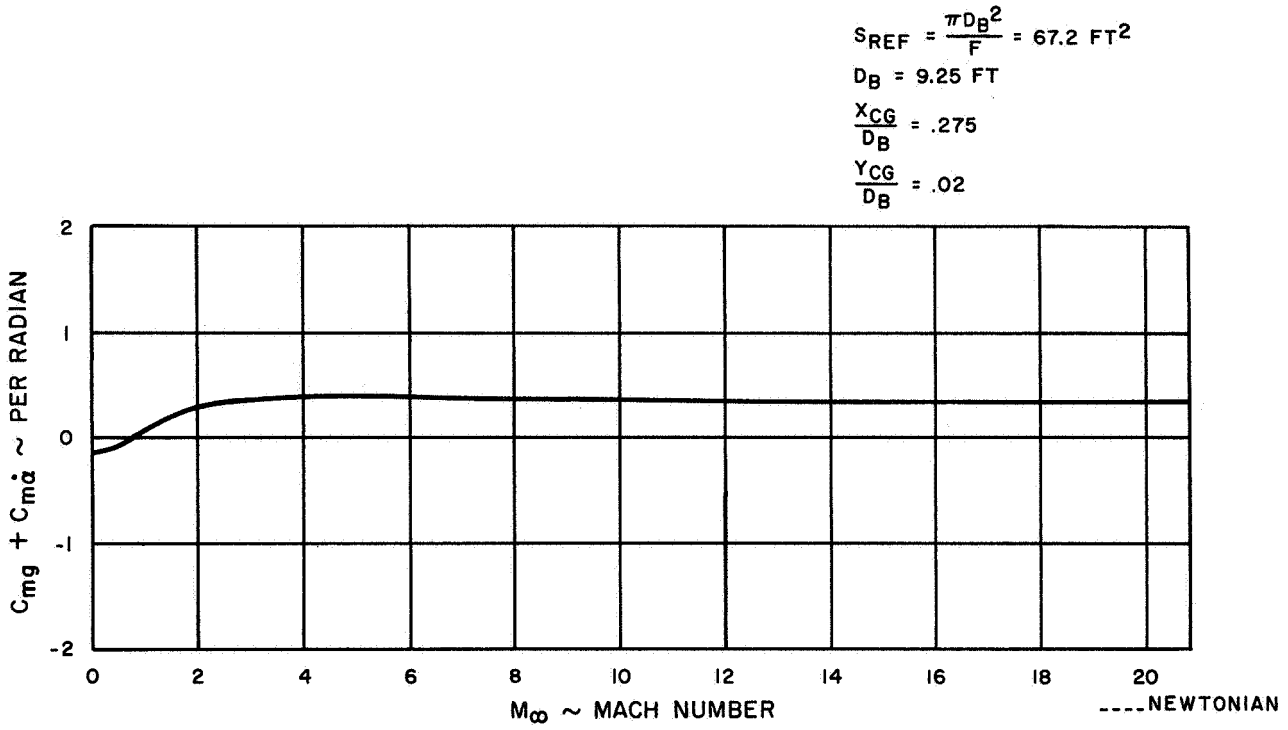

Figure I-1-24B. D-2 Configuration - Variation of dynamic damping parameter with mach number - body alone $\alpha = 0°$

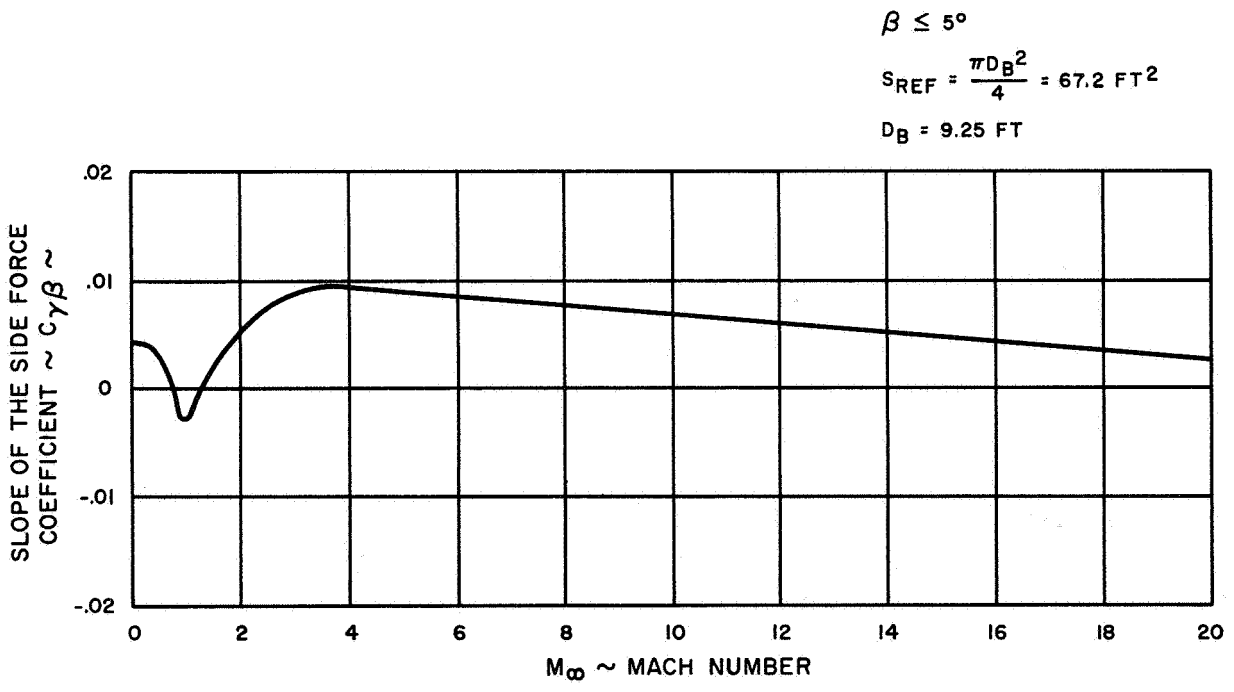

Figure I-1-25. D-2 Configuration - Variation of side force coefficient slope with mach number - body alone $\alpha = 0°$

attack, which for small angular displacements is $C_{N_\alpha} = C_{Y_\beta} = C_{L_\alpha} + C_A$. The effect of pitch flap deflections on C_{Y_β} is believed to be negligibly small up to angles of attack for $(L/D)_{MAX}$.

1.3.3.2.8 Directional Control

The directional control characteristics of the basic D-2 vehicle with and without chin flap are presented in Figure I-1-26A versus angle of attack for $M_\infty = 1.5$, 2.5 and 5.0. These results were obtained from a compilation of aerodynamic data [24] on a variety of configurations similar to the D-2 and show the complete D-2 vehicle to be directionally stable up to angles of attack for $(L/D)_{MAX}$. The estimated effect of the chin flap for the typical case of $\delta = 90°$ is observed to be small.

The directional stability characteristics of the D-2 configuration are shown as a function of Mach number for small angles of sideslip and $\alpha = 0°$, in Figure I-1-26B. This curve shows the basic vehicle to be directionally stable over the entire Mach number range. As expected, the trend of this curve follows the static longitudinal stability derivative except for small body-flap interference effects, which were considered to be slightly different in the pitch and yaw planes.

1.3.3.2.9 Lateral Stability:

The lateral stability characteristics of the D-2 vehicle (with and without flaps) are shown, respectively, as a function of angle of attack and Mach number in Figures I-1-27(A-B). The influence of the flap at $\delta = 90°$ is shown to be small. These estimates were obtained in the same fashion as the directional stability data [24] which show blunt nosed bodies with approximately the same center of gravity, as for the D-2, to be laterally stable. Again, the pitch flap effects at high angles of attack on the lateral stability is observed to be nil at hypersonic speeds.

1.3.3.3 MANEUVER CAPABILITY:

Lateral maneuvering for the D-2 vehicle is achieved by banking and pitching the vehicle, using reaction jets and chin flap respectively. More detailed explanations of the longitudinal, lateral and directional modes of maneuvering are given in the guidance and control section, Volume III, of this report.

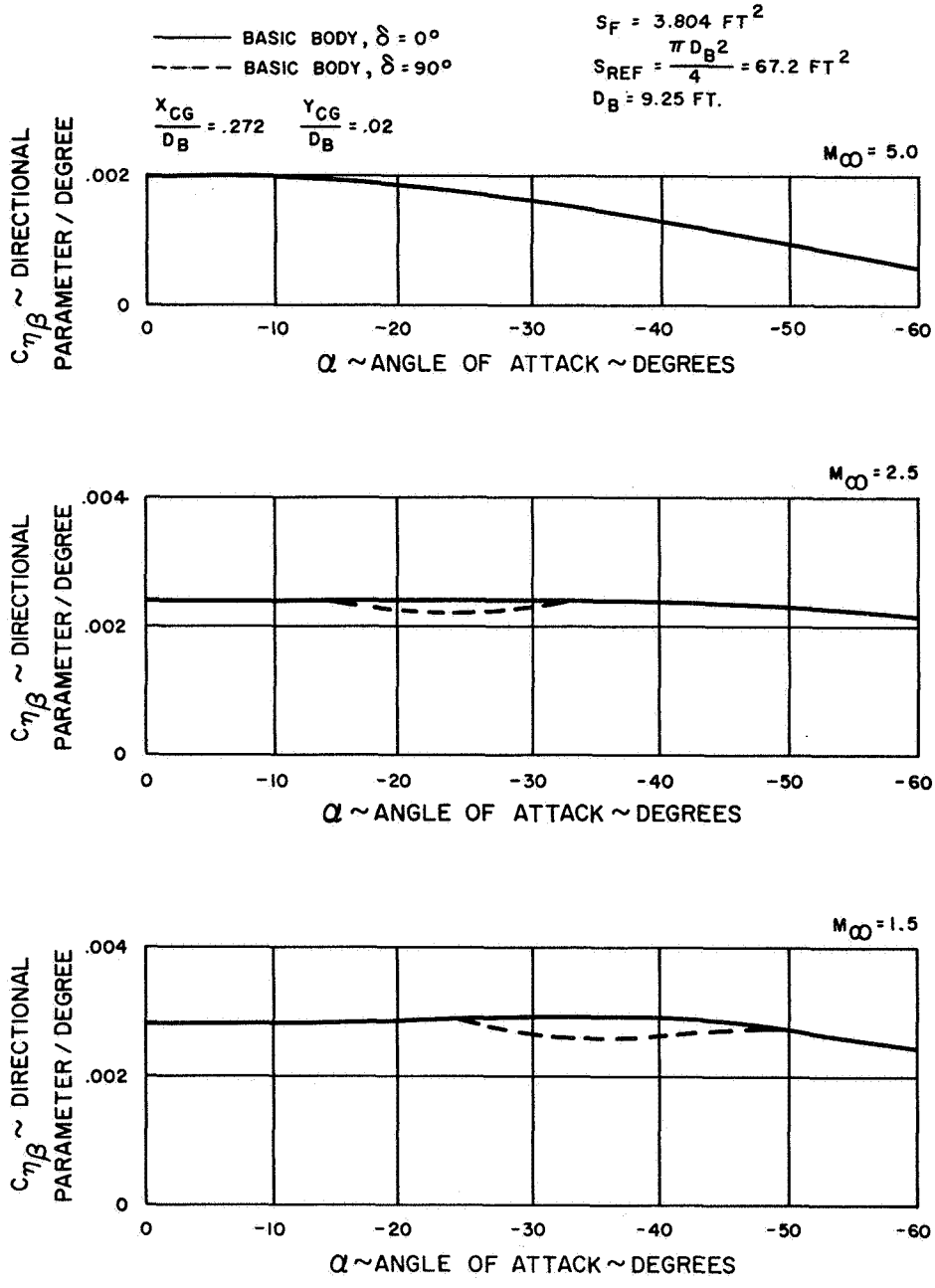

Figure I-1-26A. D-2 Configuration - Estimated directional stability characteristics of basic vehicle with and without flap deflections $-5° < \beta < 5°$

CONFIDENTIAL

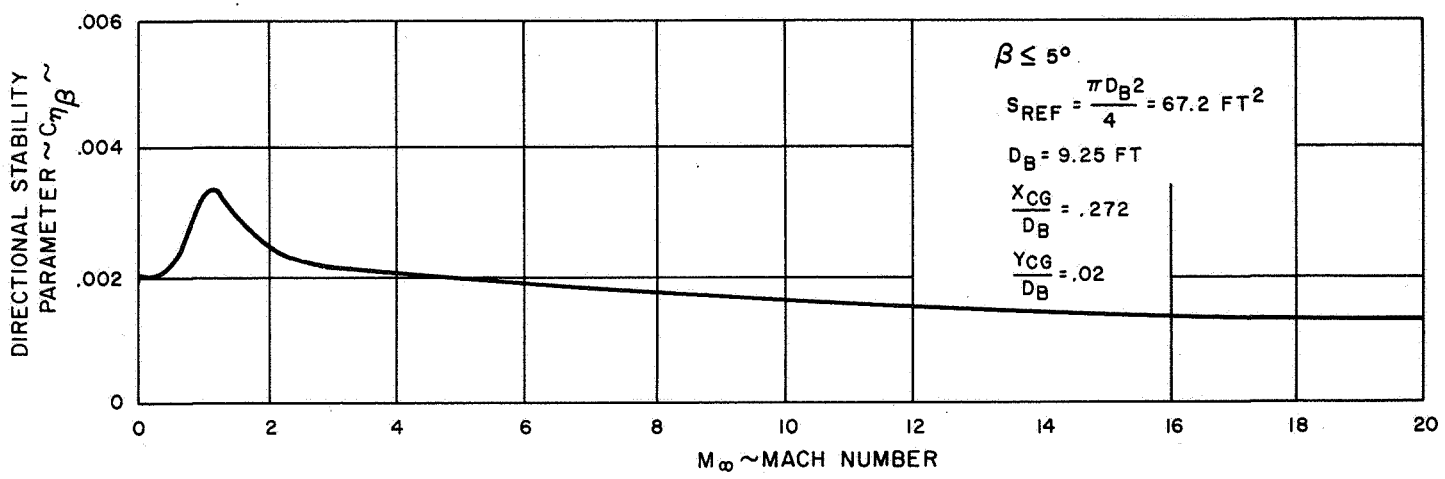

Figure I-1-26B. D-2 Configuration - Estimated variation of directional stability parameter characteristics with mach number - body alone $\alpha = 0°$

CONFIDENTIAL

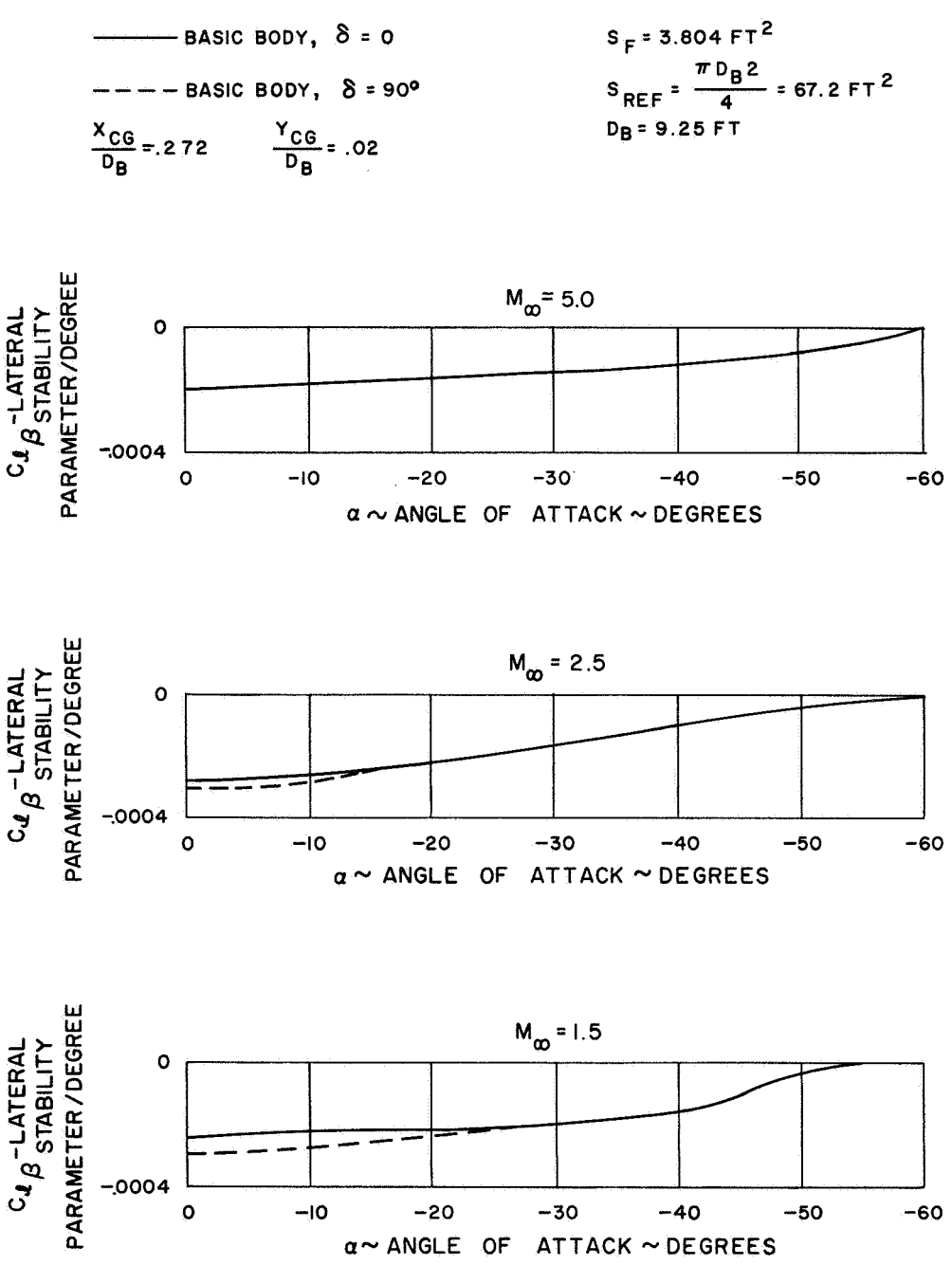

Figure I-1-27A. D-2 Configuration - Estimated lateral stability characteristics of basic vehicle with and without flap deflections $\beta \leq 5°$

1.3.3.4 PRESSURE AND LOAD DISTRIBUTION:

The pressure distributions presented in Figure I-1-28 are based on Newtonian estimates on the forward shield section of the vehicle and Prandtl-Meyer theory on both the windward and leeward surfaces, expanding through an angle of $(\alpha - \theta)$ respectively for local flow conditions existing at the shoulder.

Some differences in the estimated and actual pressure levels are expected to exist on the afterbody portion of the vehicle, inasmuch as separation is expected to occur starting at the forebody-afterbody shoulder at supersonic and hypersonic speeds.

The pressure acting on the flap when deflected at $\delta_F = 90°$ in a hypersonic stream is presented in Figure I-1-29. These estimates show that the flap, in this condition, is exposed to stagnation pressures, almost over its entire length and will require considerable heat protection.

A prerequisite of structural strength with minimum wieght necessitates definition of load distributions over the entire re-entry vehicle at peak axial, lateral and normal "g" conditions.

The accumulative axial, lateral and moment distribution loads for the D-2 vehicle presented in Figures I-1-30(A-C) for the $\alpha = 0°$ and $40°$ conditions where peak hypersonic loads are expected to occur. These plots represent the normalized distribution of the total force and moment loads up to a given body station and were obtained by the integration of the pressure distribution (Figure I-1-29) by assuming a sinusoidal distribution around the vehicle.

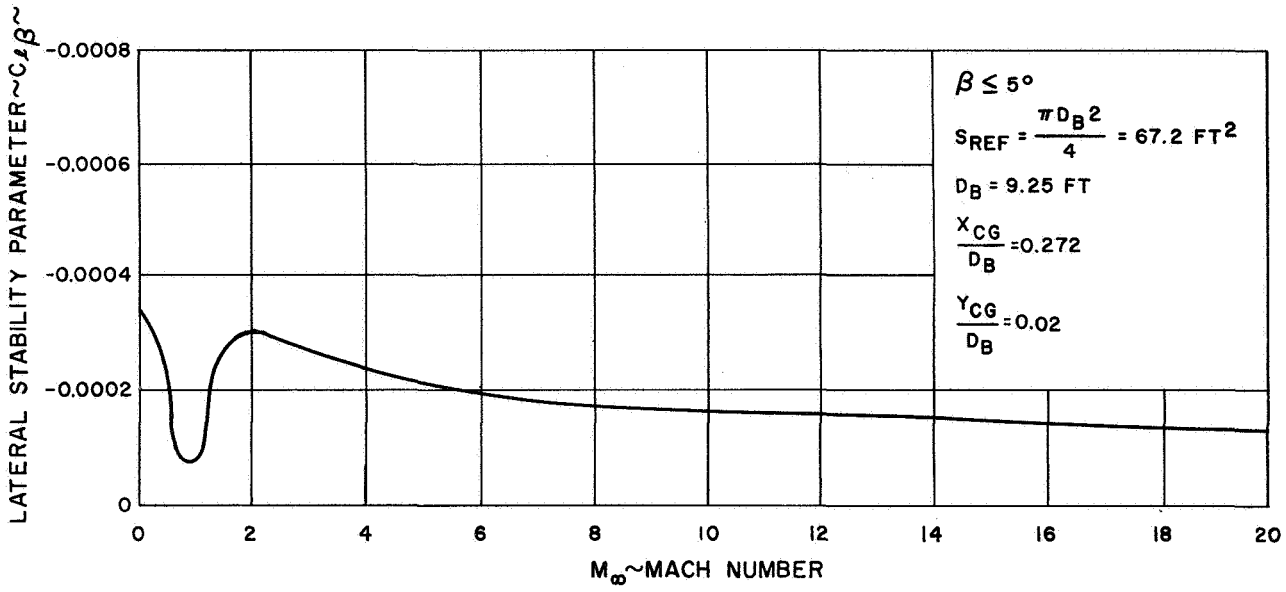

Figure I-1-27B. D-2 Configuration - Estimated variation of lateral stability characteristics with mach number - body alone $\alpha = 0°$

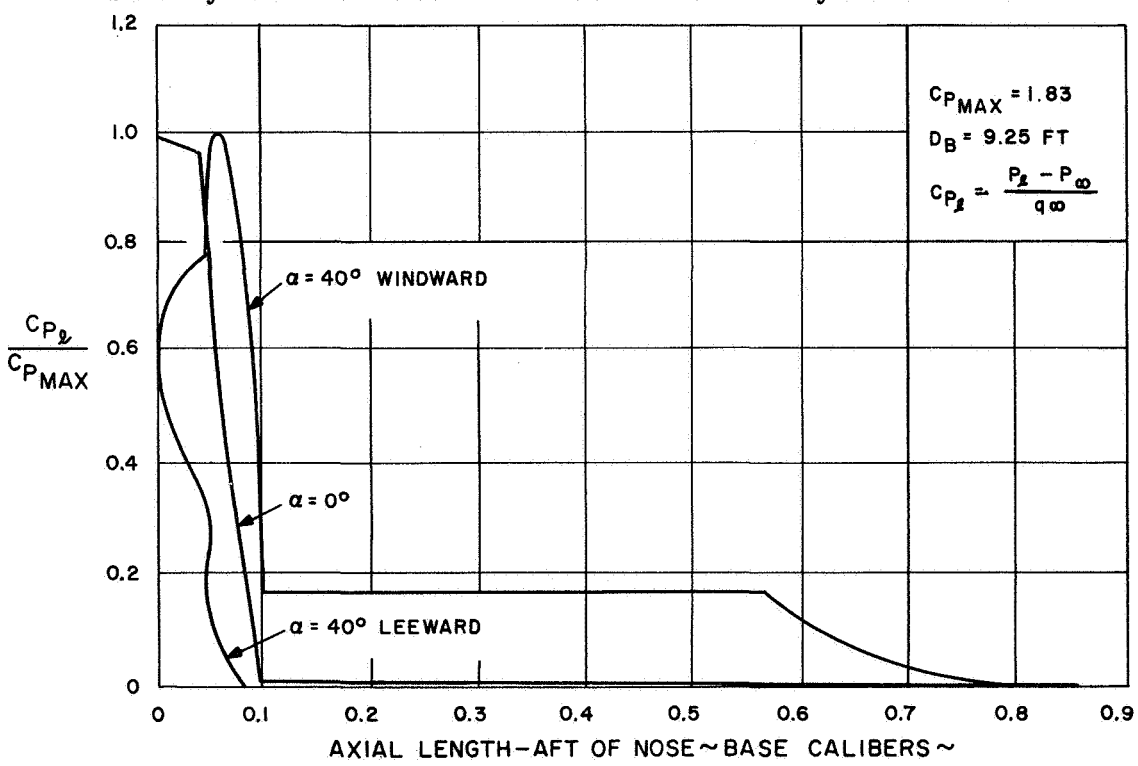

Figure I-1-28. D-2 Configuration - Variation of pressure coefficient ratio with axial length - hypersonic

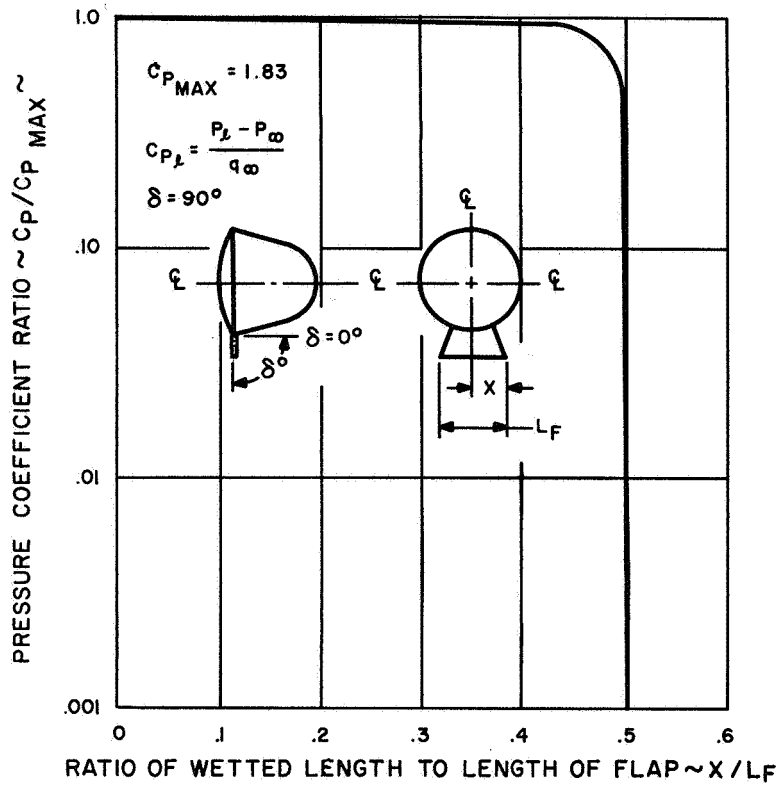

Figure I-1-29. Variation of pressure ratio for a flat flap - hypersonic

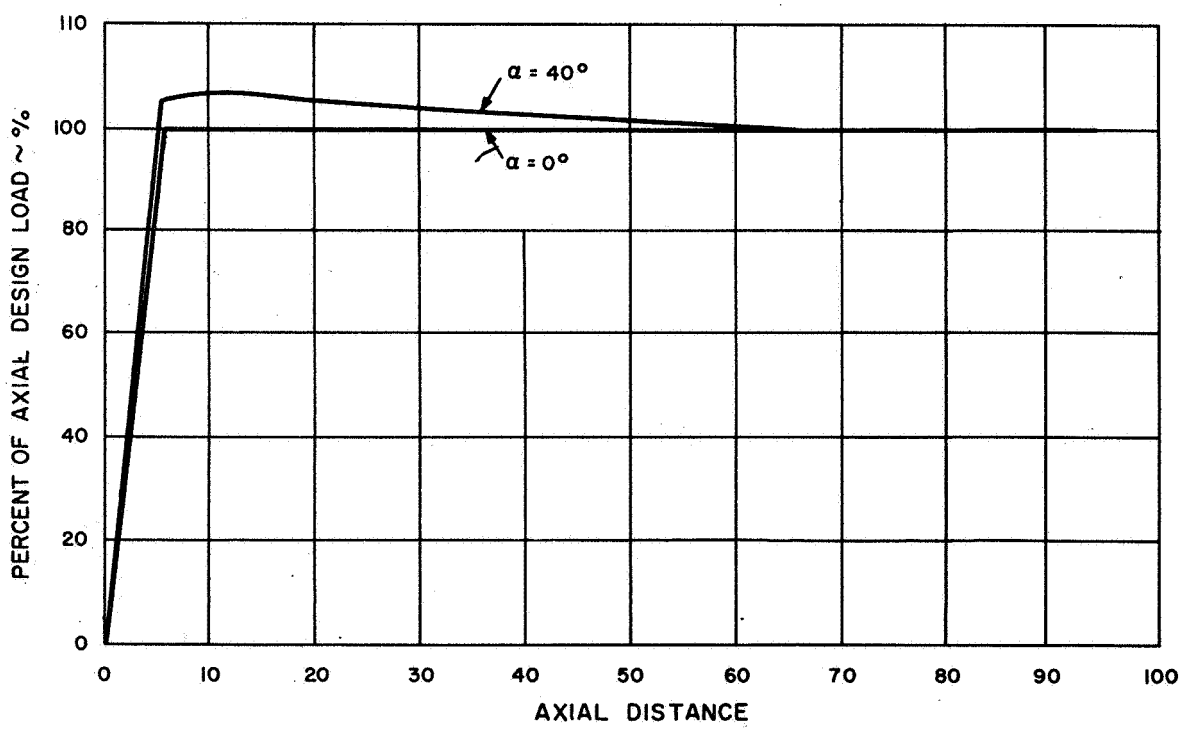

Figure I-1-30A. D-2 Configuration - Accumulative axial design loads - hypersonic α = 40°

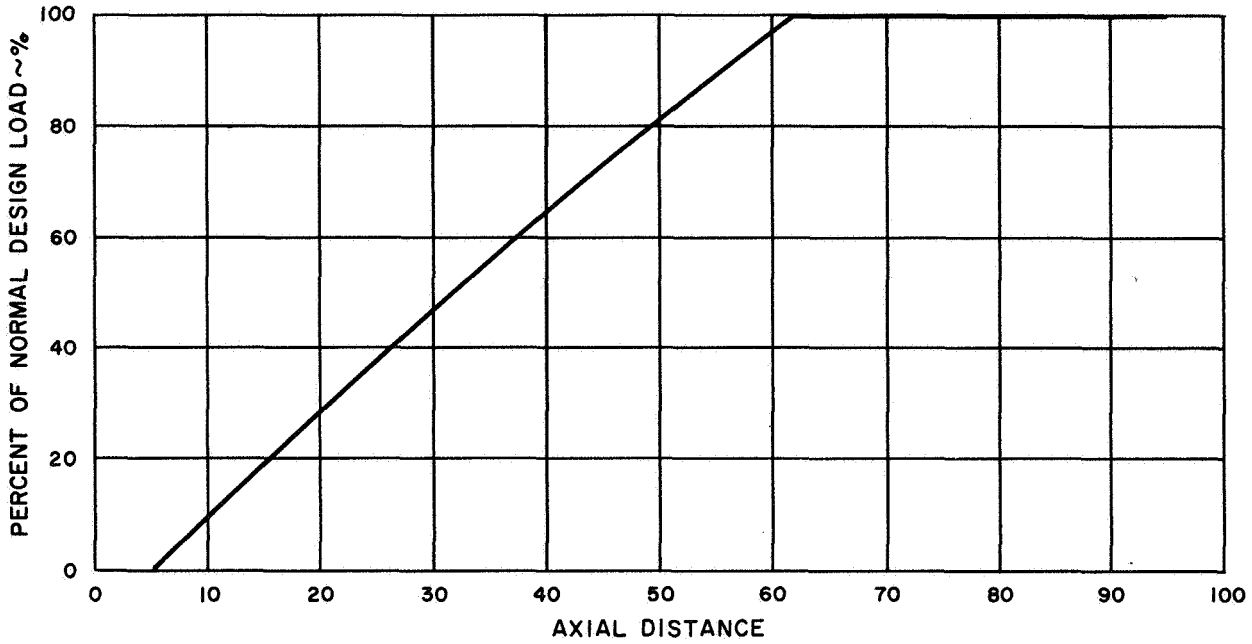

Figure I-1-30B. D-2 Configuration - accumulative normal design load - hypersonic $\alpha = 40°$

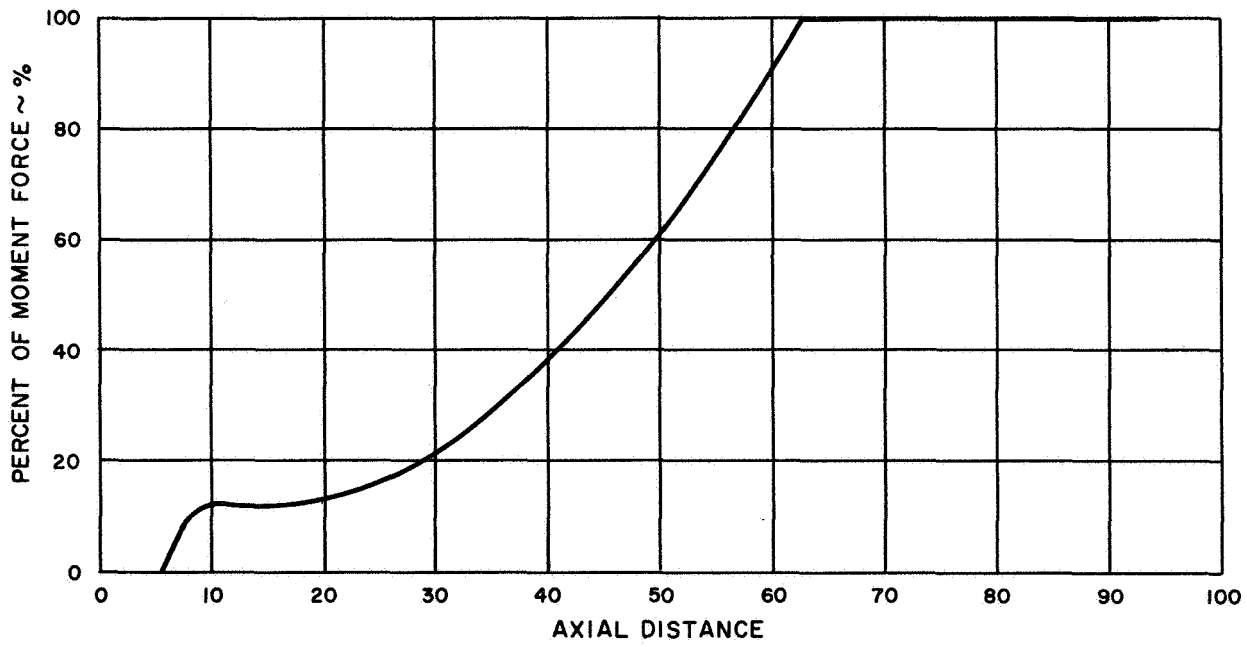

Figure I-1-30C. D-2 Configuration - accumulative moment - hypersonic $\alpha = 40°$

1.4 HIGH L/D CONFIGURATION

The high L/D glider design of Figure I-1-31 is intended to exploit to the greatest extent the advantages of L/D in providing large re-entry angle corridor (for a given allowable g) and high lateral maneuvering capability. This design re-enters and glides hypersonically at attitudes between that for maximum L/D and that for maximum C_L. It will approach and land at an attitude near maximum L/D. It is intended that the outer walls of this design operate in radiation equilibrium at least during the sub-orbital portion of the re-entry glide. For this reason, a wing loading of about 40 psf was specified in order to hold the bottom surface temperature below 3000 F.

A reaction control system provides attitude control during the low-density re-entry flight phase. Trailing edge elevons provide aerodynamic longitudinal and lateral control during the atmospheric re-entry. Aerodynamic directional control and stability augmentation are provided by the rudders throughout the hypersonic and supersonic glide. The hypersonic maximum L/D is estimated to be about 2.0 and the maximum hypersonic C_L about 0.7. The subsonic maximum L/D for approach and landing is estimated at 4.4 clean and 3.8 gear down. This configuration is similar to previous Dyna-Soar design approaches.

1.5 HIGH ATTITUDE CONFIGURATION

The high attitude configuration shown in Figure I-1-32 represents a limited departure from the high L/D design to achieve lighter weight by mild sacrifice of the highest L/D capabilities. The body is shorter and wider and comprises a larger portion of the over-all planform area than the high L/D configuration. The leading edge is curved at the front which when combined with the lower sweepback produces a somewhat higher aspect ratio vehicle. Variable geometry fin surfaces located at the wing-tips are employed for trim to low attitude and for landing. During super-orbital re-entry, these surfaces are folded on top of the vehicle to protect them from the most extreme heating conditions.

This approach is also intended to provide equilibrium hypersonic glide capability, but by high attitude super-orbital re-entry, the area exposed to critical re-entry heating is limited to the bottom surface of the vehicle. This design re-enters and glides hypersonically at attitudes between that for maximum C_L and near 90 degrees. At lower hypersonic and supersonic speeds, it trims to lower attitudes (below that for

CONFIDENTIAL

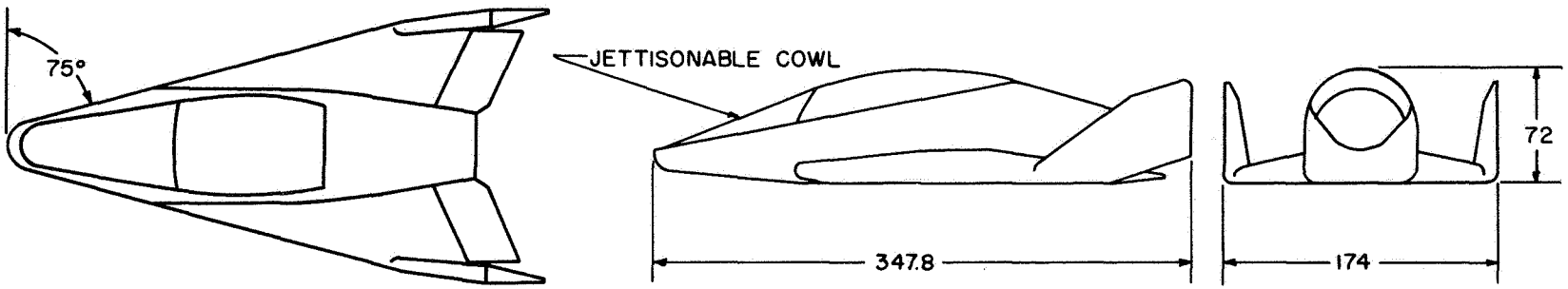

Figure I-1-31. High L/D glider design

CONFIDENTIAL

CONFIDENTIAL

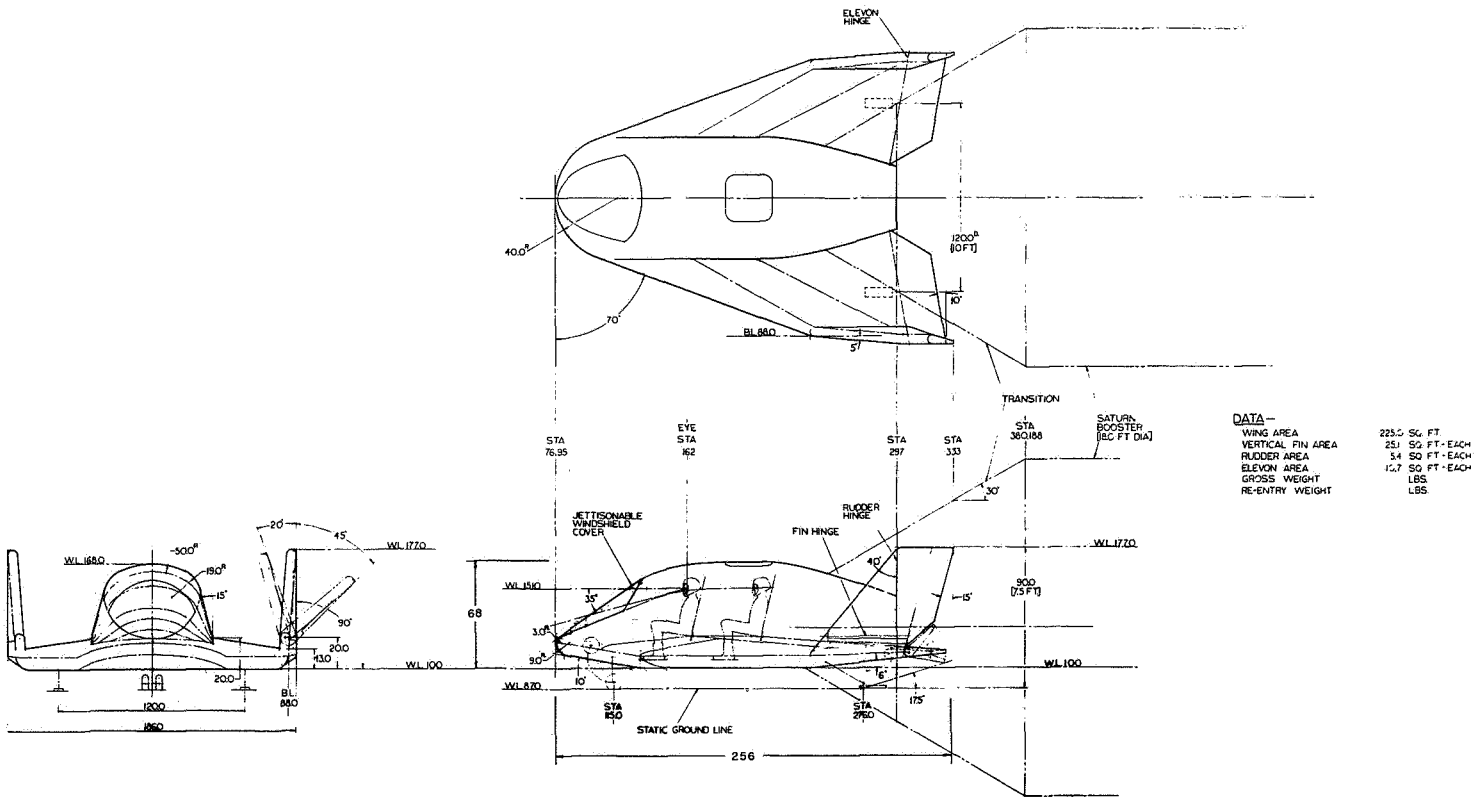

Figure I-1-32. General arrangement - high altitude re-entry vehicle - APOLLO

CONFIDENTIAL

maximum C_L) and approaches and lands near maximum L/D. The hypersonic maximum L/D is estimated to be about 1.5, but in high attitude flight, the highest useful maximum L/D will be about 0.7 at a maximum C_L of about 0.7. The subsonic maximum L/D is estimated to be 4.7 clean and 4.0 gear down.

It is evident that considerable weight penalties are incurred by the use of wings to obtain lower wing loadings and that the most densely packaged configuration tends to produce the lightest overall design. Further configuration design efforts were therefore aimed toward development of a maximum useful volume body shape tailored to the system and mission requirements and having conventional landing capability.

1.6 MODIFIED LENTICULAR CONFIGURATION (R-3)

The modified lenticular design is the result of comparative studies of the series of preliminary re-entry glider configurations designed to satisfy the requirement for conventional landing capability. The characteristics of two of these preliminary configurations, a high L/D winged glider and a high attitude winged glider, have been presented above. Table I-1-I presents an abbreviated geometric comparison of these early designs with the modified lenticular vehicle to illustrate the configuration evolution into its present form.

The modified lenticular configuration shown in Figure I-1-33 is conceived as a lightweight landable re-entry configuration having high volumetric efficiency due to its integral body design, yet possessed of sufficient aerodynamic efficiency to provide; 1) an entry α corridor of approximately four degrees, 2) guaranteed down and cross range, and 3) conventional landing capability.

The body shape is designed to accommodate the three crew members in either the side-by-side seated or supine positions, thus optimizing the tolerance to both boost and re-entry accelerations while providing conventional pilot orientation and visibility for normal approach and landing. The upper surface cross-section contour is defined by the minimum arc which encloses the crew and equipment. The bottom surface is a portion of a 370 inch radius sphere. The upper and lower surfaces are joined by a two-foot diameter curved leading edge which contributes to directional stability in the low and mid angle of attack ranges. The useful volume of this configuration for a given planform area is the highest of all conventionally landable vehicles studied. Two

TABLE I-1-I

APOLLO CONFIGURATIONS
GEOMETRIC SUMMARY TABLE

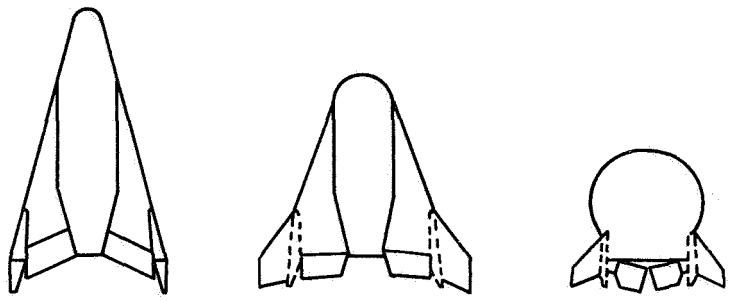

Parameter	High L/D	High Attitude	Modified Lenticular
Useful Volume (ft^3)	340	300	250
S Planform Area (ft^2) (ref.)	238.0	215.5	105 (Elevons not included)
$\bar{c}$ MAC (in.) (ref.)	231.4	187	128 (Elevons not included)
Sta LE $\bar{c}$	109.1	45.8	7.6
b Span (ft)	13.7	14.7	10.8
$\frac{S_e}{S}$ Elevon Area Ratio (Total)	.09	.0955	.116
$\frac{S_v}{S}$ Vertical Fin Area Ratio (total folding)	.229	.24	.30

NOTE: Geometric details for each configuration are given on three-view drawings in Figures 31, 32, and 33.

CONFIDENTIAL

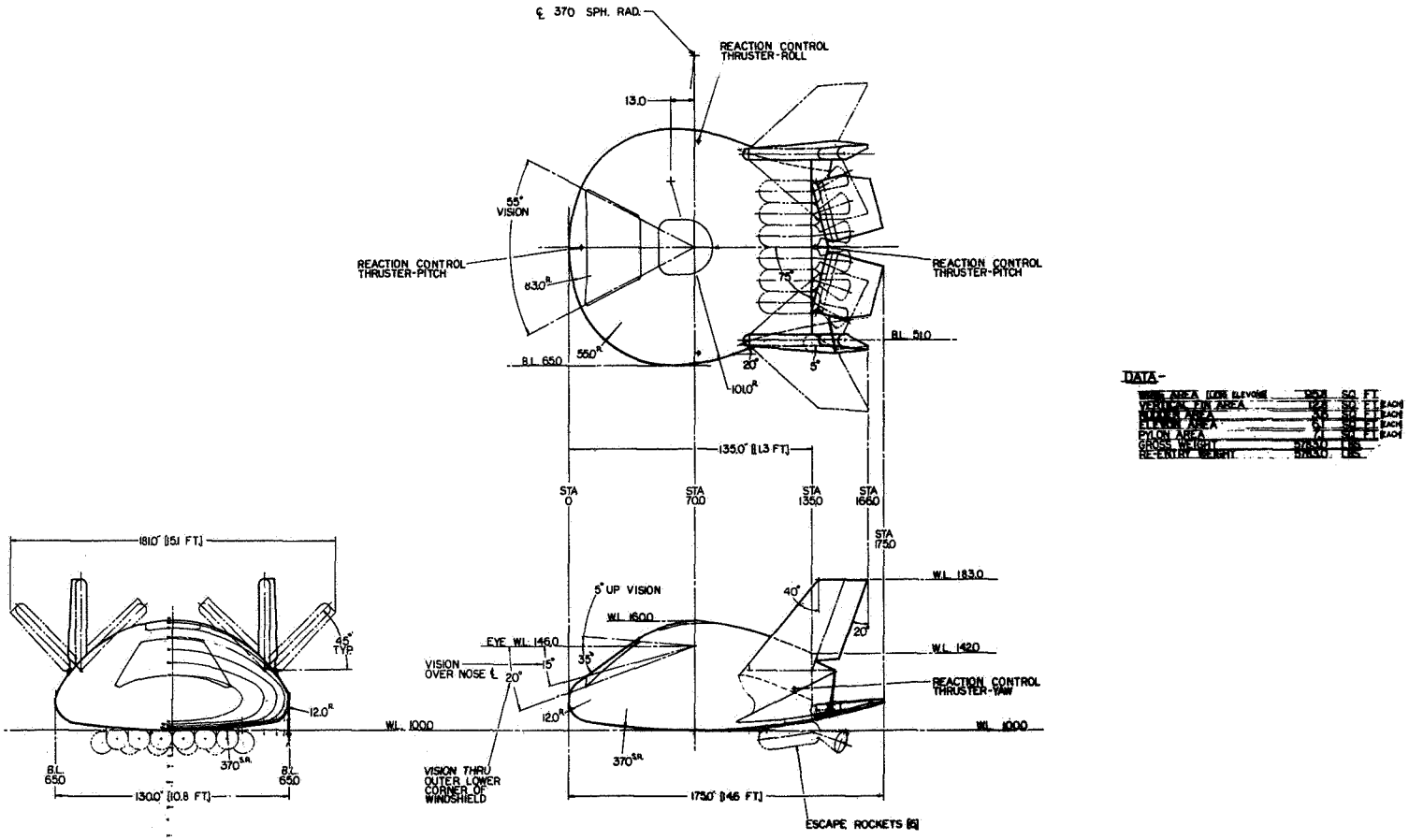

Figure I-1-33. General arrangement - APOLLO recovery vehicle - "R-3" - concept 4

CONFIDENTIAL

skewed planes compound the aft end of the body such that they provide positive directional stability at angles of attack above approximately 30 degrees to augment the diminishing directional stability contribution of the leading edge during high attitude hypersonic flight. The vehicle is equipped with elevons located behind the body for hypersonic pitch and roll control. Variable geometry fin surfaces are also provided for trim at low angles of attack during final approach and landing. The configuration is considered aerodynamically stable in pitch and yaw at all attitudes in the normal flight modes.

Initial atmospheric re-entry is accomplished in the high attitude range ($50° < \alpha < 90$). During this phase, three-axis reaction controls provide the initial high attitude orientation and supplement the elevon aerodynamic control moments during a transitional period until the aerodynamic elevon control forces reach design levels for independent operation. Because the vehicle is inherently stable in both pitch and yaw for most vehicle attitudes, the pitch and roll control moment supplied by the elevons are sufficient for flight path control. At or near $\alpha = 90°$ where the directional stability disappears, some supplementary low-level yaw control moments are supplied by the reaction control system. The maximum useful hypersonic L/D is about 0.7 in this high attitude flight phase.

The vehicle maintains high attitude flight at least until tolerable equilibrium heating conditions for low attitude flight are attained. Subsequent transition to low attitude flight then depends upon energy management, range control and flight control considerations. The variable geometry fins which are folded on top of the vehicle during the high attitude initial re-entry to protect them from the extremes of aerodynamic heating, are unfolded for the low attitude glide phase. These fins provide directional stability and roll-yaw control capability as well as the added longitudinal stability necessary for transition and trim in the low attitude range ($0° < \alpha < 50°$). Rudder-vons located at the trailing edge of these fins provide additional control capability. The maximum hypersonic-supersonic L/D in this latter glide phase approaches 1.0. Final approach and landing occurs at subsonic speeds at an L/D of about 5.0.

1.6.1 Aerodynamic Characteristics

The aerodynamic characteristics of the modified lenticular configuration have been studied in the subsonic, supersonic, and hypersonic flight regimes. In the hypersonic

regime most of the effort was devoted to high attitude characteristics whereas at sub and supersonic Mach numbers, the conventional angle of attack range was of primary interest. All of the aerodynamic data presented are applicable to the modified lenticular configuration shown in Figure I-1-33. The force and moment coefficients are based on a reference area of 105 square feet and a reference length (mac) of 128 inches. The desired center of gravity location is Station 74, Water Line 123 which corresponds to 51.8 percent of the mean aerodynamic chord of the projected planform area exclusive of fins and elevons.

1.6.1.1 GENERAL TRENDS

The trends of longitudinal and directional stability throughout the Mach range are summarized in Figures I-1-34 and I-1-35. The ability of the variable geometry fins to adequately augment both longitudinal and directional stability over the Mach range and to provide low attitude trim for final approach and landing is shown. The fin size was designed to a low-speed requirement for small but positive longitudinal and directional static margins. The present fins meet this condition with a fin position of $\phi = 50°$ which provides over-all longitudinal and directional static margins of 1.0 and 4.0 percent respectively. These margins widen appreciably through the transonic Mach number range and then decrease again to a minimum near M = 2.5. Here, the longitudinal requirement for low positive static margin can be met with a fin position of only $\phi = 31°$, and the increased directional effectiveness of the fins in this more vertical position is required to provide a directional stability margin. However, both margins are positive and a specific program of fin position versus Mach number will optimize the fin contribution to both longitudinal and directional stability to maintain the over-all static margins at acceptable levels. In the event that the present margins are not acceptable, they can be increased by a nominal increase in fin size. Although the transition from M = 2.5 to hypersonic velocities has not been investigated in detail, the vehicle will normally tend toward higher angles of attack as the angle for L/D_{MAX} increases, thereby increasing the local angle of attack on the folded out variable geometry fins and the longitudinal and directional static margins as well. In the high attitude range, the configuration is inherently stable in both planes with fins fully concealed. Therefore, it is felt that no serious stability problems will be encountered during the transition from high to low Mach numbers and attitudes.

Vehicle trim at high attitudes is controlled by the trailing edge elevons which have been designed to control the angle of attack from about 45 degrees to 90 degrees, with

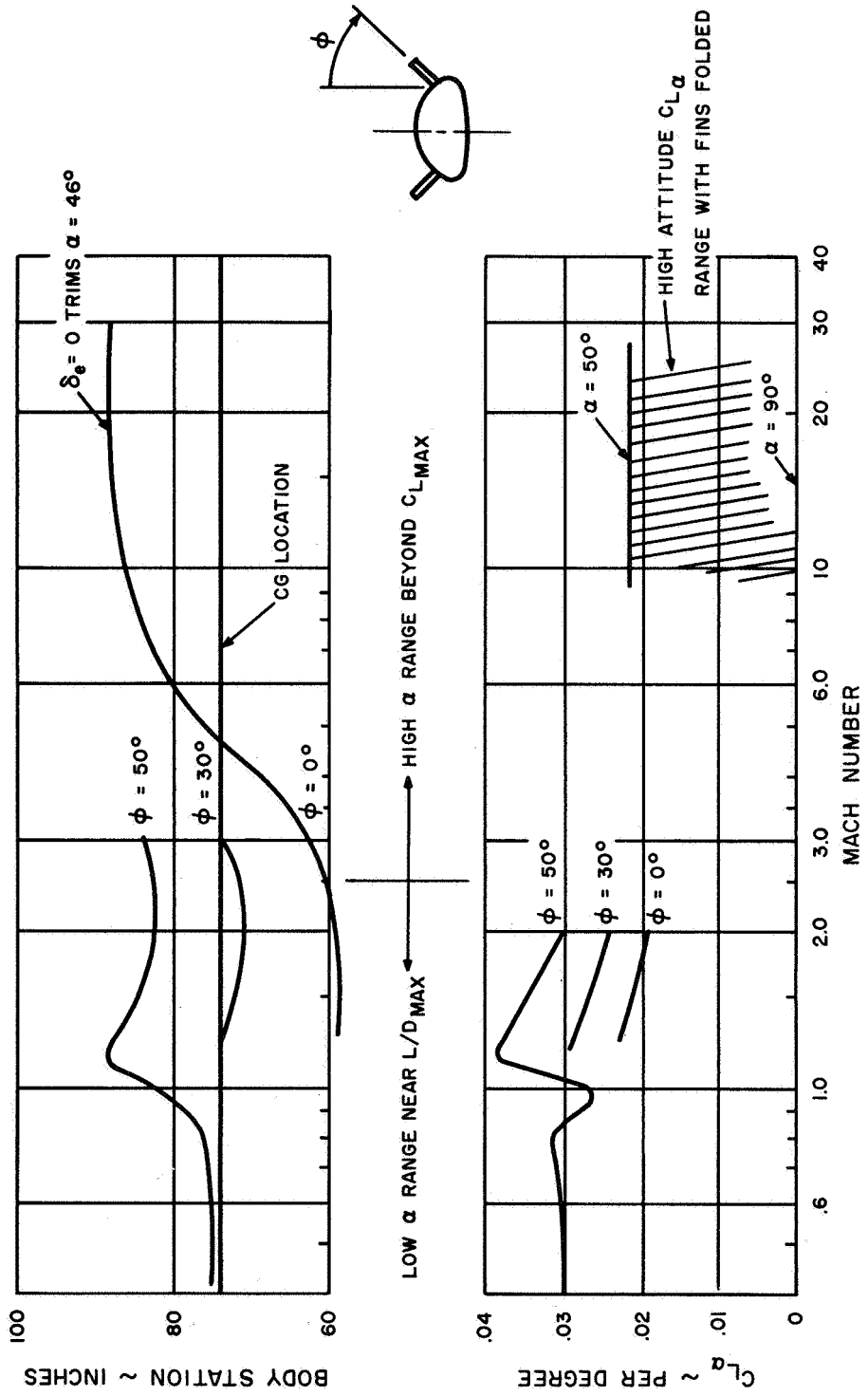

Figure I-1-34. Modified lenticular general longitudinal stability characteristics

CONFIDENTIAL

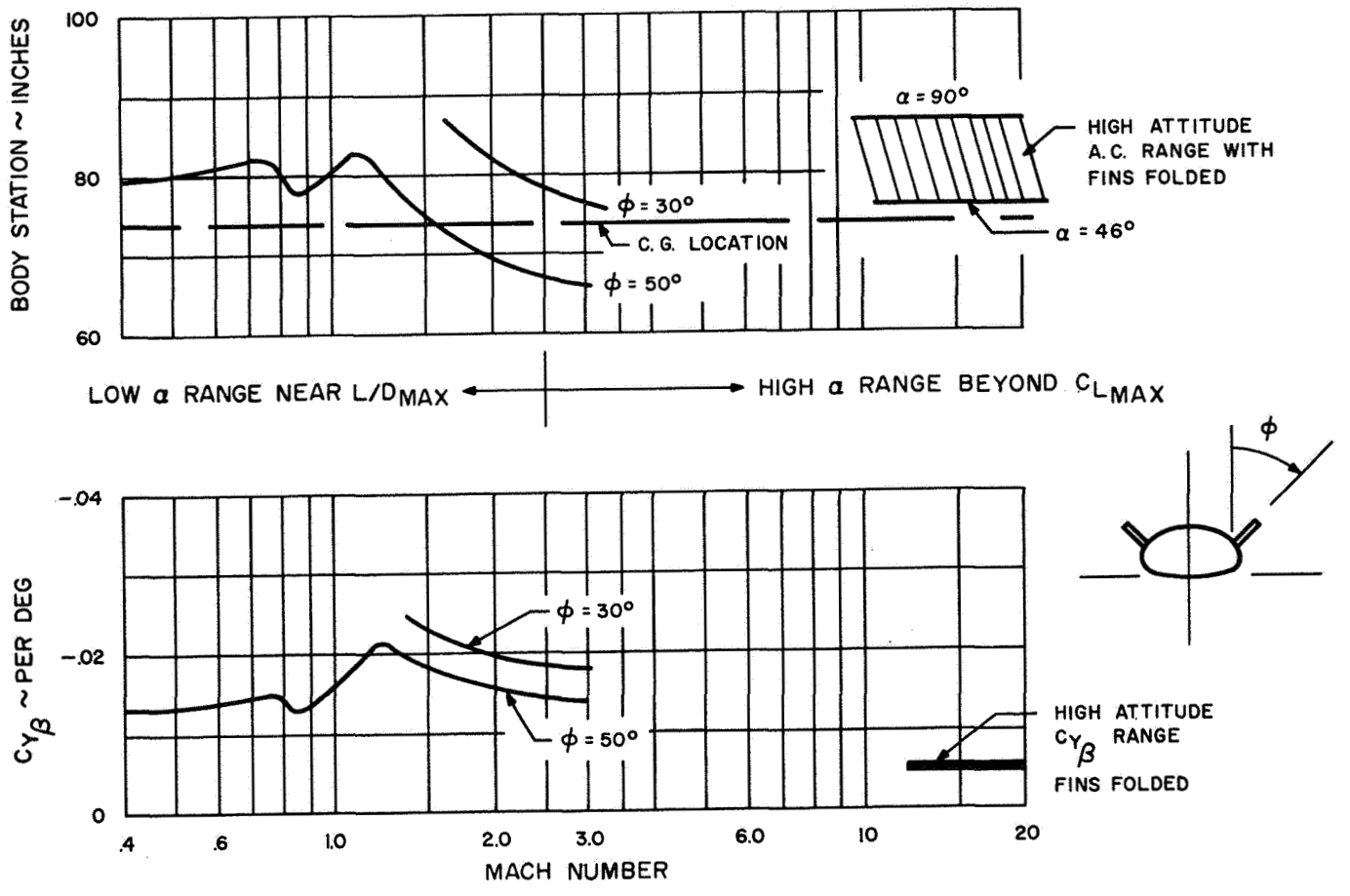

Figure I-1-35. Modified lenticular general lateral stability characteristics

CONFIDENTIAL

negative deflections only (T.E. up). Trim to lower angles of attack if desired can be accomplished at these Mach numbers with small positive deflections (T.E. down). It may be necessary to maintain the fins vertical or at slight positive ϕ 's for directional stability at angles of attack below 50 degrees. The longitudinal and directional aerodynamic center ranges for the high attitude ranges with fins fully concealed and the lift and side force curve slope trends over the Mach range are also shown in Figures I-1-34 and I-1-35.

1.6.1.2 SUBSONIC CHARACTERISTICS

1. Static Longitudinal and Directional Stability

The subsonic stability characteristics were determined by suitable modifications to existing data on lenticular shapes. Data were available in Ref. 56 and 57 for a vehicle which was similar in both shape and planform. The neutral point and lift curve slope trends with Mach number were adapted to the present configuration from these data. Stability contributions for the variable geometry fins were estimated by standard low-speed analytical techniques with suitable allowance for end plating effects of the pylon on the fins in the folded-out positions. A portion of the vertical pylon area was considered effective for directional stability. Since no directional data was available for bodies of this type, the body-alone directional characteristics were predicted using the method of Ref. 61. The variation of low-speed longitudinal and directional aerodynamic center and force coefficient slope with fin position, ϕ , is given in Figure I-1-36. The over-all lift curve slope for the $\phi = 50°$ fin position is conservatively shown as 0.030 per degree for zero angle of attack. Some non-linear increase with angle of attack is to be expected for this low aspect ratio configuration and in this case, a conservative increase of 10 percent for every 10 degree angle of attack was assumed.

2. L/D Characteristics

Preliminary tests reported in Ref. 56 through 60, have indicated L/D values ranging from 2 to 8 for lens shaped bodies. In these tests, L/D seemed to depend primarily on thickness ratio and profile shape. However, the effects of large amounts of camber and the addition of efficient lifting area, which are features of the present design, have not been sufficiently investigated to permit well substantiated predictions. The most realistic estimates which can be made at this time are given in Figure I-1-37. For the $\phi = 50°$ fin position which is recommended for final approach and

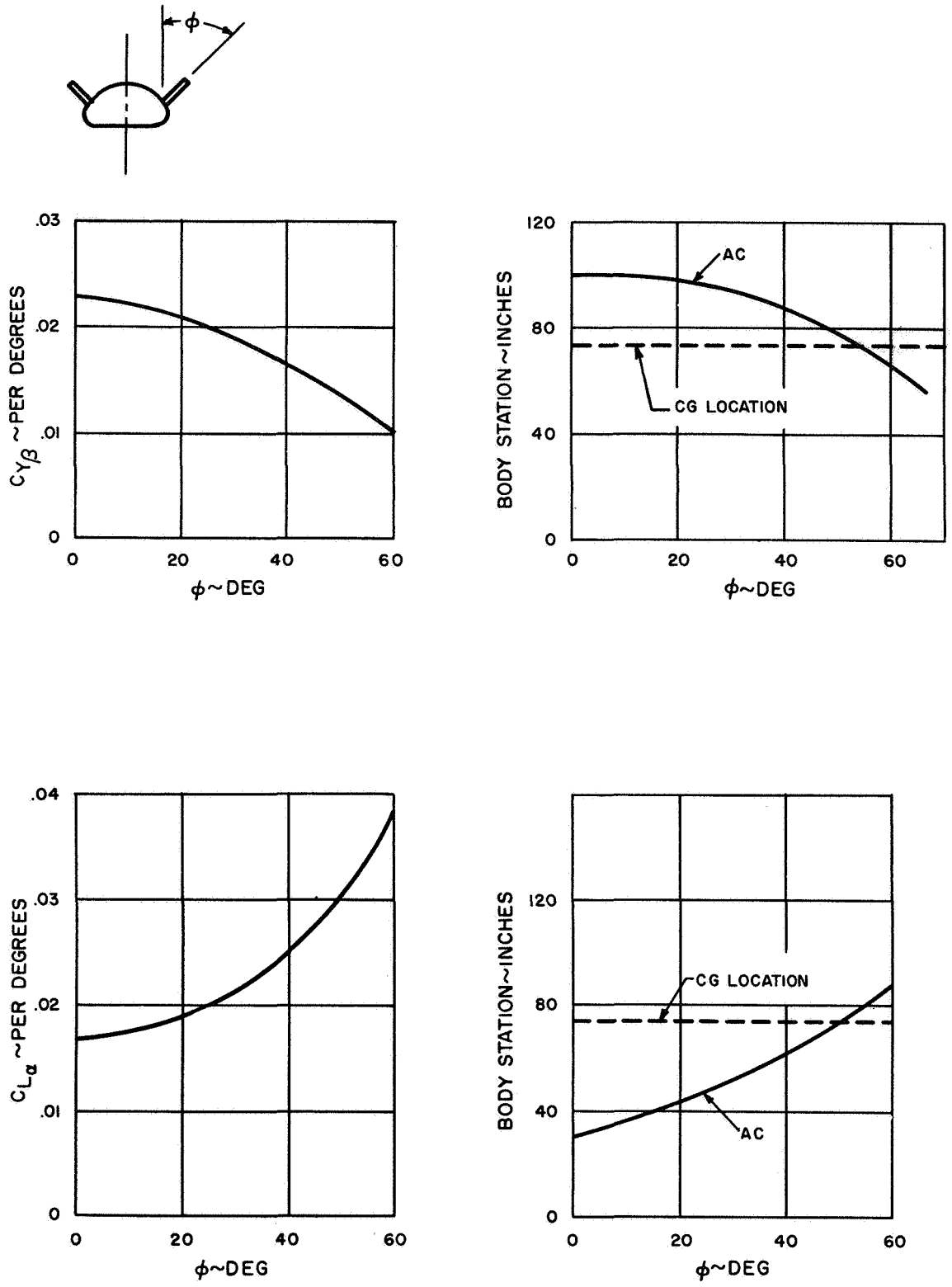

Figure I-1-36. Modified lenticular low speed effects of variable geometry on directional stability

CONFIDENTIAL

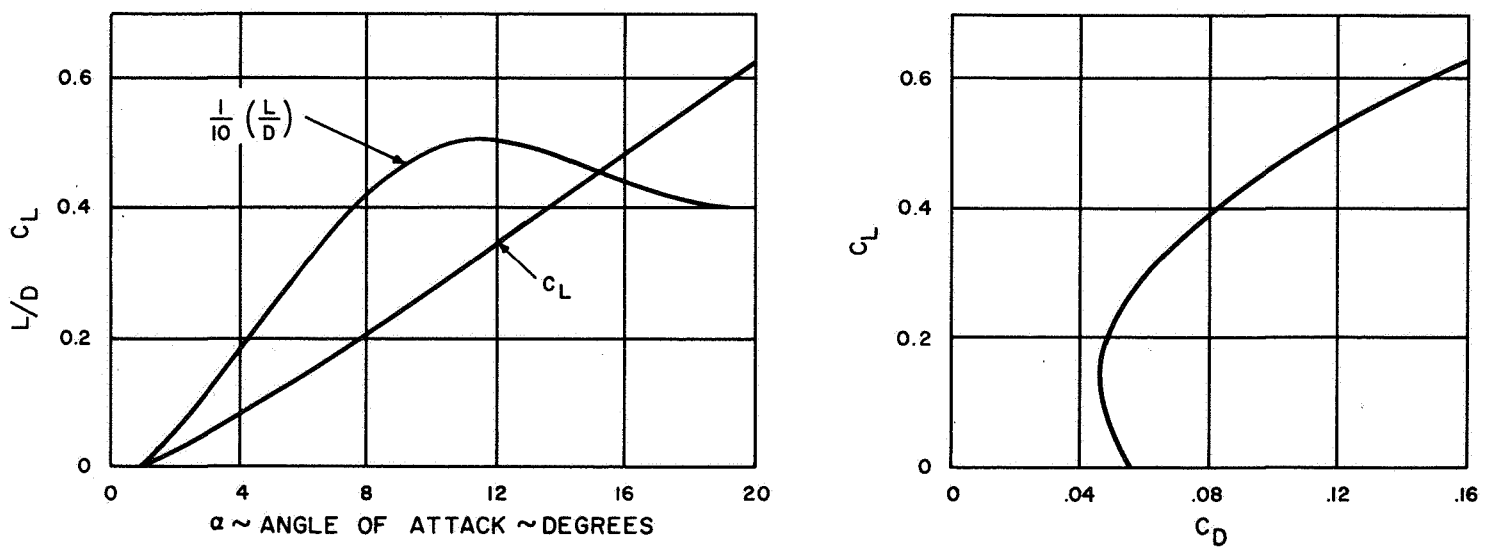

Figure I-1-37. Modified lenticular low speed longitudinal characteristics $\phi = 50°$

CONFIDENTIAL

landing, the maximum low-speed L/D is 5.0 with the peak occurring at 11.2° at a C_L of 0.32. In deriving these characteristics, consideration was given to the effects of such geometric parameters as camber, Reynolds number, transition locations, base area, and thickness ratio. No trim drag penalty is anticipated because, as is typical of most re-entry glide configurations, the low speed stability is nearly neutral and the trim control deflections required are small.

1.6.1.3 HYPERSONIC CHARACTERISTICS

The basic hypersonic longitudinal characteristics for the modified lenticular configuration are presented in Figure I-1-38. These characteristics are based on a modification to Newtonian theory in which the local pressure coefficient varied between the blunt modified and flat plate modified values depending on the local surface angle of attack. The local force coefficients were then integrated over the incident surface area to obtain force and moment characteristics. Separate contributions were obtained for the bottom surface, leading edge, upper fore-body, skewed aft sides, and the elevons in their various positions.

In determining the hypersonic L/D characteristics, the effect of altitude on the axial force coefficient was examined at M = 20 for both laminar and turbulent flow at several angles of attack. Real gas characteristics were used where applicable. The values estimated for laminar skin friction were below the turbulent values for altitudes in the 200,000 foot region. Since 200,000 feet is a good representative altitude for M = 20, the higher turbulent friction values were used for the lift and drag values presented. The skin friction contribution generally increases with angle of attack to about 40 degrees and then decreases until it becomes negligible at the very high attitudes.

The hypersonic maximum lift coefficient of 0.6 occurs at about 52 degree angle of attack at an L/D of about 0.7. Trim from this flight attitude to angles of attack near 90 degrees is provided by a range of elevon positions from tangent to the bottom surface ($\delta_e = 0$) to trailing edge full-up ($-\delta_{e_{max}}$). The maximum hypersonic L/D of 0.92 occurs at about 38 degree angle of attack which may be trimmed if desired by slight positive elevon deflections.

The hypersonic directional characteristics were determined for angles of attack above 45 degrees and are presented in Figure I-1-39. The configuration is directionally

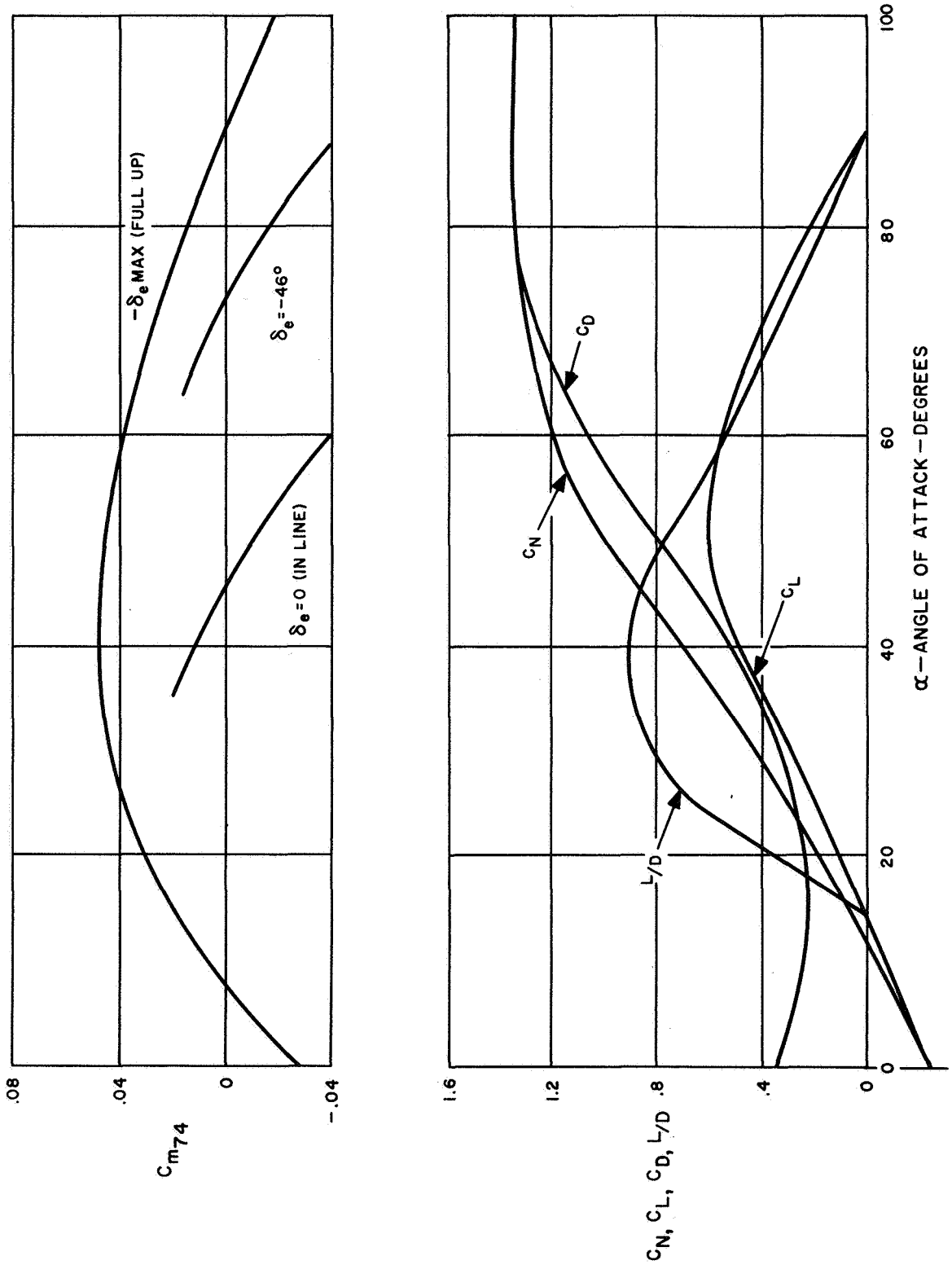

Figure I-1-38. Modified lenticular hypersonic longitudinal stability characteristics
M = 20 h = 200,000 ft fins folded

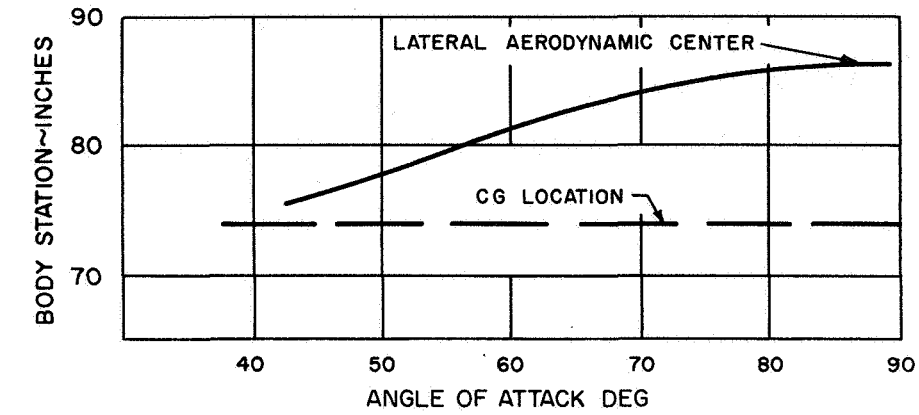

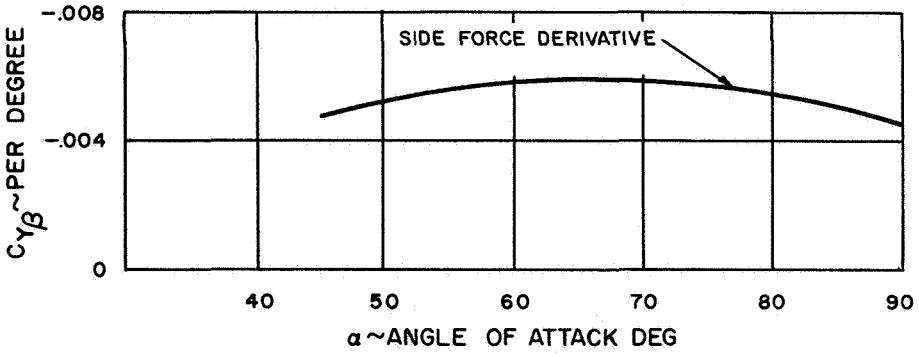

Figure I-1-39. Modified lenticular hypersonic lateral stability characteristics - fins folded

stable about Station 74 throughout the high attitude range with the fins fully concealed. The increasing static margin with increasing angle of attack derives both from the skewed planes on the side of the aft body and from the bottom surface curvature. The large curved leading edge also contributes static directional stability, but this contribution diminishes as the angle of attack increases. Since it is not ordinarily intended to trim angles of attack below that for $C_{L_{max}}$, with fins concealed, there is adequate directional stability for the entire superorbital flight range.

The modified lenticular configuration is such a compact and irregular geometric shape that the hypersonic characteristics obtained by modified Newtonian theory are subject to considerably more uncertainty than axisymmetric or more simple lifting shapes. The need for experimental confirmation, therefore, is that much more urgent. However, that the characteristics presented are reasonable for this configuration can be inferred by brief comparisons with the limited experimental data, as can be found in Ref. 60 and 62, for configurations which have some similar aspects. If experimental evidence indicates that trim characteristics for this particular shape are not optimum, it is felt that slight modifications to the basic shape can readily correct discrepancies.

1.6.1.4 DYNAMIC STABILITY AND HANDLING QUALITIES

A preliminary dynamic stability analysis was made for subsonic flight conditions. This consisted of a roots analysis of the characteristic equations obtained from the standard linearized aircraft equations of motion. As an indication of the glider's handling qualities, the results are compared with the requirements set forth in MIL-F-8785, Military Specification for Flying Qualities of Piloted Airplanes. Estimated values of stability derivatives were used for three flight conditions: 164 knots at sea level which corresponded to a landing touchdown configuration, 227 knots at sea level and 319 knots at sea level. The fin fold-out condition of the vehicle was taken as $\phi = 50$ degrees from the vertical. This condition is near optimum for pitch and yaw stability. The static longitudinal and directional stability margins were varied from the nominal estimate for the present configuration to establish trends.

The subsonic static and dynamic stability parameters that were estimated and used for this analysis are presented in Table I-1-II. The results of the roots analysis are shown in Figure I-1-40 and I-1-41. The longitudinal characteristics in Figure 40 show that with a one percent stable static margin, which is the estimated value for the

TABLE I-1-II. STABILITY DERIVATIVES USED IN ROOTS ANALYSIS

Longitudinal Nominal Values Flight Condition	1	2	3
C_D	.115	.056	.046
C_L	.51	.27	.13
α	.314	.183	.0925
C_{D_M}	0	0	0
C_{m_M}	0	0	0
C_{L_α}	1.546	1.546	1.546
C_{D_α}	.659	.235	0
C_{m_q}	-0.300	-.300	-.300
$C_{m_{C_L}}$	-.01	-.01	-.01
Values Used To Establish Trends			
C_{m_q}	-.200	-.200	-.200
$C_{m_{C_L}}$	0	0	0
$C_{m_{C_L}}$	-.02	-.02	-.02
$C_{m_{C_L}}$	-.03	-.03	-.03

TABLE I-1-II. STABILITY DERIVATIVES USED IN ROOTS ANALYSIS - Continued

Lateral Directional Nominal Values Flight Condition	1	2	3
C_{Y_β}	-.915	-.915	-.915
C_{Y_ρ}	-.0756	-.138	-.171
C_β	-.0378	-.0689	-.0853
C_ρ	-.495	-.495	-.495
C_α	.33	.33	.33
C_{n_β}	.031	.031	.031
C_{n_ρ}	.33	.33	.33
C_{n_α}	-.200	-.200	-.200
Values Used to Establish Trends			
C_{n_β}	.120 .057 .029 0	.120 .057 .029 0	.120 .057 .029 0
C_{n_α}	-.300	-.300	-.300
Inertia, Weight Data			
W	5913	5913	5913
I_x	1213	1150	1100
I_y	2049	2049	2049
I_z	2435	2516	2563
I_{xz}	-430	-261	0

TABLE I-1-II. STABILITY DERIVATIVES USED IN ROOTS ANALYSIS - Continued

Flight Conditions	
1	164.5 Knots, Sea level
2	227 Knots, Sea level
3	319 Knots, Sea level

present configuration, the glider is marginally within the MIL-8785 requirements. An increase in static margin to two percent falls slightly outside the specification; thus the smaller margin is more desirable. These results are for an estimated vehicle damping parameter, C_{m_q}, of -.30 per radian, which was estimated to be contributed by the folded-out fins. Compliance with this specification is not required but it is a useful yardstick for determining desirable stability margins.

Figure I-1-41 indicates that the lateral-direction oscillations of the present configuration will fall into the marginal region of the airplane specification also. It is known that roll-yaw damping parameters between curve A and B of the specification are acceptable from a flying qualities viewpoint. Increasing and decreasing the lateral static margin is shown to have an important effect on the roll-yaw characteristics, with increasing stability - favorable in this case. The effects of variation in vehicle velocity are shown to be small.

Finally, it should be emphasized that these results are for the basic airframe with no stability augmentation. Rate damping provided by the flight control system will normally be operative during manual control.

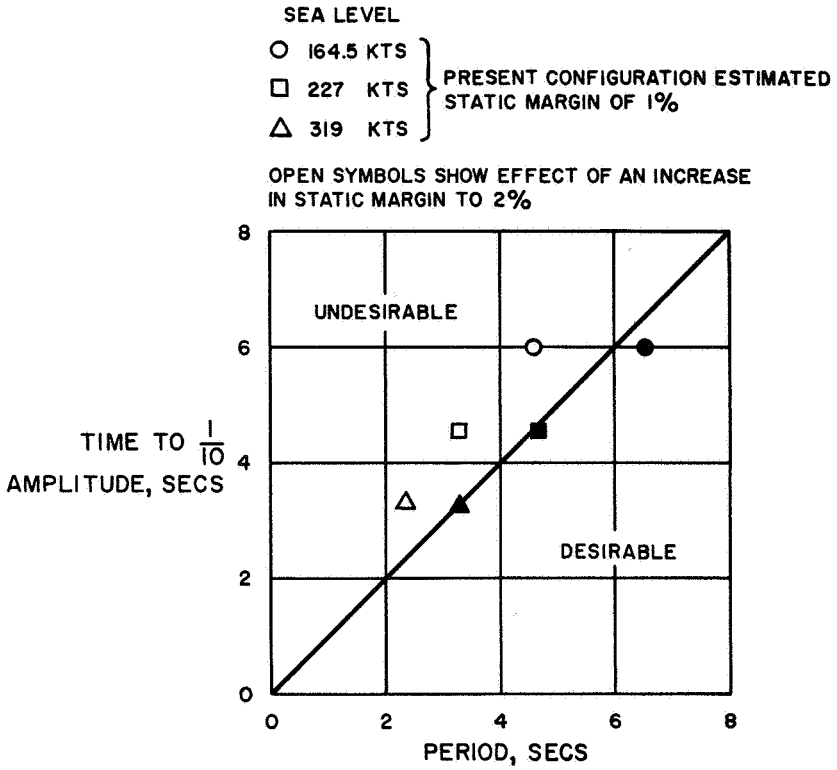

Figure I-1-40. APOLLO modified lenticular longitudinal dynamic stability characteristics - subsonic short period

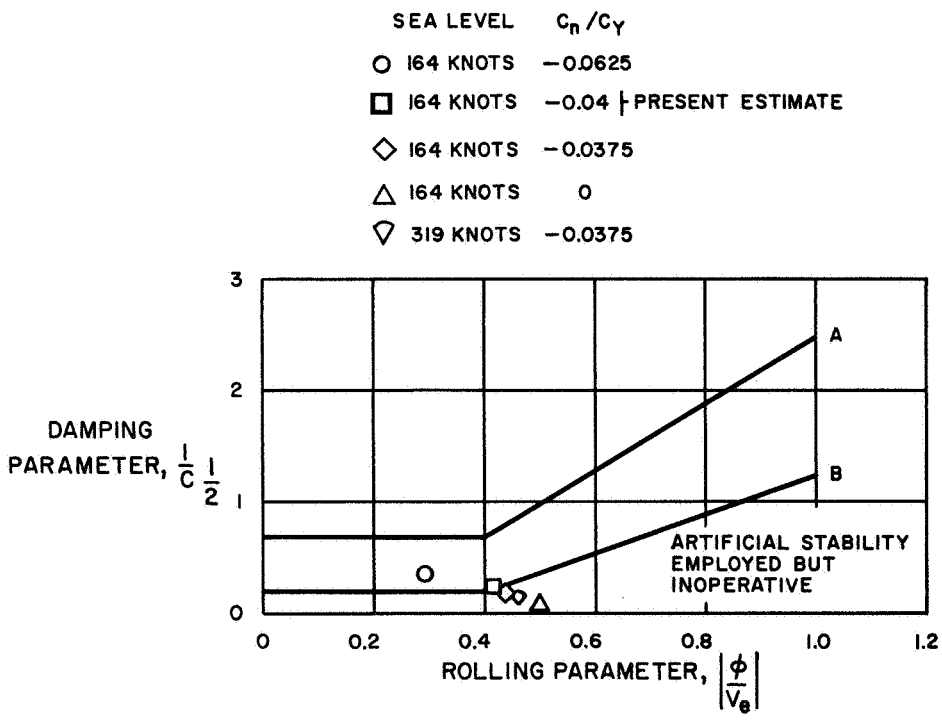

Figure I-1-41. APOLLO modified lenticular lateral directional stability characteristics - subsonic

2.0 Spacecraft

2.1 CONFIGURATION

The external geometry and general dimensions of the D-2 spacecraft are presented in Figure I-2-1. Inasmuch as aerodynamic heating does not pose a serious problem for this vehicle in composite configuration a conical nose was used to reduce the effect of nose blunting on drag. A minimum length flare was added based on the minimum static margin achieved at transonic speeds.

2.2 AERODYNAMIC CHARACTERISTICS OF THE SPACECRAFT

The center of pressure variation with Mach number for the spacecraft is shown in Figure I-2-2. This stability prediction was obtained from the vast amount of stability data available on flared bodies considered in ICBM and IRBM studies. References 36-38 are typical among the reports used in assessing the static stability of the spacecraft. The vehicle is observed to be statically stable over its entire flight speed range.

Since the space craft is the configuration that will abort off the pad and also in flight, trajectory calculations of this vehicle necessitate a knowledge of the zero lift drag coefficient and at angle of attack.

The drag coefficient vs Mach number for the launch-abort, spacecraft vehicle at zero lift ($\alpha = 0$ degree) and $\alpha = 5$ degrees and 10 degrees are presented in Figure I-2-3. These data were obtained using the semi-empirical method prescribed in Reference 19 and 20 for computing the zero lift drag coefficient for flared bodies of revolution and then adding additional increment in drag due to angle of attack effects.

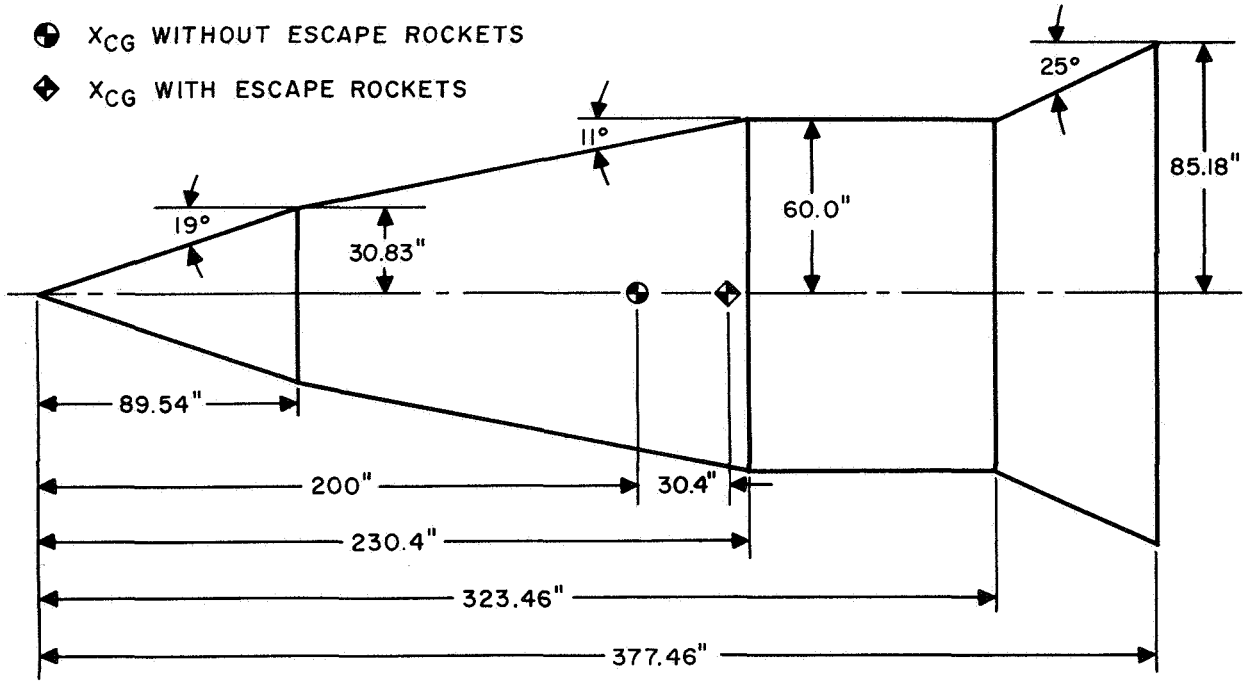

Figure I-2-1. Spacecraft and launch abort vehicle

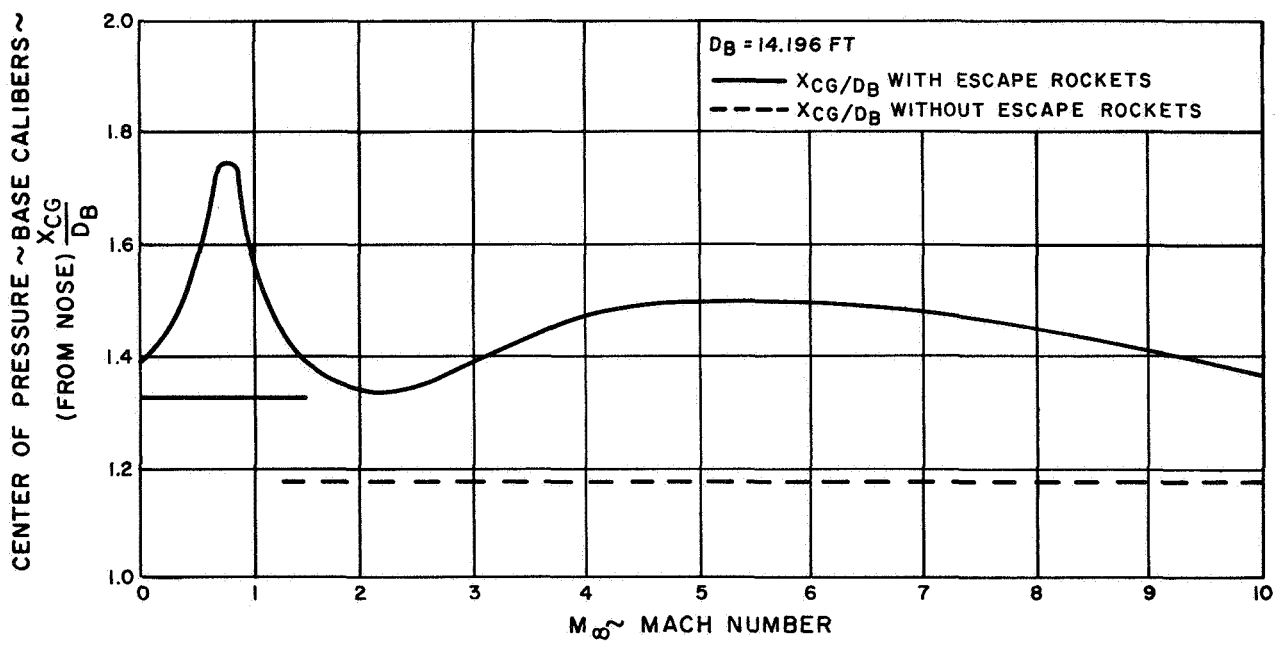

Figure I-2-2. Spacecraft and launch abort vehicle center of pressure location vs mach number $\alpha = 0°$

CONFIDENTIAL

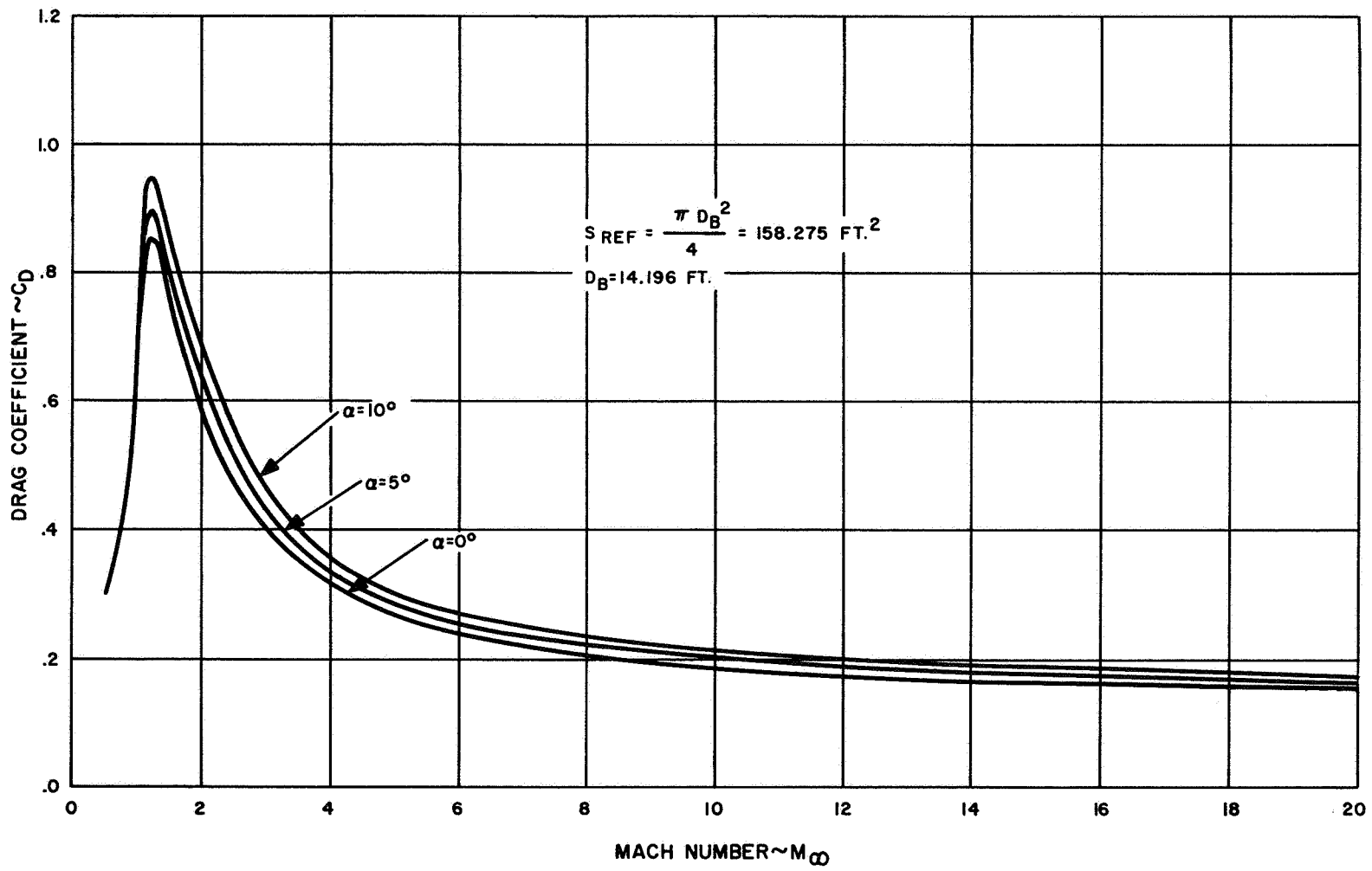

Figure I-2-3. Spacecraft - launch abort configuration variation of drag coefficient with mach number

CONFIDENTIAL

3.0 Effect of Spacecraft Aerodynamics on Booster

A study of the aerodynamic effects of the D-2 and R-3 spacecrafts on the Saturn C-2 booster (Figure I-3-1) was made to investigate the effect of winds and angle of attack on static stability. Gimballing capability of the Saturn S-1 stage[39] was found to be satisfactory -- although marginally so -- in nullifying the unstable moments of the upper stages including the D-2 spacecraft. For the R-3 spacecraft, the gimballing capability of the Saturn S-1 stage was found to be slightly deficient in this respect, for the center of gravity position assumed (e.g. between first and second stage). Inasmuch as the aerodynamic forces and moments acting on the various stages of the Saturn boost system are not accurately known, extensive wind tunnel investigations to obtain assurances of boost system static stability are recommended.

Also to achieve static stability for the Stage IV and spacecraft stage, aerodynamic fins were found to be necessary. The fin size necessary were computed to be swept 60 degrees and to have a 4.0 foot chord, a semi-span of 3.2 feet and a wedge cross section of 5 degrees semi-cone angle. These results are based on the assumption that the center of gravity for this final boost configuration was located at one-third the total vehicle length from the base.

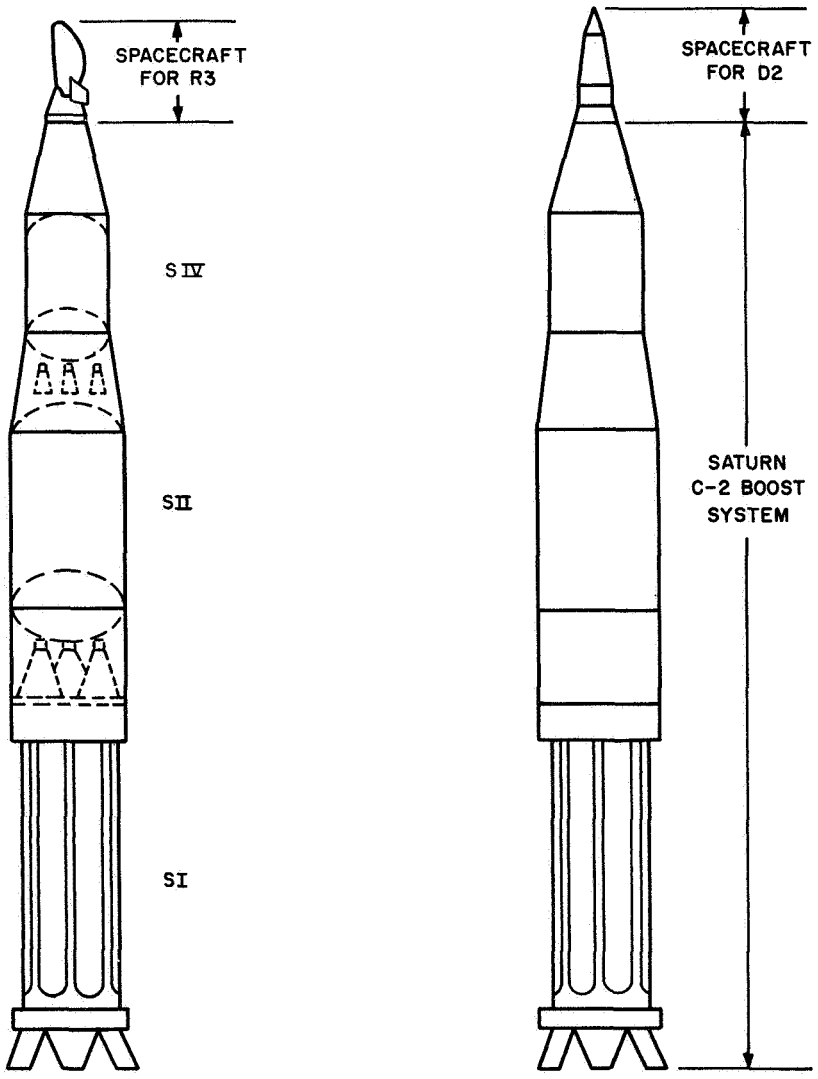

Figure I-3-1. Saturn C-2 booster system with spacecraft

REFERENCES

(1) LANGELO, V.A.

"Force And Moment Coefficients At Angles Of Attack To 180 Degrees By A Method Using Newtonian Theory." GE MSVD AERO. Fundamentals Memo No. 56.

(2) GIEGER, R.E.

"Hypersonic Lift-Drag Ratio For The APOLLO B-2 Vehicle." GE VSVD PIR.

(3) PECK, R.F., JACKSON, H.H. & STORER, E.M.

"A Review Of Some Aerodynamic Experimental Data Obtained In Support Of The G.E. - MSVD - NOSE-CONE PROGRAM." GE MSVD TIS R575D415. August 16, 1957.

(4) STORER, E.M.

"Summary Of Experimental Pressure Distribution Data." GE MSVD Addendum to ADM 2:16, July 22, 1959.

(5) GIRAGOSIAN, P.A. & FORSMAN, J.

"Preliminary Heat Transfer And Pressure Distribution Data On Configurations 3.1.C.C. (Cold) As Obtained From Tests Performed In The AEDC-GDF Hypersonic Blowdown Tunnels No. I. & II." GE MSVD PIR - 538-174, December 31, 1956.

(6) BUMBLEBEE AERODYNAMICS PANEL May 10-11, 1960.

(7) GRAVALOS, F.G., EMMONS, H. & EDELFELT, I.H.:

"The Supersonic Flow About A Blunt Body Of Revolution For Gases At Chemical Equilibrium." GE - MSVD, TIS 58SD245.

REFERENCES - Continued

(8) LAURENSON, D. I.

"Newtonian Approximation Of Aerodynamic Coefficients For Sphere-Cones And Sphere-Cone-Cylinder-Flares." GE MSVD AFM 106, August, 1960.

(9) ARMSTRONG, W.O.

"Effect Of Various Forebody Modifications On The Static Longitudinal Stability And Control Characteristics Of A Re-Entry Capsule At A Mach Number Of 9.6." NASA TM X-469.

(10) SHAW, D.S. & TURNER, K.L.

"Wind Tunnel Investigation Of Static Aerodynamic Characteristics Of A 1/9-Scale Model Of A Project Mercury Capsule At Mach Number From 1.60 to 4.65." NASA TM X-291, July, 1960.

(11) SPENCER Jr, B.

"An Investigation Of The Aerodynamic Characteristics At Subsonic Speeds Of A Non-lifting-Type Space-Capsule Model Simulating Escape And Re-Entry Configurations." NASA TM X-228, March, 1960.

(12) PEARSON, A.O.

"Wind Tunnel Investigation At Mach Numbers From 0.20 To 1.17 Of The Static Aerodynamic Characteristics Of A Possible Re-Entry Capsule." NASA TM X-262, March, 1960.

(13) LAURENSON, D.I. & McBRIDE, K.

"Newtonian Aerodynamic Characteristics Of Sphere-Cones And Cylinders At Angles Of Attack." GE MSVD ADM 1:28, February, 1961.

(14) BLANCHARD, Jr, W.S., & HOFFMAN, S.

"Full Scale Flight Test Of A Proposed Abort-Escape System For A Manned Space Capsule From Sea Level." NASA TM X-351, August, 1960.

REFERENCES - Continued

(15) ROYALL, Jr, J.F. & ENGLISH, R.D.

"Investigation Of Flight Performance Of Little Joe Booster For Project Mercury." NASA TM X-298, July, 1960.

(16) SCALLION, W.J.

"Full-Scale Wind Tunnel Investigation Of The Low-Speed Static Aerodynamic Characteristics Of A Model Of A Re-Entry Capsule." NASA TM X-220, October, 1959.

(17) SOMMER, S.C., SHORT, B.J. & COMPTON, D.L.

"Free Flight Measurements Of Static And Dynamic Stability Of Models Of The Project Mercury Re-Entry Capsule At Mach Numbers 3 And 9.5." NASA TM X-373, August, 1960.

(18) PEARSON, A.D.

"Wind Tunnel Investigation At Mach Numbers From 3.0 To 6.8 Of The Static Aerodynamic Characteristics Of Modified Mercury Exit And Escape Capsule Configurations." NASA TM X-324, September, 1960.

(19) LAURENSON, D.I.

"The Effect Of Mach Number On Aerodynamic Drag- A Compilation Of Experimental Data." GE MSVD ADM 1:14, September 8, 1959.

(20) LAURENSON, D.I.

"A Semi-Empirical Method For Preliminary Estimation Of The Drag Of Axisymmetric Ballistic Re-Entry Vehicles." GE MSVD ADM 1:24, July 7, 1960.

(21) PEARSON, A.O.

"Wind Tunnel Investigation At Mach Numbers From 0.50 To 1.14 Of The Static Aerodynamic Characteristics Of A Model Of A Project Mercury Capsule." NASA TM X-242, July, 1960.

REFERENCES - Continued

(22) PEARSON, A.O.

"Wind Tunnel Investigation At Mach Numbers From 0.40 To 1.14 Of The Static Aerodynamic Characteristics Of A Non-Lifting Vehicle Suitable For Re-Entry." NASA MEMO 4-13-59L, May, 1959.

(23) BROWN, S.W. & MOSELEY, Jr. W.C.

"Summary Of Wind Tunnel Investigations Of The Static Longitudinal Stability Characteristics Of The Production Mercury Configurations At Mach Numbers From 0.05 To 20." NASA MEMO X-491, February, 1961.

(24) LANGLEY, NASA

"Project Apollo - Preliminary Re-Entry Vehicle Force Test Results." 1927-45-2, March, 1961.

(25) DICKEY, R.R.

"The Effect Of Several Types Of Flaps On The Aerodynamics Characteristics Of An Entry Capsule With Spherical Segment Face." NASA AMES LABORATORY, January, 1961.

(26) SPENCER, Jr., S.

"An Investigation Of The Aerodynamic Characteristics At Subsonic Speeds Of A Non-Lifting-Type Space-Capsule Model Simulating Escape And Re-Entry Configurations." NASA TM X-228, March, 1960.

(27) PENLAND, J.A. & ARMSTRONG, W.O.

"Preliminary Aerodynamic Data Pertinent To Manned Satellite Configurations." NACA RM L58E132, July 21, 1958.

(28) PENLAND, J.A. & ARMSTRONG, W.O.

"Static Longitudinal Aerodynamic Characteristics Of Several Wing And Blunt-Body Shapes Applicable For Use As Re-Entry Configurations At A Mach Number Of 6.8 And Angles Of Attack Up To 90 Degrees." NASA TM X-65, October, 1959.

REFERENCES - Continued

(29) ALLEN, J.H.

"Motion Of A Ballistic Missile Angularly Misaligned With The Flight Path Upon Entering The Atmosphere And Its Effect Upon Aerodynamic Heating Aerodynamic Loads and Miss Distance." NACA TN 4048.

(30) KEHLET, A.B.

Private Communication-Summary Of Dynamic Damping-In-Pitch Data For Project Mercury To P.A. Giragosian - GE - M&SVD

(31) WEHREND, Jr., W.R. & REESE, Jr., D.E.

"Wind Tunnel Tests Of The Static And Dynamic Stability Characteristics Of Four Ballistic Re-Entry Bodies." NASA TM X-369, June, 1960.

(32) REESE, Jr., D.E. & WEHREND, Jr., W.R.

"An Investigation Of The Static And Dynamic Aerodynamic Characteristics Of A Series Of Blunt-Nosed Cylinder-Flare Models At Mach Numbers From 0.65 To 2.20." NASA TM X-110, January, 1960.

(33) EMERSON, H.F. & ROBINSON, R.C.

"The Transonic Damping In The Pitch Of Three Cylinder Flare Models With Various Degrees Of Nose Bluntness." NASA TM X-368, August, 1960.

(34) BUELL, D.A. & JOHNSON, N.S.

"An Experimental And Analytical Investigation Of The Dynamics Of Two Blunt Bodies At Subsonic Speeds." NASA TM X-18.

(35) SHORT, B.J. & SOMMER, S.C.

"Some Measurements Of The Dynamic And Static Stability Of Two Blunt-Nosed, Low-Fineness-Ratio Bodies Of Revolution In Free Flight At M-4." NASA TM X-20.

REFERENCES - Continued

(36) LAURENSON, D.I.

"Summary Of Normal Force And Center Of Pressure Data On A Variety Of Blunt Bodies." GE MSVD ADM 1.12, November 14, 1958.

(37) KIRK, D.B. & CHAPMAN, G.T.

"The Effectiveness Of Conical Flares On Bodies With Conical Noses." NASA TM X-30, September, 1959.

(38) WAKEFIELD, R.M., KNECHTEL, E.D. & TREON, S.L.

"Transonic Static Aerodynamic Characteristics Of A Blunt Cone-Cylinder With Flared Afterbodies Of Various Angles And Base Areas." NASA TM X-106. December, 1959.

(39) DONLAN, C.J.

"Preliminary Saturn C-2 Information." NASA, March 1, 1961.

(40) TAYLOR, G.I. & MACCOLL, J.W.

"The Air Pressure On A Cone Moving At High Speeds." Roy.Soc.(A) Vol 139 (1933).

(41) KOPAL, F.

"Tables Of Supersonic Flow Around Cones." MIT. Dept of Elec. Engr. TIR. No. 1. 1947.

(42) FERRI, A.

"Elements Of Aerodynamics Of Supersonic Flows." The MacMillan Co. 1949.

(43) BRONG, E.A.

"Solution Of The Prandtl-Meyer Equation For A Real Equilibrium Gas." GE MSVD, TIS R59SD445.

REFERENCES - Continued

(44) GRAVALOS, F.G., BRONG, E.A., & EDELFELT, I.H.

"The Calculation Of Flow Fields With Secondary Shocks For Real Gases At Chemical Equilibrium." GE MSVD TIS R59SD419, May, 1960.

(45) FITZGIBBON, S.

"Documented Flow Field Results." GE MSVD ADM 5:02, 1960.

(46) STORER, E.M. & RIDYARD, H.W.

"A Comparison Of Invisced And Viscous Drag Coefficient For Several Blunt Bodies." GE MSVD ADM 1:33, 1960.

(47) CROSSWELL, J.

"A Method For Determining Shock Layer Flow Variables Distribution In Axi-Symmetric Flows Around Sphere Cones." GE MSVD TIS R60SD395, 1960.

(48) NESTLER, D.E.

"Survey Of Theoretical And Experimental Determinations Of Skin Friction In Compressible Boundary Layers. Part I. The Laminar Boundary Layer On A Flat Plate." GE MSVD TIS R58SD249, 1958.

(49) IBID: PART II.

"The Turbulent Boundary Layer On A Flat Plate." GE MSVD TIS R58SD270, 1959.

(50) IBID: PART III.

"Effects Of Axial Force Variation Of Local Pressure And Surface Temperature For Laminar Boundary Layer." GE MSVD TIS 59SD339, 1959.

(51) IBID: PART IV.

"The Turbulent Boundary Layer With Axial Variation Of Pressure And Surface Temperature." GE MSVD TIS R59SD340, 1959.

REFERENCES - Continued

(52) IBID: PART V.

"The Effect Of Slip Flow." GE MSVD TIS R59SD343. 1959.

(53) TALBOT, L., STUDERIOUS, C., & SCALA, S.

"Aerodynamic Forces Due To Hypersonic Viscous Flow." American Physical Society Paper Presented at Divisional Meeting of Fluid Dynamics Section. November 21-237, 1960.

(54) EDSALL, R.H.

"Numerical Computation For Control Surface In Free Molecular Flow." GE MSVD Aero F.M. No. 99. 1960.

(55) Project Apollo Data Book Vol. II, General Electric Missile and Space Vehicle Department, March 14, 1961.

(56) WARE, GEORGE M.

"Static Stability And Control Characteristics At Low-Subsonic Speeds Of A Lenticular Re-Entry Configuration." NASA TM X-431, December, 1960.

(57) MUGLER, JOHN P., Jr., & OLSTAD, WALTER B.

"Static Longitudinal Aerodynamic Characteristics At Transonic Speeds Of A Lenticular-Shaped Re-Entry Vehicle." NASA TM X-423, December, 1960.

(58) DEMELE, FRED A., & BROWNSON, JACK J.

"Subsonic Longitudinal Aerodynamic Characteristics Of Disks With Elliptic Cross Sections And Thickness-Diameter Ratios From 0.225 To 0.425." NASA TN D-788 Advanced Distribution, March 6, 1961.

REFERENCES - Continued

(59) HOSSON, DENNIS F. & BLAKEMORE, THOMAS L.

"Static Longitudinal Stability And Control Characteristics Of Two Disk-Type Re-Entry Vehicles With Lenticular And Elliptical Cross Sections At Subsonic, Transonic, And Supersonic Speeds." NASA Proposed Memorandum (Unpublished).

(60) MAYO, EDWARD E., & BLAKEMORE, THOMAS L. Jr.

"Project Apollo Summary Of Studies Of A Lenticular Vehicle Capable Of Entry From A Lunar Mission." NASA Space Task Group Working Paper, March 3, 1961.

(61) ALLEN, JULIAN H.

"Estimation Of The Forces And Moments Acting On Inclined Bodies Of Revolution Of High Fineness Ratio." NASA RM A9126, November 14, 1949.

(62) Project Apollo - Preliminary Re-Entry Vehicle Force Test Results. NASA-Langley Field, March 1, 1961.

(63) Dyna-Soar I, Project WS 464L, Report 59RDZ11

"Flight Controls Report - Vol I" Martin Space Flight Report No. ER 10374.

4.0 Landing Retardation and Maneuvering

4.1 PROBLEM DEFINITION

The recovery of ballistic type re-entry vehicles has been successfully accomplished on a number of occasions in the RVX-1, RVX-2 and Discoverer Programs. Recently, Project Mercury joined the ranks of successful re-entry recovery demonstrating a capability for manned capsule return from outer space. It is worth noting that all of these vehicles used a straight-forward parachute approach to the solution of the retardation problem. However, it is equally important to remember that all of these programs involve mission profiles and system specifications that are considerably less stringent than those of Project APOLLO. Nevertheless, considerable insight into the solution of the landing and recovery problem for APOLLO can be gained by treating the recovery flight phase as a straight-forward retardation problem. This approach, however, must be tempered with the following four facts:

1. The recovered payload weight will be two to three times greater (or more) than the aforementioned vehicles.
2. Point landing requirements and the possiblity of large tolerances on the terminal portion of the re-entry trajectory point to the need for consideration of terminal maneuverability (possibly during the recovery phase).
3. Since human lives are at stake, fail safe abort capability is a must for any practical system design.
4. Proper consideration to impact attenuation designs must be given when the terminal (final) retardation system is designed.

Using this line of reasoning, then, in conjunction with a consideration of the overall system specifications resulted in the following list of ground rules for the recovery system design analysis:

1. Recoverable Payload Weight = 5000 to 10,000 lbs. (The final design was applied to the 5000 lb. D-2 vehicle.)

2. Vertical descent velocity not to exceed 100 ft/sec. (Final design value of 30 ft/sec was selected for the study program).
3. Axial loads not to exceed 12 g's in steady state or 20 g's in transient; lateral loads not to exceed 3 g's in steady state or 6 g's in transient.
4. Recovery system to be applicable in both normal and abort mission situation (i.e. avoid use of separate systems for abort and normal missions).
5. Maximum recovery system weight (exclusive of abort escape system) not to exceed 10 percent of total vehicle weight. (The recommended parachute system is about 5 percent of the vehicle weight.)
6. "Point" landing area to be a 20 mile square.
7. System reliability to be exceptional; thus dictating the use of proven concepts, or design techniques that are amenable to thorough experimental verification within current or projected testing capabilities (either ground or in flight).

These specifications, then, essentially define the landing and recovery problem and provide a framework within which the design analyses must function. The trajectory limitations which delineate the flight environment in which the system must operate are defined by the D-2 equilibrium glide trajectory of Figure I-4-1.

4.2 THE CONVENTIONAL RETARDATION SYSTEM OF THE SEMI-BALLISTIC RE-ENTRY VEHICLE, D-2

4.2.1 Normal Re-entry Landing

A rather straight-forward approach to a simple recovery system solution can be taken by considering the use of fairly conventional retardation devices. The equilibrium glide trajectory of Figure I-4-1, which is indicative of a typical flight path for the D-2 re-entry vehicle, indicates that severe environments for retardation actuation will not be a problem. The recovered payload weight, however, is large; 5000 lbs. for the D-2 R/V and multi-stage retardation systems become necessary in order to achieve a velocity decrease for final stage deployment, and hence a tolerable deployment shock load force. Such weights also necessitate large final stage drag areas (C_DA) for equilibrium descent velocity at impact (V_t) of 30 fps. For large C_DA values, large retardation devices are required, possibly in cluster form. The recovery system weight considerations advise the use of self inflatable devices to attain the large C_DA values necessary for the final stage. At the present time, parachutes still appear to be an optimum selection.

A series of parachute drag retardation systems have been developed as a result of the evolution of the APOLLO D-2 semi-ballistic-type re-entry vehicle. The two main considerations causing modifications of the parachute systems during the study were perturbations in vehicle weight and re-entry trajectory which occurred in the optimization of the system design. A description of the various retardation systems that were investigated is given in Table I-4-I, where initial design concepts placed the weight of the re-entry vehicle between 5,000 lb and 10,000 lb.

TABLE I-4-I

INITIAL DESIGN CONCEPTS

System I. 3 Stage - 2 Chute, Payload Weight = 10,000 Pounds

Stage and Description	Deployment Conditions	D_o (ft)	C_{D_o}	Approx. Wt.-Total (lbs)	Packing Volume (in^3)	V_t (fps)
Pilot Chute-Guide Surface	Prior to 1st Stage	3	0.7	1	50	--
1-Ribbon Chute-Fully Open	h = 60,000 ft V = 1250 fps	12	0.35(super-sonic) 0.50(sub-sonic)	50 (1000 lb ribbon)	5000	--
2-100 ft conical type - 180 gore (three each)--reefed	h = 30,000 ft V = 456 fps	6.4 each	----	600	12,400	--
3-Same as 2--fully open	h = 27,388 ft V = 218 fps	100 each	0.7 (in cluster)	Same System as #2 above	Same System as #2 above	25

System II. 4 Stage - 1 Cone + 2 Chute, Payload Weight = 7,000 Pounds

Stage and Description	Deployment Conditions	D_o (ft)	C_{D_o}	Approx. Wt.-Total (lbs)	Packing Volume (in^3)	V_t (fps)
Pilot Chute-Guide Surface	Prior to 1st Stage	3	0.7	1	50	--
1-Inflatable Cone - 90°	h = 80,000 ft V = 2400 fps	0.88 Body Dia.	1.0(super-sonic)	10(esti-mate)	---	--
2-Ribbon Chute-Fully Open	h = 75,565 ft V = 1367 fps	25	0.35(super-sonic) 0.50(sub-sonic)	30 (300 lb. ribbon)	2500	--
3-See Note						
4-77 ft. conical type-108 gore (two each) -- fully open	h = 15,000 ft V = 182 fps	77	0.7 (in cluster)	265	10,000	30

System III. 3 Stage - 2 Chute, Payload Weight = 7,000 Pounds

Pilot Chute-Guide Surface	Prior to 1st Stage	3	0.7	1	50	--
1-Ribbon Chute-fully open	h = 58,000 ft V = 1183 fps	25	0.35(super-sonic) 0.50(sub-sonic)	30 (300 lb. ribbon)	2500	--
2-See Note						
3-77 ft. conical type-108 gore (two each) -- fully open	h = 15,000 ft V = 182 fps	77	0.7 (in cluster)	265	10,000	30

NOTE: Reefing required in this stage, but preliminary analysis of System II and III did not include reefing.

System IVA. 3 Stage - 2 Chute, Payload Weight = 5000 Pounds

Stage and Description	Deployment Conditions	D_o (ft)	C_{D_o}	Approx. Wt.-Total (lbs)	Packing Volume (in^3)	V_t (fps)
Pilot Chute-Guide Surface	Prior to 1st Stage	3	0.7	1	50	--
1-Ribbon Chute-Fully Open	h = 58,000 ft V = 1183 fps	25	0.35(super-sonic) 0.50(sub-sonic)	30 (100 lb. ribbon)	3000	--
2-65 ft. conical (two each) reefed	h = 15,000 ft V = 140 fps	7 ft each	--	202	7000	--
3-Same as 2 fully open	h = 14,260 ft V = 117 fps	65 ft each	0.7 (in cluster)	202	7000	30

System IVB. 3 Stage - 2 Chute, Payload Weight = 5000 Pounds

Pilot Chute-Guide Surface	Prior to 1st Stage	3	0.7	1	50	--
1-Ribbon Chute Fully Open	h = 58,000 ft V = 1183 fps	16	0.35(super-sonic) 0.5 (sub-sonic)	10	1200	--
2-65 ft. conical (two each) reefed	h = 15,000 ft V = 178 fps	7 ft each	--	202	7000	--
3-Same as 2 fully open	h = 13,750 ft V = 114 fps	65 ft each	0.7 (in cluster)	202	7000	30

System V. 3 Stage - 2 Chute, Payload Weight ≐ 5000 Pounds

Stage and Description	Deployment Conditions	D_o (ft)	C_{D_o}	Approx. Wt.-Total (lbs)	Packing Volume (in^3)	V_t (fps)
Pilot Chute-Ribbon Type	Prior to 1st Stage	4	0.5	5	40	--
1-Ribbon Chute Fully Open	h = 25,000 ft V = 315 fps	16	0.5	10 (200 lb. ribbon)	700	--
2-Conical Type Chute-108 gore (three each) -- reefed	h = 22,953 ft V = 190 fps	19 each	0.7 Assumed	220	7000	--
3-Same as 2 above-fully open	h = 22,380 ft V = 93 fps	53	0.7 (in cluster)	220	7000	30

System VI. 3 Stage - 2 Chute, Payload Weight = 5000 lbs.

Pilot Chute-Ribbon Type	Prior to 1st Stage	6	0.5	1.5	90	--
1-Ribbon Chute Fully Open	h = 20,000 ft V = 300 fps	25	0.5	30	3800	--
2-Conical Type Chute-108 gore (three each) -- reefed	h = 19,290 ft V = 154 fps	19 each	0.7 Assumed	220	7000	--
3-Same as 2 Above-Fully Open	h = 18,600 ft V = 90 fps	53 each	0.7 (in cluster)	220	7000	30

Neglecting considerations of terminal maneuverability and abort and concentrating upon payload weight, re-entry trajectory, tolerable g conditions and impact velocity requirements, recovery systems I through III were designed for 7,000 lb and 10,000 lb vehicles. Terminal velocities at h = 0 were held to the 25-30 fps category, since early estimates of the optimum impact attenuation plus retardation system weight appeared to be located at the lower end of the terminal velocity scale. Calculation of Figures I-4-2, -3-4 and later proved this to be true. Systems IVA and IVB were designed during early phases of the study. When the nominal D-2 R/V equilibrium glide trajectory, Figure I-4-1 was developed, systems V and VI were designed. These two systems also included trade-offs with respect to the abort case and low altitude deployment. Parachute recovery system VI, described in Table I-4-I, was designed to retard the velocity of a 5,000 lb D-2 R/V to 30 fps at ground impact. More detailed information on impact attenuation studies and the selected landing and recovery subsystem appear in the landing and recovery section of Volume VII, Chapter 1. Other considerations taken into account during the design of this system were:

1. Keeping the overall deployment time as short as possible in order to present a minimum deployment time for the launch pad abort case.
2. Maintaining the ability to deploy at altitudes below 25,000 ft. in order to eliminate the possible problem of accurately sensing a pre-selected deployment altitude, thereby also allowing a maximum of altitude for maneuvering prior to retardation system actuation.
3. Retaining the ability to include a stabilization parachute if it should become necessary from a vehicle stability point of view.
4. Keeping parachute opening shock loads below the human "g" tolerance and parachute strength limitations.
5. Providing a maximum of stability and reliability to the overall recovery system.
6. Using experimental test data to determine parachute deployment and opening times where possible.
7. Keeping the recovery system weight to a minimum.

It was realized that trade-offs between the above considerations would be necessary in relation to their relative importance.

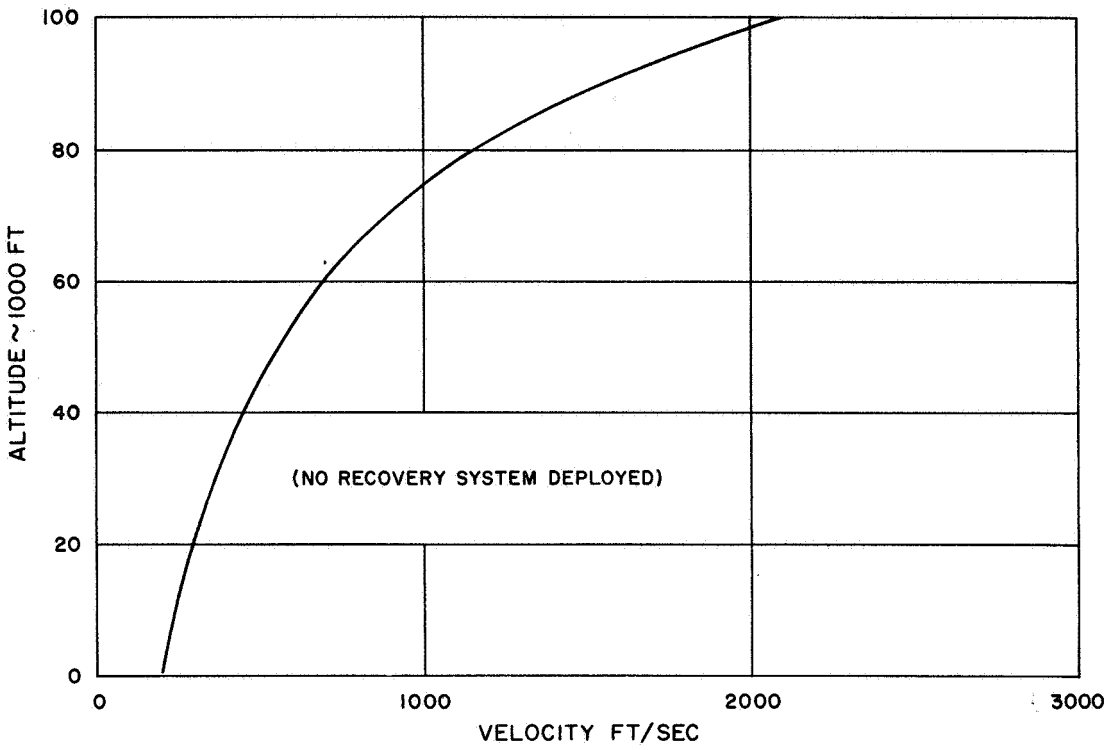

Figure I-4-1. Equilibrium glide for D-2 configuration

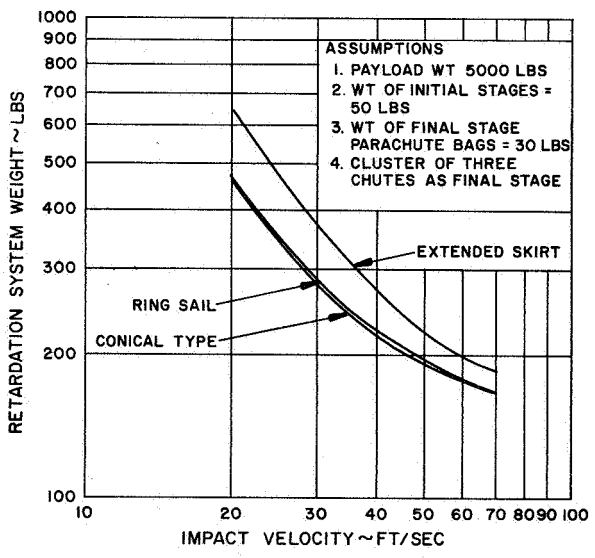

Figure I-4-2. Retardation system weight vs impact velocity

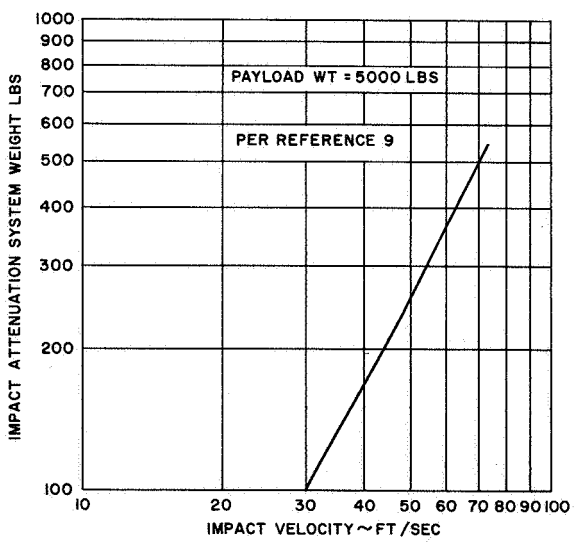

Figure I-4-3. Impact attenuation system weight vs impact velocity

Drawing upon information gained from designing systems I through V, system VI was designed in the following manner. From Figure I-4-5 it was determined that a final stage C_DA of 4673 sq ft was necessary to retard a 5000 lb vehicle to 30 fps at impact. In order to provide system stability and a measure of reliability to the final stage without an unnecessary increase in the weight, a three (3) chute cluster was chosen as the final stage. Assuming a $C_D = 0.7$ the diameter of each of three chutes of the 108 gore-conical type design was determined to be 53 ft. From experience gained from systems I through V it was felt that the minimum number of stages that could be employed while satisfying the maximum number of the above considerations was three (3). From the minimum deployment time viewpoint, a good combination of staging would be the final stage described above, a reefed version of the final stage as a second stage and a high strength chute as a first stage. Looking at the first stage it could be seen that the size of the first stage would have to be large enough to decrease the velocity of the vehicle to a point where the second stage could be deployed safely. Yet this first stage could not be so large that opening loads would limit it's deployment altitude to a narrow band of altitudes. Calculation showed that a 25 ft diameter ribbon chute having a C_D of 0.5 would satisfy the above requirements. The reefing on the second stage, necessary to minimize opening loads on the second and third stages, was then determined. A description of system VI can be found in Table I-4-I. The opening sequence of this system on normal recovery was assumed to be the optimistic case shown in the following discussion of Launch Pad Abort Recovery. These opening times were derived largely from experimental test data on chutes of similar size and deployment conditions. Picking 20,000 ft as a typical deployment altitude a trajectory was calculated and is presented in Figure I-4-6. From Figure I-4-6, it can be seen that the maximum g loading on the first stage is 3.7 and is approximately 2 for the second and third stages. Considering a shock factor of 2 (a conservative assumption), the opening load on the second and third stages would be 20,000 lb or dividing by the number of chutes would be approximately 7,000 lb per chute which is a very reasonable loading.

Looking at the range of altitude at which this system is capable of deployment, Figure I-4-7 shows that an upper limit on deployment altitude would probably be set by Mach number effects or the ability to sense the altitude accurately. No lower limit is set due to opening loads, but this no doubt would be fixed by a minimum safe deployment altitude. It can be said then that the range of deployment altitude is quite wide and would probably be limited by factors outside the recovery system itself. The range

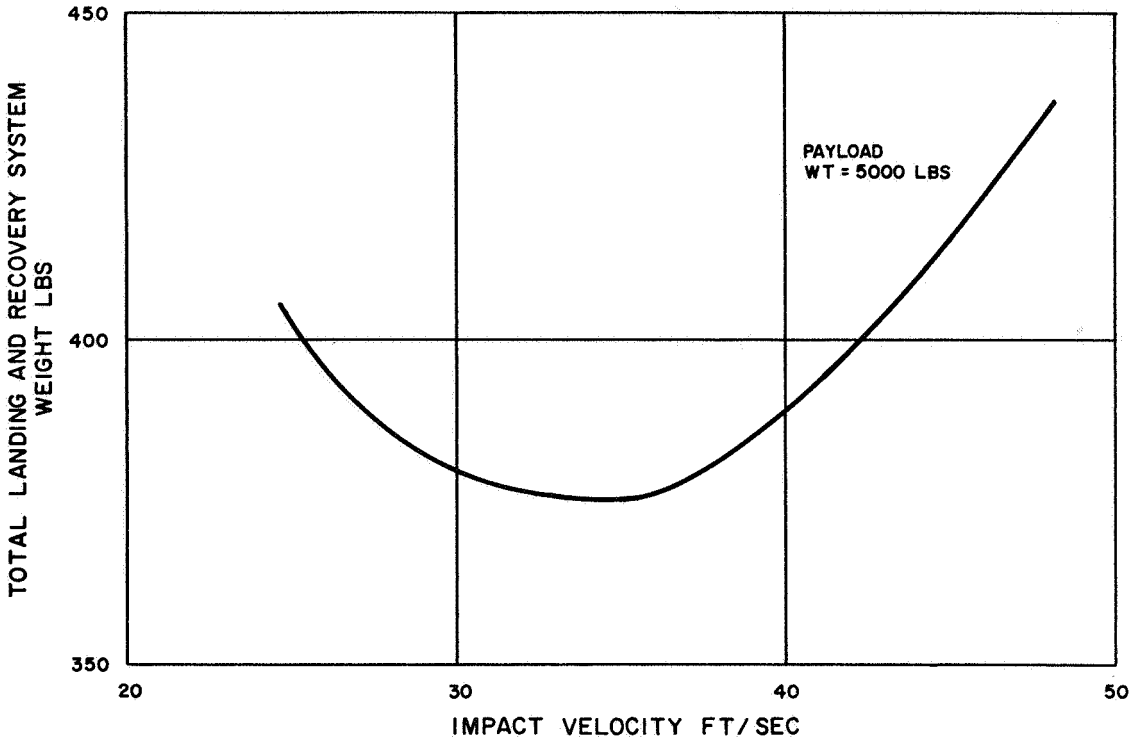

Figure I-4-4. Total landing and recovery system weight vs impact velocity

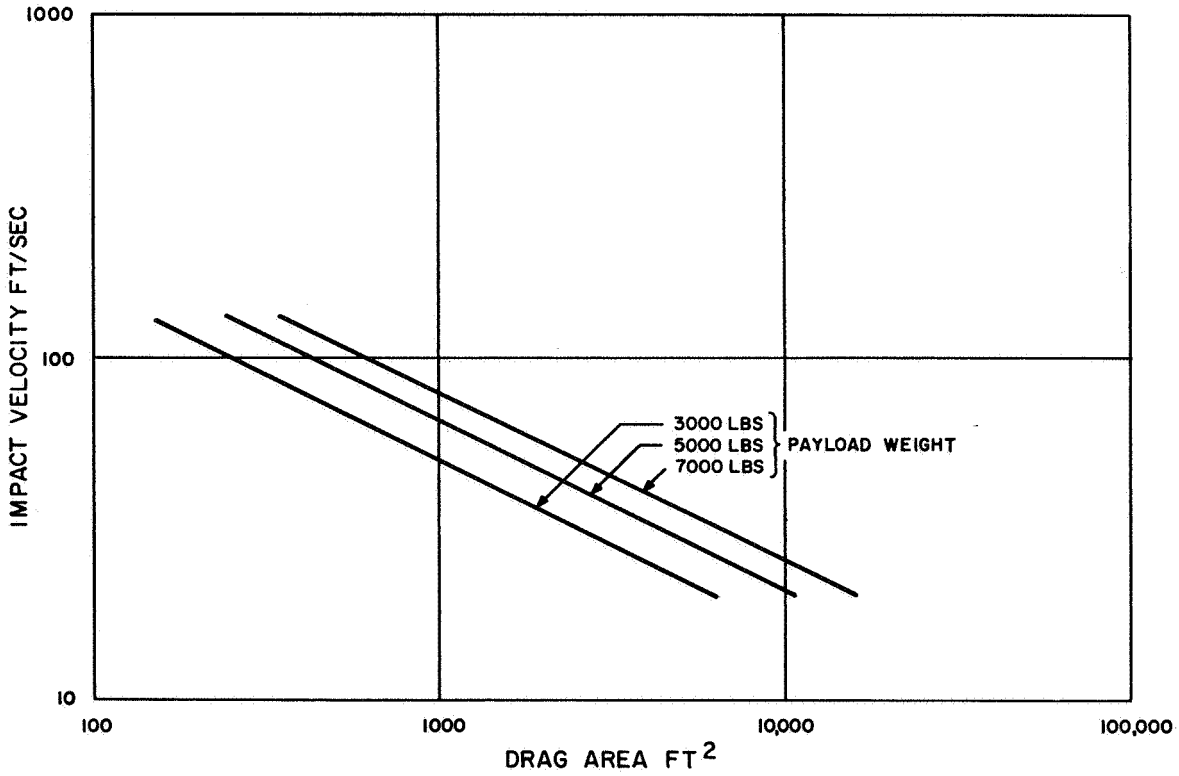

Figure I-4-5. Impact velocity vs drag area

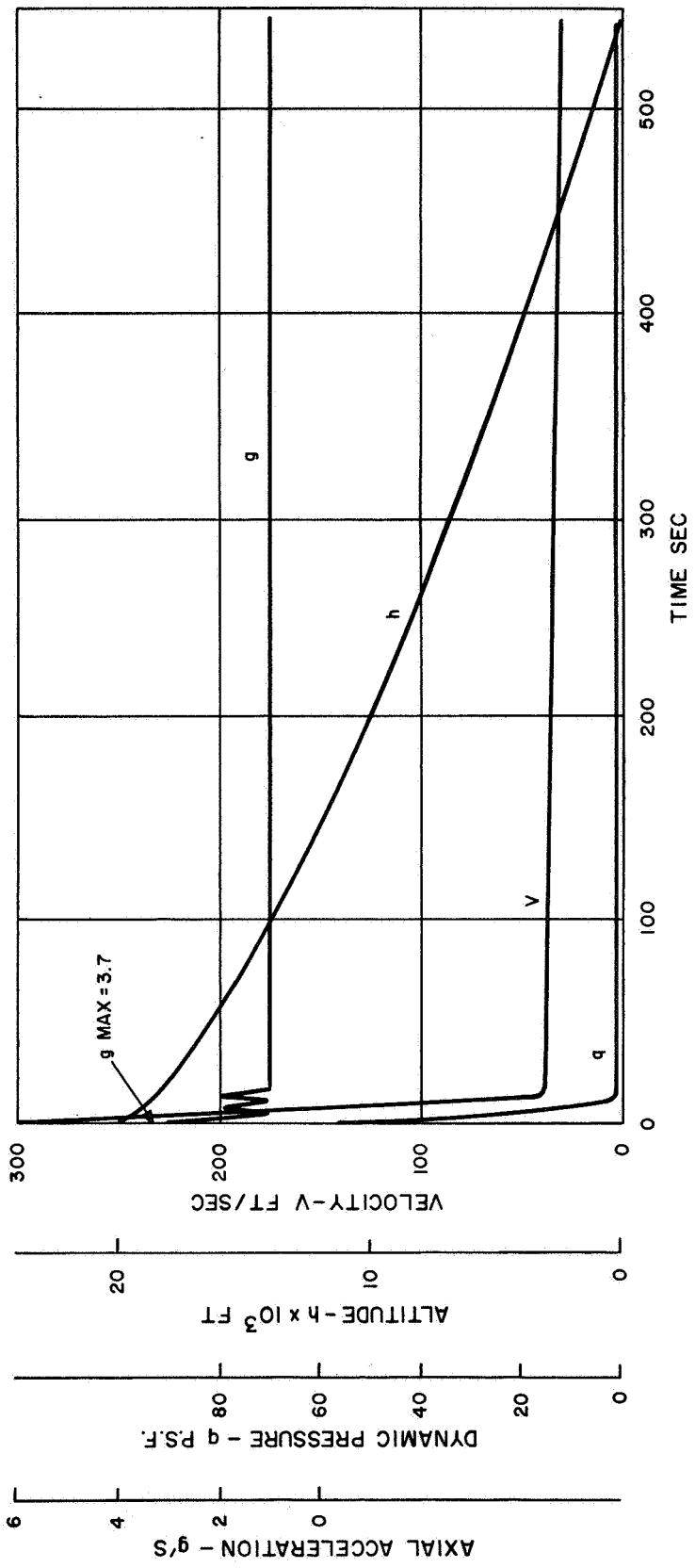

Figure I-4-6. System VI terminal (retardation) trajectory payload wt = 5000 pounds

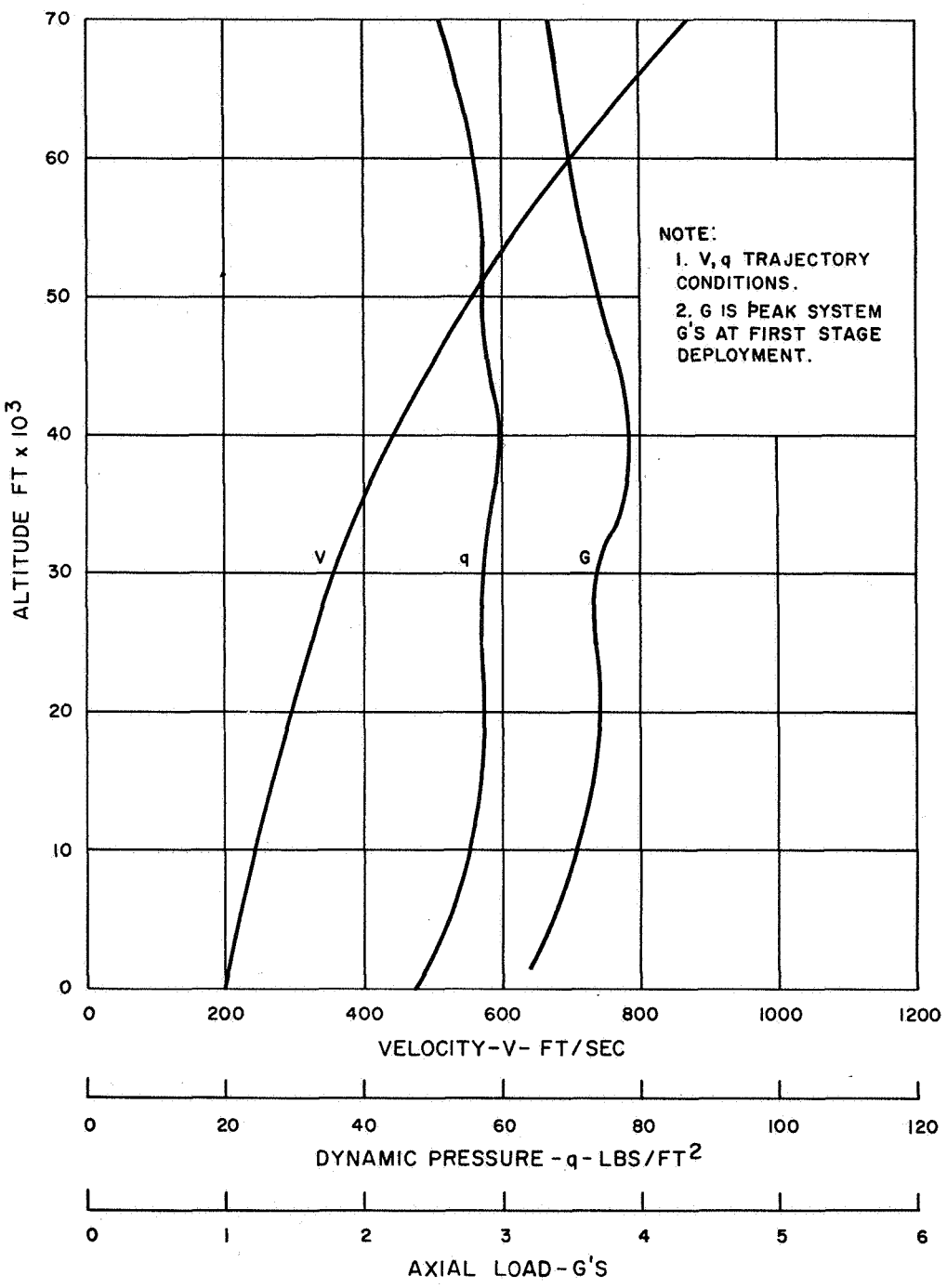

Figure I-4-7. Altitude vs velocity, dynamic pressure, axial load-System VI

that the vehicle covers after recovery system deployment is initiated is given in Figure I-4-8, for two deployment altitudes. It can be seen that the range is small and would be insignificant in relation to the range that could be induced by wind. The range due to wind could be kept to a minimum by deploying at the lowest possible altitude.

Since no back-up recovery system is proposed, it is interesting to look at the effect of failures on system capabilities. Assuming no failures until main chutes are deployed the partial failure of two or more of the main chutes might be represented by the complete failure of one chute. The result of this failure would be to increase the velocity at impact to 37 ft/sec and increase the opening loads on the other two chutes to 10,000 lb/chute. These results are not considered to be too severe in view of the magnitude of the "damage" imposed.

Further optimization of this recovery system could take place by pursuing further trade-offs between the system and mission requirements. For example:

1. Maneuvering before parachute deployment.
2. Vehicle stabilization by parachute.

4.2.2 Launch Pad Abort Recovery of the Selected Configuration, D-2

The absolute necessity for abort capability on Project APOLLO is unquestioned. From the recovery system viewpoint, it has been assumed that a "worst case" is the launch pad abort situation. This assumption is based on the fact that h = 0 at abort initiation; and this places upon the escape rocket system a requirement for attaining a minimum vehicle altitude condition that is compatible with a reliable functioning of the recovery and landing system.

A large number of launch pad abort trajectories have been calculated for various escape launch attitudes, g accelerations and rocket burning times. An analysis of the launch pad abort from the entire APOLLO system viewpoint has resulted in the selection of a group of abort trajectories which satisfy the APOLLO system requirements. It is this group that has been analyzed from the recovery system viewpoint. The recovery system used is System VI of this Section.

Due to the possible detrimental effect of low dynamic pressure on the opening times of the parachutes of Parachute Recovery System VI, two time sequences have been established for the launch pad abort case. One time sequence represents an optimistic opening for all stages of the recovery system while the other sequence represents pessimistic opening of all stages. Any combination of optimistic and pessimistic openings for the stages would, of course, fall within the envelope established by the extreme cases.

The opening times of the various stages of System VI were established in the following manner. The 1st stage (25 ft ribbon chute) nominal opening time was calculated using the filling time equation $T = \frac{8\ D_o}{V\ 0.9}$ of Reference 1. The range of opening times necessary to obtain an optimistic and pessimistic case was derived from the experimental data for the 28 ft extended skirt parachute used in the Discoverer program. Applying this range of opening times to the calculated nominal case the optimistic and pessimistic opening times for the first stage were obtained. Since the size of the chutes for the second and third stages are approximately the size of the final stage chute for the Mercury capsule, experimental data from the Mercury program was used to establish the optimistic and pessimistic opening time of these stages, i.e. shortest and longest opening time at the velocity representative of the APOLLO case. Based on the above opening times and past experience with cover ejection and parachute deployment, the following time sequences were obtained where T = 0 at apogee of the off-the-pad abort trajectory.

Time (sec.) OPTIMISTIC	Time (sec.) PESSIMISTIC	EVENT
0	0	Eject Aft Cover
2	2	Eject Pilot Chute
5	5	First Stage Extended
6.5	8	First Stage Open
10.5	14	Second Stage Open (reefed)
13.5	17	3 Sec. Reefing Time
14.5	19	Third Stage Open

It was assumed that the deployment process had no effect on the ballistic trajectory until the second stage began to open since all the force was going into deployment of the various stages. During opening of the second stage a step-wise increase in C_DA was used until the reefed C_DA of 846 sq ft was attained. A reefing time of 3 sec.

(which is fixed for either normal or abort recovery) was then used. A step-wise increase in C_DA from the reefed condition to full open was likewise assumed.

It should be noted that the time sequence for the optimistic case is identical to the time sequence used for normal re-entry recovery with the one exception being that no drag time for the first stage is assumed in the abort case. This assumption is based on the possibility of an override being employed to eliminate this drag time in the abort case.

The resulting trajectories based on the above time sequences and the indicated conditions at apogee of the abort trajectory are given in Figures I-4-9, -10, and -12. For all cases considered, the vehicle reaches equilibrium velocity with main chutes open at altitudes that are considered very safe and in fact may be excessive if drift back over the pad, caused by wind, is considered. Figure I-4-12 gives the envelope of optimistic and pessimistic openings for altitude at which the vehicle reaches V_T = 30 fps versus altitude at apogee, for a velocity at apogee of approximately 100 fps.

4.3 MANEUVER DURING LANDING OF SEMI-BALLISTIC RE-ENTRY VEHICLE, D-2

4.3.1 Introduction

Section 4.2 describes the recovery technique for the APOLLO D-2 ballistic type re-entry vehicle utilizing a drag retardation scheme. Although this scheme presents a highly reliable, and thus desirable, means of recovering the vehicle for the very terminal phase of flight, it must be recognized that it does not permit, per se, any extensive maneuver capabilities to correct for position errors or permit landing approach flexibility for the crew. For the pure retardation system to place the vehicle within a specified landing area, it must be initiated at a predetermined point in space (i.e. altitude, velocity, flight path angle and range from landing site). Through judicious selection of this point, some degree of downrange flexibility is achieved, but this is admittedly small compared to the connotation carried by the term 'maneuverability'.

If the pre-selected point of retardation actuation is not achieved with sufficient accuracy, the negligible amount of lateral maneuverability and small amount of downrange maneuverability available in the retardation system may not suffice for positioning corrections. An example of such a situation can be seen with an error in re-entry path angle (γ_e). A γ_e perturbation as small as 1/4 degree, occurring for

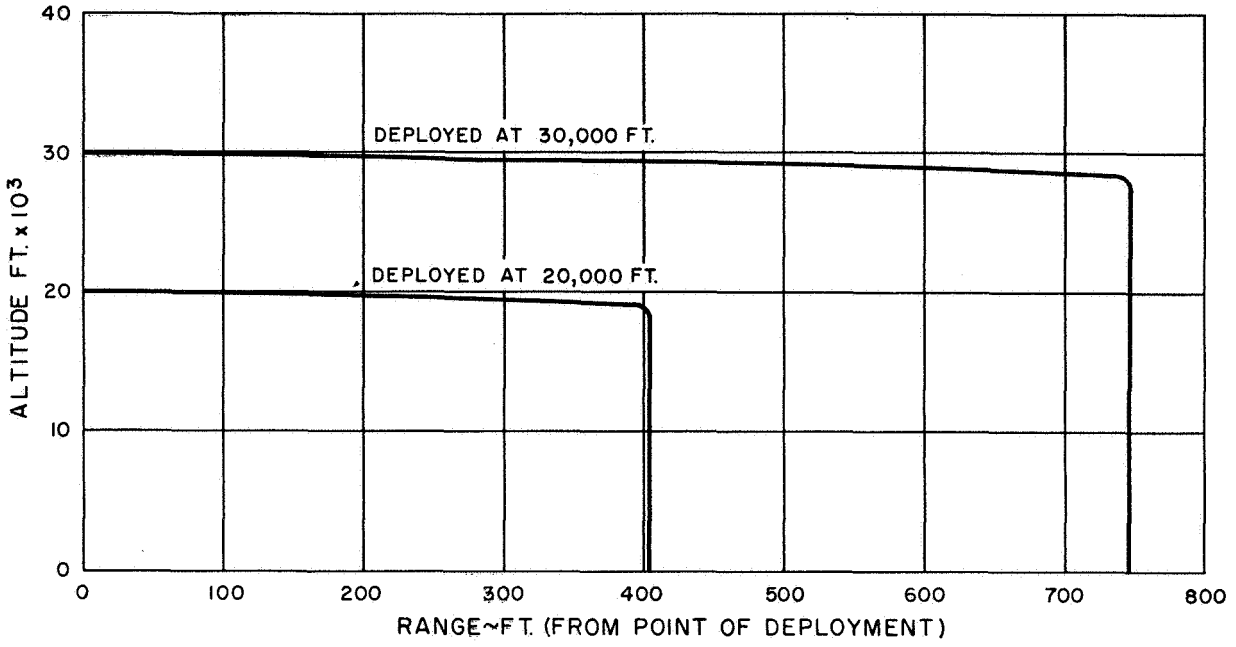

Figure I-4-8. Altitude vs range system VI

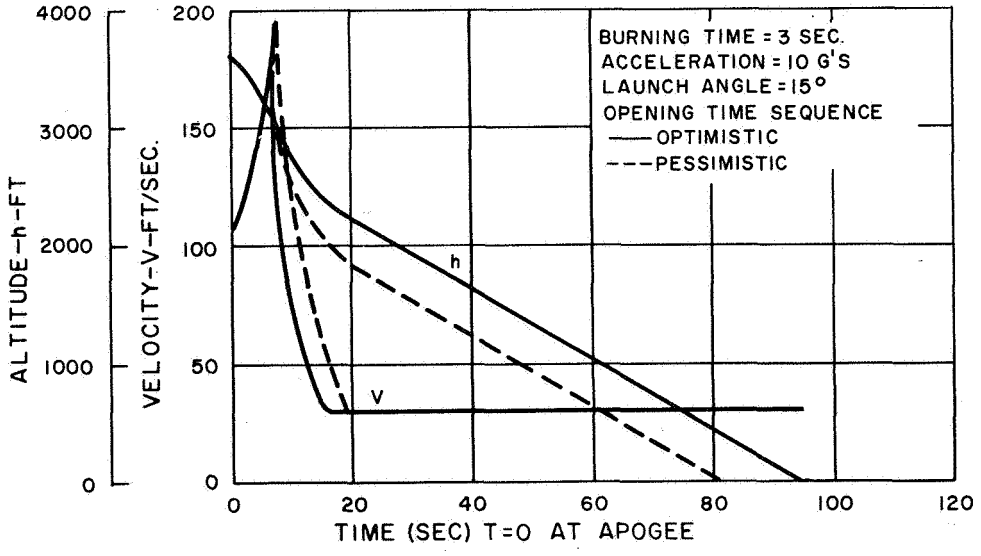

Figure I-4-9. Abort recovery trajectory - abort run no. 30

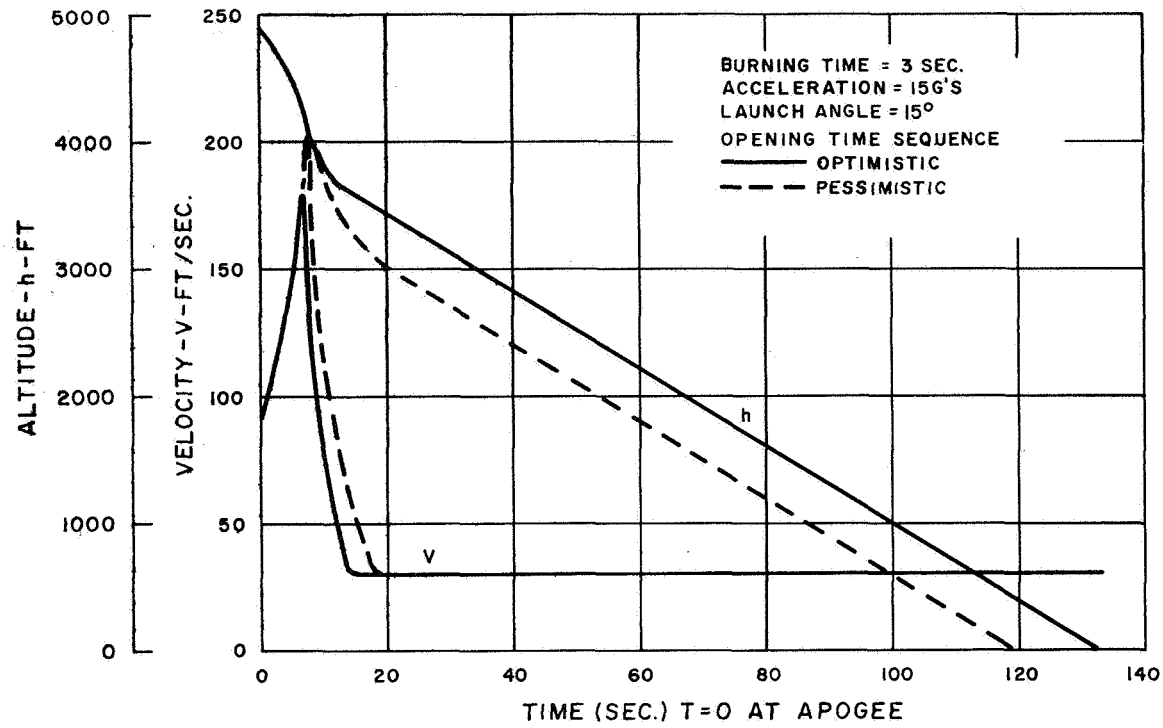

Figure I-4-10. Abort recovery trajectory - abort run no. 33

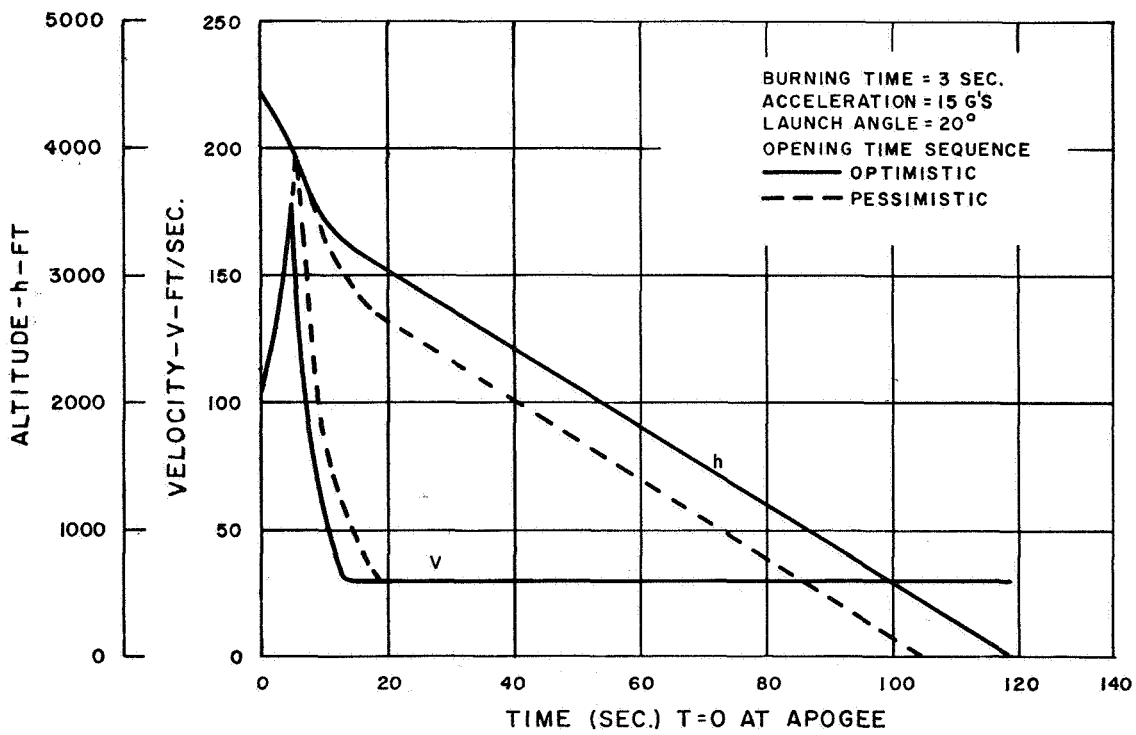

Figure I-4-11. Abort recovery trajectory - abort run no. 35

example on return from cislunar flight, may produce lateral errors on the order of 100 nmi. This type of error could be possible with a ballistic re-entry vehicle. The present day state-of-the-art in guidance and control may not be able to fully correct such errors prior to the terminal phase of flight. In order to compensate for these errors, some means of augmenting the vehicle's lift-drag ratio (L/D) during terminal flight then becomes a highly desirable feature.

During the course of this study program, the NASA parawing concept has been investigated as one possible means of achieving terminal maneuverability. Although the studies are preliminary in nature, and are based on only a limited amount of parawing performance data, it can be shown that a great deal of potential exists in the parawing concept. The following paragraphs are directed to a further review of this concept as applied to the APOLLO vehicle.

4.3.2 Equations of Motion

In order to develop an application of the parawing to specific simplified maneuvers of interest, it is well to briefly review the mathematical model of flight and the governing equations of motion.

A generalized system of motion is shown in Figure I-4-13. Here, a ballistic type body in the atmosphere is flying a certain flight path angle, γ V, and possibly a certain curved path whose radius if R. It has a weight, W = mg, and through certain lifting devices such as a parawing, a lift, L. The lifting force acts at some bank angle, ϕ. The body moves with forward velocity, V. The point mass equations of motion are:

$$m\dot{V} = W \sin\gamma - D \tag{1}$$

$$m V\dot{\gamma} = W \cos\gamma - L \cos\phi \tag{2}$$

$$\frac{m V^2}{R} = L \sin\phi \tag{3}$$

where the dot denotes a derivative with respect to time.

Equation (1) describes the forward motion along the flight path, equation (2) indicates the angular accelerations of the body with a change in γ and equation (3) gives the angular motion about the radius, R. Equation (2) has been simplified to include only the acceleration term associated with a change of γ about its instantaneous center - a similar term for rotation about the center of the earth ($\frac{V^2}{R_{earth+th}}$) has been neglected as being small.

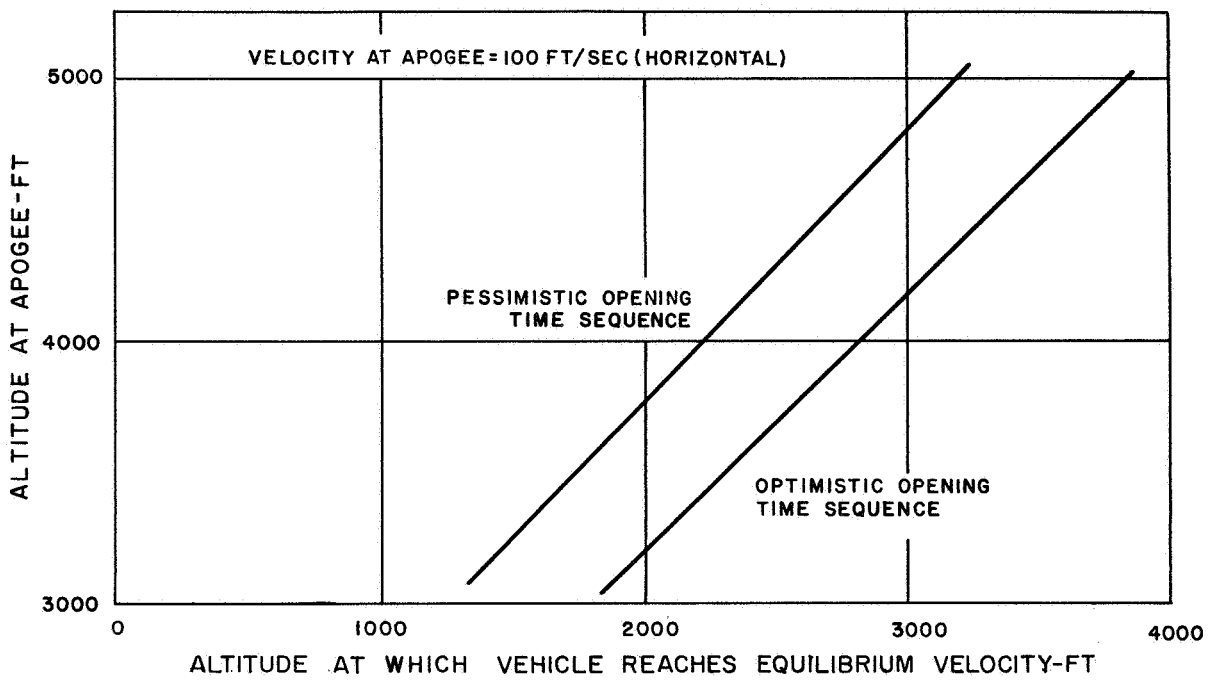

Figure I-4-12. Altitude at apogee vs altitude at V_T = 30 ft/sec

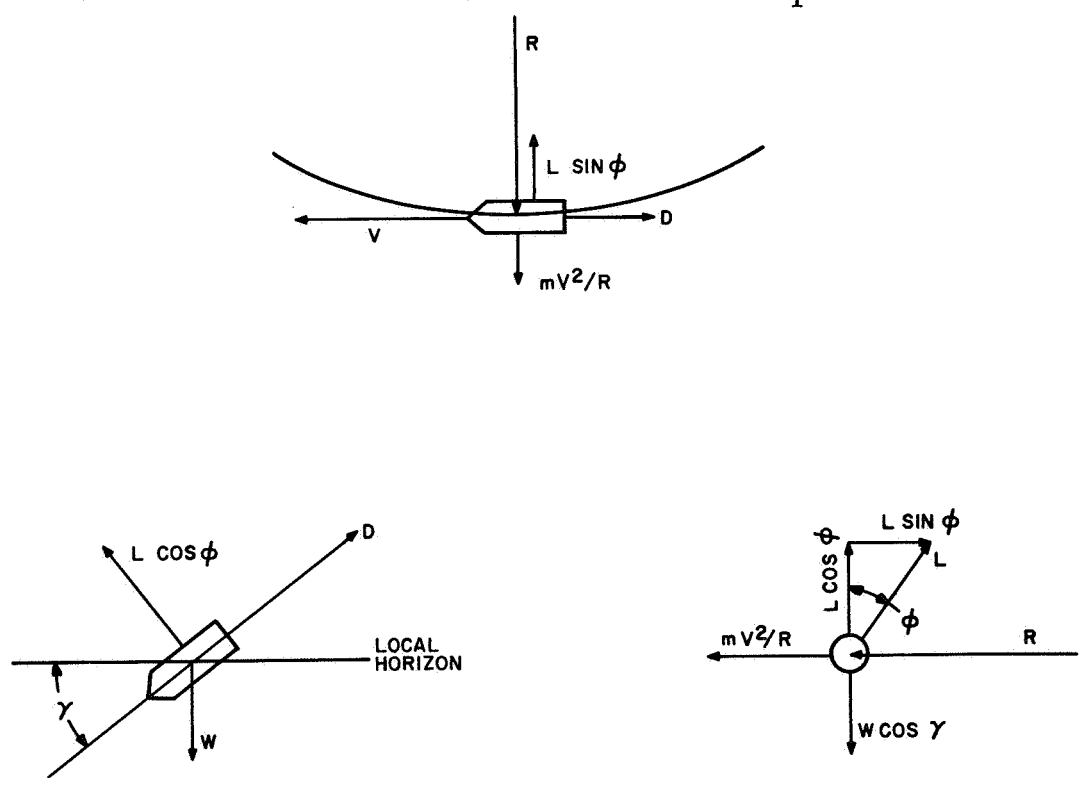

Figure I-4-13. Diagram for development of equations of motion

4.3.3 The Equilibrium Glide

Downrange and crossrange maneuvering, in excess of the basic L/D capability of the vehicle, is one area of lift augmentation via the parawing that is of interest. The basic idea has been treated here by considering an increased downrange equilibrium glide capability through an increased L/D of a body/parawing combination. For this case, equations (1) and (2) of the previous section can be used, and with $\dot{V} = \dot{\gamma} = 0$, they yield the familiar expression:

$$\tan \gamma = {}^{1}/_{(L/D)} \tag{4}$$

Hence, the vehicle can be placed into a zero deceleration, constant path angle glide and, depending upon the ability to acquire sufficient L/D and initiate the glide at a sufficiently high altitude, can augment (or correct) its range positioning within a fairly wide corridor. Figure I-4-14 presents a parametric picture of the type of range corrections that can be obtained for this situation.

The initiation of such a glide can be accomplished in several ways. It can be done before the retardation system is employed for final descent, or it could be used as an intermediary stage in the retardation system. The latter approach is illustrated in Figure I-4-15. Here, the parawing is deployed immediately after the vehicle has been decelerated from supersonic to subsonic speeds by an inflatable cone retardation stage; and, the retardation phase of recovery is continued after the desired amount of range correction has been achieved. The purpose of the initial retardation cone is twofold:

1. Decrease of velocity to subsonic speeds may be desired in order to realize the optimum performance of the parawing (and it can be shown that considerable velocity decrement can be obtained by a trailing cone without much loss in altitude).
2. Since the glide will be a $\dot{V} = 0$ maneuver, a velocity decrease to the point necessary for actuation of the next retardation stage may be required before the use of the parawing glide maneuver.

Using the D-2 configuration, Figure I-4-16 was developed to indicate the amount of L/D that must be supplied by the parawing. Utilizing this information, parawings were sized to do the job, Figure I-4-17. A more extensive analysis of this system should be performed (including crossrange maneuvering) when better definition of the parawing aerodynamic characteristics are available.

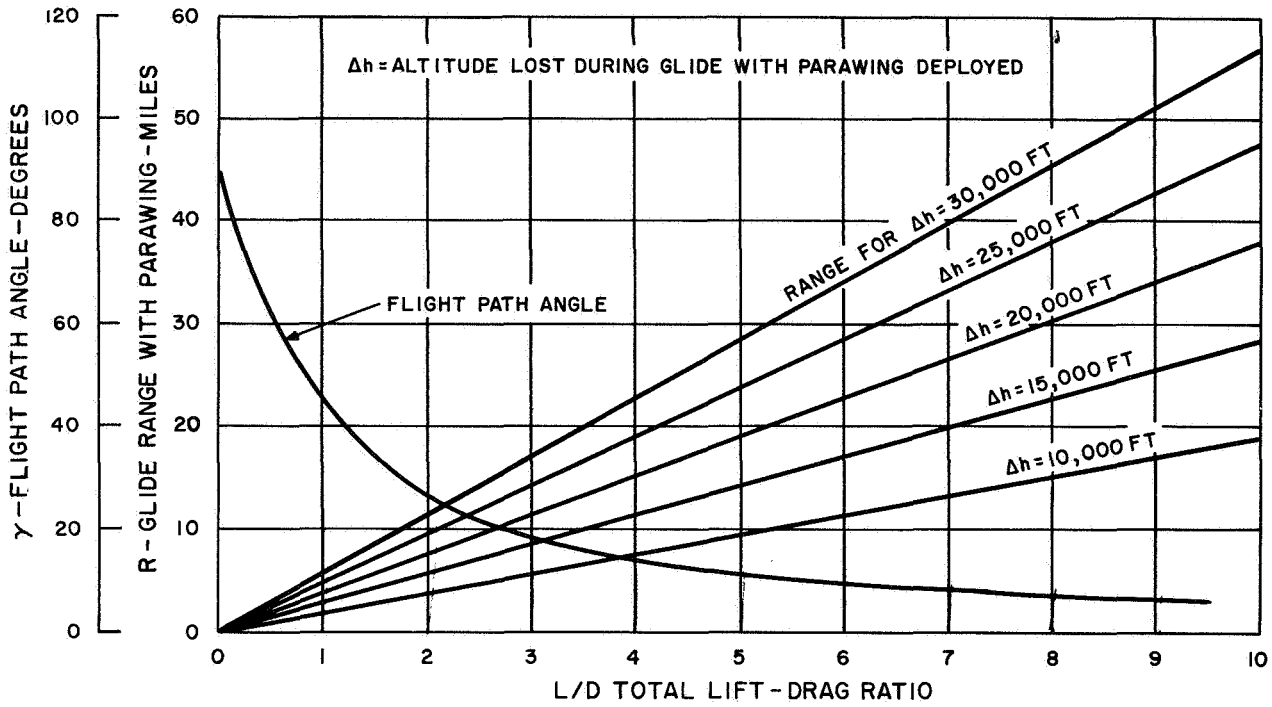

Figure I-4-14. Down-range corrections available utilizing a parawing for lift augmentation

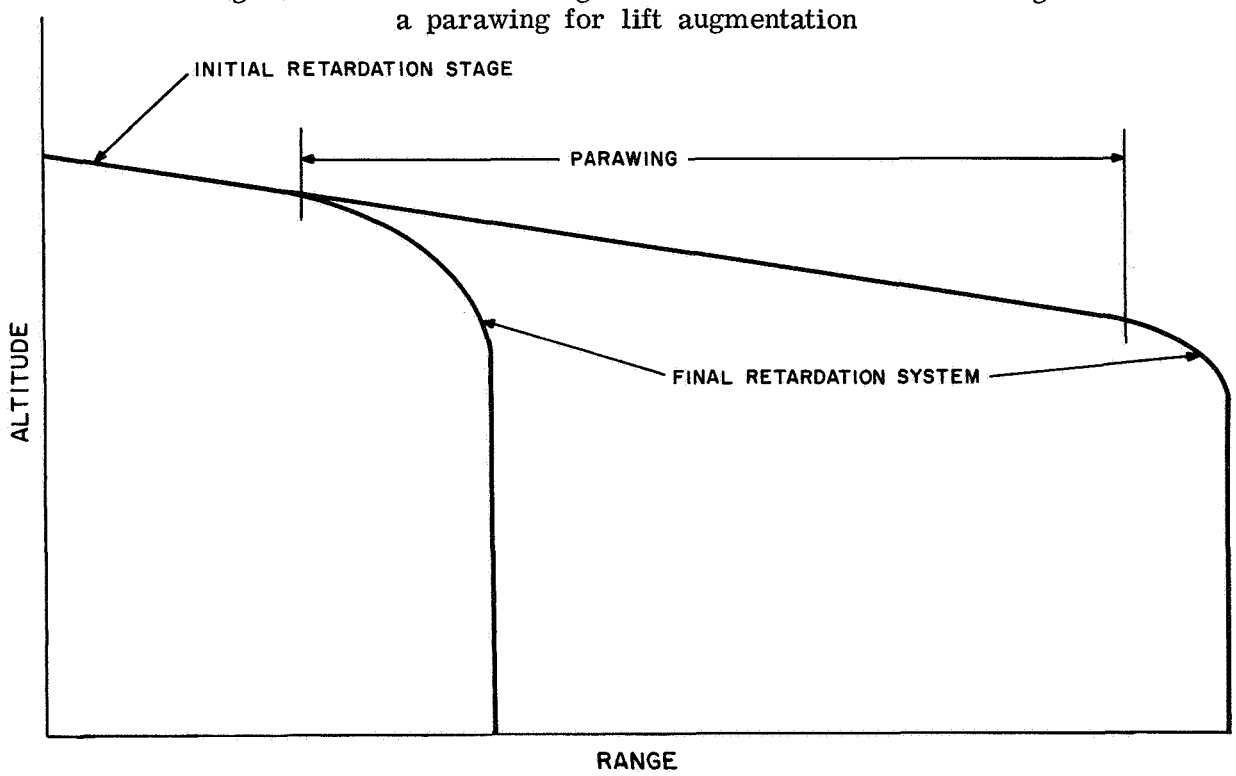

Figure I-4-15. Typical retardation trajectory utilizing parawing intermediate stage

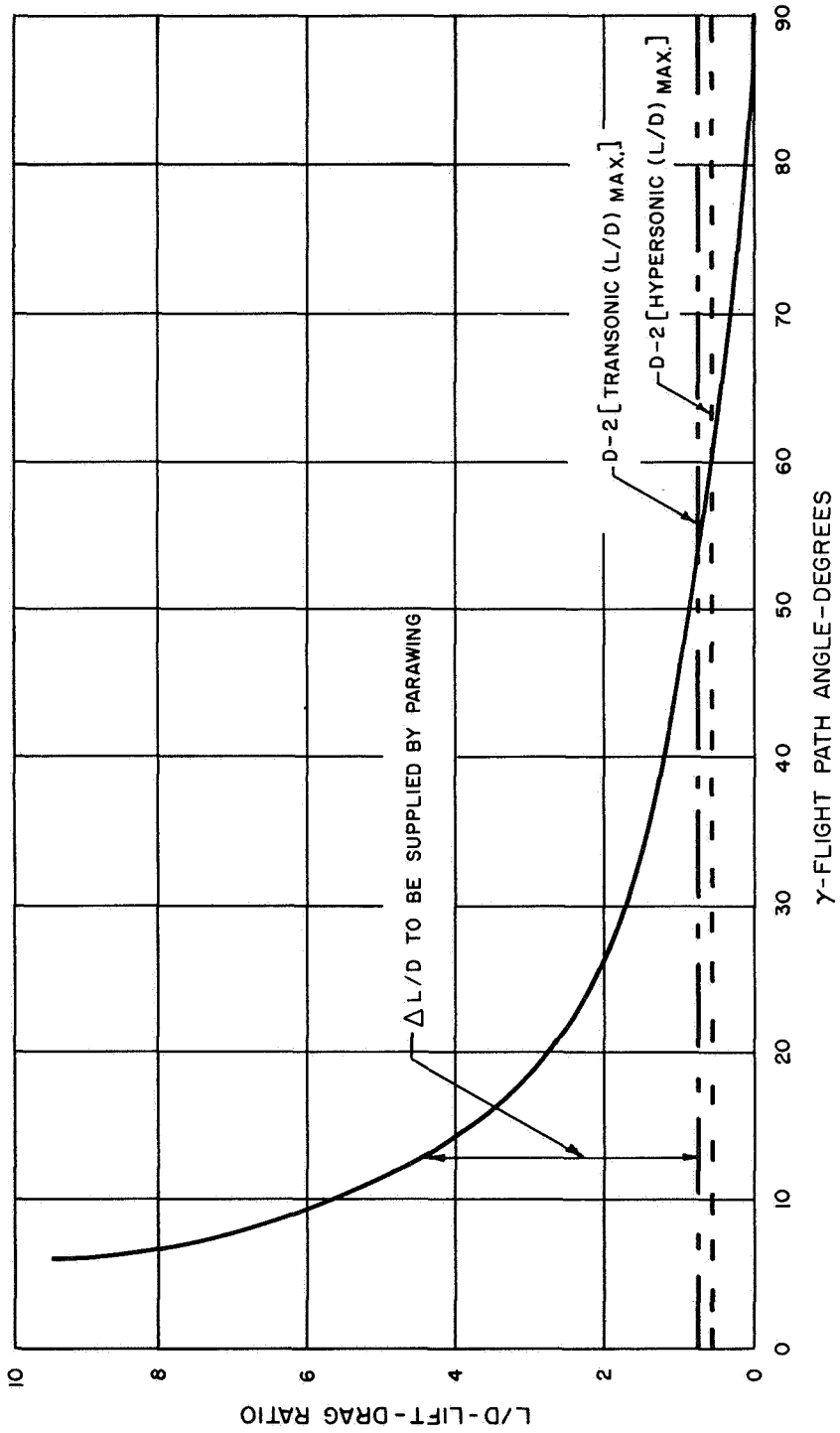

Figure I-4-16. Lift-drag required for equilibrium glide

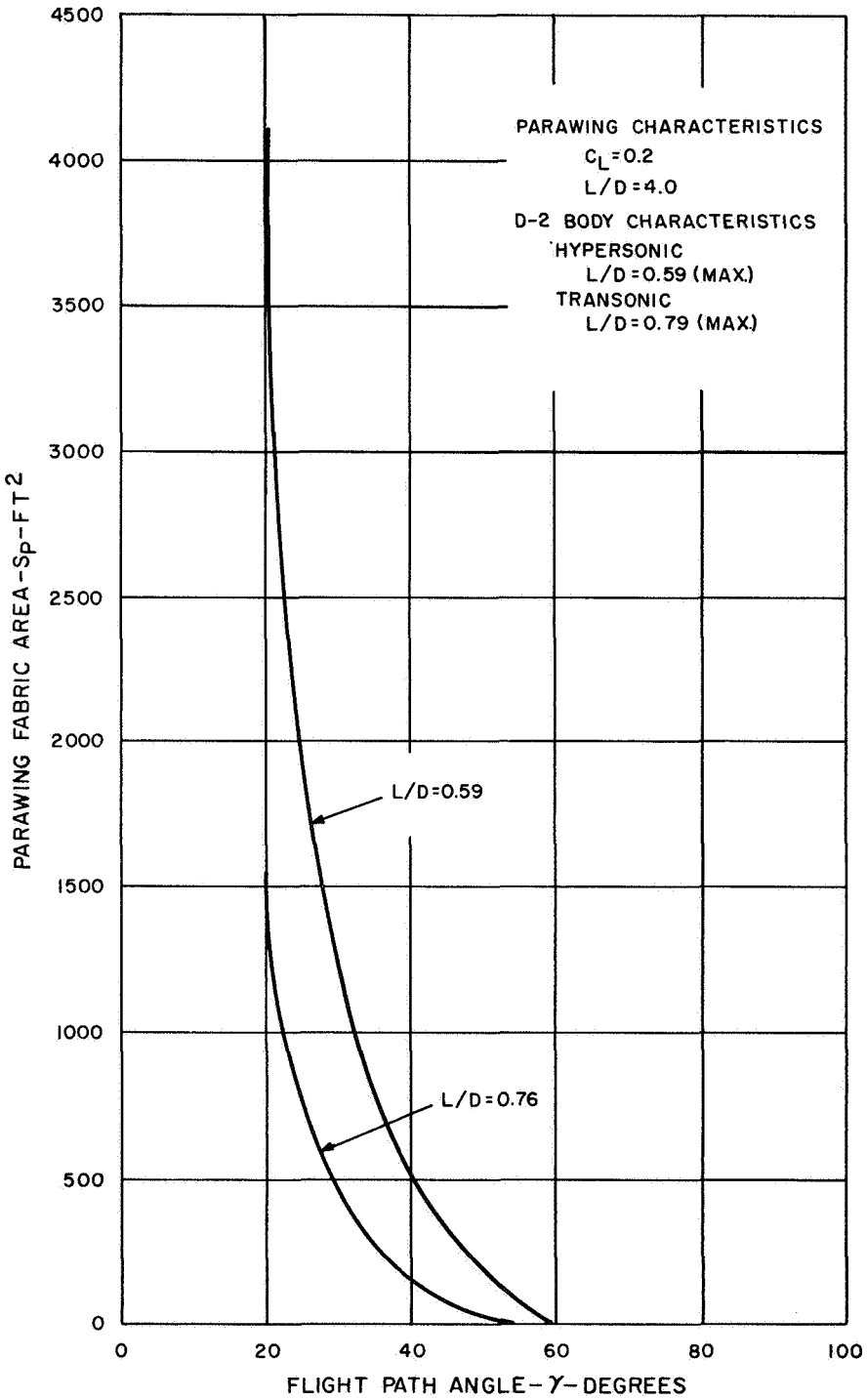

Figure I-4-17. Parawing area required for equilibrium glide D-2 configuration

4.3.4 The Spiral Descent

One rather interesting method of accomplishing the terminal phase of flight on the D-2 configuration is to fly a spiral descent maneuver about some point in the vicinity of the landing area. A schematic diagram of this maneuver is depicted in Figure I-4-18. This type of maneuver would be initiated, for some selected altitude, at a point distant from the center of the landing area equal approximately to the initial turning radius. Basically, a specified "g" limitation on the crew would define the minimum turning radius at any given velocity - and as velocity would decrease, the spiral could be drawn more closely into the center of the landing area. When the retardation sequence is initiated, the vehicle's remaining descent path would then lie entirely within the landing square.

As an initial step in analyzing this complex maneuver, a greatly simplified model system was examined. Essentially, equation (3) of Section V.2 was used for $\phi = 90°$. The "total" $C_L A$ (lift coefficient x reference area) required to actuate a 3g spiral was parametrically defined for a D-2 vehicle in terms of the free stream dynamic pressure, q $\left[\text{where } q = q\ (V,\ \text{altitude})\right]$, present at the spiral initiation point. (Note that in actuality the crew will feel a resultant g composed not only of the V^2/R term, but also the $V\dot{\gamma}$, $\dot{V}$ and gravity terms, and that this resultant acceleration is the real limiting value of interest). Figure I-4-19 shows the turning radius required for a 3g turn as a function of the tangential velocity of the vehicle. Figure I-4-20 presents the $C_L A$ required to actuate a 3g spiral as a function of dynamic pressure and also indicates the $\Delta C_L A$ deficiency of the basic D-2 vehicle for this maneuver. In order to compensate for this deficiency, a parawing has been sized in Figure I-4-21 that will furnish the $\Delta C_L A$ required to initiate the spiral.

The analyses conducted above relate only to the requirements for the initiation of a spiral maneuver at $\phi = 90°$. The complete definition of this maneuver, however, will envolve a solution of the entire set of equations given in V.2. To date, an analysis has been performed for a complete solution of these equations with $\dot{V} = \dot{\gamma} = 0$. The results, which are still unrealistic in terms of the actual flight maneuver, indicate that a rapid loss of altitude occurs during the spiral. Thus a more stringent evaluation of the equations of motion is required to account for $\dot{V}$ and $\dot{\gamma}$ terms. Such computations could be accomplished quite readily on the IBM 7090 computer if further pursuit of this concept is desired.

CONFIDENTIAL

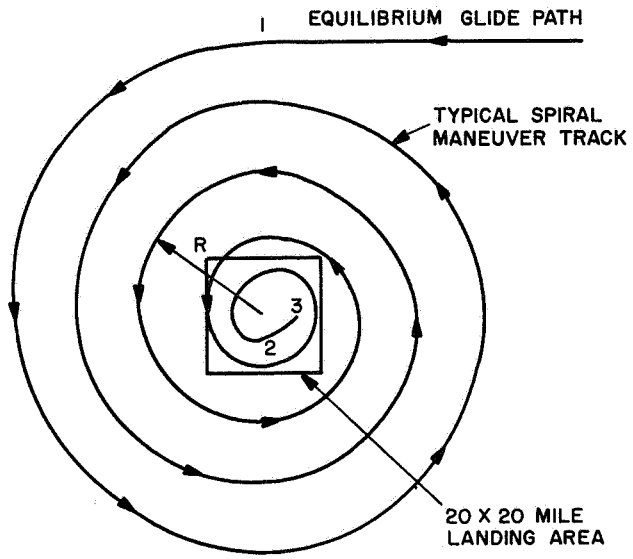

1. INITIATE A SPIRAL DESCENT MANEUVER MAINTAINING CONSTANT LOAD FACTOR. THIS MANEUVER IS INITIATED AT SOME PREDETERMINED ALTITUDE (h), VELOCITY (V), FLIGHT PATH ANGLE (γ), AND A RADIAL DISTANCE (R) FROM THE CENTER OF THE LANDING AREA

2. INITIATION OF RECOVERY SEQUENCE. THE VELOCITY HAS SUFFICIENTLY REDUCED SUCH THAT AN ENTIRE 360° TURN IS ACCOMPLISHED WITHIN THE LANDING AREA

3. VEHICLE IMPACT

Figure I-4-18. Schematic of spiral descent maneuver

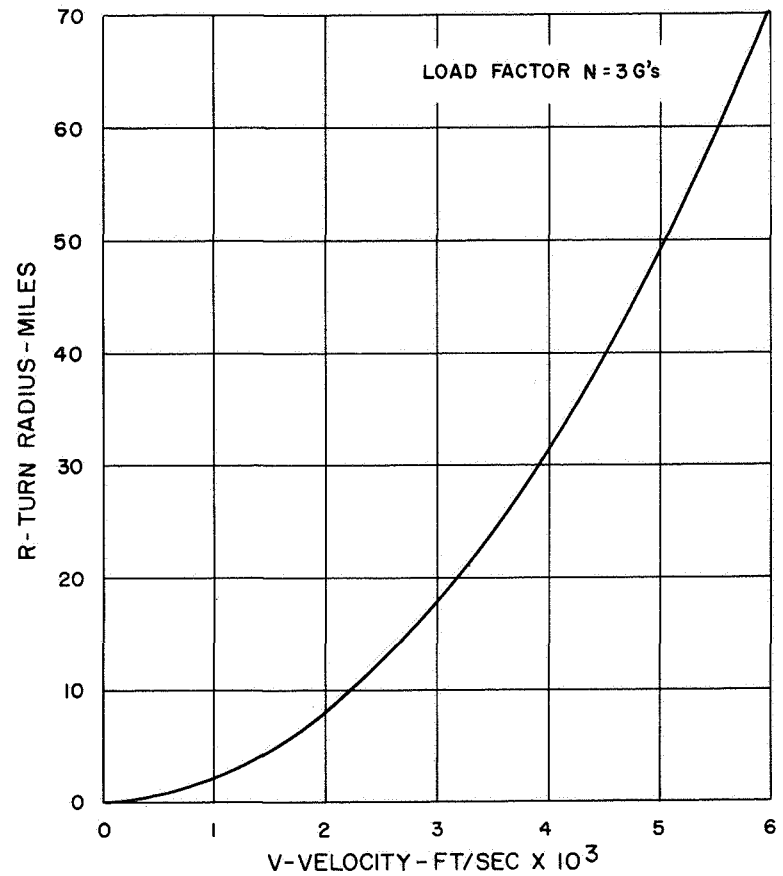

Figure I-4-19. Spiral radius as a function of velocity

CONFIDENTIAL

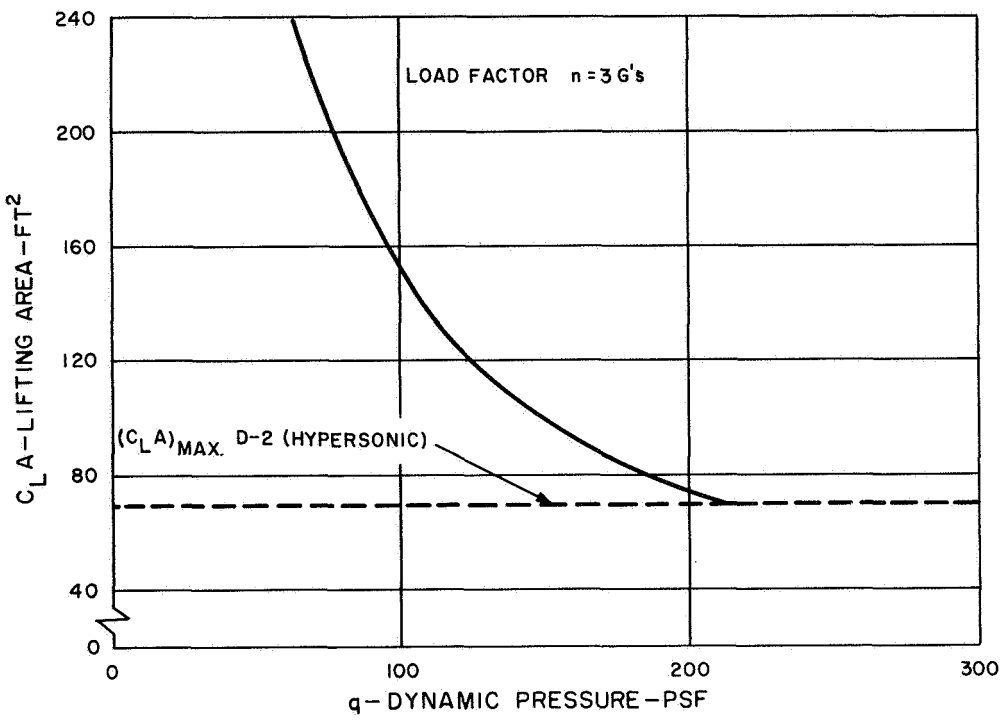

Figure I-4-20. Lift augmentation required to initiate spiral maneuver - D-2 body

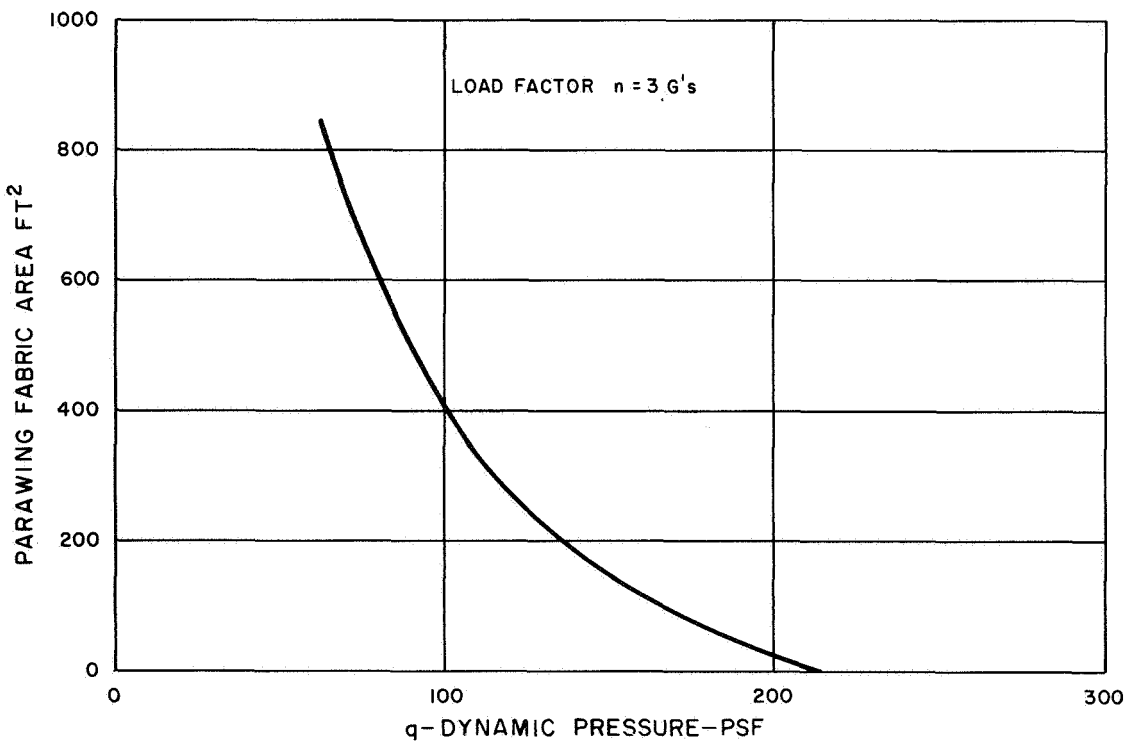

Figure I-4-21. Parawing area required for initiation of spiral maneuver - D-2 body

4.3.5 Parawing Development Problems

Although the basic parawing concept is not entirely new, its application to the APOLLO type mission does present a variety of new problems for consideration. A brief review of some of the more pertinent problem areas is given below.

In the materials area, the possible problems revolve about the combined requirement for high strength, low weight and heat resistance. The latter consideration will be important only if the parawing is to be used at high velocities, which may be the case in the spiral maneuver; for the equilibrium glide case, however, this particular problem will probably not be present. The strength problem can become quite severe, especially when one notes that wing loadings on the order of 10 to 20 may be encountered. In this regard, special consideration may also be required in the study of local stress concentrations that will occur in corners or points of line attachment. This strength problem is at odds with the desire for light weight (one of the chief advantages of the parawing) and suitable trade-off curves in this area will undoubtedly be essential.

In the structural area, the major problem will be the optimum design of the keel and leading edge members. Three types of structure can be employed; 1) the inflatable structure, 2) a solid, telescoping structure, and 3) a solid, folding type mechanical structure. Selection of the proper keel and leading edge design will involve a trade-off between strength, weight, reliability and performance suitability. There is some indication that inflatable structures may not have sufficient reliability in that full inflation may not occur unless ideal deployment of the non-inflated material is achieved. Hence, the primary effort may be required in the study of solid type structures like 2) or 3) above.

Perhaps the most critical problem area confronting a designer will be the need for more detailed parawing performance data. Aerodynamic characteristics of the parawing over a wide region of Mach number/Reynolds number conditions stand high on the list of "needs". Such information requirements would include lift, drag, stability and pressure distribution data as well as the variation of these parameters with parawing shape (this latter item being an apparent sensitive item on performance characteristics, particularly in regard to leading edge sweep angle). Deployment of the parawing is likewise a very critical problem area. Loads at deployment, parawing-body dynamic interactions, instability at deployment through pitch-up, flutter and altitude effects on deployment represent some of the more pertinent design considerations.

As a final consideration, parawing controllability must be precisely known. The ability to control the vehicle maneuvers is essential, and the degree of "line adjustments" needed to obtain this control is a vital requirement.

These problem areas outlined above are indeed significant, and considerable test work will be required to obtain a number of the answers. However, preliminary considerations of the parawing application to APOLLO definitely point to the desire for further investigations to prove or disprove feasibility of the concept.

4.4 ADVANCED RETARDATION AND LANDING FOR THE SEMI-BALLISTIC RE-ENTRY VEHICLE, D-2

4.4.1 Rotor Systems

4.4.1.1 INTRODUCTION

During the current APOLLO Study Program, the analyses of advanced recovery devices have centered, to a large extent, on the pursuit of information on rotor system concepts. These studies were performed on the basis of preliminary investigations which indicated possible performance advantages with this type of system that are highly desirable for the APOLLO mission concept. These advantages include the possible "built-in" terminal maneuvering capability that rotors possess (in addition to retardation), and the ability to flare-out prior to touchdown (thus minimizing or eliminating the impact attenuation system). The introduction of high performance launch pad abort capabilities in terms of minimum 'safe' altitude requirements and range maneuvering from the blast area may also be possible in some cases.

In order to capitalize on these advantages, it is evident that two critical questions must be raised:

1. Can critical weight and packaging requirements be met with this type of system.
2. Since the weight will undoubtedly be critical in any vehicle design, and thus preclude the use of any other type of recovery or retardation system in the vehicle, can the rotor system be utilized as the "sole source" system for the entire recovery sequence.

Preliminary study indicates solutions to both of these requirements, but extensive development programs will be required prior to the design of such recovery systems. For this reason, rotor systems were rejected for the selected configuration in favor of the proven parachute system. On the other hand, however, the obvious advantages of the rotor systems justify parallel study during the APOLLO Research and Development program.

Specifically, three rotor type systems have been investigated - all utilize a somewhat similar basic approach to use of rotors, but differ widely in the specifics of the design concept. A review of these three systems is presented in the following paragraphs.

4.4.1.2 ROCKET ON ROTOR SYSTEM (ROR)

The ROR recovery concept envisions the use of a single rotor composed of three solid blades. The rotor blades will fold 90 degrees near the hub for storage in a vehicle afterbody section. Prior to recovery, the rotor blades remain encased in the protective afterbody cover. The tip of the rotor blades contain small reaction motors. The reaction motors augment the kinetic energy of the blade during terminal descent and maneuvering. For control purposes, blade pitch (both collective and cyclic) will be applied to the blades at their hub connection, using an electrical servo system.

The profile of a typical ROR recovery is as follows: After the aerodynamic heating phase of the equilibrium glide trajectory has been completed, the afterbody protection cover will be jettisoned with explosive bolts. Blade activation and rpm buildup may be accomplished by aerodynamic forces; or if necessary, initial spin augmentation may be applied at the hub to assist in blade deployment. The rotor pitch must be set at some angle other than flat to induce rotation. Once rotation has started the centrifugal force field will complete the deployment of the rotor blades as shown in Figure I-4-22. The R/V will be retarded by the rotor until the full autorotational regime is entered. After the initiation of full autorotation, cyclic and collective pitch may be used to control the rate of descent and glide angle. As the autorotation system approaches the altitude for flare the tip rockets will be started. The added rotational energy of the blades is then used to augment the energy in the centrifugal field to provide flare, hover or powered maneuver capability of the system.

The deployment characteristics of a typical rotor is shown in Figure I-4-23. It is interesting to note that the rotor opening rpm and drag characteristics may be controlled by blade pitch adjustment. With this control, desirable values of axial loading may be maintained during deployment.

CONFIDENTIAL

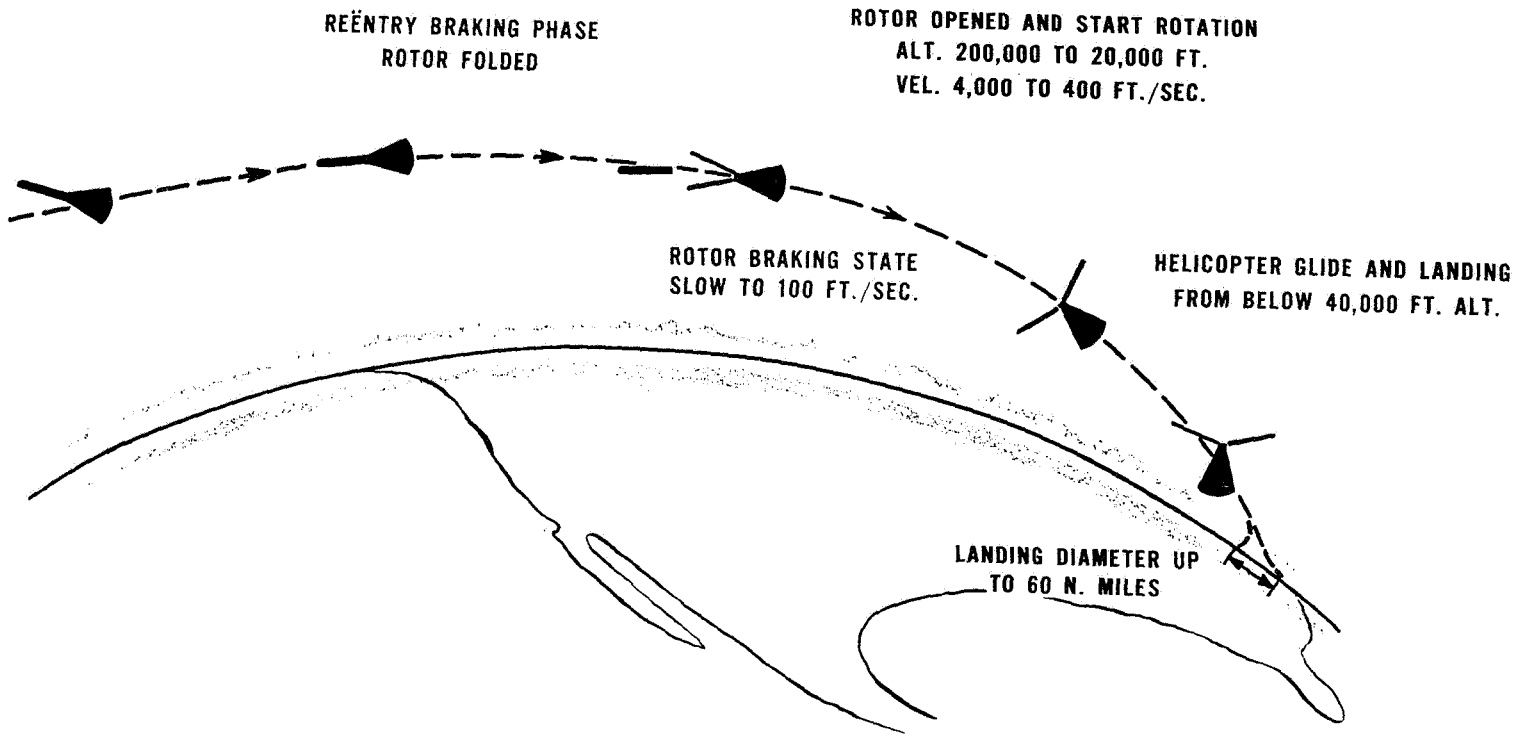

Figure I-4-22. Rotor landing system operating sequence

CONFIDENTIAL

CONFIDENTIAL

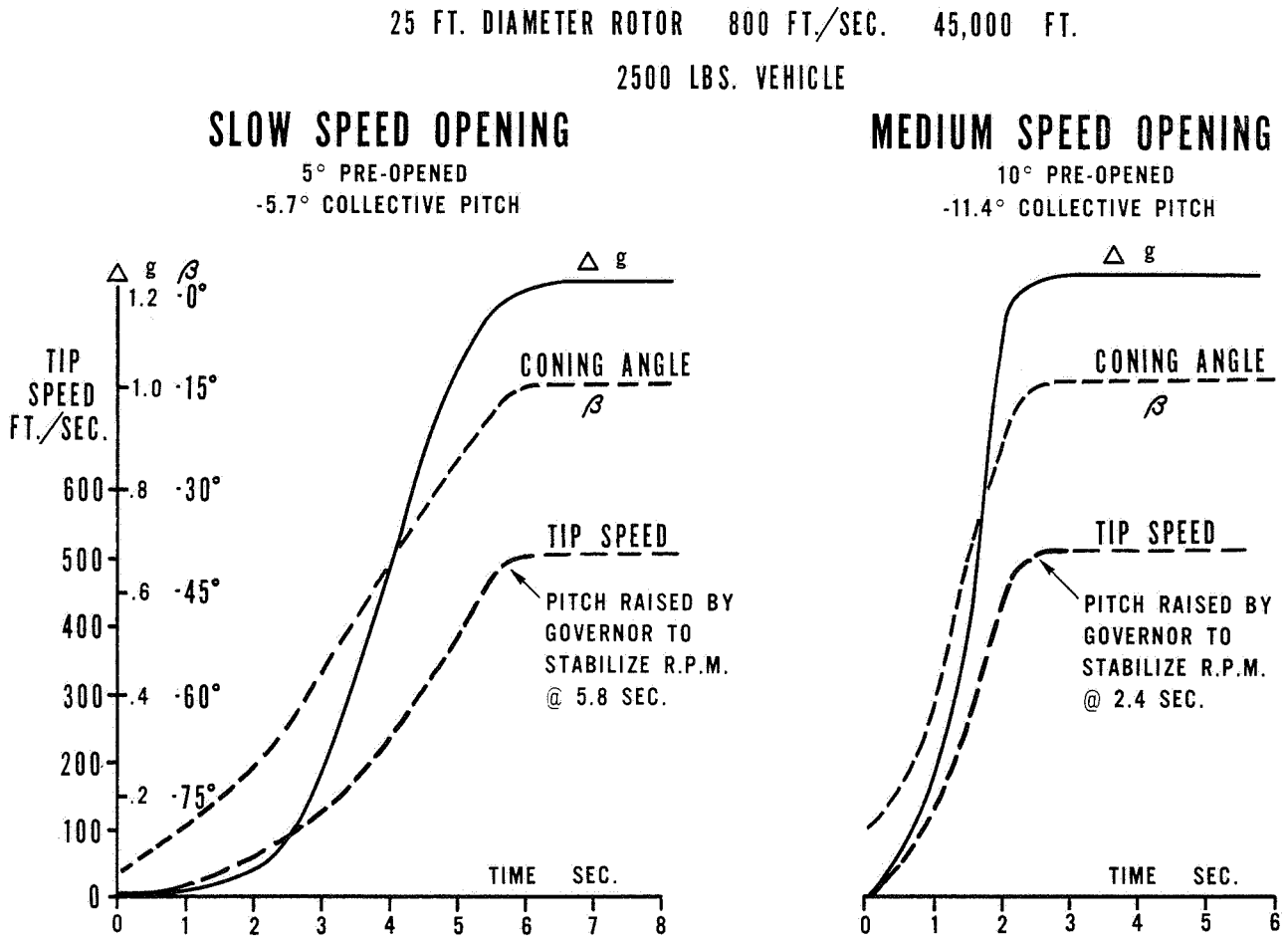

Figure I-4-23. Rotor opening characteristics

CONFIDENTIAL

When a rotor is deployed at high flight speed, the maximum induced rpm may cause centrifugal forces which are structurally intolerable. The blade pitch angle controls the induced rpm at which the rotor will stabilize. Generally there are two values of blade pitch at which rotor rpm will stabilize at less than maximum induced rpm (Reference 2). The allowable pitch settings are a very high negative pitch, where the blade chord is nearly parallel with the helix of blade motion and a zero pitch in which the rotor acts as a flat circular plate. These flight regions may be called respectively propeller windmilling and propeller braking. Figure I-4-24 shows the relative drag of a typical rotor in the windmilling and braking states. Figures I-4-25 and I-4-26 show typical mission profiles of rotor systems.

After the initiation of autorotation and the application of cyclic pitch to the rotor system, the vehicle glide potential may be investigated. The L/D ratio which may be expected is dependent on vehicle drag and rotor disk loading. The altitude where glide may be initiated depends on the blade loading of the rotor. Figure I-4-27 (Reference 2) shows L/D ratios which may be expected. Assuming a glide ceiling of 25,900 ft and L/D = 3 a glide range of some 14 miles would be available. The use of the tip rockets will provide as much low level flight capability (i.e. flare, hover or maneuver) as necessary. The penalty, of course, is fuel weight. To show order of magnitude calculations of fuel weight necessary in the flare or glide approach, the following assumptions may be made:

Descent velocity = V_v = 100 ft/sec
Weight of Vehicle = W_v = 5000 lb
Blade tip speed = V_T = 800 ft/sec
Rotor radius = R = 10 ft
Number of blades = 3
Air density = ρ_a (slugs/cu ft) = sea level
Time required to flare = t_f = 3.42 sec (per analysis from Reference 3)
Change in Kinetic Energy = ΔKE

For flare, assume that rotor ΔKE must equal $4\Delta KE$ of the vehicle in vertical descent (per equations from Reference 3 for 2g flare). The thrust required for a 2g flare may be written as:

$$T_f = \frac{\Delta KE_{rotor}}{t_f \; V_T} = 1130 \text{ lb}$$

CONFIDENTIAL

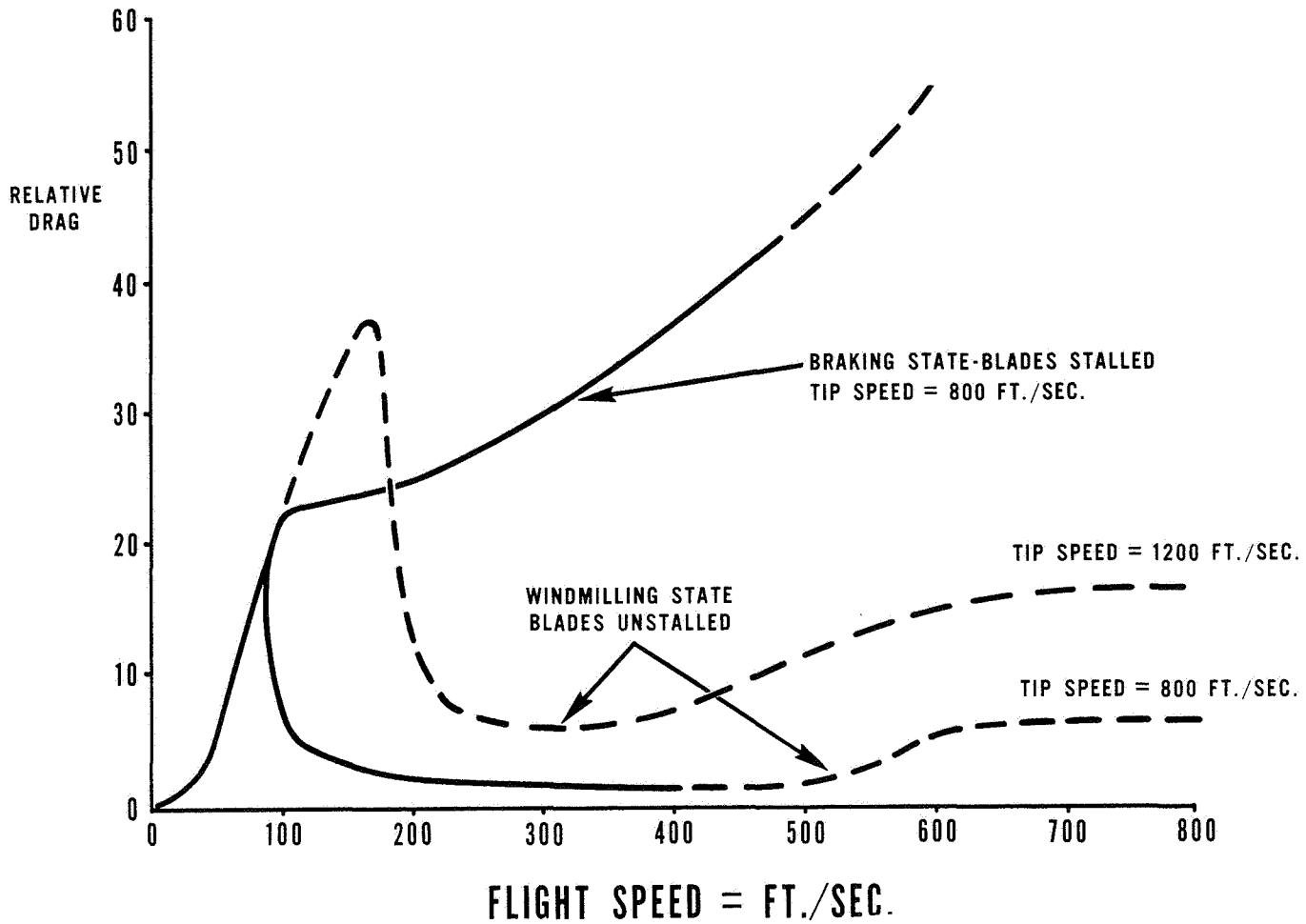

Figure I-4-24. Rotor drag characteristics in propeller braking and windmilling state

CONFIDENTIAL

CONFIDENTIAL

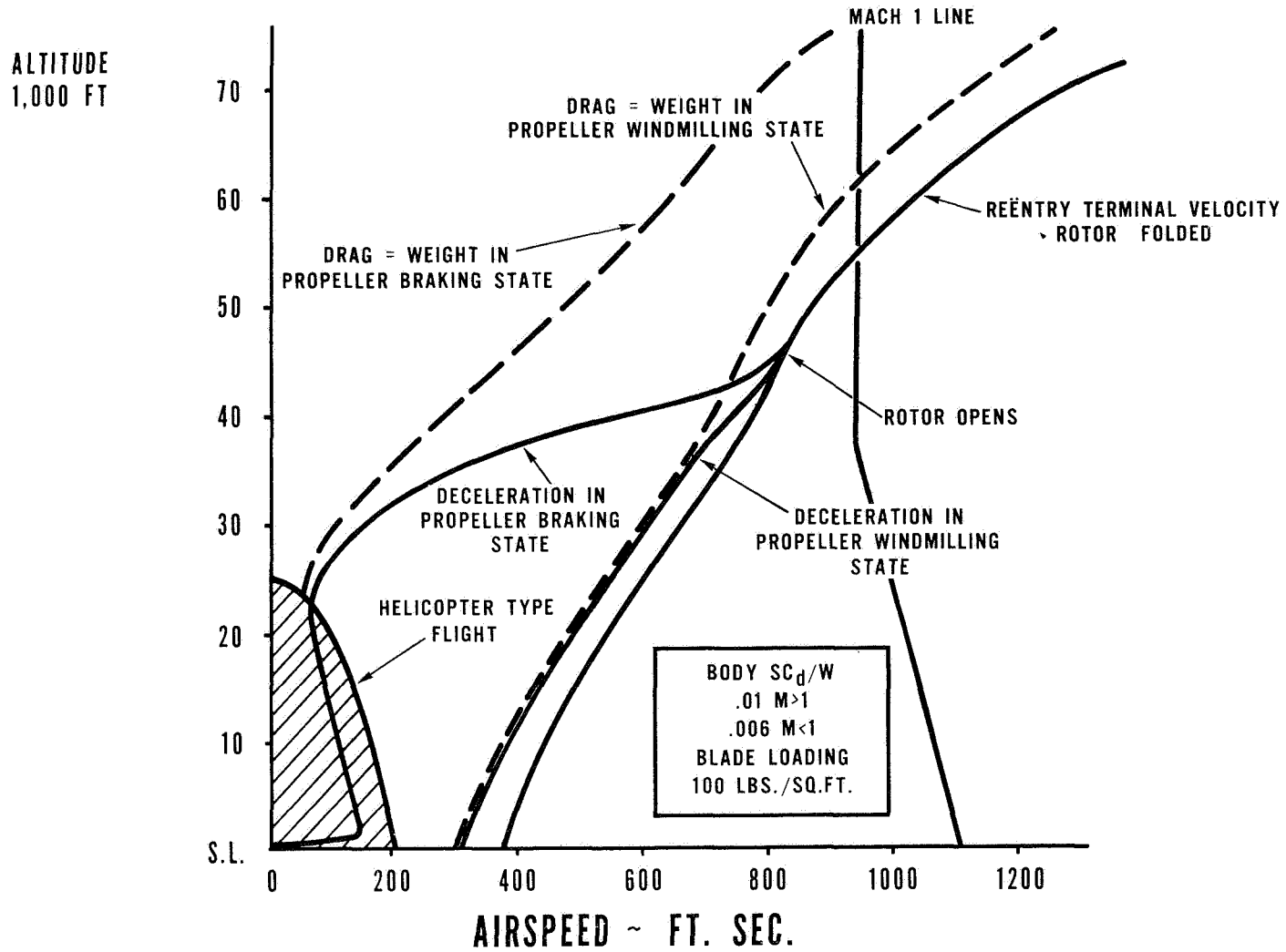

Figure I-4-25. Variation of airspeed with altitude - subsonic opening case

CONFIDENTIAL

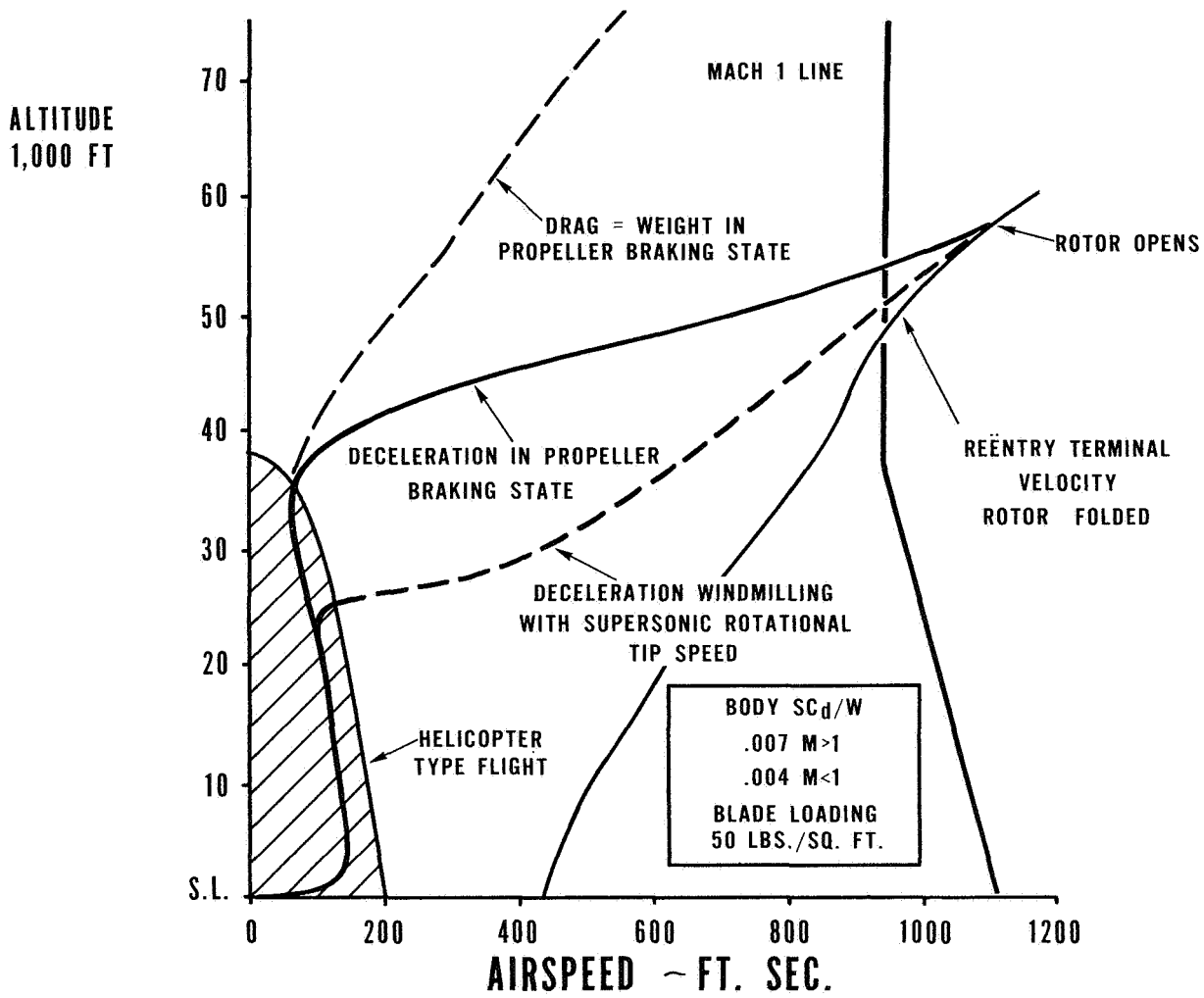

Figure I-4-26. Variation of airspeed with altitude supersonic opening case

The weight of propellant may now be calculated from:

$$W_p = \frac{T_f \, t_f}{I_{SP}}$$

where I_{SP} is the specific impulse rating of the rocket fuel. Reference 3 also states that the thrust required for a glide approach with forward velocity is 50 percent of that for vertical flare. The glide thrust reduction is due to the decrease of rotor induced drag as discussed in Reference 12. The values of propellant weight required for the flare and glide approach maneuvers are shown in the table below:

		Weight Propellant (lb)	
	Thrust	I_{SP} = 130	I_{SP} = 230
Glide Approach	565 (lb)	12.9	8.4
Flare Maneuver	1130 (lb)	25.8	16.8

For a launch pad abort situation, the ROR system would apparently perform quite well. For any recovery system, the abort rockets will be necessary to remove the capsule from the danger area. At the apogee of the abort ballistic trajectory the ROR system could be deployed. Reference 3 states 200-300 ft will be needed to attain steady descent velocity, after full autorotation has started. The remainder of the abort apogee altitude will be available for the initiation of autorotation which in the case of the ROR system can be augmented by the use of the tip rockets. The rocket motors could also be used as desired for increased lift and terminal maneuvering.

The glide, terminal maneuverability, and flare performance of this system look quite attractive. Figure I-4-28 from Reference 4 shows an expected system weight for a wide range of vehicle weights. Figure I-4-29 from Reference 3 gives a comprehensive analysis of ROR weight in terms of the desired capabilities.

Assuming the weight distribution with rotor disk loading is the same for 5000- and 10,000-lb vehicles, Figures I-4-28 and I-4-29 may be used to estimate the weight of the necessary blades and root retention fittings. Having calculated the propellant weights necessary for the forward velocity glide and flare maneuvers and assuming

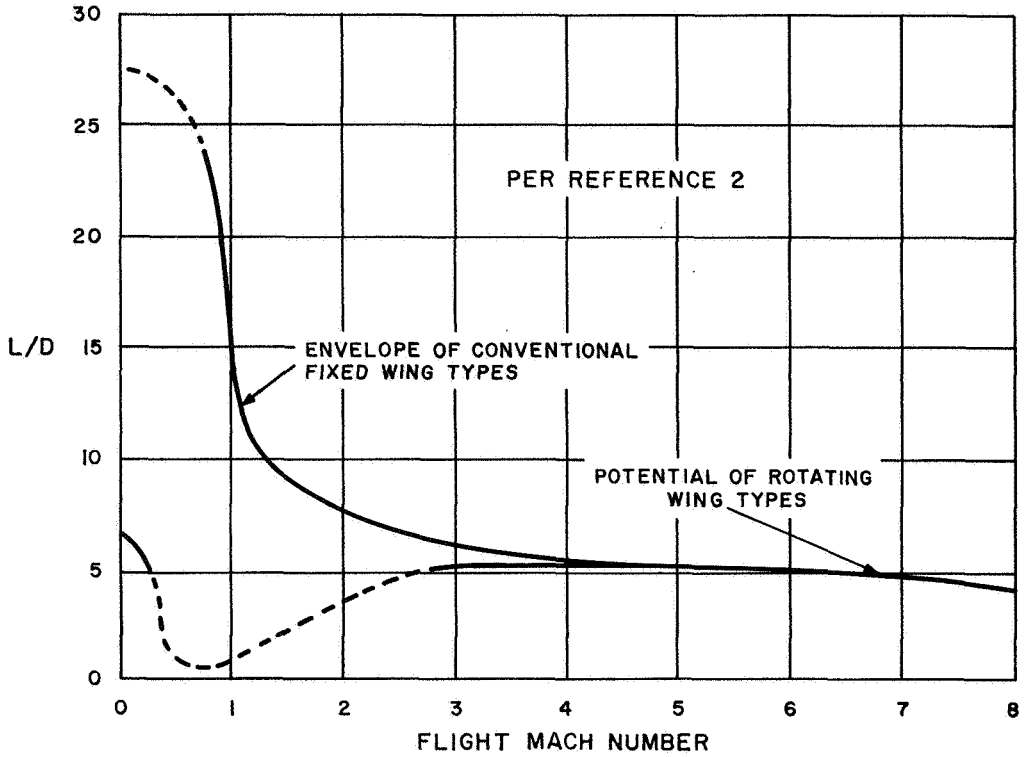

Figure I-4-27. Comparison of lift-drag ratios of fixed and rotating wing aircraft

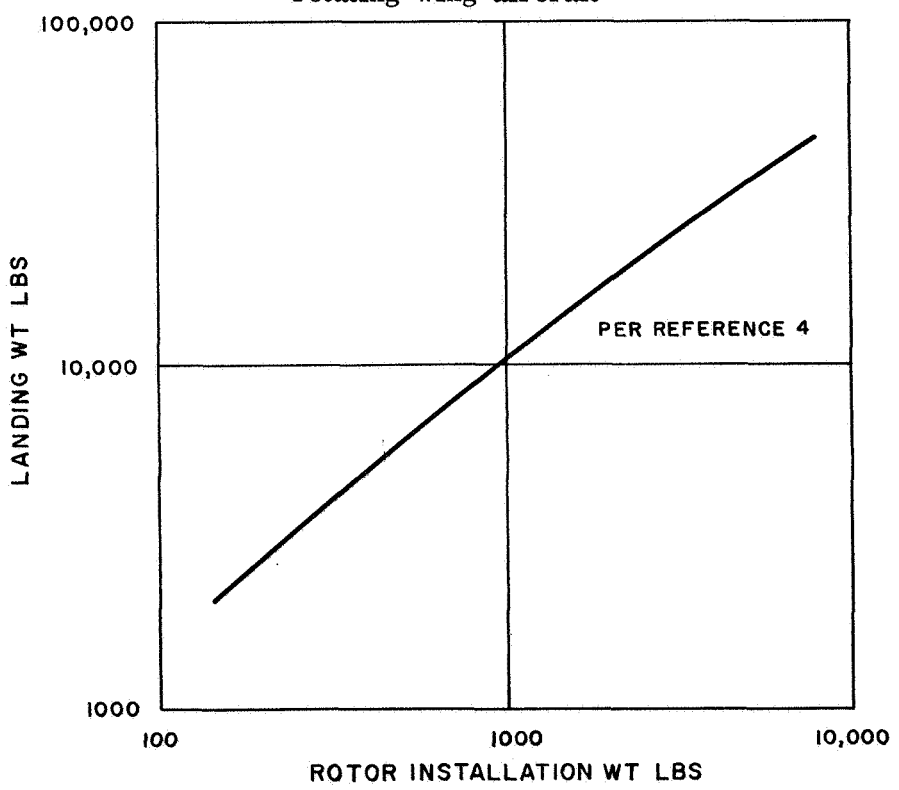

Figure I-4-28. Preliminary weight estimates of rotor recovery system vs vehicle landing weight

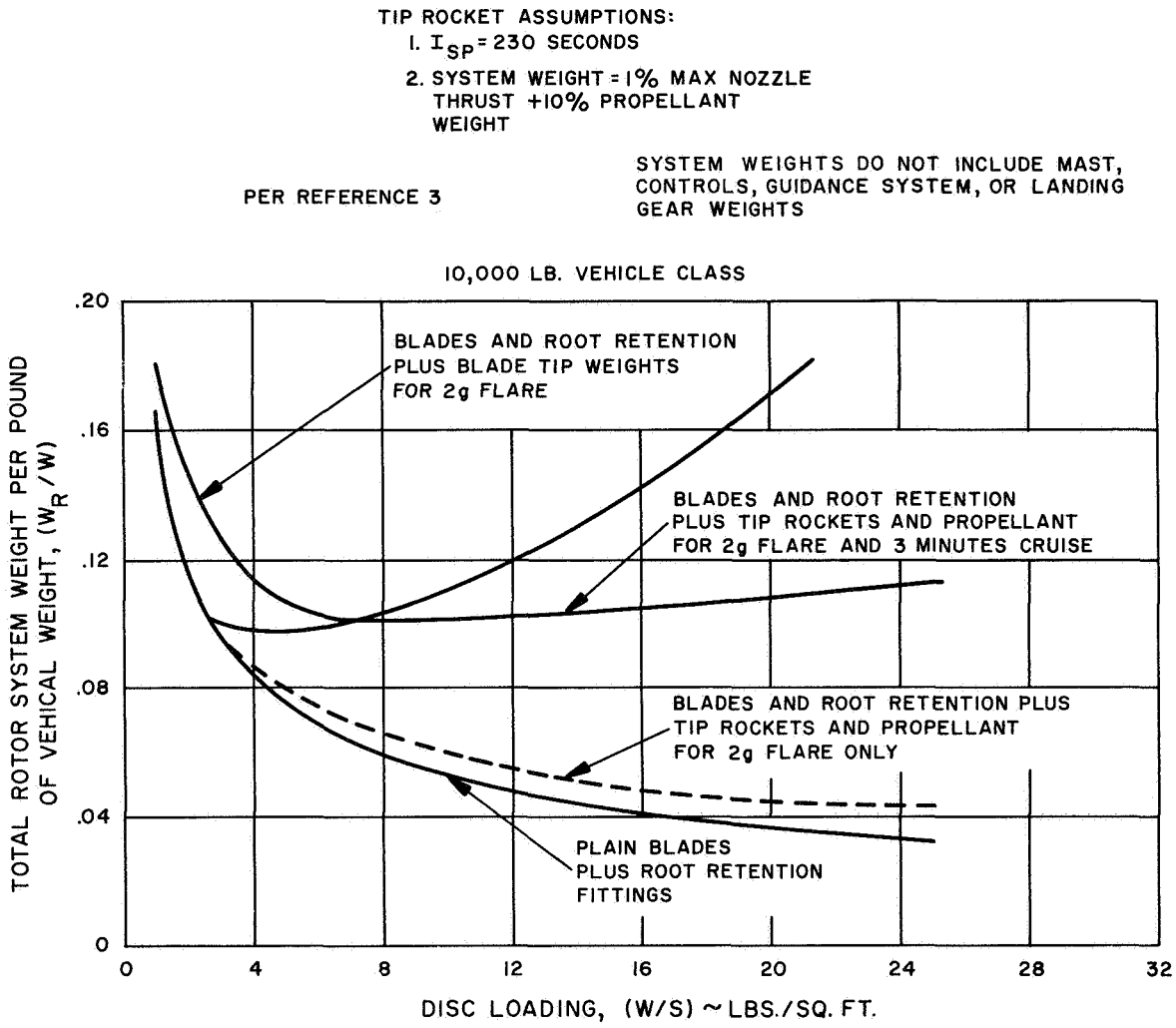

Figure I-4-29. Preliminary comparison of rotor recovery system weights using tip weights or tip rockets

the rocket motor weights given in Reference 3, the following Table may be made:

		Rotor Radius (ft)	Total Blade Weight (lb)	Total Rocket Motor Weight (lb)	Tankage fuel lines & misc. hardware weight (lb)	Weight Propellant (lb)	Total ROR System Weight (lb)
Forward velocity	I_{SP}=150	10	155	21	100	12.9	288.9
glide approach	I_{SP}=230	10	155	21	100	8.4	284.4
Flare	I_{SP}=150	10	155	21	100	25.8	301.8
Maneuver	I_{SP}=230	10	155	21	100	16.8	292.8

Investigations of the ROR concept are being pursued in conjunction with the Reaction Motors Division of Thiokol Chemical Corporation and the Bell Helicopter Company. Application of the ROR concept to helicopter systems has already been successfully achieved, and continued development of this concept for the APOLLO vehicle appears to be a feasible and desirable course of action to pursue. Such development should lie in the areas of rotor mechanization, storage and protection of blades, and system tests.

4.4.1.3 AUTO ROTATIONAL REELABLE ROTOR SYSTEM (RRS)

The RRS under consideration during the APOLLO study was first investigated for GE-MSVD by the Vertol Div. of Boeing Airplane Co. for the 2700 pound RVX-2 vehicle.

The RRS rotor consists of two flexible stainless steel blades. The blades are terminated by tip weights which assist in blade deployment, centrifugally stiffen the blades, and store kinetic energy which is dissipated in the flare maneuver at touchdown. To decrease the packaging problems the blades are stowed on rollers. These rollers, geared together, are mounted on a hub which may rotate independent of the APOLLO vehicle. Also mounted on the hub are small solid rocket motors, which provide rotational energy for blade deployment. Pitch control (both collective and cyclic) is applied by servo tabs at the rear of the tip weights. The servo tabs are controlled by an electric motor clutch mechanism housed in the tip weights.

A recovery mission profile may now be investigated in terms of the functional interrelationships of the components. When the aerodynamic heating phase of the re-entry flight has been completed, either a drogue parachute or explosively jettisoned doors are used to remove the system from its stowed location and position it at the base of the R/V for blade deployment. When the RRS attains proper orientation, solid rockets will ignite, spinning the hub and initiating blade deployment. Deployment loading may be controlled by pitch setting and/or rate of blade extension. As the system enters the autorotational regime, cyclical pitch may be applied resulting in either a vertical or gliding descent. As the vehicle approaches the touchdown, the kinetic energy of the rotor will be dissipated by an abrupt rotor pitch change. The RRS flare thrust that is developed is directly proportional to an integration of blade torque decay.

During an on the pad abort, the normal escape rocket system would be utilized to remove the R/V from the danger area. RRS deployment would be initiated as soon as possible allowing maximum time for autorotation. Due to the autorotational nature of the system, however, the deployment altitude required in this case may become a problem. Terminal maneuverability will decrease considerably under the abort conditions, but the RRS will maintain its inherent ability to combat adverse wind conditions.

The determination of the size and weight of the RRS system necessary to recover a particular R/V becomes most critical at terminal flare. An order of magnitude system has been designed for the APOLLO R/V based on the following conditions:

Rotor Radius = R (ft)

Air Density = $\rho\alpha$ (slugs/cu ft) - sea level

Blade Thickness = t = 0.032"

Number of Blades = 2

Blade chord = c (ft)

Blade Tip Speed = V_T = 800 ft/sec.

Material Safety Factor = SF = 3

Ultimate Tensile Strength = T_S = 180,000 lb/in^2 (stainless steel)

Density of Stainless Steel = ρ_{SS} = 490 lb/cu ft

Vehicle Weight = W_V = 5000 lb.

Time required to flare = $t_f = 0.059 \sqrt{\dfrac{W_V}{2\pi R^2}}$ (sec.) - Reference 3

Blade Weight = $W_B = ctR\rho$ (lb)
Tip Weight = W_T (lb)
Gravitational Constant = g (ft/sec^2)

The maximum allowable tip weight is calculated from:

$$\frac{ct\ T_S}{SF} = \frac{V_T^{\ 2}}{Rg} \sqrt{\frac{W_B}{2} + W_T} \qquad (1)$$

The solution of (1) is shown on Figure I-4-30. The time required to perform a 2g flare maneuver with a 5000 pound R/V may be found from the above equation for t_f. This time is shown in Figure I-4-31 as a function of rotor radius, R. Also shown in Figure I-4-31 is the time of flare endurance (which includes the time required to flare) as a function of rotor radius as obtained from Reference 5. At the intersection of the time required to flare and the flare endurance curves we have the minimum Rotor radius allowable. The rotor radius selected from Figure I-4-31 may now be used to enter Figure I-4-32 which gives total RRS weight. From the conditions used, two systems could be chosen for the APOLLO mission:

Rotor Rad ft.	Blade Chord ft.	Number Blades	Blade Weight (lb)	Total Tip Weight (lb)	Component Wt* (lb)	Total Syst. Wt. (lb)
21	2	2	113	42	177	333
18	3	2	141	54	177	372

*Note: Weight of hub spin rockets and other mechanical component considered constant at 177 lb.

4.4.1.4 FLEXIROTOR RECOVERY SYSTEM (FRS)

Barish Associates, under subcontract to GE-MSVD, has studied the applicability of a flexible rotor to recovery systems. A preliminary flexirotor design for a APOLLO vehicle has been accomplished.

The FRS as shown in Figure I-4-33 consists of a drogue parachute, Vortex ring parachute and 4 synthetic fiber (nylon or dacron) blades. Each blade contains a leading and trailing edge fiber reinforcement to increase its tensile strength and rigidity. The blade tips contain aerodynamically stabilized weights which provide the rotor kinetic energy for a flare maneuver. The vortex ring parachute acts as the rotating

CONFIDENTIAL

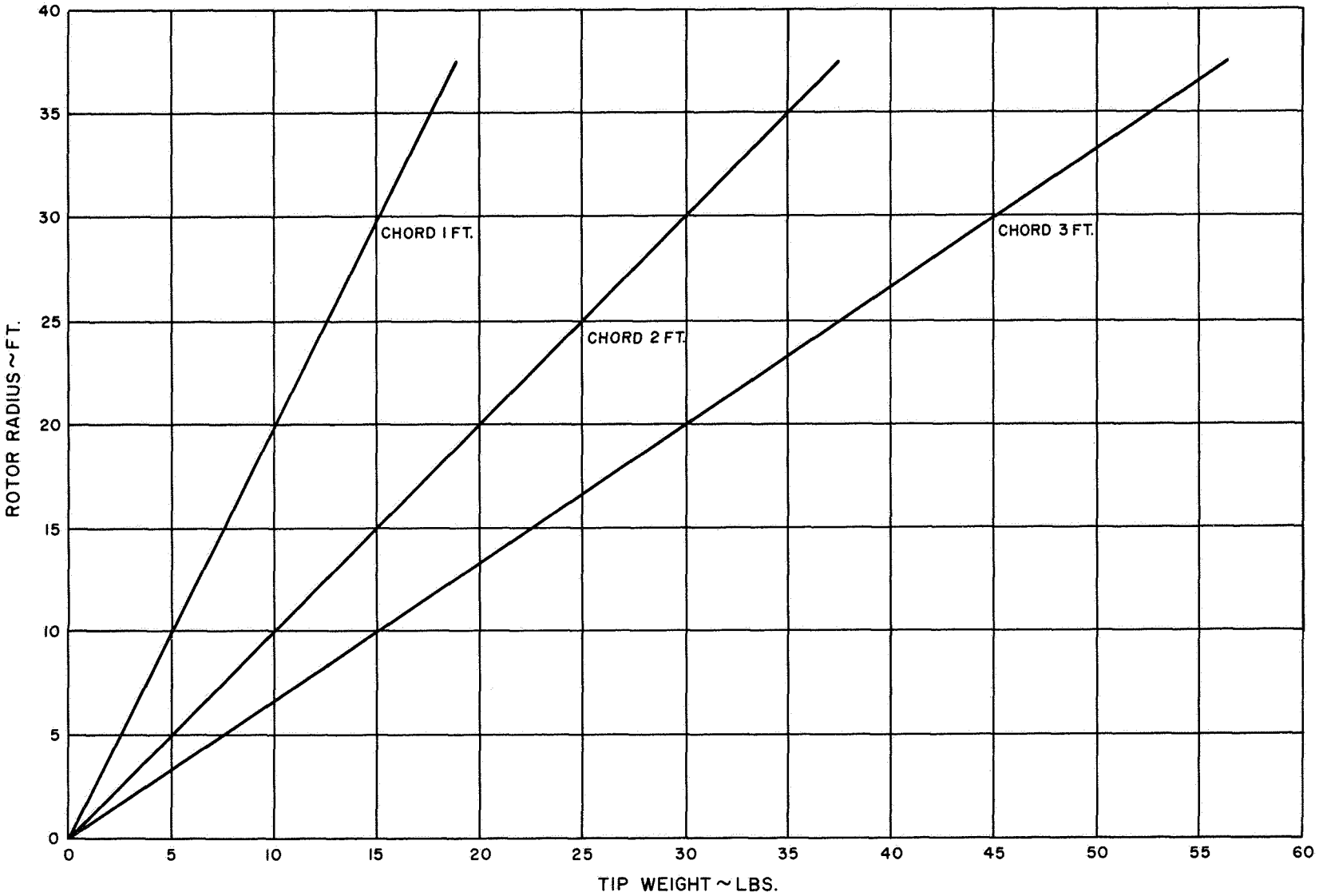

Figure I-4-30. RRS maximum tip weight (lb) considering blade strength

CONFIDENTIAL

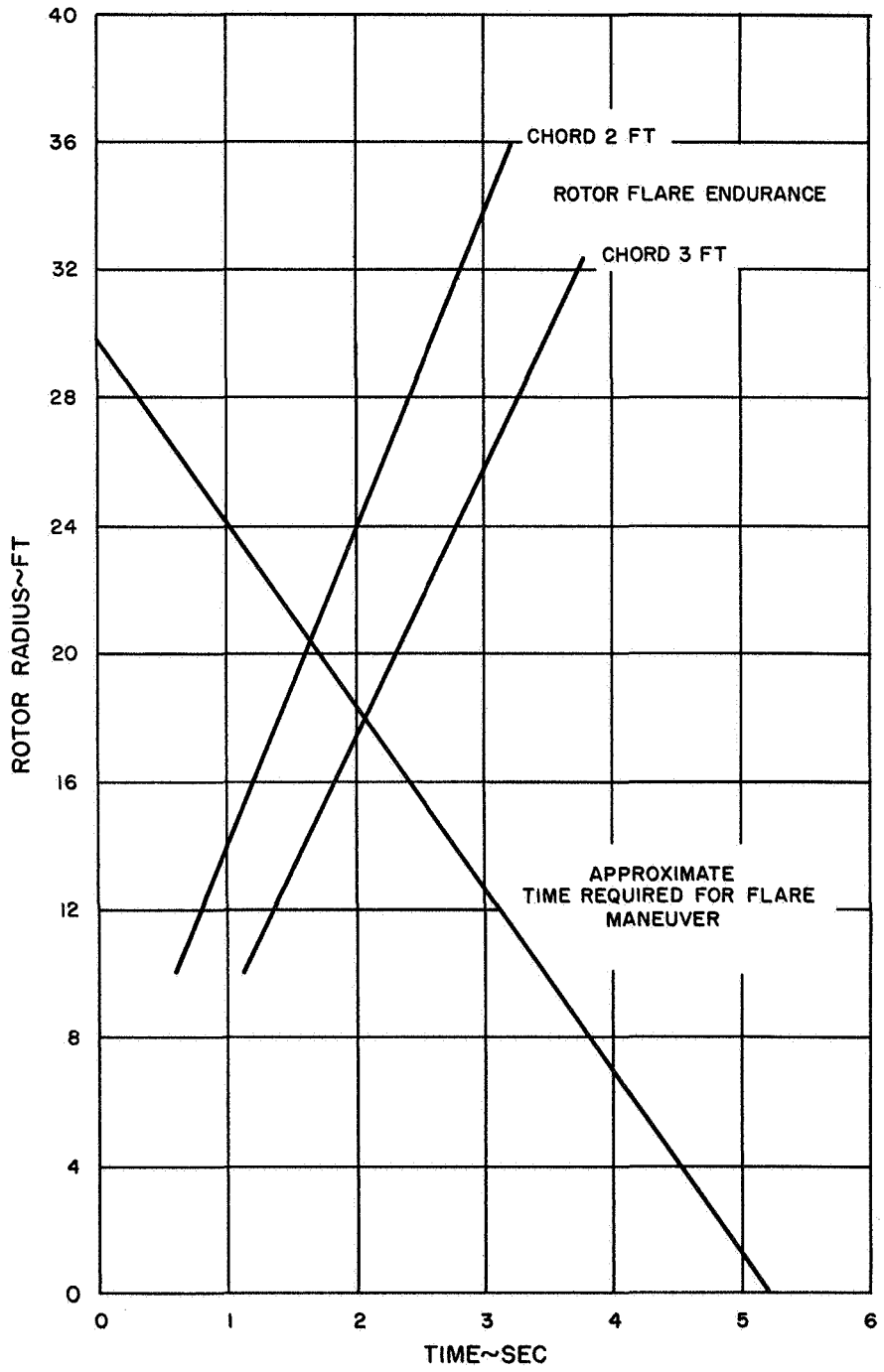

Figure I-4-31. RRS rotor length selection

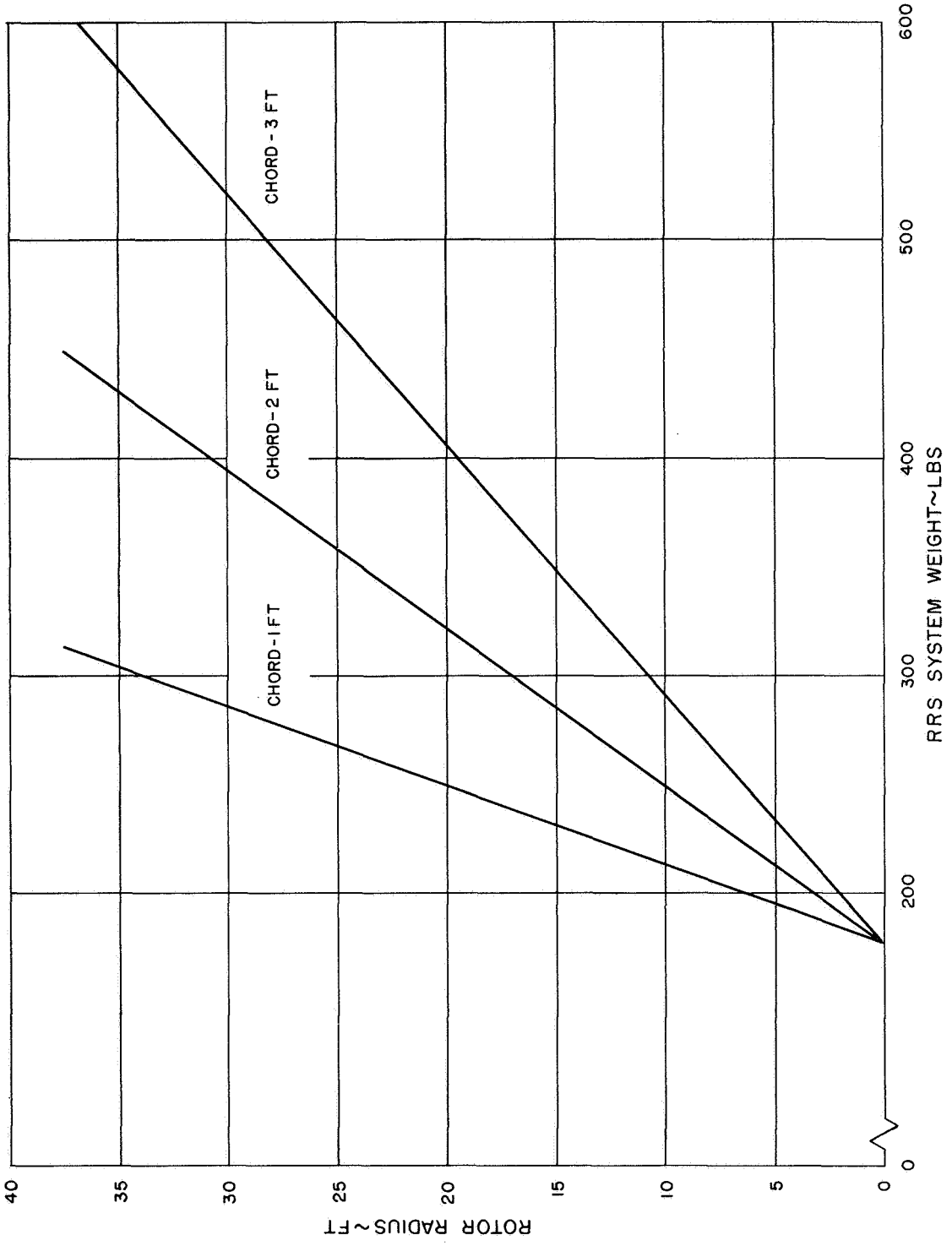

Figure I-4-32. RRS weight estimation

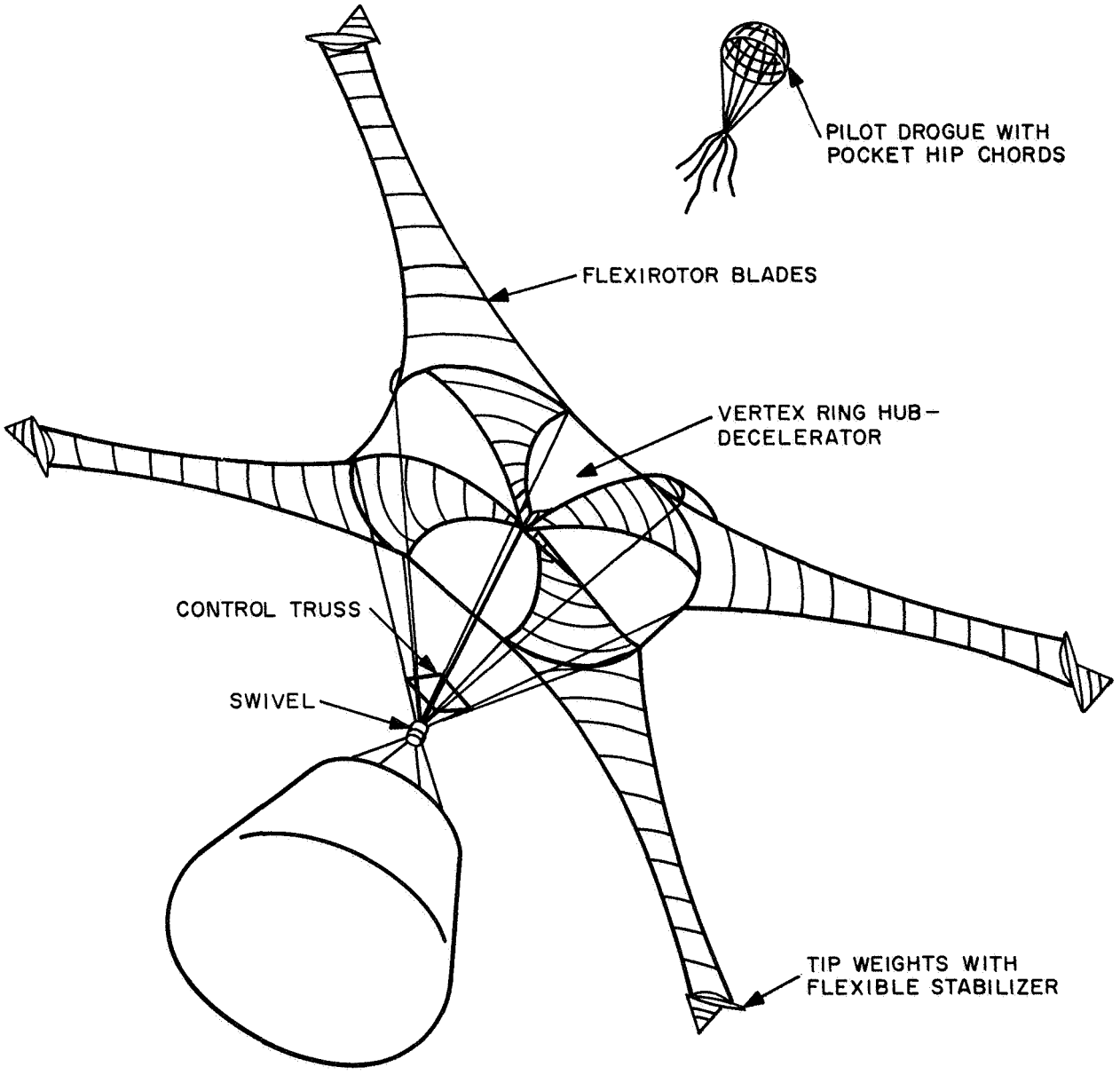

Figure I-4-33. APOLLO recovery system with flexirotor recovery system

hub of the system. The FRS is connected to the R/V by suitable riser lines and a low friction swivel to prevent high induced R/V rotational speeds. Prior to recovery, the drogue and vortex ring parachutes are packed in a conventional manner while the blades are packed in pockets on the periphery of the vortex ring parachute.

Under the conditions of normal recovery the FRS will operate as follows: - After the re-entry heating phase of the recovery mission has been completed, the drogue parachute of the FRS is deployed with a mortar charge. Some R/V velocity retardation may be gained from the drogue parachute but its main function is to deploy the rotating hub (vortex ring parachute) of the FRS. When the vortex ring parachute attains the proper rotational velocity and altitude the blades are deployed by centrifugal force. As the blades extend, the system drag area increases, and vehicle vertical velocity is further reduced. The FRS with full blade extension becomes fully autorotational and descends at equilibrium velocities approximately equal to those obtained with a parachute of FRS diameter. Near ground zero a step change in blade pitch is effected for a flare-out by using pyrotechnic cutters and snubbing lines to increase the length of the blade leading edge member. Glide may be achieved by repositioning the control truss (Figure I-4-33) relative to the R/V.

For an on the pad abort mission, the escape rocket system will be used to remove the vehicle from the danger area. At the apogee of the ballistic abort trajectory, FRS deployment would be initiated. Under a worst case condition, i.e. velocity = 0 at apogee, approximately 1000 ft would be needed to deploy the FRS and bring it to equilibrium descent; 200 feet would also be needed to perform the flare maneuver. The minimum abort altitude for FRS deployment will thus be about 1200 ft.

To use the FRS gross navigational error correction capability in a normal recovery sequence, the vehicle must be decelerated to reasonable subsonic speeds in order to deploy the blades. The ability to rapidly acquire this subsonic speed then leads to the use of the vortex ring parachute as the hub for initial supersonic retardation. This chute has been deployed in tests at M = 2.2 by NASA and M = 1.5 by Cook Research Laboratories. The vortex ring parachute chosen for this application has an inflated diameter of 18 ft, a subsonic drag area of 200 sq ft, a weight of 30 lbs and an ultimate canopy strength of 60,000 pounds.

Table below shows the parachute loading for deployment at various points on a typical APOLLO equilibrium glide trajectory.

Altitude (1000 ft)	p/p_o	Velocity ft/sec	Dynamic Pressure (lb/sq ft)	Drag (lb)
80	.036	2400	250	50000
60	.094	1240	171	34200
40	.25	830	86.5	17300
20	.53	590	22.4	4480

From the table it may be noted that supersonic deployment of the vortex ring chute at $V \doteq 2400$ ft/sec or less should give adequate structural safety. If position error corrections are applied to the vehicle, blade deployment must be delayed to the subsonic speed regime to preclude the possibility of sonic blade tip speeds and excessive centrifugal forces.

Since the flare is the most critical portion of the recovery, rotor blades designed to flare properly will perform acceptably under all other conditions. From calculation based on the assumption that the change in rotational kinetic energy must equal twice the vertical kinetic energy of the R/V, blade size and weight may be found for a four blade rotor system and a 5000 lb vehicle:

Rotor Radius = 27.5 ft
Vertical descent Velocity, V_V = 41.8 ft/sec
Total Rotor weight = 55 lb (Reference 8)

The maximum allowable tip weight is calculated from blade strength consideration, and was found to be 12.1 lb/blade or 48.4 lb total. The flexirotor has been tested for autorotation gliding at Princeton and at NASA Langley. The maximum glide ratio measured was about 8:1 for the rotor alone. Profile drag of the body will reduce the above mentioned glide ratio but if glide is initiated at 20,000 ft, an area of approximately 20 miles radius should be available for mission termination.

The flare maneuver will be accomplished by a step change in rotor pitch. This change will produce high values of lift to decelerate the vehicle vertically while the blade decelerates in rotation. The upwash through the blades will be changed to a downwash giving hover capability until the blades can no longer sustain rotation. Figure I-4-34 shows the time relationship of blade pitch and drag during flare.

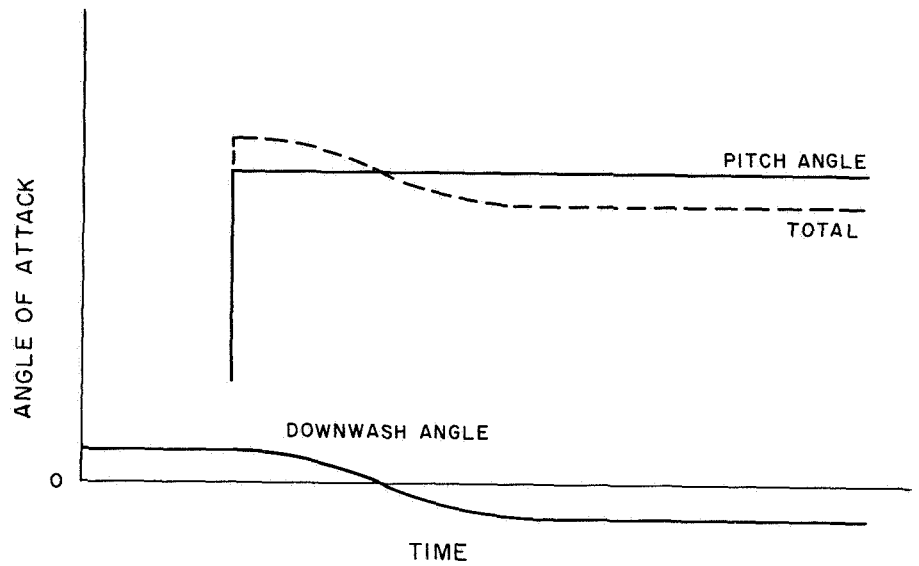

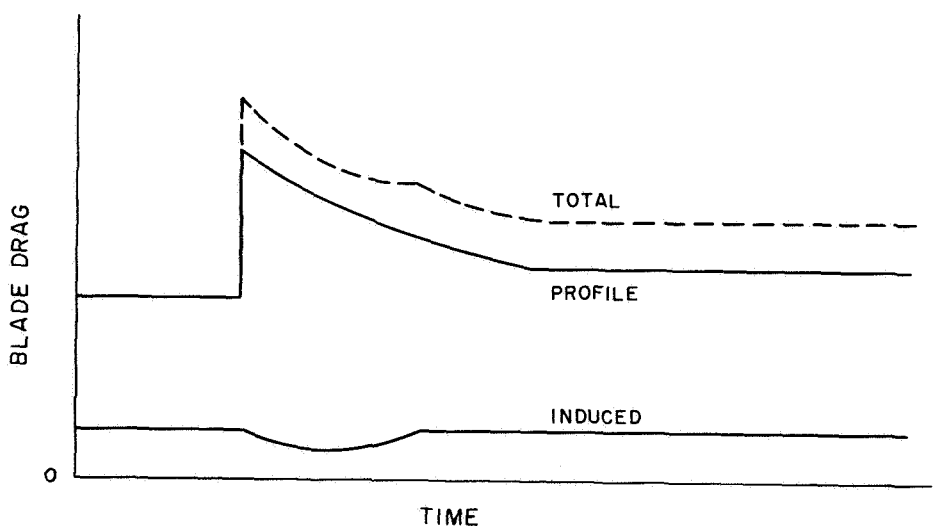

Figure I-4-34. Expected rotor performance during flare

Having previously defined the approximate weights of the principal system components, a total system weight analysis may be made for a 5000 lb vehicle:

Vortex Ring Parachute (18' dia)	30 lb
Rotor Blades (including structural members)	55 lb
Rotor blade tip weights	48 lb
Drogue Parachute	15 lb
Bags, Swivel, Misc Hardware	52 lb
Approximate Total FRS Weight =	200 lb

Barish Associates are currently investigating the FRS system for Army and Air Force recovery applications. A 6 foot diameter FRS model has recently completed the initial phase of a test program in the 20 foot vertical wind tunnel at the NASA Langley Research Center. Other tests have also been performed at the Princeton and United Aircraft Wind tunnels (Ref. 6 and 7). Another test program soon to be started will establish performance and stability of the FRS in the 12' stability tunnel. Following the completion of the current wind tunnel tests, a full scale FRS will be built and a drop test program conducted for a vehicle in the APOLLO weight class.

4.4.2 Parachutes and Other Retardation Devices

4.4.2.1 SUPERSONIC APPLICATION

The extension of the operational region of parachutes, especially at supersonic velocities, has been recognized as a desirable addition to the retardation state-of-the-art for some time. Numerous investigators have concluded that chute operation at $M > 2$ can be extremely critical; chute opening is unreliable or, if it opens, stability characteristics are poor in connection with unstable or random oscillations, structural instability and eventual canopy destruction. To alleviate this problem, a supersonic retardation device has been proposed by Dr. H.G. Heinrich of the University of Minnesota, which would increase the static pressure of the captured air in a series of smaller pressure changes, and finally allow the entire air mass to escape through the vent of a parachute like cup. A sketch of this design, known as a spiked parachute, is shown in Figure I-4-35. Testing of the flow details about the configuration have been accomplished with a water table, and wind tunnel tests at $M = 3.0$ have

been conducted. To date, the results are very encouraging in that stable conditions have been obtained for reasonable values of drag coefficient (0.28). The continued development of the spike parachute could certainly contribute to an optimization of the APOLLO retardation system in those cases where added deceleration at $M>2$ would be desirable - for example, in connection with the need for a first stage decelerator prior to the use of the parawing in the equilibrium glide maneuver situation.

Other trailing drag devices have also been proposed for supersonic application. These devices are mostly of the forced inflation or solid body type of structure. They include cones, spheres (balloons), latticed plates and cones, and other like schemes. One of the most promising of these devices is the inflatable cone. Maynard of the NASA Langley Research Center has obtained drag coefficients in excess of 1.0 at supersonic Mach numbers up to 5. Further investigation of these devices would be desirable, especially in regard to the inflatable structures and the design approach for obtaining reliable inflation with a minimum weight penalty for the system. These devices would have an APOLLO application similar to that previously mentioned for the supersonic parachute.

4.4.2.2 CONTROLLABLE PARACHUTES

The attractive weight, packaging and reliability aspects of parachutes make them the optimum selection as recovery devices at the present time. However, conventional parachutes have two undesirable features as a recovery device in that they possess:

1. Little capability to maneuver and avoid obstacles on landing such as rocks, trees, power lines, etc.
2. Little capability of correcting for wind drift.

The importance of the first feature above, can be appreciated if the effects on impact attenuation caused by the above mentioned obstacles, are considered. The second parachute characteristic, wind drift, can also affect the operation of the impact attenuation device by imparting a horizontal velocity to the vehicle which certain impact devices find undesirable. The wind drift could also cause drift back over the pad on launch pad abort missions. It is, therefore, clear that the parachute recovery system would become even more attractive if some means were available to overcome wind drift and provide last minute maneuvering capability. One method of handling

such a situation is to modify a conventional parachute so that it will be capable of glide maneuvers with preferential orientation. This type of parachute is referred to as a controllable or dirigible parachute. Two investigators presently working with this type of parachute are Radioplane Division of Northrop Corporation and Sandia Corporation, Ref. 10, 11.

The Sandia system is a conventional parachute with a gore or gores removed to provide the thrust for gliding. The directional control is obtained by pulling on a guide line which is attached to the parachute skirt at the corner of the removed gore, thereby giving rotational control in two directions. Wind tunnel and drop tests have shown that glide angle and rotational response were good for a small solid, flat circular chute. Figure I-4-36 shows glide path drop test results obtained with this particular chute. The selected APOLLO Recovery System VI of Table I has a canopy loading of 0.75 lb/sq ft, which approaches the optimum loading value shown in the Figure I-4-36 for maximum glide angle.

The Radioplane dirigible parachute is a second type being investigated. This type of controllable parachute has a section of the canopy which is hinged to the main canopy near the canopy vertex. For normal descent it is held in its normal position by control lines. For initiation of the glide the control lines are played out allowing the skirt of the hinged section to rise. This produces a "hole" in the side of the chute producing a thrust and, therefore, gliding. Directional control is achieved by varying the length of the control lines so that the skirt of the hinged section is pulled down on one side. This produces a twist of the hinged section which changes the direction of the thrust vector so that rotation of the chute is obtained. Qualitative drop tests have been made on single and clustered parachutes of this type. Typical results obtained were:

$V_{horizontal}$ = 8.5 ft/sec

$V_{vertical}$ = 15.8 ft/sec

average glide angle = 28 degrees

for a conical type parachute approximately 40 ft in diameter.

A parachute recovery system using controllable chutes is slightly heavier than one with conventional chutes due to the necessary control devices. However, the increased

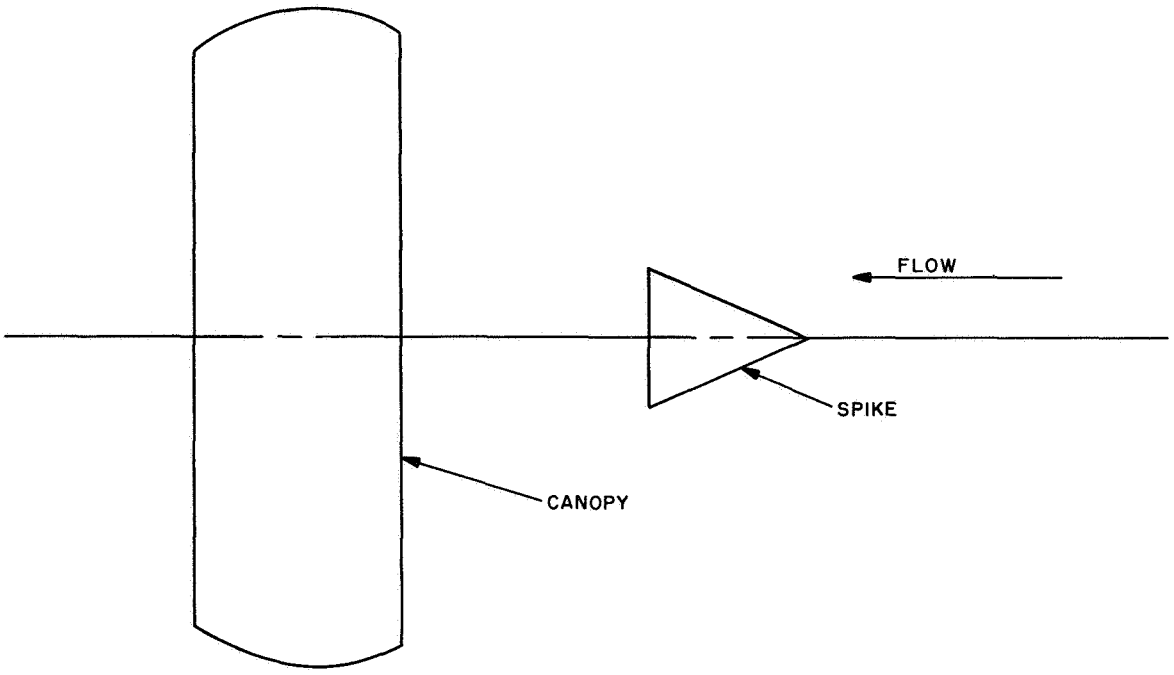

Figure I-4-35. Supersonic spiked parachute configuration illustrative sketch

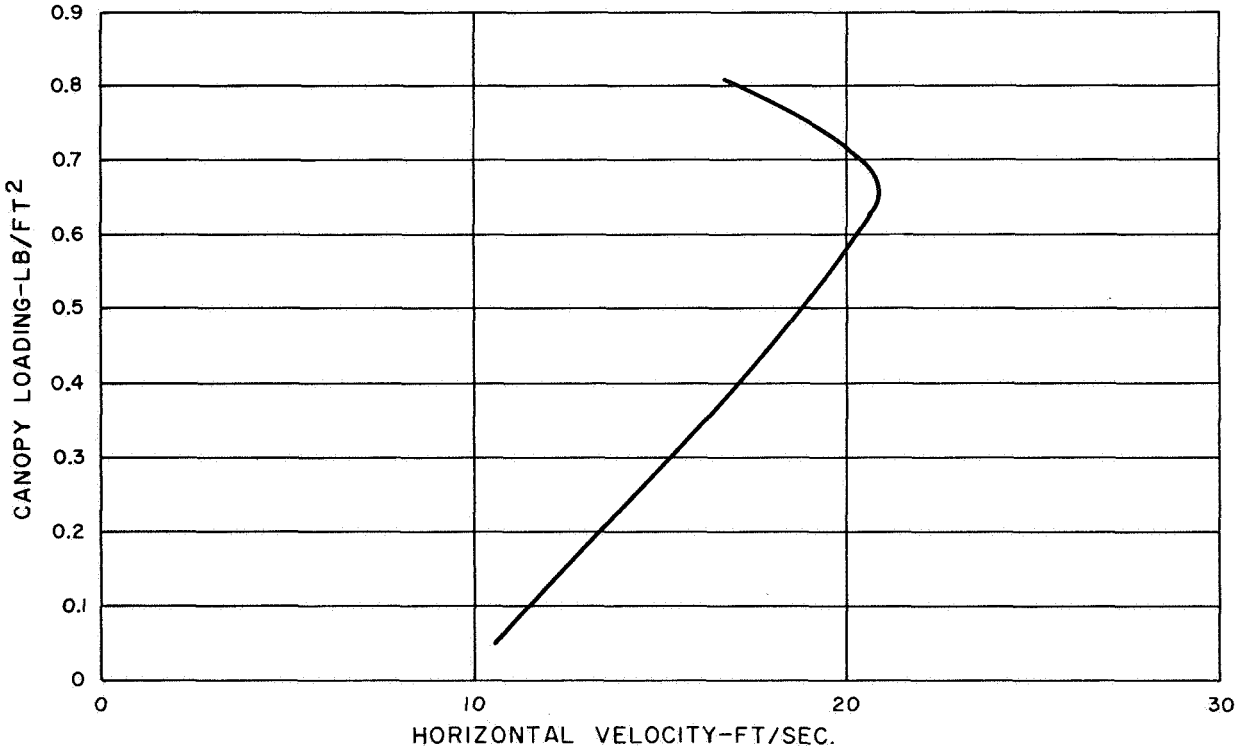

Figure I-4-36. Effect of canopy loading on horizontal velocity - per reference 11

capability, which the unrefined tests to date have indicated, is well worth the small increase in weight that is suffered. The increased capability also allows a parachute recovery system to compete more favorably with glide type recovery systems now being considered for advanced recovery.

4.4.3 Approach and Landing — R-3 Configuration

4.4.3.1 L/D CONSIDERATIONS

To establish the subsonic L/D requirements for satisfactory landing characteristics of hypervelocity vehicles, the results of two approaches to a quality rating were reviewed; that used in the Dyna Soar Phase Alpha study and that discussed in NASA TM X-334. These were based on the results of X-15 flight tests and flight tests of an F-104A and an F-102 which were simulating low L/D aircraft landings. The L/D and approach velocity boundaries within which the landing characteristics are deemed acceptable differ in each approach although there is a considerable overlap of acceptable area. They differ partly because one approach apparently uses only flight test data while the other includes additional calculations and assumptions relating to hypervelocity vehicles. Further differences were undoubtedly introduced in the analyses of flight tests and pilot opinion both of which offer considerable data "scatter". Both approaches appear sound and the R-3 configuration has been designed to have subsonic characteristics that are acceptable to either rating system.

A summary chart which is a composite of the results of both analyses is presented in Figure I-4-37. The results have been modified to reflect the present wing loading of the R-3 configuration. This figure shows the L/D ratios and corresponding limits of flare-initiation speeds which will permit acceptable landings to be made. The minimum L/D for good landing capability is indicated. From this composite plot, the minimum acceptable L/D is 3 and for good landing capability the minimum L/D is 4. The estimated L/D_{max} of the R-3 configuration is 5 which should provide good landing capability with the range of flare-initiation speed from about 210 knots to 325 knots.

4.4.3.2 LANDING PERFORMANCE OF THE R-3 CONFIGURATION

The subsonic glide characteristics of glide velocity, flight path angle and rate of sink have been calculated for the R-3 configuration based on the estimated subsonic aerodynamic parameters and are presented in Figure I-4-38. Glide at L/D_{max} which

CONFIDENTIAL

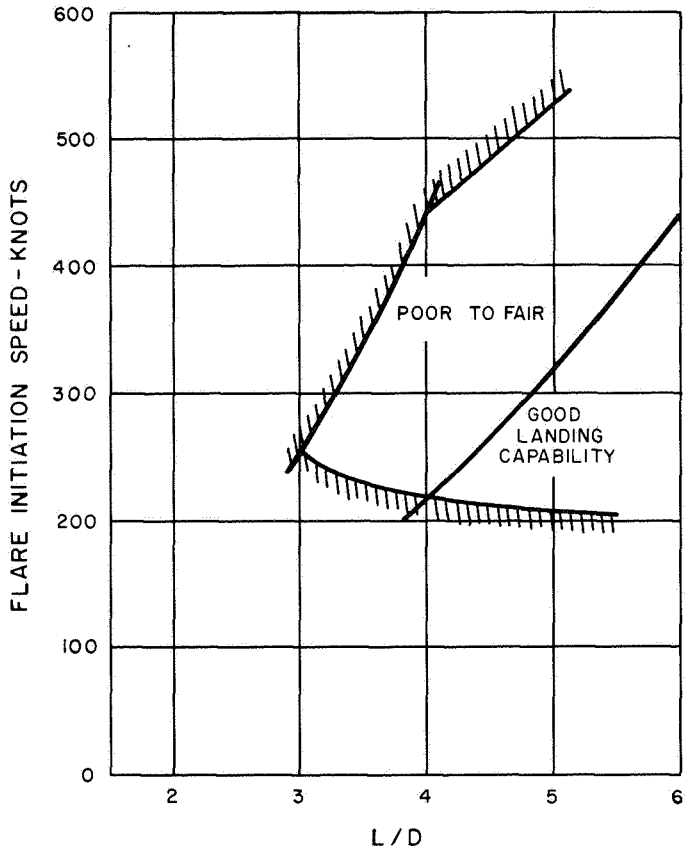

Figure I-4-37. L/D and approach speeds for acceptable landing characteristics

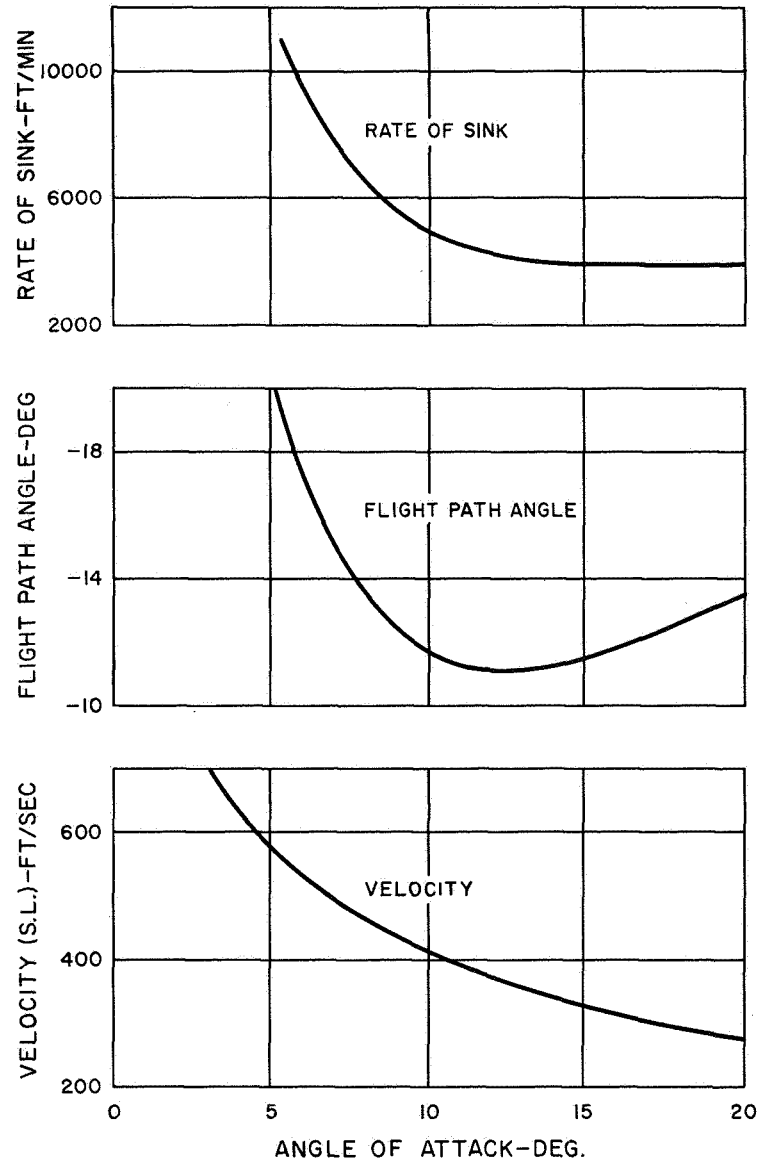

Figure I-4-38. Modified lenticular vehicle subsonic glide characteristics

CONFIDENTIAL

occurs at 12 degrees angle of attack, results in a flight path angle of 11.17 degrees, a sea level velocity of 370 ft/sec (219 knots) and a rate of sink of 4290 ft/min. Minimum sink occurs at 18 degrees angle of attack and is 3840 ft/min with a corresponding velocity of 290 ft/sec (172 knots) and a flight path angle of -12.74 degrees.

Using these characteristics, a terminal glide from 4300 feet to touchdown was calculated for an abort from the launch pad and is shown in Chapter 3 of Volume II under "Supplemental Data for the R-3". This glide was calculated at L/D_{max} and is not considered a nominal path since it leaves no means of extending range by varying L/D. The flare and touchdown were calculated with an angle of attack of 20 degrees which was assumed to be the touchdown attitude. With an assumed 20 percent increase in C_L at touchdown for ground effect, the touchdown occurred at 252 ft/sec (149 knots) with about 200 feet altitude being required for the flare. A nominal path would of course be at a lower angle of attack and correspondingly higher velocity to permit either extending or decreasing range in order to touchdown at the proper point. As mentioned above, the touchdown angle of attack was assumed to be 20 degrees. Since this configuration has no landing gear, the tail end of the vehicle will touchdown first and then the vehicle will rock forward on the curved bottom suface. It will require a shock absorbing device at the tail end to prevent it from bouncing and the rocking characteristics will depend on the vehicle aerodynamic, dynamic and physical characteristics.

For normal landings at pre-selected sites, 20 degrees angle of attack will probably be sufficient. However, in emergency landings on unprepared land areas or in water it will be desirable to decrease the forward velocity as much as possible prior to touchdown. The optimum conditions of attitude, velocity and sink speed for touchdown can probably best be determined by tests with full scale models instrumented to measure longitudinal, normal and rotational accelerations. Such tests should also include the use of parachutes. No analyses of these emergency landings have been made. However, experimental studies currently being conducted by the NASA - Langley on similar configurations are providing useful data.

SPECIFIC REFERENCES USED IN TEXT

(1) "United States Air Force Parachute Handbook", WADC TR No. 55-265, December, 1956.

(2) Haig, Chester R., Jr., "The Use of Rotors for the Landing and Re-entry Braking of Manned Spacecraft", IAS Paper No. 60 - 17.

(3) Fletcher, C. J., Tesch, E. C., Jr., "ROR-Chute Concept for Recovery Systems", Reaction Motors Division TR 3740, 27 January 1961.

(4) Haig, C., McDowell, E., Lynn, R., Dukes, W., "Proposed Researches to Investigate Stored Energy Rotor Recovery Systems", Bell Helicopter Company Report No. 299-099-132, Vol. II, 12 April 1960.

(5) Anom., "Preliminary Study of an Autorotative Reelable Rotor as a Lift/Drag Device for Nose Cone Recovery", Vertol Division of Boeing Airplane Company, Report R - 230, 3 January 1961.

(6) Barish, D.T., "Technical Report on Model Tests of the Vortex Ring Parachute in the Princeton 4' x 5' Wind Tunnel", Barish Associates, February, 1959.

(7) Barish, D.T., "Technical Report on Vortex Ring Parachute Tests at United Aircraft Wind Tunnel", Barish Associates, 1959.

(8) Barish, D.T., "Diaphragm Rotor Blades - Performance and Weight Estimates", Barish Associates, 1959.

(9) Coppa, A.P., "Apollo Landing System", GE-MSVD PIR 290-007, 2 February 1961.

(10) Ewing, E.G., "Radioplane Dirigible Parachute Development", Radioplane Report No. PTM - 332, February, 1961.

(11) Kane, Milton T., "A Guided Parachute System", Proceedings of the Recovery of Space Vehicles Symposium, 1960.

(12) Gessow, Alfred and Myers, Garry C., Jr., "Aerodynamics of the Helicopter", The MacMillan Company, New York, 1952 (First Printing).

GENERAL LIST OF REFERENCES EMPLOYED

(1) Heinrich, H.G. et al, "Theoretical Parachute Investigations", Progress Reports 1 - 15, University of Minnesota, 1957-1960.

(2) "ARDC Atmospheric Model, December, 1951", GE-MSVD PIBA-2.

(3) Maynard, Julian D., "Aerodynamics of Decelerators at Supersonic Speeds", Proceedings of the Recovery of Space Vehicles Symposium, 1960.

(4) Smith, Anthony M., "Some Aerodynamic Considerations in the Recovery of Re-entry Vehicles", GE-MSVD TIS R60SD423, 1960.

(5) Ewing, E.G., "A Minimum Weight Landing System for Interplanetary Spacecraft", Proceedings of the Recovery of Space Vehicles Symposium, 1960.

(6) Gimalouski, Edward G., "Development of a Final Stage Recovery System for a 10,000 Pound Weight", WADC TR 59-109, December, 1958.

(7) Howell, R., "Parachute Recovery System Bomb Tests", The Martin Company, Engineering Report No. 10197, June, 1958.

(8) Engrstrom, B.A. and Meyer, R.A., "Performance of Trailing Aerodynamic Decelerators at High Dynamic Pressures", WADC TR 58-284, Parts I, II, III, 1959.

(9) Wiant, Harry W. and Fredette, Raymond O., "A Study of High Drag Configurations as First Stage Decelerators", WADC TN 56-320, July, 1956.

(10) Cilmi, P., "Results of Wind Tunnel Tests to Determine the Forces and Moments on the Discoverer Mark 2 and 4 Heat Cover Configurations", GE-MSVD Aerodynamic Data Report 60SD665 Revised, 1960.

(11) Bondurant, Stuart et al, "Human Tolerance to Some of the Accelerations Anticipated in Space Flight", WADC TR 58-156, April, 1958.

(12) Lysdale, C.A., "Launch Vehicle Recovery Techniques", IAS Paper No. 61 - 51.

(13) Penlande, Jim A. and Fitterman, David E., Jr., "The Effects at a Mach Number of 6.88 of Drag Brakes on the Lift, Drag and Pitching Moment of an Ogive Cylinder", NACA RM L55K23, 1956.

(14) Kurbjun, Max C., "High Altitude Performance of a 64 Foot Diameter Ring Sail Parachute", NASA TM X-232, 1959.

(15) Musil, Jay L., "Requirements and Considerations for Testing Hypersonic Retardation Devices for Re-entry Vehicle Recovery", AFFTC TR 59-4, March, 1959.

(16) Heinrich, H.G. and Riabokin, Toma, "Analytical and Experimental Considerations of the Velocity Distributions in the Wake of a Body of Revolution", WADC TR 60 - 257, December, 1959.

(17) Rogallo, F.M. and Lowry, J.G., "Flexible Re-entry Gliders", Paper Presented at the SAE National Aeronautics Meeting, N.Y., 1960.

(18) Naeseth, Rodger L., "An Exploratory Study of a Parawing as a High Lift Device for Aircraft", NASA TN D-629, November, 1960.

(19) Rogallo, Frances M., Lowry, John G., Croom, Delwin R., Taylor, Robert T., "Preliminary Investigation of a Paraglider", NASA TN D-443, August, 1960.

(20) Taylor, Robert N., Judd, Joseph H., Hewes, Donald E., "Flexible Gliders", AF/NASA Joint Conference on Lifting Manned Hypervelocity and Re-entry Vehicles, April, 1960.

(21) Mandell, Donald S., "A Study of the Maneuvering Performance of Lifting Re-entry Vehicles", Part I, "Initial Atmospheric Re-entry", General Electric Company, Flight Mechanics Data Memo 2:23, October, 1960.

(22) NASA unpublished data, "Project Apollo, Summary of Studies of a Lenticular Vehicle Capable of Entry from a Lunar Mission", NASA STG Langley Field, Va., March 3, 1961.

II. HEAT PROTECTION SYSTEMS

1.0 Summary and Conclusions

The objectives for the design of the heat protection system were to arrive at a light weight, passive, configuration for which there would be a high confidence level. It would be resistant to meteorite damage, could be manufactured with current technology, and could be proven with a minimum of proof testing, both ground and flight. Most important of all it would not require "scheduled" breakthroughs in materials.

The recommended system for the D-2 selected configuration meets these requirements.

The design studies for the D-2 configuration were based on two trajectories. These represent the flight corridor limits for entry angles of 4.7 and 8.4 degrees. The 4.7 entry angle, or skip limit trajectory, has lower peak heat fluxes to the vehicle but a larger integrated heat flux due to the increased flight time. The 8.4 degrees entry angle conversely has higher heating rates and a lower total heat flux. Intermediate trajectories, such as the 8 "g" trajectory, have maximum heat rates less than the 8.4 entry but a total heat flux approximately the same as the skip limit trajectory. The final design will be based on a thorough analysis of the complete family of trajectories falling between the corridor limits. However, investigation of the limit conditions is sufficient to establish system concepts and weights. For the D-2 configuration the skip limit trajectory imposes the more stringent requirements on the heat protection system and establishes the system weight.

The APOLLO re-entry vehicle is initially subjected to a short high heating rate followed by a long low heating rate during re-entry. This suggests that the heat protection design should be a combined ablation-radiation system. For maximum efficiency the heat protection system material should be characterized by;

a) a high Q*
b) a high outer surface re-radiation temperature
c) a low conduction temperature for the insulation required for thermal protection of the inner compartments

d) and a low thermal diffusivity to give maximum insulation effiency.

A comprehensive study of four basic classes of heat protection systems, Thermosetting Plastics, Thermoplastics, Refractory Oxides, and Refractory Metals was conducted and results are included herein. A system utilizing thermosetting plastics, as typified by phenolic nylon and G.E. 100 series, was chosen for the APOLLO design, primarily because this class of materials best meets the over-all system requirements. They have a high Q* for both laminar and turbulent flow; the surface char temperature is high, yet decomposition at the char-virgin material interface occurs at a low temperature giving a low driving temperature for the insulation; and they have a low thermal diffusivity thus serving as good insulators. In addition, they can be readily manufactured by casting, winding, molding, or hand layup and have been extensively flight tested since 1958.

The refractory metals, pyrolytic-graphite also possess the desirable combination of performance characteristics. However, full advantage of their potential weight savings for protection of manned or low temperature internal compartments is contingent upon the development of a high temperature, high efficiency insulation or cooling system. Furthermore, solutions of problems associated with manufacture and structural integrity and attachment must be further developed before they can be extensively used.

The heat fluxes and ablation material distribution were determined for several points on the re-entry vehicle. Calculations were based on an angle of attack of 40 degrees, an effective heat of degradation for the ablative material of 5000 Btu/lb, and an adiabatic back face with a temperature at touchdown of 500 F. Calculations were based on the generally accepted theoretical equations as modified by General Electric Co., to give better correlation with flight test results.

A large percentage of the total heat protection system weight is necessitated by the insulation requirements for the large areas of the afterbody. To optimize this system, studies were made of the total insulation system from the char-virgin material interface to the manned compartment wall. The total weight can be reduced by using high efficiency insulations or active cooling systems. However, this requires higher bond temperatures for the ablative material structural attachment. Consistant with the heat protection system design criteria, a system utilizing a bond temperature of 500 F and multiple layer radiation barrier insulation was chosen for the APOLLO re-entry vehicle.

To determine the potential improvement in the heat protection system, advanced thermal protection systems were investigated. These included the use of higher, theoretically predicted, effective heats of degradation for the ablative material, pyrolytic-graphite-hot structure systems, and "super insulations" and cooling systems for internal compartment protection. Perhaps the most significant aspect of these studies is their highlighting of areas that need further development before these systems can be brought to reality. The more important items are:

a) verification of effective heats of degradation of ablative materials at high enthalpy levels,
b) development of large sheets of pyrolytic-graphite and means of attaching to hot structure,
c) development of high temperature bonding methods for ablative materials,
d) development of high temperature "super insulations" and methods of installation,
e) and development of a passive, high efficiency, low temperature (100 F) cooling system.

The heat fluxes to the control surfaces (flap) were calculated, based on free stream conditions modified by results from experimental data. Since there is no requirement for low temperature protection behind the flap a high temperature construction eliminating insulation requirements is very desirable from the weight and overall thickness viewpoints. Consequently, a pyrolytic graphite shield bonded to a columbium substructure was chosen for the flap heat protection system.

The temperature of various points on the spacecraft surface were determined for the powered launch trajectory. The forward nose cone, which is later ejected, is coated with a thin layer of epoxy to limit its temperature to 500 F. The maximum temperature on the remainder of the vehicle is 365 F on the aft flare.

Several configurations other than the D-2 were investigated during the APOLLO study. The heat protection system for the B-2 and C-1 configurations were reported at the Mid-Term review and are summarized here for completeness. The D-1 is a larger version of the D-2 with the Command Module and Mission Module integrated into a single vehicle. The R-3 is a lenticular shaped vehicle which initially re-enters at a very high angle of attack, 90 degrees, and subsequently flies at low angles of attack to develop a high subsonic L/D for horizontal landing.

The APOLLO heat protection system performance and weight have been based on certain assumptions, extrapolations, and theories for the calculation of the magnitude of the local aerodynamic and radiant heat transfer and system material performance at super orbital velocities. An analysis of the requirements and a recommended test program for development of the APOLLO heat protection system has been included. This program, or a similar one, must be implemented at the start of the APOLLO design to achieve a high confidence - minimum weight system.

2.0 The Selected Configuration, D-2

2.1 RE-ENTRY VEHICLE

2.1.1 Introduction

Two re-entry thermal environments experienced by the D-2 vehicle, whose configuration is presented in Figure II-2-1, were investigated. The extreme trajectories, minimum (skip) and maximum (12g limit) re-entry path angles, were considered and are presented in Figures II-2-2 and II-2-3, respectively. A constant angle of attack (α) of 40 degrees was assumed to exist throughout the entire heating period of each trajectory. Although this angle of attack is a conservative assumption for the windward meridians of the vehicle, it should be noted that this assumption is not conservative for the leeward sections.

At a 40 degree angle of attack, the D-2 vehicle's stagnation point lies upon a 5 inch radius which serves as the forebody-afterbody junction. This stagnation point is designated as Pt. 1 in Figure II-2-1 and will be referred to as such throughout this section of the report.

2.1.2 Heat Fluxes Along the Windward Meridians

Angle of attack convective heat fluxes to the D-2 vehicle were calculated, considering both extreme trajectories, for representative body locations along the forebody and most windward afterbody meridian by a digital computer trajectory-flux program [(1)] (Ref. 1).[(2)] The effect of wall temperature on these convective heat fluxes was found to be small (Ref. 2) due to the high enthalpy levels attained during the heating period of each

---

[(1)] This program is basically designed for axisymmetric configurations at zero angle of attack; however, the selection of appropriate body geometry and pressure distribution permits a reasonable simulation of conditions imposed by an angle of attack on meridians where no cross-flow occurs.

[(2)] References will be found at the end of Section 2.1.

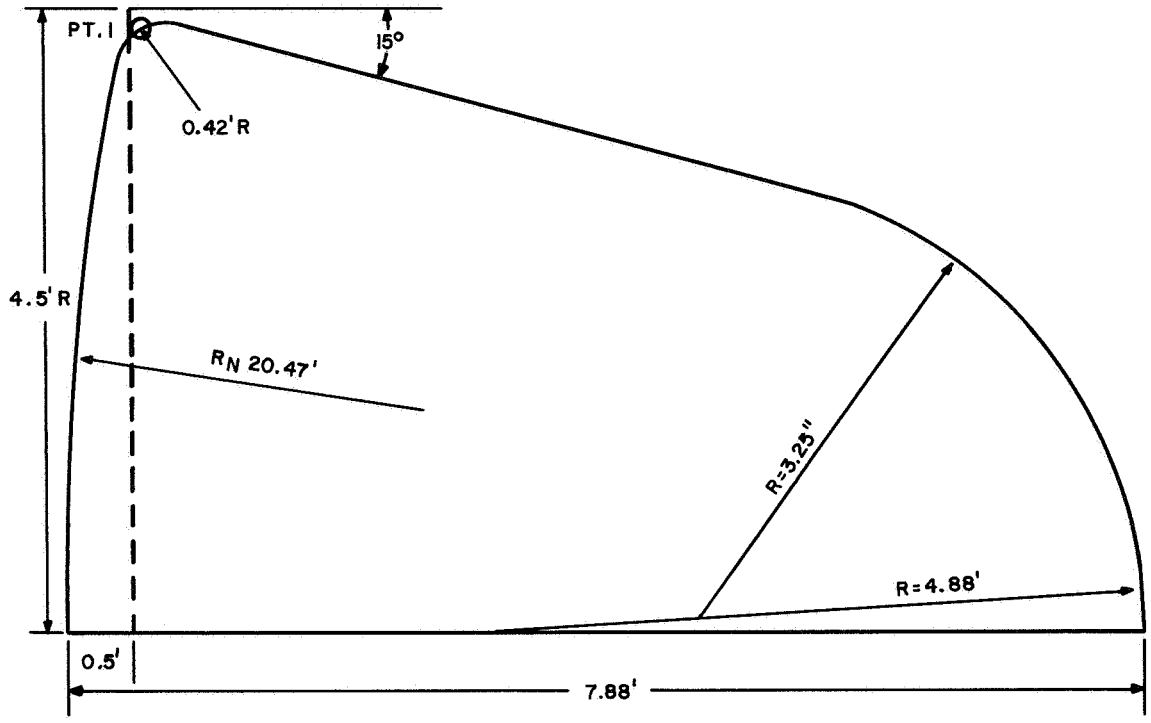

Figure II-2-1. APOLLO - D-2 Re-entry configuration

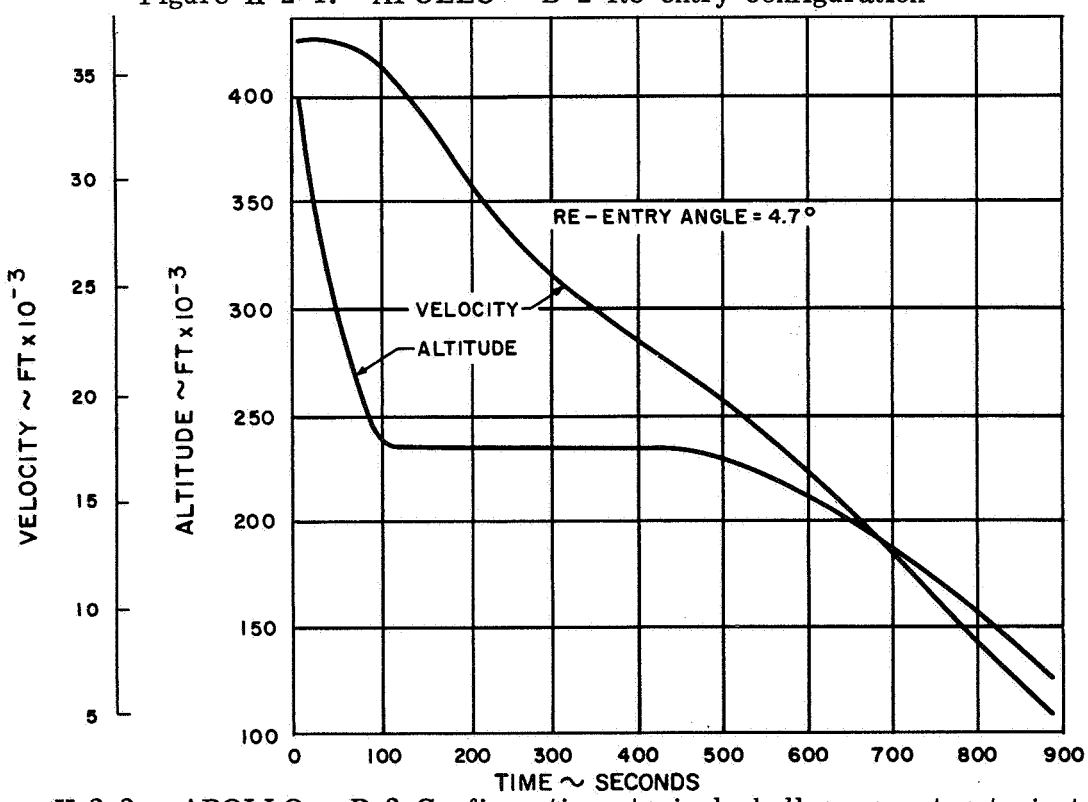

Figure II-2-2. APOLLO - D-2 Configuration, typical shallow re-entry trajectory

trajectory. Therefore, an average wall temperature of 4000 degrees R was assumed for all convective heat flux calculations.

The heat transfer relationships used are essentially the same as those employed by General Electric Co., MSVD in previous ballistic missile re-entry vehicle and satellite re-entry vehicle thermal studies.[1]

The digital trajectory-flux program calculates stagnation point heat transfer rates with the following equation

$$\dot{q}_s = \frac{0.779}{(Pr)^{2/3}} (\rho_e{}^* \mu_e{}^* U'_o)^{1/2} (h_s - h_w)$$

which is based upon Lees' classical solution of hypersonic heating, Ref.(3), with properties evaluated at E. Eckert's reference enthalpy state (Ref. 4). Laminar heat transfer rates to body locations along the forebody and most windward afterbody meridian were calculated by

$$\dot{q}_L = \frac{0.389}{(Pr)^{2/3}} \frac{\rho_e{}^* \mu_e{}^* U_e \, y \, (h_r - h_w)}{\left[\int_o^3 \rho_e{}^* \mu_e{}^* U_e y^2 \, ds\right]^{1/2}}$$

which is a compressible reference enthalpy equation also based upon Lees' solution.

The inviscid flow field at the edge of the boundary layer was defined by a Newtonian pressure distribution with local velocity and air property values obtained by an isentropic expansion from the stagnation point to the local enthalpy level obtained from the pressure field. Transition from laminar flow to a turbulent boundary layer flow was assumed to occur when a Reynolds No. (R_{e_s})[2] of 150,000 was reached. Turbulent heat transfer rates were calculated when $R_{e_s} \geq 150,000$ by

---

[1] The coefficients in the stagnation and laminar laws are 10 percent greater than those in Lees' classical solution. This increase is based upon flight test data, Ref. (14).

[2] Based upon wetted length and local edge of boundary layer values. Transition at 150,000 is based upon flight test results from ablating re-entry vehicles.

$$\dot{q}_T = \frac{0.0296}{(Pr)^{2/3}} \quad \frac{\rho_e U_e (\mu_e)^{1/4} \left(\frac{\mu_e^*}{\mu_e}\right)^{1/5} \left(\frac{\rho_e^*}{\rho_e}\right)^{4/5} y^{1/4} (h_r - h_w)}{\left[\int_0^s \rho_e U_e (\mu_e)^{1/4} y^{5/4} \, ds\right]^{1/5}}$$

which is the General Electric axisymmetric compressible reference enthalpy equation.

All heat transfer predictions are based upon real gas relationships. Properties of dissociated air in chemical equilibrium were obtained from Tables published by J.G. Logan and C.E. Treanor of Cornell Aeronautical Laboratory (Ref. 6). However, any increased heating due to electronic heat conduction which may occur at escape velocities was not included. A preliminary estimate of this increased heating would possibly be on the order of 15 percent. The most significant effect of this ionization is to increase the thermal conductivity of air (Ref. 7) which may occur at velocities of 30,000 ft/sec or more. The re-entry peak heat transfer rates of the D-2 vehicle are reached before the velocity falls below 30,000 ft/sec; therefore, it is apparent that electronic heat conduction influences on aerodynamic heating is an area which bears further investigation.

It was necessary for the digital computer to extrapolate the air properties given in the Logan and Treanor Tables, over a particular portion of each trajectory, to accommodate the extreme conditions imposed by escape velocity re-entry. However, a comparison of heat flux calculations using the extrapolated values to heat flux calculations based upon Moeckel and Weston charts (Ref. 8) showed differences within engineering accuracy for the two extreme thermal environments studied.

Thermal radiation from the hot gas cap surrounding the vehicle was calculated at representative body locations by the Stefan Boltzman Law

$$\dot{q}_{\text{hot gas}} = \sigma \alpha_W \epsilon_g T_e^4$$

where

$\sigma = 4.76 \times 10^{-13}$ BTU/ft^2 sec °R^4

$\alpha_w \sim$ Wall Absorptivity (0.8)

$\epsilon_{gas} \sim$ Gas Emissivity

$T_e \sim$ Local Temperature °R

Local temperature histories at the edge of the boundary layer at each body location was determined, for the two extreme trajectories, through the use of the aforementioned Moeckel and Weston charts. Corresponding gas emissivity histories for optically thin gas layers were taken from B. Kivel and K. Bailey Tables (Ref. 9) and corrected to non-optically thin layers through the use of an emissivity correction factor (k) which varies as a function of shock detachment distance (L). The corrected gas emissivities were computed by

$$\epsilon_g = K L \left(\frac{\epsilon g}{L}\right)_{O.T.}$$

Shock detachment distances were obtained from AEDC wind tunnel data for a similar configuration (Mercury Vehicle) and analytical scaling factors.

Non-equilibrium radiation effects were not considered in this analysis due to an insufficient amount of fundamental data which would make an assessment of these effects conjecturable. Some preliminary investigations for satellite velocity conditions have shown that these effects may increase the radiation heating by an order of magnitude. Therefore, to determine realistic heat rate predictions within the escape velocity re-entry regime, where the hot gas radiation contributes significantly to the total heat input, non-equilibrium effects demand further exploration.

Hot gas radiation to the D-2 vehicle, considering the maximum (12g limit) re-entry path angle, is approximately 25 percent of the convective heating over the forebody and 5 percent of the convective heating over the most windward meridian of the afterbody.

The minimum (skip) re-entry path angle trajectory is such that the hot gas radiation amounts to no more than 2 percent of the convective heating to the forebody or most windward afterbody meridian.

Gross (convective plus hot gas radiation) heat fluxes to the stagnation point, most windward afterbody meridian and forebody locations considering each of the extreme trajectories and an angle of attack of 40 degrees are presented in Figures II-2-4 to II-2-7.

2.1.3 Heat Fluxes Along the 90 Degree and leeward Meridians

Heat transfer rates along the 90 degree meridian (which lies midway between the most windward (0 degrees) meridian and most leeward (180 degrees) meridian) were

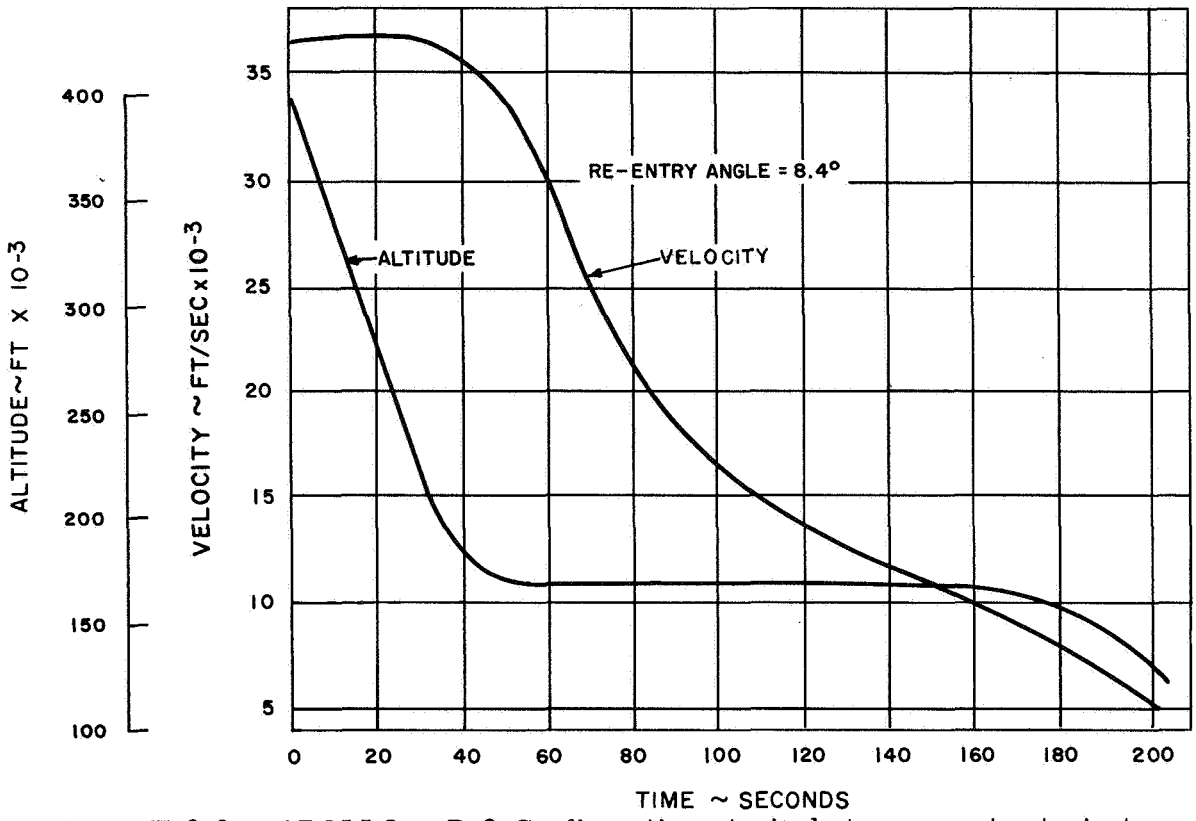

Figure II-2-3. APOLLO - D-2 Configuration, typical steep re-entry trajectory

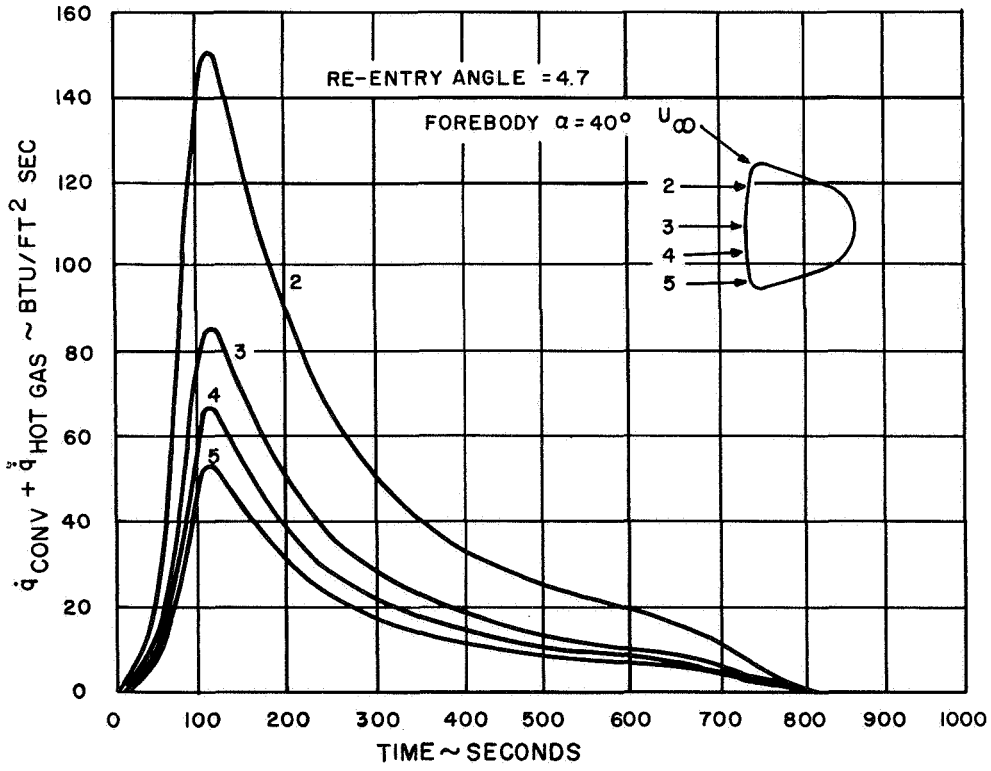

Figure II-2-4. APOLLO - D-2 Configuration, gross heat fluxes during re-entry

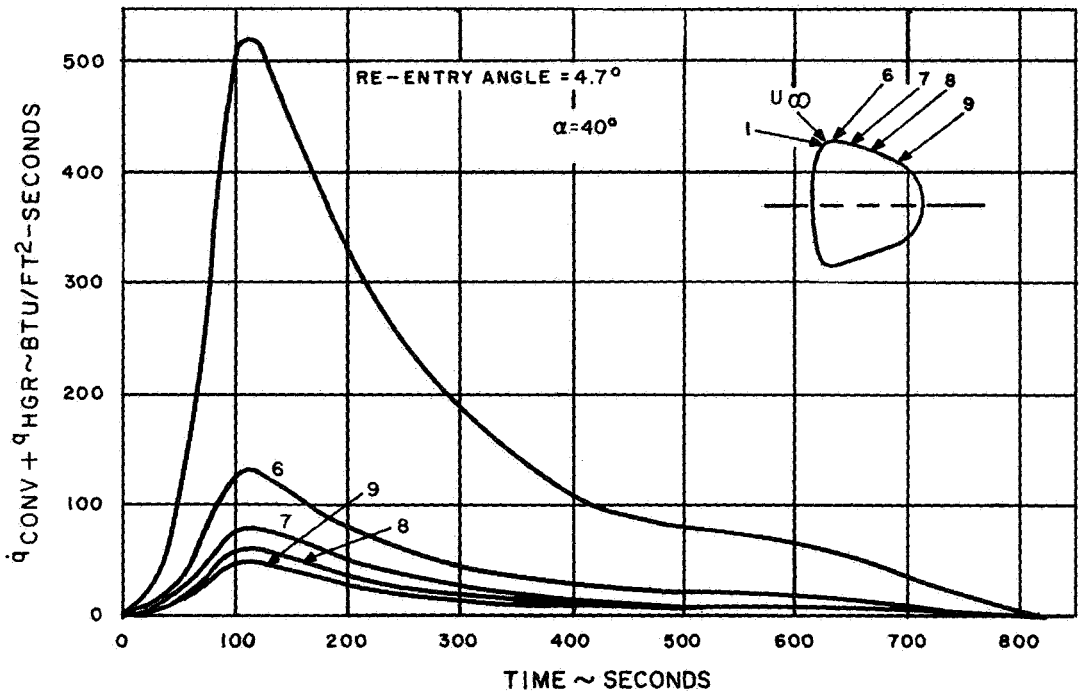

Figure II-2-5. APOLLO - D-2 Configuration, gross heat fluxes during re-entry - afterbody

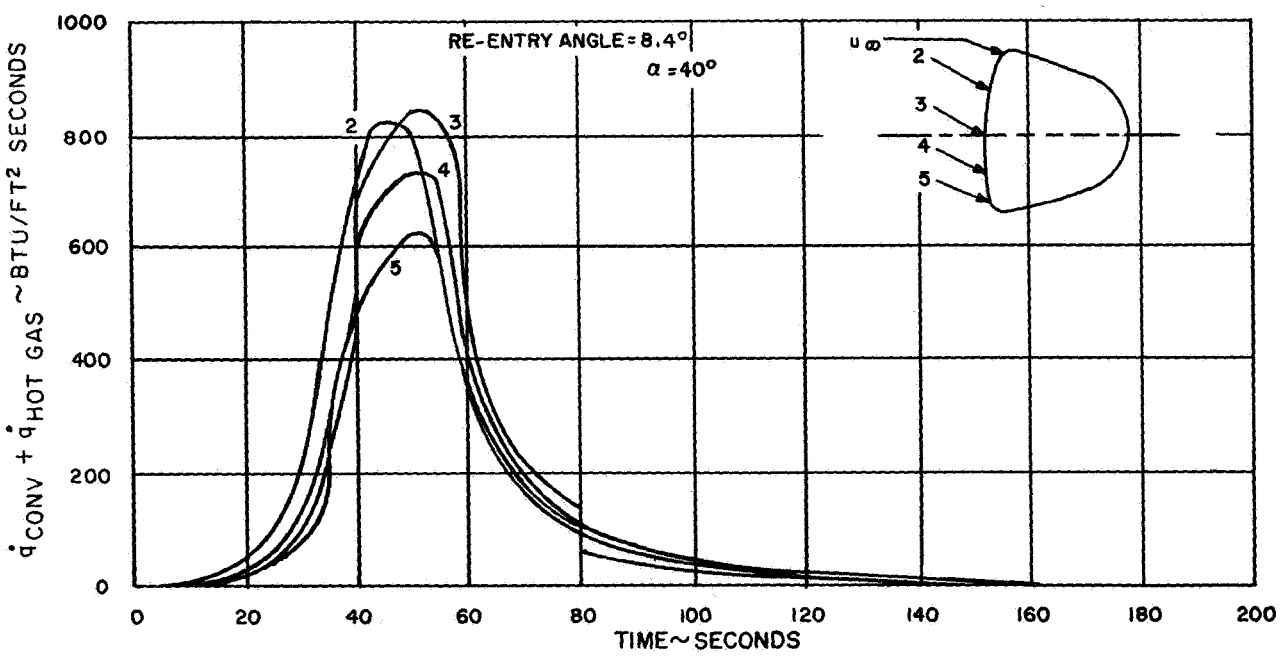

Figure II-2-6. APOLLO - D-2 Configuration, gross heat fluxes during re-entry - forebody

assumed to be equal to the zero angle of attack values for an axisymmetric body, a Newtonian assumption.

Considering each of the extreme trajectories, zero angle of attack convective heat fluxes to the D-2 vehicle were calculated for representative body locations along the afterbody by a digital computer afterbody flux-conduction program (Ref. 10). Turbulent attached flow was conservatively assumed over the entire afterbody for the duration of the heating period. The hypersonic coefficient of pressure ratio ($C_p/C_{p\ max}$) distribution used for these zero angle of attack calculations is given in Figure II-2-8. This digital program uses the following flat plate equation

$$\dot{q}_{T.A.} = \frac{0.0296}{(Pr)^{2/3}} (U_e \rho_e^*)^{4/5} \left(\frac{\mu_e^*}{s}\right)^{1/5} (h_o - h_w)$$

for turbulent attached (T.A.) flow. These turbulent attached heat fluxes to body locations along the 90 degrees meridian, considering both extreme trajectories, are given in Figures II-2-9 and II-2-10.

Hot gas radiation to the afterbody's 90 degrees and leeward meridians was assumed to be negligible based on the small amount of hot gas radiation for the windward meridian case.

Heat transfer rates along the most leeward afterbody meridian were conservatively evaluated to be 20 percent of those calculated at the 90 degree afterbody meridian. This evaluation is based upon previous angle of attack studies made for the Discoverer and Mk 6 vehicles. Gross heat fluxes to body locations along this most leeward meridian considering both extreme trajectories are shown in Figures II-2-11 and II-2-12.

2.1.4 Effective Heat of Degradation

The capacity of a charring-ablative type material to absorb thermal energy may be expressed as an "effective heat of degradation" and defined by the relation

$$H_e = \frac{Q_{gross}}{\rho_x}$$

where Q_{gross} is the integrated convective and hot gas radiation heat flux ($\int \dot{q}_{gross}\, dt$), ρ is the density of the virgin material, and x is the total degradation depth. A detailed discussion and physical representation of the charring-ablation process is offered

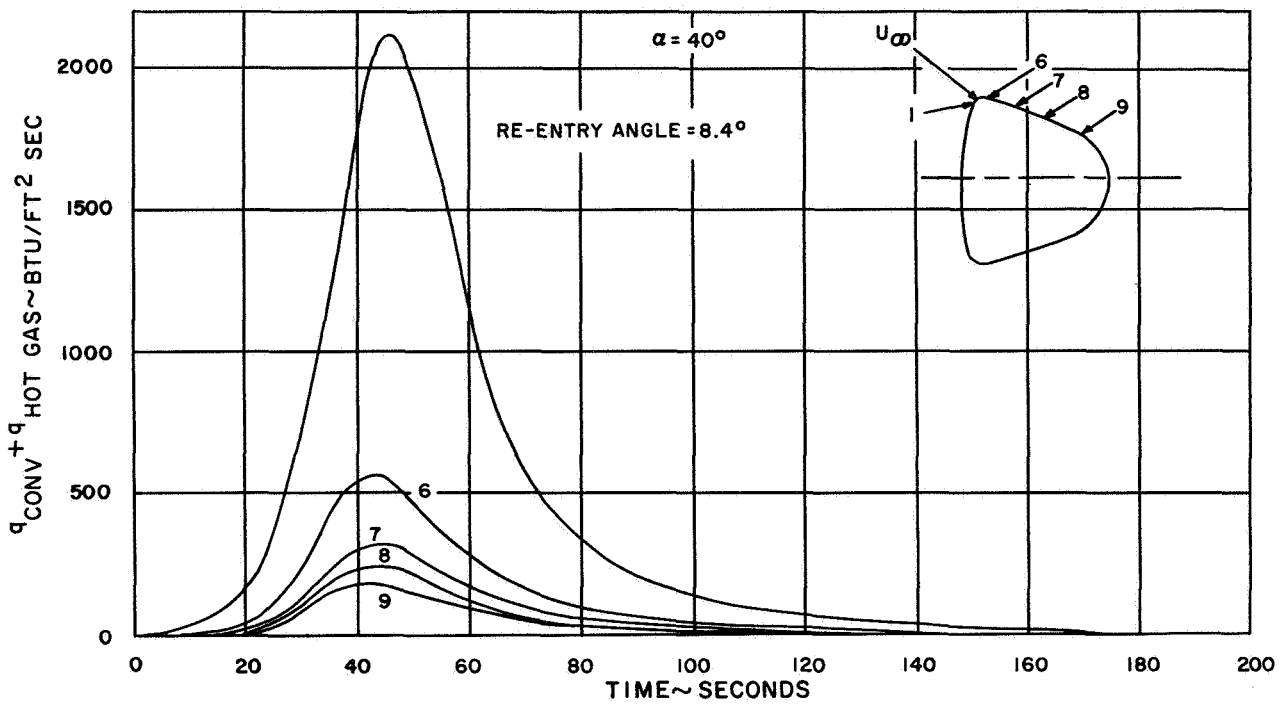

Figure II-2-7. APOLLO - D-2 Configuration, gross heat fluxes during re-entry - afterbody - most windward meridian

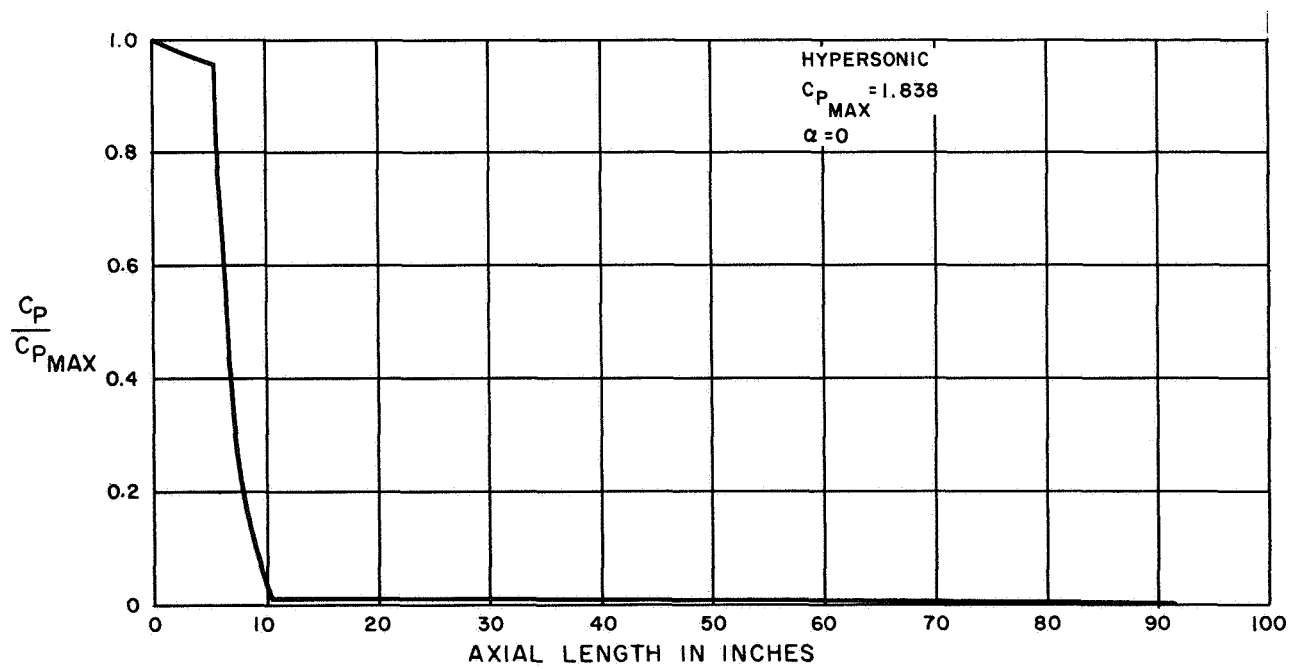

Figure II-2-8. APOLLO - D-2 Configuration, coefficient of pressure ratio distribution

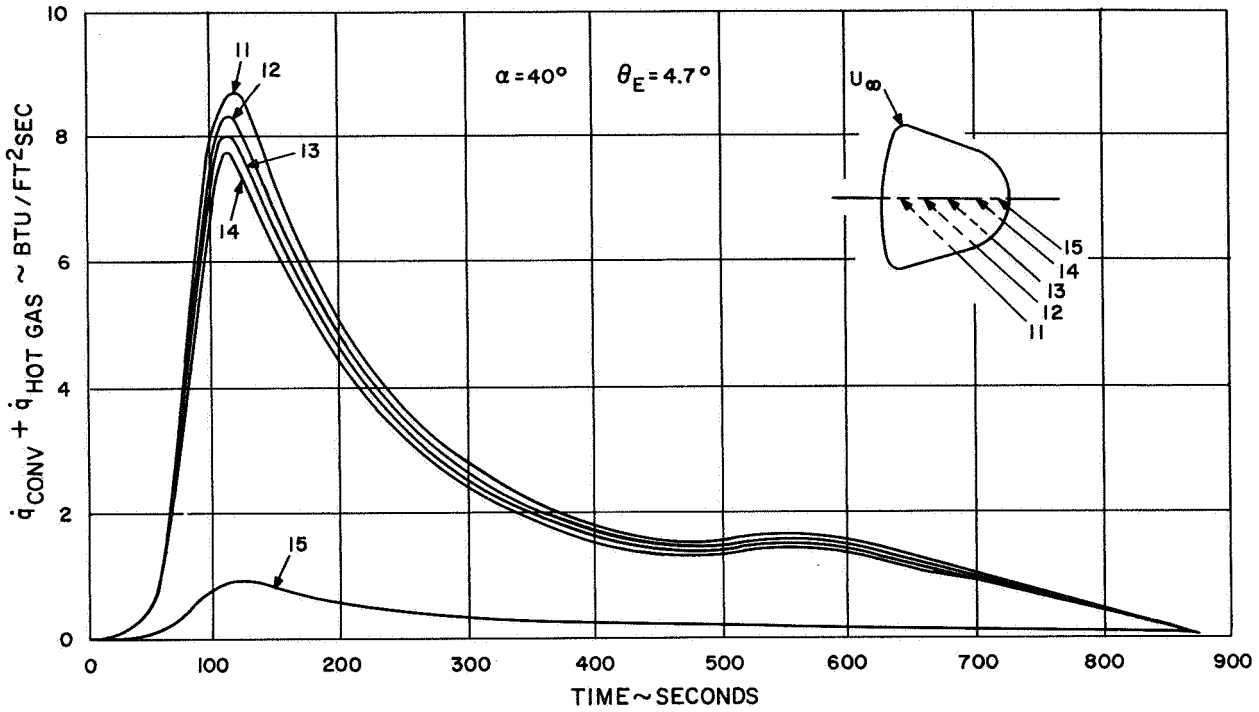

Figure II-2-9. APOLLO - D-2 Configuration, gross heat fluxes during re-entry - afterbody - 90 degree meridian

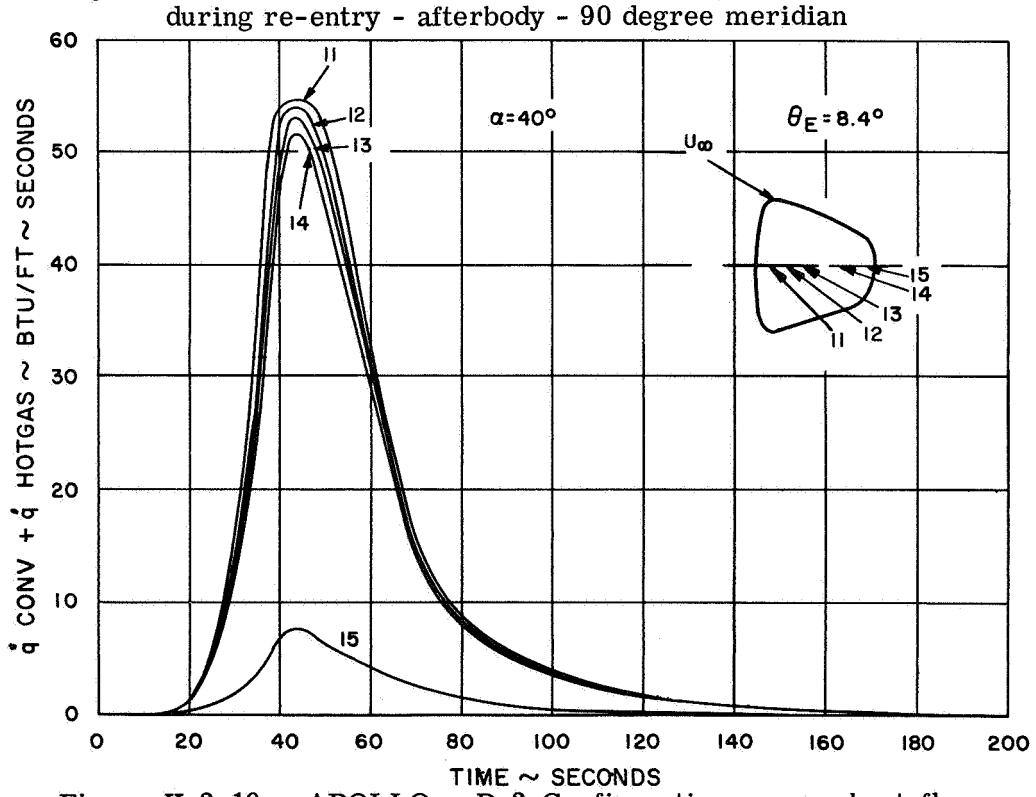

Figure II-2-10. APOLLO - D-2 Configuration, gross heat fluxes during re-entry afterbody - 90 degrees meridian

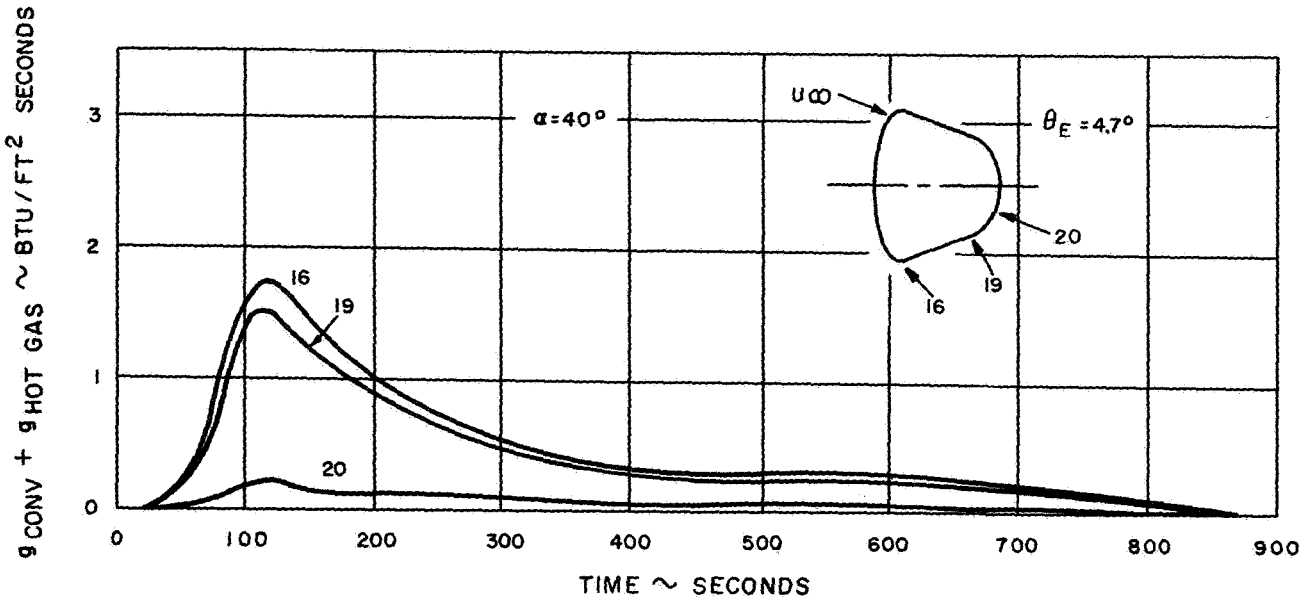

Figure II-2-11. APOLLO - D-2 Configuration, gross heat fluxes during re-entry afterbody - leeward

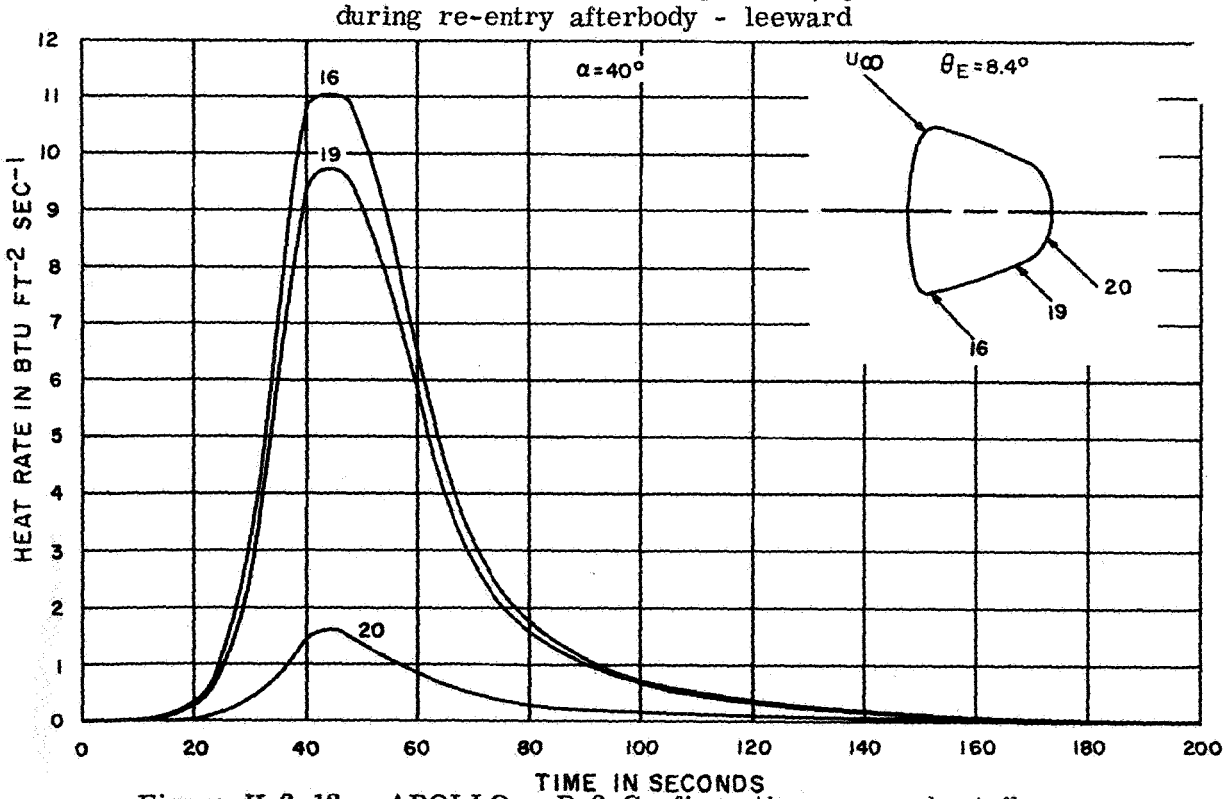

Figure II-2-12. APOLLO - D-2 Configuration, gross heat fluxes during re-entry afterbody - leeward

in Section II-4.0. Figure II-2-13 presents some flight and ground test data for a typical charring-ablative type material (Refs. 11 and 12). The effective heat of degradation design curve used in this study is shown in Figure II-2-13 as a function of stagnation enthalpy level. The thicknesses of ablated and charred thermal shield material are based upon this curve (H_e = 5000 BTU/lb) using gross (convective plus hot gas radiation) heat input, a wall temperature of 4000 degrees R, and no re-radiation from the wall. This approach is considered conservative because an extrapolation of effective heats of ablation from flight test data points, based upon several analytical considerations, indicates that the stagnation enthalpy levels attained by the D-2 during re-entry would result in an average effective heat of ablation of more than 10,000 BTU/lb. However, considering the nature of the payload, it was deemed advisable to maintain the highest feasible confidence level in the design values. No safety factor has been included in the ablation material requirements other than that obtained by using the conservative value of the effective heat of degradation.

2.1.5 Temperature Responses

A digital computer conduction-char-ablation program (Ref. 13) was employed to calculate front face recession and temperature histories of the thermal shield. This program consists of an approximate solution to the one dimensional heat conduction problem with one boundary undergoing melting or vaporization. Temperature histories of approximately 40 nodes within the shield and a front face recession history at one body location are simultaneously calculated. A sufficient number of body locations were investigated to generate a shield thickness distribution around the entire D-2 vehicle. Typical examples of these histories are presented in Figures II-2-14 to II-2-21, considering each of the extreme trajectories with a 40 degree angle of attack. Figure II-2-22 shows the locations of all body points studied on the D-2 vehicle. All temperature calculations were based upon an adiabatic backface of the shield with a maximum allowable temperature of 960 degrees R.

2.1.6 Assumptions and Results

Thermal properties and assumed conditions are presented in Table II-2-I. Table II-2-II gives the required total thicknesses of a charring-ablative thermal shield for the D-2 vehicle for the two extreme re-entry trajectories considered.

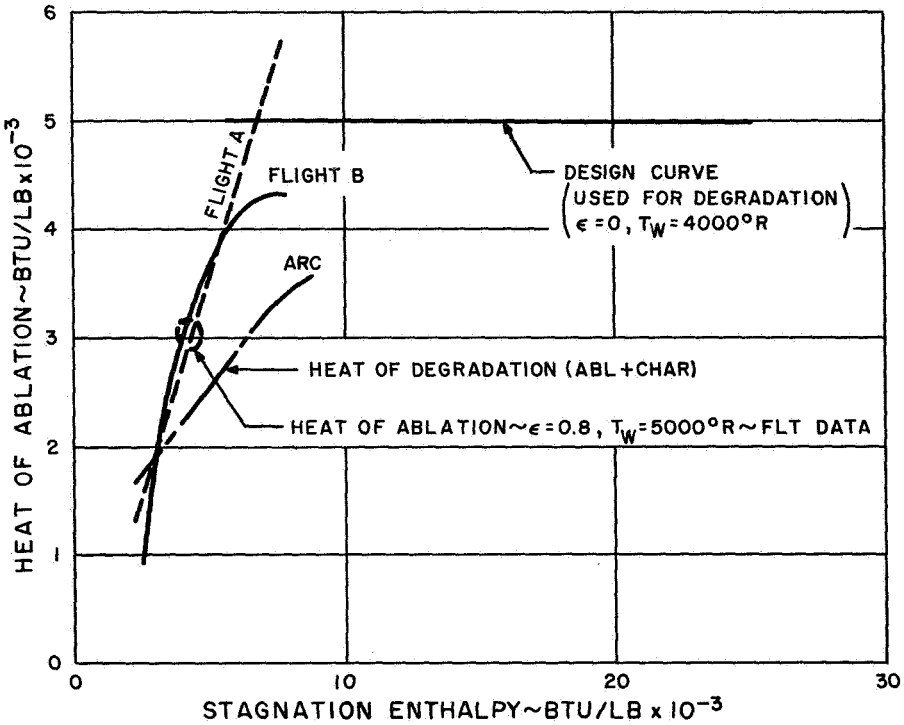

Figure II-2-13. Heats of ablation

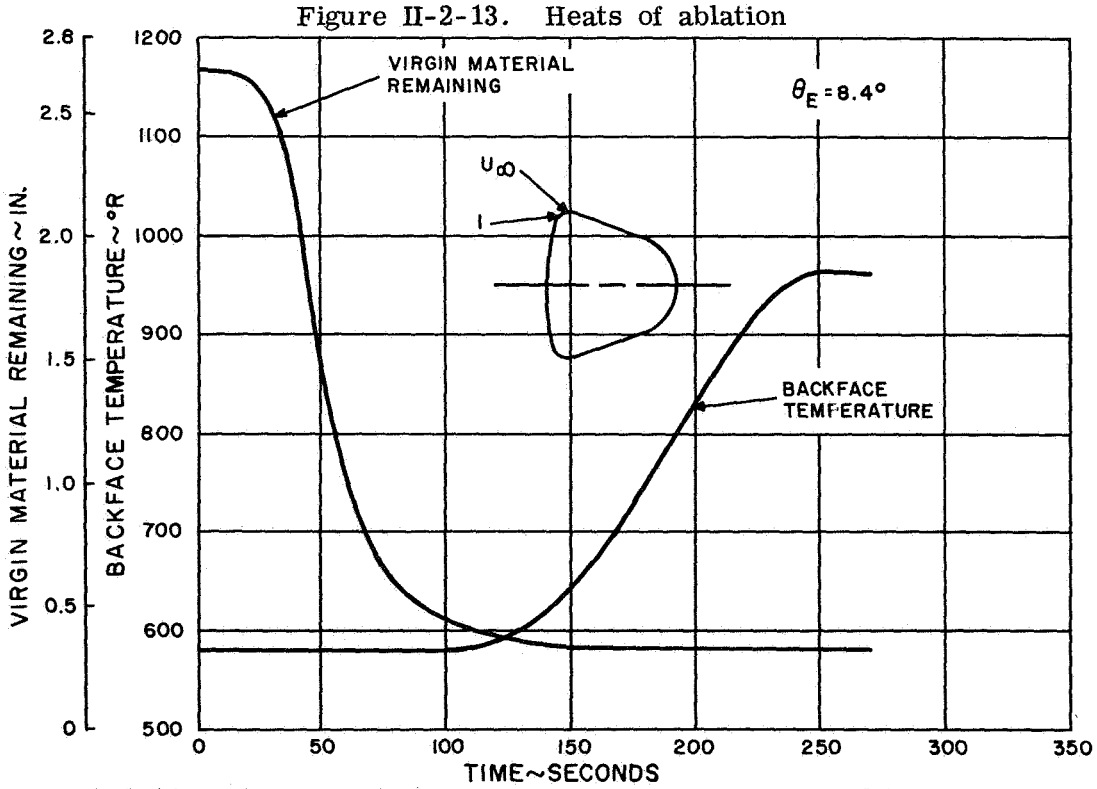

Figure II-2-14. APOLLO - D-2 Configuration, temperature and front face recession histories during re-entry, afterbody - windward meridian

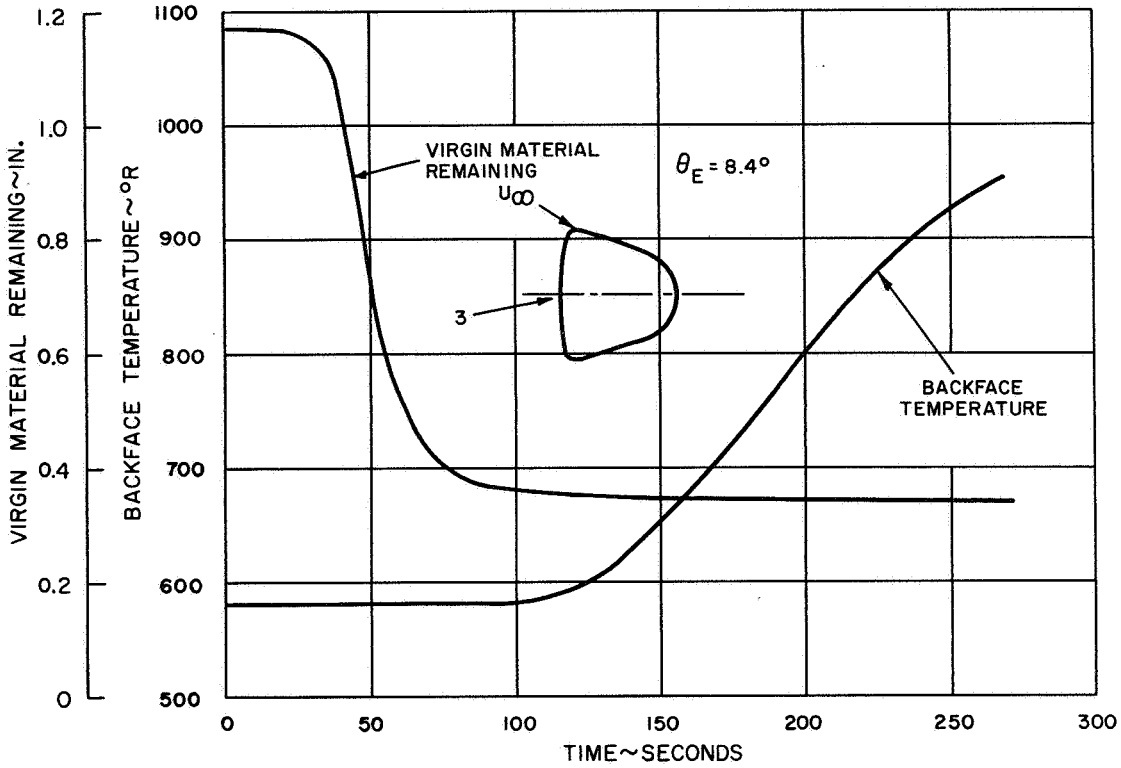

Figure II-2-15. APOLLO - D-2 Configuration, temperature and front face recession histories during re-entry, forebody

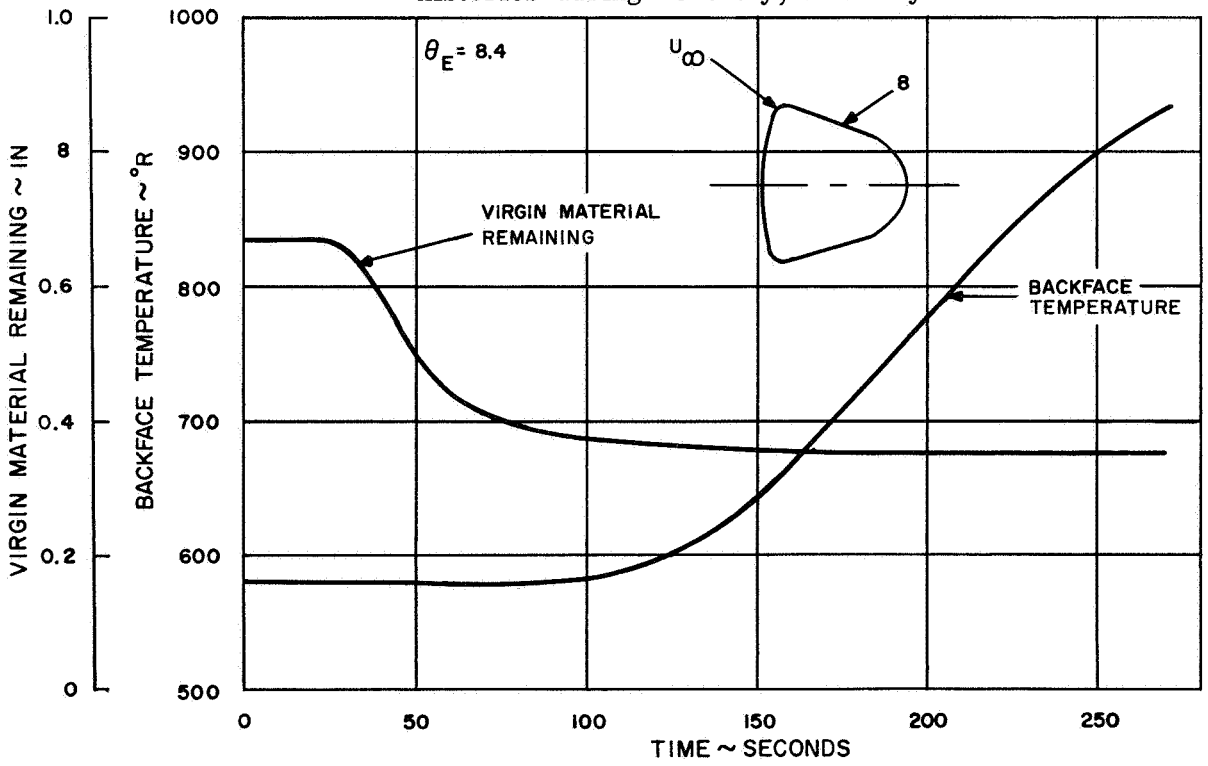

Figure II-2-16. APOLLO - D-2 Configuration, temperature and recession histories during re-entry, afterbody - windward meridian

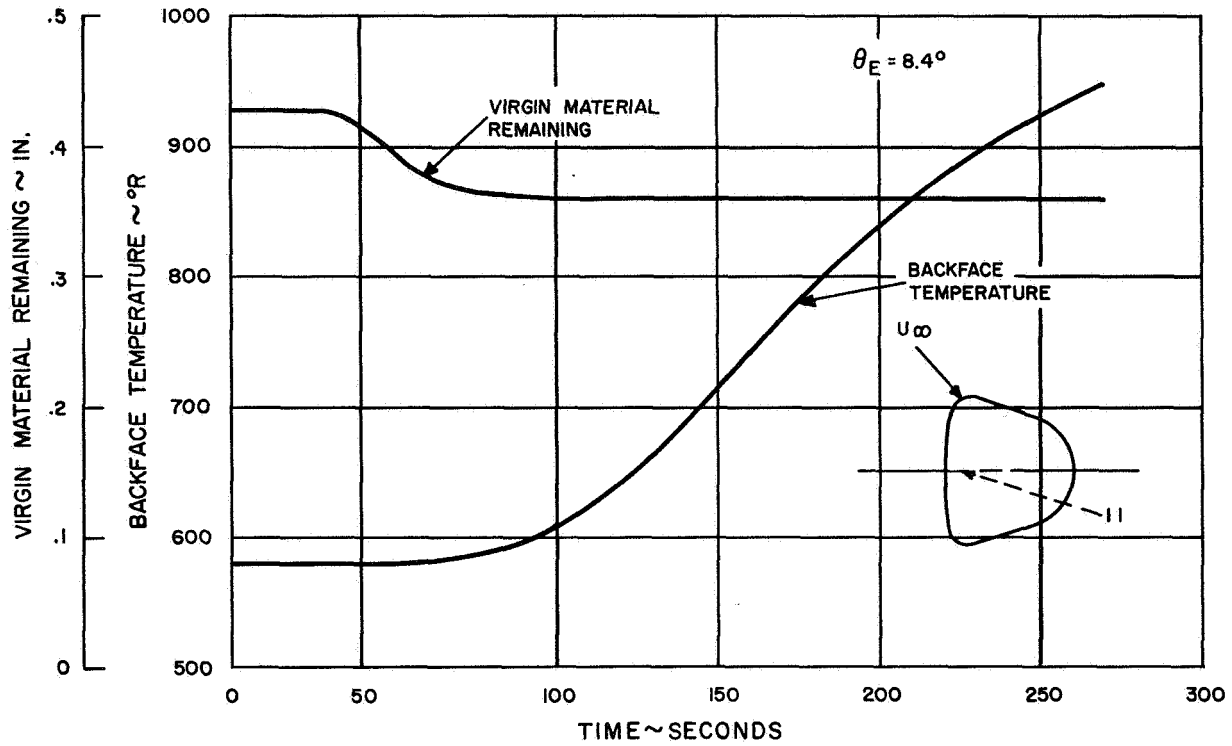

Figure II-2-17. APOLLO - D-2 Configuration, temperature and recession histories during re-entry, afterbody - 90 degree meridian

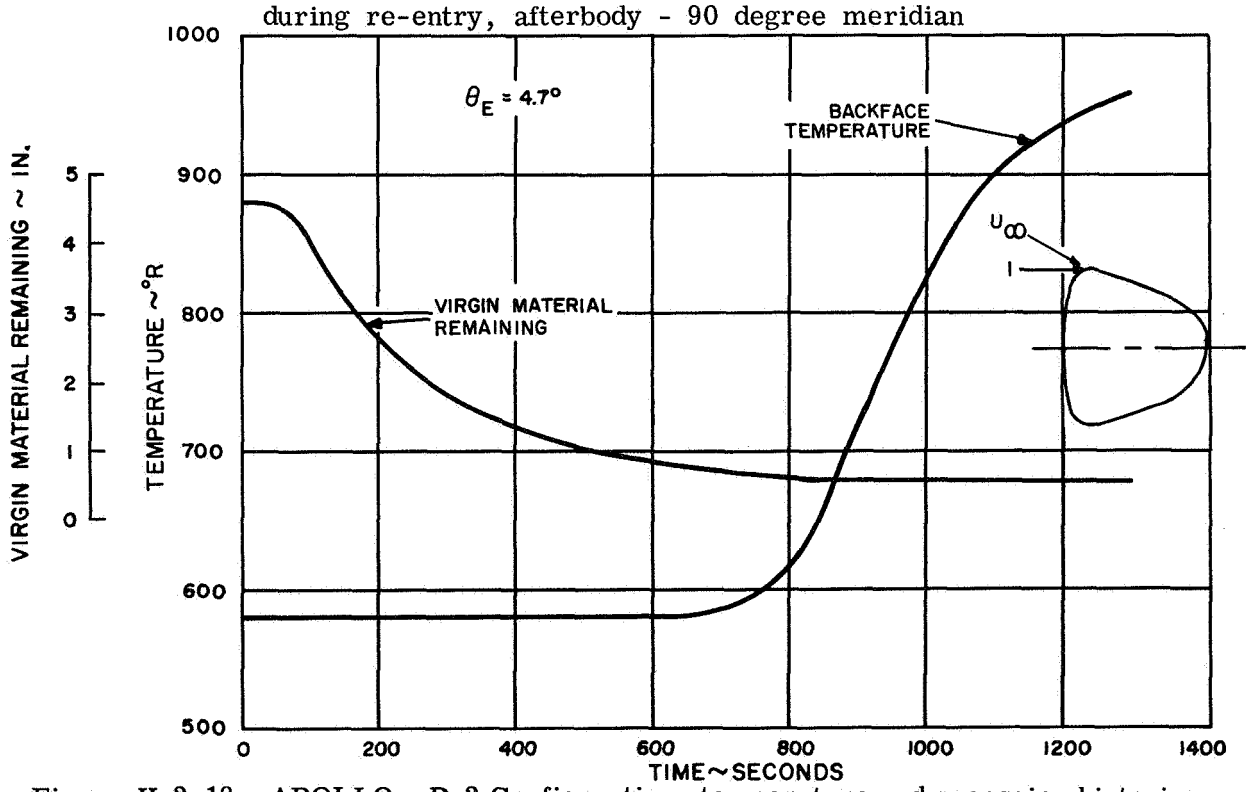

Figure II-2-18. APOLLO - D-2 Configuration, temperature and recession histories during re-entry, afterbody - windward meridian

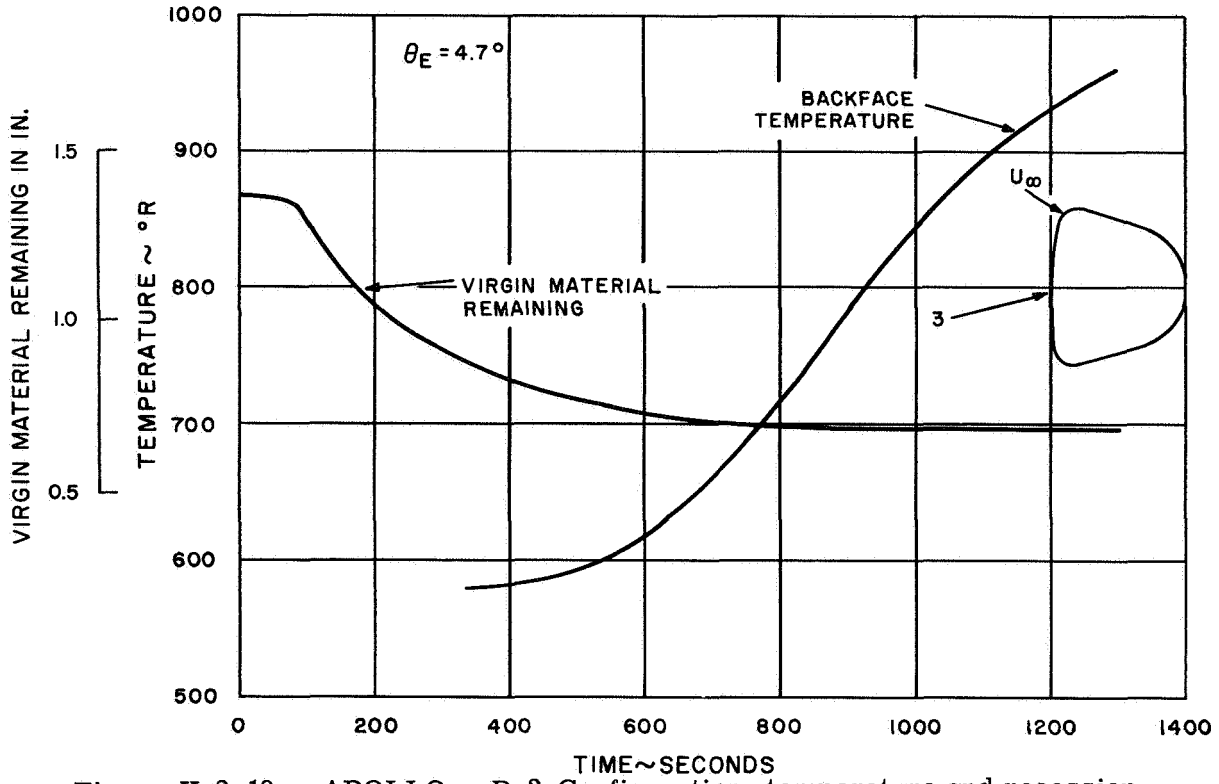

Figure II-2-19. APOLLO - D-2 Configuration, temperature and recession histories during re-entry - forebody

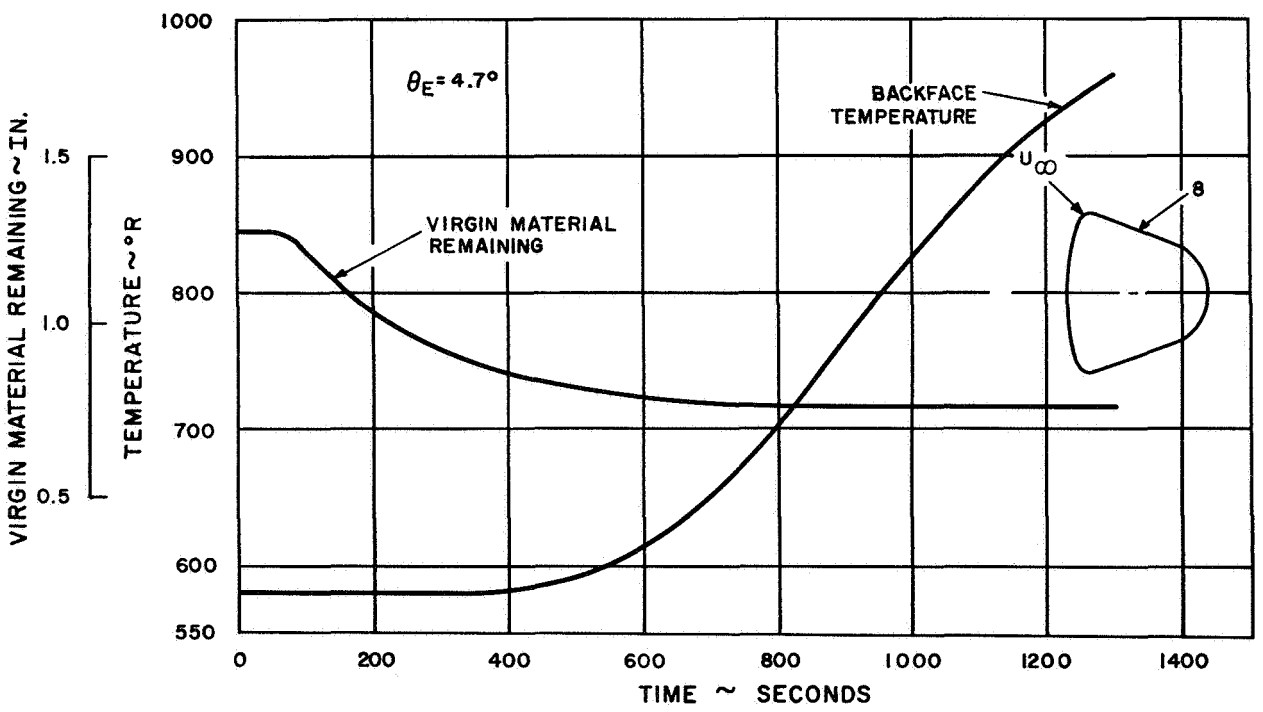

Figure II-2-20. APOLLO - D-2 Configuration, temperature and recession histories during re-entry, afterbody - windward meridian

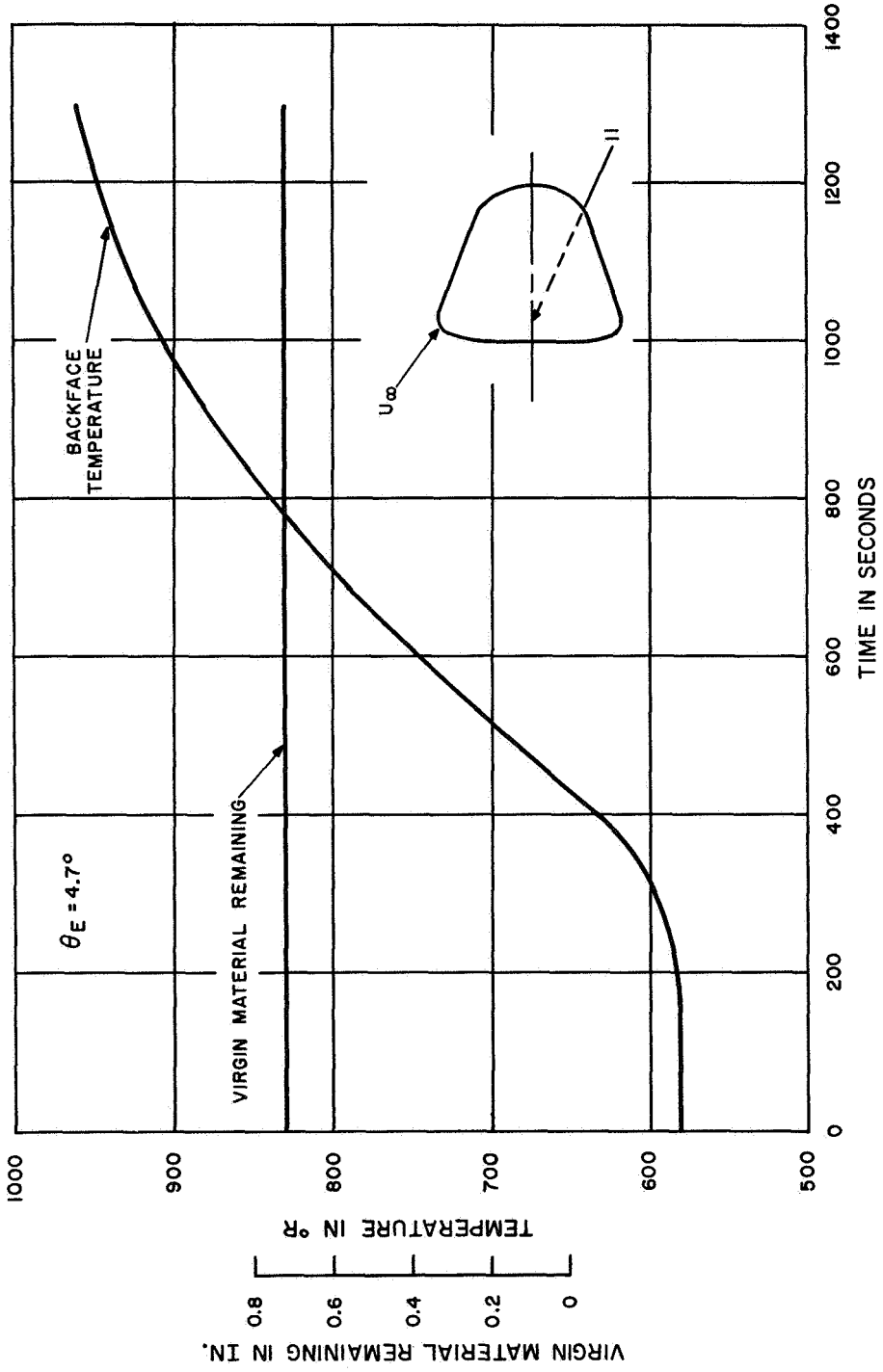

Figure II-2-21. APOLLO - D-2 Configuration, temperature and recession histories during re-entry, afterbody - 90 degree meridian

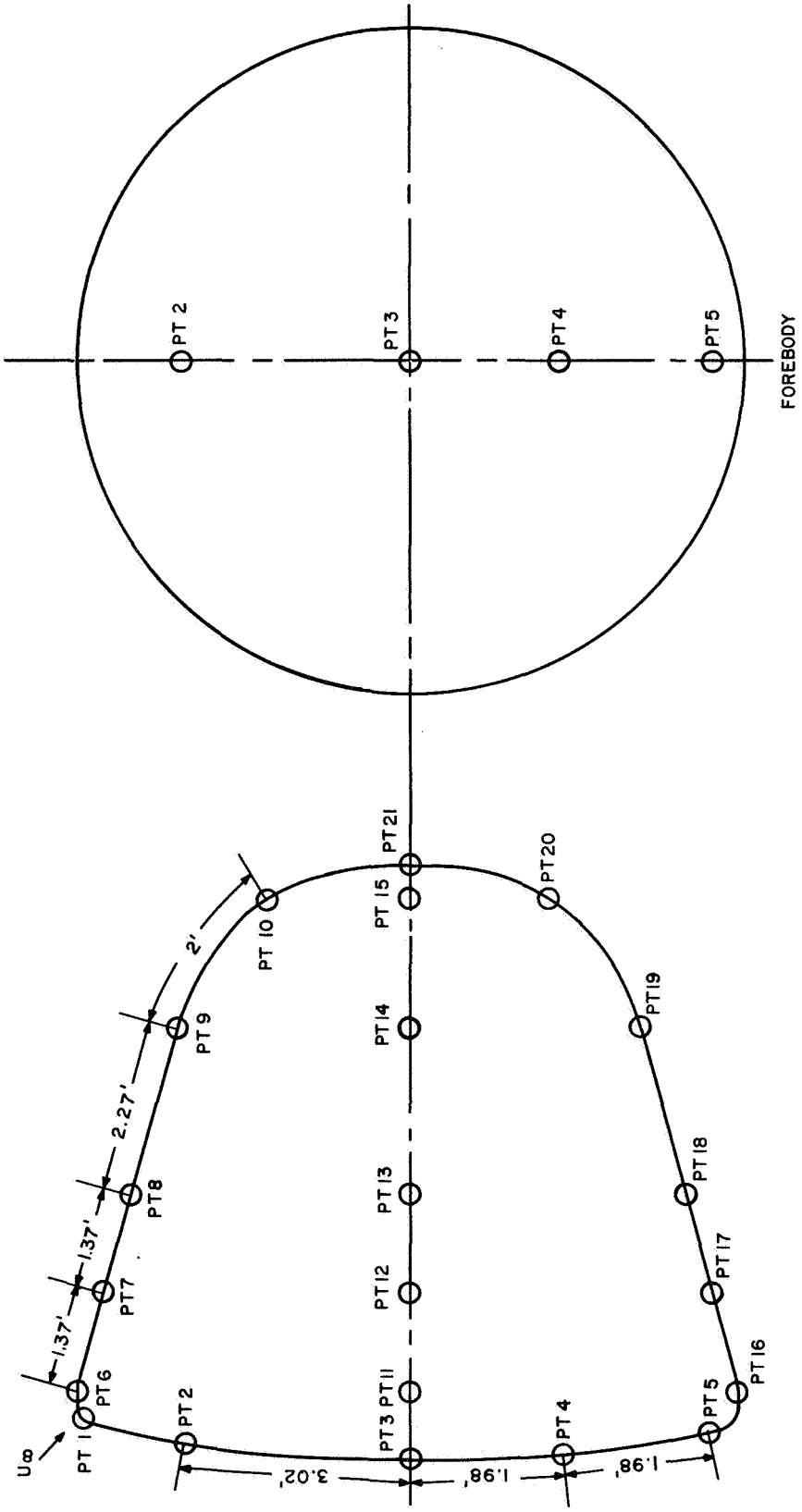

Figure II-2-22. APOLLO - D-2 Configuration, body locations studied

TABLE II-2-I

THERMAL PROPERTIES AND ASSUMPTIONS USED FOR RE-ENTRY

Properties	Charring-Ablative Material
Density ~ lb/ft^3	75
Specific heat ~ BTU/lb-°R	0.38
Thermal Conductivity ~ BTU/ft^2-sec-°R/ft	0.000035
Effective Heat of Degradation[1] ~ BTU/lb	5000
Degradation Temperature ~ °R	1700

Assumptions:

1. Transition Reynolds Number ~ 150,000
2. Back-face of charring-ablative material-adiabatic
3. Initial Temperature ~ 580°R

Note: These material properties are typical of thermosetting plastics in use in current re-entry vehicles.

[1] Estimated values of the D-1 vehicle were based upon an H_e = 5,000 BTU/lb.

TABLE II-2-II

APOLLO D-2

Charring-Ablative Material Required to Maintain a Maximum Back-Face Temperature of 960°R to Impact

(Thicknesses based on an H_e = 5000 BTU/lb)

Pt.[1]	Body Location	Total Shield Thickness ~ inches	
		θ_E = 4.7°	θ_E = 8.4°
1	Stagnation Pt.	4.61	2.66
2	Forebody	1.82	1.17
3	Forebody	1.37	1.17
4	Forebody	1.27	1.08
5	Forebody	1.20	0.98
6	Afterbody (Windward)	1.75	0.99
7	Afterbody (Windward)	1.38	0.75
8	Afterbody (Windward)	1.28	0.67
9	Afterbody (Windward)	1.21	0.58
10	Afterbody (Windward)	0.31	0.15
11	Afterbody (90° Meridian)	0.72	0.43
12	Afterbody (90° Meridian)	0.72	0.43
13	Afterbody (90° Meridian)	0.72	0.43
14	Afterbody (90° Meridian)	0.68	0.42
15	Afterbody (90° Meridian)	0.18	0.11
16	Afterbody (Leeward)	0.46	0.25
17	Afterbody (Leeward)	0.46	0.25
18	Afterbody (Leeward)	0.46	0.25
19	Afterbody (Leeward)	0.44	0.23
20	Afterbody (Leeward)	0.11	0.06
21	Afterbody (Sphere)	0.18	0.11

[1] Point locations are shown in Figure II-2-22.

DEFINITIONS

Symbol	Identification	Units
h	enthalpy	BTU lb^{-1}
H_e	effective heat of degradation	BTU lb^{-1}
K	correction factor	
L	shock detachment distance	ft
P_r	Prandtl Number	
$\dot{q}$	heat flux	BTU/ft^{-2} sec^{-1}
R_{e_s}	Reynolds Number	
S	wetted length	ft
T	temperature	°R
U	velocity	ft sec^{-1}
U_o'	velocity gradient	sec^{-1}
x	total degradation	ft
y	radius of revolution of an axisymmetric body	ft
α	angle of attack	deg (°)
ϵ	emissivity	
ρ	density	lb ft^{-3}
μ	viscosity	lb ft^{-1} sec^{-1}

Subscript	Identification
e	local conditions
g	gas
H.G.R.	hot gas radiation
L	laminar
O.T.	optically thin
r	recovery
s	at Stagnation Point
T.	turbulent
T.A.	turbulent attached
W	wall conditions

Superscript	Identification
*	Reference conditions

REFERENCES

(1) Dewees, L., "Re-entry Vehicle Design (Ablating) Program", G.E.-MSVD TIS R59SD391, dated July, 1959. DiCristina, V., "Addendum to the Ablation Design Digital Computer Program", G.E.-MSVD Aerophysics Engineering Tech. Memo. No. 152, dated March, 1960.

(2) General Electric, Missile and Space Vehicle Department, "Project APOLLO Data Book", Volume II, 14 March 1961.

(3) Lees, L., "Laminar Heat Transfer over Blunt-Nosed Bodies at Hypersonic Speeds", Jet Propulsion, dated April, 1956.

(4) Eckert, E.R.G., "Engineering Relations for Heat Transfer and Friction in High Velocity Laminar and Turbulent Boundary Layer Flow Over Surfaces with Constant Pressure and Temperature", ASME Paper No. 55-A-31, dated, 1955.

(5) Walker, G.K., "A Particular Solution to the Turbulent-Boundary Layer Equations", Journal of the Aerospace Sciences, Vol. 27, No. 29, dated September, 1960.

(6) Logan, J.G., Treanor, C.E., "Tables of Thermodynamic Properties of Air from 3000°K to 10000°K at Intervals of 100°K", Cornell Aeronautical Laboratory, Inc., Report No. BE-1007-4-3, dated January, 1957.

(7) Adams, M.C., "A Look at the Heat Transfer Problem at Super Satellite Speeds", AVCO - Everett Research Laboratory, AMP 53, dated December, 1960.

(8) Moeckel, W.E., Weston, K.C., "Composition and Thermodynamic Properties of Air in Chemical Equilibrium", NACA TN 4265, dated April 1958.

(9) Kivel, B., Bailey, K., "Tables of Radiation from High Temperature Air", AVCO Research Laboratory, Research Report 21, dated December, 1957.

(10) Dewees, L. "Afterbody Design Program", G.E. - MSVD TIS R59SD393, dated July, 1959.

REFERENCES (Cont)

(11) Shaw, T.E., Mertz, W.S., "Thermal Flight Test Summary Report", G.E.-MSVD TIS R60SD403, dated August, 1960, SECRET.

(12) Allen, C.C., Lewis, M.I., Eagles, A.E., "Materials Evaluation for Mark VI Program", G.E.-MSVD Aerophysics Data Report 60SD498, dated December, 1960, SECRET.

(13) DiCristina, V., "A One Dimensional Conduction Melting Solution with Internal Air Gap", G.E.-MSVD Aerophysics Engineering Tech. Memo. No. 174, dated November, 1960.

(14) Walker, G.K., Shaw, T.E., "Final Summary Report Aerothermodynamic Analysis", G.E.-MSVD TIS R60-SD481, dated January 1961, SECRET.

2.2 RE-ENTRY VEHICLE CONTROL SURFACES

The local flow environment surrounding control surfaces in the shock layer of a hypersonic vehicle represents a complex combination of shock wave-boundary layer interaction, local flow conditions which vary across the shock layer, local separation, and three-dimensional cross flow. Since the shock layer flow is supersonic, a detached shock stands in front of the control surface and interacts with the body boundary layer. The flap acts as an obstruction to the boundary layer, causing it to separate as the flap is approached, if the pressure rise to separation is sufficient. The presence of a highly curved bow shock causes gradients in all flow properties within the shock layer, which in turn causes cross-flow over the flap surfaces. The resulting boundary layer condition on the flap and adjacent body surfaces is extremely difficult to predict theoretically with any degree of confidence.

A comprehensive survey of available heat transfer to fin and wing types of control or lift surfaces is contained in Ref. 1.[1] Although the summary excludes data on flaps, many of the phenomena associated with these types of protuberances hold for flap configurations.

A sketch of the flap and vehicle configuration and vehicle flight altitude is shown in Figure II-2-23. The relative position of the bow shock about the body, without flap, was based on schlieren and luminosity photographs of the Mercury Configuration (Ref. 2). The shock detachment distance was adjusted to higher Mach number ($M_\infty = 32$) by use of data presented by Nestler, Ref. (3).

When the flap was superimposed on the shock shape and body configuration shown, it was found that the flap was enveloped in the shock layer.

It would appear that streamlines entering at the "stagnation" point and expanding over the body will see an appreciable pressure rise at the flap due to the large turning angle involved. For purposes of analysis it was assumed that the maximum pressure on the flap surface that could sustain an attached boundary layer was given by pressure rise to separation data presented on page 1157 by Shapiro, Ref. (4). The aerodynamic heating along the centerline, given by this attached flow would represent a nominal design condition, from which, other possible variations in heat transfer could be estimated. The heat transfer based on the above hypothesis was estimated for flight conditions at $M_\infty = 32$ and an altitude of 176,000 feet.

[1] References will be found at the end of Section 2.2

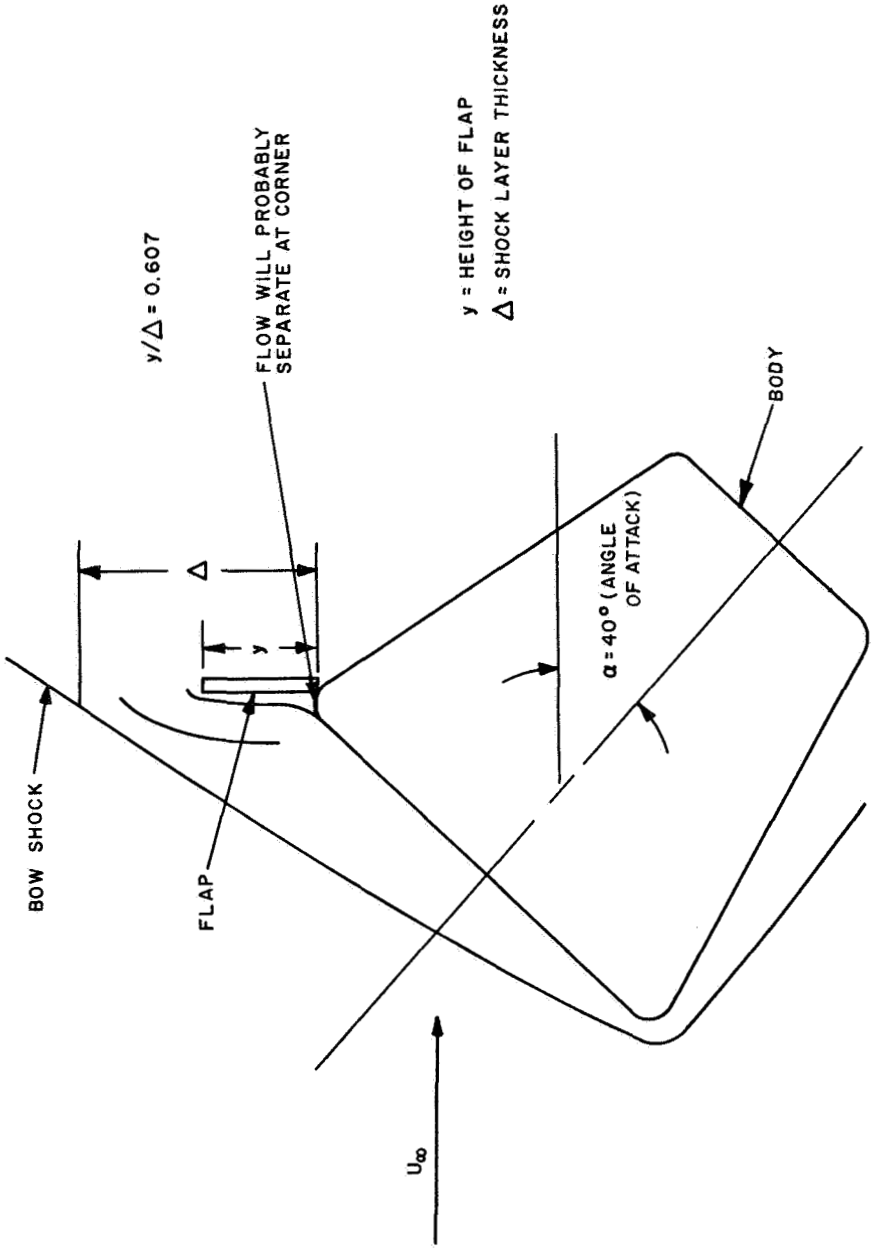

Figure II-2-23. Schematic of re-entry vehicle with flap

For turbulent flow the maximum pressure rise that can exist without separation may be related to the local dynamic pressure as

$$\frac{P_2 - P_1}{q} = \frac{4.5}{R_{e_s}^{1/5}} \qquad \text{(Ref. 5)} \qquad (1)$$

In laminar flow,

$$\frac{P_2 - P_1}{q} = \frac{1.4}{R_{e_s}^{1/2}} \qquad \text{(Ref. 5)} \qquad (2)$$

From equations 1 and 2 above it is obvious that the highest pressure that could be sustained on the flap without separation would be for a turbulent boundary layer. The local Reynolds number on the front face of the configuration (considering the centerline) would appear to be turbulent from about 200,000 feet down in altitude when it is considered that an ablation system is used which may trigger transition to turbulent flow at Reynolds numbers, R_{e_s} (based on wetted length from the "stagnation" point) of approximately 100,000 - 150,000. At 176,000 feet the local Reynolds number was about 200,000. Because of the small variation in $R_{e_s}^{1/5}$ during the trajectory, the maximum pressure rise for separation is comparatively insensitive to the local Reynolds number before the flap.

For purposes of estimating the pressure on the flap (for attached flow) it was assumed that the flow had expanded approximately 50 degrees which is the local angle of inclination on the vehicle prior to the small turning radius.* Applying equation 1 the local pressure on the flap was calculated. Within fairly narrow limits the pressure on the flap was approximately 40 percent of the stagnation pressure. No variation with spanwise location was assumed or calculated. With a knowledge of the local pressure on the flap the turbulent heat transfer rate was calculated at the flap centerline assuming boundary layer growth from the stagnation point. If, for example, a wetted length was selected arbitrarily as 1 foot in front of the flap, then the local heating would be increased approximately 50 percent. A comparison of the former heating rate, with that to the flap, assuming it were in an undisturbed stream (i.e.,

*Note that this procedure tacitly assumes a very localized region of separated flow at the base of the flap; otherwise the turning angle would exceed 90 degrees.

outside the shock layer) at this and two other trajectory points indicated that the heat transfer to the flap ranged from 0.75 to 1.5 times that to the flap in free stream. Because of the assumptions used in the analysis and the absence of experimental data for a comparable configuration it was decided that a constant ratio relative to the free stream flap heating of 1.5 should be used. If the flow separates over a major portion of the flap the heat transfer in the separated zone should be approximately 60 percent of the attached value (Ref. 6). If separation occurs, reattachment may occur at some location on the flap. Larson, (Ref. 6) has indicated that for turbulent flow that the heat transfer at reattachment may be as high as 2 1/2 times the corresponding attached value. However, ablation tests of blunt fins in which flow attachment occurred on the leading edge have not shown such increases (Ref. 1). Further, the zone of higher heat transfer, if it should exist, should be localized and with the use of materials such as graphite or pyrolytic graphite, able to absorb such local discontinuities.

Heat transfer in the region about the base of the flap, based on the analysis of protuberance data summarized in Ref. 1 was estimated to be 2-3 times the local turbulent heat transfer at the corner of the blunt forward face.

Heat transfer rates to the center line of the control flap (oriented normal to the flow for the entire heating period) were calculated for each of the limiting trajectories and are shown in Figure II-2-24 and II-2-25. These calculations are based upon the method outlined above.

A pyrolytic graphite - columbium bonded composite was considered because of its excellent high temperature properties and high oxidation resistance. The pyrolytic graphite shield would be either brazed or bonded with a high temperature graphite cement to an F - 50 columbium support structure. Techniques of brazing pyrolytic graphite to itself and also to high temperature refractory metals such as columbium are presently being investigaged by GE-MSVD.

The required thickness of pyrolytic graphite to reduce the bond temperature to 2500 degrees R are listed below:

Re-entry Angle	Pyrolytic Graphite	F-48 Columbium	Type Bond
4.7°	0.30 in.	0.10 in.	C-9 graphite cement (National Carbon Co.) or braze
8.4°	0.10 in.	0.10 in.	(same as above)

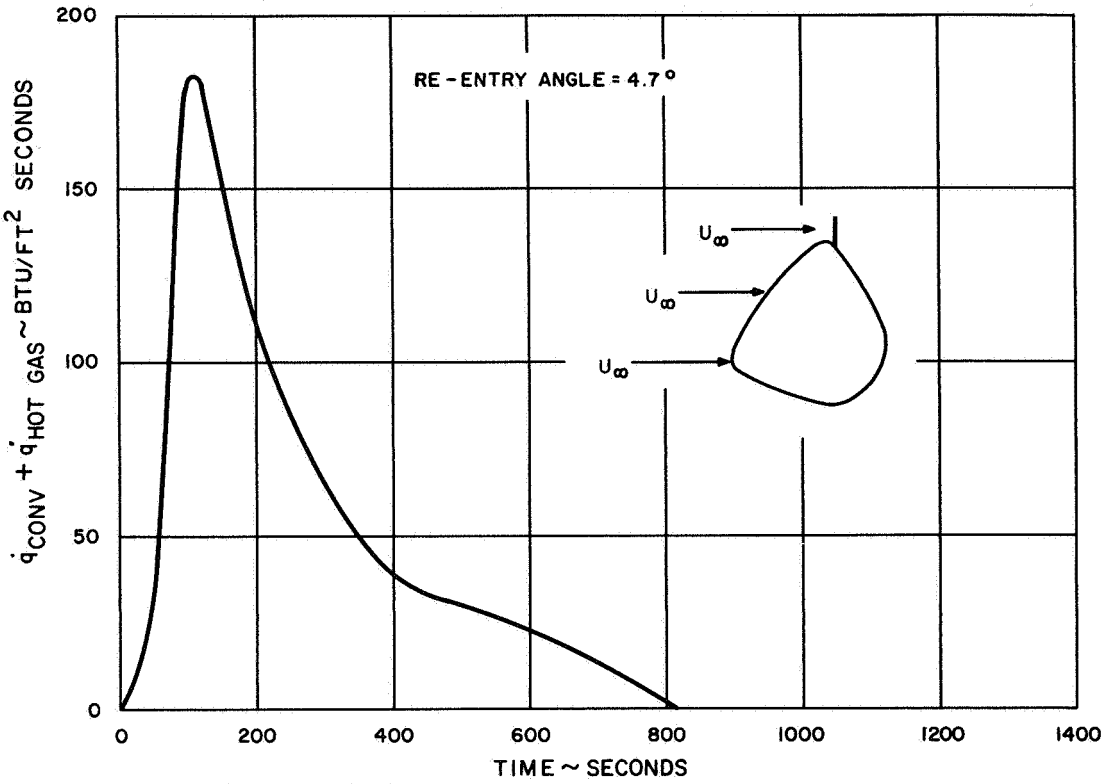

Figure II-2-24. APOLLO - D-2 Configuration, gross heat fluxes to flap during re-entry

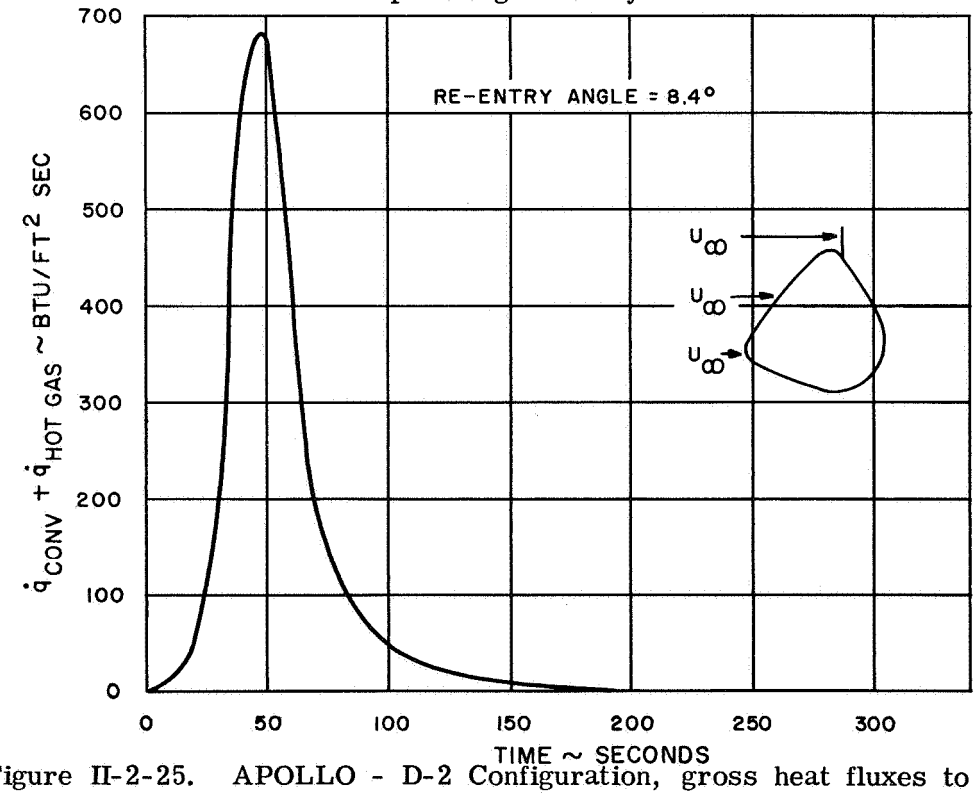

Figure II-2-25. APOLLO - D-2 Configuration, gross heat fluxes to flap during re-entry

The geometry of this type of control surface suggests that a charring-ablative material could be employed without experiencing a detrimental shape change during re-entry. Thicknesses of a charring-ablative material required to maintain a maximum bond temperature of 960 degrees R, based upon an H_e = 5000 BTU/lb, are as follows:

Re-entry Angle	Charring-Ablative Material
4.7°	2.0"
8.4°	1.1"

If the control system employs an aluminum support structure, it will be necessary to coat the back-face of the aluminum with approximately 0.06" of an epoxy coating to absorb the wake heating and limit the aluminum structure's back-face to 960 degrees R.

REFERENCES

(1) Shaw, T.E. and Nestler, D.E., "Heat Transfer and Ablation Phenomena in the Interaction Zones of Fin-Body Configurations in Hypersonic Flow" GE-MSVD Aerophysics Eng. Tech. Memo 198, April 1961.

(2) Pritts, O.R. and Mallard, S.R., "Pressure and Heat Transfer Distribution on a One-Tenth Scale Mercury Capsule at Mach Number 8" AEDC-TN R59-164".

(3) Nestler, D.E., "Correlations for Convective Heat Transfer, Pressure Distribution and Shock Detachment Distance for Blunt Axisymmetric Forebodies", GE-Aerophysics Eng. Tech Memo No. 194, January 1960.

(4) Shapiro, A., "The Dynamics and Thermodynamics of Compressible Fluid Flow" Vol. II.

(5) Donaldson, C. duP., and Lange, R.H., "Study of the Pressure Rise Across Shock Waves Required to Separate Laminar and Turbulent Boundary Layers", NACA TN 2770, 1952

(6) Larson, H.K., "Heat Transfer in Separated Flows", IAS Report No. 59-37, January, 1959.

2.3 POWERED LAUNCH

A thermal study was made to determine the thermodynamic performance, during powered flight, of the APOLLO D-2 boost configuration shown in Figure II-2-26.

The boost trajectory and coefficient of pressure ratio ($C_p/C_{p\ max}$) distribution used in the calculation of heat transfer rates to this vehicle are presented in Figures II-2-27 and II-2-28 respectively. Although the pressure values shown in Figure II-2-28 are theoretically correct at a free stream Mach. No. of 5, this distribution is assumed constant over the entire powered flight range. Peak heating occurs at the stagnation point at $M\infty = 5$.

Aerodynamic heat fluxes to five representative body locations of the boost vehicle (Pts. 1, 8, 13, 18, 23) were evaluated through the use of two digital computer programs. A digital computer trajectory-flux program (Ref. 1)[1] was employed to calculate aerodynamic heat transfer coefficients and recovery enthalpy levels for 25 body locations along one meridian of the vehicle during the entire heating period. This program incorporates heat transfer equations based upon Lees' classical solution of the hypersonic heating problem for a laminar boundary layer and the G.E. axisymmetric relationship for turbulent flow. The equations used are as follows:[2]

Stagnation Pt. Heating

$$\dot{q}_s = \frac{0.779}{(P_r)^{2/3}} (\rho_e^* \mu_e^* U_o^*)^{1/2} (h_s - h_w)$$

Laminar Heating

$$\dot{q}_L = \frac{0.389}{(P_r)^{2/3}} \frac{\rho_e^* U_e^* y (h_r - h_w)}{\left[\int_o^s \rho_e^* U_e^* y^2 \, ds\right]^{1/2}}$$

---

[1] References will be found at the end of Section 2.3

[2] Nomenclature for this section is identical to that in Section II-2.1

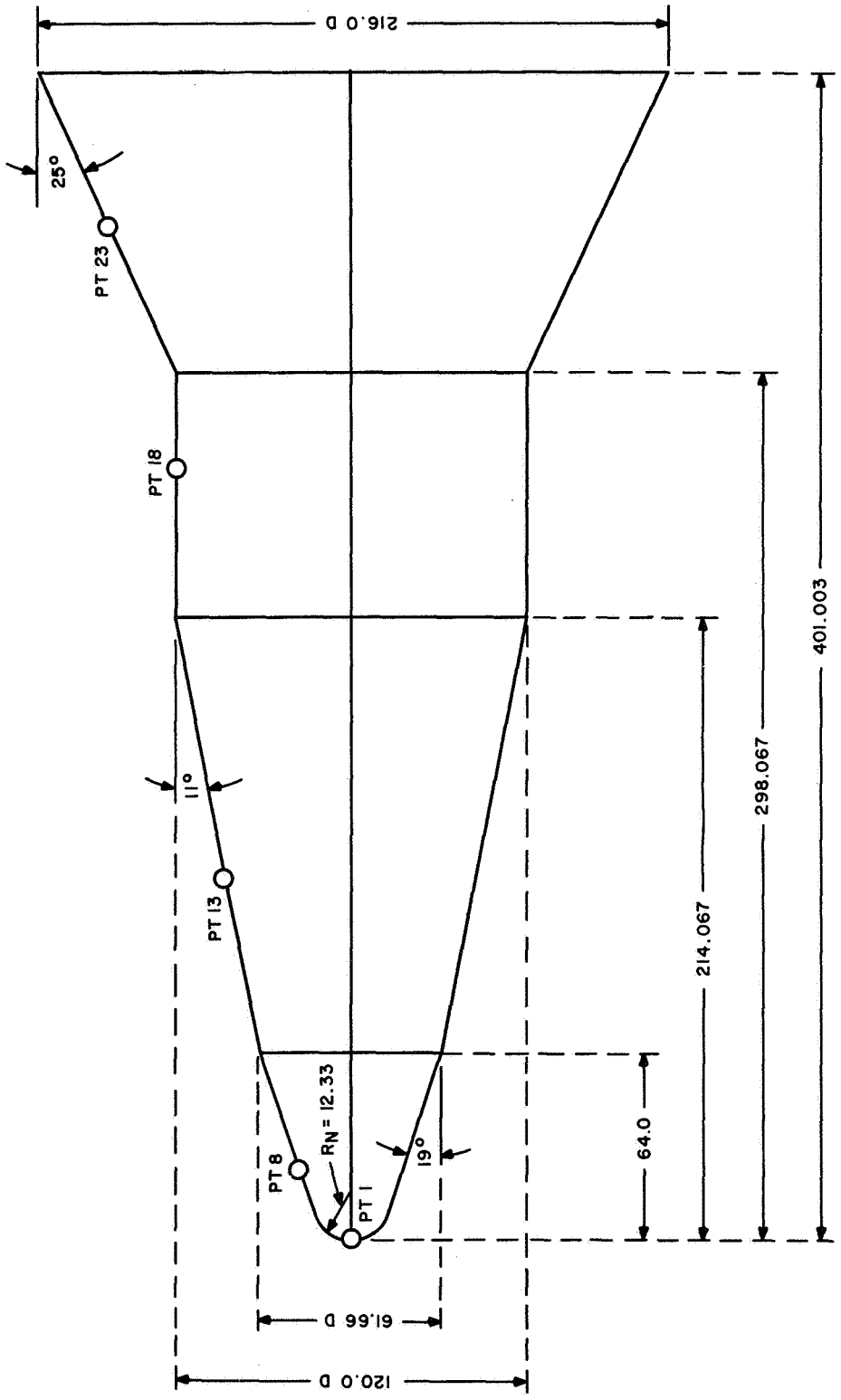

Figure II-2-26. APOLLO - D-2 Configuration, boost configuration

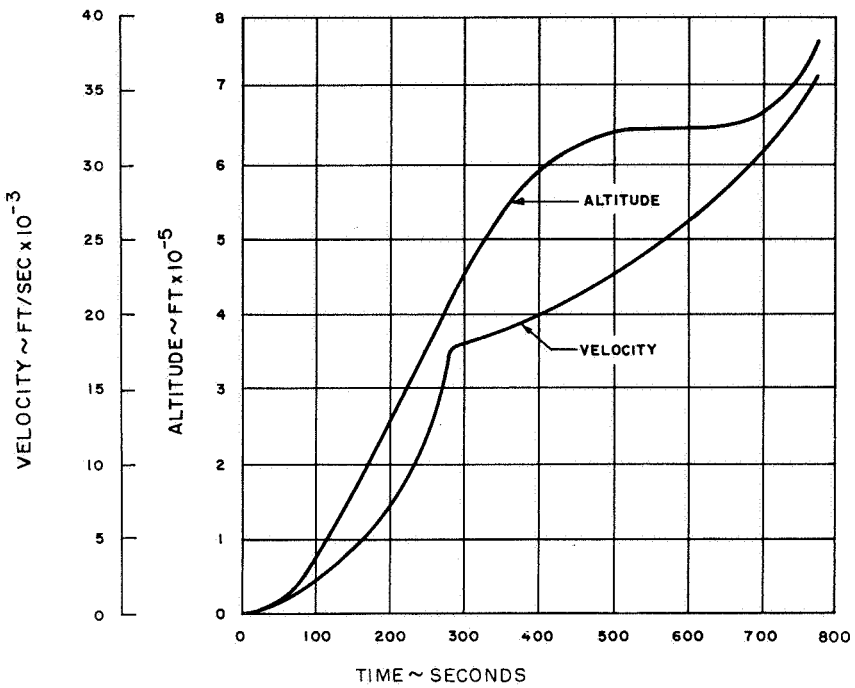

Figure II-2-27. APOLLO - D-2 Configuration, trajectory during powered flight

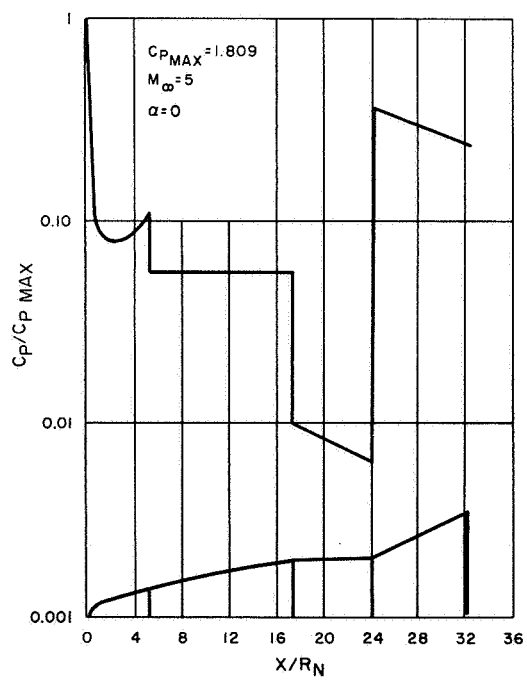

Figure II-2-28. APOLLO - D-2 Configuration, coefficient of pressure distribution

G.E. Axisymmetric Turbulent Heating

$$\dot{q}_T = \frac{0.0296}{(P_r)^{2/3}} \frac{\rho_e U_e (\mu_e)^{1/4} \left(\frac{\mu_e^*}{\mu_e}\right)^{1/5} \left(\frac{\rho_e^*}{\rho_e}\right)^{4/5} y^{1/4} (h_r - h_w)}{\left[\int_o^s \rho_e U_e (\mu_e)^{1/4} y^{5/4} ds\right]^{1/5}}$$

It was assumed that the air stream expanded isentropically from the stagnation point of the vehicle and that stabilization of turbulent flow to laminar flow occurred when a local Reynolds No. (Re_s)[1] of 150,000 was reached. Atmospheric properties are represented by the 1959 ARDC Model atmosphere. Zero angle of attack was assumed throughout the launch trajectory.

A form of heat transfer coefficients $(\dot{q}/h_r - h_w)$ and recovery enthalpies (h_r) at each of the five body locations, combined with experimentally determined thermal properties of the shield materials, were used as primary inputs to a digital computer conduction-char-ablation program (Ref. 2). This program constitutes an approximate solution to the one dimensional heat conduction problem and, if required, one boundary undergoing melting or vaporization. A closed loop method uses the input and a self-generated surface temperature to calculate the instantaneous heat flux to one body location. Temperature histories of approximately 40 nodes within a multi-layer slab (and front face recession history, if melting occurs) at this location are simultaneously calculated based upon the self-generated instantaneous heat fluxes. All shield temperature calculations are based upon an adiabatic back face.

The hot gas radiation to the vehicle is small when compared to the aerodynamic powered flight heating, therefore it was neglected.

Temperature histories were calculated assuming an aluminum honeycomb structure, shown in Figure II-2-29 over the first conical section, cylindrical section and flare assembly which correspond to body locations 8, 18, and 23 shown in Figure II-2-26. The second conical section, body location 13, was assumed to be an aluminum skin with a minimum structural thickness of 0.08". The spherical section of the nose cap may employ a minimum thickness of an epoxy coating over the honeycomb or a heat sink (0.2" of aluminum) to maintain a tolerable temperature response in this region.

---

[1] Based upon wetted length and local edge of boundary layer values.

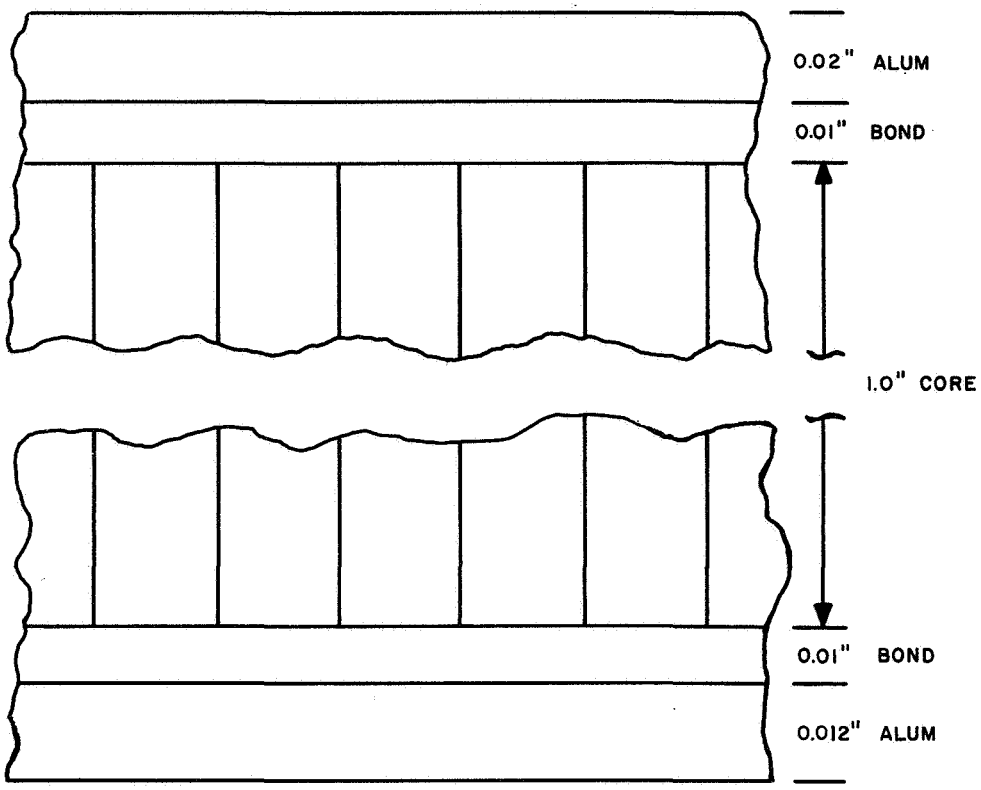

Figure II-2-29. Composite of spacecraft honeycomb structure

The surfaces of the aluminum skin and honeycomb structure were assumed to be coated to have an emissivity of 0.85. This coating was assumed to afford no thermal protection to the aluminum other than its relatively high emissivity whereby re-radiation from the vehicle was increased.

The net heat fluxes to the body locations studied are shown in Figure II-2-30.

Surface and back face temperature histories of the honeycomb at body locations 8, 18, and 23 are presented in Figures II-2-31, II-2-32, and II-2-33.

The temperature history of the aluminum skin at body location 13 is shown in Figure II-2-34.

Thermal properties and assumed conditions for the powered flight portion of this study are given in Table II-2-III.

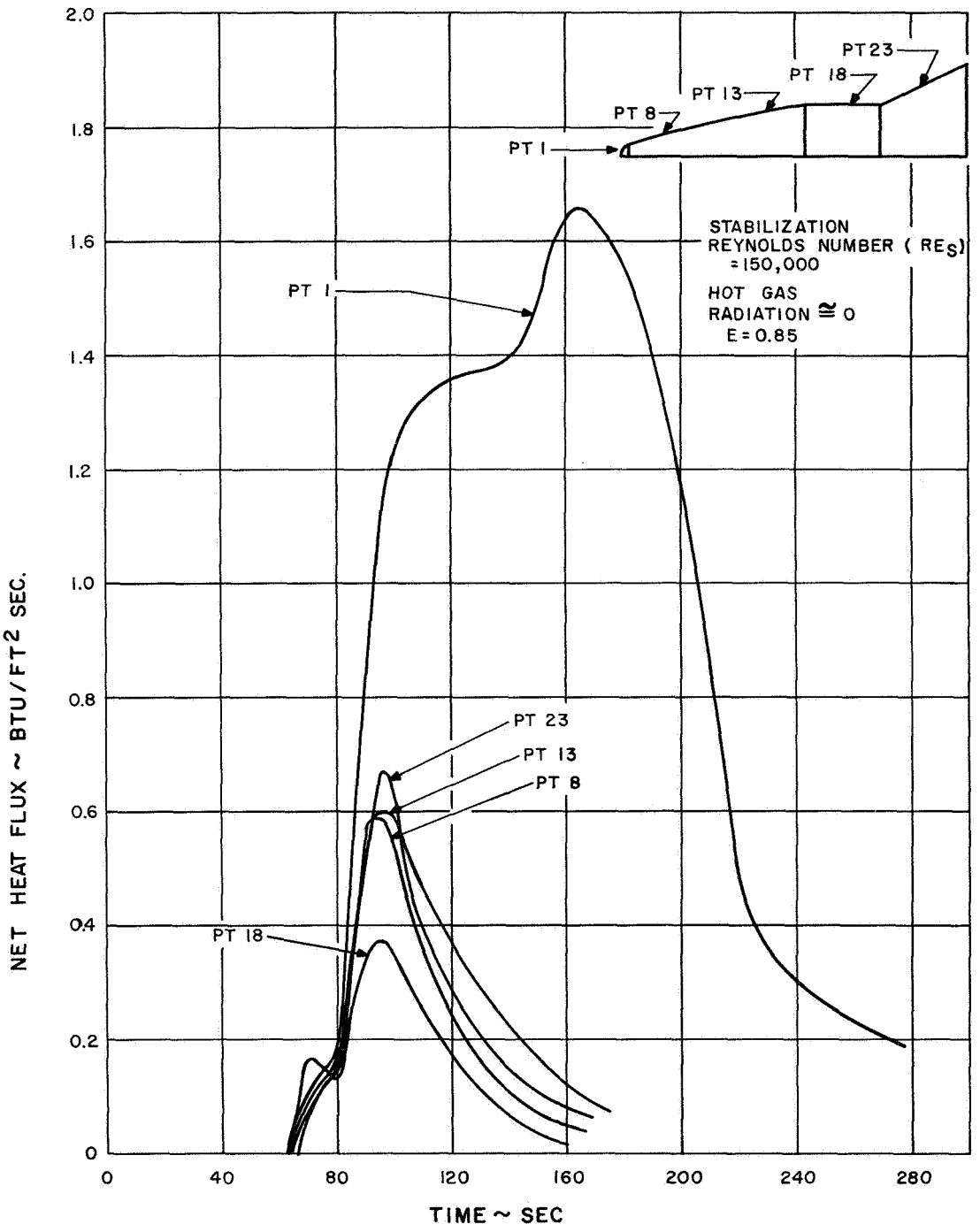

Figure II-2-30. APOLLO - D-2 Configuration, net heat fluxes during powered flight

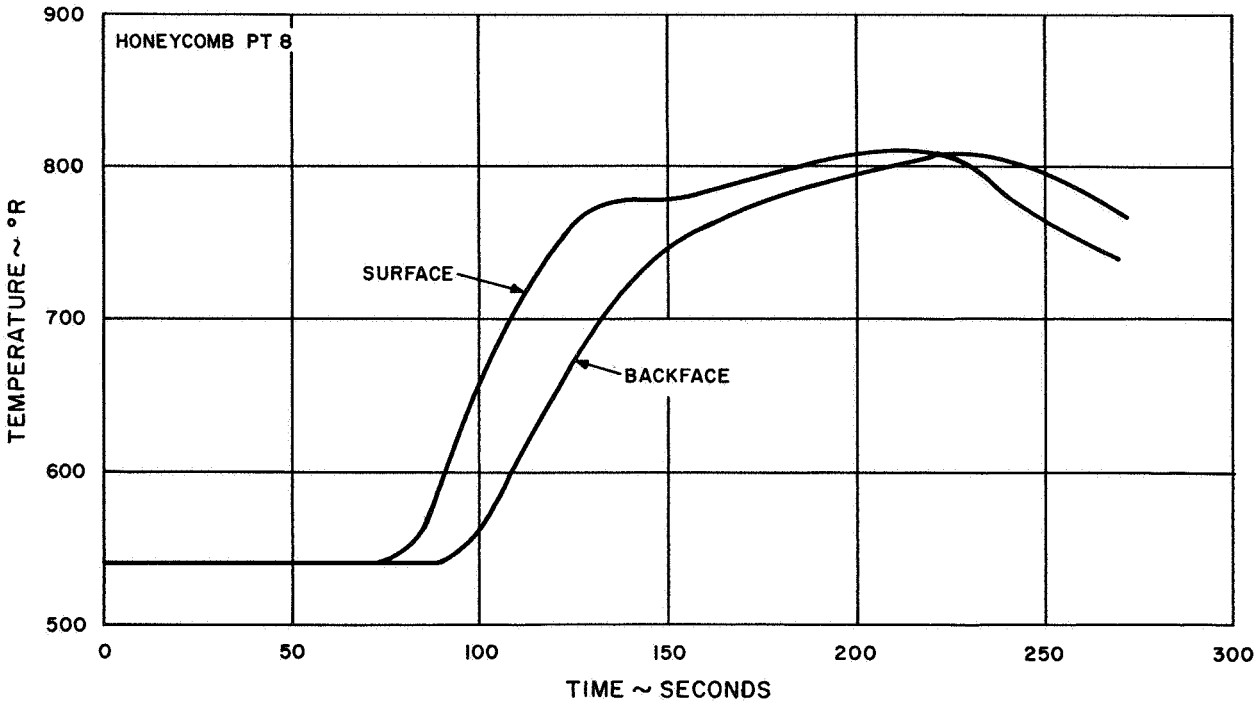

Figure II-2-31. APOLLO - D-2 Configuration, temperature histories powered flight

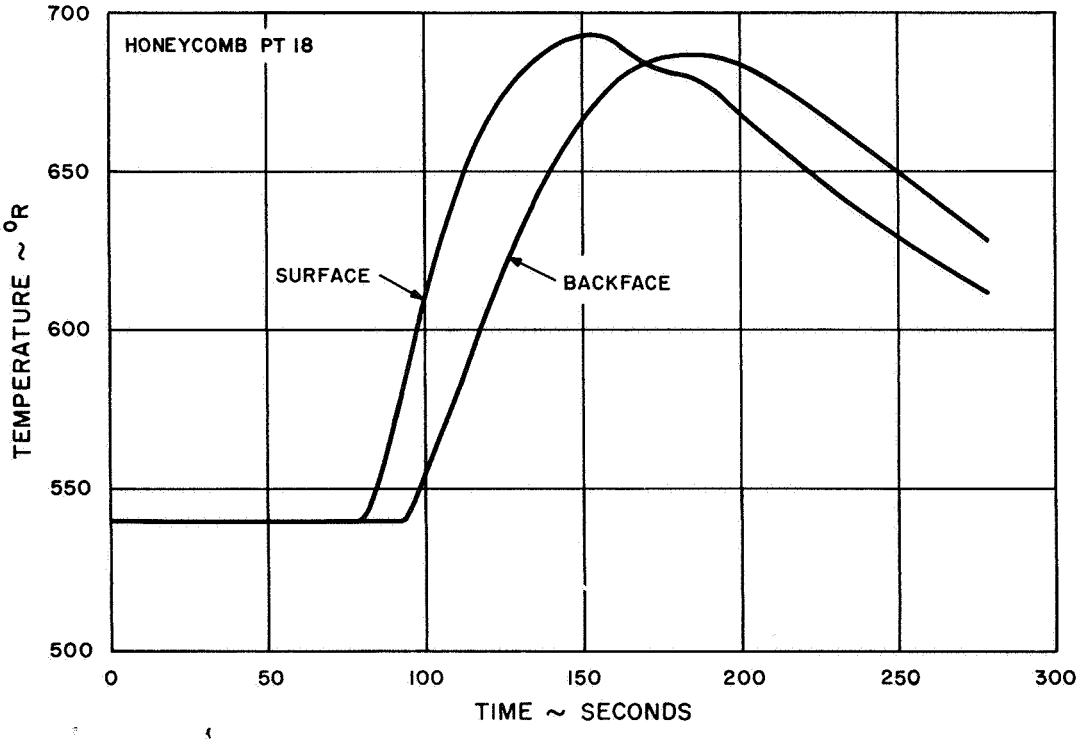

Figure II-2-32. APOLLO - D-2 Configuration, temperature histories powered flight

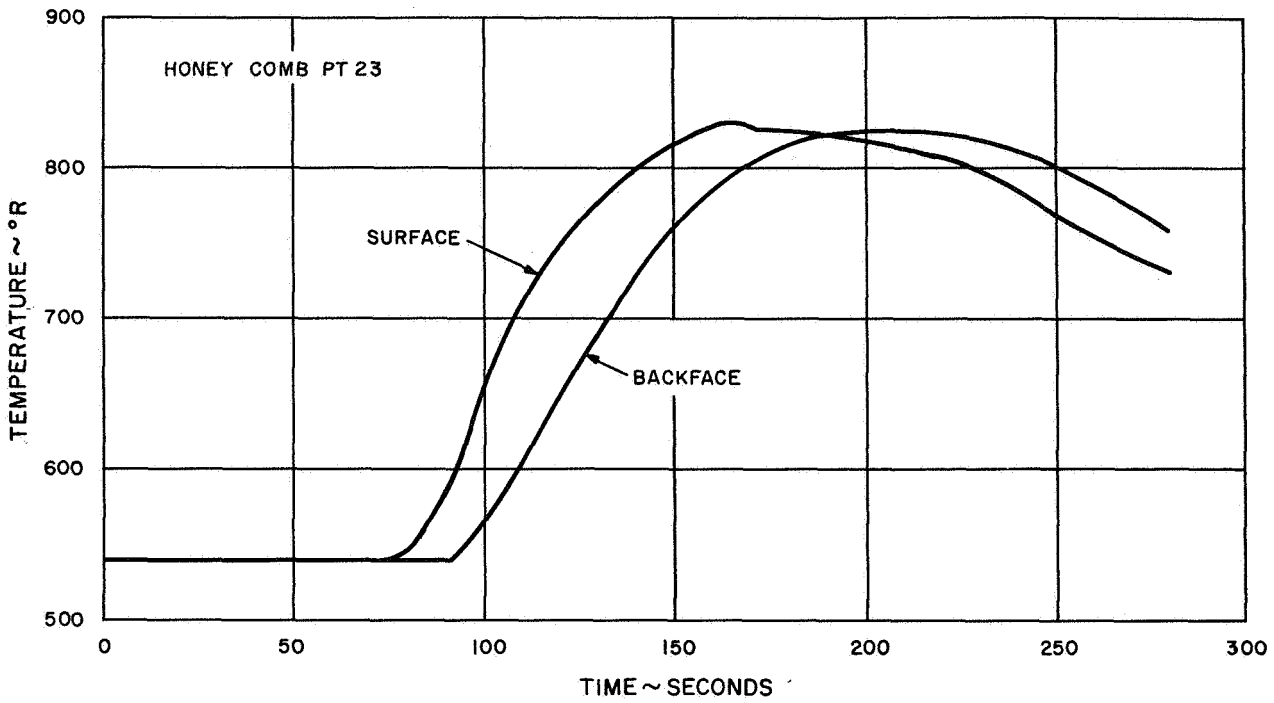

Figure II-2-33. APOLLO - D-2 Configuration, temperature histories powered flight

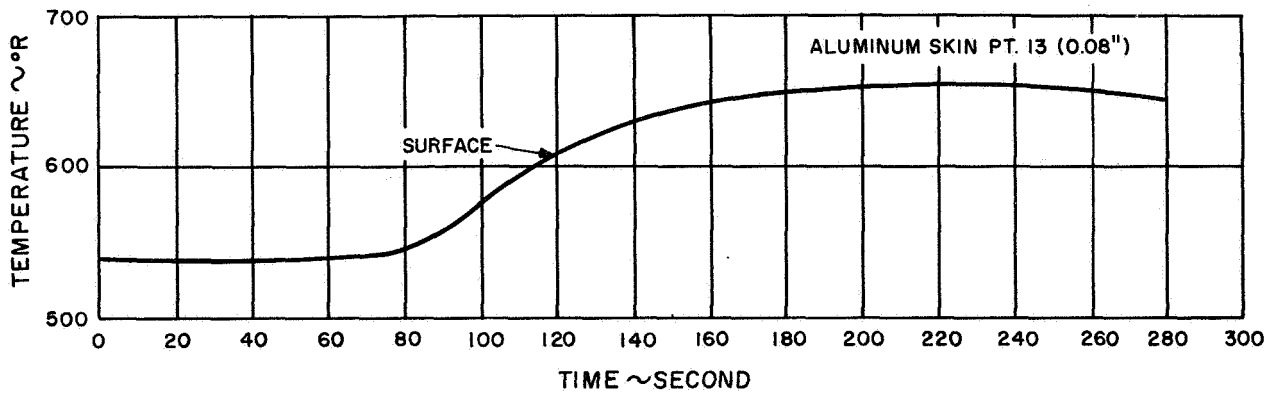

Figure II-2-34. APOLLO - D-2 Configuration, temperature histories powered flight

TABLE II-2-III

THERMAL PROPERTIES AND ASSUMPTIONS USED FOR POWERED FLIGHT

PROPERITES	ALUMINUM[1]	BOND
Density lb/cu ft	167	77
Specific Heat BTU/lb-°R	460°R - - .209 960°R - - .241 1460°R - - .273	.47
Thermal Conductivity BTU/sq ft-sec-°R/ft	460°R - - .0286 960°R - - .0367 1460°R - - .0439	.000028
Surface Emissivity	0.85	- - -

Assumptions:

1. Stabilization Reynods Number - 150,000
2. Back face of honeycomb - adiabatic
3. Initial temperature -540 degrees R

[1] The thermal response of the honeycomb was determined assuming a core cell size of 1/4" and a core density of 1.6 lb/cw ft.

REFERENCES

(1) Dewees, L., "Re-entry Vehicle Design (Ablating) Program", G.E. - MSVD TIS R59SD391, dated July 1959.

DiCristina, V., "Addendum to the Ablation Design Digital Computer Program", G.E. - MSVD Aerophysics Engineering Tech. Memo. No. 152, dated March 1960.

(2) DiCristina, V., "A One Dimensional Conduction Melting Solution with Internal Air Gap", G.E. - MSVD Aerophysics Engineering Tech. Memo. No. 174, dated November, 1960.

2.4 INTERNAL THERMAL PROTECTION

The re-entry vehicle structural arrangement is shown in Chapter III. Basically it consists of a thermal shield including its structural support and an inner pressure shell which houses the crew and associated equipment. The thermal protection system must not only maintain the load carrying structure within stress limits during re-entry but it must prevent the crew from being exposed to excessive temperatures and heat loads.

The design of the thermal shield from the aspect of external influences was discussed above. This section is primarily concerned with the inner structure and crew protection aspects of the thermal shield. As shown in Figures II-2-14 through II-2-21, additional ablative material is added for insulation to achieve low bond and structural support temperatures for the thermal shield (500 F). Since the weight of the "insulation portion" of the thermal shield is significant it becomes mandatory to arrive at an optimum configuration for the overall thermal protection system. Consequently the effect of various insulations, bond temperatures, and crew protection systems were investigated to determine the most feasible systems, and what methods or approaches might produce significant weight reductions with future development.

During the re-entry trajectory the ablative material chars to a finite depth. Time temperature histories of this point of maximum char depth were obtained for several points on the re-entry vehicle. A typical point is shown in Figure II-2-35. This char-virgin material interface temperature was then used as the driving force to study various inner heat protection systems. An analog program was written, utilizing standard heat transfer equations, and included the effects of varying the virgin ablative material thickness, emissivity of the structural supports, variable insulations and/or heat sinks, and the compartment wall and air temperatures.

A design goal of a maximum crew compartment wall temperature of 105 F at impact was established by the Human Factors group to maintain a shirt sleeve environment. The amount of insulation required for various thicknesses of virgin material were determined. Figure II-2-36 shows the reduction in total system weight that can be achieved by replacing the ablative material with a more efficient insulation. However, as the relative thickness of the virgin ablative material is decreased the bond temperature increases. The performance of a similar system but using a multiple layer radiation barrier type insulation, is shown in Figure II-2-37.

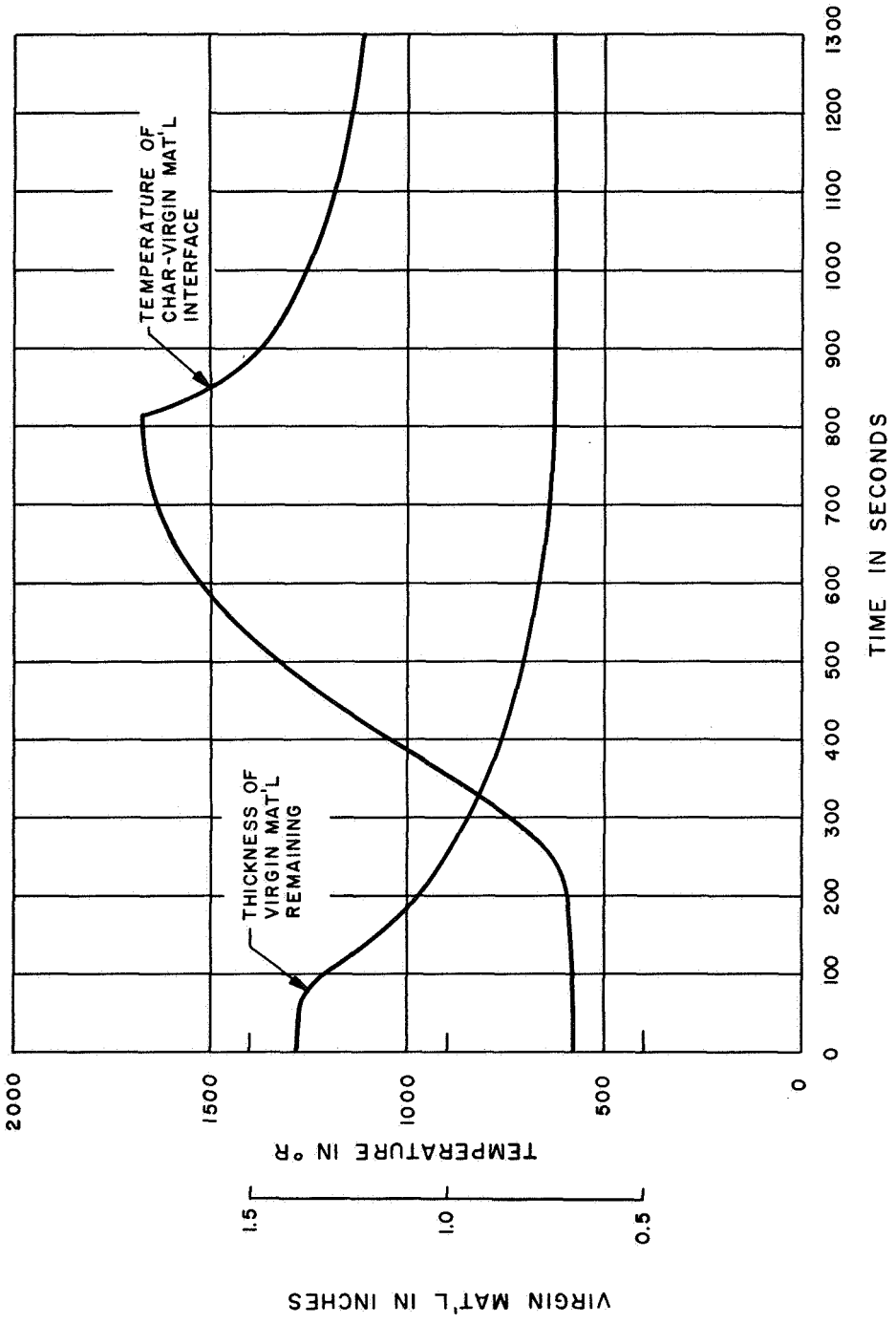

Figure II-2-35. Temperature of the char-virgin material interface vs time for a typical point on the D-2 afterbody

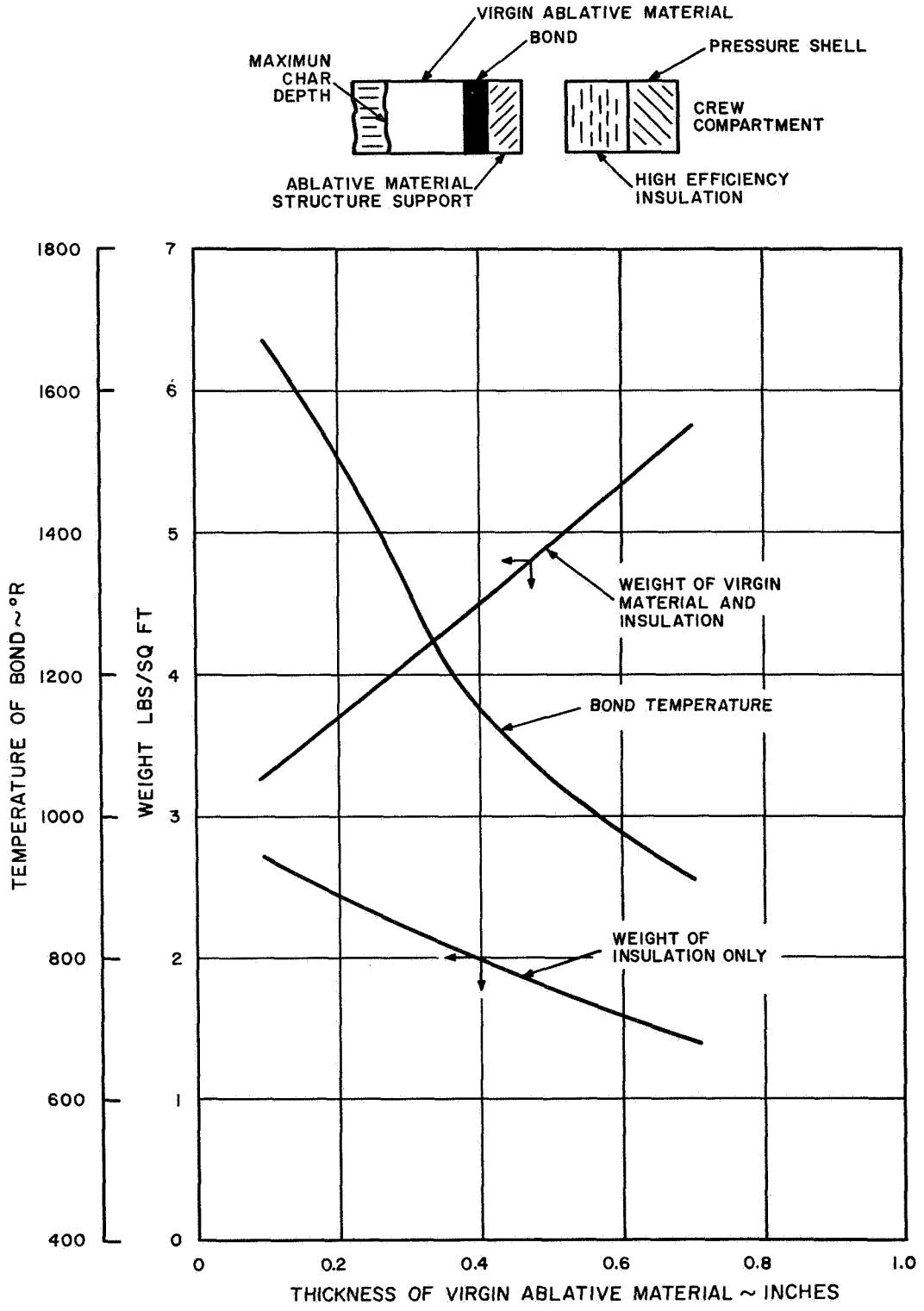

Figure II-2-36. Effect of virgin material thickness on overall system weight and bond temperature, insulation ~ Min K

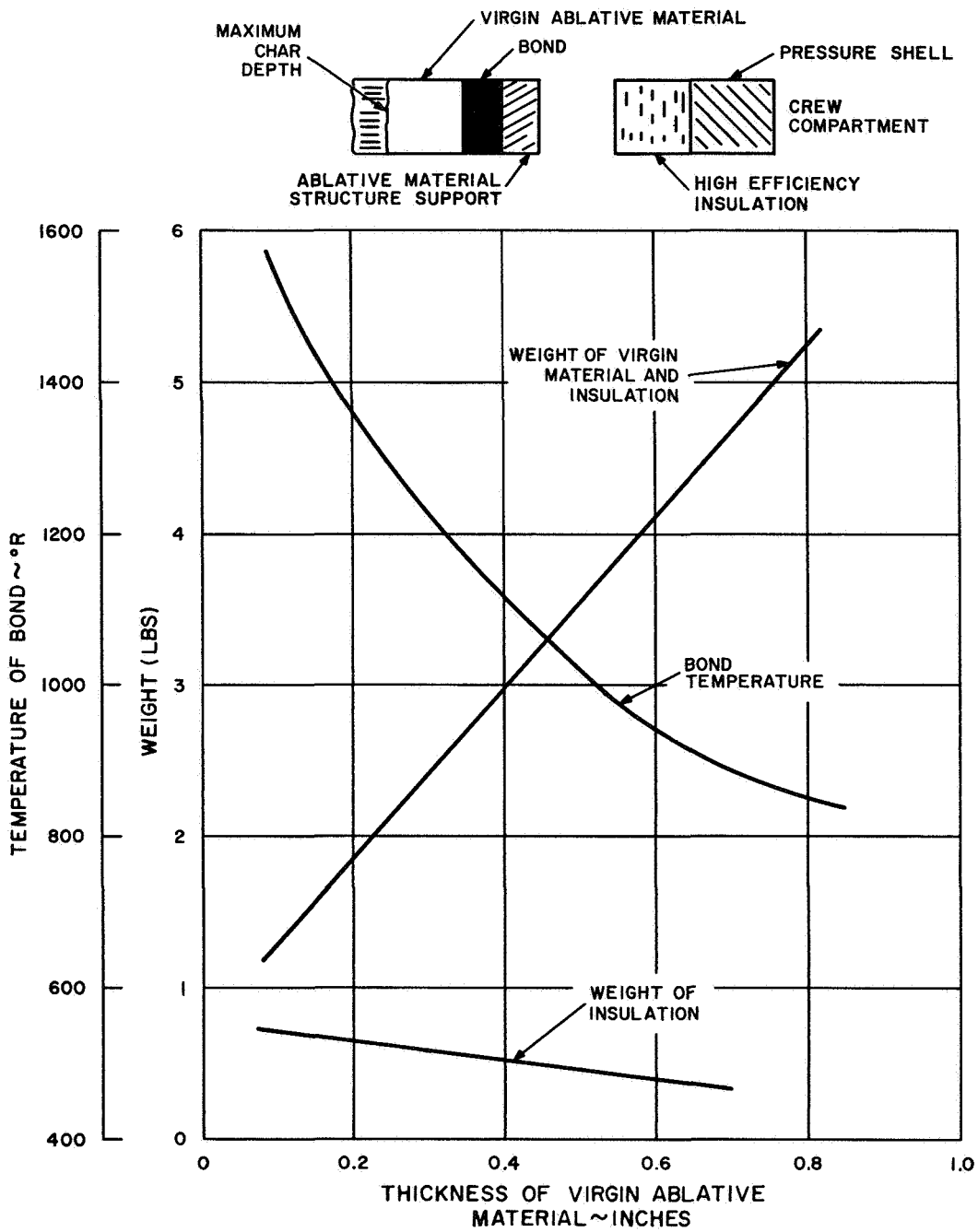

Figure II-2-37. Effect on virgin material thickness on overall system weight and bond temperature, insulation ~ multiple layer radiation barrier

For a bond temperature of 500 F the weight of the insulation system is reduced from 5.5 to 4.3 pounds per square foot with the use of multiple layer radiation barrier type of insulation in place of Min K. If the bond temperature could be raised to 1200 F the multiple layer radiation barrier insulation system weight could be dropped to 1.3 pounds per square foot. The advantages of using high bond temperatures and replacing the virgin ablation material with the high efficiency, so called super-insulations, becomes apparent. However, the total potential weight saving is mitigated somewhat by the necessity to use higher temperatures for the design of the ablative material structural support and thus increases the structural weight accordingly.

The use of an active cooling system to further reduce the weight was investigated. Figure II-2-38 shows the results obtained by using a "solid" water blanket for low temperature evaporative cooling of the pressure shell while maintaining the bond temperature at 500 F. The minimum total weight for virgin ablative material and water was also obtained for bond temperatures of 800 F and 1100 F and is shown in Figures II-2-39 and II-2-40 respectively.

A comparison of the two insulations and the active cooling system versus bond temperature is shown in Figure II-2-41. The difference between the two water cooling system curves is that the high weight curve is based on radiation as the sole means of transferring heat from the thermal shield to the water. The optimum curve assumes sufficient conductance exists between the thermal shield and the water to produce the minimum over-all weight as shown in Figures II-2-38, II-2-39, and II-2-40.

A system similar to that shown in Figure II-2-37 was chosen for the APOLLO design. The bonds currently available are limited to a maximum temperature of 500 F. The multiple radiation layer radiation barrier insulation was assumed to have a thermal conductivity of 25×10^{-5} BTU/sq ft F hr/ft, density of 4.7 lb/cu ft and a specific heat of .22 BTU/lb F. An analog trace of the wall and compartment temperatures are shown in Figure II-2-42 as a function of time for the minimum entry angle trajectory with the selected system. The pressure shell wall temperature reaches a temperature of 105 F at touchdown, but the temperature continues to rise for some time. Thus it will be necessary to cool the interior of the cabin to prevent excessive wall and air temperatures after touchdown. A system similar to the Mercury capsule using external air ventilation during parachute descent should provide adequate cooling for a reasonable weight.

CONFIDENTIAL

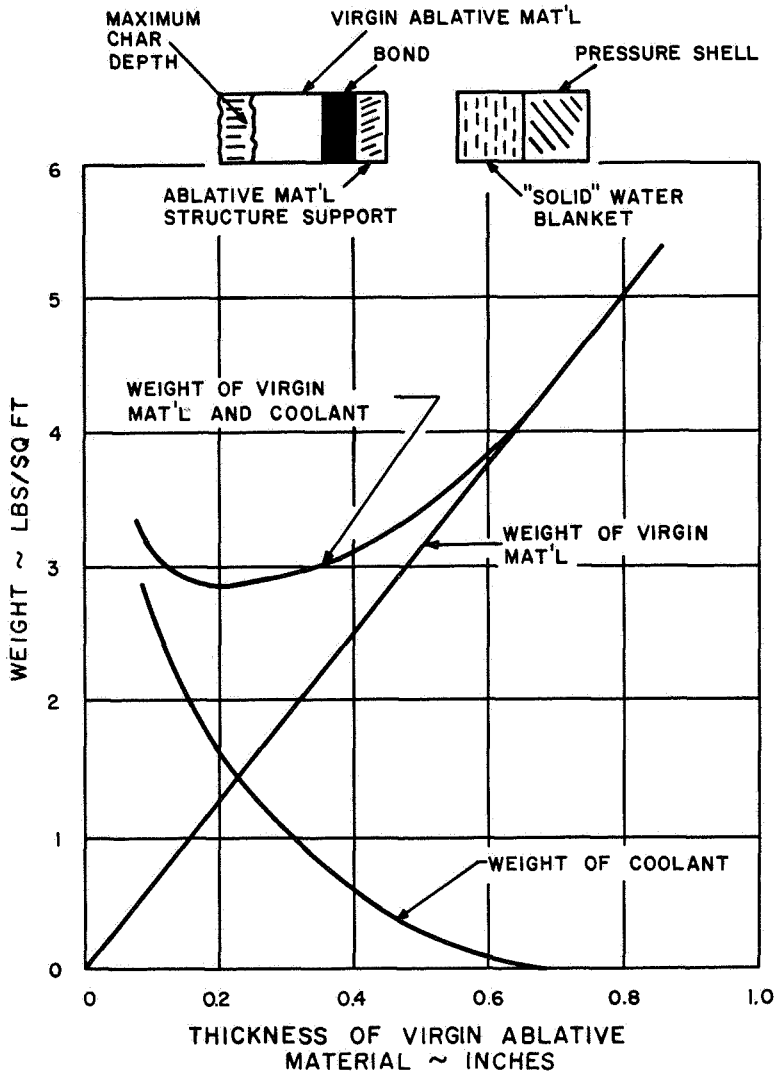

Figure II-2-38. Effect of active cooling system on overall system weight, temperature of bond = 500 F

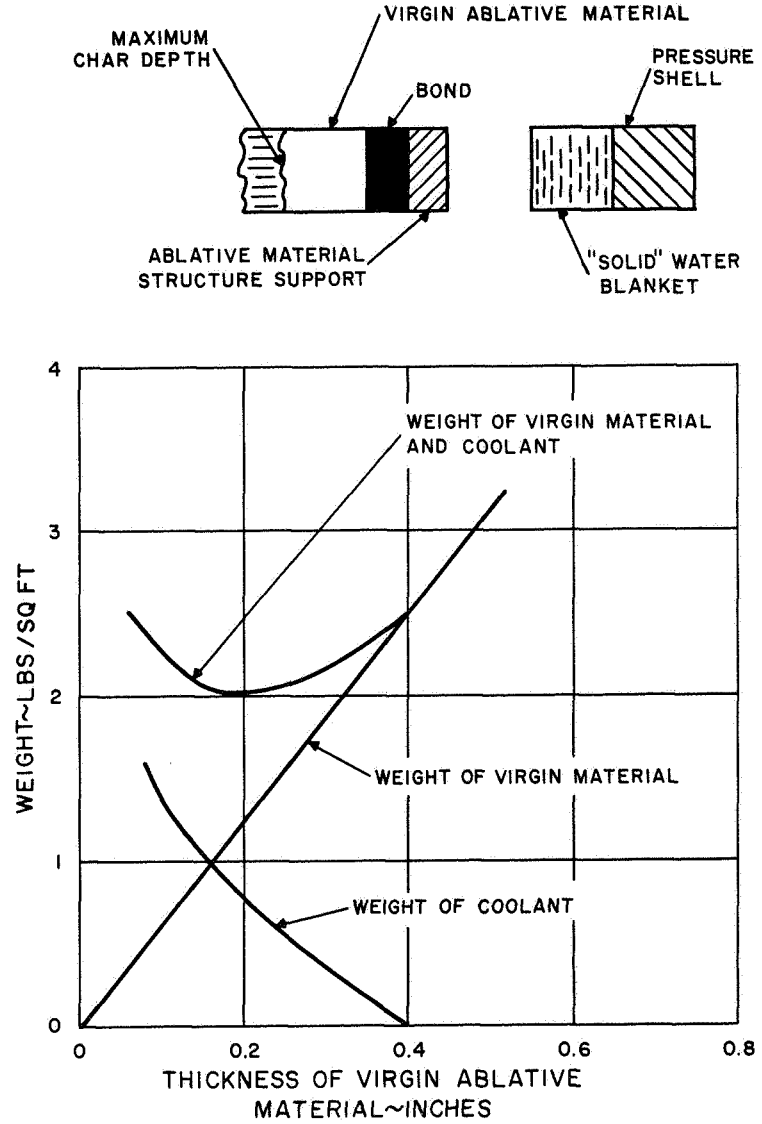

Figure II-2-39. Effect of active cooling system on overall system weight, temperature of bond = 800 F

CONFIDENTIAL

CONFIDENTIAL

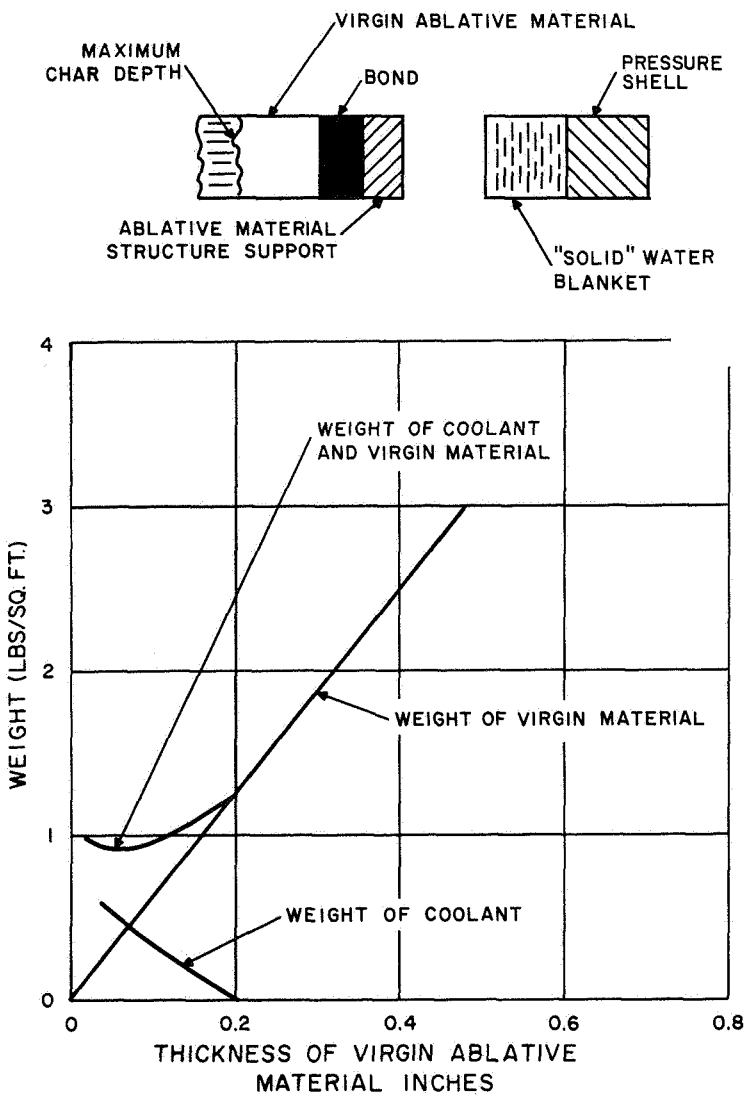

Figure II-2-40. Effect of active cooling system on overall system weight, temperature of bond = 1100 F

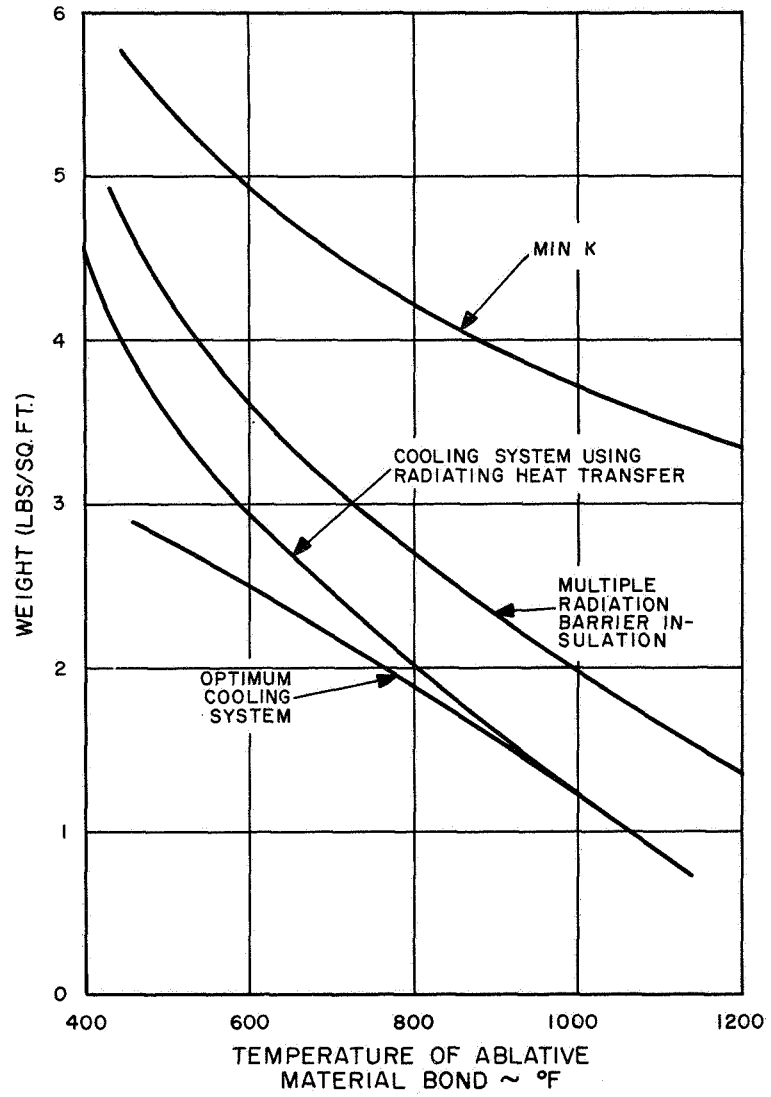

Figure II-2-41. Comparison of overall system weight vs ablative material bond temperatures for different insulations and cooling systems

CONFIDENTIAL

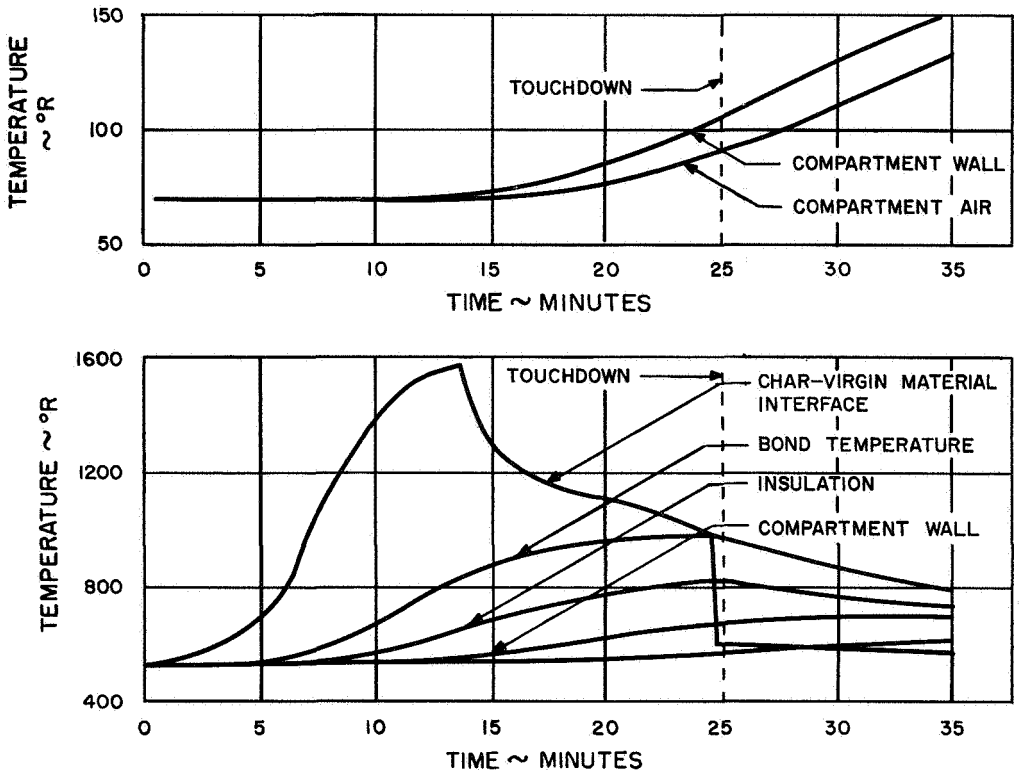

Figure II-2-42. Analog trace of wall and compartment

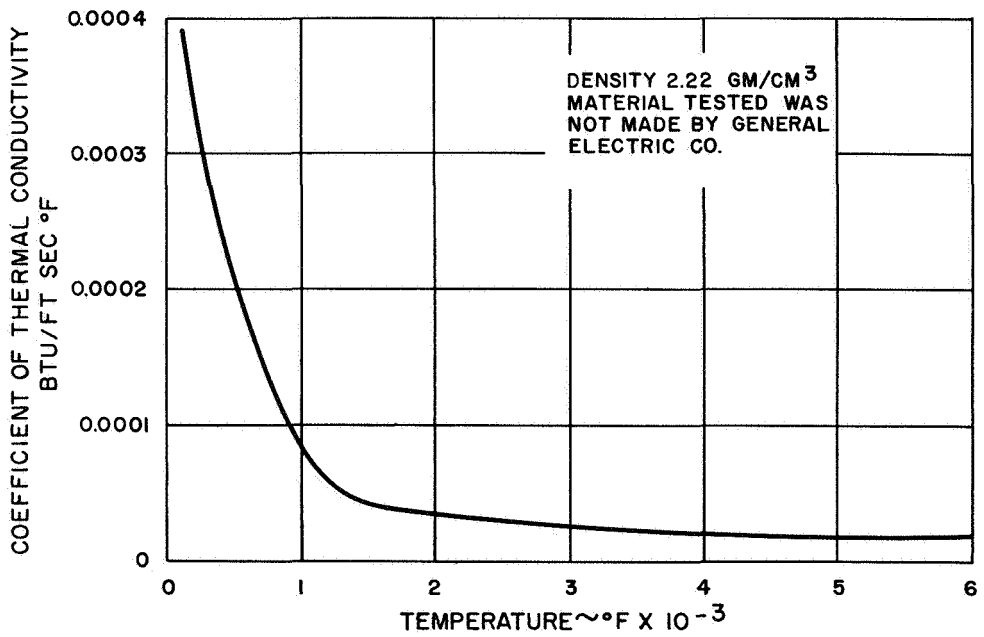

Figure II-2-43. Thermal conductivity vs temperature, pyrolytic graphite, across planes "C" direction

From the results obtained during the APOLLO study for the D-2 configuration it appears that;

1) The development of higher bond temperatures for the ablating material will allow the substitution of high efficiency insulations for the virgin ablation material and result in significant weight savings and

2) The use of active cooling systems for thermal protection of the crew can result in lighter weight systems if the means of installing the cooling systems can be developed for reasonable weights.

2.5 ADVANCED THERMAL PROTECTION SYSTEMS

2.5.1 Reinforced Plastics

The effective heat of degradation (H_e) was conservatively estimated at 5000 BTU/lb for the studies reported above in Section 2.1. However, to determine the effect of the effective heat of degradation on the APOLLO re-entry vehicle design the performance of the reinforced plastics was extended, by theory, to the APOLLO flight regime. In this manner an extrapolated value of H_e = 11,500 BTU/lb was obtained. A detailed discussion of ablative material performance is reported in Section 4.0 below.

The shield thicknesses for the D-2 re-entry vehicle are presented in Table II-2-IV.

2.5.2 Refractory Metals (Graphites)

Graphite materials are especially attractive as a heat protection system because of their high oxidation resistance which results in a negligible mass loss during ballistic and semi-ballistic re-entry. Since a commercial graphite shield acts as a heat sink and approaches radiation equilibrium temperatures during re-entry, a high temperature insulation is required to reduce the internal shield temperature to a tolerable level. Present investigations at General Electric regarding the preparation and properties of pyrolytic graphite have demonstrated the feasibility of utilizing the excellent high-temperature insulation characteristics of pyrolytic graphite, Figure II-2-43 in conjunction with a commercial graphite subtrate to form a light weight, minimum erosion heat protection system. The pyrolytic liner may be deposited directly on the commerical graphite substrate, bonded with a high temperature graphite cement, or brazed.

TABLE II-2-IV

APOLLO D-2

Charring-Ablative Material Required to Maintain a Maximum Back-Face Temperature of 960 degree R to Impact

(Thicknesses based upon an H_e = 11500 Btu/lb)

		Total Shield Thickness ~inches	
Pt.(1)	Body Location	$\theta_E = 4.7°$	$\theta_E = 8.4°$
1	Stagnation Pt.	2.38	1.35
2	Forebody	1.27	0.71
3	Forebody	1.12	0.71
4	Forebody	1.08	0.68
5	Forebody	1.05	0.64
6	Afterbody (Windward)	1.24	0.64
7	Afterbody (Windward)	1.12	0.54
8	Afterbody (Windward)	1.08	0.51
9	Afterbody (Windward)	1.05	0.49

(1) Point locations are shown in Figure II-2-22

A low density insulation placed behind the pyrolytic graphite liner performs the remaining required temperature reduction to the manned capsule.

Figures II-2-44 and II-2-45 illustrate the temperature distributions at the back-face of the commercial graphite shield, pyrolytic graphite liner, and the Min-K-2000 insulation at the stagnation point. The combined weights of the heat protection system for both the 4.7 degrees and 8.4 degrees re-entry angle trajectories to maintain an internal temperature of 500 F in the region of the stagnation point are 12.7 lbs/sq ft and 6.7 lbs/sq ft, respectively.

Using the techniques discussed in Section 4.2 below, the mass loss for both commercial graphite and pyrolytic graphite were predicted at the stagnation point for

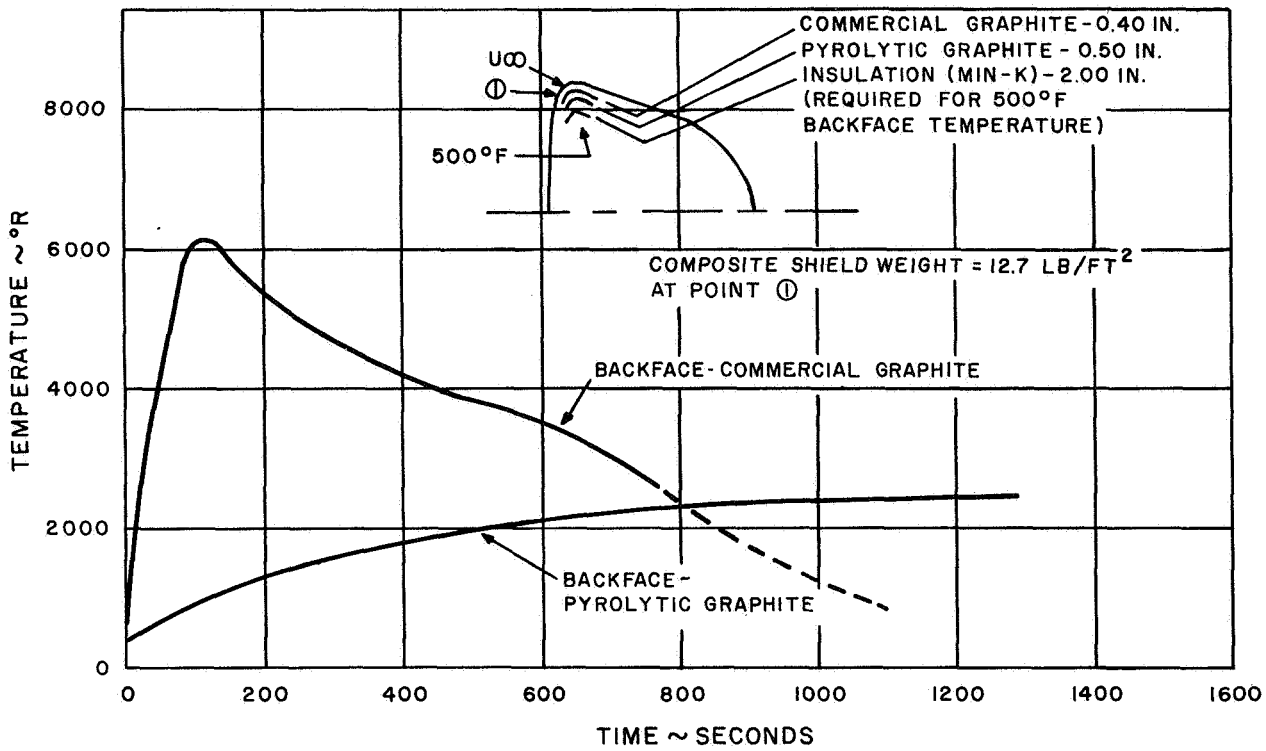

Figure II-2-44. APOLLO - D-2 Configuration, temperature vs time during re-entry, re-entry angle = 4.7 degrees

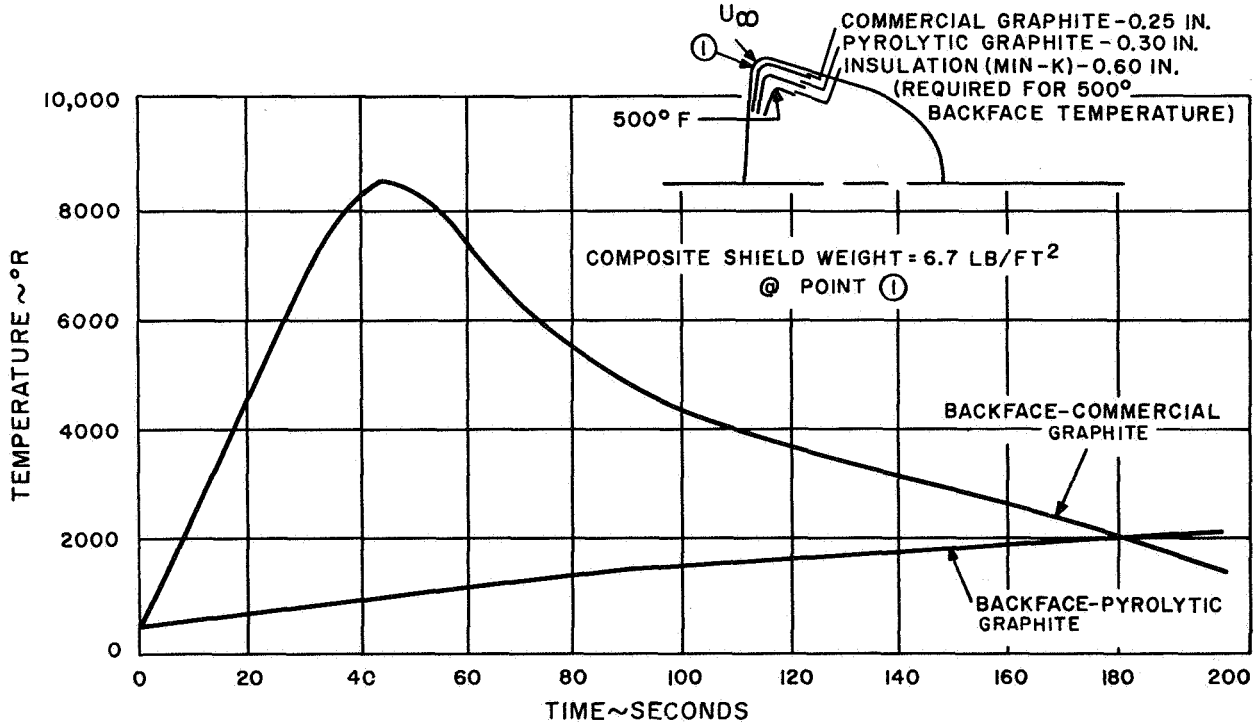

Figure II-2-45. APOLLO - D-2 Configuration, temperature vs time during re-entry, re-entry angle = 8.4 degrees

the D-2 configuration and are illustrated in Figures II-2-46, 47, 48, 49. It should be noted that the mass loss in the sublimation regime is approximately 50 percent and 80 percent of the total erosion for the 4.7 degrees and 8.4 degrees re-entry angle trajectories, respectively.

The length loss of both commercial and pyrolytic graphite at other body locations on the D-2 configuration are illustrated in Tables II-2-V and II-2-VI. The length loss of pyrolytic graphite is included to illustrate its superior oxidation characteristics. Possibly, the "state-of-the-art" for manufacturing large pieces of pyrolytic graphite will be advanced in the next few years to allow a single pyrolytic graphite shield to be fabricated. (See Appendix A-C.) The composite weight at locations other than the stagnation point will be considerably less because of the negligible erosion and low heating rates in these regions.

The inherent high emissivity, and high oxidation resistance of the graphite composite, as well as its minimum weight characteristics make it a particularly attractive heat protection system which bears further investigation. The feasibility and performance of graphite for re-entry is discussed in considerable detail in Paper number 1 of Volume XI.

TABLE II-2-V

EROSION D-2 CONFIGURATION

RE-ENTRY ANGLE = 8.4°

Station Body Position (1)	Pyrolytic (inches)	Commercial (inches)
1. Stag. pt.	0.144	0.205
2. Pt 2 Forebody	0.023	0.029
3. Pt 3 Forebody	0.023	0.029
4. Pt 4 Forebody	0.042	0.054
5. Pt 5 Forebody	0.036	0.046
6. Pt 6 Afterbody (Windward)	0.018	0.023
7. Pt 7 Afterbody (Windward)	0.011	0.014
8. Pt 8 Afterbody (Windward)	0.009	0.012
9. Pt 9 Afterbody (Windward)	0.006	0.008

(1) NOTE: Station body positions are illustrated in Figure II-2-22 of Section 2.1

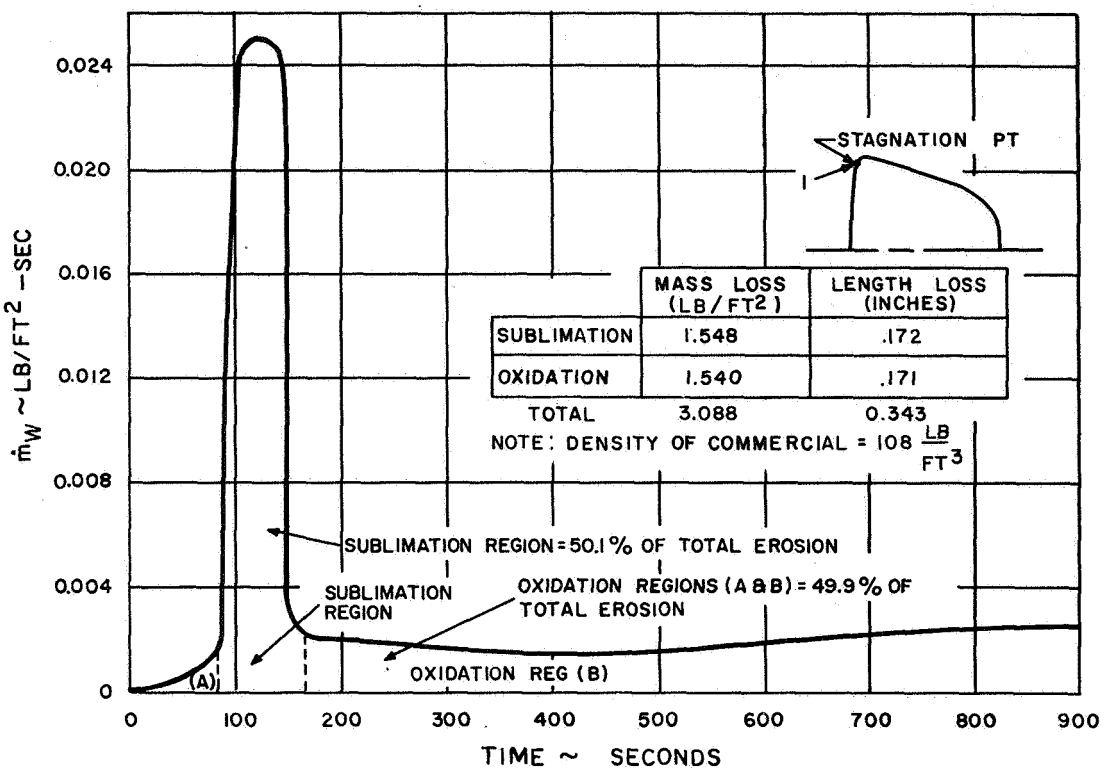

Figure II-2-46. APOLLO - D-2 Configuration, mass loss vs time during re-entry, re-entry angle = 4.7 degrees, commercial graphite

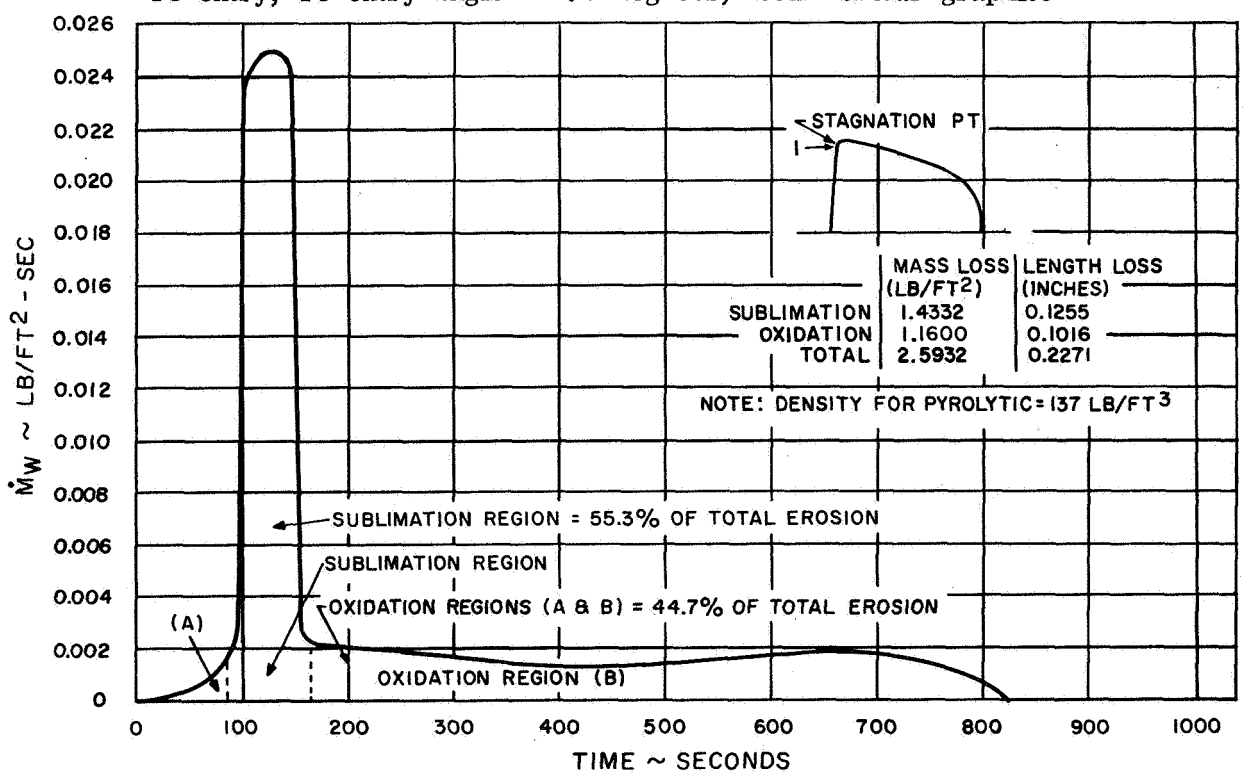

Figure II-2-47. APOLLO - D-2 Configuration, mass loss vs time during re-entry, re-entry angle = 4.7 degrees, pyrolytic graphite

CONFIDENTIAL

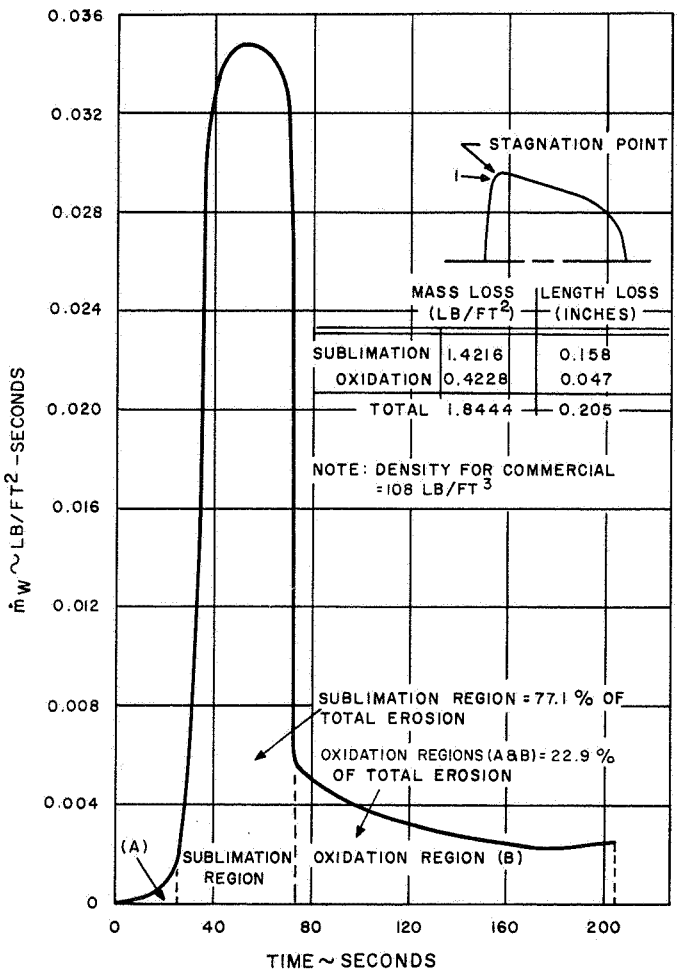

Figure II-2-48. APOLLO - D-2 Configuration, mass loss vs time during re-entry, re-entry angle = 8.4 degrees, commercial graphite

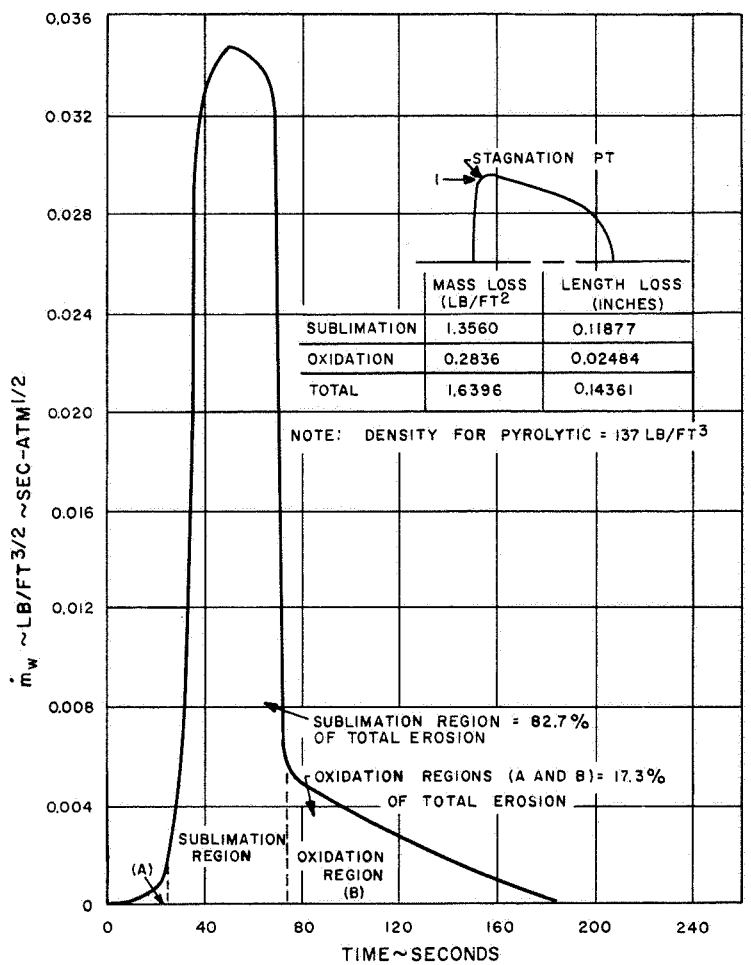

Figure II-2-49. APOLLO - D-2 Configuration, mass loss vs time during re-entry, re-entry angle = 8.4 degrees, pyrolytic graphite

CONFIDENTIAL

TABLE II-2-VI

EROSION D-2 CONFIGURATION

RE-ENTRY ANGLE = 4.7°

Station Body Position (1)	Pyrolytic (inches)	Commercial (inches)
1. Stag. Pt.	0.227	0.343
2. Pt 2 Forebody	0.042	0.054
3. Pt 3 Forebody	0.024	0.031
4. Pt 4 Forebody	0.018	0.023
5. Pt 5 Forebody	0.015	0.019
6. Pt 6 Afterbody (Windward)	0.039	0.050
7. Pt 7 Afterbody (Windward)	0.023	0.029
8. Pt 8 Afterbody (Windward)	0.018	0.023
9. Pt 9 Afterbody (Windward)	0.014	0.018

(1) NOTE: Station body positions are illustrated in Figure II-2-22 of Section 2.1

3.0 Additional Vehicle Configuration Studies

3.1 D-1 CONFIGURATION

To explore the feasibility of the integrated vehicle approach, i.e. Mission and Command Module combined, the thermal protection system for the D-1 configuration was investigated. The required shield thicknesses were estimated for the D-1 vehicle using the D-2 extreme trajectories with a constant 40 degrees angle of attack. These values, given in Table II-3-I, are based on the results obtained for the D-2 considering the similar thermal environments experienced by these vehicles. Convective and hot gas radiation heat transfer rates were corrected for the change in geometry and shock detachment standoff distances. Figure II-3-1 shows the body locations considered.

3.2 B-2 AND C-1 CONFIGURATIONS

The thermal shield requirements for the B-2 and C-1 semi-ballistic configurations were previously evaluated and the results published in the General Electric Project APOLLO Data Book, dated 14 Mar. 1961. The configurations, trajectories, and angles of attack used in the evaluation are presented in Figures II-3-2 through II-3-11. A summary of the heat protection systems is shown on Tables II-3-II and II-3-III for the C-1 and B-2 respectively.

3.3 R-3 CONFIGURATION

The R-3 configuration is described in Chapter 1 of this Volume. The methods for calculating heat transfer for the R-3 configuration are not identical to those used for the D-2 configurations. However, for the purpose of preliminary analysis they are adequate for the study conducted and give numerical results that agree reasonably well with the methods reported above.

TABLE II-3-I

APOLLO D-1

Charring-Ablative Material Required to Maintain a Maximum Back-Face Temperature of 960° R to Impact

(Thicknesses based upon an H_e = 5000 BTU/lb)

Pt.[1]	Body Location	Total Shield Thickness $\theta_E = 4.7°$	Inches $\theta_E = 8.4°$
1	Stagnation Pt.	4.23	2.50
2	Forebody	1.82	1.20
3	Forebody	1.37	1.18
4	Forebody	1.27	1.11
5	Forebody	1.20	1.00
6	Forebody	1.17	0.99
7	Afterbody (Windward)	1.75	0.99
8	Afterbody (Windward)	1.28	0.67
9	Afterbody (Windward)	1.21	0.58
10	Afterbody (Windward)	1.19	0.55
11	Afterbody (90° Meridian)	0.72	0.43
12	Afterbody (90° Meridian)	0.72	0.43
13	Afterbody (90° Meridian)	0.72	0.43
14	Afterbody (90° Meridian)	0.68	0.41
15	Afterbody (Leeward)	0.46	0.25
16	Afterbody (Leeward)	0.46	0.25
17	Afterbody (Leeward)	0.46	0.25
18	Afterbody (Leeward)	0.44	0.23
19	Afterbody (Sphere)	0.31	0.15
20	Afterbody (Sphere)	0.18	0.11
21	Afterbody (Sphere)	0.11	0.06
22	Afterbody (Sphere)	0.18	0.11

[1] Point locations are shown in Figure II-3-I

CONFIDENTIAL

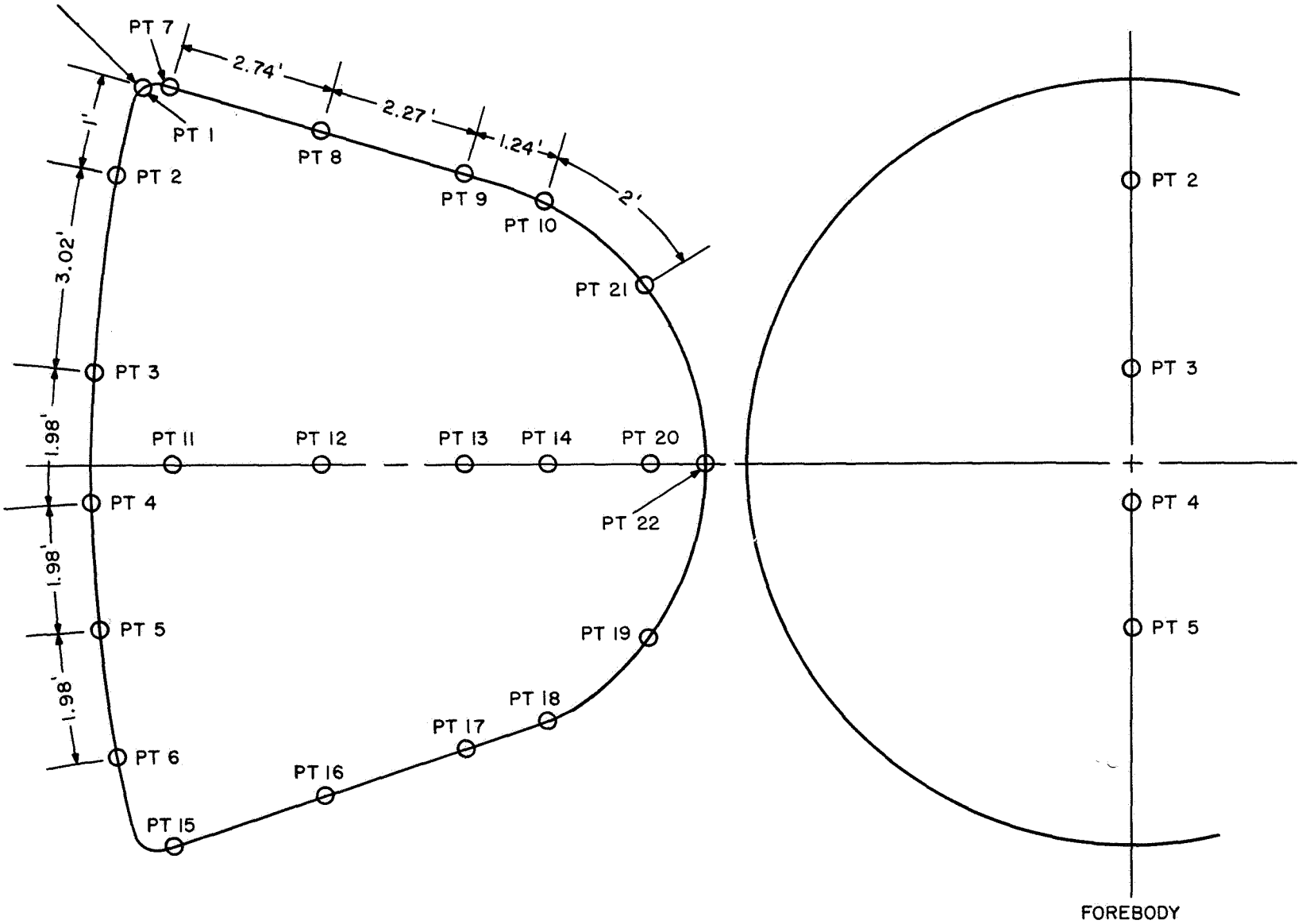

Figure II-3-1. APOLLO - D-1 Configuration, body locations studied

CONFIDENTIAL

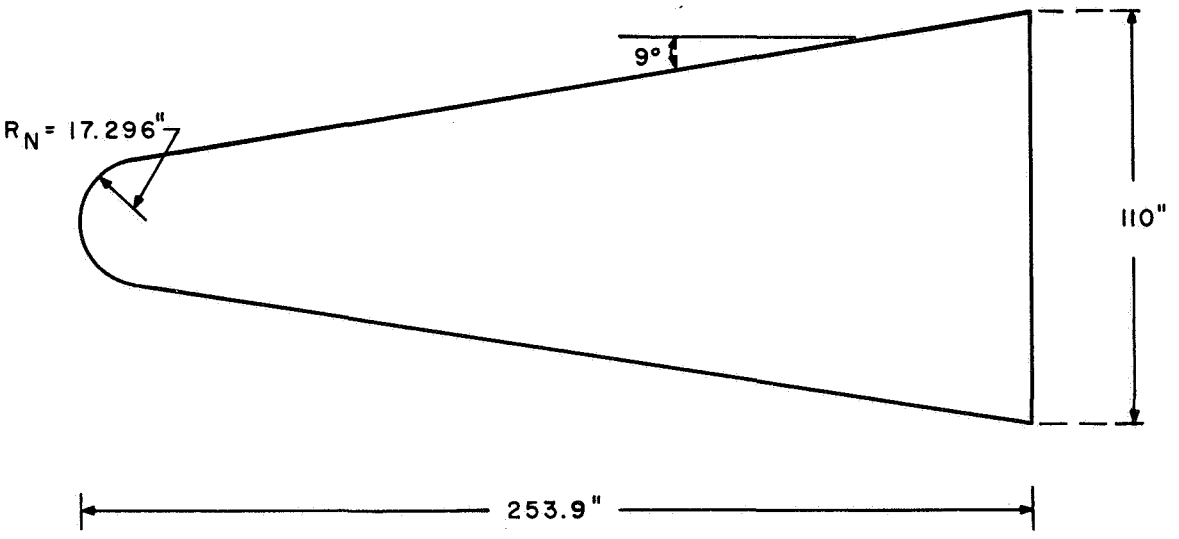

Figure II-3-2. APOLLO - C-1 Configuration, re-entry configuration

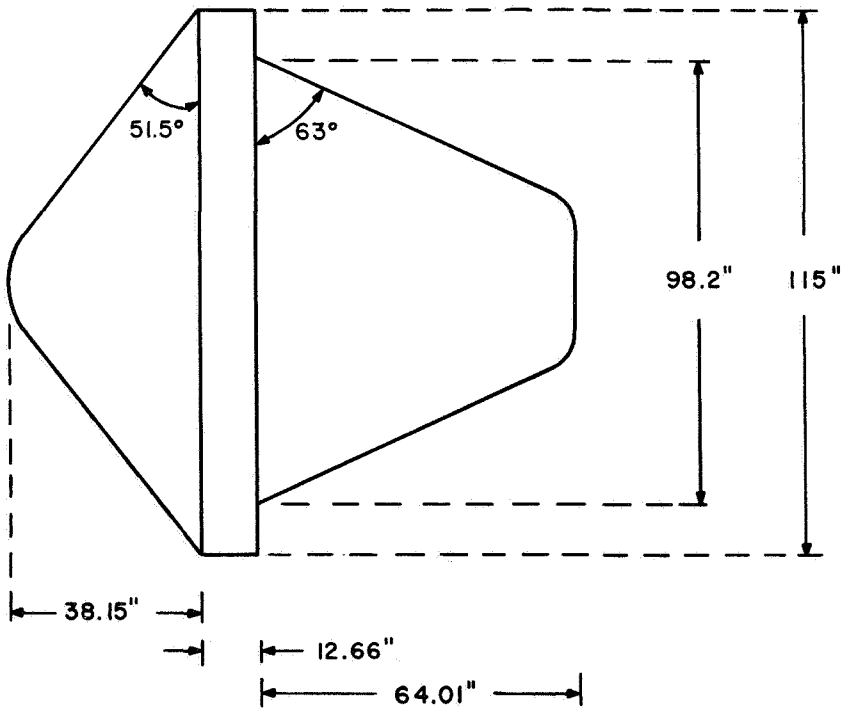

Figure II-3-3. APOLLO - B-2 Configuration, re-entry configuration

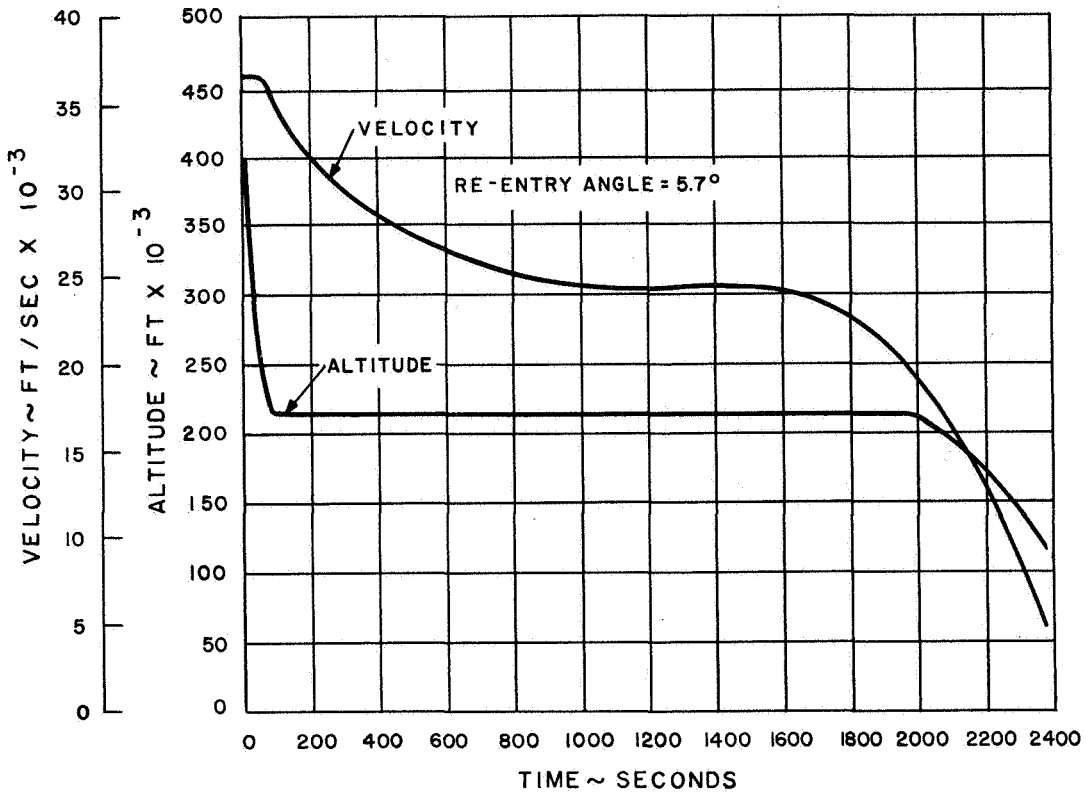

Figure II-3-4. APOLLO - C-1 Configuration, re-entry trajectory

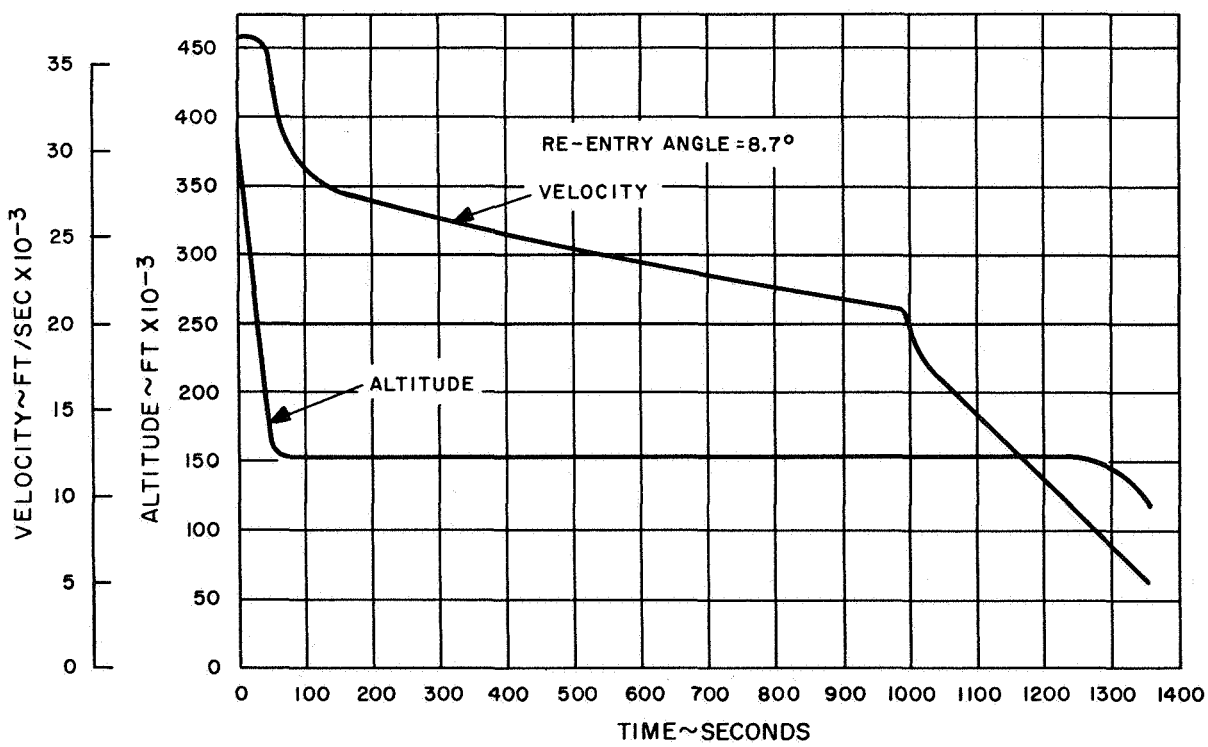

Figure II-3-5. APOLLO - C-1 Configuration, re-entry trajectory

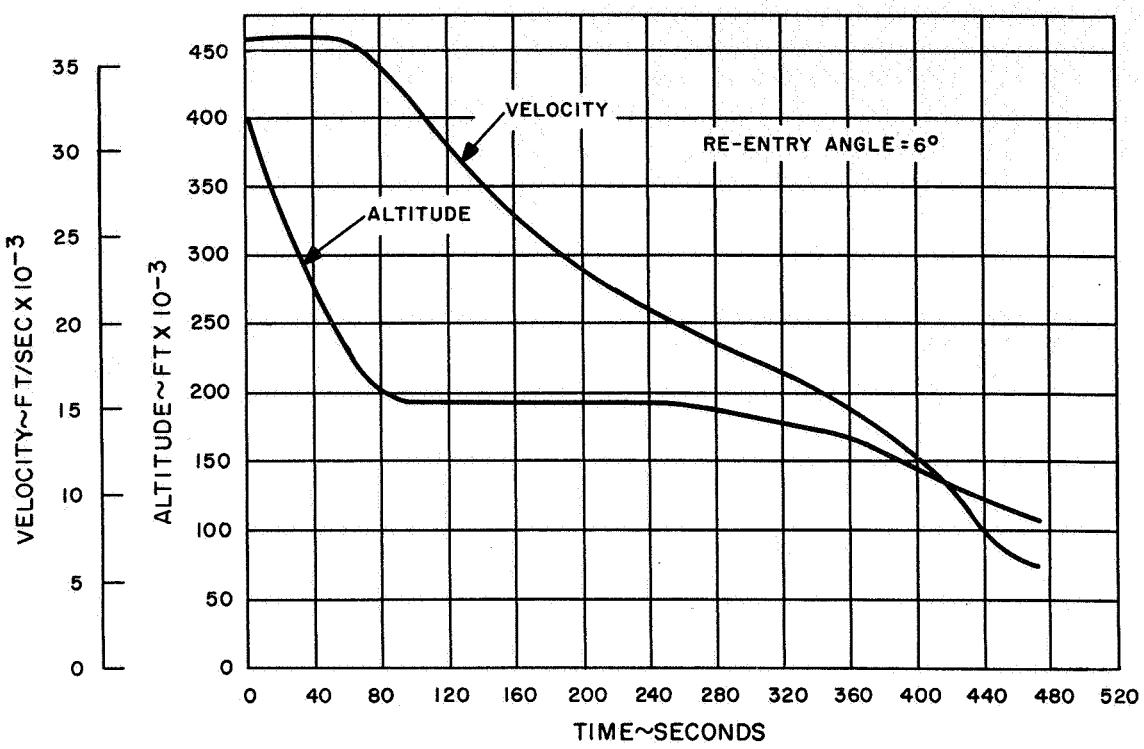

Figure II-3-6. APOLLO - B-2 Configuration, re-entry trajectory

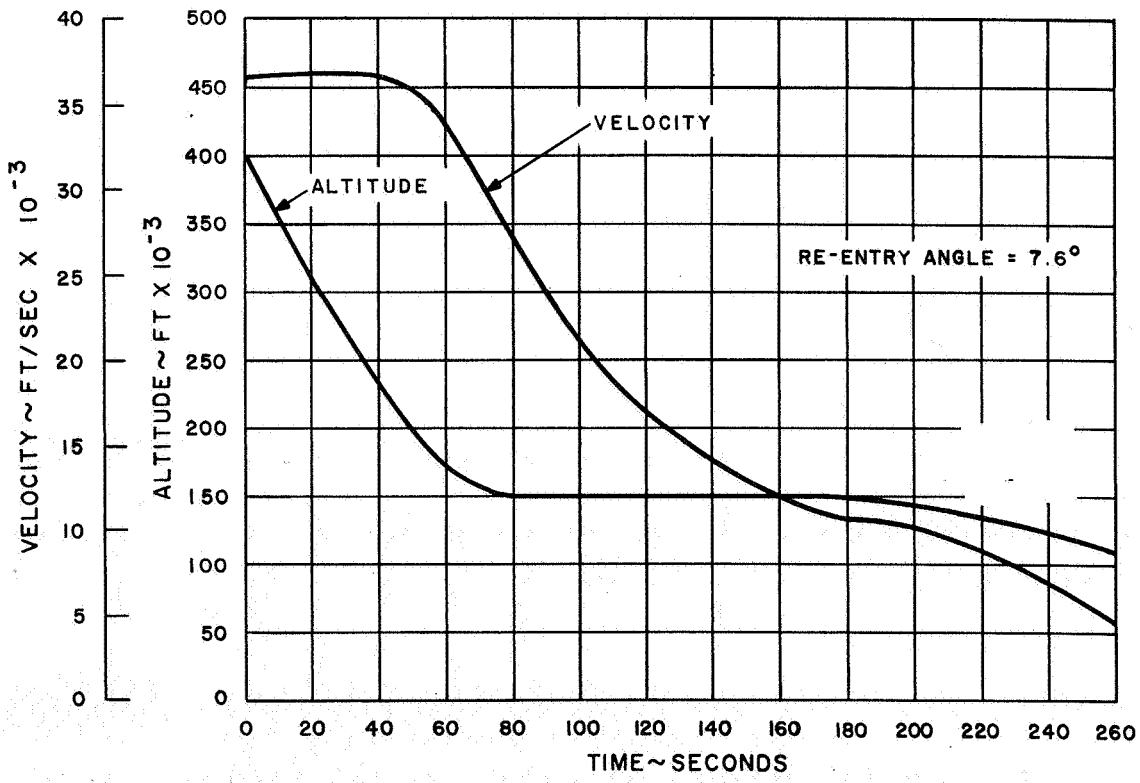

Figure II-3-7. APOLLO - B-2 Configuration, re-entry trajectory

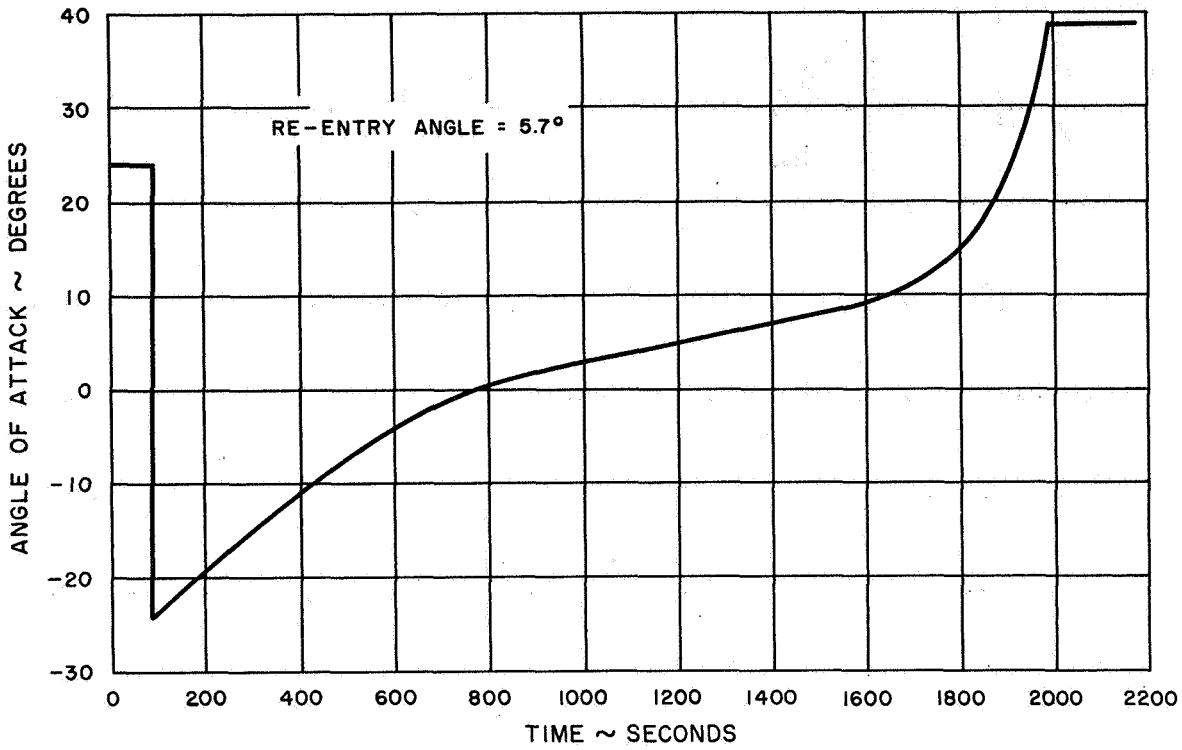

Figure II-3-8. APOLLO - C-1 Configuration, angle of attack vs time

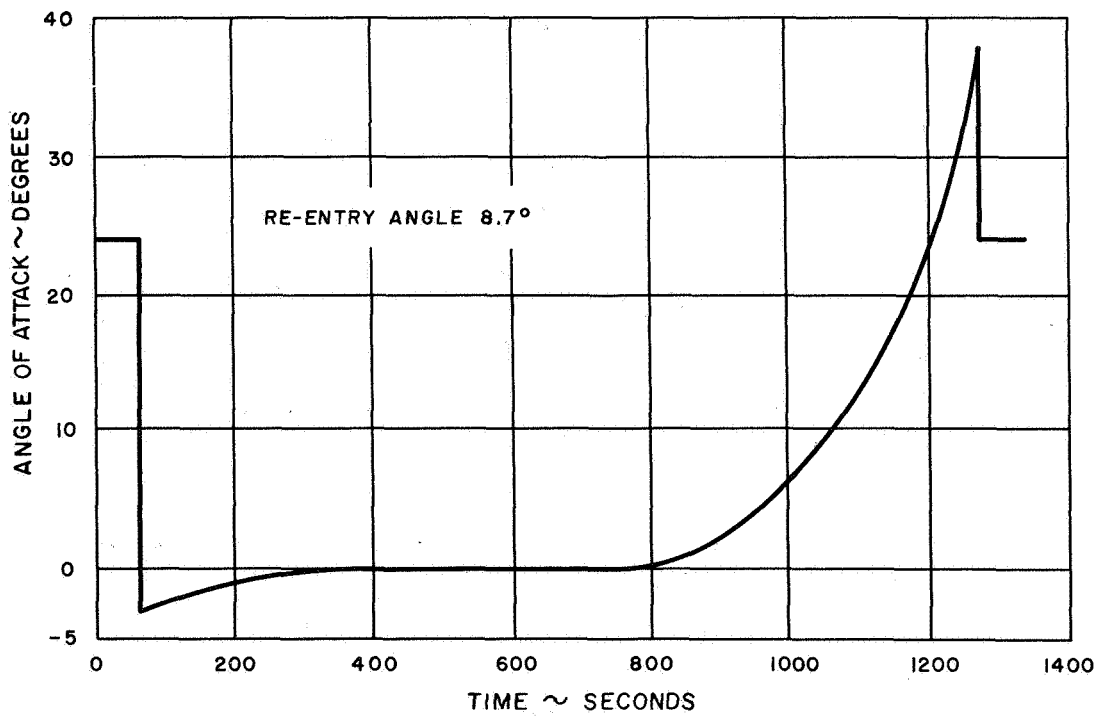

Figure II-3-9. APOLLO - C-1 Configuration, angle of attack vs time

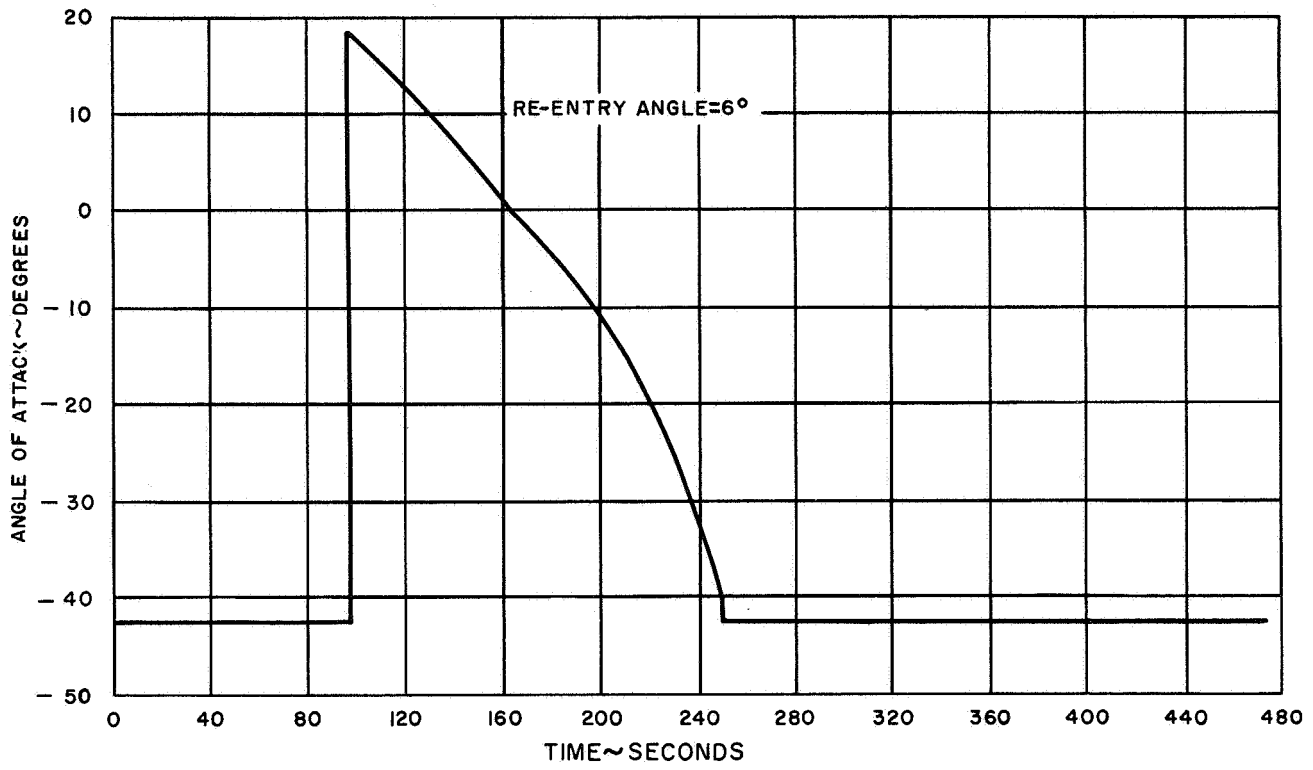

Figure II-3-10. APOLLO - B-2 Configuration, angle of attack vs time

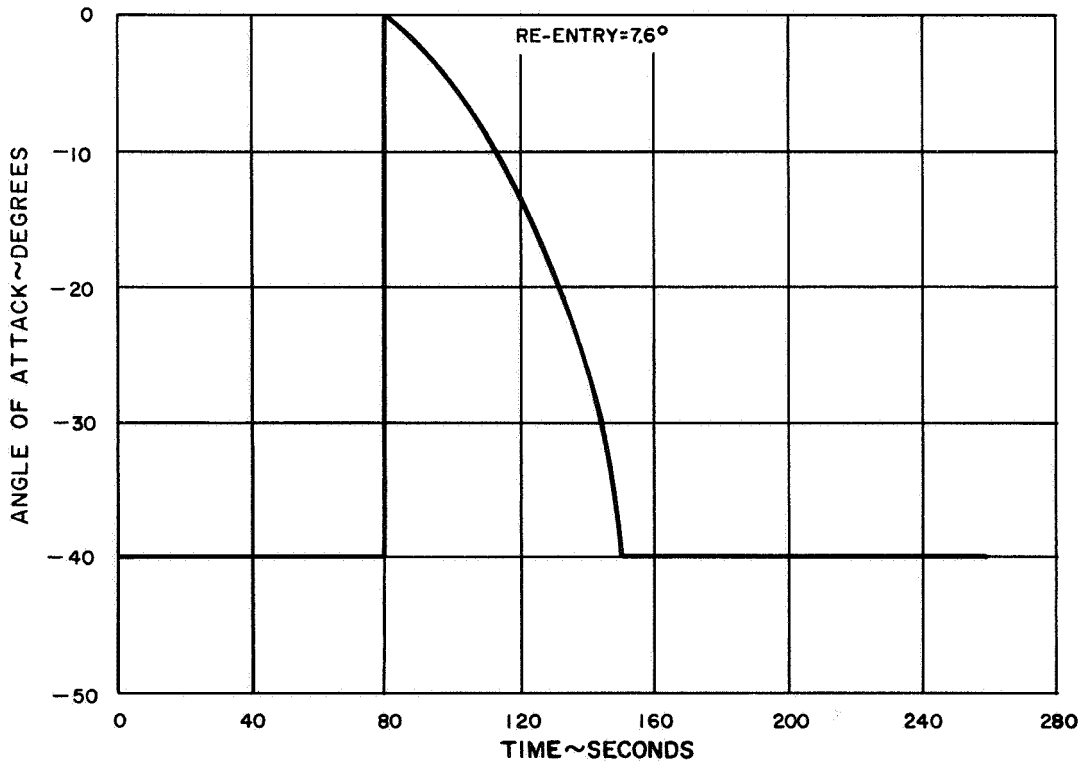

Figure II-3-11. APOLLO - B-2 Configuration, angle of attack vs time

TABLE II-3-II

HEAT PROTECTION FOR C-1 CONFIGURATION

	Station	Reinforced Plastic Shield Thicknesses Req'd to Maintain* 960°R Back Face					
		Windward (0°)		Between W & L (90°)		Leeward (180°)	
		Amt. Ablated + Char	Insula-tion	Amt. Ablated + Char	Insula-tion	Amt. Ablated + Char	Insula-tion
$\theta_E = 5.7°$	0'	---	---	---	---	---	---
	1.216"	2.72"	0.55"	1.63"	0.71"	0.77"	0.81"
	7.199"	1.30"	0.69"	0.66"	0.82"	0.32"	0.96"
	21.158"	0.80"	0.80"	0.34"	0.94"	0.18"	1.05"
$\theta_E = 8.7°$	0'	---	---	---	---	---	---
	1.216'	2.82"	0.49"	2.30"	0.50"	2.04"	0.51"
	7.199'	1.92"	0.50"	1.36"	0.51"	1.08"	0.53"
	21.158'	1.54"	0.51"	1.12"	0.53"	0.90"	0.56"

*At impact

CONFIDENTIAL

CONFIDENTIAL

CONFIDENTIAL

TABLE II-3-II

HEAT PROTECTION FOR C-1 CONFIGURATION (Continued)

	Station	Amount Oxidized	Graphite Insulation Commercial	Graphite Insulation Pyrolytic	Low Density
$\theta_E = 5.7°$	0'	0.41"	0.19"	0.2"	7"
	1.216'	0.12"	0.13"	0.15"	7"
	7.199'	0.07"	0.12"	0.1"	7"
	21.158'	0.05"	0.14"	0.1"	7"
$\theta_E = 8.7°$	0'	0.55"	0.20"	0.2"	5"
	1.216'	0.15"	0.15"	0.15"	5"
	7.199'	0.11"	0.08"	0.1"	5"
	21.158'	0.08"	0.11"	0.1"	5"

TABLE II-3-III

HEAT PROTECTION FOR B-2' CONFIGURATION

	Section	Graphite Commercial	Graphite Pyrolytic	Low Density Ins.	Reinforced Plastic
$\theta_E = 6.0°$	Entire Forebody	0.19"	0.05"	3.6"	1.4"
	Cylinder	0.19"	0.05"	3.6"	0.6"
		Reinforced Plastic	Columbium	Low Density Ins.	
	Afterbody	0.15"	Min. Thick.	3.6"	0.5"

CONFIDENTIAL

TABLE II-3-III

HEAT PROTECTION FOR B-2 CONFIGURATION (Continued)

	Section	Graphite		Low Density Ins.	Reinforced Plastic
		Commercial	Pyrolytic		
$\theta_E = 7.6°$	Entire Forebody	0.19"	0.05"	2.8"	1.3"
	Cylinder	0.19"	0.05"	2.8"	0.6"
		Reinforced Plastic	Columbium	Low Density Ins.	
	Afterbody	0.15"	Min. Thick.	2.8"	0.5"

CONFIDENTIAL

CONFIDENTIAL

3.3.1 Method of Analysis

1) Basic Relations

Approximate relations for the convective heating to the nose and flat plate bottom surface of an entry vehicle, which can be evaluated simultaneously with the entry trajectory computations on the high speed digital computer, have been established. These are simplified curve fits (by AVCO and Bell Aerosystems) to the relatively well established analytical methods.

The stagnation-heat convection equation may be used for the nose cap or can be modified to be used for the bottom surface if the vehicle is at high angle of attack.

The flat plate heat convection relations that are of primary concern are those associated with turbulent flow because at the initial pullout where maximum heating occurs, the Reynolds numbers are reasonably high. The laminar representation is given only for completeness. The relationships presented are reasonably accurate in the range of α from 0 to 30. Beyond that, there is considerable outflow and the bottom surface begins to behave as a flat-faced nose of large diameter.

(a) Stagnation Region Convective Heating

The heat flux to the nose of a body of revolution has been determined using the following equation:

$$\dot{q}\ \dot{R} = \sqrt{17,600}\ \sqrt{\rho/\rho_o}\left(V/V_c\right)^{3.15}\left[\frac{h_s - h_w}{h_s - h_w = 500\ R}\right]\frac{Btu}{ft^{1.5}sec}$$

(b) Flat Plate Convective Heating

The following is a discussion of the curve fit approximation that has been made of the Reference Temperature method for determining heating rate to the bottom surface. It is based on Bell Aircraft Report 7006-3352-001 and curve fitting by Blessing and Schmidt. Although this analysis is based upon ideal gas relations, the heat flux is estimated rather well in spite of the fact that the recovery temperature and heat transfer coefficients are not well represented. Particularly, the resulting formulation of heat flux as a function of V_∞, p_∞, α, and x is felt to be adequate up to $V_\infty \approx 25,000$/sec. As will be pointed out later, the vehicle is not expected to be flown at low altitudes at super-orbital velocities so that an extension of moderate wedge angle methods to extreme velocities does not appear to be required.

For laminar flow, the process is rather straightforward because:

$$\dot{q}_{conv} = h\ (T_r - T_w)$$

where

$$h = \frac{.00963\ (P_\delta\ V_\delta)^{0.5}}{(T')^{.904}\ x^{0.5}}$$

and T_r is proportional to V^2.

Therefore at high velocity where $T_r \gg T_w$

$$\dot{q}_{conv} = C_1\ P_\delta^{0.5}\ V_\delta^{2.5} = C_1\ P_\infty^{0.5}\ V_\infty^{2.5}\ f\ (M, \alpha)$$

because $(T')^{.04}$ is nearly constant over a wide range of M and α by virtue of the small exponent.

For turbulent flow, the curve fitting is not so straightforward because:

$$q_{conv} = h\ (T_r - T_w)$$

and

$$h = \frac{.0334\ (P_\delta\ V_\delta)^{0.8}}{(T')^{.576}\ x^{.2}}$$

Since the T', which is of the form

$$T' = 1/2\ (T_w + T_\delta) + .22\ r\ (T_o - T_w)$$

is raised to a significant power, it is necessary to consider its variation with α and M. Therefore, to formulate an analytic expression for $\dot{q}_{conv}$ (turbulent flow) the following was postulated:

$$\dot{q} = \dot{q}_{\alpha = o} \cdot f_1(\alpha,\ M)$$

where

$$\dot{q}_{\alpha = o} = g\ (P_\infty,\ V_\infty,\ x) = \frac{C_1}{x^{.2}}\ V_\infty^{\ a}\ P_\infty^{\ b}$$

Through judicious curve fitting procedures, it was found that $\dot{q}_{\alpha = o}$ could be represented as

$$\dot{q}_{\alpha = o} = .00032\ V^{1.735}\ P^{.8}$$

for an x = 10 ft. In general it would be

$$\dot{q}_{\alpha} = o, \; x = \frac{.000507}{x^{.2}} V^{1.735} P^{.8}$$

It can be seen immediately that the exponent on pressure should be 0.8. The velocity exponent would be 1.648 if the T' were simply a velocity squared term; however, it is not, therefore there was a minor adjustment in the exponent and coefficient to provide a better approximation.

The function f_1 (α, M) was developed with good correlation because the heat flux is based on local flow conditions which can be expressed well as a power of Mach number and polynominal in α.

The results of considerable correlation efforts can be stated as follows:

$$f_1 (\alpha, M) = 1 + f_2 (\alpha) M^{1.732}$$

The function f_2 (α) can be represented by the following cubic

$$f_2 (\alpha) = .00274333 \alpha + .0003615 \alpha^2 - .0000067833 \alpha^3$$

This was found to correlate results very well for $0 \leq \alpha \leq 30$ degrees and $15 \leq M \leq 35$. Therefore, the heat flux to an element on h, the compression side of a flat bottomed vehicle, can be represented as

$$\dot{q} (\alpha, x, V, h) = \frac{.000507}{X^{.2}} V_{\infty}^{1.735} P_{\infty}^{0.8} \left[1 + (.0027433 \alpha + .0003615 \alpha^2 - .0000067833 \alpha^3) M^{1.732}\right]$$

where M, of course, could be replaced by $\frac{V_{\infty}}{a}$.

This appears to be a rather complicated function but with the use of high speed digital computation, the solution of this equation is very simple and can be calculated simultaneously with the computation of a trajectory. This has been done by this contractor. Also, it is very simple to either integrate this heat flux over the flight path and/or determine the radiation equilibrium temperature.

The units for $\dot{q}$ in the relations for the flat plate are BTU/ft^2 hr.

2) Geometry and Distribution Considerations

To determine the heat load to the bottom surface of the R-3 vehicle during flight at very high angles of attack, one may consider the vehicle as a flat disc and apply the methods such as have been forwarded by Stoney, Ref. 1*, Lees, Ref. 2, Stine and Wanlass, etc. Figure II-3-12 illustrates the heat flux over a circular flat face as compared to the heat flux to the stagnation point of a sphere of similar radius. This curve was obtained using the method of Lees, basing the transport properties upon the Reference Temperature of Eckert. It is seen to be very similar to that illustrated in Ref. 1.

This curve indicates that the average heat flux to a flat face is appreciably less than that for the stagnation point of a sphere, in fact, 0.6 of it. However, one must bear in mind that this is applicable only for laminar flow and that for a vehicle which has approximately an 11-foot diameter, the chances of triggering transition on the front face would appear to be good. This is particularly so for recovery from steep entry angles which inevitably forces the vehicle to plunge rather deeply into the atmosphere before first perigee is reached.

Figure II-3-13 illustrates the turbulent flow heat flux per unit area on a flat face ratioed to that which would occur at the stagnation point of an 11 foot diameter sphere using the integral method of Bromberg, Fox and Ackerman, Ref. 3, again with the fluid properties evaluated at the Reference or T' temperature.

As is well known, the method breaks down near the center of the disc, giving a value of zero at the center. As the Reynolds number increases, i.e., the altitude decreases, the ratio of turbulent-flow heat flux to laminar stagnation heat flux increases as one would expect. The dashed line that has been superimposed upon this carpet represents the locus of points where turbulent and laminar flow heating are identical. Anywhere below this line, the laminar flow method predicts higher heating rates. For this particular diameter of vehicle, using the aforementioned methods, no consideration of turbulent flow need be made above 238,000 feet altitude. However, at lower altitudes, the possibility of having turbulent flow must be considered. In fact, to demonstrate this more clearly, Figure II-3-14 illustrates a composite of this picture. The ordinate is the ratio of average flat-face heat flux to the stagnation point of a hemisphere, laminar flow.

* References will be found at the end of Section 3.3.3

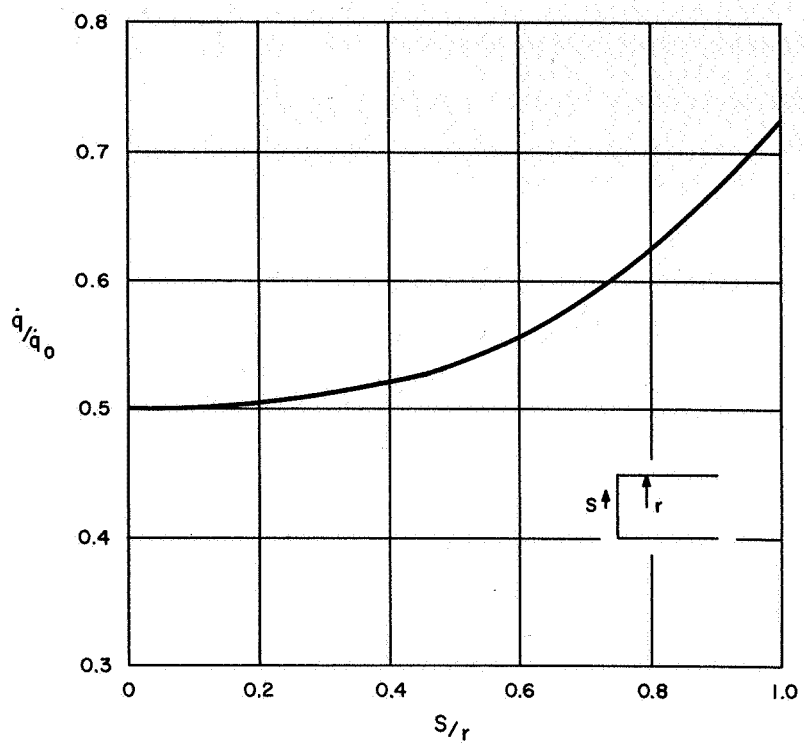

Figure II-3-12. APOLLO - R-3 Configuration, flat face heat flux distribution, laminar flow

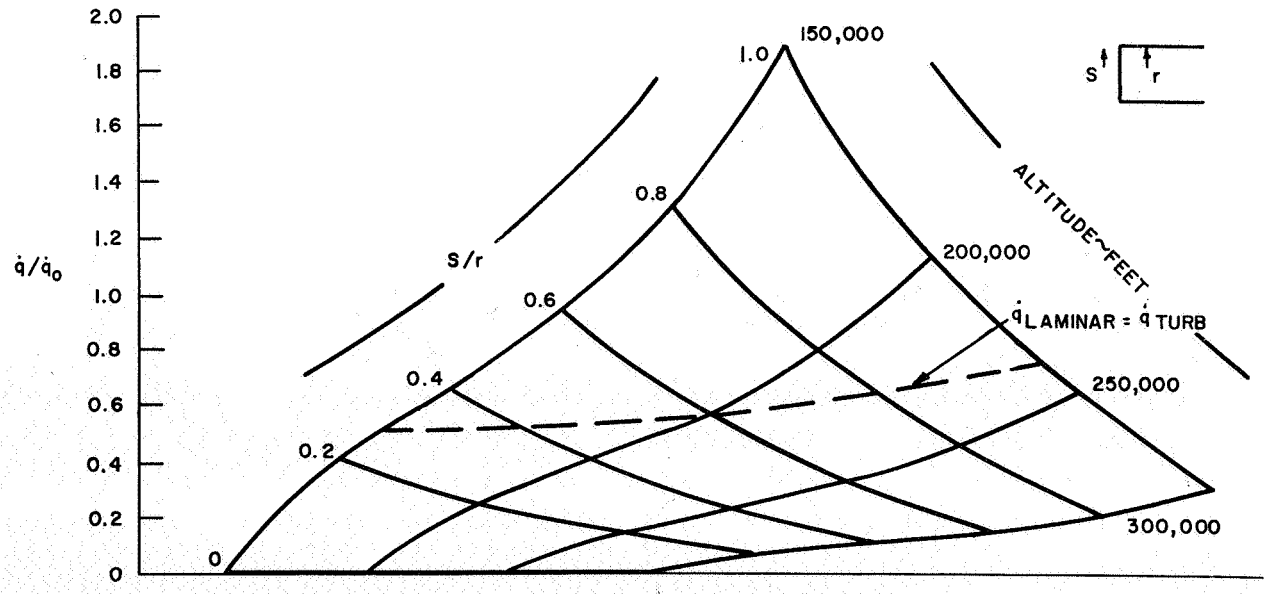

Figure II-3-13. APOLLO - R-3 Configuration, flat face heat flux distribution, turbulent flow

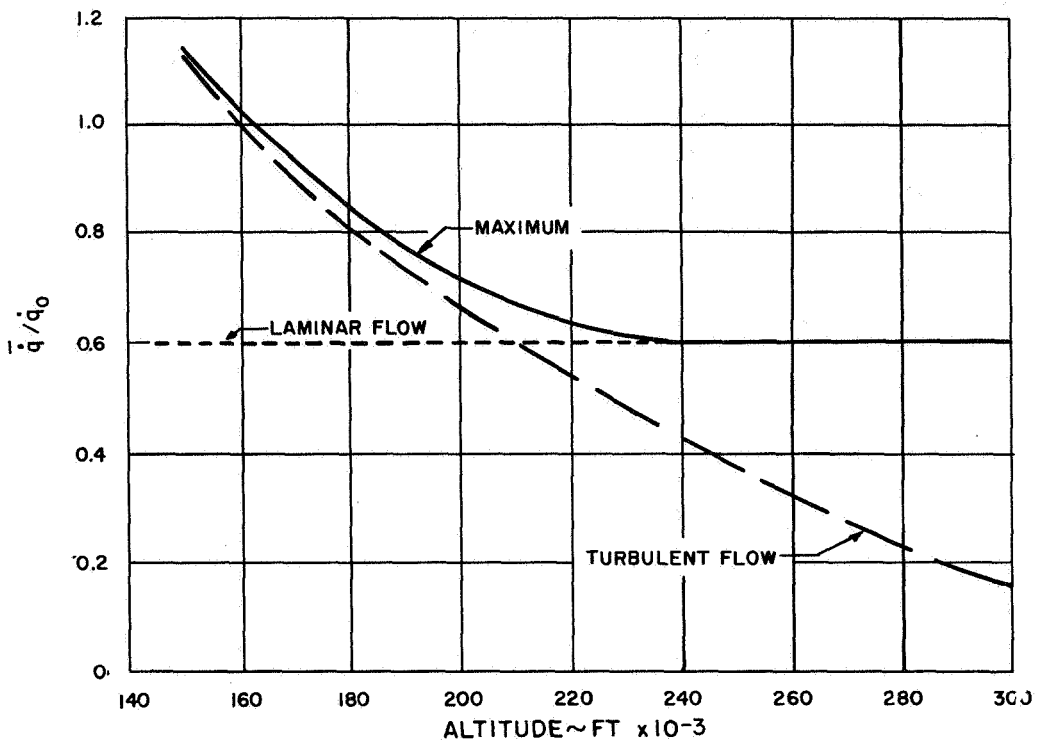

Figure II-3-14. APOLLO - R-3 Configuration, average flat face heat flux distribution

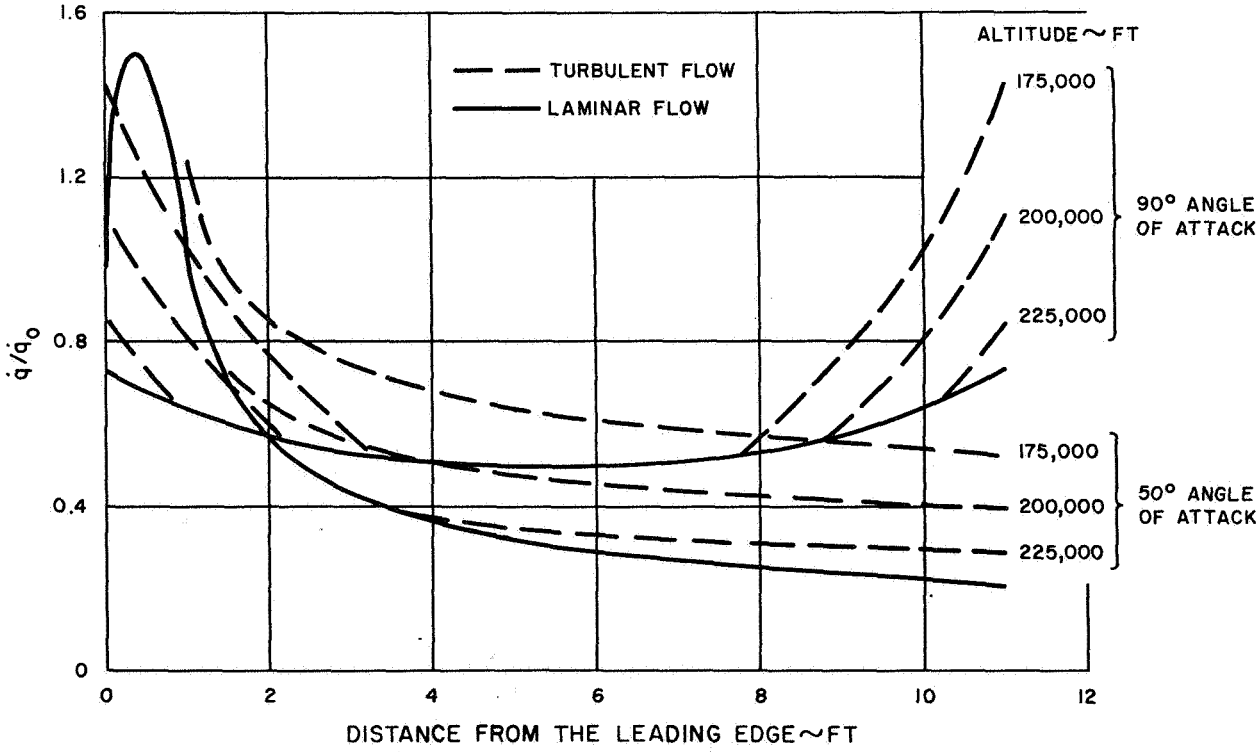

Figure II-3-15. APOLLO - R-3 Configuration, heat flux rate to the bottom surface referenced to A 5.5' radius sphere

As stated before, the average, using laminar flow, is altitude invariant and is shown as having a value of 0.6. All turbulent flow theory gives a rapidly increasing ratio of the heat flux with decreasing altitude. The envelope of maximum average heat flux to the disc is shown by the solid line which is coincident with the laminar-flow curve above 238,000 ft and becomes asymtotic to the turbulent-flow curve at low altitudes. This work has been done assuming M_∞ is infinite. However, by examining the effect of M_∞ on the ratio of both laminar and turbulent heat flux to the heat flux at the stagnation point of a sphere, it can be shown that the ratios are nearly invariant for M_∞ greater than 12.

As will be discussed later and also in the Structures Section thermal protection systems, the value of $\bar{\dot{q}}/\dot{q}_0$ that was used for the current investigation to obtain system weights, was 0.7. This would appear to be conservative because the flights near the skip limit are the ones that are most taxing to the thermal protection system due to the protracted "in atmosphere" flying time at moderate heating intensities. Perigee is reached at approximately 250,000 ft for this case. Near the "g" limit on entry, the perigee is lower, approximately 200,000 ft; however, decelerations are so rapid for these flights that the total convective heating is not as great.

It is felt that the above curves are representative for the lenticular design at angles of attack from 75 degrees to 90 degrees. Additional testing must be done to verify and to expand this knowledge to angles of attack as low as 50 degrees.

Estimates of the bottom surface heat flux distribution at 50 degrees angle of attack have been estimated using Lees method for laminar flow and assuming the flat plate relations are valid for the turbulent flow regions. Pertinent to these estimates, it was postulated, based on the work of Stoney, Ref. 1, that the heat flux to the leading edge over the angle of attack range would vary as a cosine function between that for leading edge radius stagnation heating at zero angle of attack and that at the edge of a flat face 90 degrees to the flow, so that the value of $\bar{\dot{q}}/\dot{q}_0$ was chosen to vary from 1.94 at $\alpha = 0$ to .725 at $\alpha = 90°$. It is possible then to assume that the nose or leading edge of the vehicle may be replaced by a fictitious spherical nose of appropriate radius for all intermediate angles of attack. These radii were also used to compute gas cap radiation at the leading edge.

The convective heat flux along the bottom center-line is shown in Figure II-3-15. The solid lines indicate all laminar flow for both $\alpha = 50°$ and $90°$. These curves are

invariant with altitude as discussed earlier. The dashed lines represent turbulent flow heating which are of course altitude dependent. From this, it can be seen that for the R-3 vehicle flying at $\alpha = 50°$, the heating rate is higher in the region of the leading edge but that the average heat flux to the bottom surface is less than the average $\bar{\dot{q}}/\dot{q}_o$ of 0.7 which has been chosen for the comparisons that will be discussed subsequently.

3) Gas Cap Radiation

An investigation of the additional heating that might be experienced in the stagnation region of the vehicle due to gas cap radiation has been made. From Kivel's work, Ref. 5, Figure II-3-16 was constructed based on a 5.5 feet radius sphere. Superimposed on these curves are typical entry paths spanning the width of entry corridor. It can be seen that according to this work the radiation becomes particularly significant for the nominal and steep re-entries.

These estimates are for equilibrium conditions in the radiating gas cap layer. The intensity of radiation from a non-equilibrium layer has been variously theorized to be as much as an order of magnitude greater than the equilibrium radiation. Much testing is required in order to ascertain the real magnitude and the best means of designing for it. The choice of entry path may be restricted to a narrow band near the skip limit and it may be distinctly advantageous to reconsider the vehicle configuration based on the results of such research work. For example, a sharper nosed vehicle with a smaller wing loading that can enter from a shallower entry angle may become more appropriate. The class of heat protection materials that will be sought will be those that are good reflectors of the radiant energy emanating from the gas cap. These may or may not be related to the current ablation materials. This is a broad problem area that must be given top priority to assure a successful solution.

3.3.2 Heat Flux to the Lenticular Vehicle

The remainder of this discussion pertains to the amount of heat flux and the heat flux rate to the vehicle surface assuming that the surface is cold. In the suborbital portion of the flight, equilibrium temperatures are also enumerated.

A time history of heat flux for the steepest entry has been constructed. Figure II-3-17 illustrates the heat flux and heat flux rate to the bottom surface of the vehicle for this flight path if the vehicle were oriented at 90 degree angle of attack.

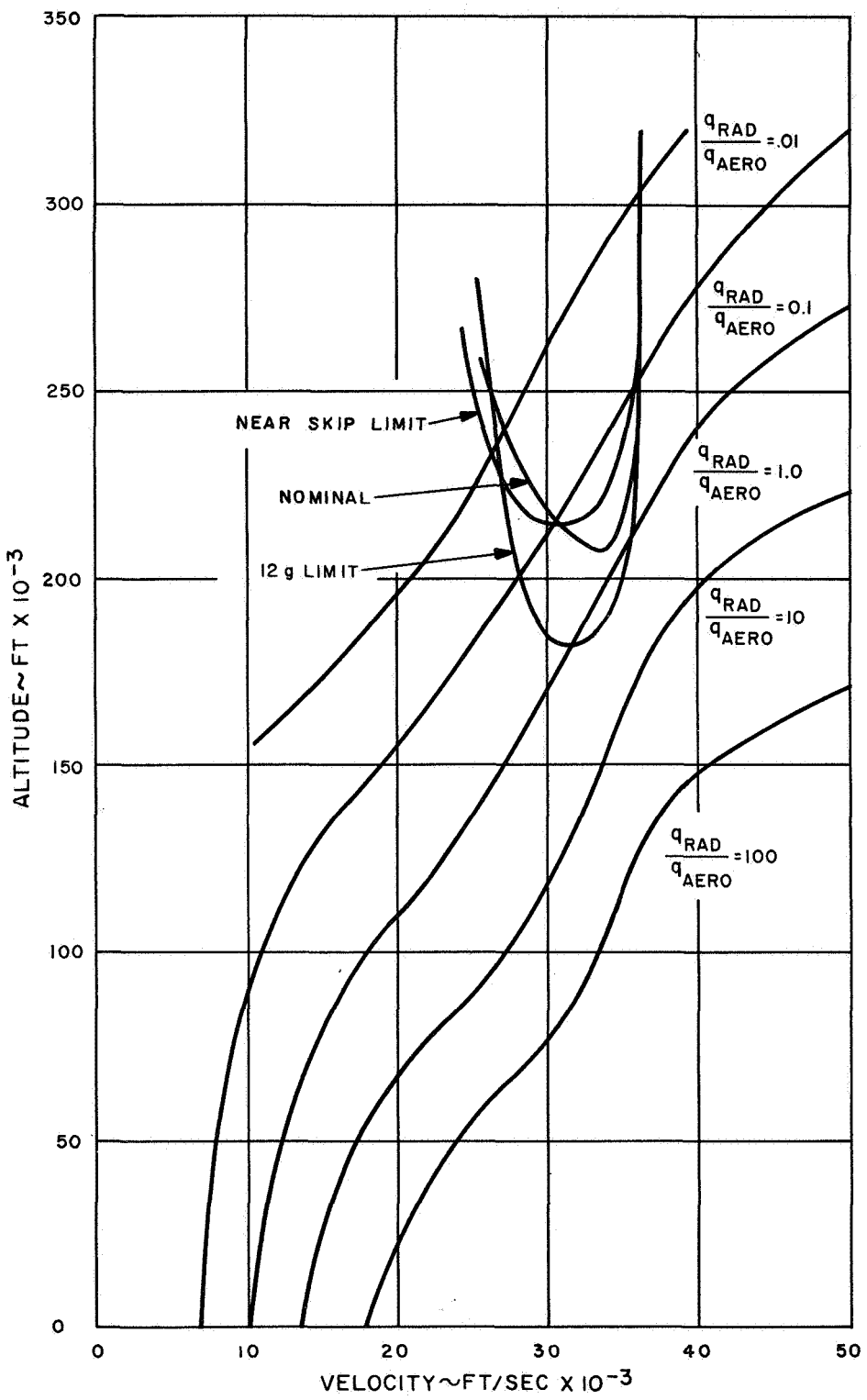

Figure II-3-16. APOLLO - R-3 Configuration, nose cap radiation intensity and typical entry trajectories

CONFIDENTIAL

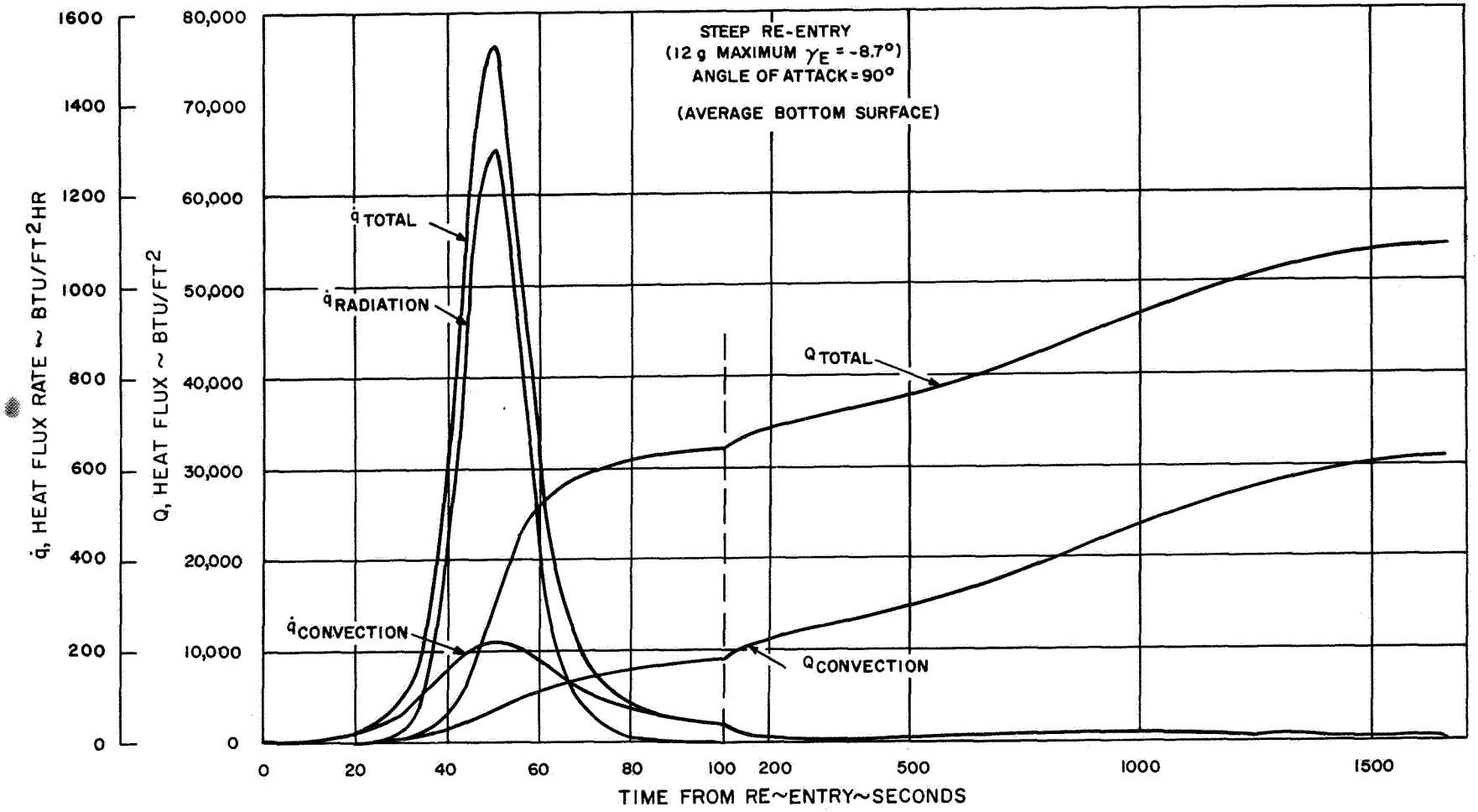

Figure II-3-17. APOLLO - R-3 Configuration, time histories of heat flux and heat flux rate

CONFIDENTIAL

These are average values over the bottom surface. It can be readily seen that for a steep entry such as this, and for a large rather flat bottomed vehicle that is at or near $\alpha = 90°$, the gas cap radiation may be the major contributor to the maximum heat flux rate and accounts for nearly half of the total flux. If the thermal protection system relies upon a radiation equilibrium scheme, once the heat flux rate is less than 30 Btu/sq ft hr, (approximately the capability of coated molybdenum,) then the total flux for this flight would be about 33,000 Btu/sq ft of which only 1/3 is by convection. Furthermore, if as was stated earlier the non-equilibrium radiation is much greater, consideration must be given to further restrict the steepness of the entry path and to reduce the effective nose diameter to reduce the shock stand-off distance.

Figure II-3-18 is presented to illustrate a point concerning the extreme opposite limit, $\alpha = 0°$, from that of Figure II-3-17. Although neither of these cases are representative of the actual flight condition which has been used to calculate the flight path in question, they serve to provide bounds to the problem. It may be noted, as one would expect, that for such a hypothetical case as this, the convective heat flux rate is much higher than it was for the previous flat face case and also is large compared to the gas cap radiation because of the small standoff distance. Interestingly enough, however, the total heat flux rate for this case is significantly less than for the previous one. However, the convective heating remains at a sufficiently high rate that if such a flight could be flown with the vehicle oriented in this manner the total flux over the leading edge area would be large compared with the average value over the bottom surface mentioned previously, i.e., 84,000 vs 33,000 Btu/sq ft. Of course the applicable area is local rather than total.

The next series of Figures, II-3-19 to II-3-21 are summary curves of heat flux and heat flux rate for three typical flights. The first has already been discussed as a time history. These figures illustrate maximum heat flux rate, (dashed curves) that would be encountered by each of these flights if the vehicle were oriented at any angle. This would be possible if for some reason the vehicle inadvertently assumed an angle of attack that was not expected. The maximum convective heating to the leading edge of course decreases with increasing α, the gas cap radiation increases. The maximum total rate remains relatively constant but does increase significantly near 90 degrees for the steep entry where the gas cap radiation is rather overpowering. The integrated heat fluxes are also illustrated, however, they are only directly

CONFIDENTIAL

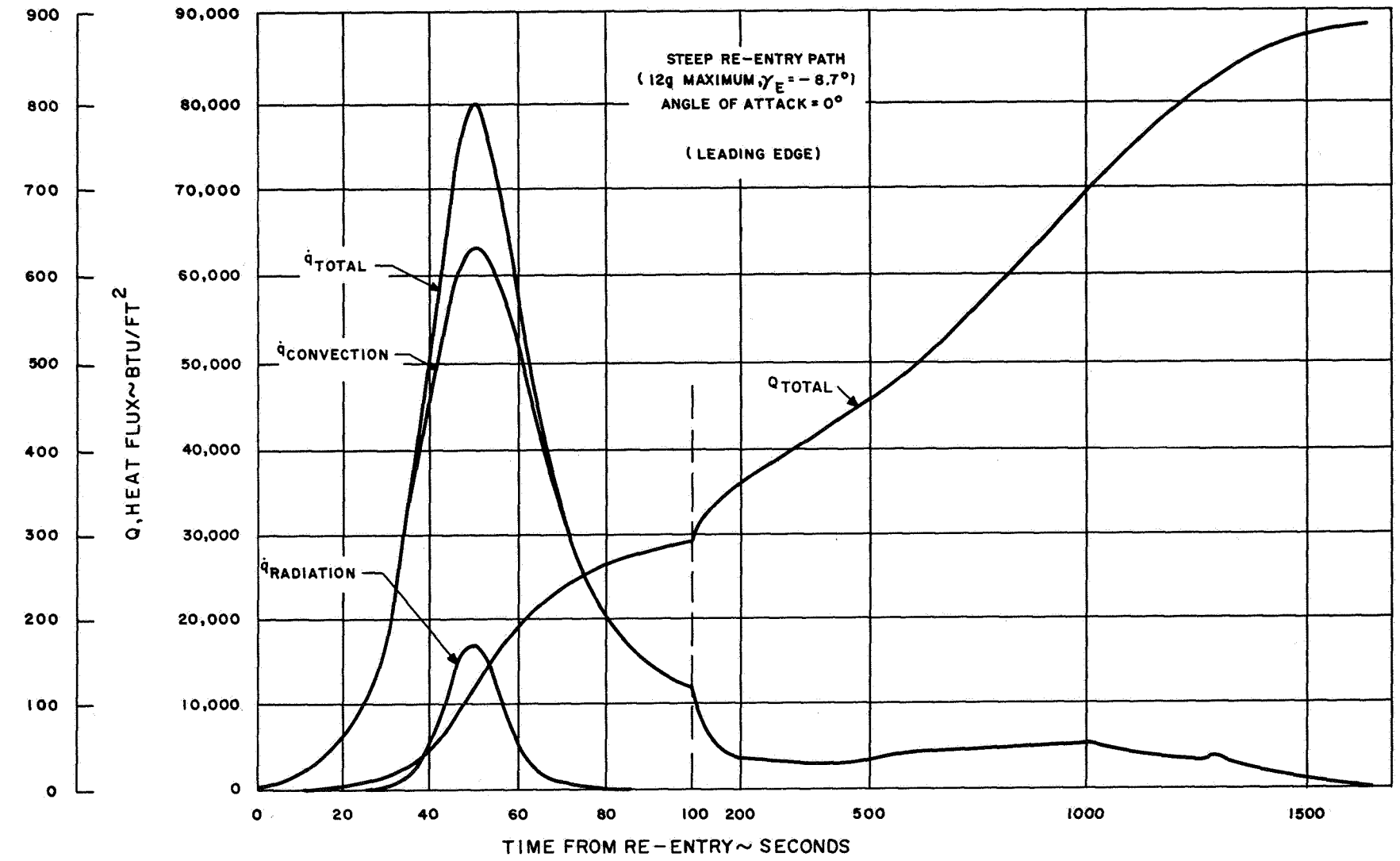

Figure II-3-18. APOLLO - R-3 Configuration, time histories of heat flux and heat flux rate

CONFIDENTIAL

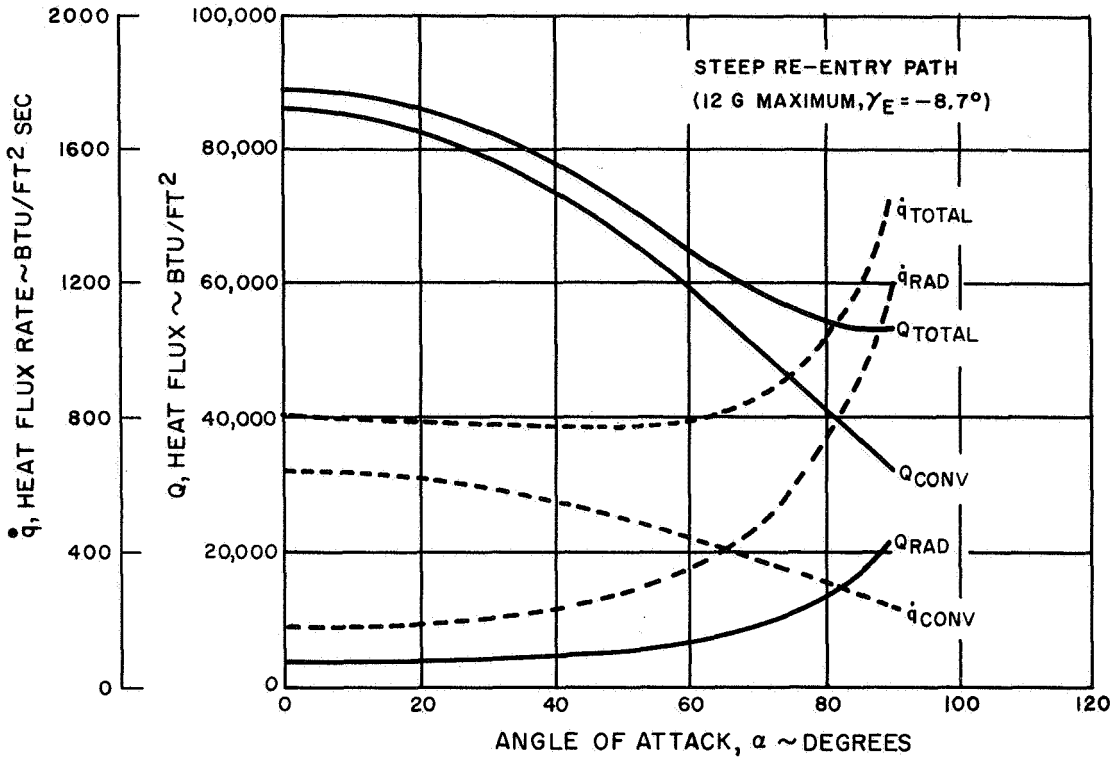

Figure II-3-19. APOLLO - R-3 Configuration, heat flux and heat flux rate to the leading edge

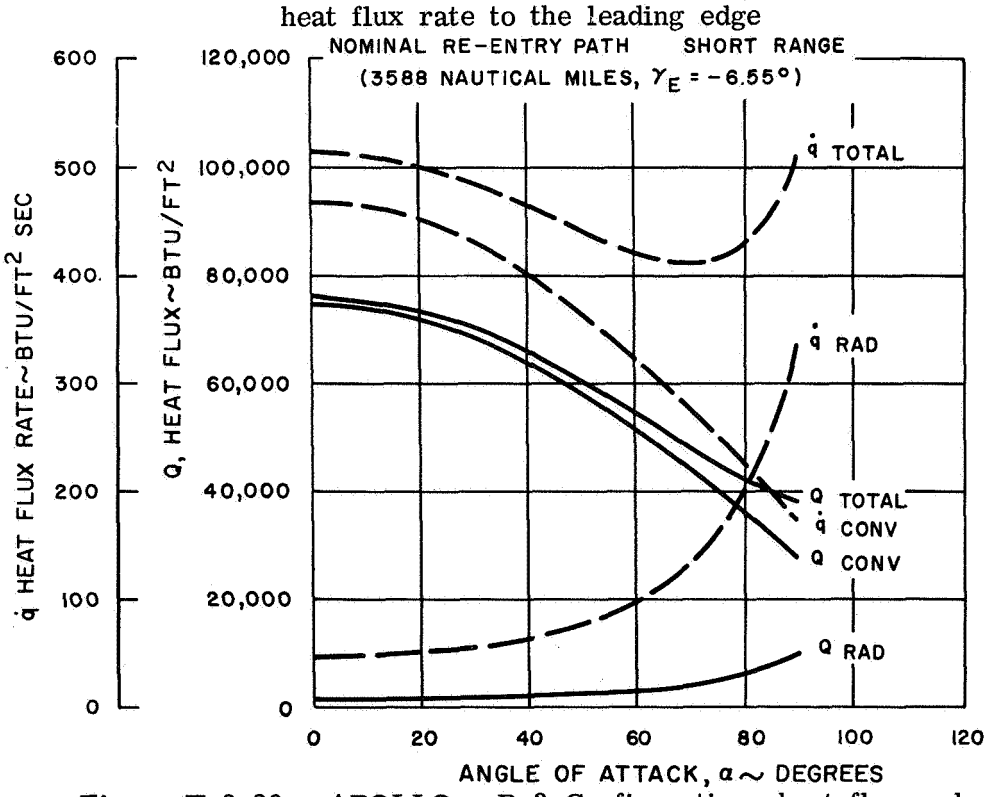

Figure II-3-20. APOLLO - R-3 Configuration, heat flux and heat flux rate to the leading edge

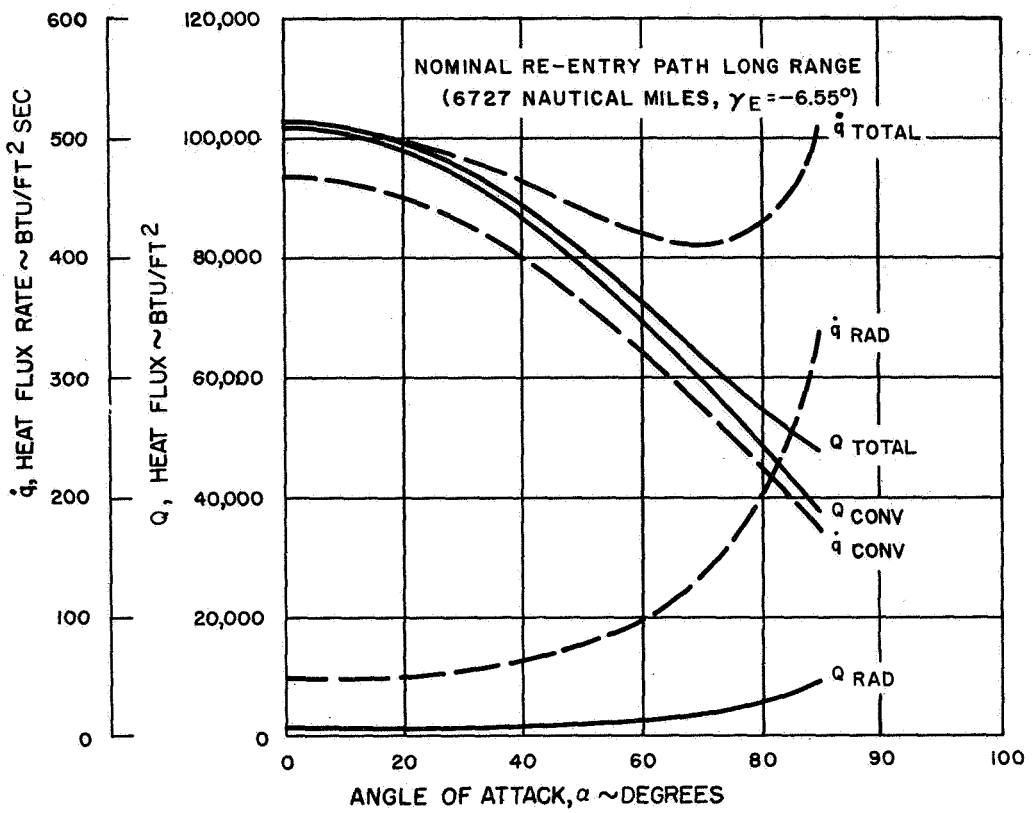

Figure II-3-21. APOLLO - R-3 Configuration, heat flux and heat flux rate to the leading edge

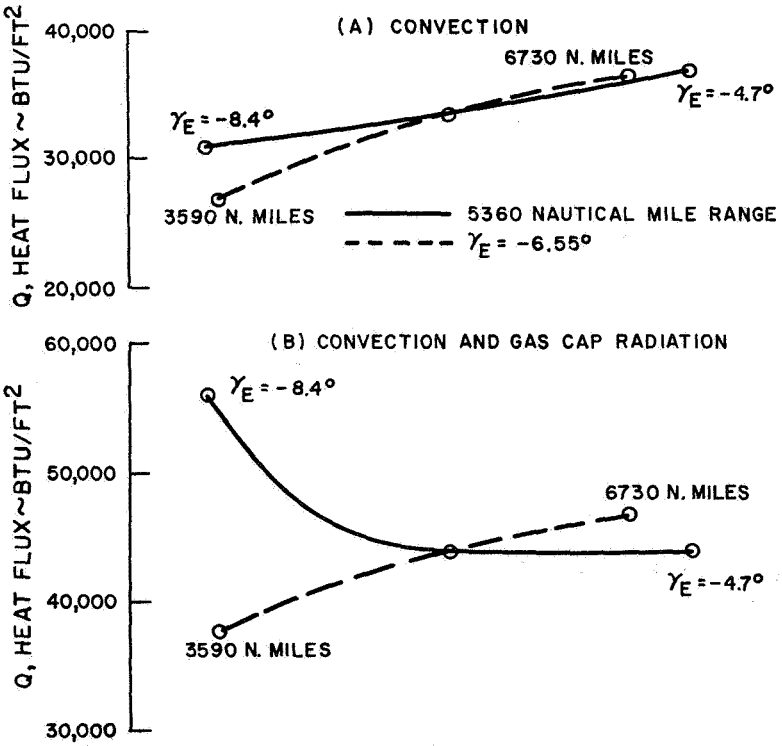

Figure II-3-22. APOLLO - R-3 Configuration, heat flux to the bottom surface of vehicle oriented at 90 degrees to airstream

applicable for a range of angle of attack near $\alpha = 50°$, i.e., an L/D = .7. For other angles of attack the L/D varies, hence the flight time varies. By properly taking this into account however, it is possible to use these curves to determine total heat flux to the leading edge stagnation region for other angles.

The effect of entry angle and in-atmosphere range upon the total average heat flux to the bottom surface, again assuming that $\alpha = 90°$ is shown in Figure II-3-22. The upper part of the figure illustrates that the convective heating increased slightly as the entry angle is decreased, if constant range is maintained. For the same entry angle, more range results in more heating as would be expected. The second part of this figure includes also the gas cap radiation. The character of the constant range curve is identical because the radiation intensity and total flux is largely a function of entry angle and vehicle geometry both of which are fixed for this case. However, the total flux increases sharply with increasing entry angle but is essentially constant at lower entry angles. These conclusions will be even more pronounced if the non-equilibrium gas cap radiation postulations materialize. In that case it may no longer be the maximum accelerations that limit the steepness of the entry angle.

During the hypersonic portions of flight where the heating intensity is too great to allow operation of radiation-equilibrium surfaces, it is advantageous to fly at high attitudes to keep the time of flight short and the total heat to the vehicle within bounds. At some suborbital velocity, depending upon the surface material capability and the wing loading, the vehicle may be flown in a more normal attitude gliding like a Dyna-Soar, thus effecting a higher L/D with more cross range potential.

Figure II-3-23 illustrates the maximum velocity at which this mode of operation may be begun depending upon the temperature tolerance of the outer surface material. Assuming that the vehicle should be capable of lifting twice its apparent weight the upper curve becomes a design curve. For example if the outer surface material will tolerate 2200 F and has a surface emissivity of 0.9 it can initiate normal attitude flight at any point below a velocity of 10,800 ft/sec.

Figure II-3-24 gives a similar representation for the load factor of 2 curve except that it illustrates the effect of other emissivities. Using this curve, it is simple to convert a maximum allowable temperature and any emissivity to an effective allowable temperature with an emissivity of 0.9.

CONFIDENTIAL

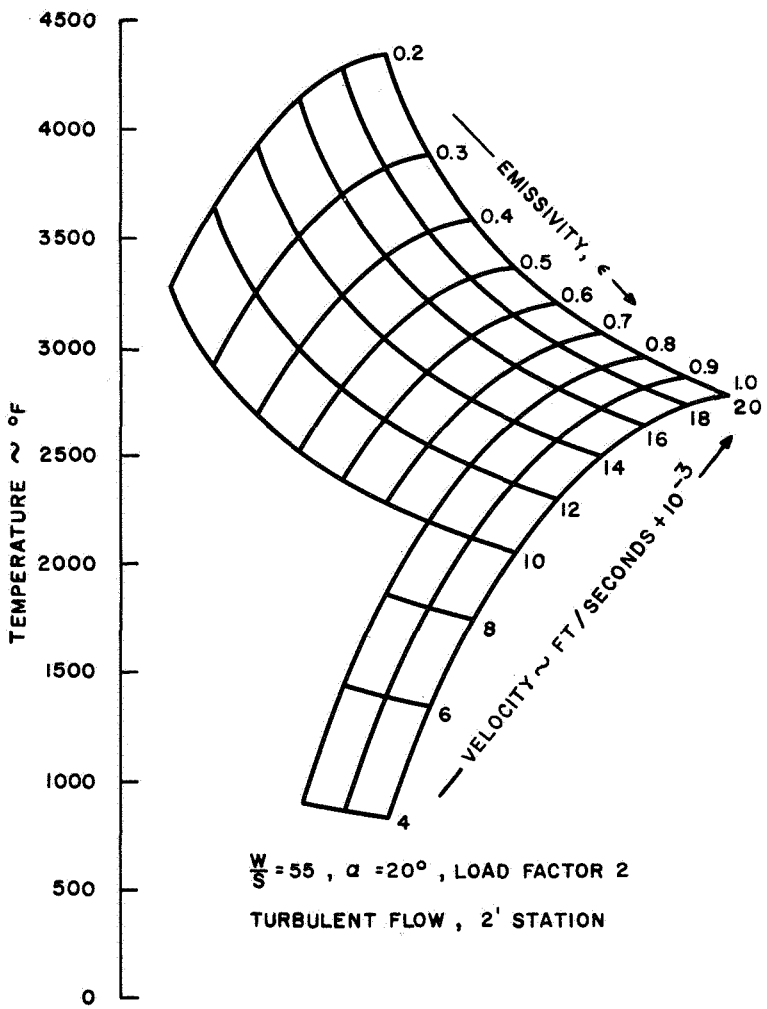

Figure II-3-23. APOLLO - R-3 Configuration, equilibrium wall temperature

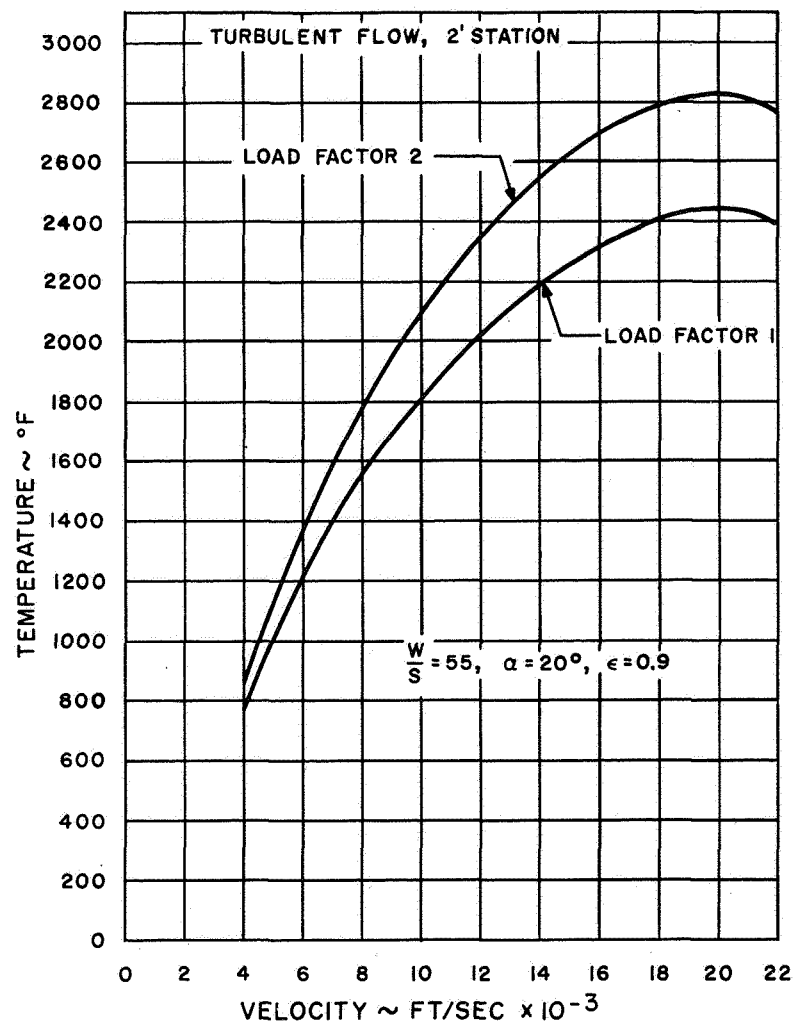

Figure II-3-24. APOLLO - R-3 Configuration, equilibrium wall temperature

CONFIDENTIAL

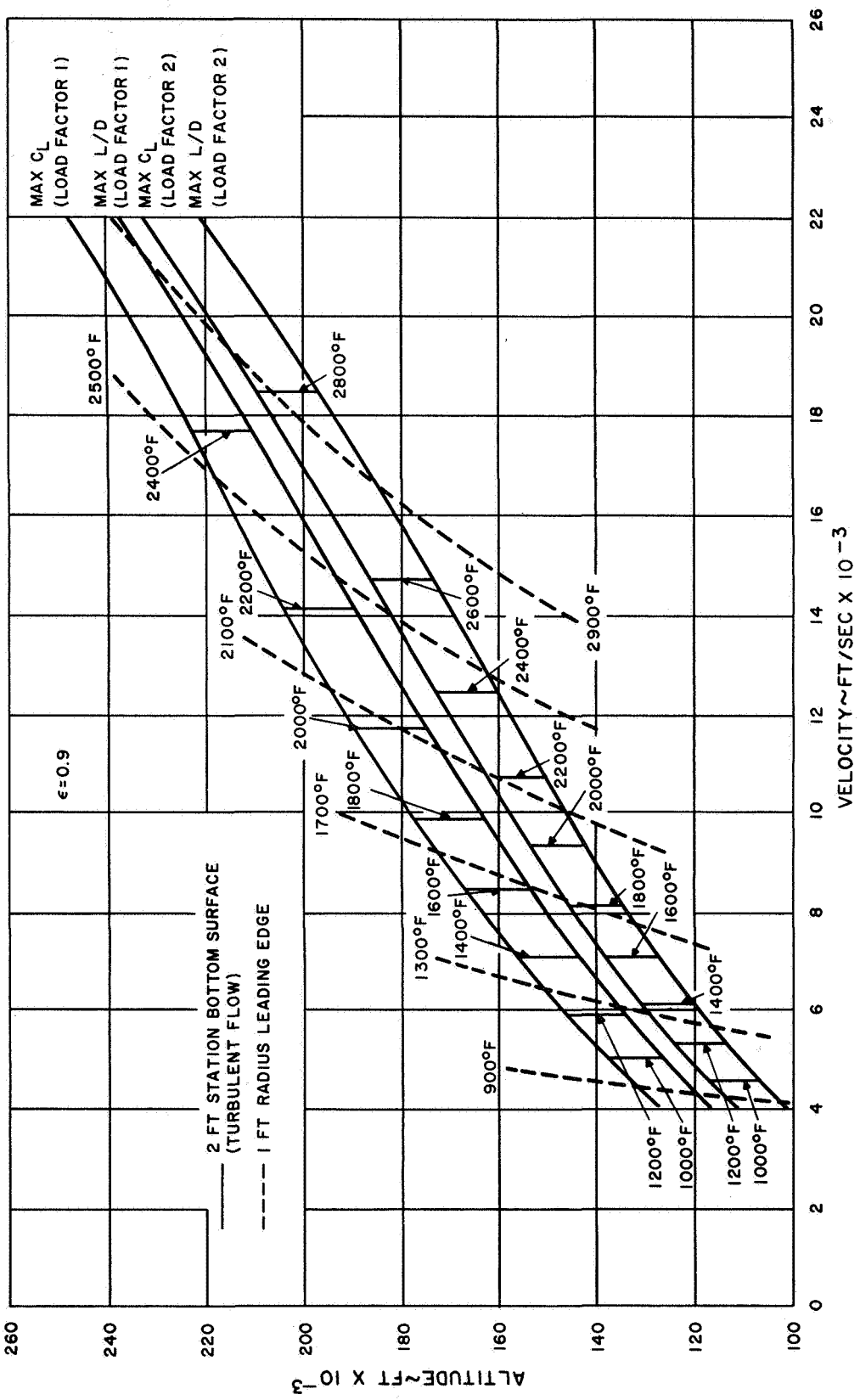

Figure II-3-25. APOLLO - R-3 North - South flight

A corridor plot of permissible initiation of this normal attitude flight is illustrated in Figure II-3-25. This chart may be used to aid in the trade-off investigation of maximum maneuverability vs. maximum allowable radiation equilibrium temperature that may be achieved. More exotic materials (higher temperature tolerance) will of course allow a larger maneuvering capability for greater landing site selection.

REFERENCES

(1) Stoney, W.E., "Aerodynamic Heating of Blunt Nose Shapes at Mach Numbers up to 14", NACA Conference on High Speed Aerodynamics, March 1958.

(2) Lees, Lester, "Laminar Heat Transfer Over Blunt Nosed Bodies at Hypersonic Flight Speeds", Jet Propulsion, Vol. 26, No. 4, April 1956.

(3) Bromberg, R., Fox, J.L., and Ackermann, W.O., "A Method of Predicting Convective Heat Input to the Entry Body of a Ballistic Missile", Ramo-Wooldridge Corporation, Transactions of the First Technical Symposium on Ballistic Missiles, Vol. IV. June 1952.

(4) Reshotko, Eli, "Heat Transfer to a General Three-Dimensional Stagnation Point", Jet Propulsion, January 1958.

(5) Kivel, B, "Radiation from Hot Air and Stagnation Heating", A.F. BMD-TR-59-20 Avco Research Report 79. October 1959.

4.0 Ablation Materials

4.1 INTRODUCTION

The successful design of a hypersonic vehicle for manned re-entry requires "a priori" knowledge of the behavior of high temperature materials subjected to a severe aerothermochemical environment. The three general classes of materials currently being contemplated for high temperature application to re-entry vehicles includes metals, ceramics and plastics. Metals and the crystalline forms of certain ceramics are typical crystalline solids. Graphitic materials and the general category of ceramic oxides, carbides and nitrides are typical amorphous solids. The plastics are essentially thermosetting resins, which are sometimes reinforced with organic or refractory fibers in varying proportions and orientations.

The response of a given material in each of the broad classes listed above will depend critically on the rate of application, magnitude, duration and nature of the heating load. That is, the response of a material to a thermal load during hypersonic re-entry is not so much dependent on the total integrated heat transfer during the time of flight as it is on the precise combination of the instantaneous enthalpy and pressure of the chemically reacting gas which envelops the vehicle as it re-enters.

If the coefficient of thermal conductivity of an oxidation resistant material is sufficiently high relative to the rate of heat transfer, then equilibration of the heat transfer with the heat sink capacity of the material occurs, and the temperature of the material rises with time. If the surface temperature remains below the softening point or below the vaporization temperature during the entire heating cycle, this type of material retains its structural integrity and ablation does not occur. Most metals can, in fact, behave in this fashion. At higher heating rates, the temperature near the surface of the material rapidly rises to the point where thermal degradation of one form or another begins.

The use of metals for heat protection has been largely confined to heat sink and radiative type systems. Heat sink heat protection systems are usable where the

heat transfer rate and total thermal load is small, and weight limitations are not severe. Although radiative systems are generally light weight the level of temperature which existing metals are capable of surviving is limited to approximately 3000 F so that radiation systems are unusable above heating rates of 30 Btu/sq ft. sec. As a result of these system limitations considerable theoretical and experimental effort has been devoted to the investigation of ablation heat protection systems.

In general ablation materials can be divided into 4 categories:

1. Refractory Vaporizing Oxides - such as quartz.
2. Refractory Metals - such as graphite
3. Reinforced Plastics - such as phenolic nylon, phenolic refrasil and General Electric Series 100 materials
4. Thermo Plastics - such as teflon, polyethylene

4.1.1 Refractory Vaporizing Oxides

For this class of refractory materials, the ablation process will usually consist of melting followed by vaporization from the interface between the gas and liquid phase boundary layers. The fraction of solid that enters the gas phase during the ablation process comprises the most effective utilization of the heat absorbing and heat blocking action of the entire mass transfer process. When the fractional part of the solid which gasifies, called, Γ the gasification ratio, approaches unity, the process is called sublimation. When the gasification ratio is zero, the phenomenon is one of pure melting. The value of the gasification ratio is not a fixed constant for a given material but is a function of the material and its environment. That is, Γ depends critically on the enthalpy, pressure and chemistry of the environment in which the material performs. Quartz-like crystalline and amorphous refractories are typical of this class of materials.

4.1.2 Refractory Metals

Certain refractory materials, such as graphite, do not melt but undergo heterogeneous chemical reactions. The rate of mass loss from the surface of this type of material will depend on an oxidation process, which is rate-controlled at low surface temperatures, but rapidly becomes diffusion-controlled as the surface temperature rises. In this type of ablation process, the chemical heat release during the oxidation process and the blocking action of the mass transfer process due to the thickening

of the boundary layer will depend critically on the heterogeneous reaction rates. When it is assumed that the rates of reaction are infinitely fast, then the equilibrium constants of the various combustion reactions will yield sufficient constraints to make the solution to the problem determinate.

4.1.3 Reinforced Plastics

Reinforced plastics, which generally combine a thermosetting plastic resin with various inorganic reinforcements (such as glass or quartz) and/or organic reinforcement (such as nylon) degrade thermally in a pyrolysis of the solid organic phase. This results in the formation of gaseous products such as methane, ethylene, acetylene and hydrogen, leaving a solid residue behind in the form of a non-uniform cross-linked char sponge and inorganic fiber matrix. The thermal degradation of reinforced plastics is also complicated by combustion reactions which occur between the gaseous hydrocarbons and the atomic and molecular oxygen present in dissociated air. Further, an understanding of the coupling of the liquid layer formed with glass or quartz reinforcement phase and the thermosetting resin phase is required for complete description of the ablation process.

4.1.4 Thermoplastics

Thermoplastic resins decompose by means of a process called depolymerization. In this case, a complex hydrocarbon polymer undergoes chemical reactions leading to the formation of monomer. This monomer can subsequently undergo combustion reactions with the oxygen in the gas which flows around the vehicle, resulting in an increase in heat transfer to the ablating plastic.

4.2 STATE-OF-THE-ART OF ABLATION

Over the past several years theoretical and experimental investigations have provided a fairly clear insight into the ablation of the classes of materials discussed above. This information is summarized in the following sections to provide a reference for the assumptions made in the current design of the heat protection system of the APOLLO Spacecraft.

It has now become common practice to use the symbol Q* to represent the "effective heat of ablation", which may be defined as the heat blocked or absorbed per unit mass loss from the ablating material. The quantity Q* represents the complex

interaction between a material and its environment, and consequently is not a constant property of a given material, but rather its magnitude depends on both the material properties and the environmental conditions to which the material is exposed during flight.

The "effective heat of ablation" may be defined by the ratio:

$$Q^* = \frac{\text{heat transfer to a non-ablating calorimeter}}{\text{total mass ablated}} \tag{1}$$

where the calorimeter is assumed to have the same surface temperature, emissivity and catalytic efficiency as the ablating material. The total effectiveness of the material is then due to the separate contributions of:

(a) heat blocking due to "boundary layer thickening" caused by mass transfer
(b) heat absorption within the material, including phase changes
(c) heat absorption or release due to heterogeneous and homogeneous reactions between the injected species and dissociated air
(d) heat blocking due to convection in the liquid phase (if one exists)

The magnitude of each of these terms is of course different for each class of material.

In quasi-steady ablation an energy balance between the incident aerodynamic heating and the energy absorption processes of the material are expressed by Equation (1)

4.2.1 Mass Transfer in Laminar and Turbulent Flow

Before the current state of theoretical and experimental work on the four classes of ablation materials is presented, the effectiveness of mass transfer into the boundary is discussed ((a) above) since it represents the most important energy absorption term for many ablation materials, particularly in the super orbital velocity range.

For hypersonic flight, Scala, Ref. (1), has established rigorously the precise magnitude of this term for the injection of air molecules into the dissociated hypersonic boundary layer. The mass transfer effectiveness may be expressed by the quotient $\left(\frac{\Delta\tilde{Q}}{\Delta\dot{m}}\right)$ which represents the unit change in the energy function $\tilde{Q}$ per unit mass transfer. This function was correlated by the relation

$$\frac{\Delta\tilde{Q}}{\Delta\dot{m}} = \frac{30}{\bar{M}} \left[240 + 0.48\,(h_s - h_w)\right] \tag{2}$$

where $\bar{M}_w$ is the mean molecular weight of the gas at the surface and the enthalpies h_s and h_w are expressed in Btu/lb.

It has been assumed that this form of the equation is approximately valid for predicting the effect of the mass transfer of gases other than air, since the mean molecular weight of the gas at the wall appears in the denominator.

This equation predicts that the injection of light-weight gases acts to increase the "effectiveness quotient", but only insofar as it alters the mean molecular weight of the gas at the wall from that of dissociated air. This is clearly a non-linear effect, since at high mass transfer rates, $\bar{M}_w$ is affected more strongly by foreign species than at low mass transfer rates.

Finally, it is sufficient to observe that the enhanced "effectiveness quotient" produced by light-weight gases is due to the larger heat capacity and larger diffusion coefficients of gases having a low molecular weight.

Although the correlation equation presented by Scala, Ref. (2)(Equation 2) strictly applies to the stagnation point, similar results were obtained by Scala and Ashley Ref. (3) for the local laminar boundary layer.

Rigorous theoretical solutions for the mass transfer effectiveness in turbulent flow are significantly more complex than that for laminar flow because of the inherent complexity of the turbulent process. Currently available techniques for estimating the effect of mass transfer in turbulent flow have been reviewed by Stewart, Ref. (4) Walker, Ref. (5) and Hidalgo, Ref. (6). Each has presented engineering correlations for determining the reduction in skin friction and heat transfer in turbulent flow. Each investigator found that laminar mass transfer is significantly more effective than turbulent mass transfer. If mass transfer were assumed to be the

primary mode of energy absorption by an ablation material (for a gas with the molecular weight of air) then the heat of ablation can be expressed approximately[1] as

$$Q^* = 0.5\ (h_s - h_w) \quad \text{laminar flow} \tag{3}$$

$$Q^* = 0.3\ (h_s - h_w)\ m/\rho_e \mu_e = 0.005 \quad \text{turbulent flow}$$

Although this hypothetical heat of ablation is significantly less in turbulent flow, as compared to laminar flow, at velocities of 35,000 ft/sec even the turbulent heat of ablation approaches 7000 Btu/lb. The implication of these analyses is that materials that depend almost entirely on mass transfer into the boundary layer are relatively inefficient in turbulent flow, although, at superorbital velocities, the mass transfer effect becomes significant, particularly for low molecular weight gases.

4.2.2 The Ablation of a Refractory Vaporizing Oxide — Quartz

The ablation of quartz in laminar flow has been rigorously analyzed by Scala, Ref. (2), and Bethe, Ref. (8). No further discussion of this phase is warranted. It is however, informative to compare the theoretical predictions with available test data. This is shown in Figure II-4-1, where the stagnation ablation of quartz is compared with the average integrated heat of ablation of quartz from selected flight tests, data for an effective velocity of 18000 ft/sec. Within the limitations of the data accuracy, excellent agreement exists. Also, as shown in Figure II-4-1, the heat of ablation of quartz increases significantly with enthalpy, but decreases with increasing pressure. This is a result of two somewhat compensating characteristics. The effective heat of vaporization of quartz increases with flight speed or enthalpy,

(1) For example, Steg, Ref. (7), has correlated the effective heat of ablation of a material such as phenolic nylon as

$$Q^* = 1500 + 1/2\ h_s$$

for laminar flow.

At high enthalpy levels (high velocity) it is seen that the primary contribution to Q* is that a mass addition as given by the second term on the right.

For a material such as phenolic nylon, the ratio $\Gamma / \frac{30}{\overline{M}}$ is approximately 1.0.

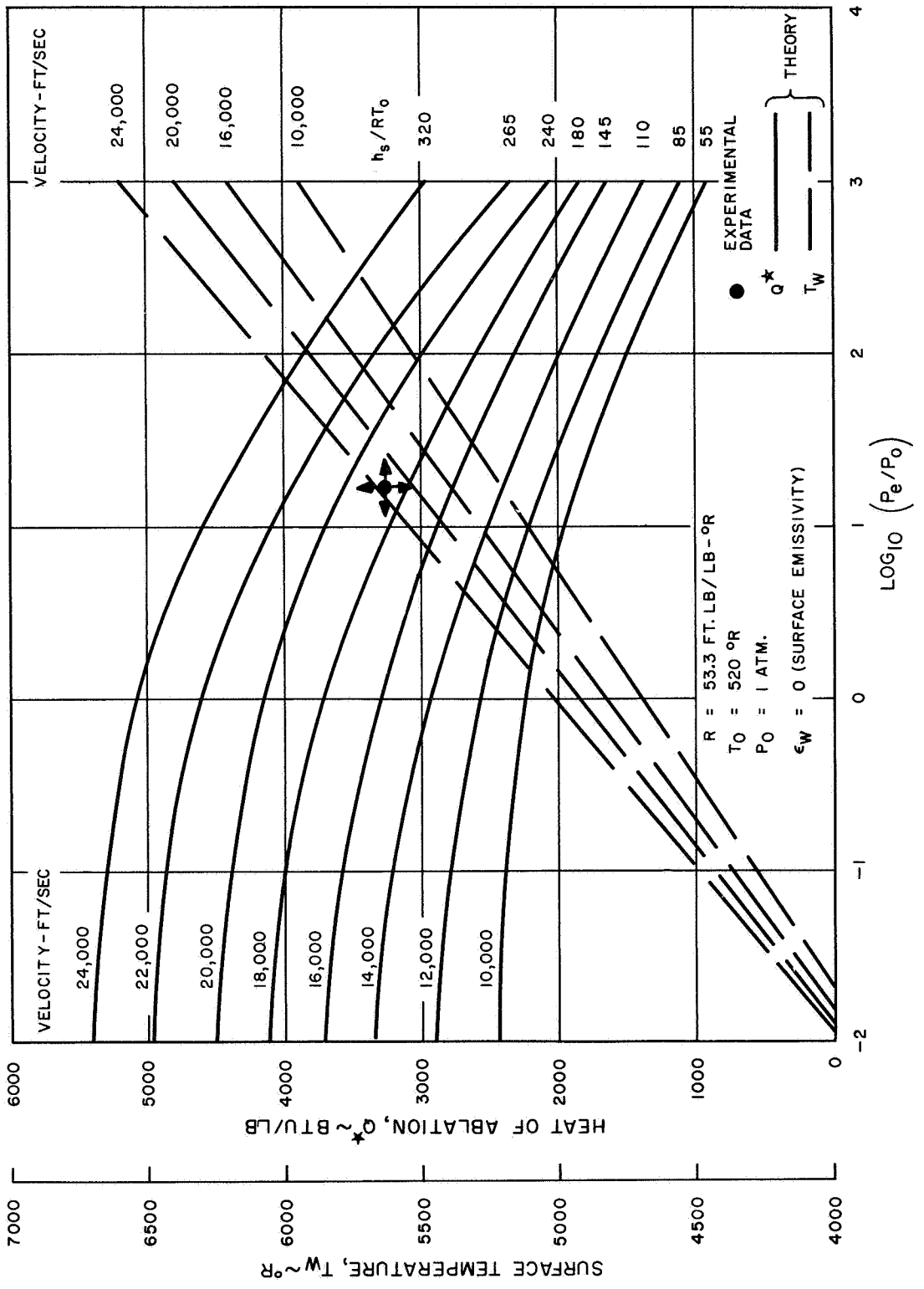

Figure II-4-1. Heat of ablation of a refractory vaporizing oxide - quartz (stagnation point)

but the gasification of the liquid layer decreases with increasing pressure at constant enthalpy. However, the degree of gasification depends on the precise transport properties utilized for the liquid phase. The gasification ratio is large when the Prandtl number of the liquid is large. Further, deceleration of the re-entry vehicle also tends to increase the gasification ratio.

The ablation of quartz under turbulent flow conditions has been investigated by Adams et al, Ref. (9), in which the solutions for convection in the liquid layer are coupled with the local viscous boundary layer equations. Upon adjustment of the quartz-viscosity temperature relation, generally good agreement was obtained between test data and theory. Typical results are presented in Ref. (10). As in laminar flow, the heat of ablation increases significantly with enthalpy.

4.2.3 The Ablation of a Refractory Metal — Graphite

The thermal degradation of graphitic materials occurs not primarily as a consequence of heat transfer but rather by means of an oxidation process. Thus, during hypersonic flight, the net heat transfer into the surface is modified by the fact that exothermic combustion reactions occur in the boundary layer.

In an investigation of the behavior of graphite during re-entry, one requires data on the nature and extent of the chemical reactions between carbon and the primary products of dissociated air, including atomic and molecular oxygen and nitrogen. The reaction between carbon and oxygen produces both CO and CO_2. A number of different mechanisms are possible and these include the following:

1. The formation of both CO and CO_2 is a surface reaction between C(s) and O_2 or O.
2. The formation of CO_2 from C(s) and O_2 and O at the surface, followed by the dissociation of CO_2 to CO, O_2 and O in the gas phase, or reduction of CO_2 to CO at the surface.
3. The formation of CO at the surface from C(s) and O_2 or O, or C(s) and CO_2, the CO being oxidized to CO_2 in the gas phase.

Fortunately both the mass transfer and heat transfer at the surface can be predicted without specifying the specific oxidation mechanism.

It is commonly accepted that the manner in which the oxidation of graphite proceeds depends on the type of graphite, the environmental conditions (e.g. the pressure, temperature, velocity and composition of the stream), the surface temperature; and at high surface temperatures, on the geometry of the model. The temperature at which a measurable mass loss first occurs, is called the threshold temperature (1000-1800 R) and is not a constant but depends on the partial pressure of the reacting gas at the surface.

At low surface temperatures, the mass loss increases rapidly with surface temperature, and the ablation rate is limited by the speed of the chemical processes, including absorption, reaction and desorption.

At somewhat higher temperatures (1400-3200 R), the speed of the chemical processes is comparable to the rate at which fresh reactant is brought to the surface and the products of reaction are removed by convection and diffusion. Therefore, the overall process is in a transition regime, where the speed of the overall oxidation process is limited by the presence of two resistances in series, one chemical and the second gas dynamic.

At temperatures above 3200 R, the chemical oxidation processes are overshadowed by the gas dynamic processes. In this diffusion controlled regime, the mass loss is relatively insensitive to the surface temperature.

Eventually, when the surface temperature is sufficiently high (5500-8000 R), the sublimation rate of carbon atoms and molecules can exceed the surface oxidation rate, and these species are then present in the gas phase. These regimes are illustrated in Figure II-4-2.

In the rate controlled regime, the rate of mass loss is determined by reaction kinetics, where the governing equation may be written in the form:

$$\left(\dot{m}_w\right)_{\text{React.}} = k \left(P_{o_2}\right)_w^n \tag{5}$$

where k is the specific reaction rate, $\left(P_{o_2}\right)_w$ is the partial pressure near the surface, and n is the order of the reaction.

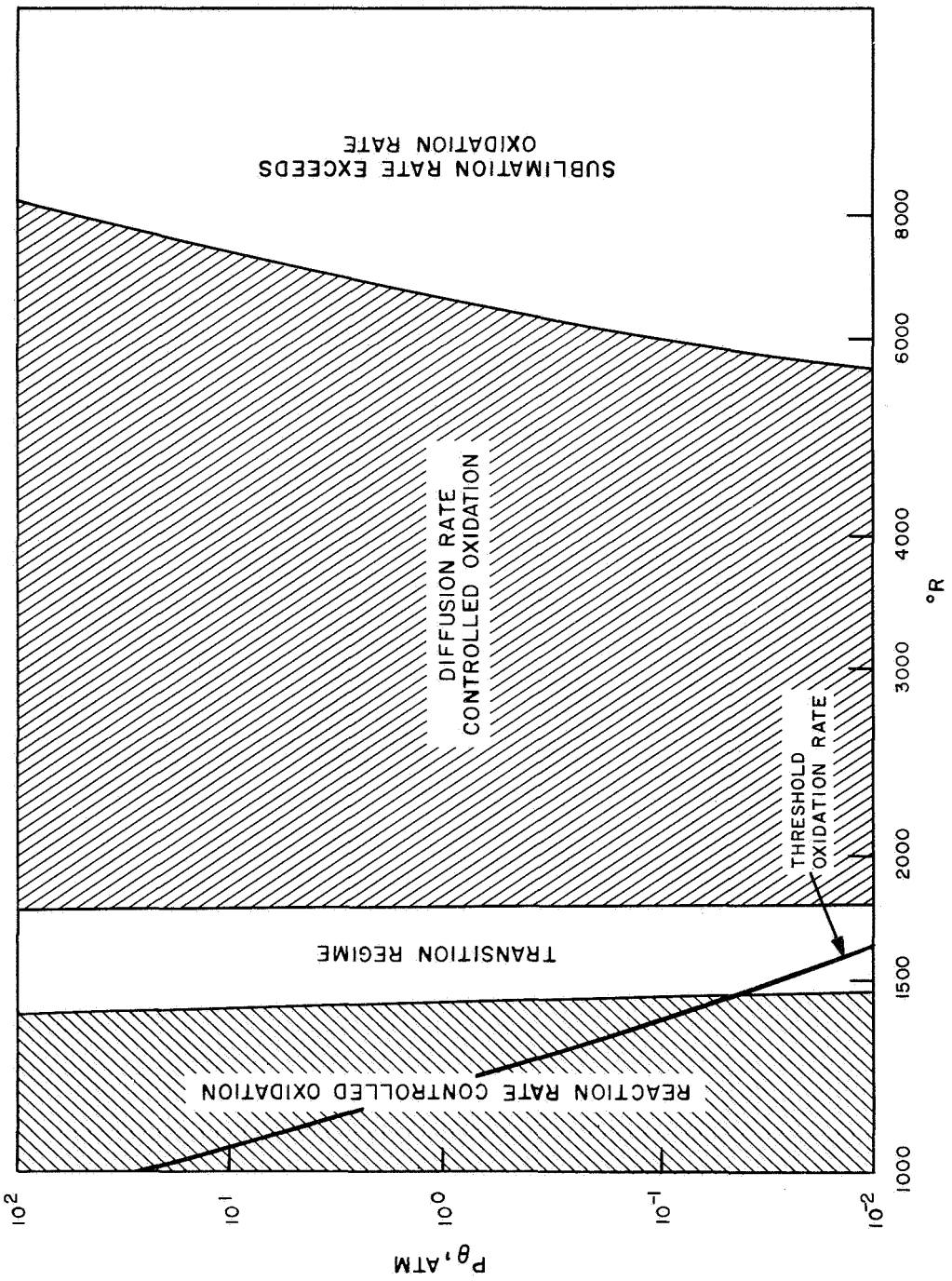

Figure II-4-2. Mass transfer regimes for ablating graphite

The specific reaction rate k can be written in the Arrhenius form:

$$k = k_o e^{-\frac{E}{RT_w}} \tag{6}$$

and hence assuming n = 1/2, (6) becomes

$$\frac{(\dot{m}_w)\ \text{React.}}{P_e^{1/2}} = k_o \left(X_{o_2}\right)_w^{1/2} e^{-\frac{E}{RT_w}} \tag{7}$$

where $X_{o_{2_w}} = 0.21$ for low surface temperatures. As the surface temperature rises, the overall process rapidly goes through a transition regime into a diffusion controlled regime.

In the diffusion controlled regime, it has been found that the mass loss could be correlated in the form: (Ref. 11)

$$\frac{(\dot{m}_w)\ \text{Diff.}\ \sqrt{2R_B}}{P_e^{1/2}\ f(\Omega)} \left[\frac{f(\Omega)}{\sqrt{2}}\right]^{\delta} = 6.2 \times 10^{-3}\ \frac{\text{lb.}}{\text{ft.}^{3/2}\ \text{sec.}\ \text{atm}^{1/2}} \tag{8}$$

which applies to both axially-symmetric ($\delta = 1.0$), and two-dimensional ($\delta = 0$) geometries, for laminar flow where $f(\Omega)$ represents the effect of yaw. Note that Equation (5) which represents the rate controlled oxidation rate is independent of the geometric factors, whereas the diffusion controlled mass loss, Equation (8) is not.

The overall mass loss is then dependent on the separate contributions of the rate controlled and diffusion controlled processes.

Upon introducing the concept of resistances in series, one has immediately for the total mass loss:

$$\dot{m}_w = \frac{1}{\frac{1}{(\dot{m}_w)\ \text{React.}} + \frac{1}{(\dot{m}_w)\ \text{Diff.}}} \tag{9}$$

where the reaction term predominates at low surface temperatures, and the diffusion term predominates at high surface temperatures.

In computing the mass loss for commercial graphite it is permissible to eliminate the rate controlled reaction since commercial graphite becomes quickly diffusion controlled due to its extremely high collision frequency $\left(k_o = 6.73 \times 10^8 \frac{lb}{ft^2 - sec}\right)$. For pyrolytic graphite, however, whose collision frequency is $4.47 \times 10^4 \frac{lb}{ft^2\ sec}$, equation (7) must be used to calculate the reaction rate oxidation.

When the stagnation pressure and surface temperature become sufficiently high, the sublimation regime is reached. In this regime, it has been found that the principal gaseous species in the equilibrium vapor over graphite are the following: C1, C2, C3, C4, and C5. The procedure to calculate the mass loss in this regime is as follows:

(1) Compute the vapor pressure of the appropriate carbon specie (C1, C2, C3, C4, C5) from the vapor pressure temperature data reported in Ref. (12).
(2) Next, using Raoults law, compute the mole fraction of the particular specie assuming that the total pressure is equal to the vapor pressure.
(3) Using Daltons law and the conservation of mass, compute the mole fraction of air in the mixture and hence the average molecular weight of the subliming mixture.
(4) Next, compute the mass fraction of the individual specie from a knowledge of the average molecular weight of the mixture and the individual molecular weight of the given specie.
(5) Finally, the mass loss of the individual specie is computed using the relationships developed in Ref. (13).

The mass loss of graphite for turbulent flow may be approximated from the following mass-heat transfer analogy:

$$\dot{m}_{\substack{\text{Local}\\ \text{Turbulent}}} = 2\,\dot{m}_{\substack{\text{Laminar}\\ \text{Stagnation}}} \left(\frac{\dot{q}_{\text{Local Turbulent}}}{\dot{q}_{\text{Laminar Stagnation}}} \right) \tag{10}$$

4.2.4 The Ablation of a Thermoplastic — Teflon

The general category of thermoplastic resins includes acrylics, cellulosics, fluorocarbons, Nylon, polyethylene and the vinyls. An ablation material representative of this category is Polyethafluoroethylene-Teflon. For laminar flow, Scala, Ref. (2), has conducted a rigorous analysis of the rate controlled pyrolysis of teflon. In the analysis of Scala, it was assumed that the ablation of Teflon occurs as a quasi-steady depolymerization process, in which the Teflon polymer (C_2 F_4) undergoes a rate controlled pyrolysis in which the solid gasifies to the nonomer C_2F_4 and that the nonomer C_2F_4 combusts with oxygen to form COF_2. The heat of ablation of Teflon and its surface temperature response is shown in Figure II-4-3. The surface temperature correlates as an increasing function of the logarithm of the stagnation pressure, in a manner quite similar to quartz. Consequently, the heat of ablation is weakly dependent upon stagnation pressure. The variation of the heat of ablation with enthalpy is shown in Figure II-4-4 for both laminar and turbulent flow. The turbulent line is an estimate by Offenhartz, Ref. (14). Note that in general, the experimental results agree quite closely with the laminar theory of Scala. The estimated line, for turbulent flow was obtained from an analysis of the blocking action of the gases of pyrolysis and does not include the effects of combustion.

4.2.5 The Ablation of a Reinforced Thermosetting Plastic

During the exposure to severe heat of the cured thermosetting plastics, a degradation known as pyrolysis occurs. This causes a breaking of the cross linked molecules and results in the formation of gases such as carbon monoxide, hydrogen, and various other low and high molecular weight hydrocarbons. A solid "char" remains which is a rather carbonaceous structure that is porous and refractory in nature.

As shown by Gruntfest and Shenker Ref. (15), a variety of reinforcing fibers may be added to these resins to improve the strength of the resin and char. These additives introduce additional variables to the solution of the problem, depending upon the appropriate properties such as: (a) the presence of a molten layer; (b) the vapor pressure of the various chemical species: (c) the contribution of the additives to the thermal properties of the char layer and virgin plastic. It should be noted that the char layer, being carbonaceous, may also undergo a combustion reaction.

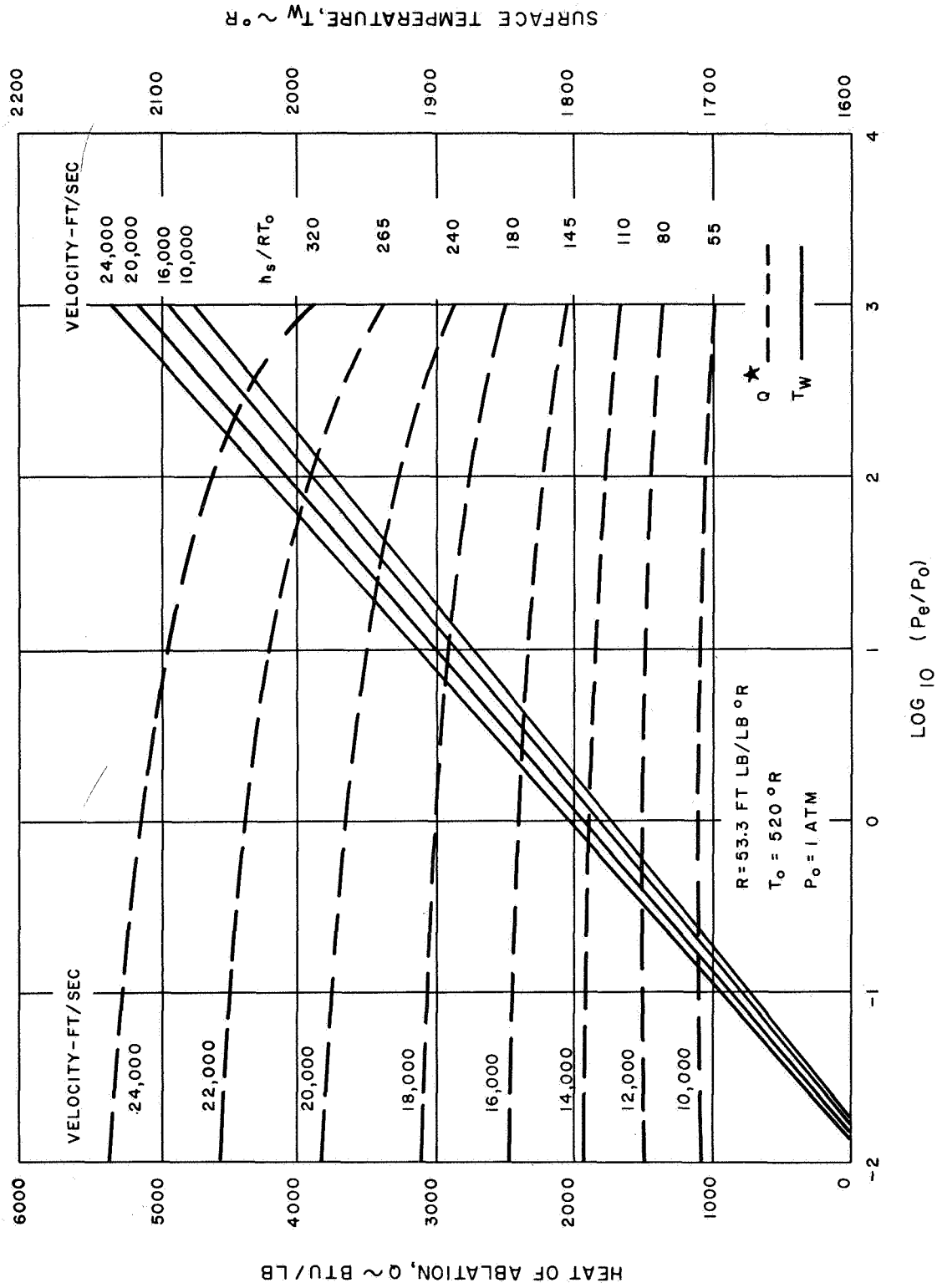

Figure II-4-3. Theoretical heat of ablation of teflon (stagnation point)

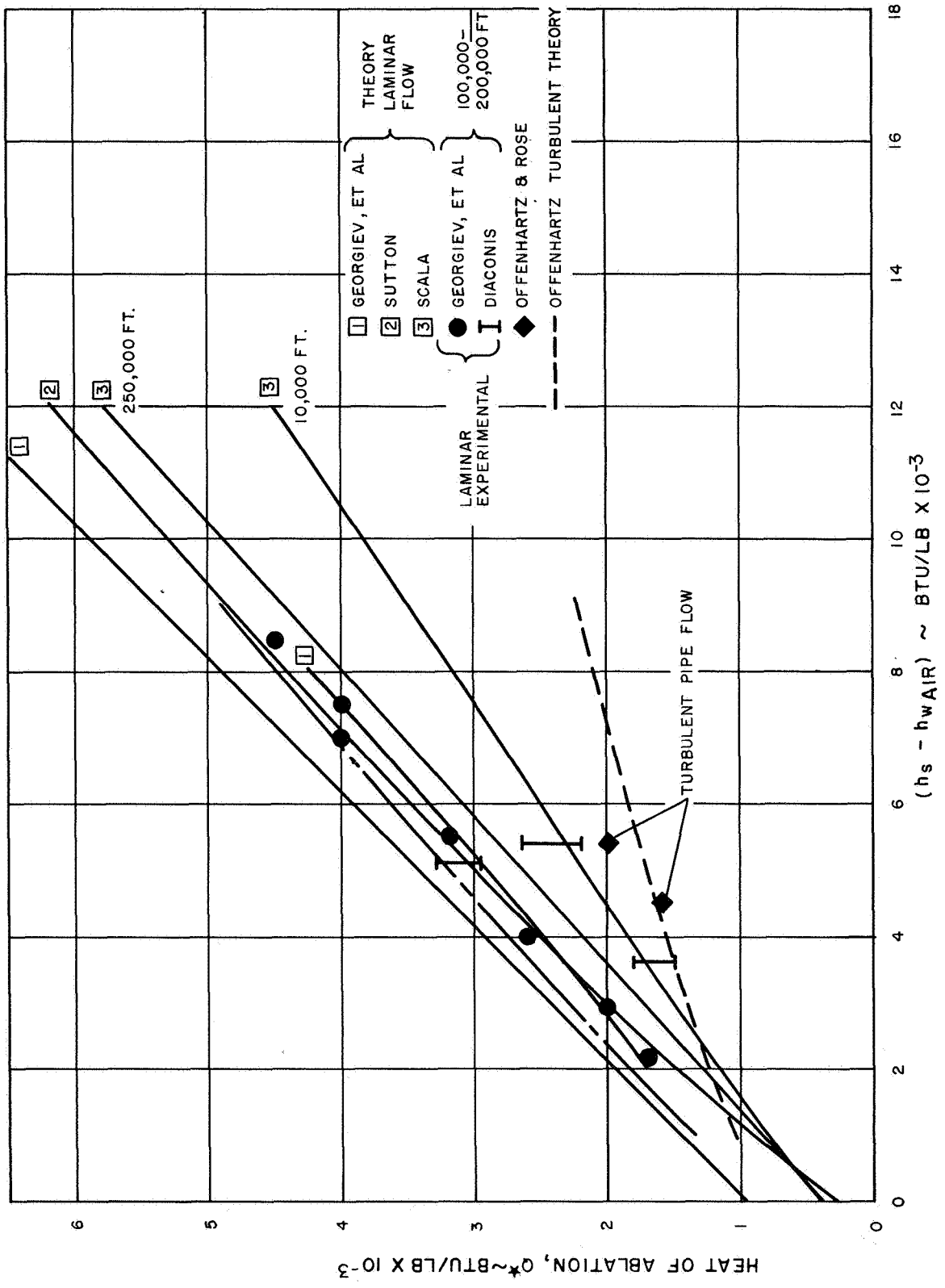

Figure II-4-4. Heat of ablation of teflon

Scala Ref. (2) has analyzed this problem and has found that the ablation rate of a reinforced plastic is different from that of pure sublimation, since gasification occurs in several distinct steps including pyrolysis and combustion. Thus, a certain portion of plastic $(1 - \Gamma - E)$ does not gasify but remains as char. The gasification process that occurs immediately below the char layer is temperature dependent in depth, and the pyrolysis obeys the usual conservation of mass and energy laws. The local rate of pyrolysis is determined by:

$$\frac{\partial \rho_i}{\partial t} + \Delta\left(\rho_i \underset{\rightarrow}{v_i}\right) = \dot{w}_i \tag{11}$$

$$\rho\, C_p \left(\frac{\partial T}{\partial t} + \underset{\rightarrow}{V}\, \Delta T\right) = \nabla (K \nabla T) - \Sigma_i\, w_i\, h_i \tag{12}$$

Each of the chemical source terms, w_i, obeys a kinetics law which introduces rate constants having an exponential dependence on temperature. Once these are solved the mass of gas which flows through the char layer and eventually appears in the boundary layer in one form or another may be determined. Scala Ref. (2) has made a qualitative estimate of the behavior of reinforced plastic by equating the total mass loss of pyrolyzed plastic to the injected chemical species into the boundary layer plus the mass of char which combusts and injects products of combustion into the boundary layer. Q^* then becomes:

$$Q^* = \frac{Q_{cal}}{\dot{m}_p} = \left(\Gamma + \epsilon\right)\left[\left(\frac{\Delta Q}{\Delta \dot{m}}\right)_w + h_w\right] - hvp \tag{13}$$

where $\dot{m}_p$ is the mass of solid pyrolyzed; Γ is the fraction gasified; ϵ is the fraction of pyrolyzed char that combusts.

The Q^* given by equation (13) pertains to the thermosetting resin portion of a reinforced plastic; or for materials such as phenolic nylon or unreinforced General Electric Series 100 materials in which the heterogeneous combination (such as phenolic and Nylon) can be treated as a thermosetting plastic. When the thermosetting resin is combined with an inorganic reinforcement the solution of the inorganic and thermosetting plastic must be coupled together. Although an "exact" solution cannot be obtained for a material such as phenolic Nylon adequate engineering results can be obtained once the decomposition rate of phenolic Nylon has been determined and an estimate made of the gaseous species and their enthalpy at the surface of the char. The equations governing the degradation of the plastic can

then be coupled with the hypersonic boundary layer equations and the rate of thermal degradation calculated.

4.2.6 Applied Engineering Techniques for the Prediction of the Ablation of a Reinforced Thermosetting Plastic

As an example of application of the available analytical techniques to a prediction of the thermal history of a re-entry vehicle with an ablating-type heat shield, the analysis used to predict the thermal history of a thermosetting resin such as phenolic-resin and General Electric Series 100 materials will be outlined. This analysis has been used successfully by General Electric to predict the thermal history of ICBM type re-entry vehicles.

As a re-entry vehicle with a heat shield fabricated from a material containing thermosetting resins starts to re-enter the earth's atmosphere (about 300,000 ft), the temperature of the body is relatively low (550 to 1000 R). The energy transferred to the body during the initial part of the re-entry simply increases the body temperature, i.e., the vehicle behaves like a heat sink.

The surface temperature of the plastic continues to increase, during re-entry, to the point where the plastic starts to decompose at a significant rate. Thermosetting resins decompose to form a carbon-like char and gas. The fraction of the virgin plastic converted to gas, the composition of the evolved gases, and the chemical kinetic expression that describes the decomposition rate of the plastic can all be determined by independent laboratory experiments. To describe the thermal behavior of the material, it is necessary to solve the transient-heat conduction equation through the char and the virgin plastic continuously and simultaneously throughout the remainder of the re-entry period. In order to solve these two second-order differential equations simultaneously, it is necessary to prescribe three boundary conditions, two of which are common to both equations. These boundary conditions are: (1) the net heat-transfer rate to the charred surface of the vehicles is the aerodynamic heat-transfer rate to a non-ablating calorimeter reduced by surface re-radiation, and the "blocking action" effect of the injection of the decomposition gases into the boundary layer; (2) the coupling boundary condition is that the heat conducted out of the char into the virgin plastic is equal to the sum of the heat stored in the plastic, the heat conducted into the plastic, and the energy required to decompose the plastic. The latter is incorporated into the heat conduction equation within the virgin plastic as a heat absorption term, i.e., the amount of energy absorbed in the decomposition

of a unit volume of plastic per unit time. This, in turn, can be formulated in terms of the chemical kinetics which describe the decomposition rate (an exponential function of the temperature) and the heat of decomposition of the plastic. It was assumed that this term is significant only in a narrow region of the virgin plastic near the char-virgin plastic interface. The decomposition term also determines the rate of gas injection into the boundary layer (and therefore the magnitude of the "blocking action" term and the gasflow rate in the porous char). This is valid since it was assumed that the char is sufficiently porous so as not to restrict the gas flow, i.e., the rate of mass injection into the boundary layer and the gas flow rate in the char are determined only by the plastic decomposition rate; (3) the third boundary condition is that the heat conducted out of the backface of the virgin plastic is zero.

The heat conduction equation in the porous char is:

$$\rho_c \, C_{pc} \frac{\partial T}{\partial t} = K_{cg} \frac{\partial^2 T}{\partial^2 x} - \rho_g \, v_g \, c_{pg} \frac{\partial T}{\partial x} \tag{14}$$

where the second term on the right-hand side is the heat absorbed by the gas as it flows from the decomposition zone at the char-virgin-plastic interface to the surface and where it was assumed that the char and gas are always on thermal equilibrium with each other. The heat conduction equation in the virgin plastic is:

$$\rho \, VC_{vp} \frac{\partial T}{\partial t} = K_v \frac{\partial^2 T}{\partial x^2} - A \tag{15}$$

where the second term on the right hand side is the heat absorbed in decomposing a unit volume of the virgin plastic. It can be shown that the quantity A is given by:

$$A = H_v \, \rho_v \, k_o \, e^{-E/RT} \tag{16}$$

where $k_o \, e^{-E/RT}$ is the first-order reaction-rate constant for the decomposition rate of the plastic into char and gas. The boundary conditions for the simultaneous solution of (1) and (2) are:

$$\dot{Q}_s = \dot{Q}_{Aero} - \sigma \, \epsilon_s \, T_s^4 - \dot{m}_g \left[\frac{\Delta Q}{\Delta \dot{m} \, \epsilon} \right] \tag{17}$$

where $\Delta Q / \Delta \dot{m}$ is the "blocking action" term discussed by Scala, Ref. (1). The aerodynamic heat-transfer rate Q_{Aero} can be determined by means of the methods described by Walker, Ref. (16). The common boundary condition is:

$$k_e\left(\frac{\alpha T}{\alpha x}\right)_c = \rho_\nu c y \rho \frac{\alpha T}{\alpha t} + kv \frac{\alpha T}{\alpha x} - A \tag{18}$$

and as mentioned above, the plastic decomposition was assumed to occur in a narrow region near the char-virgin plastic interface. This is a reasonable assumption since the virgin plastic is a poor thermal conductor and, thus, the temperature gradient is large while the reaction rate is exponential. The third boundary condition is:

$$k_V \left(\frac{dT}{dx}\right)_{BF} = 0 \tag{19}$$

where the subscript "BF" refers to the backface of the virgin plastic. The "blocking action" term in Equation 17 has been discussed previously and given by Equation (2) for the stagnation point of an axisymmetric body.

This correlation formula has been developed for "air-to-air" injection and has been corrected for the injection of other gases by the molecular weight correction shown. Also, as pointed out previously, it has been found that the stagnation point relationship is valid around the body, again, for the laminar boundary layer. In those cases where the boundary layer flow is turbulent, the "blocking action" effectiveness defined by Walker, Ref. (5) appears to be a reasonable assumption, for air, i.e.,

$$\frac{\Delta Q}{\Delta \dot{m}} = \frac{-150 + 0.58\ (hs - hw)}{0.88 + 1.27\ (m/\rho_e\ V_e)} \tag{20}$$

The molecular weight correction by Hidalgo, for example, can be used to adjust for gas molecular weights different from air.

The mass decomposition rate of the virgin plastic, m, can be shown to be:

$$\frac{\rho\ H_v\ k_o\ e^{-E/RT}}{H_v}\ \Delta X = m \tag{21}$$

where Δx is the distance which the char-virgin-plastic interface moves in time Δt. The fraction of plastic converted to gas is known experimentally, so that the gas evolution rate is simply:

$$\Gamma \dot{m} = \dot{m}_g \tag{22}$$

where Γ is the function of virgin plastic converted to gas.

Thus, from a knowledge of the aerodynamic heat-transfer rate throughout the re-entry period, the behavior of material can be predicted by using an analog or digital computer program developed from the analysis described above provided that three assumptions are made. Those assumptions are: (1) the temperature gradient in the char layer is linear, (2) the surface of the char is not "ablated", i.e., the material does not suffer any substantial dimensional change (of course, the material is "ablated" in the sense that there is a mass loss), and (3) the char layer thickness can be prescribed or controlled.

With these three assumptions, the time variation of the surface temperature, the char-virgin plastic interface temperature, the temperature profile through the virgin plastic, as well as the rate of growth of the char layer can be predicted for any arbitrary aerodynamic heat pulse. As an example of these calculations, this program has been applied to a prediction of the behavior of a phenolic-Nylon model in a relatively low heat flux facility (a low density air arc tunnel $\cong$ heat flux = 60 Btu/sq ft-sec) in which there was very little surface recession but a considerable amount of char formation Ref. (17). The predictions of the program were in good agreement with the observed temperature-time history of the model surface, as well as the final char layer thickness as shown in Figure II-4-5. The predicted char-virgin plastic interface temperature was also in good agreement with the values obtained in other laboratory experiments. The agreement of the analysis with these test results corroborates the validity of the analysis and indicates that the values of the material properties used (thermal conductivity, heat capacity, decomposition rate expression, etc.) are reasonably correct, particularly with respect to the values used for the char layer.

Of course, during the high heating, high shear portions of re-entry, there is a considerable amount of surface erosion of the charred vehicle at least for ballistic ICBM flights, particularly in the nose region. For this case the complete behavior of the material can be predicted with the program described above, if the processes by which the char is ablated can be described adequately or if the char layer thickness can be prescribed. The char is ablated by one or more of several mechanisms: (1) surface oxidation; (2) mechanical "scrubbing" of the char from the surface of the vehicle since the char from phenolic nylon is quite fragile; (3) aerodynamic shear; and (4) mechanical effect.

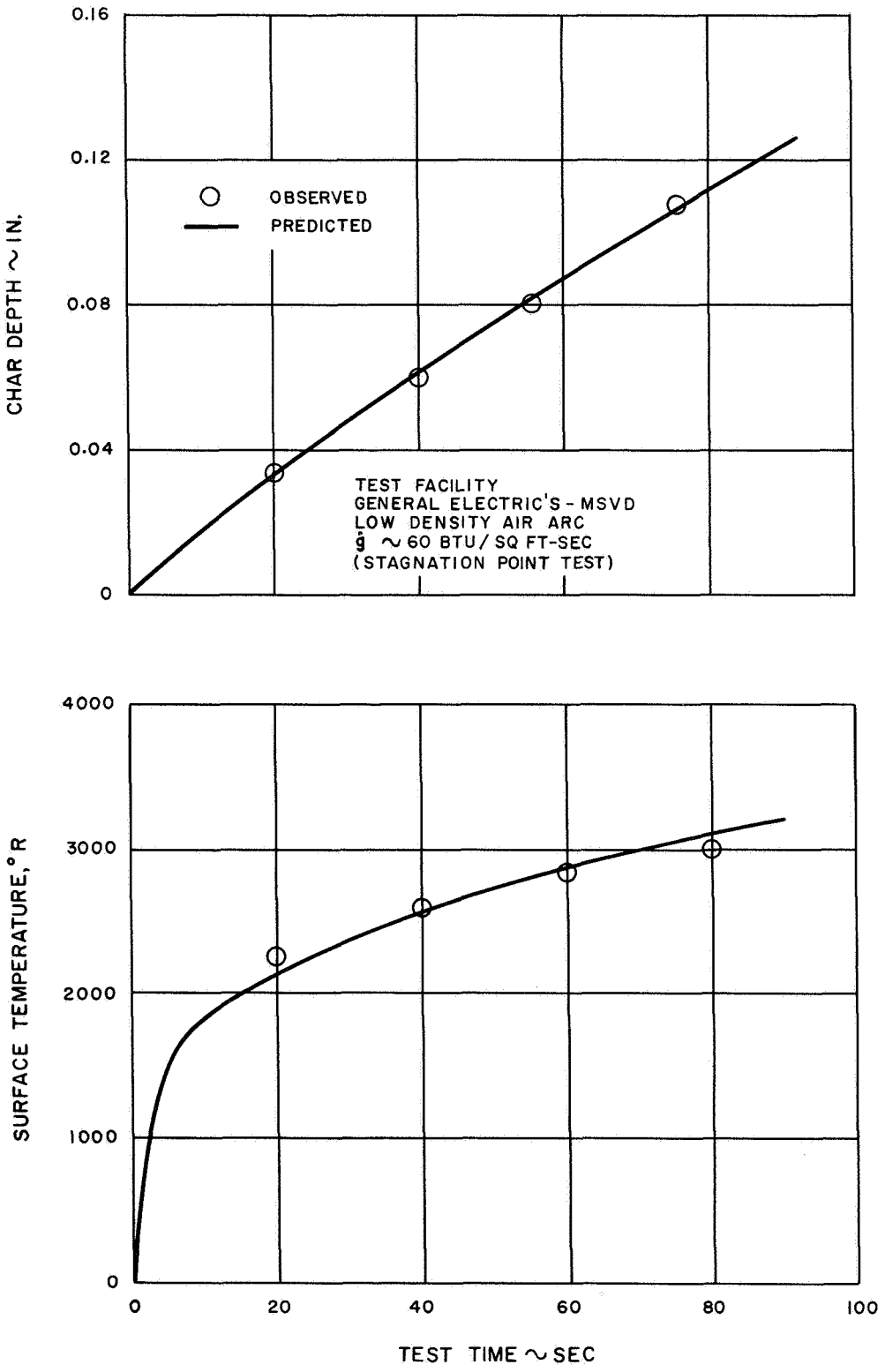

Figure II-4-5. Correlation of air arc results with theory (typical thermosetting plastic)

Thus far, it has not been possible to analytically describe the ablation of the char. On the basis of analysis of phenolic Nylon data from re-entry vehicle flight test, it appears that aerodynamic shear is the primary factor in char removal. Although combustion of the char may also occur, and tend to remove the char, examination of recovered vehicles such as the Thor Able RVX-1, Ref.(18) indicates that oxidation in the low heat transfer regions of the vehicle, $\dot{q}_{max} \approx$ 200 Btu/sq ft. sec is negligible since no char was removed. At this point then, it would appear that the phenolic Nylon char will grow, with little or no surface erosion, until the shear level reaches a certain value. Based on current analysis of test data, this value appears to be on the order of 10-12 lb/sq ft. The char thickness will then be reduced in thickness in a few seconds, then remain relatively constant during the remainder of re-entry heating. Based on observation of test data, where the shear levels were high, τ = 50-75 lb/sq ft, the char layer thickness was on the order of 0.003 to 0.006 inches. It has been found that ablation observed in flight tests can be predicted quite accurately, by utilizing this concept of a "thin" char with the other properties of the char and gas determined from air arc experiments such as the one described above. An example is shown in Figure II-4-6 for a typical test using a thermosetting type material. Ablation and char in a comparatively low level heat transfer environment for the same type of test is shown in Figure II-4-7. Generally good agreement is obtained with the observed results. A by-product of the ablation and char calculation are the surface and subsurfaces temperatures, also shown on both figures. In this case only the surface and interface temperature between the char and virgin Nylon is shown. The partition of the heat transfer to the thermosetting plastic during the tests is shown in Figures II-4-8 and II-4-9 for both cases. This partition of energy reveals several interaction aspects of the ablation of thermosetting plastics. The most important is that the energy absorbed by the gases in reaching the surface temperature of the char is more significant than that observed by the blockage of heat from mass transfer effects. (In laminar flow, of course, the mass transfer effect would be approximately a factor of two greater). Also, at the lower heat transfer level, the energy radiated from the surface is a highly significant portion of the total incident to the surface.

Further, the effect of char layer thickness on surface temperature is readily apparent from examination of Figures II-4-6 and II-4-7. Although the aero heat transfer rate was a factor of 5 greater in Figure II-4-6, the maximum surfaces temperature for both heat transfer histories was approximately the same.

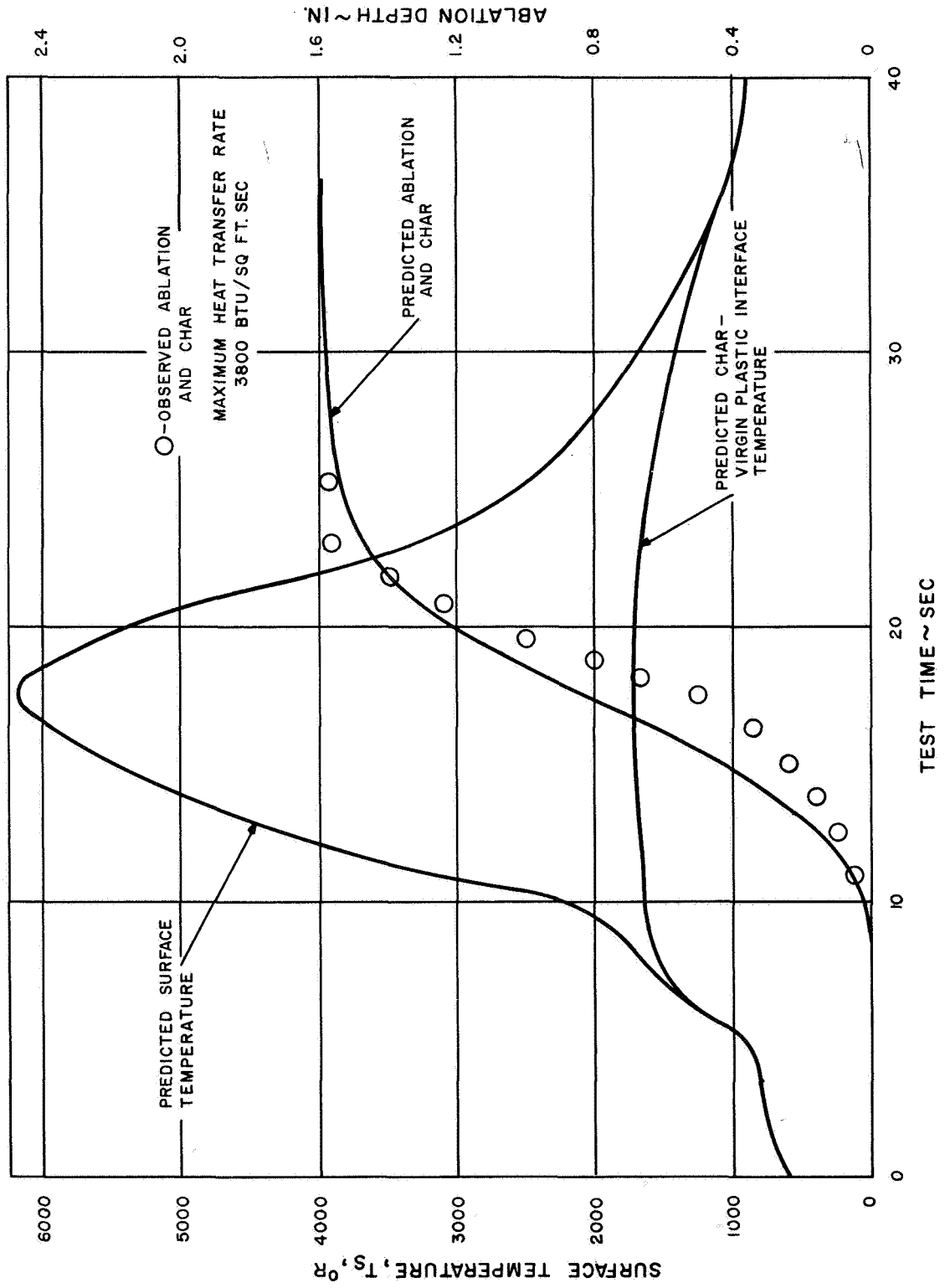

Figure II-4-6. Observed and predicted ablation and temperature of a typical plastic foil simulated re-entry heating thermosetting

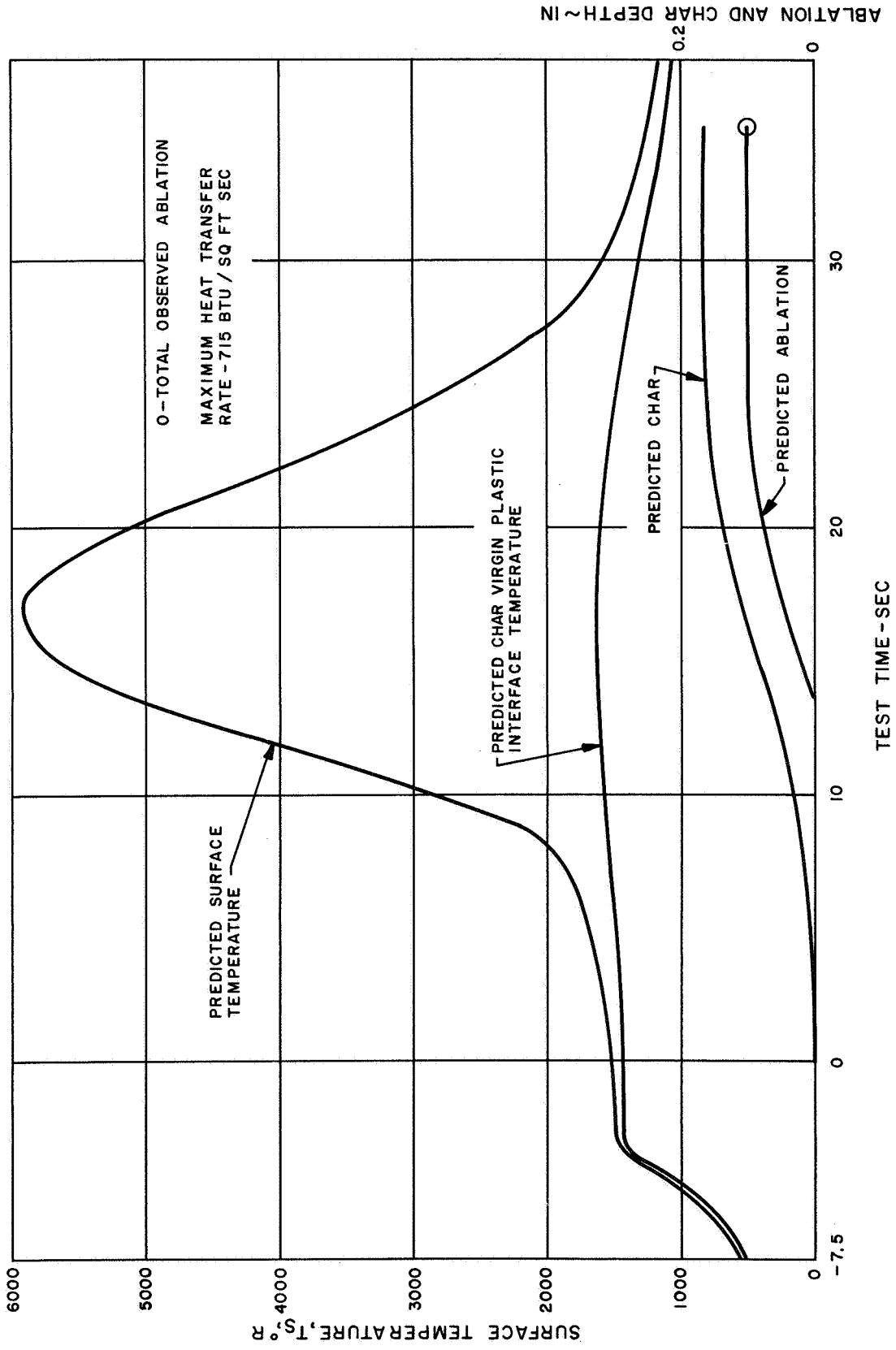

Figure II-4-7. Observed and predicted ablation and temperature of a typical thermosetting plastic for simulated re-entry heating

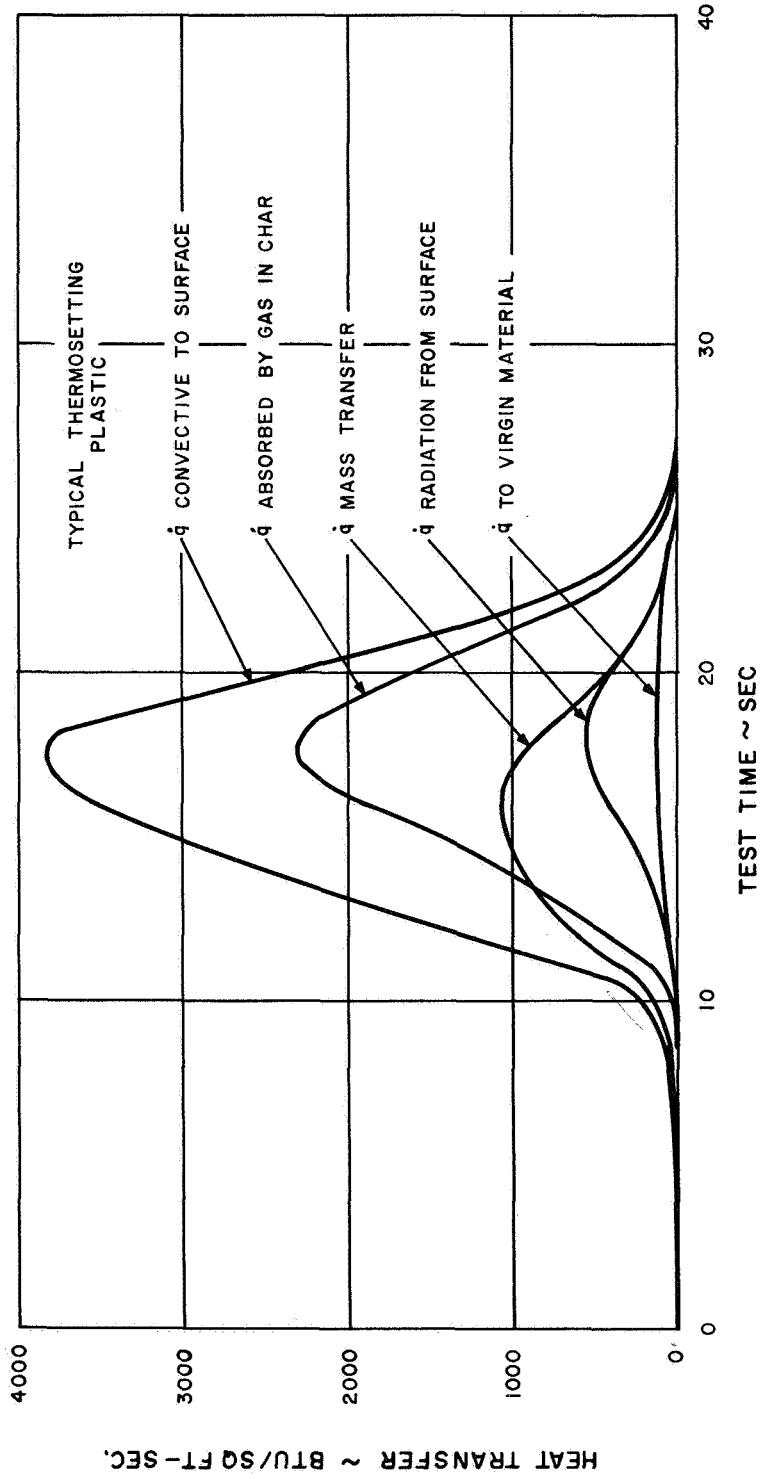

Figure II-4-8. Predicted partition of aerodynamic heating for simulated re-entry

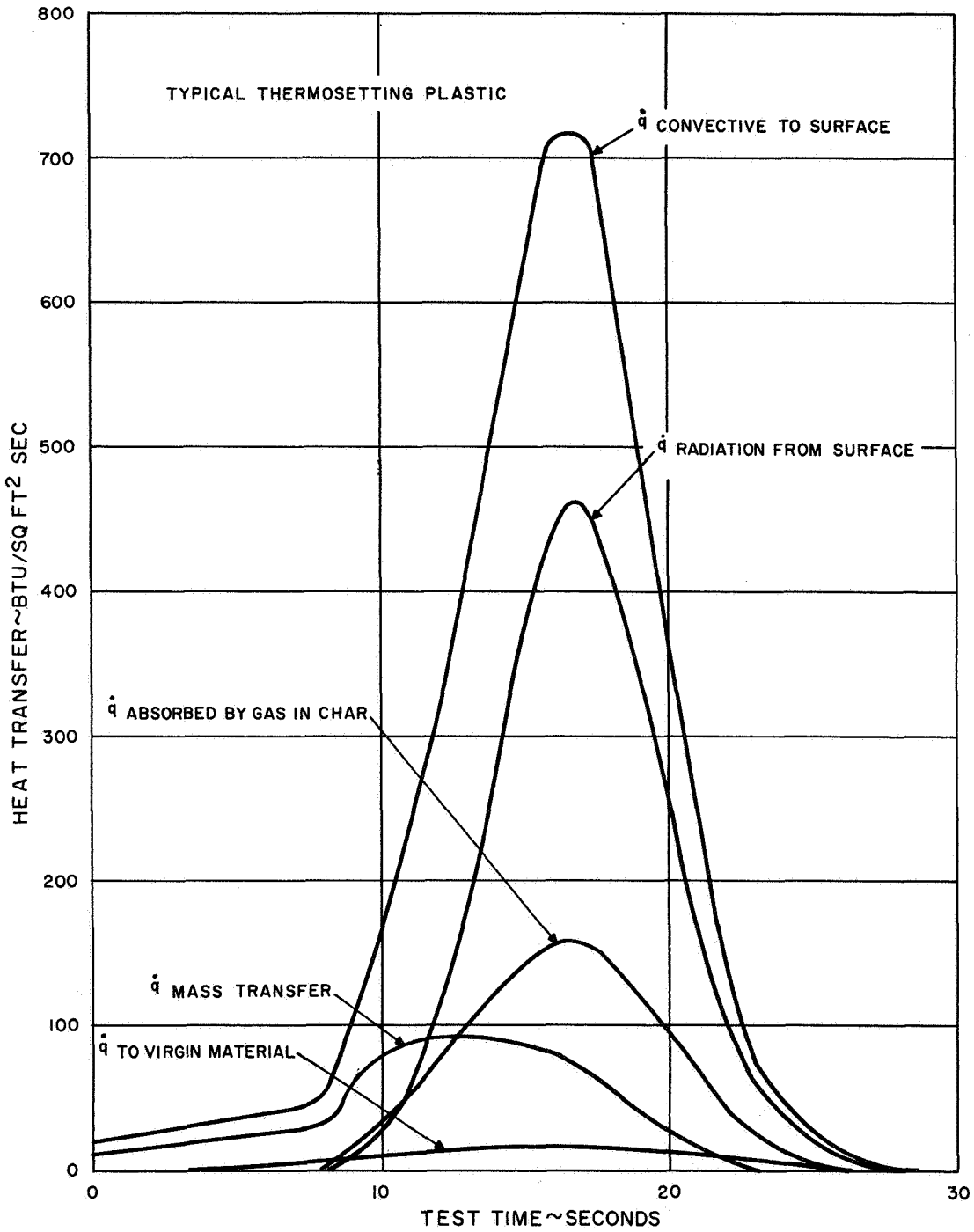

Figure II-4-9. Predicted partition of aerodynamic heating for simulated re-entry

A parametric study of the variation of a typical thermosetting plastic char peak surface temperature with peak aerodynamic heat transfer rate is shown in Figure II-4-10 for a constant char layer thickness of 0.006 inch. Two values of the mass transfer effectiveness parameter ($\Delta Q/\Delta \dot{m}$) are shown in Figure II-4-10 to point out the relative effect of mass injection into the boundary layer on peak surface temperature. Qualitatively, Figure II-4-10 shows that the char temperature is a strong function of aerodynamic heat transfer.

Parametric studies also showed that the char surface temperature decreased with char layer thickness for a given heating history. Figure II-4-10 shows the variation of char surface temperature with char layer thickness for a peak heating rate of 440 Btu/sq ft-sec. Results presented in Figure II-4-10 also show that for thin char layers ($\cong$ 0.005 inch), a large error in the estimation of the char layer thickness ($\approx$ 100 percent) would change the maximum surface temperature less than 300 to 500 F. This is significant since it is not possible to determine exactly the char layer thickness. Based on the analysis described above, then, a reasonable engineering approach for the prediction of the thermal degradation of thermosetting plastics, such as phenolic Nylon and General Electric Series 100 exists. With the analysis and results described above as a reference to the behavior of thermosetting materials, it is worthwhile to examine effective heat of ablation values of these materials obtained from ground facility and flight test as a function of enthalpy. These are summarized in Ref. (19). All of the data shows the expected increase with enthalpy as defined by the role of mass transfer.

Similar results were observed for the effective heat of ablation of inorganically reinforced thermosetting plastic such as phenolic refrasil as shown in Figure VI-2-8. The data in this figure illustrates the effect of combining a thermosetting resin and a quartz fiber. The effective heat of ablation increases with enthalpy due to mass addition effects from the thermosetting resin and the vaporization of the inorganic, quartz, as previously discussed. On the basis of analysis and flight test results, it would be expected that a similar increase with enthalpy would exist at even higher enthalpies, assuming that severe effects in depth are not incurred due to the high radiant energy emitted from the ionized gas cap at very high velocities.

4.2.7 Conclusions

With the previous discussion serving as essentially a review of the current

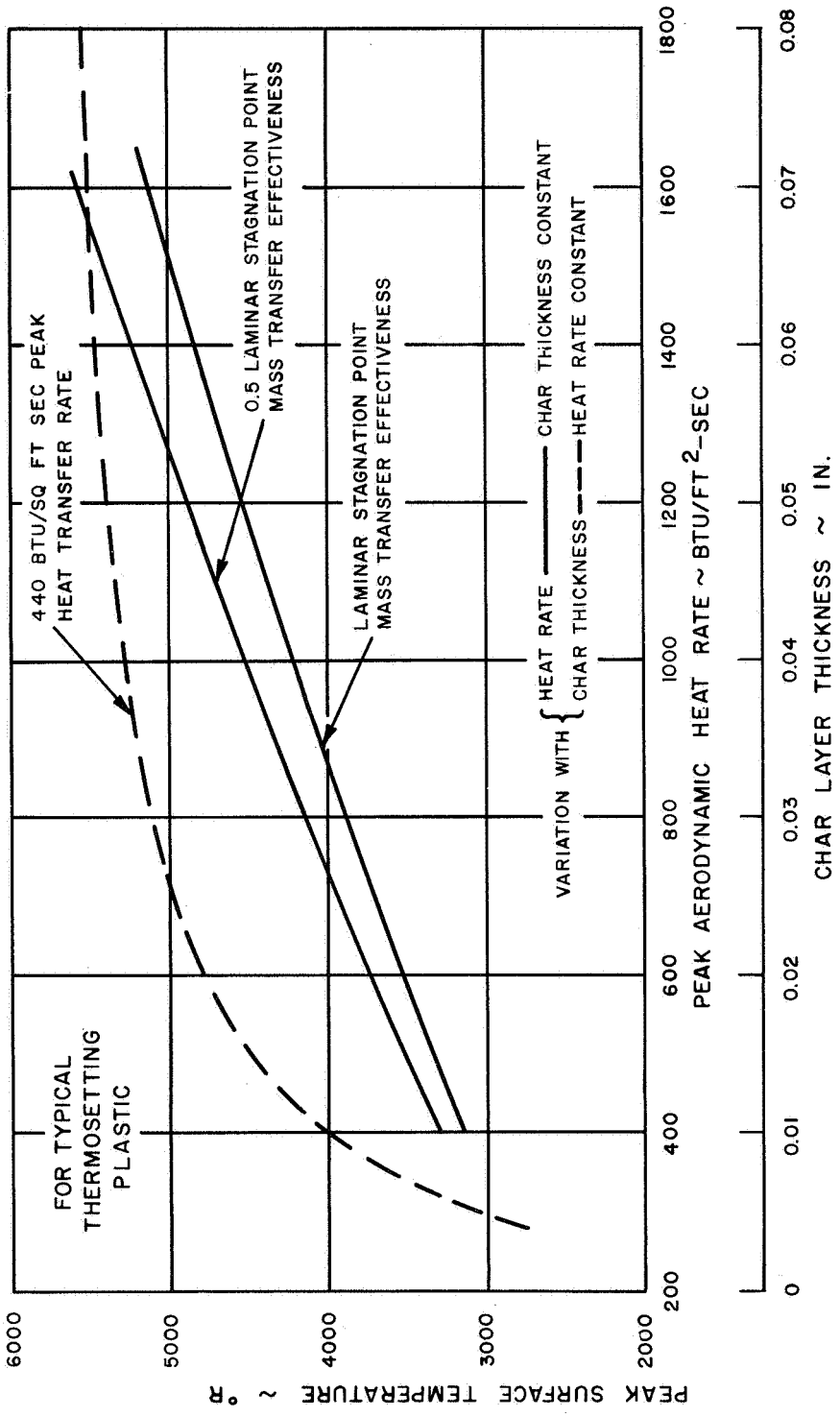

Figure II-4-10. Variation of surface temperature with heat rate and char thickness

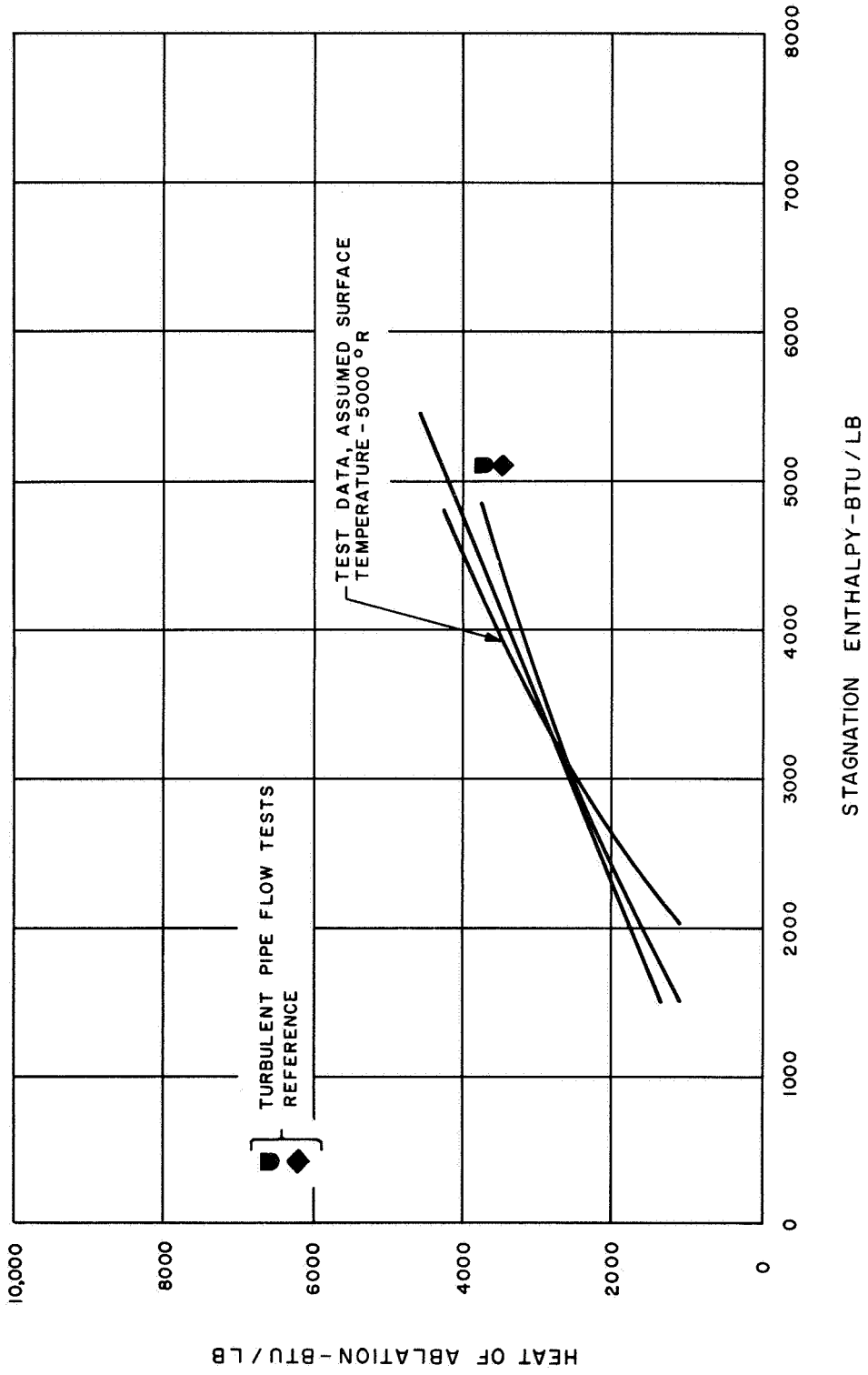

Figure II-4-11. Heat of ablation variation of typical thermosetting resin combined with quartz type reinforcement (turbulent flow)

state-of-the-art in the prediction of the performance of materials representative of four major classes of ablation materials it is possible to draw several conclusions relative to their desirable characteristics and their application to re-entry vehicles operating at the satellite and sub-orbital velocity regimes:

(1) Ablation materials should have high gasification ratios and yield gaseous products of low molecular weight. These gaseous products thicken the viscous boundary layer and reduce the rate of heat transfer.

(2) Ablation materials should have good thermal insulation properties in order to localize the ablation process and should degrade in a reasonably uniform fashion.

(3) Ablation materials should have a high resistance to thermal and mechanical shock and be easy to fabricate in large sizes.

(4) Sufficient theoretical, experimental and flight test data has been accumulated (with the possible exception of the refractory materials such as graphite) so that reasonably accurate engineering designs analysis for a given mission can be made.

(5) For ICBM application, many of the practical materials considered have comparable ablation performance, excepting quartz, in turbulent flow, which has approximately 50 percent higher values of Q* than materials such as phenolic Nylon and phenolic refrasil.

(6) For short re-entry times and high heating rates, ablation is an obvious selection; for long re-entry times and low heating rates, radiation cooling is an obvious selection. The nature of the heating pulse experienced during manned satellite or lunar re-entry conditions suggests a material which will act predominantly as an efficient re-radiator at low heating rates and as an efficient self-regulating mass transfer system at the higher heating rates. The combined ablation-radiation system should also have good insulation properties since the need for insulation will degrade the heat protection system.

(7) For comparatively low level heat transfer environments, the concept of Q* for describing material performance may be used for preliminary design purposes but more complete and accurate solutions for the material viscous boundary layer solutions. This is of particular importance in describing sub-surface temperature characteristics.

(8) The high surface temperature which thermosetting plastics can achieve, with their low interface temperature regulated by the decomposition characteristics are particularly effective for low level heat transfer regimes since much of the incident energy is radiated back to space while the interior temperature remain low.

4.3 NOMINAL PERFORMANCE OF ABLATION MATERIALS IN THE SUPERORBITAL VELOCITY REGIME

Based on experience gained from theoretical and experimental investigation conducted as part of ICBM re-entry vehicle programs nominal ablation heat protection performance in the super-orbital regime may be estimated, based on an extrapolation of current theory and experimental data to the super-orbital regime.

Figures II-4-12 A and B show an approximate extrapolation of theoretical and experimental results obtained for ablation performance in dissociated air. At high enthalpy levels, the primary contribution to the heat of ablation of the thermosetting and thermoplastic materials stem from the mass addition effect. In contrast to the sub-orbital regime the enthalpy of the gases at the material surface temperature is small compared to the blocking action effectiveness.

For laminar flow, the thermosetting plastic class of materials offers several advantages:

1. A high heat of ablation and high surface temperature
2. Low interface or conduction temperature and low thermal diffusivity.

Although the heats of ablation of both teflon and quartz type materials are about 30 percent lower than the typical thermosetting plastics for laminar flow, this difference is not as important as the high diffusivity and conduction temperature of quartz, compared to the thermosetting types of material and the low surface temperature of Teflon, which is highly ineffective for radiating the energy back to free space. In turbulent flow the thermosetting plastics have heats of ablation lower than quartz type materials, but are appreciably higher than the thermoplastic class of materials. As noted in the previous discussion the quartz type material performance from a system basis is hampered by its high conduction temperature and higher than thermoplastic diffusivity. A system comparison of these four classes of materials

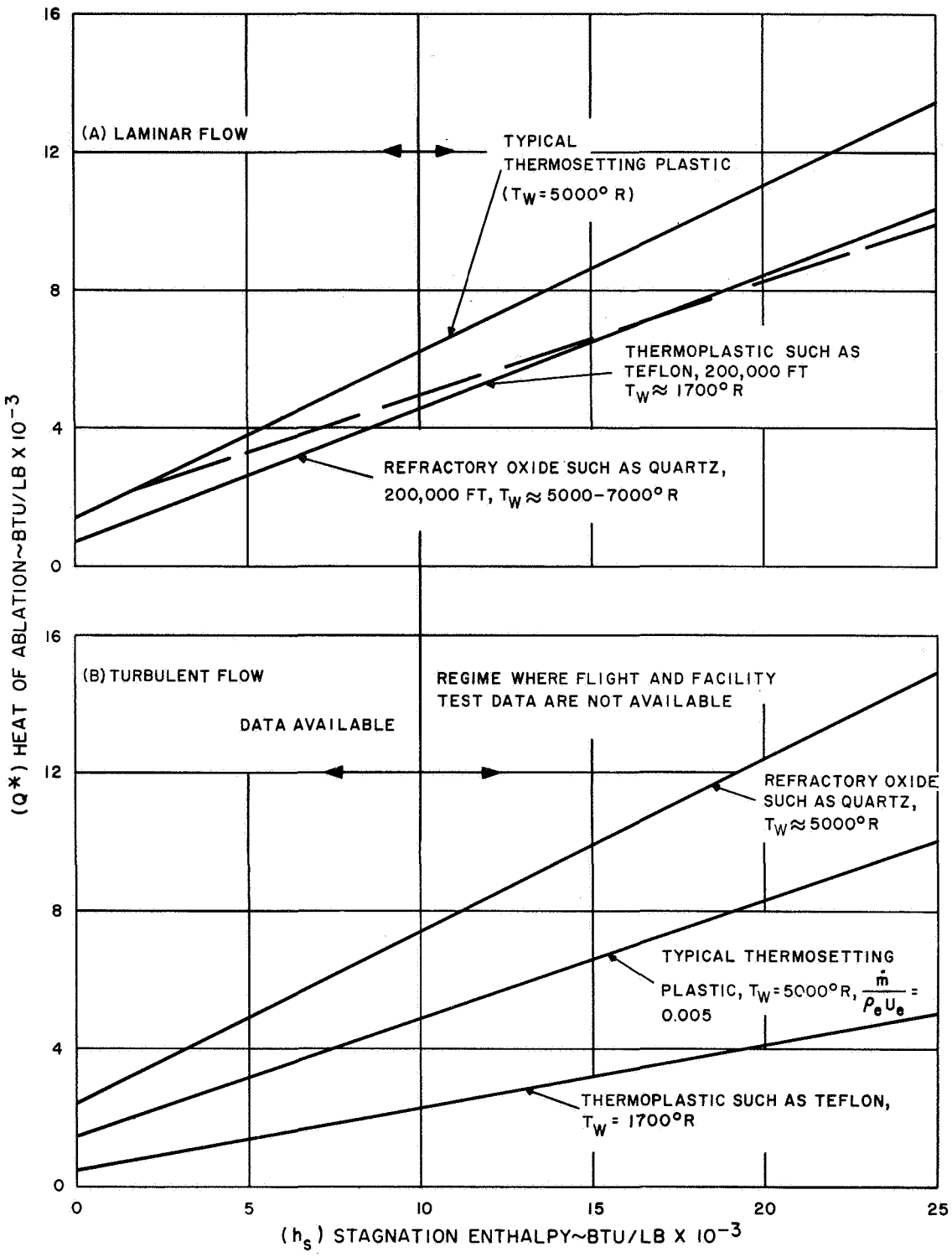

Figure II-4-12. Heat of ablation, typical heat protection system materials

for satellite application is given in Ref. (1). Excluding radiation, or other unforseen ionization effects the thermosetting class of ablation materials on the basis of present day knowledge appear to show to best advantage in orbital and/or super orbital velocity regimes. Including radiation it would appear that materials such as Teflon or quartz may be relatively transparent to radiative emission, although these materials may be "doped" to minimize such effects. Both reinforced plastics which char upon degradation and graphite act to block this radiation and localize its effects at the surface. From the standpoint of radiation effects on material performance it is obvious that experimental data must be obtained in the super-orbital velocity regime. For organically based materials immediate sub-surface damage may occur. However, as noted previously, the formation of thick char layers may tend to minimize this phenomena.

REFERENCES

(1) Scala, S.M. "TRANSPIRATION COOLING IN THE HYPERSONIC LAMINAR BOUNDARY LAYER", See General Electric MSVD TIS R59SD438, Sept. 30, 1959

(2) Scala, S.M. "A STUDY OF HYPERSONIC ABLATION", General Electric MSVD TIS R59SD438, Sept. 30, 1959

(3) Scala, S.M. and Ashley, W.R. Private Communication

(4) Stewart, J.D. "TRANSPIRATION COOLING - AN ENGINEERING APPROACH" General Electric TIS Report No. R59SD338, May 1959

(5) Walker, G.K. Schumann, B.A. "A DISCUSSION OF MKS'S ANALYSIS FOR A TURBULENT FOUNDARY LAYER WITH MASS ADDITION", General Electric TIS R61SD49, April 1961

(6) Hidalgo, H. "A THEORY OF ABLATION OF GLOSSY MATERIAL FOR LAMINAR AND TURBULENT HEATING" AVCO-EVERETT RESEARCH LABORATORY, Research Report 62, June 1959.

(7) Steg, L. "MATERIALS FOR RE-ENTRY HEAT PROTECTION OF SATELLITES" ARS Journal, Vol. 30, No. 9, Sept. 1960 pps. 815-823

(8) Bethe, H.A. and Adams, N.C. "A THEORY FOR THE ABLATION OF GLOSSY MATERIALS" J. of the Aero/Space Sci., Vol. 26, No. 6 June 1959, pp 321-328

(9) Adams, M.C., Georgiev, S., Hidalgo, H. and Powers, W. "A STUDY OF QUARTZ AS AN ABLATING MATERIAL" AVCO-Everett Research Laboratory Semi-Annual Report On Re-Entry Problem, Section II, June 1958. (Secret)

(10) Final Test Evaluation Report, AVCO RAD RVX 1-3 Flight of 11 June 1959, AFMTC Flight test No. 2006, Project Able, phase II, RAD-SR-9-59-43, 24 July 1959. (Secret)

REFERENCES (Continued)

(11) Scala, S. M., "The Ablation of Graphite in Dissociated Air", (to be published).

(12) Vidale, G. L., "The Vaporization of Graphite, TiC, ZrC. and Hfc, General Electric TM No. 155, June 1960.

(13) Scala, S. M. and Vidale, G. L. "Vaporization Processes in the Hypersonic Laminar Boundary Layer", International Journal of Heat and Mass Transfer", Vol. I, pp 4-22, 1960.

(14) Offenhartz, B., and Rose, P. H. "ABLATION MEASUREMENTS IN TURBULENT FLOW" Transactions at the Fourth Symposium on Ballistic Missile and Space Technology, Vol. II, Entry Vehicles and Hypersonics 24-27 August 1959.

(15) Gruntfest, I. J. and Shenker, L. H. "BEHAVIOR OF REINFORCED PLASTICS AT VERY HIGH TEMPERATURES" Part I, Modern Plastics, Vol. 35, No. 10, pp. 155-166, June 1958.

(16) Walker, C. K., "SOME COMMENTS ON LAMINAR AND TURBULENT HEAT TRANSFER EQUATIONS" General Electric Co., Aerophysics Engineering Tech Memo #147, Dec. 1959.

(17) Warren, V. R. and Diaconis, N. S. "THE PERFORMANCE OF ABLATION MATERIALS AS HEAT PROTECTION FOR RE-ENTERING SATELLITES", General Electric Co. IAS Paper No. 60-49.

(18) Shaw, T. E., and Stewart, J. D. "SUMMARY ANALYSIS OF G. E. -MSVD RVX-1 THERMO-DYNAMIC DATA, FLIGHTS 3 and 5" Transactions of the 4th Symposium on Ballistic Missile and Space Technology 24-27 August 1959.

(19) Shaw, T. E., et. al Flight and Ground Test Summary Analysis General Electric TIS Doc 60SD490, - to be published.

SYMBOLS

A	defined by Equation (16)	
C_p	specific heat -	Btu/lb°R
ϵ	Fraction of combustible pyrolized char	
E	activation energy	Btu/mole or calories/mole
g	acceleration of gravity -	32.2 ft/sec^2
h	enthalpy	Btu/lb
H_v	enthalpy of decomposition of virgin plastic	Btu/lb
k	specific reaction rate	
k_o	collision frequency	lb/sq ft-sec
K	thermal conductivity	Btu/ft-sec °R
m	mass transfer	lb/ft
$\dot{m}$	mass loss rate	lb/sq ft-sec
$\overline{M}$	mean molecular weight of gas	lb/mole
n	order of reaction Equation (5)	
P	pressure	lb/sq ft or atmospheres
(P_{O_2})	partial pressure of oxygen	
$\dot{q}$	heat transfer rate	Btu/sq ft-sec
Q^*	effective heat of ablation	Btu/lb
Q	energy function	Btu
R_N	nose radius	ft
R_B	base radius	ft
R	gas constant	ft-lb/lb-°R
T	Temperature	°R or °K

t	time	seconds
V	velocity	ft/sec
$\dot{W}$	rate of pyrolysis	lb/sq ft-sec
$(X_{O_2})_w$	Concentration of oxygen at wall	
x	length	ft
Γ	gasification ratio	
$f(\Omega)$	function of yaw angle - Equation (8)	
τ	shear stress	lb/sq ft
ϵ	emissivity	
σ	Stefan-Boltzman constant	Btu/sq ft °R ^{4}sec
ρ	density	lb/cu ft

SUBSCRIPT

c	denotes char
e	denotes conditions at edge of boundary layer
g	denotes gas
i	denotes i^{th} species
p	denotes plastic
s	denotes stagnation conditions or surface conditions
w	denotes wall conditions
v_p	virgin plastic
BF	back face

5.0 Recommended Tests for the APOLLO Heat Protection System

Estimates of the APOLLO heat protection system performance and weight have been based on certain assumptions for the calculation of the magnitude of the local aerodynamic and radiant heat transfer and the heat protection system material performance. The assumptions used have been based upon extrapolations of results of theoretical and experimental investigations conducted at sub-orbital enthalpy levels. For design purposes realistic system safety margins were applied consistent with the nature of the system mission. The success of these "a priori" estimates of system performance and margin can only be measured by those tests which fully simulate the mission profile.

Unfortunately, no experimental data has been obtained in the super-orbital velocity regime in the key technical areas which determine re-entry systems performance. These key technical areas are summarized in Table II-5-I. Note that several are included in addition to those directly associated with the thermal protection system such as aerodynamic heating and material performance.

The question may be logically asked as to what is "unique" or different about the super-orbital regime as contrasted to the sub-orbital regime. In brief, the phenomena "unique" to the super-orbital velocity regime, possible effects and the status of theoretical and experimental investigations are summarized in Table II-5-II. The primary unknowns then, are those associated with the high degree of ionization and air temperature. The extent of ionization (for equilibrium air) and the relation of current flight and facility test data to the proposed APOLLO lunar mission are shown graphically in Figures II-5-1 and II-5-2. A summary bar graph of these comparisons is shown in Figure II-5-3.

Key re-entry systems design information needs associated with the heat protection and related structural subsystems are itemized in Table II-5-III along with the required significant simulation parameter. General facility and/or flight test specifications for simulation are shown in Table II-5-IV.

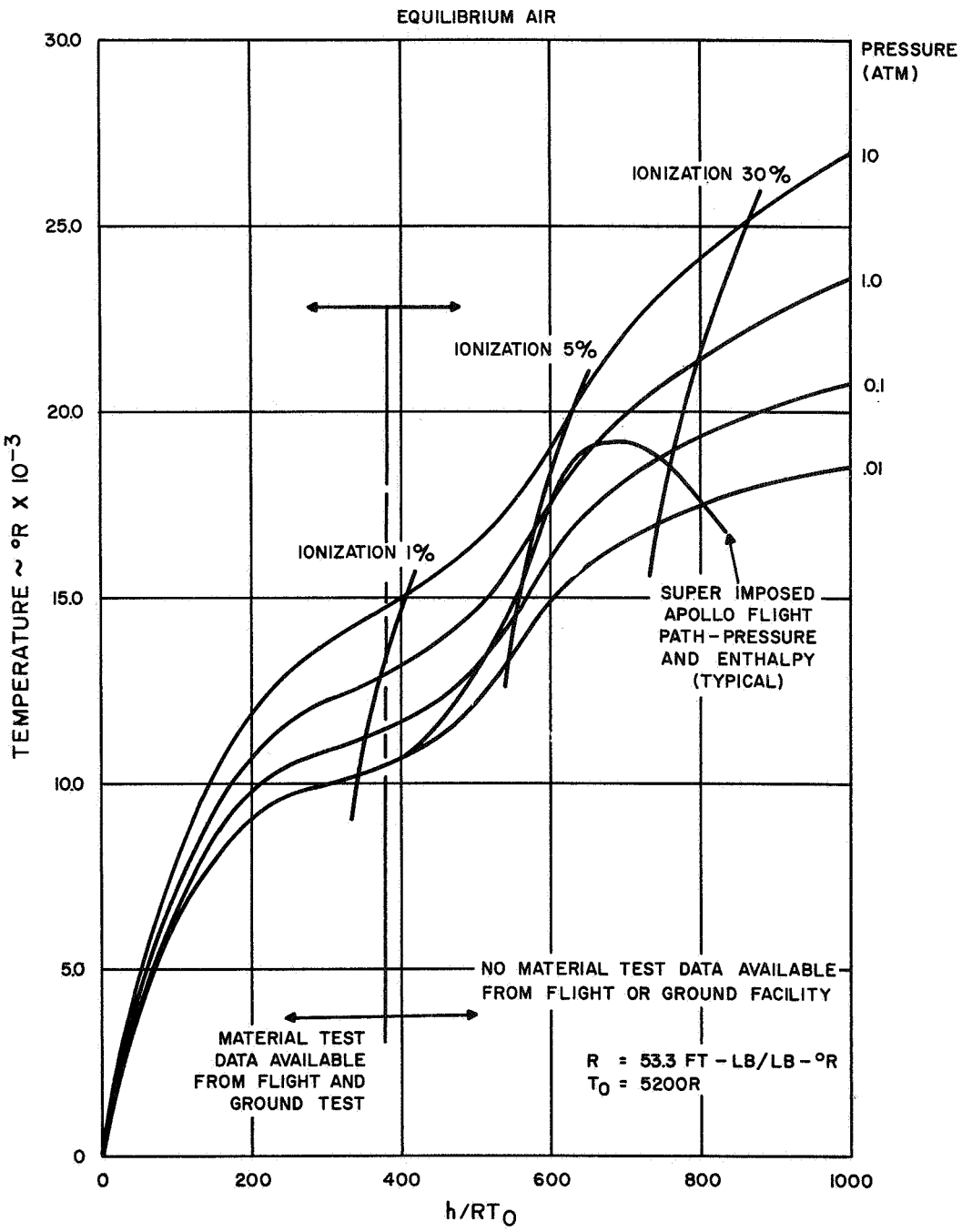

Figure II-5-1. Variation of temperature with enthalpy and extent of ionization

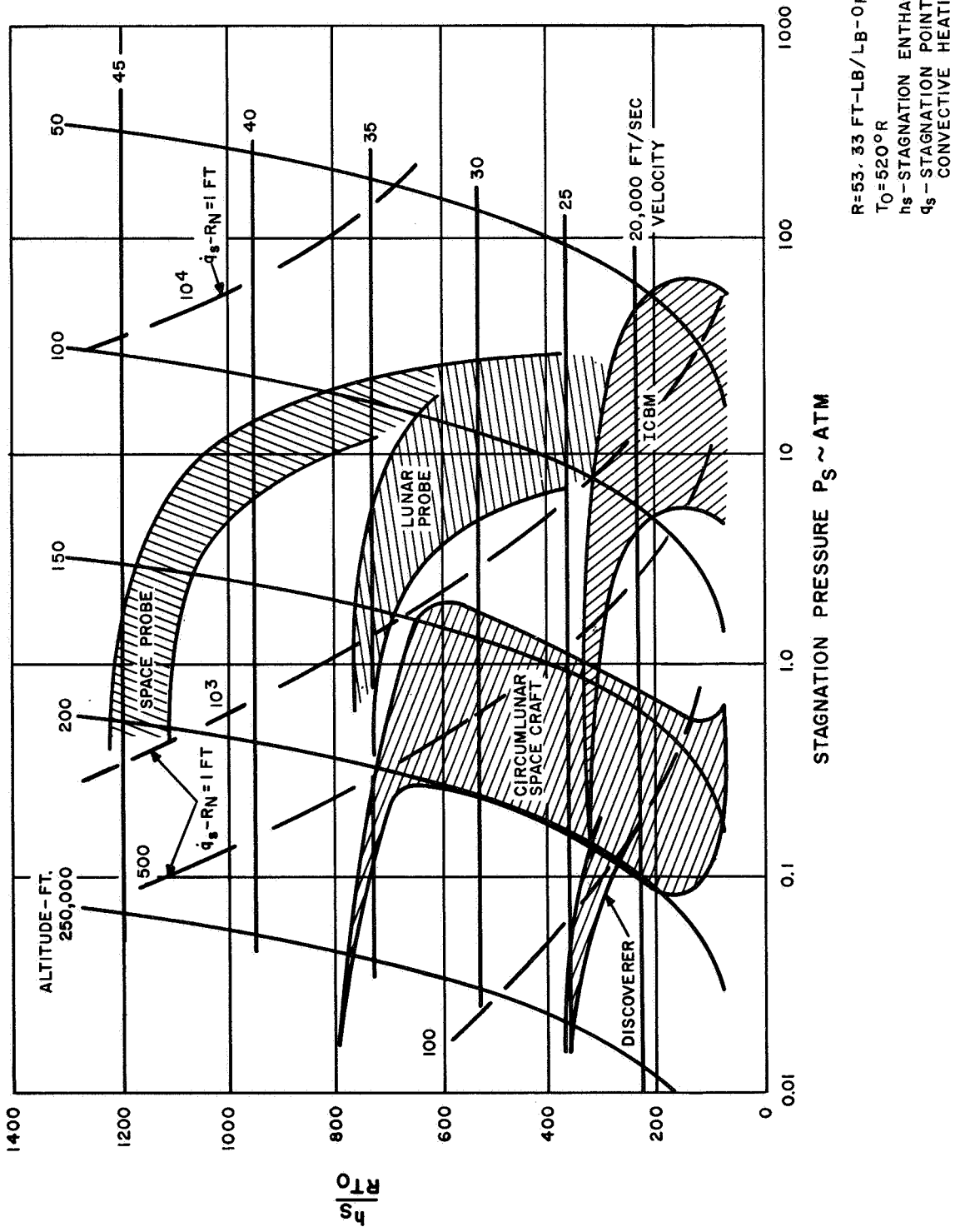

Figure II-5-2. Pressure enthalpy environment of re-entry

CONFIDENTIAL

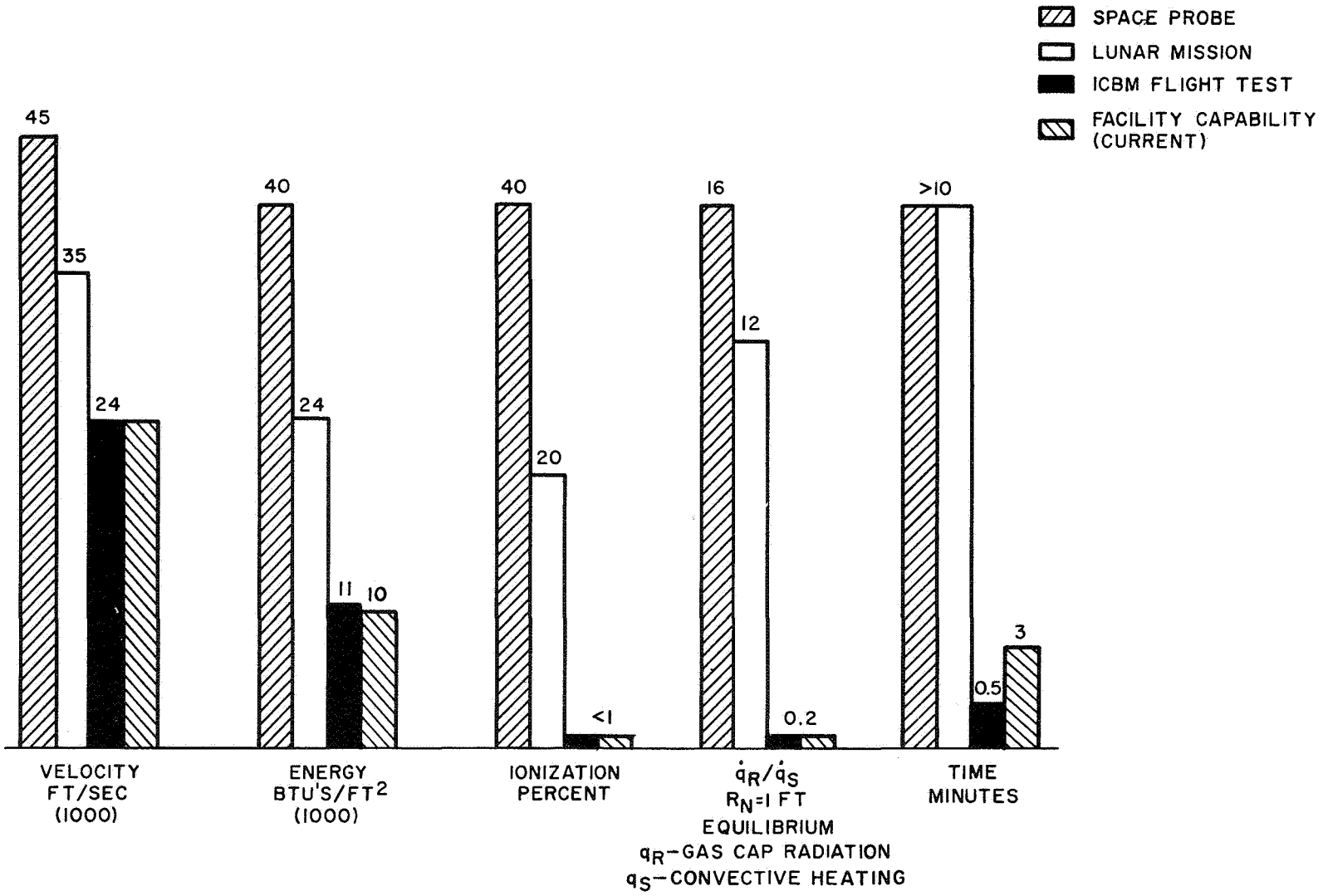

Figure II-5-3. Comparison of super orbital environment with current facility and flight test

CONFIDENTIAL

TABLE II-5-I

KEY TECHNICAL PROBLEMS OF THE SUPER ORBITAL VELOCITY REGIME

1. AERODYNAMIC HEAT TRANSFER
2. GAS RADIATION HEAT TRANSFER
3. HEAT PROTECTION SYSTEM RESPONSE
4. ELECTROMAGNETIC PROPAGATION
5. INSTRUMENTATION QUALIFICATION
6. FLOW FIELD CHARACTERISTICS
7. AERODYNAMIC CHARACTERISTICS
8. AEROTHERMOSTRUCTURAL SIMULATION

TABLE II-5-II

PHENOMENA "UNIQUE" TO SUPER-ORBITAL VELOCITY REGIME

1. HIGH AIR IONIZATION

EFFECTS:

A. SIGNIFICANT INCREASE IN CONVECTIVE HEATING
B. INTERACTION OF ENERGIZED PLASMA WITH HEAT PROTECTION MATERIALS
C. INTENSIFIED COMMUNICATION PROBLEM
D. INTERACTION OF ENERGIZED PLASMA WITH DIAGNOSTIC AND INFORMATION SENSORS

CURRENT STATUS:

Theory

1. EXTRAPOLATION OF EXISTING HEAT TRANSFER AND MATERIAL PERFORMANCE PREDICTION TECHNIQUES
2. THEORETICAL SOLUTIONS EXTREMELY DIFFICULT BECAUSE OF MANY COMPONENT BOUNDARY LAYER AND INVISCID FLOW

TABLE II-5-II

PHENOMENA "UNIQUE" TO SUPERORBITAL VELOCITY REGIME (Cont'd)

Experimental

1. NO DATA AVAILABLE
2. NO LARGE, LOW CONTAMINATION, HIGH ENTHALPY, GROUND FACILITY AVAILABLE
3. NO QUALIFIED DIAGNOSTIC OR INFORMATION SENSORS AVAILABLE FOR FUTURE FLIGHT TESTS

2. HIGH AIR TEMPERATURE

EFFECTS:

A. HIGH THERMAL RADIATION FROM AIR TO BODY (UP TO 10-20 TIMES CONVECTIVE FLUX)

B. HIGH NON THERMAL RADIATION EFFECTS ON MATERIALS

C. MATERIAL TRANSPARENCY AT SELECTED WAVE-LENGTHS

STATUS:

SAME AS AIR IONIZATION

TABLE II-5-III

DESIGN INFORMATION NEEDS

TECHNICAL AREA	SIGNIFICANT SIMULATION PARAMETER
AERODYNAMIC HEATING	VELOCITY, PRESSURE CONFIGURATION
RADIATION HEATING	VELOCITY, PRESSURE CONFIGURATION
HEAT PROTECTION SYSTEMS (INCLUDING COMPATIBLE INSTRUMENTATION AND INFORMATION SYSTEMS)	VELOCITY, PRESSURE CONFIGURATION MATERIAL TIME VELOCITY AND PRESSURE VARIABLE WITH TIME
AEROTHERMOELASTIC EFFECTS	VELOCITY, PRESSURE CONFIGURATION, MATERIAL STRUCTURAL DESIGN, EXPOSURE TIME VELOCITY AND PRESSURE VARIABLE WITH TIME
AERODYNAMIC AND FLOW FIELD CHARACTERISTICS	VELOCITY, MACH NUMBER, PRESSURE, CONFIGURATION

TABLE II-5-IV

GENERAL SPECIFICATION FOR SIMULATION

1. TOTAL AND VARIABLE ENTHALPY DUPLICATION
2. TOTAL HEAT FLUXES AND CONVECTIVE AND/OR RADIATIVE HEAT TRANSFER RATE SIMULATION
3. FLOW FIELD SIMULATION
4. TESTS WITH LARGE SCALE MODELS AND SEGMENTS OF THE VEHICLE
5. DUPLICATION OF RE-ENTRY ATMOSPHERE (AIR FREE OF CONTAMINATION)
6. TEST TIME COMPATIBLE WITH RE-ENTRY CYCLE

In obtaining design solutions for a given re-entry problem area, three parallel paths of investigation are usually followed: theory, ground facility tests, and flight tests. The results of these investigations are then reduced to engineering design techniques. For the APOLLO re-entry trajectory the aerothermodynamic properties (and hence the structural properties) of a given material are critically dependent on the environment in which the material must perform. Further, the aerodynamic performance may be critically dependent on the structural configuration selected. Thus, an integrated horizontal approach is recommended at the onset of the APOLLO program, to insure that all necessary data will be generated simultaneously for each category of materials which qualify for careful scrutiny. The broad relationships and responsibilities are illustrated in Table II-5-V. Such an integrated horizontal approach to material development is presently being followed at MSVD, for re-entry and space vehicle application. As shown in Table II-5-I there are many areas in which further theoretical effort may be expended. However, in the regime of complete dissociation and high ionization rigorous theoretical treatments become very complex and difficult. It is apparent, then, that an integrated, comprehensive test program is required to provide timely, technical support for APOLLO systems development.

Both ground facility and flight tests are required. Ground facility tests are a necessary complement to flight tests for the broad reasons presented in Table II-5-VI. The capability and flexibility of such a facility should be close to that listed in Table II-5-VII, Table II-5-VIII and Figure II-5-4. Unfortunately a ground facility with the capability of simulating conditions in the super-orbital velocity regime does not yet exist.

However, preliminary design of such a facility has been underway for some time at several installations throughout the country including GE-MSVD.

The flight test program associated with the APOLLO project should have the following primary objective in the areas of heat transfer and materials:

Obtain heat transfer and material performance data to compare with heat transfer and material performance extrapolated from sub-orbital theoretical and experimental investigations.

TABLE II-5-V

SYSTEMS APPROACH TO APOLLO MATERIALS RESEARCH

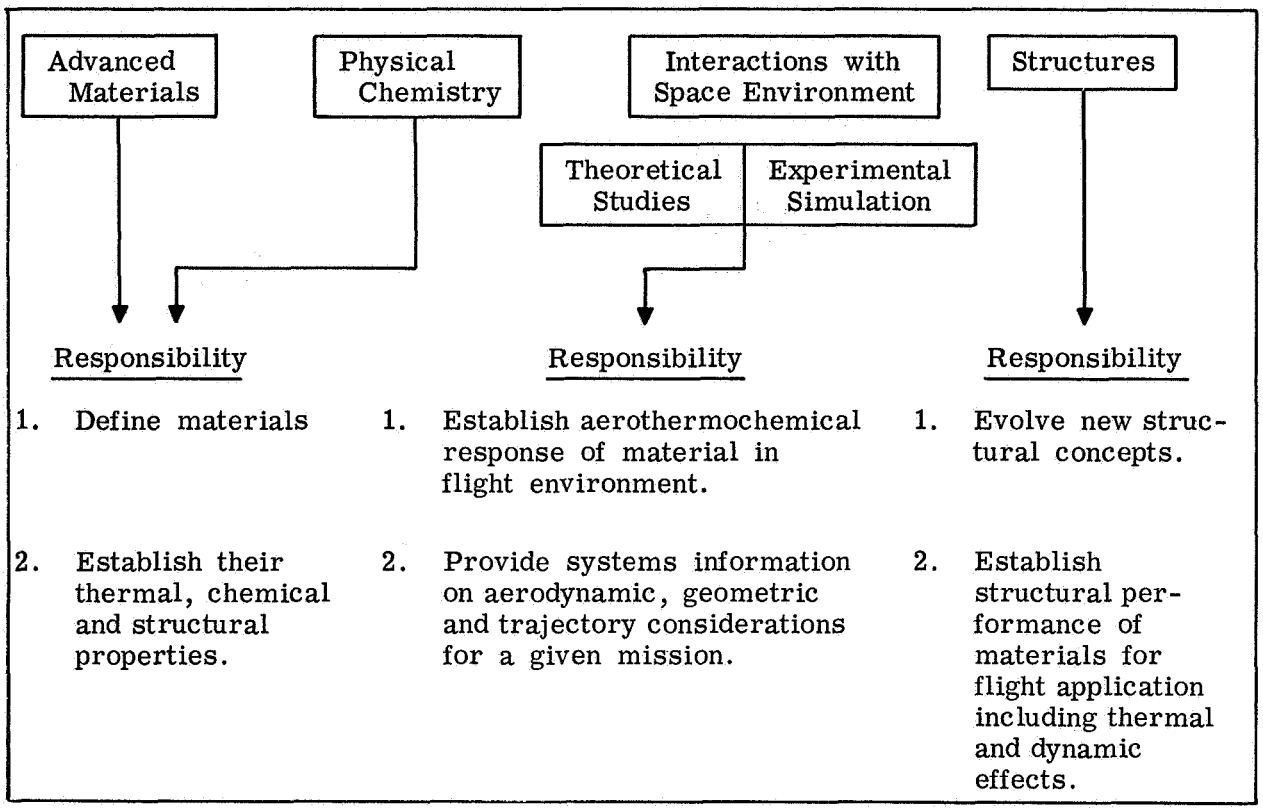

TABLE II-5-VI

UTILITY OF HIGH ENTHALPY GROUND FACILITY

I. DETERMINE RE-ENTRY SYSTEMS PERFORMANCE
   - A. SUPER-ORBITAL VELOCITY
   - B. SUB-ORBITAL VELOCITY

II. MINIMIZE EXTENT OF LARGE SCALE FLIGHT TESTS
   - A. REDUCE PROGRAM COST
   - B. MINIMIZE MANPOWER REQ'D.
   - C. MINIMIZE TIME TO DATA

III. PROVIDE TIMELY TECHNICAL SUPPORT FOR ADVANCED SYSTEM DEVELOPMENT

IV. COMPLEMENT EXISTING FACILITY CAPABILITY AND AVAILABILITY

TABLE II-5-VII

REQUIRED FACILITY CAPABILITY TO OBTAIN DESIGN INFORMATION NEEDS

REQUIREMENT	VALUE	FOR
CLEAN GAS	0.1 mass	ATMOSPHERIC SIMULATION
HIGH ENTHALPY (h/RT_0)	700	IONIZATION EFFECTS RADIATION HEATING-HEAT PROTECTION SYSTEM PERFORMANCE FLOW FIELD CHARACTERISTICS INSTRUMENTATION QUALIFICATION
LONG TEST TIME (MINUTES)	10-20	TIME DEPENDENT MATERIAL PERFORMANCE AEROTHERMO-ELASTIC EFFORTS
LARGE MODEL (DIAMETER-INCHES)	5-10	RADIATION HEATING STRUCTURAL AND HEAT PROTECTION SYSTEM PERFORMANCE
VARIABLE TEST CONDITIONS	ENTHALPY PRESSURE TIME	MATERIAL PERFORMANCE AERO-THERMOELASTIC EFFECTS
HYPERSONIC MACH NUMBER	7-8	FLOW FIELD SIMULATION MATERIAL PERFORMANCE (MASS TRANSFER)

TABLE II-5-VIII

REQUIRED FLEXIBILITY OF A HIGH ENTHALPY (AIR ARC) TO OBTAIN DESIGN INFORMATION

MODE OF OPERATION	FUNCTION
(1) FREE JET M_∞ ~1-3 MODEL SIZE → 2 INCHES PRESSURE → 50 ATMOSPHERES	CONVECTIVE AND RADIATION HEAT TRANSFER MEASUREMENTS
(2) SHROUD M_∞ <1.0 MODEL SIZE → 3-5 INCHES PRESSURE → 50 ATMOSPHERES	STRUCTURAL INTEGRITY INSTRUMENTATION QUALIFICATION MATERIALS TESTING AEROTHERMOELASTIC EFFECTS
(3) TUNNEL M_∞ ~7 MODEL SIZE → 8-10 INCHES PRESSURE → 50 ATMOSPHERES	STRUCTURAL INTEGRITY AEROTHERMOELASTIC EFFECTS HEAT PROTECTION SYSTEM PERFORMANCE INSTRUMENTATION QUALIFICATION FLOW FIELD-CONTROL SURFACE INTERACTION
(4) PIPE TEST M_∞ <1.0 MODEL SIZE → 4-6 INCH DIAMETER PRESSURE → 50 ATMOSPHERES	MATERIALS SCREENING - TURBULENT FLOW MATERIAL PERFORMANCE

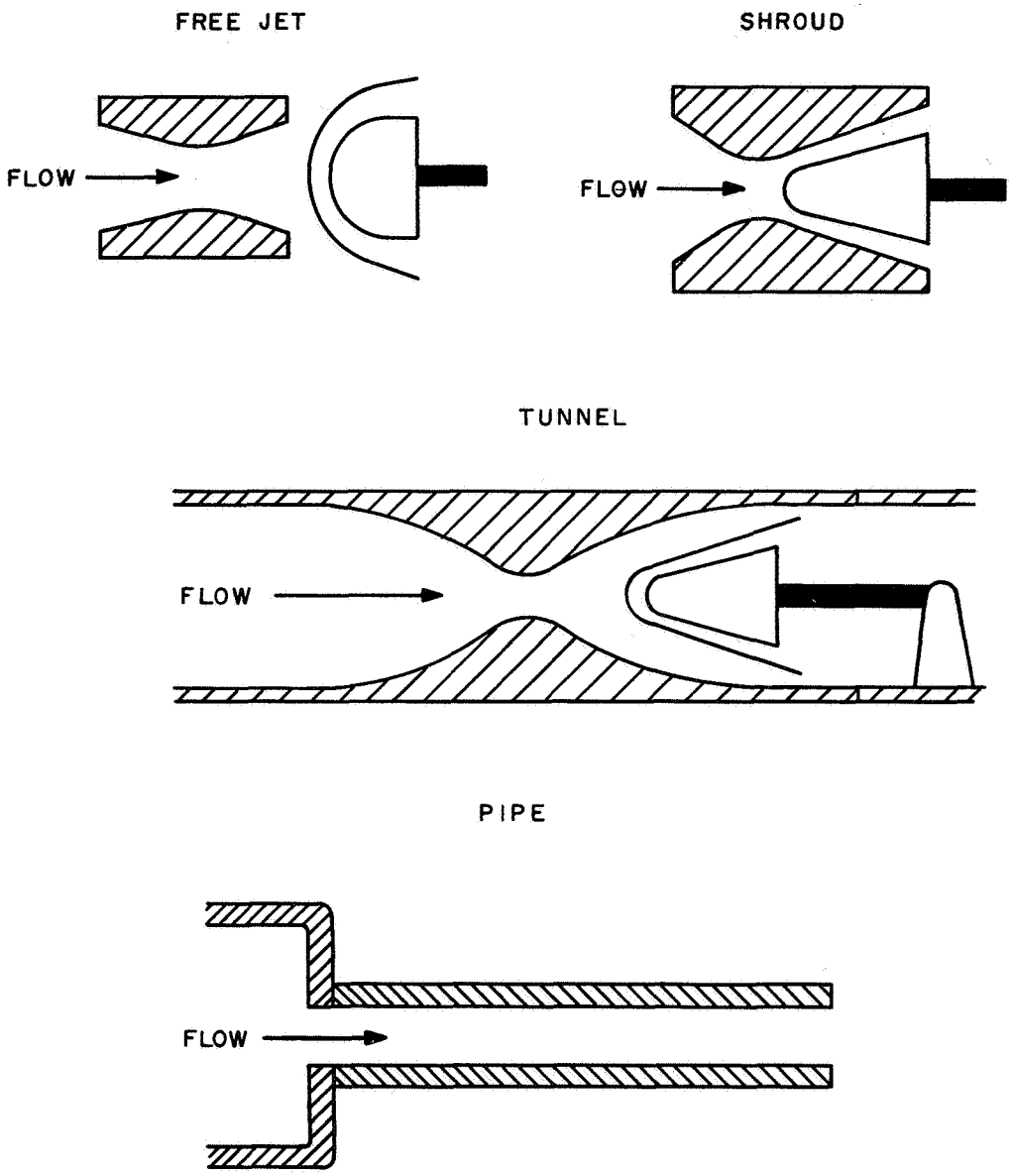

Figure II-5-4. Hypersonic arc configuration

Once preliminary information of this type is obtained, the direction of further ground and flight test programs can be determined and the validity of current facilities and data clearly defined. Specifically, then, the following specific tests are strongly recommended:

1) Aerodynamic heat transfer on a basic shape in the super-orbital velocity regime with an immediate velocity goal of 35,000 ft/sec.
2) Radiant heat transfer measurements in the super-orbital regime with an immediate velocity goal of 35,000 ft/sec.
3) Heat of ablation and thermal degradation of ablation materials with an immediate velocity goal of 35,000 ft/sec.

Extensions of current plasma arc facilities to meet the criteria of Tables II-5-VII and II-5-VIII should be initiated concurrently with flight test programs to assure that key design information can be acquired. This procedure is believed necessary as a complementary source of information if flight sensors, transmission problems and/or recovery problems prove extremely difficult and costly in time.

III. STRUCTURES AND MATERIALS

1.0 Structural Description

This section describes the structural arrangement, materials, type of construction, critical loading conditions, and design criteria for vehicles utilizing the selected D-2 semi-ballistic and the R-3 modified lenticular configurations.

1.1 SPACECRAFT STRUCTURAL DESCRIPTION — D-2 CONFIGURATION

The spacecraft structure exploits present state-of-the-art materials and fabrication techniques. The major portion of the spacecraft shell is conventional bonded aluminum honeycomb. As discussed below, studies indicate this to be the lightest structure and a very effective means of meteoroid protection. The forward conical section, Station (88.50) to (128.80) consists of an aluminum skin and eight longerons that support the mission module. The forward ejectable nose fairing, Station (0.00) to (46.00), is of semi-monocoque aluminum construction. This fairing is attached to the structure at Station (46.00) with a Marman-type splice. Ejection is accomplished by two explosive bolts on the Marman band and a spring loaded release system. The forward conical section, Station (0.00) to (88.50), is coated with epoxy to protect the structure during exit heating. The D-2 spacecraft structure is shown on Figure III-1-1.

The propulsion system, (discussed in detail in Volumn IV), consisting of hydrogen and oxygen tanks, engines, and associated hardware, is located in the aft cylinder and flare sections. The propulsion module is supported by a stiffened conical shell that joins the propulsion ring to the spacecraft shell frame at Station (379). The use of the cone results in lightest support structure since it affords a continuous attachment to the spacecraft structure, thereby reducing the frame size and longerons required for multiple leg supports.

1.1.1 Separation Device

For the large diameter sections requiring separation, Stations (238.57), (376.57), and (379.17), the shaped charge separation system is proposed. This system uses a ring of preformed RDX explosive of predetermined cross sectional area and shape to completely sever the shell structure circumferentially. Extremely small quantities of explosives may be used, with proper development of shape, and the inherent stability of the explosive virtually eliminates danger during and after installation with proper interlocks, shorting devices, and safearm initiators. This type of separation device is currently used on the Minuteman program and has been employed extensively in warhead applications. Multiple charges may be employed to assure reliability of separation, and an aluminum back-up ring containing the charge would be employed to minimize internal blast and fragmentation effects. The back-up ring may not be required if the proper charge is developed for the desired blast propagation. Advantages of the shaped charge are much lighter weights than the Marman clamp system and higher reliability over multiple explosive bolts or mechanical linkage systems. In addition, the shaped charge does not interfere with the shell structural continuity as would local bolt fittings and load redistribution members.

1.1.2 Radiator

The radiator, discussed in Volume VII, is an integral part of the spacecraft honeycomb shell structure extending approximately from Station (238) to (376) and 150 degrees around the circumference. Choice of this location was based on a requirement for continuous radiator structure, for light weight, non-interference with separation joints and suitable radiator area. The radiator consists of a series of aluminum tubes brazed to the inner surface of the outer honeycomb face. The core is notched to allow clearance of tubing resulting in a clean, structurally sound composite honeycomb panel.

1.1.3 Solar Collector

The solar collector is shown on Figure III-1-2. The collector assembly consists of three basic components; the solar cell panel, a reflector, and a collimator. This primary assembly is deployed and supported by a telescoping central support column stabilized by three or four support cables as shown on Figure III-1-3. This solar cell panel and collimator are of rigid aluminum construction and the large parabolic reflector is a collapsible reflective-coated mylar structure. The reflector is extended

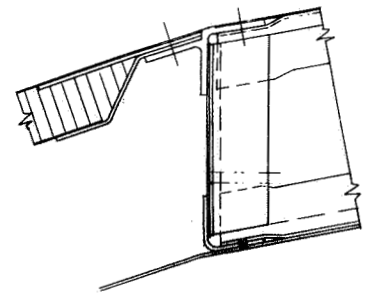

DETAIL B

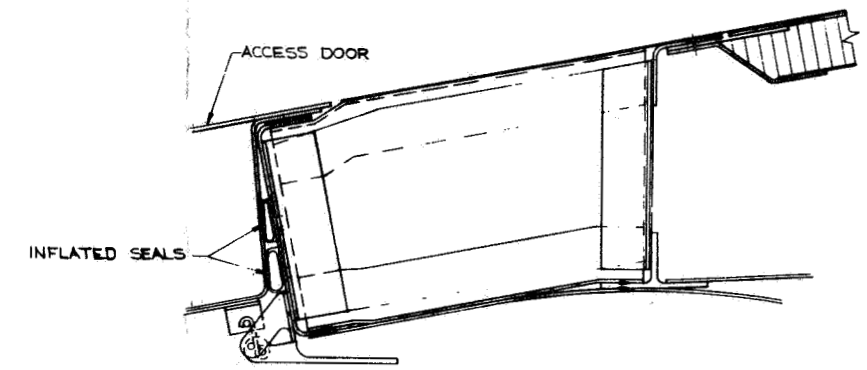

DETAIL C

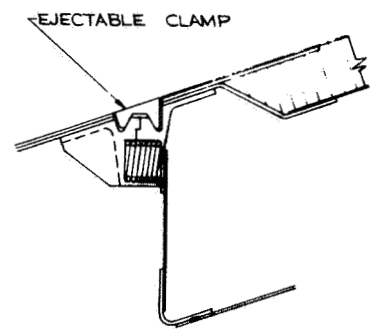

DETAIL A

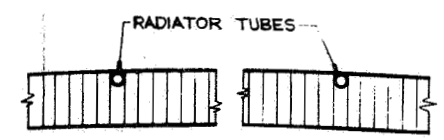

SECTION N-N

DETAIL G
SCALE 1=4

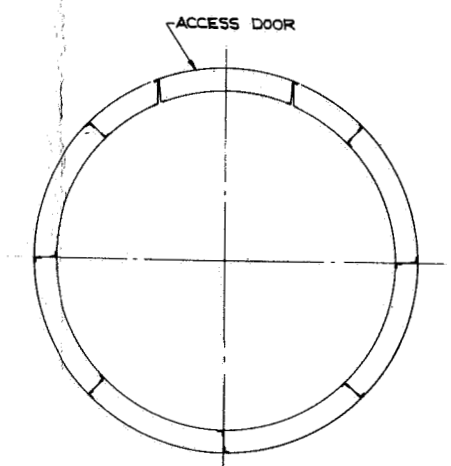

SECTION M-M
SCALE 1=10

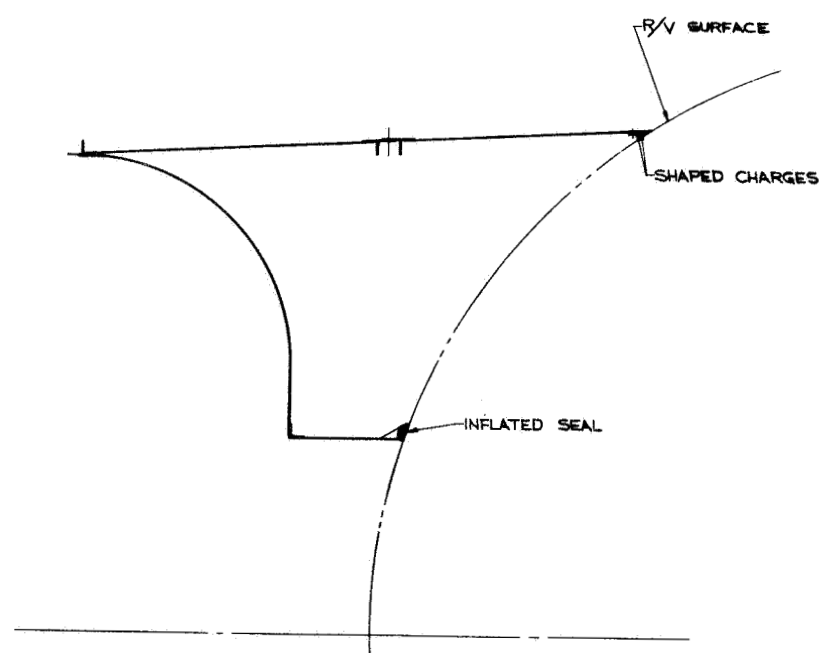

VIEW E
SCALE 1=4

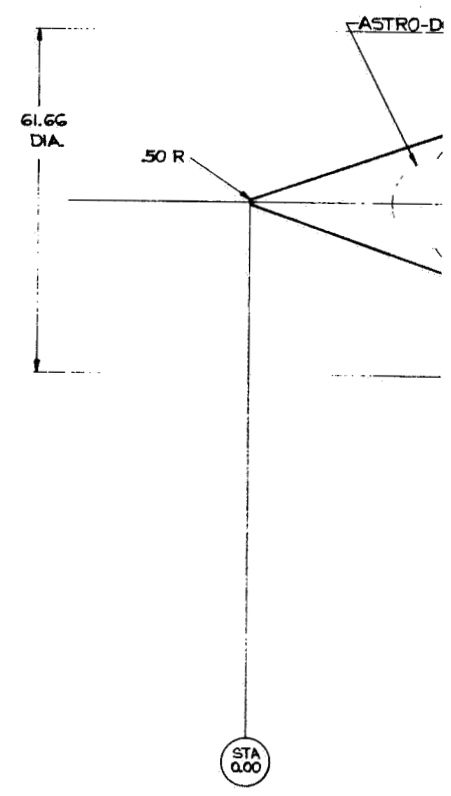

~~CONFIDENTIAL~~

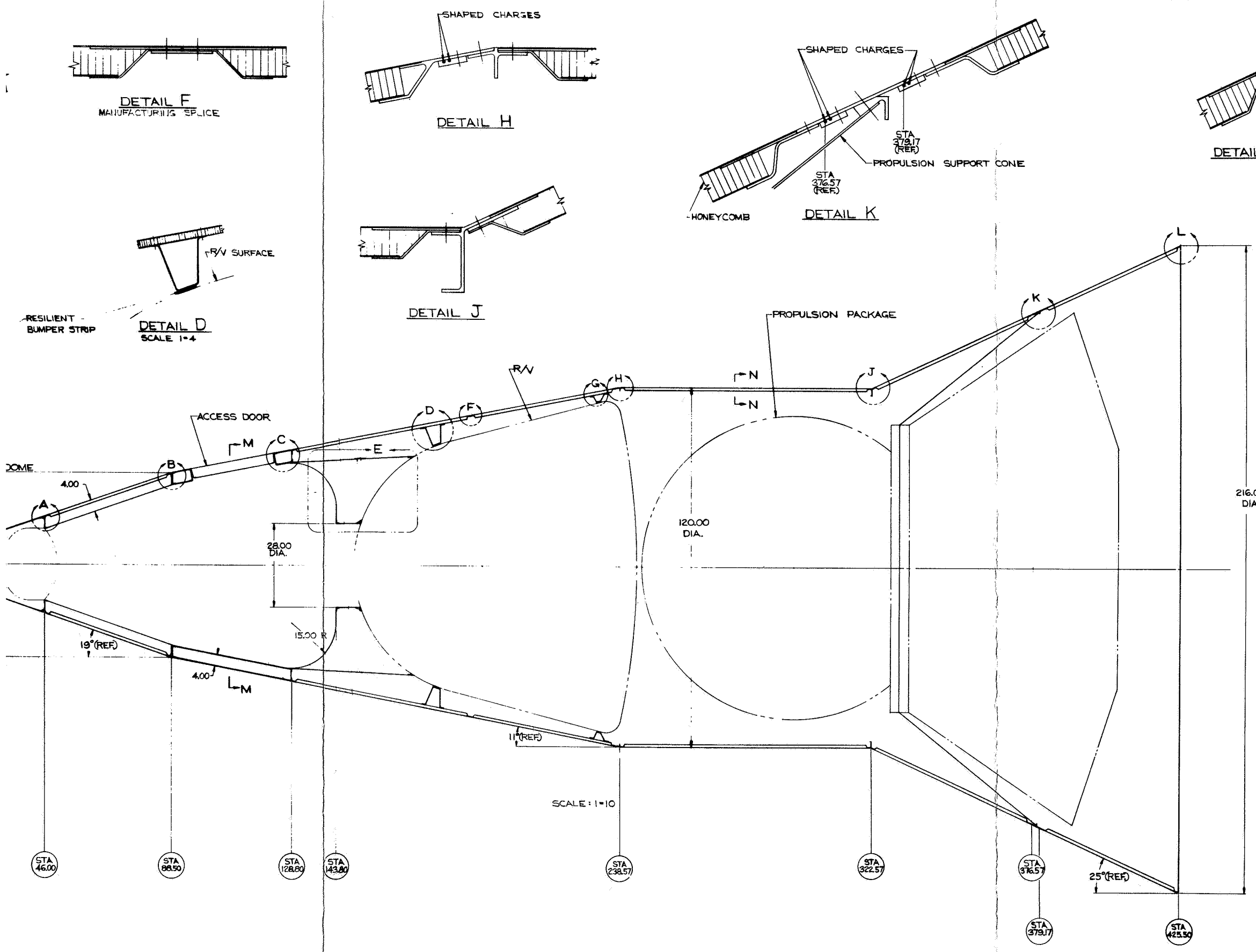

Figure III-1-1. D-2 Configuration - structural arrangment, space vehicle

~~CONFIDENTIAL~~

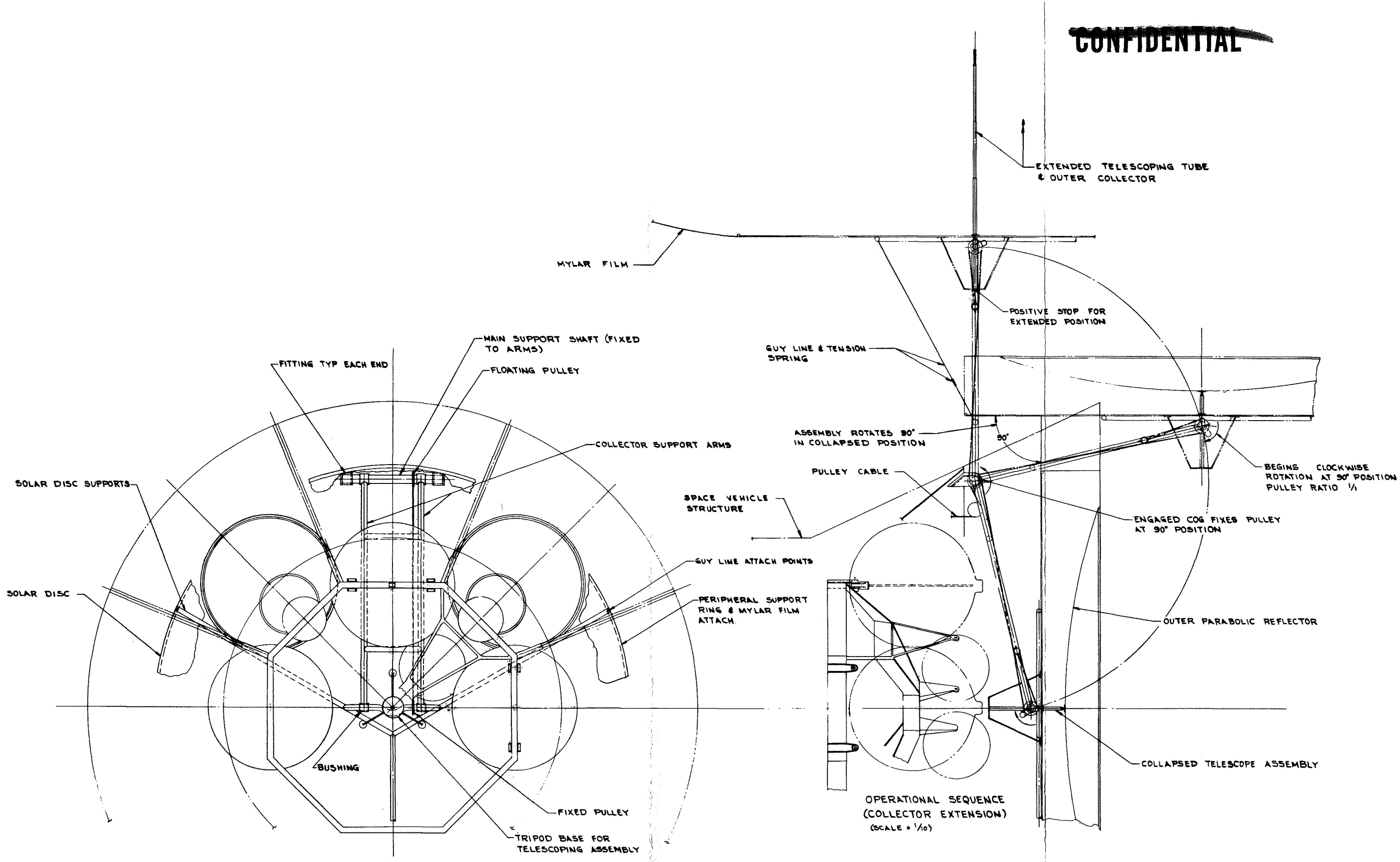

Figure III-1-2. Design proposal solar concentrator

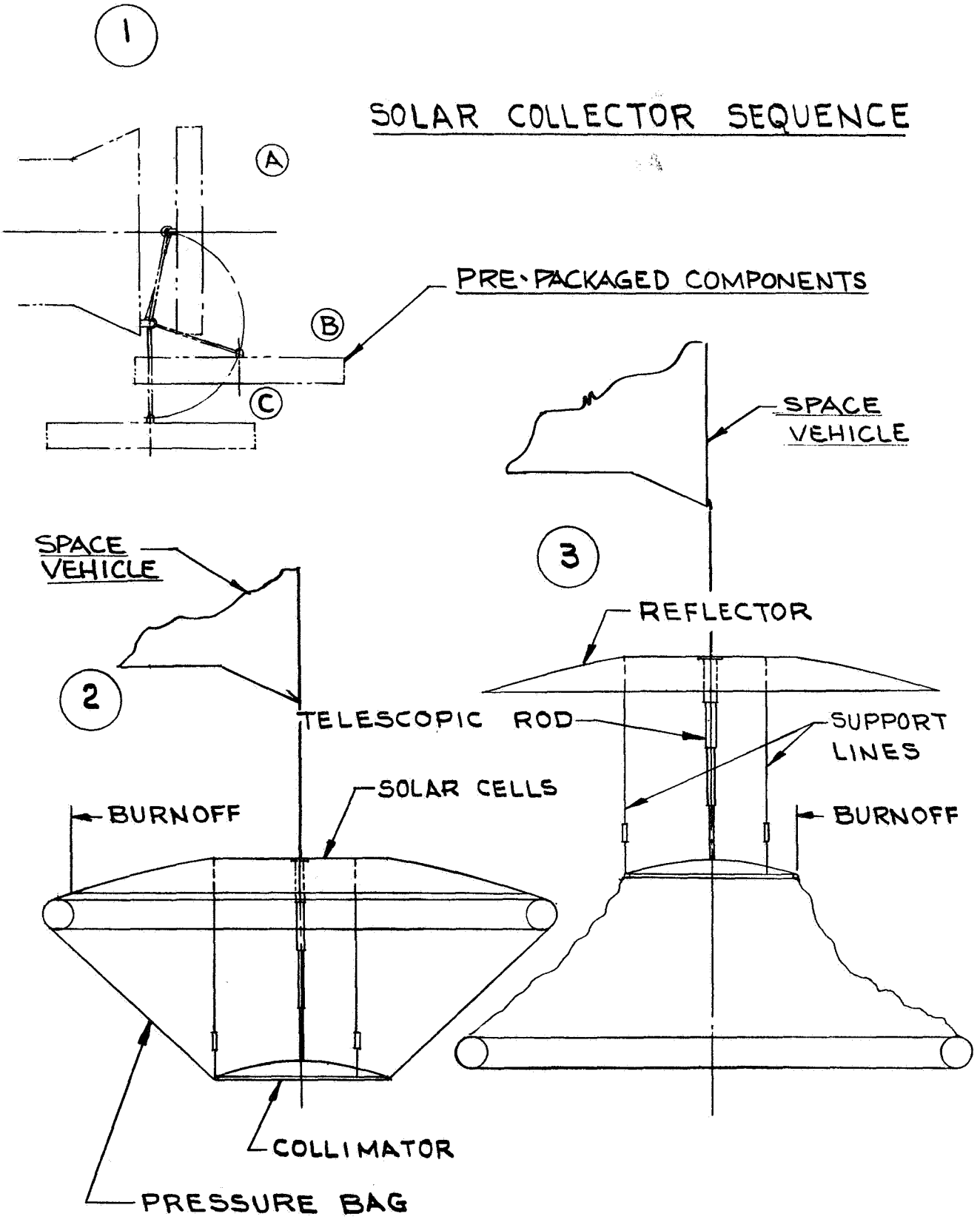

Figure III-1-3. Solar collector sequence

after deployment of the assembly by an inflating mylar bag. The reflector surface is rigidized by a heat-hardenable coating or by a foam-in-place back-up. After rigidizing, the inflation bag is burned off, leaving the operational collector configuration.

1.1.4 Communication Antenna

The communication antenna, Figure III-1-4, is located in the aft flare section and is extended after separation from the S-IV stage and solar collector extension. The antenna must point toward earth and therefore is provided with capability for two axis gimbal orientation by the crew.

1.2 MISSION MODULE STRUCTURAL DESCRIPTION — D-2 CONFIGURATION

The mission module is of welded aluminum construction. All frames and support members will be either spot or seam welded to the pressure shell. Since pressure leakage must be kept to a minimum, welded structure was chosen and close control and inspection will be required to insure welding integrity. Access to the mission module is through an access door that is integral with the spacecraft and mission module structure. The door is of aluminum construction and is pressure sealed by the use of two inflatable tubes providing positive sealing between the door and mission module structure.

The re-entry vehicle tunnel is welded to the aft section of the mission module pressure shell. The tunnel is a 28 inch diameter aluminum tube.

1.3 RE-ENTRY VEHICLE STRUCTURE — THE SELECTED SYSTEM, D-2

The structural drawing, Figure III-1-5, shows the basic load carrying structure, the thermal shield and the insulation installation proposed for the D-2 re-entry vehicle. The re-entry vehicle structure, utilizing conventional types of construction, materials, and fabrication techniques, is designed for the loads and environmental conditions discussed in the previous chapters of this volume. The re-entry vehicle re-entry heating environment, thermal shield distribution, thermal shield materials, and the internal insulation are described in Volume VI, Chapter II. The design of the thermal shield, a thermosetting plastic such as phenolic nylon or GE series 100 is based on an allowable maximum substructure temperature of 400 F to permit the use of aluminum shell structure. The pressure cabin structural skin temperature is held to a maximum temperature of 105 F by the use of an insulation barrier externally attached to the pressure cabin skin.

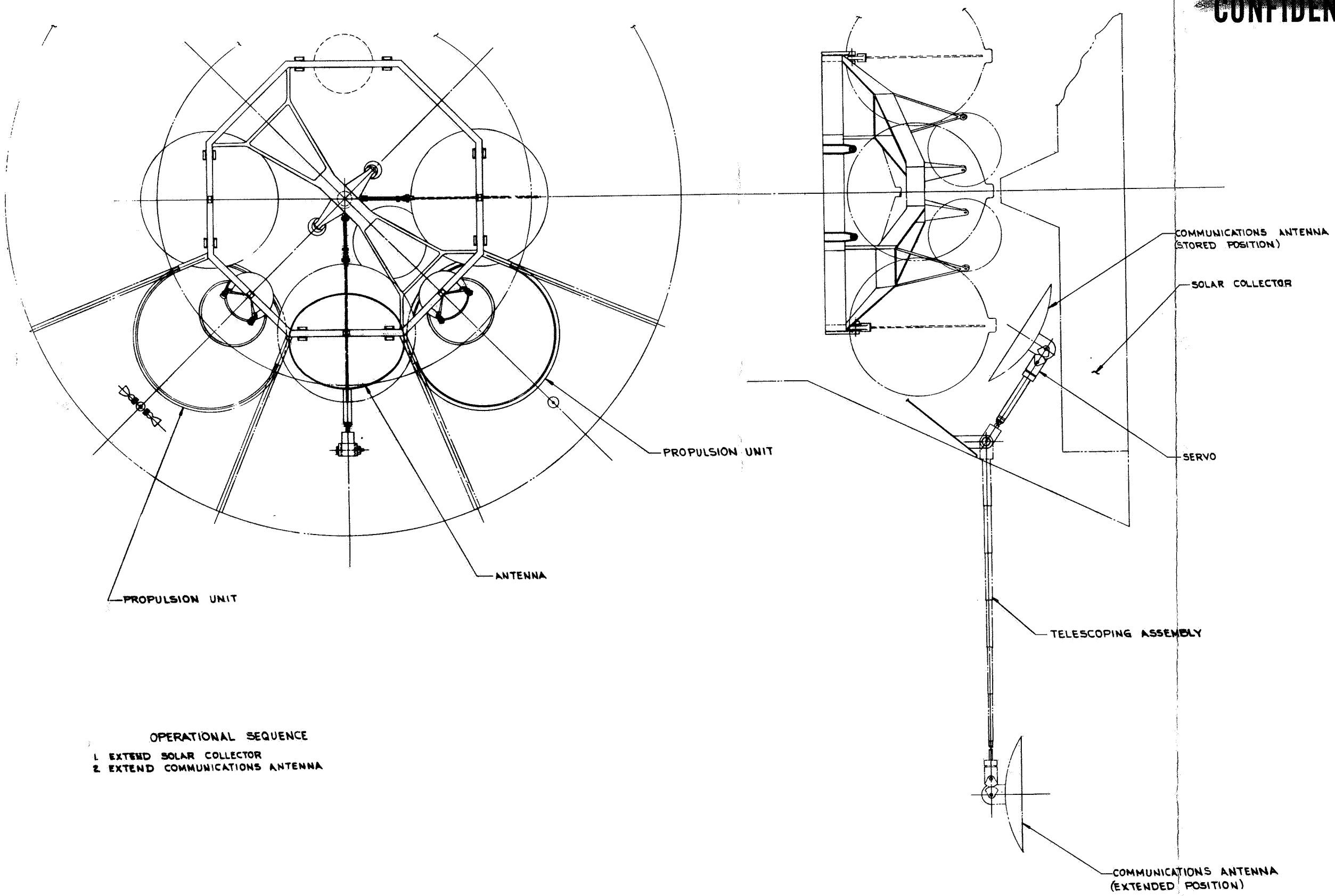

OPERATIONAL SEQUENCE

1. EXTEND SOLAR COLLECTOR
2. EXTEND COMMUNICATIONS ANTENNA

Figure III-1-4. Communications antenna arrangement

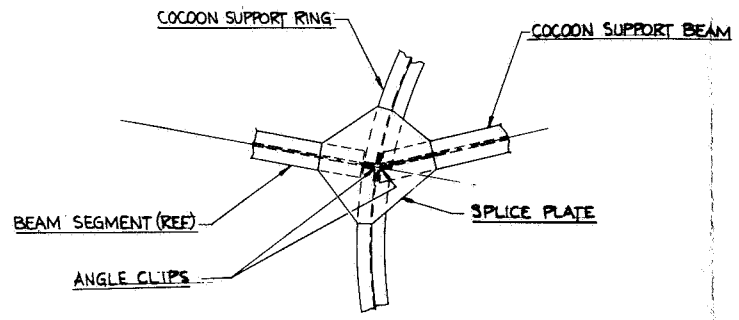

VIEW 'F'
COCOON SUPPORT BEAM JOINT
TYPICAL 8 PLACES

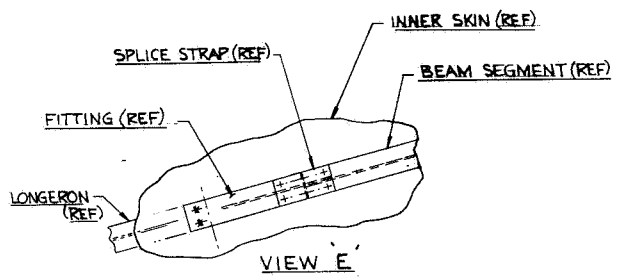

VIEW 'E'
TYP. SPLICE STRAP - 8 PLACES

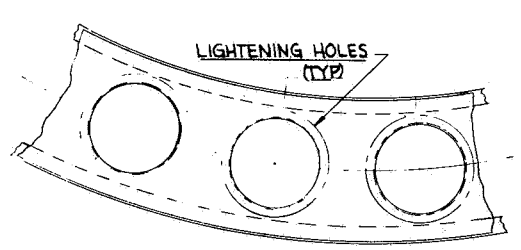

VIEW 'G'
FRAME CONFIG.

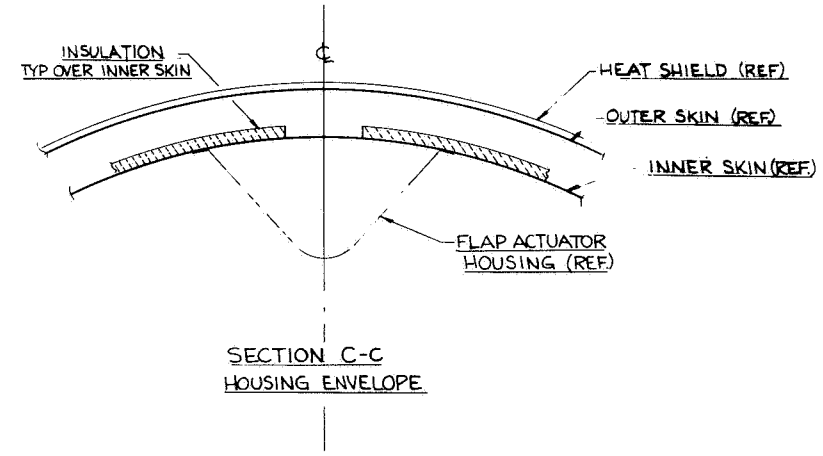

SECTION C-C
HOUSING ENVELOPE

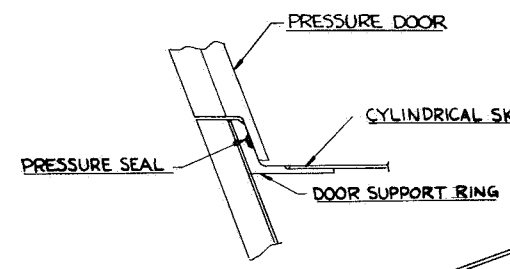

DETAIL 'A' (ENLARGED)

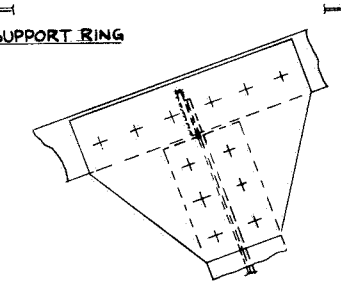

TYP GUSSET INST'L
8 PLACES

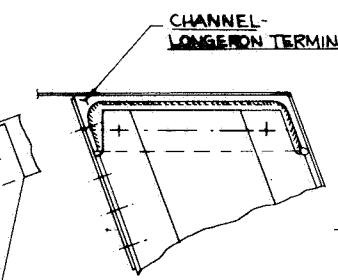

DETAIL 'B' ENLARGED

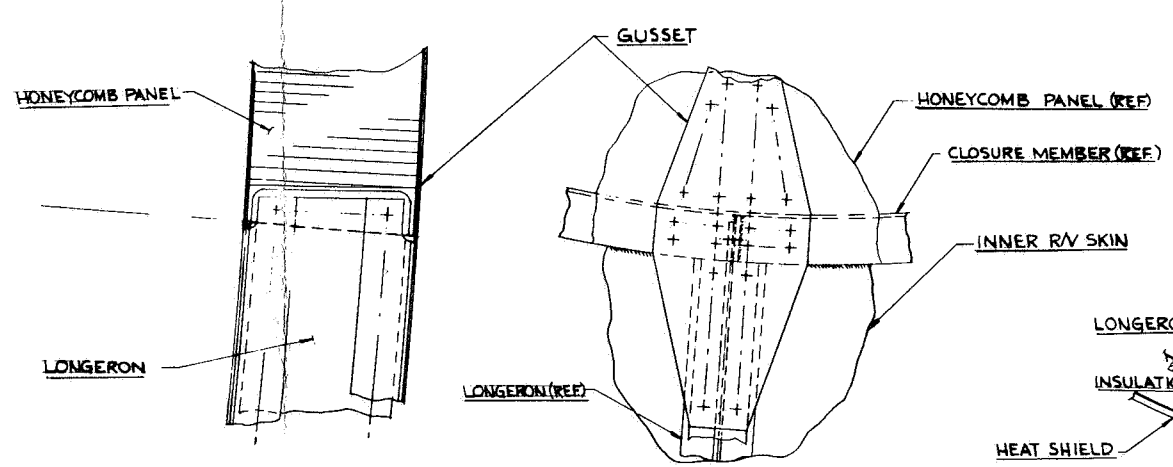

DETAIL 'C' ENLARGED

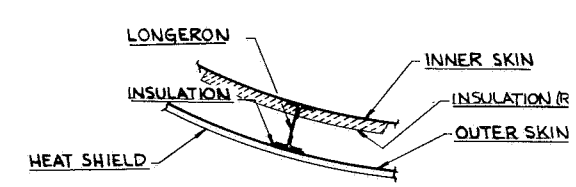

SECTION B-B
LONGERON - TYP 8 PLACES

2

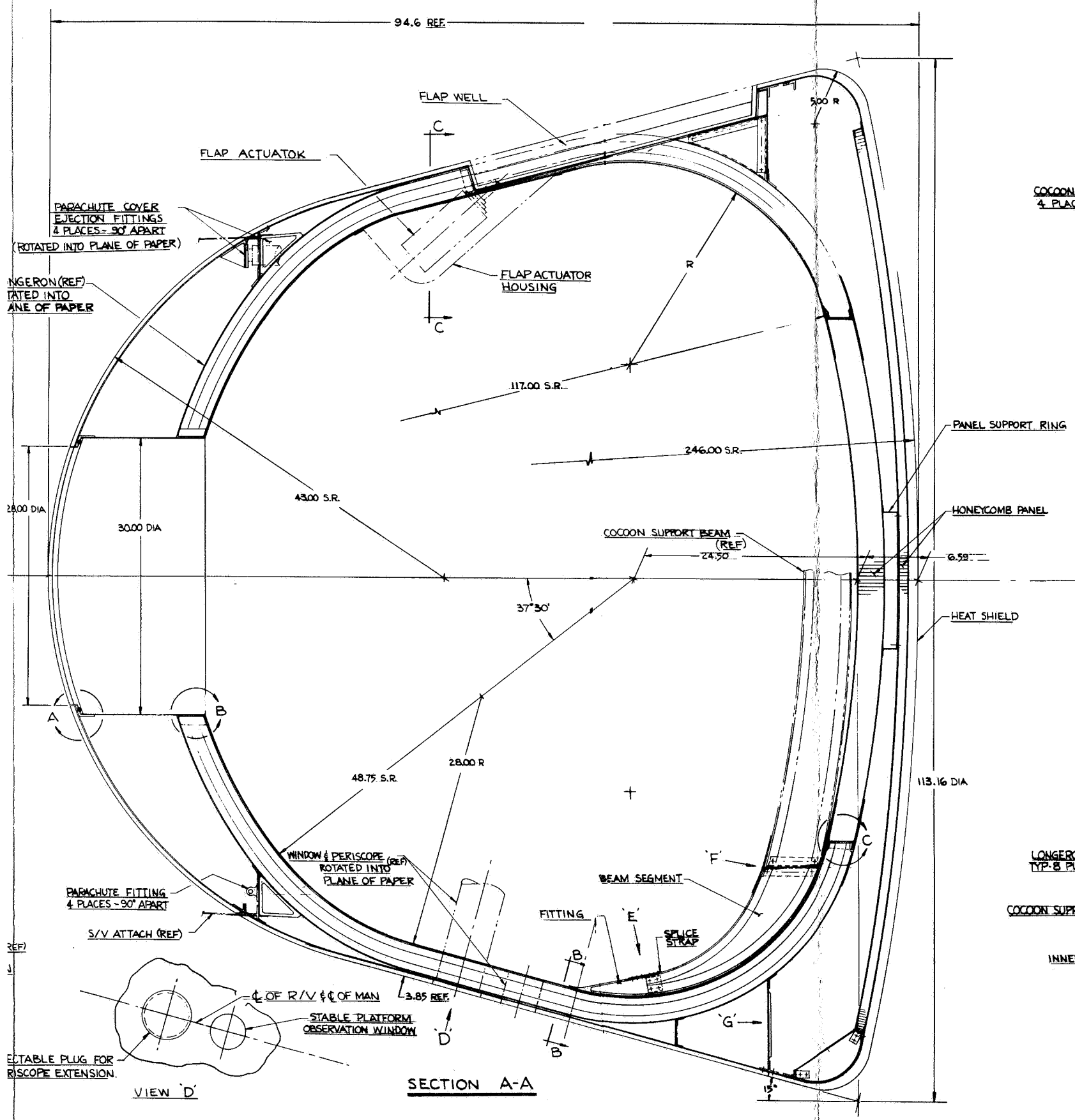
94.6 REF.
FLAP WELL
FLAP ACTUATOK
PARACHUTE COVER EJECTION FITTINGS 4 PLACES - 90° APART
(ROTATED INTO PLANE OF PAPER)
NGERON (REF)
TATED INTO
ANE OF PAPER
FLAP ACTUATOR HOUSING
5.00 R
R
117.00 S.R.
246.00 S.R.
43.00 S.R.
28.00 DIA
30.00 DIA
COCOON SUPPORT BEAM (REF)
24.50
6.59
37°30'
PANEL SUPPORT RING
HONEYCOMB PANEL
HEAT SHIELD
113.16 DIA
48.75 S.R.
28.00 R
WINDOW & PERISCOPE (REF) ROTATED INTO PLANE OF PAPER
PARACHUTE FITTING 4 PLACES - 90° APART
S/V ATTACH (REF)
BEAM SEGMENT
FITTING
SPLICE STRAP
3.85 REF.
℄ OF R/V & ℄ OF MAN
STABLE PLATFORM OBSERVATION WINDOW
ECTABLE PLUG FOR
RISCOPE EXTENSION
VIEW 'D'
SECTION A-A
15°

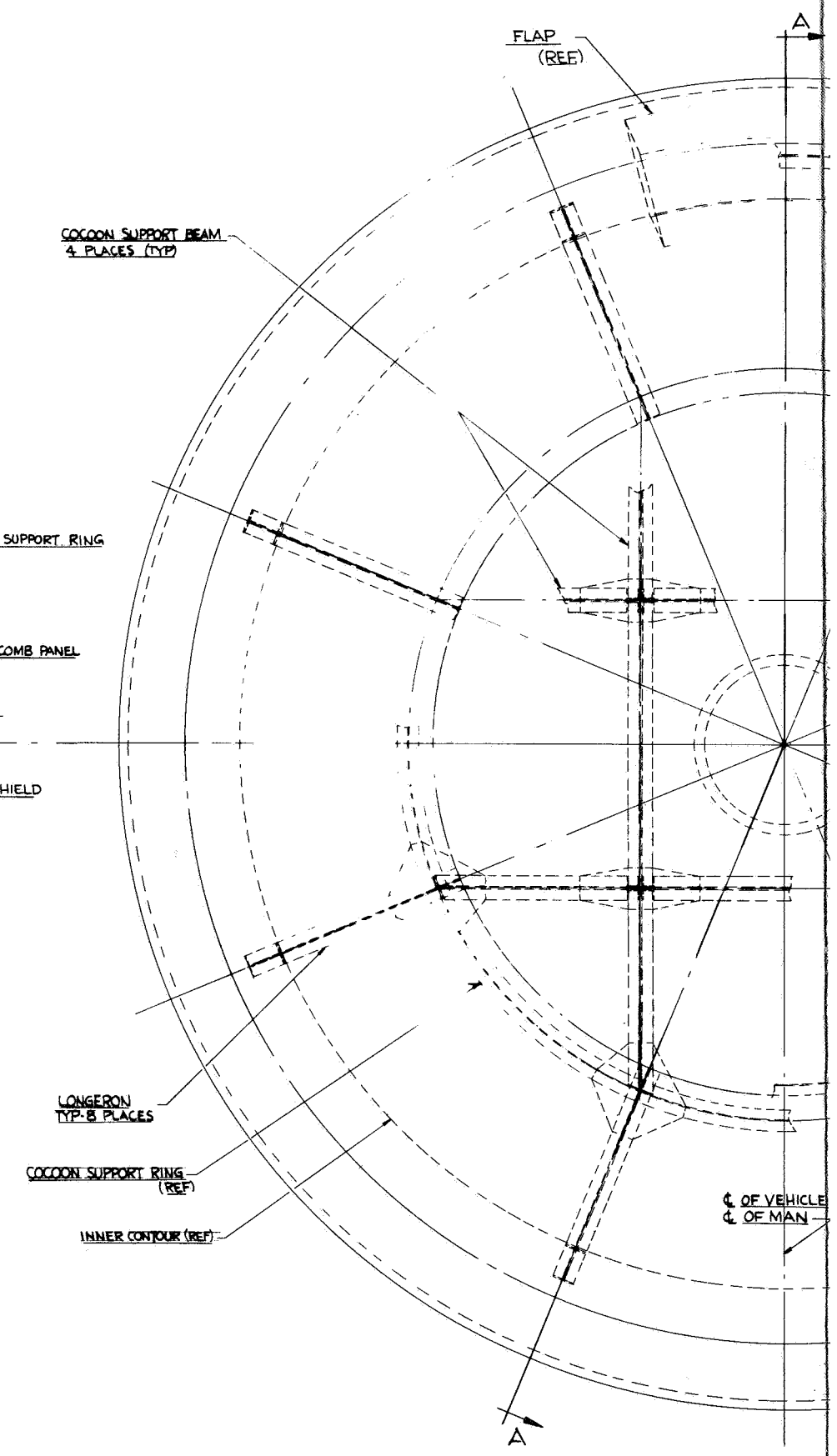
FLAP (REF)
COCOON SUPPORT BEAM 4 PLACES (TYP)
LONGERON TYP-8 PLACES
COCOON SUPPORT RING (REF)
INNER CONTOUR (REF)
℄ OF VEHICLE
℄ OF MAN

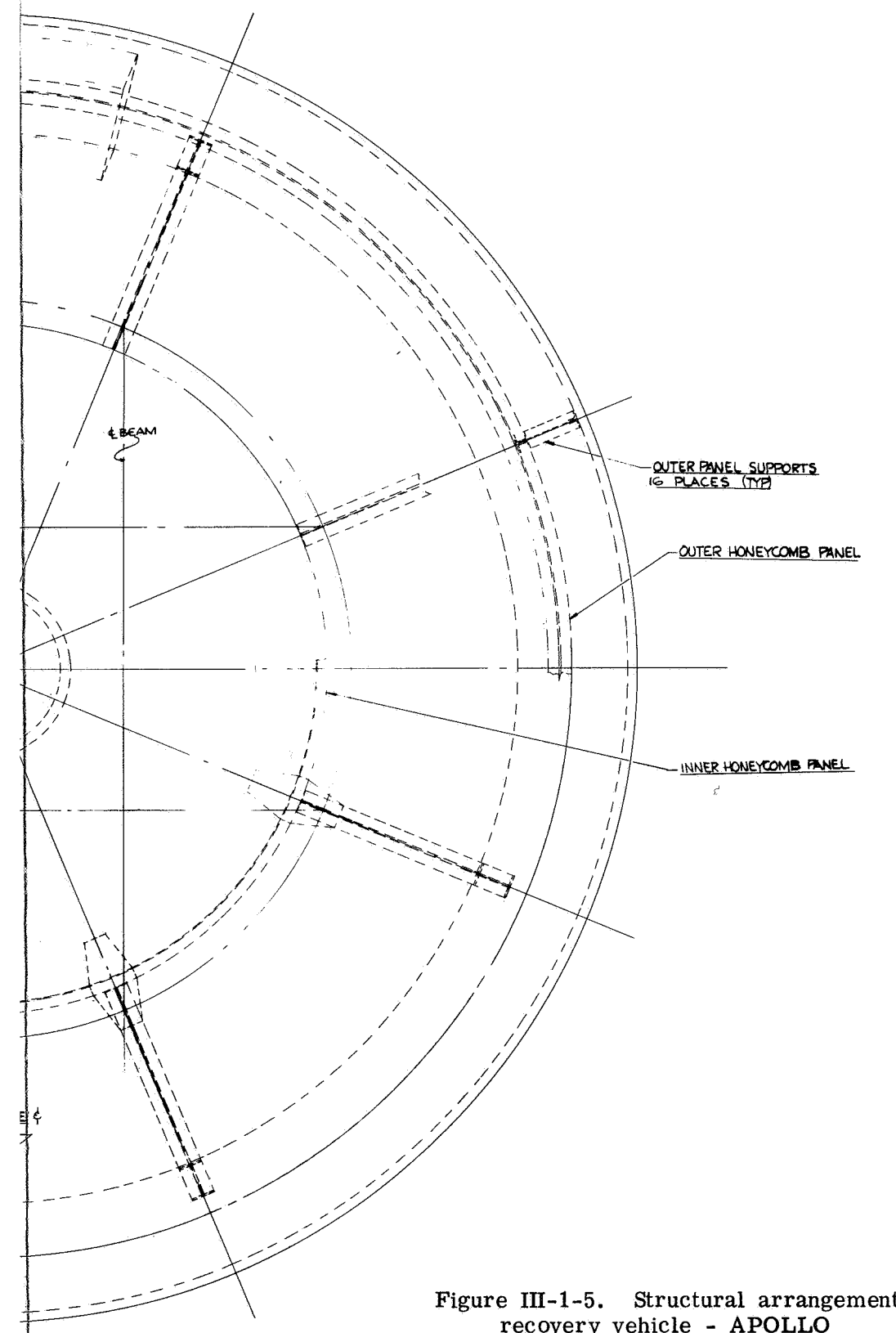

Figure III-1-5. Structural arrangement, recovery vehicle - APOLLO D-2 configuration

The structure of the re-entry vehicle consists of the following primary elements:

1. Outer shell skin
2. Forward honeycomb panel
3. Pressure shell skin
4. Pressure shell honeycomb panel
5. Longerons (8)
6. Parachute fittings (4)
7. Support cylinder
8. Bulkheads
9. Lateral supports
10. Hatch
11. Internal support beams
12. Control flap

The external shell structure of the re-entry vehicle, on which the thermal shield is soft bonded, consists of a forward aluminum honeycomb panel and an aluminum skin for the afterbody. Honeycomb was chosen for the large forward structural panel as the lightest type of construction to react the critical pressure loads due to booster explosion. The afterbody shell is stablized with aluminum bulkheads which also resist the re-entry vehicle lateral support frames loads and support the pressure cabin structure for the lateral loads.

The pressure cabin consists of a welded aluminum pressure vessel with eight seam welded external longerons.

The forward panel of the pressure cabin is of aluminum honeycomb construction. Honeycomb was chosen for the large relatively flat panel to give the lightest structure to resist internal pressure and the external pressure loads due to impact.

Four parachute fittings are attached to a ring bulkhead mounted between the external shell and the pressure cabin longerons. An aluminum cylinder is attached to this bulkhead to provide the primary axial support load path between the re-entry vehicle and mission module load re-distribution longerons. These eight longerons transfer axial loads from both re-entry vehicle and mission module into the space vehicle external shell. The vehicle entrance hatch, located at the aft end of the re-entry vehicle, is of aluminum construction and uses a breech-lock type latching system and sealing is accomplished with an "O" ring that is compressed as the door is latched.

The aft portion of the external shell is attached with piston-type ejection devices. To permit release of the parachutes the skin is severed by a shaped charge adjacent to the support cylinder interface, and is ejected aft from the re-entry vehicle.

The shaped charge separation system is also used for separation of the forward shell structure to release the impact system, and for severing the re-entry vehicle support cylinder.

Internal beams in the pressure cabin support the three cocoons and some of the internal equipment. These beams are welded to the pressure cabin skin at the longeron locations. Remaining internal equipment is mounted to brackets that are welded to the cabin skin.

1.3.1 Heat Protection Thermo — Structural Design

The heat protection material for the shield of the APOLLO re-entry vehicle will be a thermo setting plastic such as phenolic nylon or GE Series 100 material. The properties of these materials have been learned through extensive tests and flights of vehicles such as RVX-2, RVX-2A, MARK 3, NERV, etc. The ablative performance of these materials is discussed in Volume VI.

A flexible foamed Neoprene sheet bonds the heat shield to the aluminum sub-structure. A "soft" bond is required so temperature extremes and the associated differential expansion may be tolerated without shield failure. The bond, having a low thermal diffusivity, contributes to the shield insulation requirement, resulting in a negligible weight penalty for the thicker flexible bond.

All antenna windows in the re-entry vehicle will be made of quartz to provide maximum heat protection with a transmittable material.

1.3.2 Flap Structure

The flap, as shown on Figure III-1-6 utilizes a re-radiative heat protection system to resist the higher local heating for the deflected flaps as discussed in the previous two chapters of this volume. The flap assembly consists of a refractory metal sub-structure and a pyrolytic graphite heat shield covering the surfaces exposed to direct airflow. The sub-structure assembly consists of built-up sheet metal beams and frames covered by a thin surface skin, similar to an aircraft speed brake structure. The pyrolytic graphite heat shield is attached mechanically, or with a high temperature

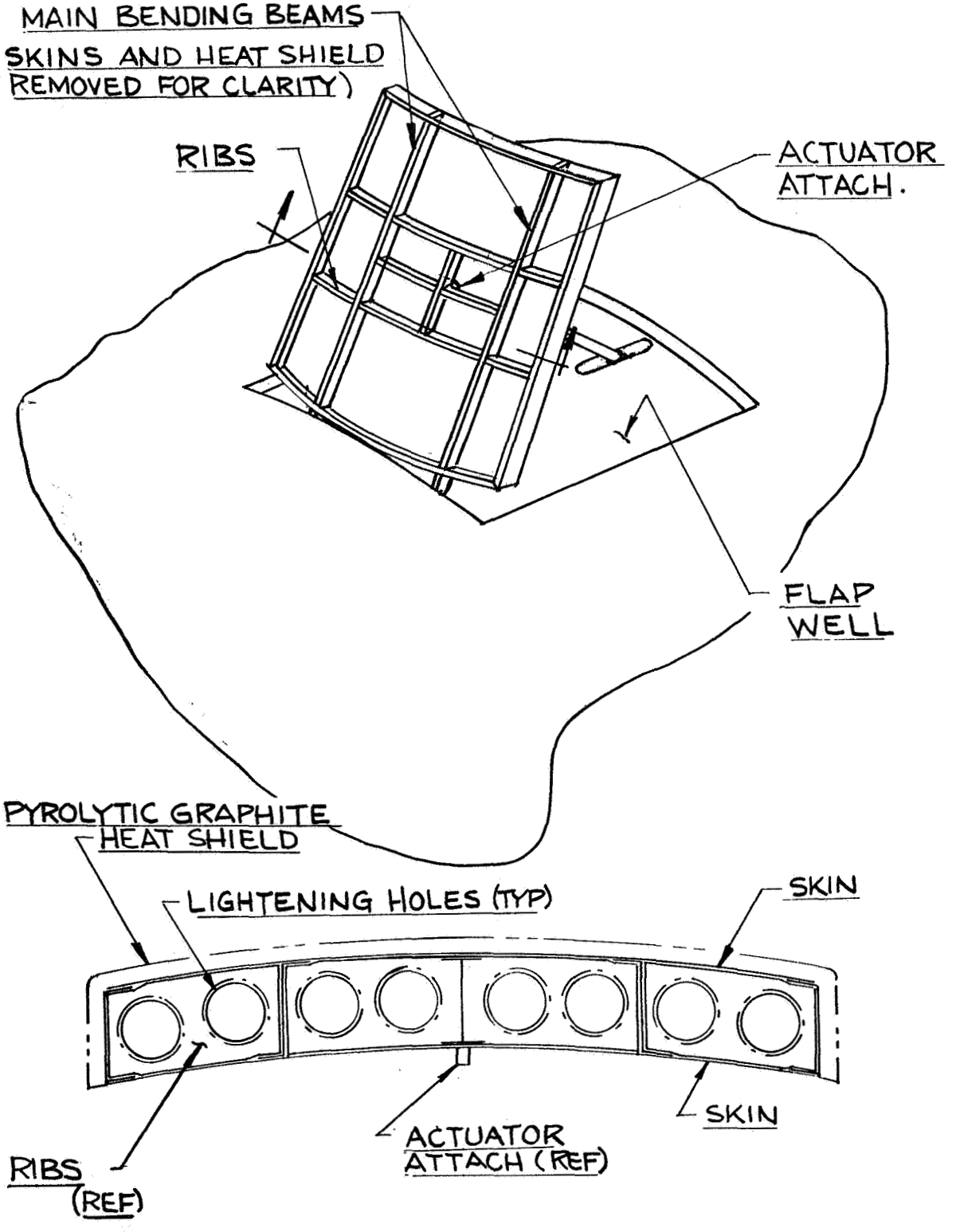

Figure III-1-6. Control flap structure

ceramic bond, to the sub-structure. The graphite laminations are oriented parallel to the flap surface. Columbium appears to be the most promising refractory metal presently available due to its superior oxidation resistance, acceptable fabrication characteristics, and high strength at temperatures above 2000 F. Columbium, as well as all other refractory alloys, requires a protective coating to preclude excessive oxidation of the metal surfaces. Adequate coatings exist, but major problems must be solved before fabrication of complex refractory assemblies is feasible. Typical problem areas are: methods of coating application and inspection, coating over joints and similar discontinuities, and local repair procedures. These problems are currently under study by many agencies and usable solutions are expected well within the APOLLO design and development period. Pyrolytic graphite is proposed for the control surface heat shield due to its desirably low thermal conductivity normal to the laminations. This material is currently under extensive development by GE and others for advanced re-entry heat protection systems. Uses to date have been limited to relatively small elements and much additonal research and testing will be required tc develop the fabrication and assembly techniques for application to larger structural components.

If sub-structure temperatures can be limited to lower values, less costly alloys such as Rene 41, M-252, and many others are available.

1.4 STRUCTURAL DESCRIPTION — R-3 VEHICLE

The structural design of the modified lenticular vehicle is shown in Figure III-1-7. Basically, this design features a low temperature primary structure covered by a thermal protection system. The primary structure consists of a pressure membrane skin, supported by frames at 10-inch spacing, with upper and lower longerons at Buttock Lines ±15 and ±40. Tension ties between the upper and lower longerons serve to balance the internal pressure load on the upper surface against that on the lower surface and thus materially reduce the bending moments in the frames. The tension ties are spaced every 20 or 30 inches along the longerons at locations chosen to permit free movement of the crew throughout the interior of the vehicle. Since tension ties are not supplied at every frame, the longerons are designed as continuous beams to span the pressure loads from these intermediate frames to the tension ties.

Except for the control surfaces and their pylons, the entire vehicle is pressurized to 8 psi working pressure. Ultimate design pressure is 16 psi and this is the critical

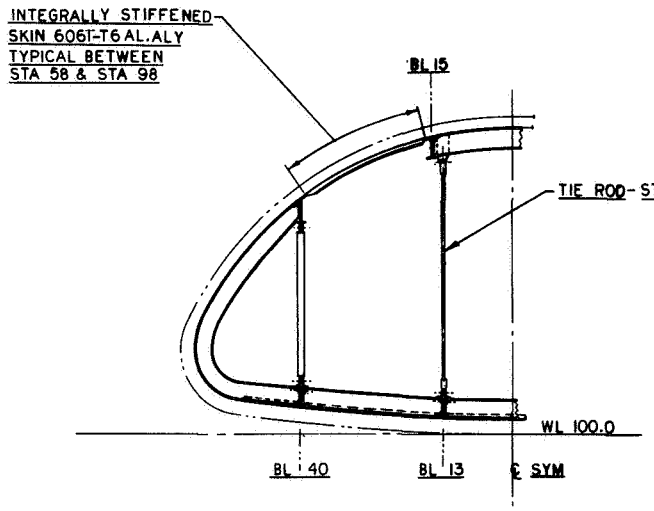

STA 78.0
TYPICAL FOR STA 88.0
EXCEPT TIE RODS OMITTED

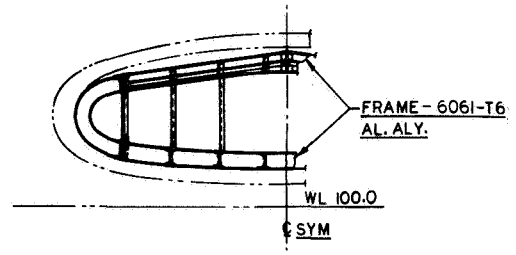

STA 14.0

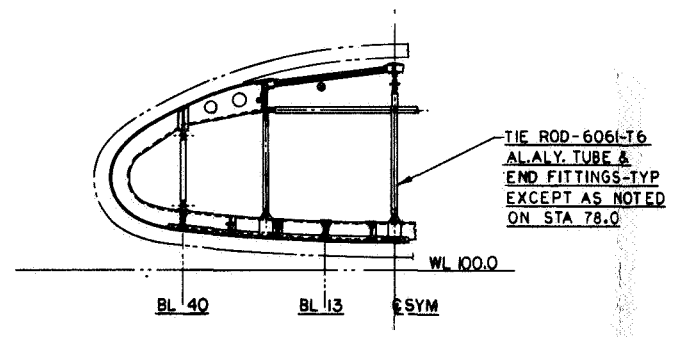

STA 28.0

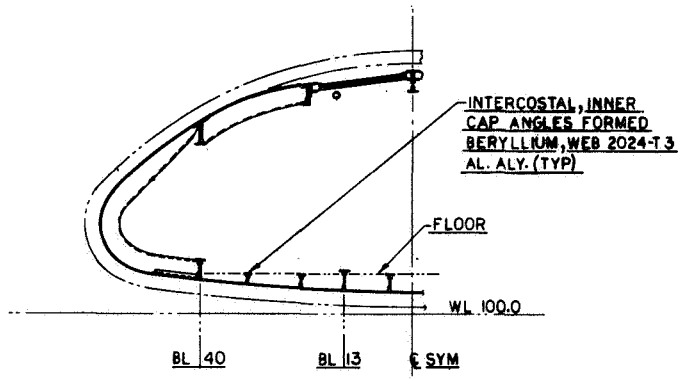

STA 38.0

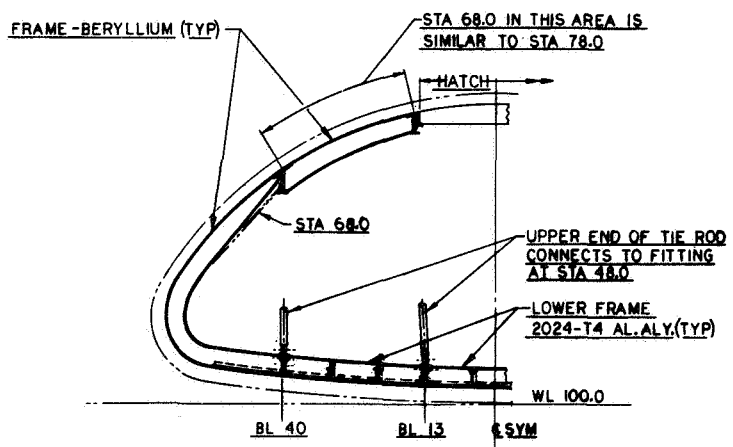

STA 58.0
TYPICAL FOR STA 68.0 EXCEPT
TIE RODS OMITTED & AS NOTED

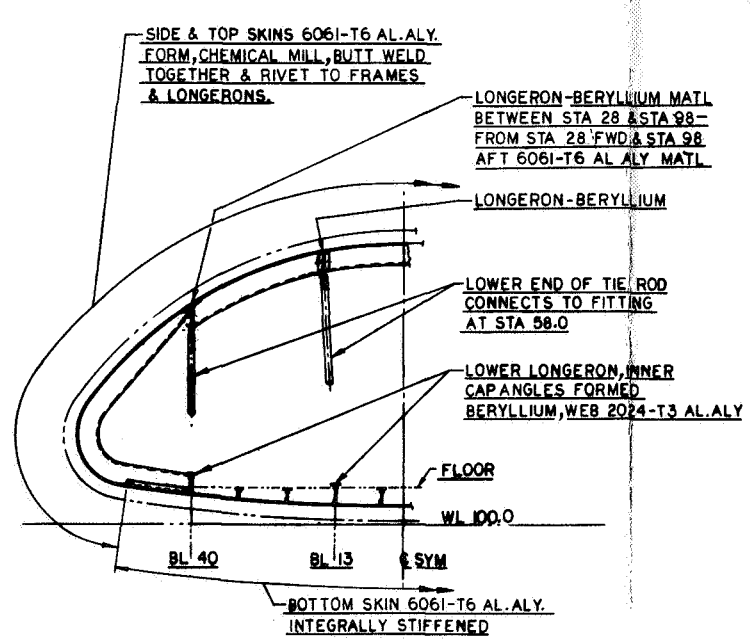

STA 48.0

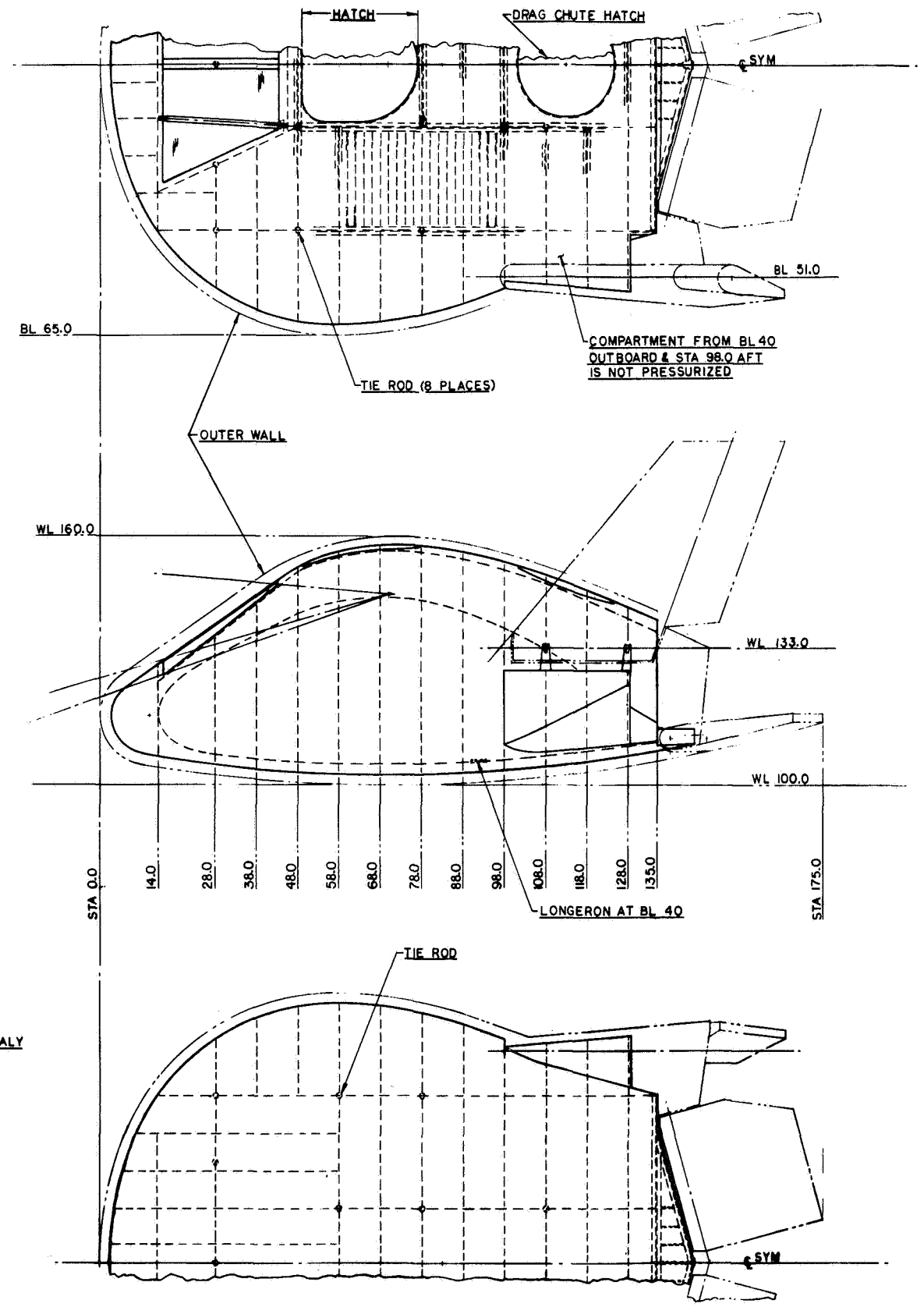

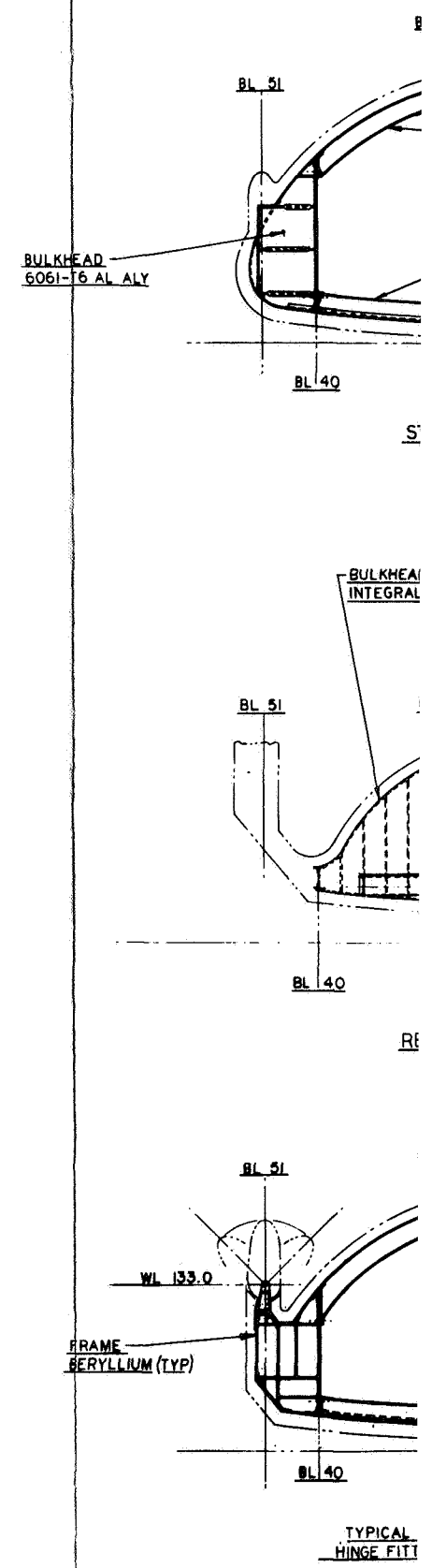

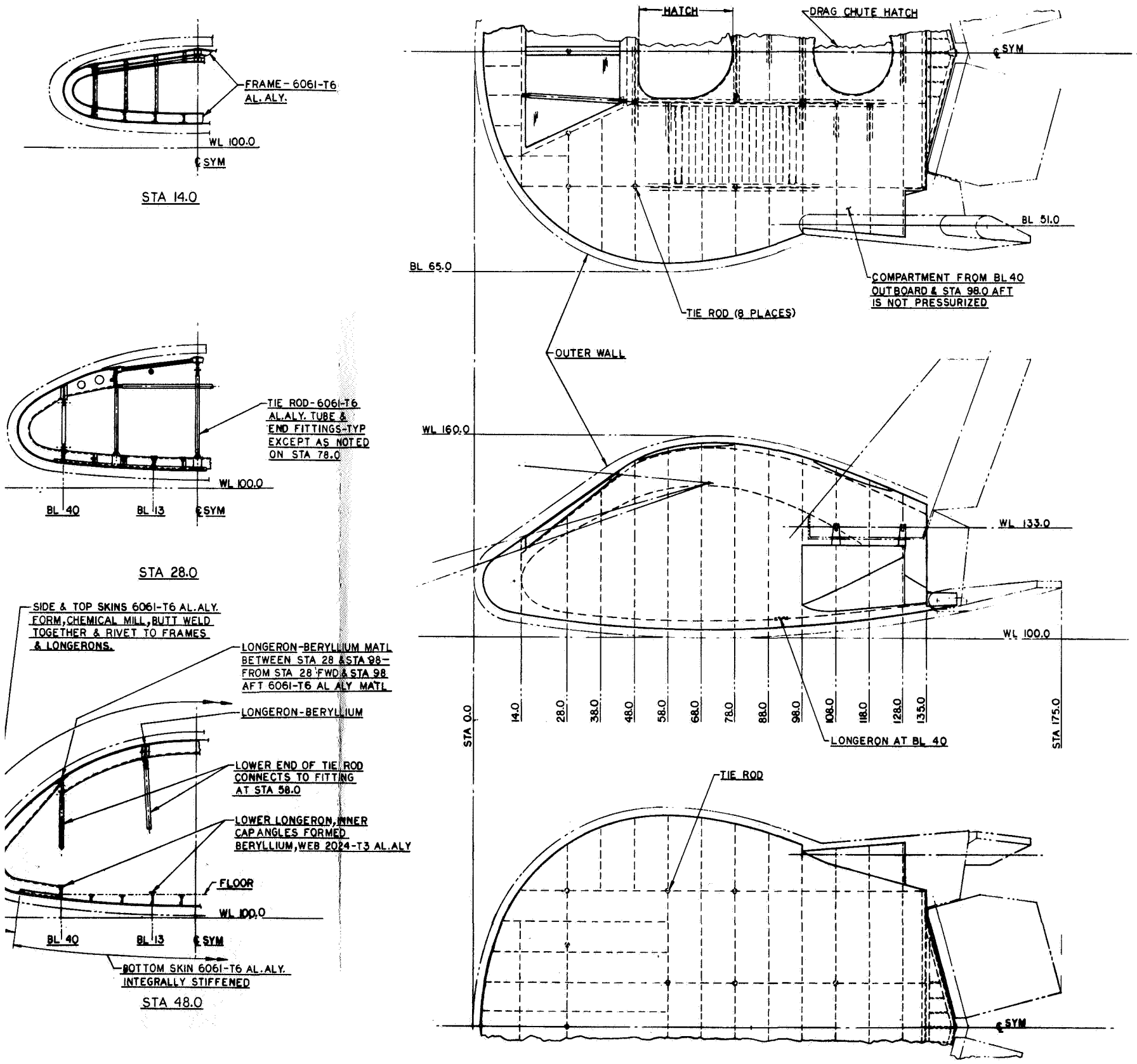

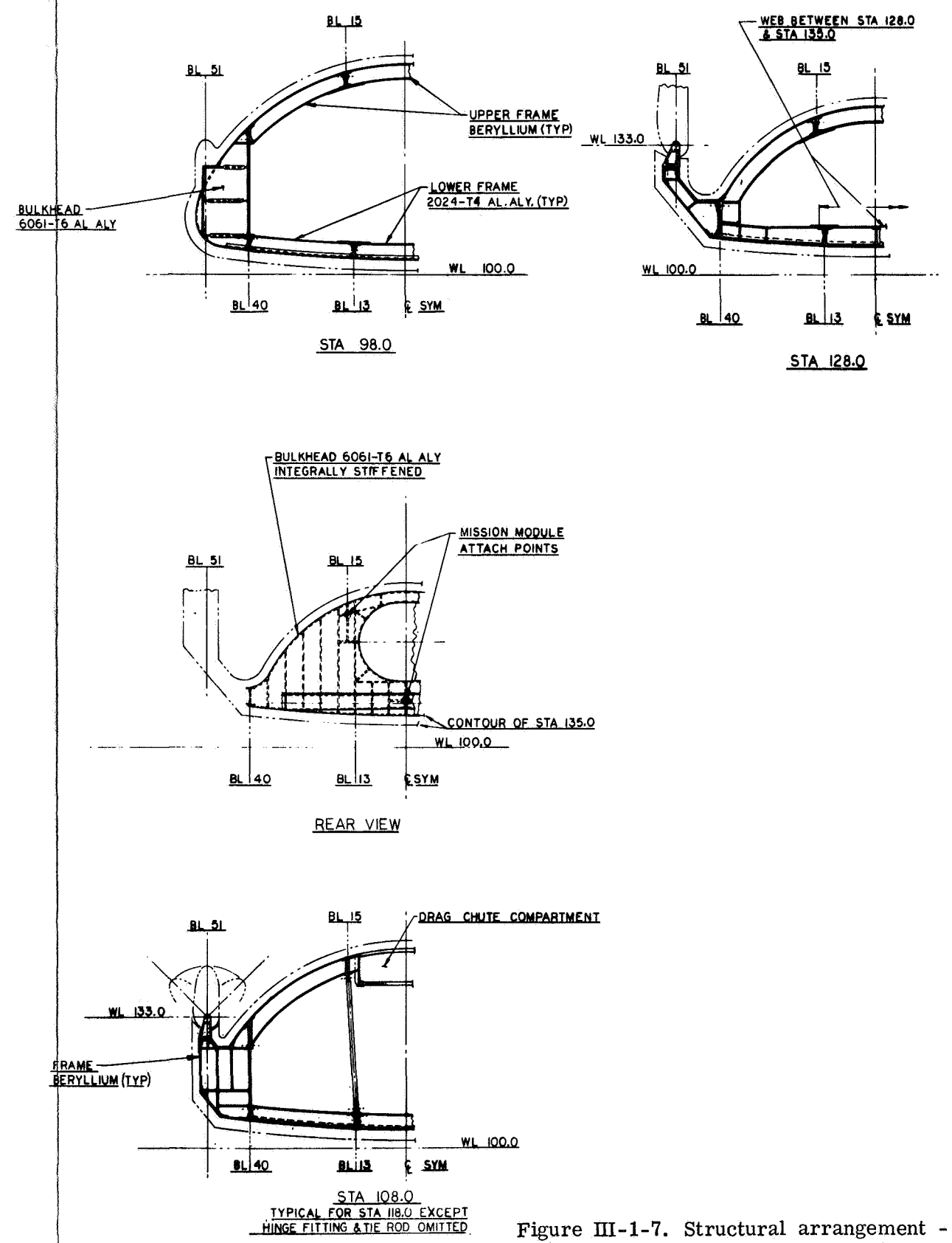

Figure III-1-7. Structural arrangement - APOLLO recovery vehicle R-3, concept # 4

design condition for most of the airframe. The aft end of the longerons, the pylons, and the control surfaces, are critical for the condition of maximum dynamic pressure during boost.

Construction details are shown in Figure III-1-7. The lower surface is a section of a large radius sphere and the skin is machined and chem-milled in one piece with integral upstanding flanges for riveting to the webs of the frames and longerons. The outboard caps of the frames and longerons are thus integral with the skin and the lower surface is therefore a zero leakage structure since no attachements pierce the skin. Longeron webs are aluminum and the inboard caps are beryllium. Aluminum is used for both the webs and inboard caps of the frames which are spliced at each longeron.

The sides and top of the vehicle are of compound curvature and cannot be be machined as integral skin and caps. Instead the skin is stretch formed and chem-milled in several large sections which are welded together on assembly. Butt welds are not used but flanges are provided around the edge of each skin section and the edges of the flanges are welded to one another. The flanges are normal to the skin and extend outboard into the area immediately below the insulation packages of the thermal protection system. Attachment to the frames and longerons is by riveting and the rivets are sealed by bonding the head to the outside skin surface or by welding the edge of the head to the skin. The frames and longerons are I-sections which permits a symmetrical attachment to the skin by two rows of rivets thereby minimizing the probability of leakage resulting from distortions due to internal pressure. The upper longerons are each a machined beryllium member and the frames in the sides and top are machined beryllium sections which are spliced at each longeron. In the regions over the heads of the outboard crew members the frames are eliminated, to provide clearance, and the skin is supported by closely spaced one inch deep stiffeners spotwelded to the skin and riveted to a beryllium sheet which form the inboard cap of the stiffeners and makes a smooth ceiling for the crew.

The aft bulkhead is machined like the lower surface with stiffeners attached to integral flanges on the forward side. Integral flanges on the aft side are provided to attach the elevon pylon.

The fin pylons are machined beryllium frames covered with the thermal protection system outer wall panels and insulation. The fins are conventional aluminum

construction protected by outer wall panels and insulation. Only the lower surfaces of the elevons are protected with outer wall panels and the elevons are of heat sustaining construction.

The thermal protection system consists of heat sustaining outer wall panels, which form the outside contour of the vehicle, and insulation packages which are mounted between the outer wall panels and the primary structure. Relatively small size panels are used for the outer wall with alternately overlapping stepped edges to permit unrestrained thermal expansion of each panel. Only three or four supports are used to attach the outer wall panels to the primary structure in order to minimize heat transfer to the primary structure. Three types of outer wall panels are used on the vehicle: (1) Haynes 25 brazed honeycomb sandwich panels for regions of low heating, (2) molybdenum alloy panels composed of a number of parallel channel sections which are riveted to a pair of transverse hat-section beams, for regions of moderate heating, and (3) molybdenum alloy panels covered with a layer of ablative material for regions of severe heating. Type 1 panels are used on the upper surface of the body and the inside surface of the fins and fin pylons. Type 2 panels are used on the fin outer surface. Type 3 panels are used on the body and elevon lower surface and the fin pylon outer surface.

1.4.1 Primary Structure and Thermal Protection

1.4.1.1 GENERAL

Structures work conducted to date for the APOLLO study has been concerned principally with the re-entry vehicle, since this is considered a more critical structural problem than the mission module due to the aerodynamic heating problems of re-entry. The work has had two principal objectives; first, to provide structural concepts, structural arrangements and airframe weight data in support of configuration studies, and second, to investigate various approaches to the more critical problem areas. The problem areas which have been emphasized are those of airframe weight and aerodynamic heating during re-entry. Preliminary consideration has also been given to the micrometeorite problem and the problem of pressure retention for long periods of time with negligible losses. No consideration has been given at present to the problem of space radiation as it affects airframe materials.

With respect to re-entry heating the protected structure concept was selected at the beginning of the study as the general solution. Protected construction involves a low

temperature primary structure which carries all major loads, in addition to housing the vehicle contents. This primary structure is protected from aerodynamic heating effects by an external system of insulation and radiation panels.

It is expected that the choice of protected construction will be verified later in the study by a consideration of alternate approaches. For the moment the choice is based on past experience which includes both the development, fabrication and testing of protected structures and also studies of their application to a number of hypersonic and re-entry vehicles. Based on this experience it is believed that protected construction offers simple and reliable subsystems, since these all operate at low temperature. It further simplifies manufacturing problems since 50% of the airframe weight is conventional construction, and the high temperature elements are small and of simple shape. This approach also offers important growth potential in terms of higher temperature capability and reduced airframe weight since it separates strength and temperature requirements and makes possible the use of a wide range of materials. Past studies have also shown that this approach offers important weight advantages where a cool interior must be provided for crew, equipment and propellants, and with an efficient vehicle configuration this condition holds for most of the airframe.

With the protected construction approach established, the airframe study work divides into two parts; the study of the basic primary structure and the study of the protection system.

Studies of the primary structure have included the conventional construction methods of stringers, longerons, frames and skin, using the standard aluminum alloys. Consideration has also been given to a more advanced concept involving the use of pressure supported shells and the use of beryllium for a large portion of internal structure. Significant benefits have been shown by using this concept for a high L/D wing configuration which involved a more or less cylindrical fuselage. Consequently to exploit more fully these advantages the same approach has been applied to the present low L/D lenticular configuration.

With respect to the thermal protection system the problem of lifting re-entry from escape velocities, in combination with significant maneuvering capability for landing accuracy, requires what might be termed a "wide range" protection system. This term refers to a system which simultaneously has the temperature capability to resist very severe heating for short times, and also the protective efficiency to sustain moderate heating for long periods of time with practical weights.

Normally, protection systems based on heat absorption would be used for high intensity short-time conditions, since such systems are not particularly sensitive to heat intensity and their relatively poor efficiency is not serious for times of 1 to 2 minutes. Similarly the long time heating condition would require the use of a radiative system, which is normally limited in the heating intensity which can be sustained, by the temperature capability of surface materials.

For the present application, which involves the combination of high intensity for short times and moderate intensity heating for long times, both of these systems have been considered but advanced forms have been assumed in order to improve the deficiencies of each. Absorptive systems have been considered with materials which have good insulative or radiative capabilities in order to improve weight efficiency. Also radiative systems have been extended considerably in temperature capability by considering non-metallic materials and by accepting some deterioration of these materials in order to accommodate the maximum heat fluxes. In addition to these extended forms of absorptive and radiative protection systems, combinations of both have also been introduced in an effort to find the minimum weight arrangement.

1.4.1.2 PRIMARY STRUCTURE

A structural arrangement for the modified lenticular configuration is shown in Figure III-1-8. A low temperature primary structure is protected by heat sustaining outer wall panels and insulation packages. The primary structure features a pressure membrane skin supported by transverse frames at 10 inch spacing. The frames are, in turn, supported by eight longerons, four on the upper surface and four on the lower surface, and finally, the upper and lower longerons are connected by tension tubes which effectively balance the pressurization load on the upper surface against that on the lower surface.

Fundamentally the modified lenticular configuration is a dual capability vehicle which is designed to re-enter the atmosphere at near 90 degrees angle of attack and also achieve an airplane type landing under the direct control of the pilot. This capability is reflected in the configuration and the corresponding structural arrangement. In general the basic shape of the vehicle is set by the requirement of a large radius lower surface for re-entry, the control surface arrangement, and the windshield required for pilot controlled landing. Around these requirements the lines of the vehicle are chosen to provide two things: a shape no larger than necessary for the crew and equipment;

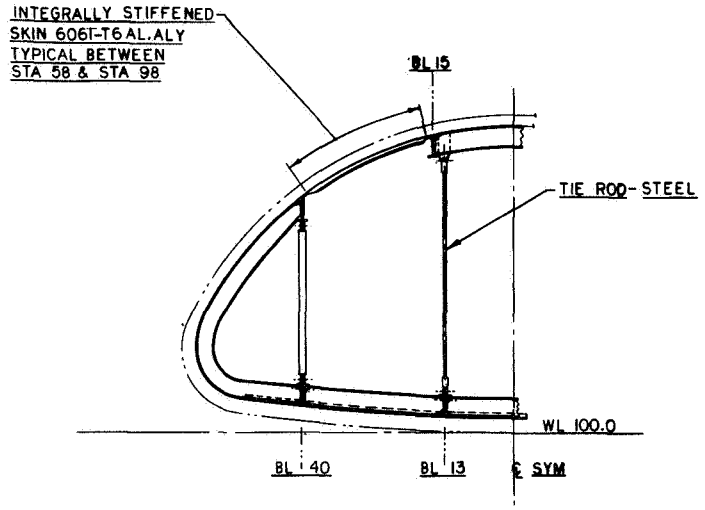

STA 78.0
TYPICAL FOR STA 88.0 EXCEPT TIE RODS OMITTED

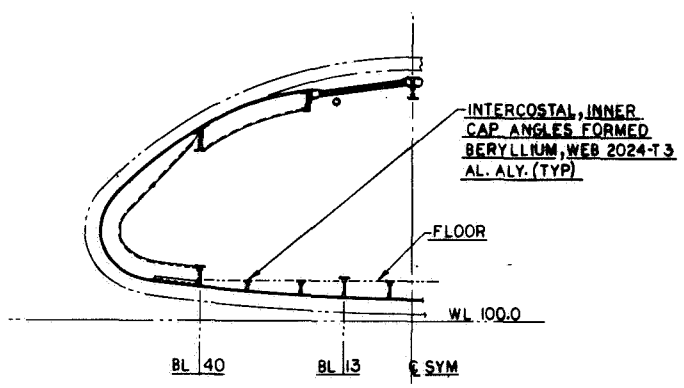

STA 38.0

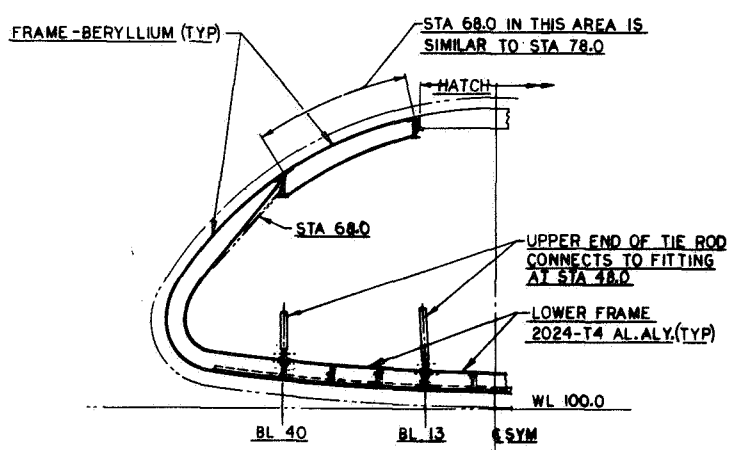

STA 58.0
TYPICAL FOR STA 68.0 EXCEPT TIE RODS OMITTED & AS NOTED

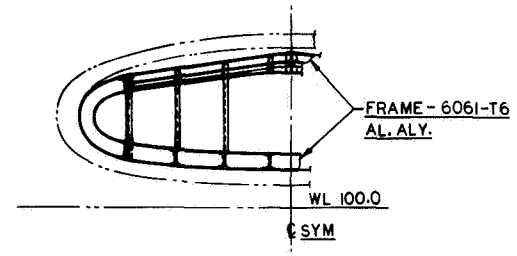

STA 14.0

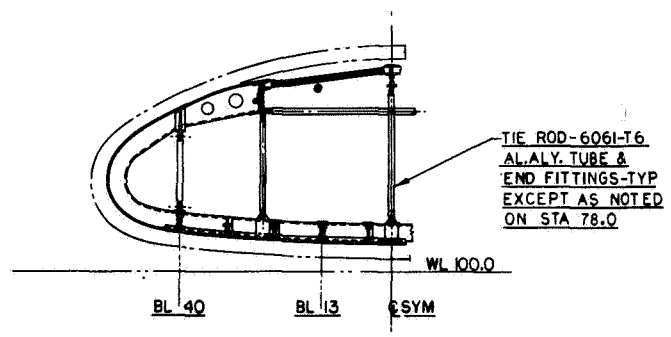

STA 28.0

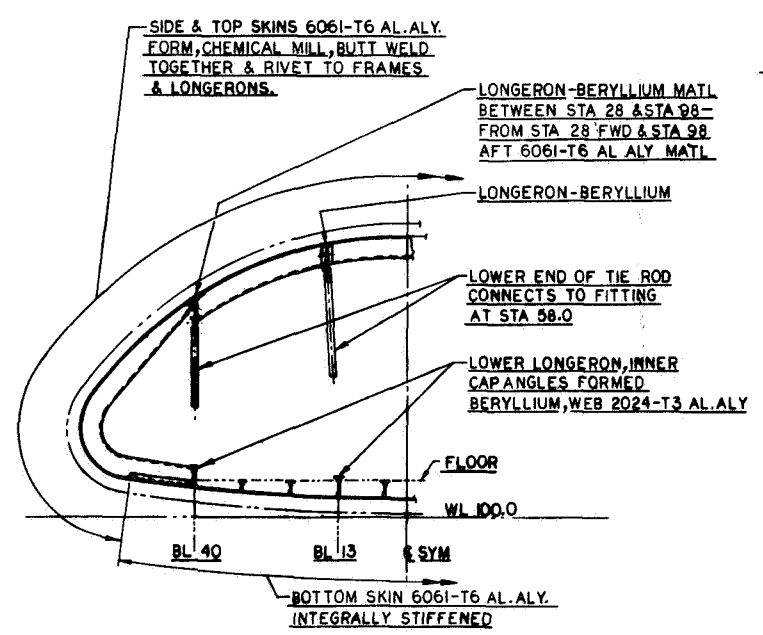

STA 48.0

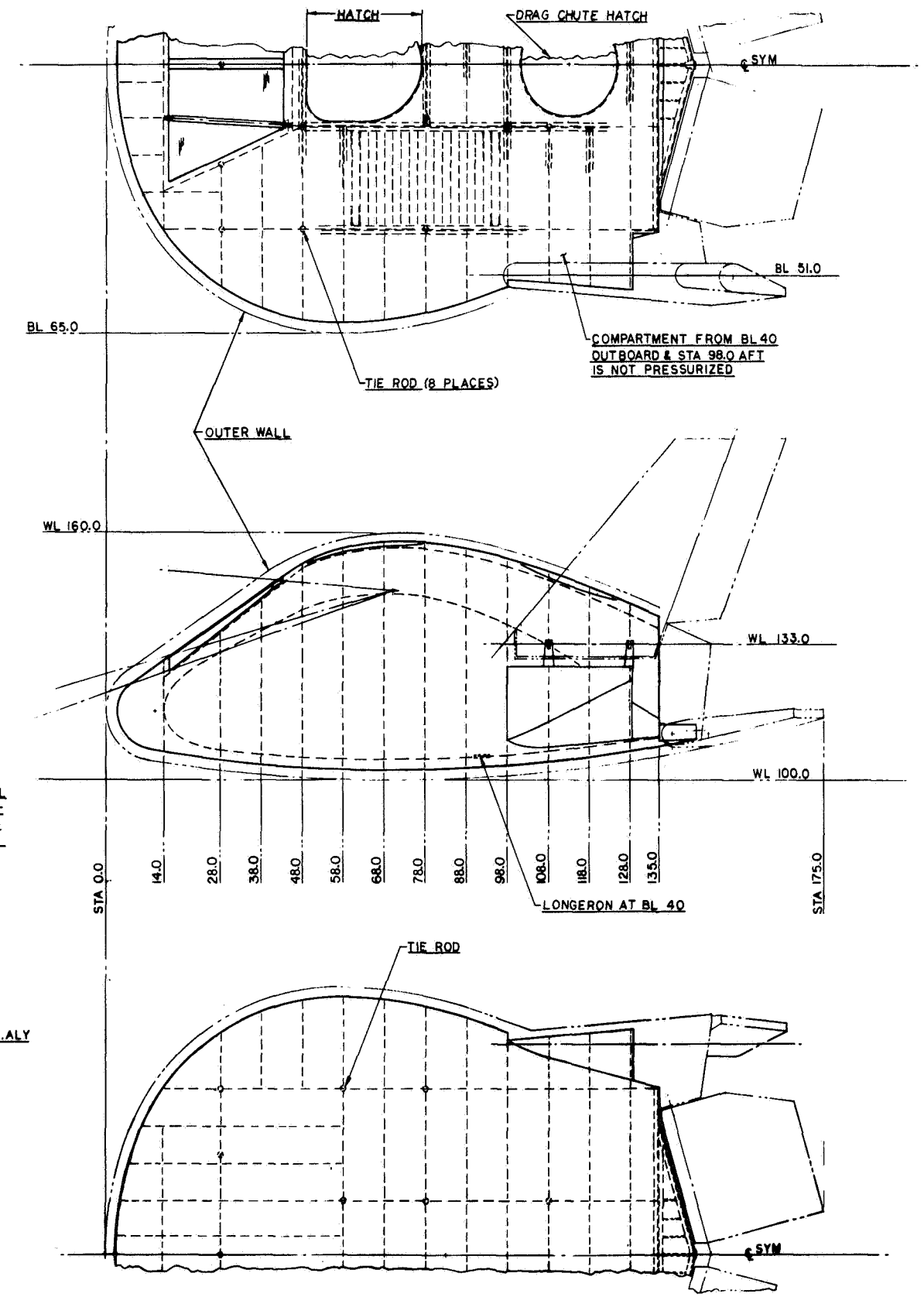

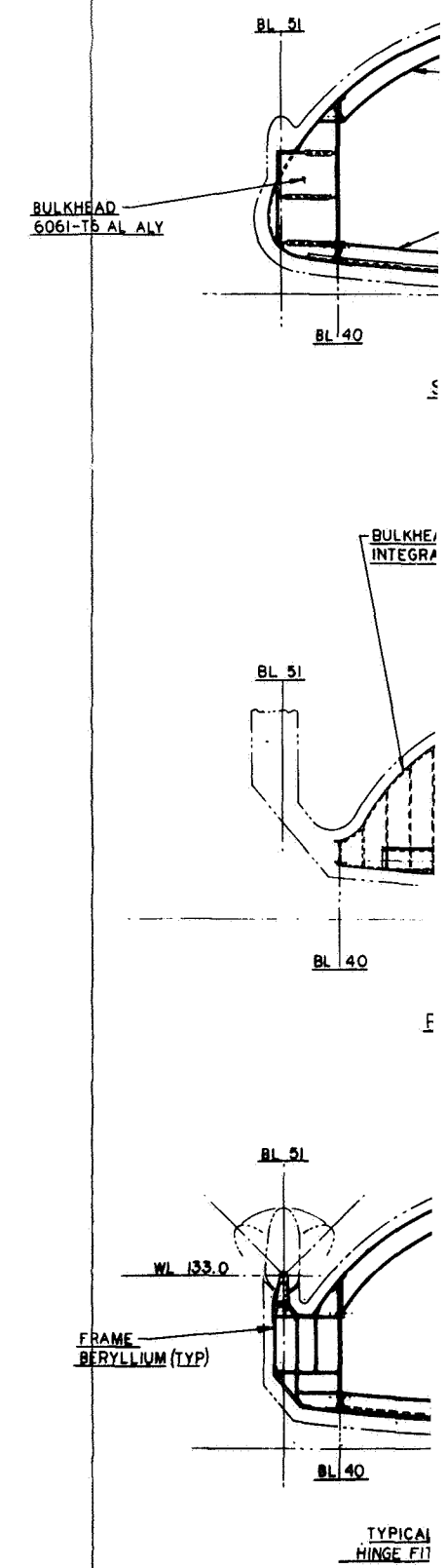

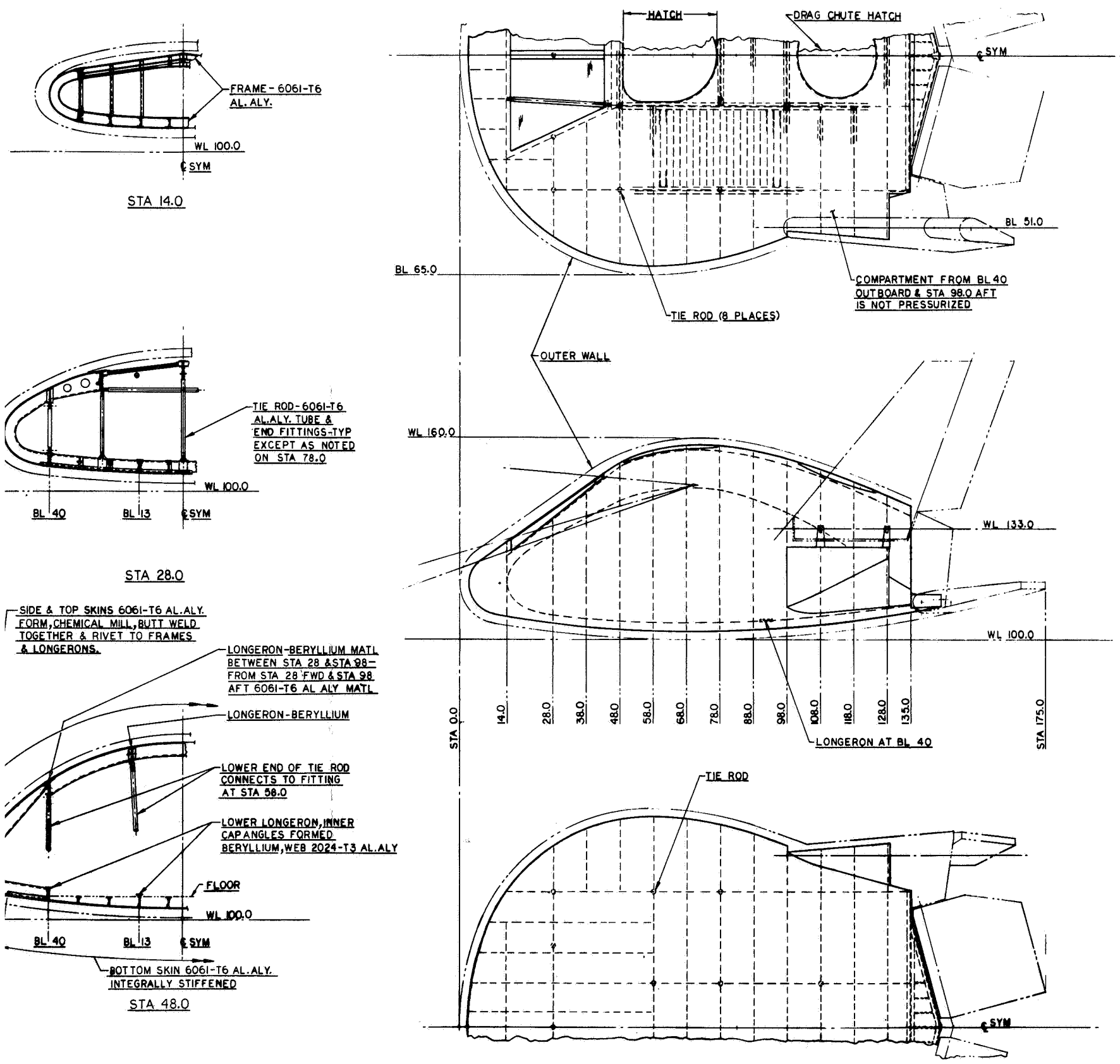

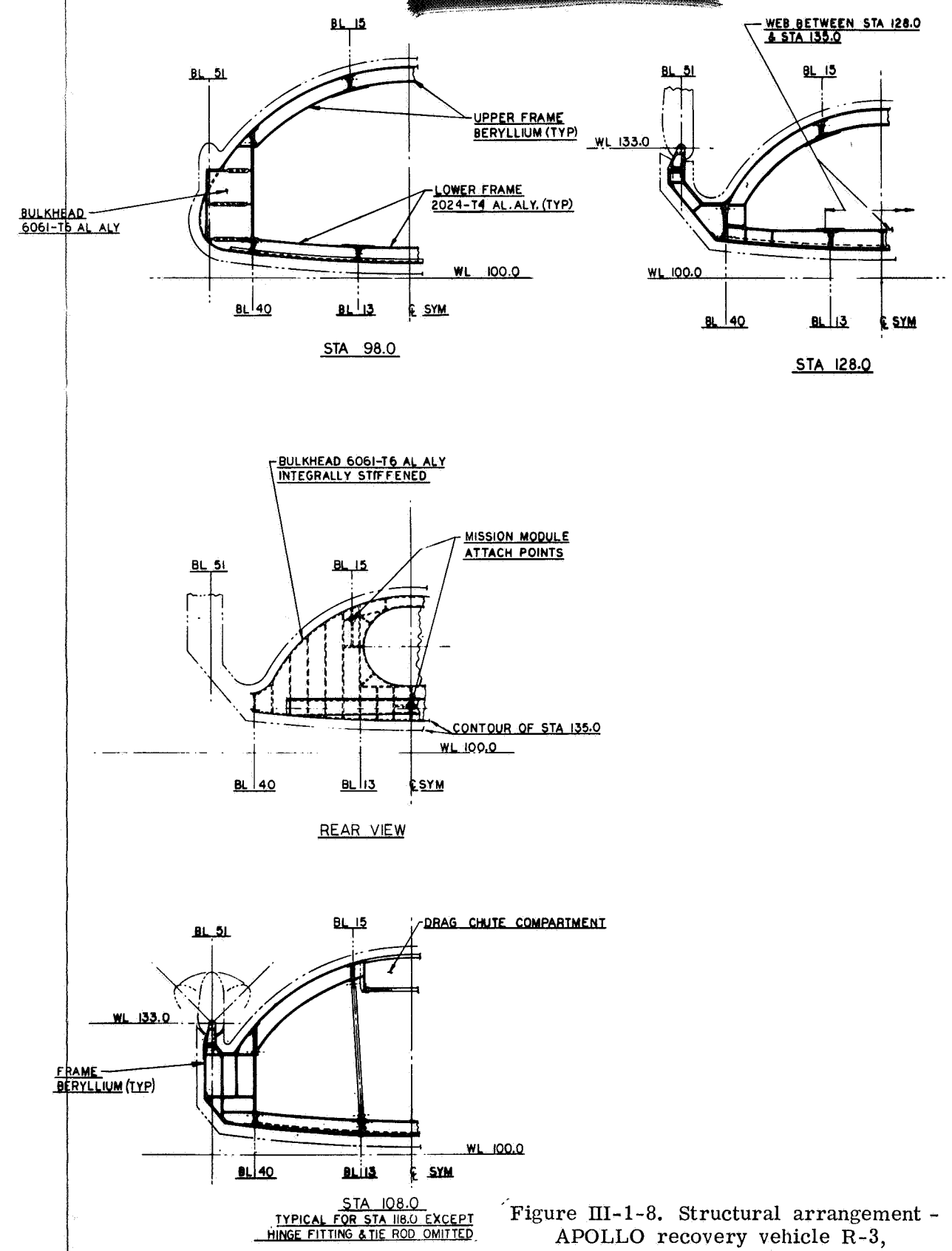

Figure III-1-8. Structural arrangement - APOLLO recovery vehicle R-3, concept # 4

and, also, a shape with an L/D suitable for an airplane type landing. This does not necessarily result in a minimum weight structure, which would be a body of revolution with no cutouts. However, the use of tension ties between the upper and lower surfaces does minimize the structural weight for the chosen shape.

Since the vehicle is of minimum size for the contents, and therefore the entire vehicle must be pressurized, there is no duplication of structure (by having a pressurized shell surrounded by non-pressurized primary structure) except in the region of the control surface pylons where it is more efficient to leave the pylons unpressurized. Another significant benefit to having the entire vehicle pressurized is that external airloads are not critical since the structure behaves as a pressure stabilized shell (i.e., tension stresses due to internal pressure are greater than compression stresses due to external airloads). Exceptions to this general statement are thrust loads during low altitude abort, bending moment loads in the aft portion of the body at maximum dynamic pressure during boost, and landing loads when no differential pressure exists. However, the entire primary structure forward of Station 98 is critical for the ultimate internal pressure of 16 psi (8 psi working pressure x 1.33 x 1.5). Aft of Station 98 the primary structure is critical for the condition of ±5 degree pitch at maximum dynamic pressure during boost combined with 8 psi internal pressure. This 5 degree pitch at maximum dynamic pressure produces the design loads on the control surface also, since the fins are deployed to landing position during boost to provide stability during abort, and the elevons are deflected to a down position to clear the mission module.

Aside from the design loads the most severe problems faced in the structural design are the requirement for zero leakage, the requirement for minimum weight, and the problem of fabrication, all of which are interrelated. For instance, zero leakage could be achieved by welding the entire skin to the frames and longerons. However, this requires matching several score compound curvature formed and chem-milled skin panels to compound curvature flanges with sufficient accuracy to butt weld. Although the resulting buckles in such a weldment would not be objectionable from an appearance standpoint, since the primary structure is covered with outer wall panels anyway, the weld induced buckles and thermal strains would be potential sources of cracks. The welding would also destroy the heat treat of the flanges and thus result in a heavier structure.

The type of construction chosen for the primary structure is shown in Figure III-1-8. Since the lower surface contour is a portion of a large radius sphere, it is possible to machine the outer caps for the frames and longerons integral with the skin thus obtaining zero leakage of the lower surface. The lower surface frames and longerons can then be built-up assemblies with aluminum webs riveted to the upstanding leg of the machined outer cap, and either beryllium inner caps riveted to the webs or aluminum caps integral with the webs. (Beryllium webs cannot be used in this combination since the ratio of the modulus of elasticity of beryllium to that of aluminum is such that the working stress in the aluminum outer cap would be limited to 10,000 or 12,000 psi to avoid overstressing a beryllium web.) As shown in Figure III-1-8 the longeron webs and beryllium inner caps are continuous and the frame integral aluminum webs and caps are spliced at the longerons. This results in the least loads in the splices since there is more shear in the longerons than the frames due to the spacing of the tension ties along the longerons at every second or third frame.

Since the sides and upper surface of the vehicle are of compound curvature it is not considered feasible to make a machined integral skin and cap component. The approach chosen is a stretch formed and chem-milled skin fabricated in several sections and welded on assembly to preclude leakage at the skin joints. The skins are not butt welded, but flanges are provided around the edge of each skin section and the edges of the flanges are welded to one another. The flanges are normal to the skin and extend outboard into the area immediately below the insulation packages. Attachment to the frames and longerons is by riveting. Although each rivet is a potential source of leakage, it is felt that the manufacturing and weight advantages of riveting outweigh the disadvantage of sealing each rivet. Several methods are feasible for sealing the rivets: (1) bonding the rivet to the skin, (2) heli-arc welding around the edge of the rivet head, (3) chem-milling flanges along each row of rivets to which a cover can be welded after riveting. Also distortion at the joint which might precipitate leaks can be minimized by making the skin thicker over each longeron and frame, and using a machined tee section for the frame or longeron cap. This makes the attachment symmetrical about the web of the frame or longeron and prevents rolling of the attachment which further reduces the possibility of distortion and leakage.

Attaching the skins by spotwelding is not considered feasible because of the thickness of the skins and flanges and the inaccessibility of some of the spots.

A distinct advantage of riveting is that the upper longerons and frames can be fabricated of beryllium which does save weight. As shown in Figure III-1-8, the upper longerons are each a one piece machined I section, and the frames are assembled of machined I section pieces which extend between the longerons and are spliced at each longeron.

A study of a typical frame with various arrangements of tension ties is summarized in Figure III-1-9. The spanwise spacing of tension ties (and longerons) is dictated by the crew seating arrangement and the longitudinal location of tension ties along the longerons is also dictated in part by the necessity of permitting crew movement throughout the vehicle interior. Results are given in Figure III-1-9 for a continuous frame with no tension tie, with tension ties at Buttock Lines ±40, and with tension ties at Buttock Lines ±40 and ±15. Results are also given for a frame pinned at Buttock Lines ±40, top and bottom, with tension ties at the same location; and for a frame with tension ties at Buttock Lines ±15 and ±40 and pinned at the top at the latter locations. This last frame more nearly represents the frames used in the vehicle and it has the lowest bending moments along with the continuous frame with no tension ties. An inspection of the actual structure in Figure III-1-8 shows that not one frame is complete across the ship due to interruptions by the windshield, hatch, crew heads, parachute hatch, crew foot wells, and fin pylons. However, the curves of Figure III-1-9 show a trend and indicate a definite weight saving by use of the tension ties.

The frame spacing shown in Figure III-1-8 is 10 inches. This was picked as a possible required support spacing for outer wall panels based on panels of 20 inch size. There is a trade-off possible in the weight of skins, frames, and outer wall panels and 10 inch spacing may not be the optimum. However, previous studies of other types of primary structure showed that minimum overall weight is achieved with the biggest possible outer wall panels.

In the regions over the heads of the outboard crew members the frames are eliminated to provide clearance and the skin is supported by closely spaced one inch deep stiffeners spotwelded to the skin and riveted to a beryllium sheet which forms the inboard cap of the stiffeners and makes a smooth ceiling for the crew. This construction is not used throughout the entire vehicle as it is heavier than the skin and frames. However, in this particular application it saves weight as the entire vehicle would be larger and therefore heavier if clearance were provided for conventional frames.

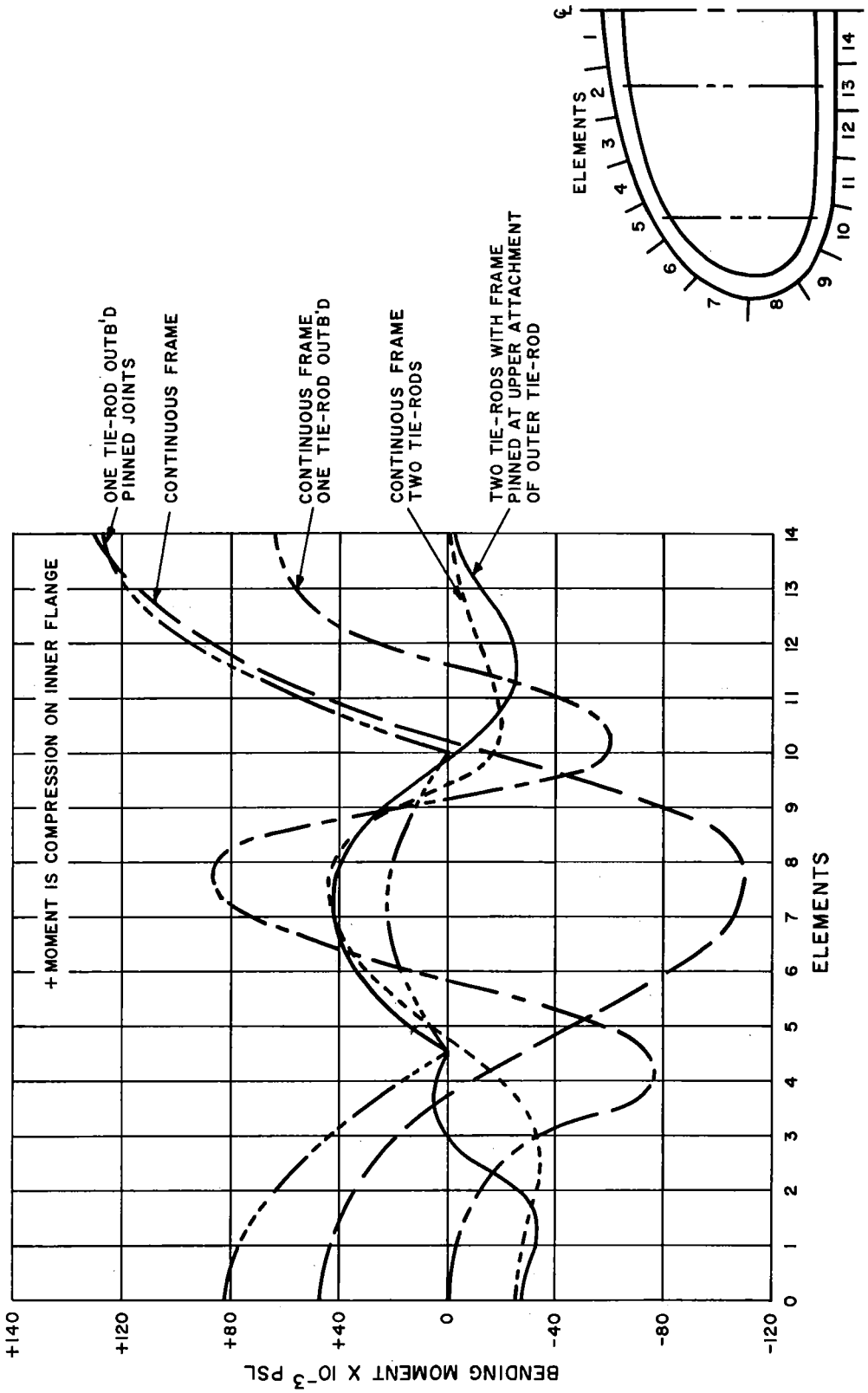

Figure III-1-9. Bending moment distribution for various frame configuration

The aft bulkhead is machined like the lower surface with stiffeners attached to integral flanges on the forward side. Integral flanges on the aft side are provided to attach the elevon pylon.

The fins pylons are beryllium frames covered with outer wall panels and insulation. The fins are conventional aluminum construction protected by outer wall panels and insulation. The elevons have outer wall panels on the lower side only and are of heat sustaining construction.

2.0 Structural Design Criteria

To assure a structural design which will exhibit both high reliability and minimum weight, an ultimate factor of safety of 1.5 and a yield factor of safety of 1.15 were selected. The following additional criteria are used to insure structural integrity in detail design areas.

15 percent margin for all shear joints at ultimate
50 percent margin for all tension joints at ultimate
50 percent margin for the support structure of components whose dislodging could endanger the crew

Design ultimate factor of safety = 2.0 for cabin internal pressure loading.

The loading conditions for which the structure has been analyzed are described below and in Table III-2-I. The spacecraft axial load, side shear, and side bending moment curves are shown on Figure III-2-1. The maximum axial shell loads, maximum side shear flow and maximum external shell pressure curves are shown in Figure III-2-2. The external pressure distribution on the re-entry vehicle for critical conditions is shown in Figure III-2-3. Loads shown are for the selected D-2 configuration.

The forward portion of the external shell of the spacecraft to sta. 238.6 was designed to resist overpressure due to a booster explosion after the craft has aborted. The midportion of the external shell of the spacecraft from sta. 231 to sta. 322.6 has been analyzed for aborting of the craft during maximum dynamic pressure during boost. The spacecraft's external shell aft of sta. 322.6 as well as the adapter section have been designed for boost loading during maximum dynamic pressure with a 100 fps, side gust. No relieving lateral inertia is assumed acting for this condition due to booster dynamic response to the initial gust loading.

The maximum axial acceleration condition during boost provided the criterion for design of the support structure for the propulsion package.

CONFIDENTIAL

TABLE III-2-1

SUMMARY OF DESIGN CONDITIONS (LIMIT LOADS)

VEHICLE	COND.	DESCRIPTION	N_{AFT}*	N_{SIDE}*	WEIGHT 1000 LB	CRITICAL STRUCTURE
LAUNCH 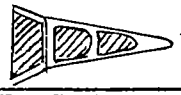	I	BOOST AT MAX. "Q" 100 F.P.S. GUST LOAD	2.0	1.0	20.0	SHELL AND ADAPTER STRUCTURE AFT OF STA. 322.6
	II	BOOST - MAX. AXIAL ACCELERATION	5.1	1.0	20.0	PROPULSION PACKAGE SUPPORT STRUCTURE
ABORT IN BOOST PHASE	III	ABORT OFF LAUNCHING PAD - MAX. AXIAL ACCELERATION	15.0	4.0	9.4	(1) SUPPORT STRUCTURE FOR MISSION MODULE (2) REENTRY VEHICLE LATERAL SUPPORT STRUCTURE (3) INTERNAL MOUNTS IN MISSION MODULE
	IV	ABORT AT MAX. "Q" DURING BOOST 100 F.P.S. GUST	3.4	1.0	9.4	SHELL STRUCTURE BETWEEN STA. 231.0 AND STA. 322.6
	V	10 P.S.I. OVERPRESSURE DUE TO BOOSTER EXPLOSION	-	-	9.4	(1) SHELL STRUCTURE FWD. OF STA. 238.6 (2) FWD. FACE OF R.V. (3) R.V. AXIAL SUPPORT STRUCTURE
RE-ENTRY VEHICLE 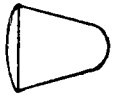	VI	RE-ENTRY AT MAX. "Q"	8.15	1.4	5.1	(1) SHELL STRUCTURE OTHER THAN FWD. FACE (2) FLAP, FLAP ACTUATOR AND SUPPORT STRUCT.
	VII	MAX. CHUTE LOADING	5.7	1.6	5.1	CHUTE ATTACHING STRUCTURE
	VIII	MAX. IMPACT ON LAND	10.0	1.0	5.1	(1) IMPACT BAG STRUCTURE (2) CABIN INTERNAL COMPONENT MOUNTING
PRESSURE CABIN	IX	7 P.S.I INTERNAL PRESSURE	-	-	-	INTERNAL SHELL OF R.V. AND MISSION MODULE

NOTE: NO RELIEVING LATERAL INERTIA IS ASSUMED ACTING FOR SIDE GUST LOAD CONDITIONS.

CONFIDENTIAL

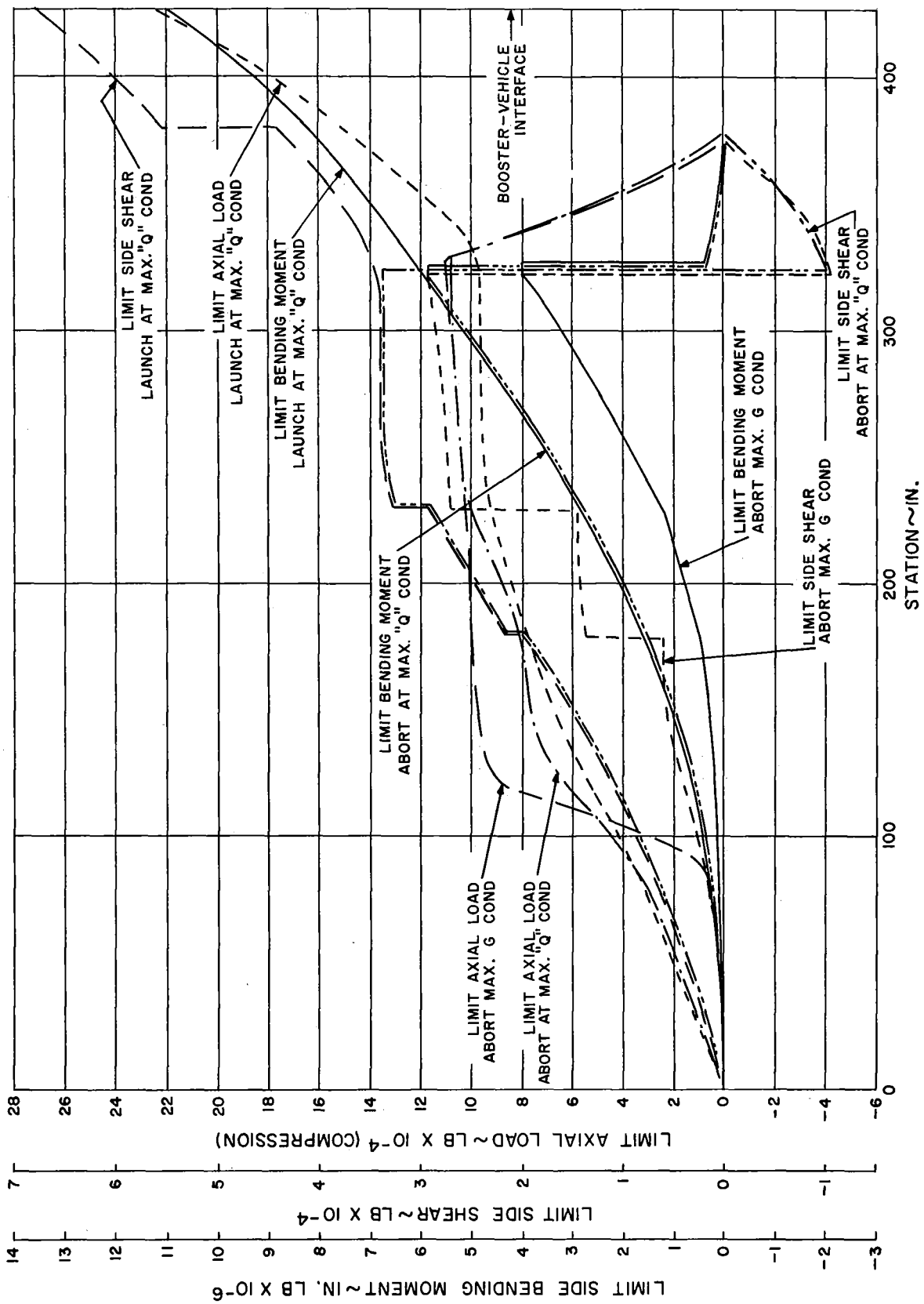

Figure III-2-1. Spacecraft launch and abort conditions axial load, side shear and bending moment

CONFIDENTIAL

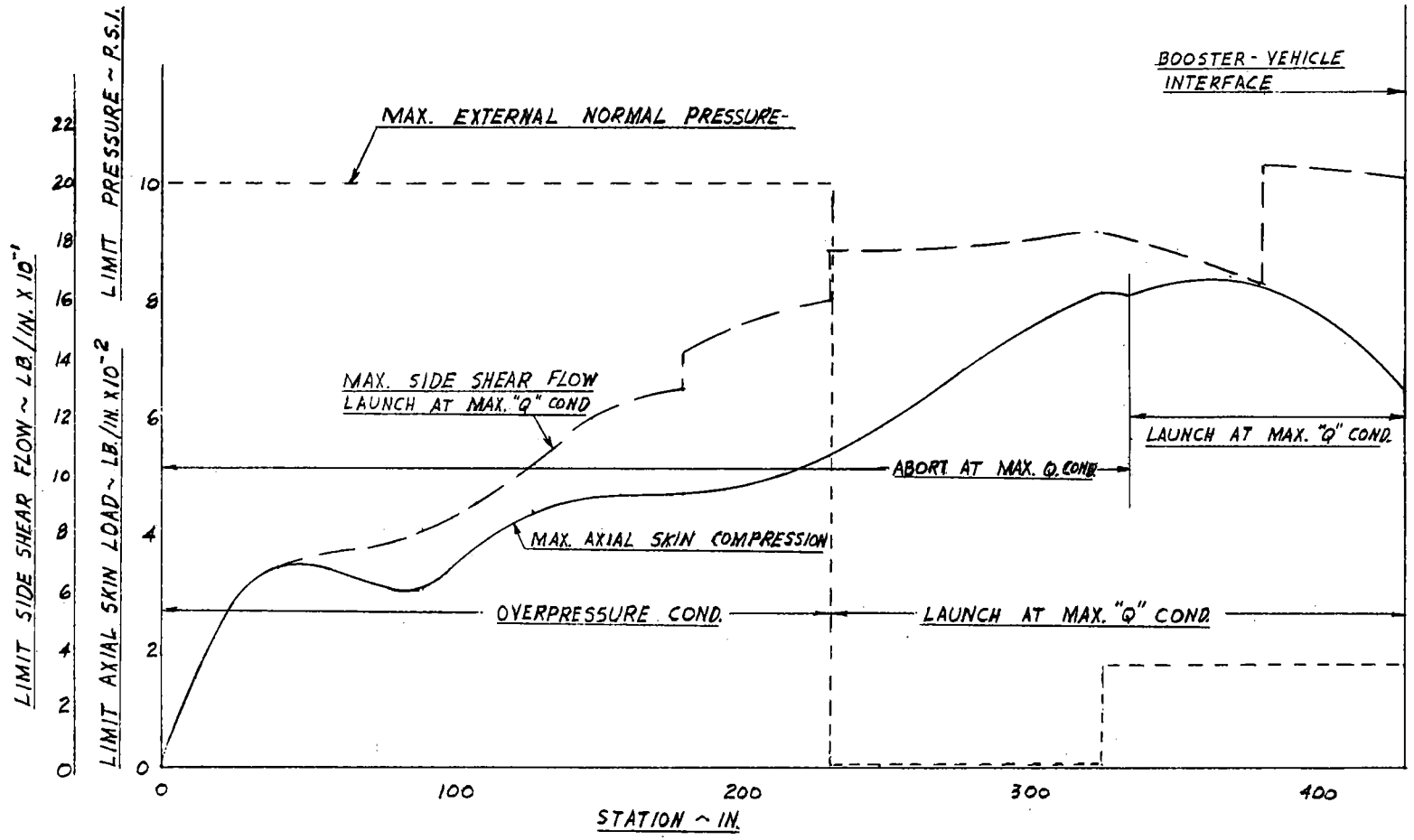

Figure III-2-2. Spacecraft axial skin load, side shear flow and external normal pressure for critical conditions

CONFIDENTIAL

CONFIDENTIAL

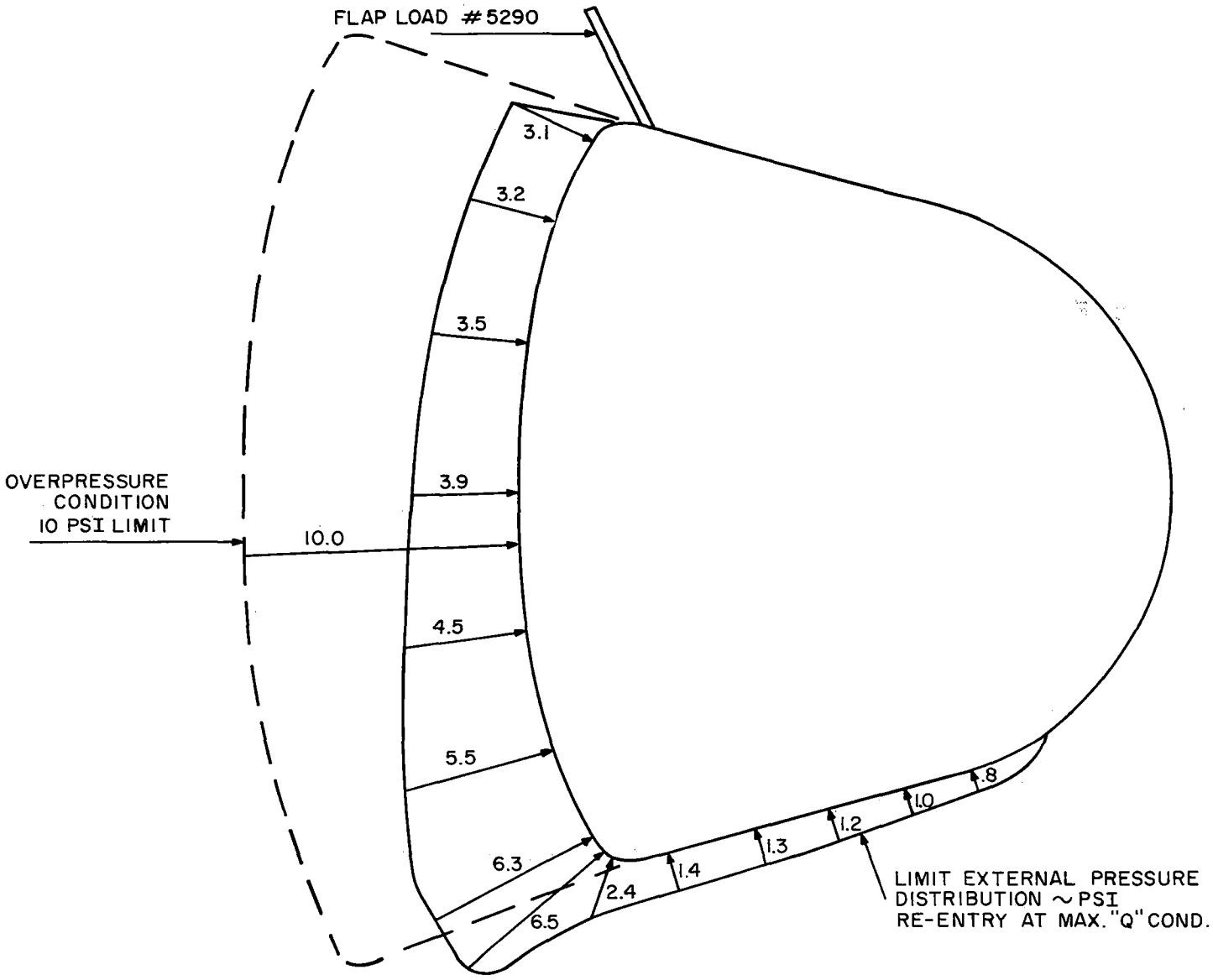

Figure III-2-3. Limit external pressure distributions re-entry vehicle

CONFIDENTIAL

When the craft aborts from the launching pad, maximum axial acceleration is felt on the abort craft. The support structure for the mission module as well as its internal mounting structure and the side support structure for the re-entry vehicle are designed to this condition.

The overpressure condition due to booster explosion after the craft has aborted designs the re-entry vehicles forward face as well as its axial support structure.

The re-entry vehicle shell other than its forward face was designed to re-entry conditions at maximum dynamic pressure. The flap with its actuator and support structure were also designed to this condition. The parachute attaching structure was analyzed for maximum chute dynamic load at chute opening.

The environment pressure required in the cabin during space flight determines the cabin shell design of the re-entry vehicle as well as the shell of the mission module. The impact of the re-entry vehicle on land determines the internal component mounting structure in the re-entry vehicle in addition to the impact bag structure.

2.1 ENVIRONMENTAL CRITERIA

Booster Shock and vibrations from the booster will establish requirements for the design, mounting, and qualification of all components and structure. Predicted levels are below the values currently applicable in ballistic missile weapon systems design.

Space Environment - Effects of high vacuum, radiation, meteoroids and temperature extremes will be considered in all phases of design and qualification of structure, materials, and components. Radiation effects are discussed in Volume V. Present testing of structural materials for the Advent Program indicate that for the APOLLO exposure time of 14 days, no significant effects of vacuum or radiation exposure is expected for either organic or inorganic materials. Results of meteoroid studies are presented in a subsequent section of this chapter.

3.0 Summary of Structural Characteristics

Table III-3-I summarizes the materials, type of construction, and development status for the proposed APOLLO structure.

Heat shield materials are either phenolic nylon currently in use on the Mark 3 ballistic R/V program, or the G.E. series castable materials under development for the Mark 6 R/V Program. These materials have been flight tested on the Mark 3 and RVX-2 programs and represent present design capability. Subsequent development of the G.E. series materials may result in increased weight savings in addition to the lower production costs.

Space vehicle and R/V internal structural materials are conventional aluminum and magnesium alloys and the outer shell aluminum honeycomb is in wide spread usage.

Columbium and pyrolytic graphite are used for the control flap and require extensive research and development, as will the large collapsible solar collector.

3.1 WEIGHT ANALYSIS

3.1.1 Weight Statement — D-2 Configuration (The Selected Configuration)

Overall vehicle weight estimates and a detailed weight breakdown are shown in this section.

Table III-3-II shows the subsystem weights for both present and predicted design capabilities. The predicted weight capabilities are based on state of the art improvements such as limited use of beryllium for sub-structure, heat shield materials improvements, propulsion system optimization, and miniaturization in all subsystem areas.

Table III-3-III lists the distribution of present subsystem weight between the re-entry vehicle, spacecraft, and abort configuration. Note that a significant portion of the total weight remains with the booster for launch pad abort.

Table III-3-IV lists the weight breakdown for the APOLLO Mission Profile. Tabulated are weights for the various vehicle modes throughout the mission sequences.

TABLE III-3-I

SUMMARY OF STRUCTURAL CHARACTERISTICS

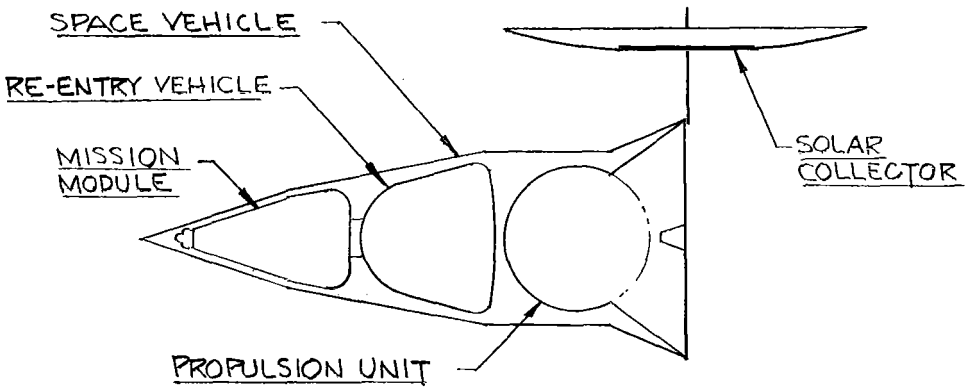

	ITEM	MATERIAL	CONSTRUCTION	MAX. LOAD	MAX. TEMP.	DEVELOPMENT STATUS
RE-ENTRY VEHICLE	HEAT SHIELD	GE SERIES 100 OR 500	MOLD-CAST	RE-ENTRY	RE-ENTRY	RVX FLIGHT TESTED MARK VI DEVELOPMENT
		PHENOLIC NYLON	BONDED TAPE WOUND			IN HOUSE USAGE ON NERV, RVX & MARK III
	OUTER-SHELL	ALUMINUM MAG-THOR	CONVENTIONAL SHEET METAL	RE-ENTRY (PRESSURE)	RE-ENTRY	STATE OF THE ART
	INTERNAL STRUCTURE	ALUMINUM	WELDED SHELL BONDED SHEET METAL FRAMES	ABORT & LANDING IMPACT	ENVIRONMENT CONTROL 70° F	STATE OF THE ART MATL'S. DEVELOPMENT OF PRESSURE SEALS, & SELF SEALANT MAT'L. & REPAIR TECHNIQUES FOR PUNCTURES
	CONTROL FLAP	COLUMBIUM PYROLYTIC GRAPHITE	BUILT-UP SHEET METAL SUB STRUCTURE	RE-ENTRY	RE-ENTRY	CURRENTLY UNDER DEVELOPMENT FOR ADVANCED RE-ENTRY VEHICLES
MISSION MODULE	SHELLS SUPPORT STRUCTURE	ALUMINUM	WELDED SHELL BONDED SHEET METAL FRAMES	POWERED FLIGHT & ABORT	ENVIRONMENT CONTROL 70° F	SAME AS R/V INTERNAL STRUCTURE
SPACE VEHICLE	OUTER SHELL	ALUMINUM HONEYCOMB	BONDED ALUMINUM CORE & FACES	POWERED FLIGHT & ABORT	2ND STAGE BOOST	GENERAL USAGE AT PRESENT DEVELOPMENT OF LARGE BONDED ASSEMBLIES
	INTERNAL SUPPORT STRUCTURE	ALUMINUM OR MAGNESIUM	CONVENTIONAL SHEET METAL	POWERED FLIGHT & ABORT	2ND STAGE BOOST	STATE OF THE ART POSSIBLE BERYLLIUM USAGE
SOLAR COLLECTOR	PARABOLIC REFLECTOR WITH SOLAR CELLS	EPOXY HARDENED SHEEL WITH ALUMINIZED SURFACE	SPIN MOLD FORMED WITH INFLATABLE MYLAR BAG	POWERED FLIGHT	LUMAR SPACE FLIGHT	1.) SPACE INFLATABLE STRUCTURE & REFLECTOR DEVELOPMENT 2.) RELATED IN HOUSE PROGRAMS STEPS, SOLAR SIMULATOR & AIR FORCE - MSVD R&D ON INFLATABLE SOLAR REFLECTORS

III-38

TABLE III-3-II

WEIGHT SUMMARY, D-2 CONFIGURATION

SUBSYSTEMS	PRESENT DESIGN CAPABILITY WEIGHT	PREDICTED DESIGN CAPABILITY WEIGHT
PROPULSION SYS.	12225	11508
LIFE SUPPORT EQUIP.	1931	1720
NAV. AND CONTROL SYS.	336	270
POWER SUPPLY SYS.	782	630
SEARCH AND RECOVERY SYS.	625	550
ELECTRICAL SYS.	285	250
INSTR. AND COMM. SYS.	159	150
STRUCTURE	4177	3750
GROSS WEIGHT	20,520	18,828
ESCAPE WEIGHT	18,000	16,300

TABLE III-3-III

WEIGHT BREAKDOWN, D-2 CONFIGURATION

SUBSYSTEM	R/V	- WEIGHT - S/V (Total)	S/V (Abort)
STRUCTURE	2275	1902	1365
INSTR. AND COMM. SYS.	107	52	36
POWER SUPPLY SYS.	357	425	---
SEARCH AND RECOV. SYS.	625	---	---
PROPULSION	---	12225	2208
NAV. AND CONTROL SYS.	190	146	146
ELECTRICAL SYS.	75	210	130
LIFE SUPPORT EQUIP.	1489	442	442
TOTAL	5,118	15,402	4,327

GROSS WT = R/V + S/V_{Total} = 20520

ABORT WT = R/V + S/V_{Abort} = 9445

Preliminary center of gravity locations and moments of inertia are shown in Tables III-3-V and III-3-VI for the present re-entry vehicle and spacecraft.

Table III-3-VII is a detailed weight breakdown of the subsystem components summarized in the previous tables.

3.2 WEIGHT STATEMENT — R-3

The APOLLO Vehicle Weight Data contained in the following pages is a result of several configuration studies conducted during the past several months. Table III-3-VIII presents a chart of the vehicle subsystems and gross weights of a development version and an ultimate 1966 version. The chart shows that a weight saving of 1633 pounds will be achieved by 1966. Table III-3-IX presents a Summary Weight and Balance for both the Recovery Vehicle and the Space Vehicle which when combined give the APOLLO gross weight. The Recovery Vehicle moments of inertia are also summarized therein. The Detail Weight and Balance of the Recovery Vehicle is shown in Table III-3-X.

The configuration studies were conducted to obtain, among other considerations, an optimum weight. The major Bell Responsibility for obtaining weight optimization occurs in the structural concept. Therefore, several structural designs were studied in order to select the optimum arrangement which is reflected in the weight estimates herein. The structural concepts, including heat protection, are discussed in Section 1.4 of this chapter.

The subsystem weights, provided by the General Electric Company, are used in their entirety where possible, and modified to be compatible with the Bell configuration in some instances. The propulsion subsystem weights were obtained from Bell Aerosystems Report 7110-945003. If a lox-hydrogen system is used with the modified lenticular configuration, the propulsion system weights should be obtained from the Aerojet Propulsion report.

TABLE III-3-IV

APOLLO MISSION WEIGHT PROFILE

SUBSYSTEM	GROSS (ON PAD)	LUNAR ORBIT (FREE FLIGHT) (ESCAPE)	LUNAR ORBIT PRIOR TO RE-ENTRY	ABORT	ABORT (LESS ROCKETS)
R/V	5118.0	5118.0	5118.0	5118.0	5118.0
S/V	---	---	---	---	---
STRUCTURE	1576.0	1547.0	1547.0	1365.0	1365.0
INSTR. AND COMM.	52.0	52.0	52.0	36.0	36.0
PWR. SUPPLY	425.0	425.0	425.0	---	---
NAV. AND CONTR.	146.0	146.0	146.0	146.0	146.0
PROPULSION	12225.0	10060.0	2140.0	2208.0	91.0
LIFE SUPPORT	442.0	442.0	442.0	442.0	442.0
SEARCH AND RECOV.	---	---	---	---	---
ELEC. SYS.	210.0	210.0	210.0	130.0	130.0
ADAPTER	326.0	---	---	---	---
TOTAL	20,520.0	18,000.0	10,080.0	9,445.0	7,328.0

CONFIDENTIAL

CONFIDENTIAL

[redacted]

TABLE III-3-V

WEIGHT AND BALANCE SUMMARY, D-2 RE-ENTRY VEHICLE

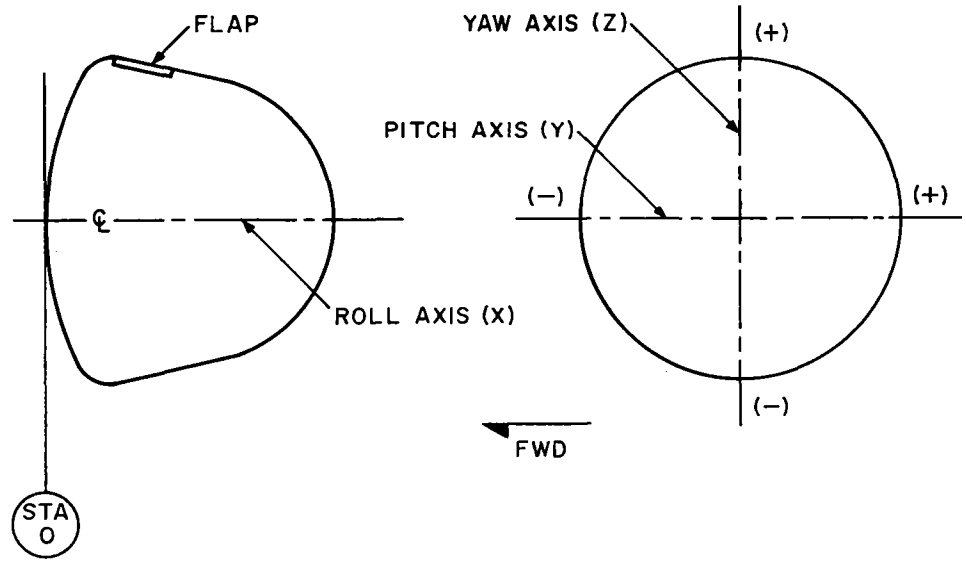

WEIGHT AND BALANCE SUMMARY
(R/V)

WEIGHT	CENTER OF GRAVITY			MOMENT OF INERTIA [1]			PRODUCT OF INERTIA [1]		
	ROLL FROM STA. O	YAW FROM	PITCH FROM	ROLL ABOUT	YAW ABOUT C. G.	PITCH ABOUT C. G.	ROLL-YAW	ROLL-PITCH	PITCH-YAW
5118.0	29.2	-2.6	0.5	1172	1149	1357	-153	52	-7

[1] ALL MASS MOMENTS OF INERTIA ARE IN SLUG FT^2 UNITS.

[redacted]

TABLE III-3-VI

WEIGHT AND BALANCE SUMMARY, D-2 SPACECRAFT

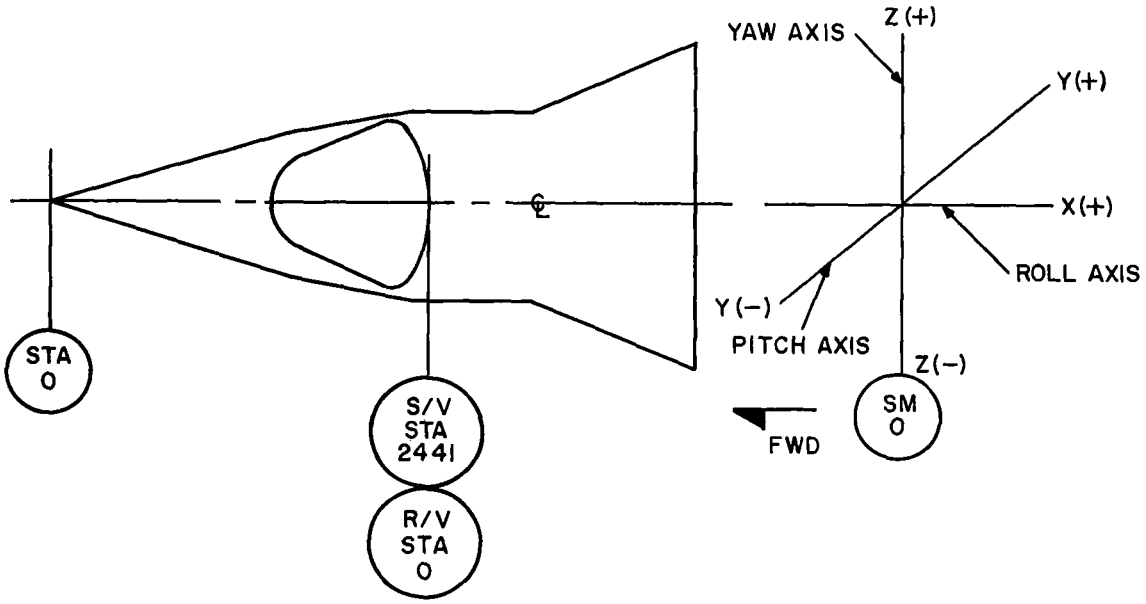

WEIGHT AND BALANCE SUMMARY
S/V

ITEM	WEIGHT	CENTER OF GRAVITY			MOMENT OF INERTIA [1]			PRODUCT OF INERTIA [1]		
		ROLL FROM STA. O	YAW FROM	PITCH FROM	ROLL ABOUT	YAW ABOUT C.G.	PITCH ABOUT C.G.	ROLL-YAW	ROLL-PITCH	PITCH-YAW
GROSS (ON PAD)	20563.0	(285.3)	(-0.8)	(4.3)	6407	29878	30444	-1592	11558	-22
LUNAR ORBIT FREE FLT. (ESCAPE)	18000.0	(279.4)	(-0.9)	(-0.1)	2994	22900	23106	-1558	-492	-7
LUNAR ORBIT ANT. AND COLL. EXT.	18000.0	(278.6)	(4.2)	(-0.1)	13733	35373	39505	11048	-648	-7
LUNAR ORBIT PRIOR TO RE-ENTRY	10080.0	(233.6)	(8.2)	(-0.2)	13670	27334	31403	10329	-633	-10
ABORT	9445.0	(230.3)	(-1.7)	(9.3)	4818	15842	16513	-1407	10720	-40
ABORT LESS ROCK.	7328.0	(204.6)	(-2.2)	---	2157	6684	6897	-1321	-361	-7

[1] ALL MASS MOMENTS OF INERTIA ARE IN SLUG FT^2 UNITS

TABLE III-3-VII

DETAIL WEIGHT BREAKDOWN
D-2 CONFIGURATION

STRUCTURE			2275.0
R/V			
HEAT SHIELD			
INSULATION (INTERNAL)		1450.0	
FLAP		250.0	
FLAP INCL. (STR. AND ABL.)		25.0	
SKIN (HEAT SHIELD SUPT.)		130.0	
HONEYCOMB (HEAT SHIELD SUPT.)		82.0	
HATCH ASS'Y.		15.0	
FITTING		36.0	
HATCH	(35)		
SEPARATION AND CHUTE	(28.3)		
CHUTE TIE	(4.2)		
BULKHEAD		44.5	
STA. 72.0	(11.0)		
STA. 26.5	(14.5)		
STA. 16.5	(19.0)		
SHAPED CHARGE ASS'Y.		12.5	
HEAT INSULATOR		0.5	
PRESSURE VESSEL		229.5	
SKIN	(110.0)		
HONEYCOMB	(30.0)		
LONGERON (8)	(52.0)		
LONGERON (Fig)	(20.0)		
BEAMS (4)	(17.5)		
S/V			1576.0
NOSE FAIRING		29.0	
SHELL		745.6	
HONEYCOMB	(680.6)		
SKIN	(65.0)		

TABLE III-3-VII

DETAIL WEIGHT BREAKDOWN
D-2 CONFIGURATION - Continued

STRUCTURE (Cont'd)			
S/V (Cont'd)			
FRAMES (RINGS)		276.5	
ACCESS DOOR		20.0	
ACCESS DOOR INC'L.		11.0	
PROPULSION SUPT'S.		156.5	
MISSION MODULE		188.4	
SKIN	(132.0)		
LONGERON	(20.0)		
FLOOR AND SUPT'S.	(36.4)		
R/V SUPPORT		149.0	
CONE	(76.0)		
BUMPERS	(73.0)		
TOTAL STRUCTURE (BASIC)			3851.0
ADAPTER (INTER-STAGE)		326.0	
FRAMES (RINGS)	92.5		
HONEYCOMB	233.5		
GROSS STRUCTURE			4177.0
INSTRUMENT AND COMMUNICATION			
R/V SECTION			107.0
EMERGENCY TRANS-RCVR		10.0	
PWR. SUPPLY		4.0	
DATA RECORDER		22.0	
PCM MULTIPLEX-ENCODER (5)		35.0	
250 MC XMTR (2)		7.0	
250 MC RCVR		5.0	
250 MC DIRECTIONAL FILTER		5.0	
ANT. (5)		19.0	

TABLE III-3-VII

DETAIL WEIGHT BREAKDOWN
D-2 CONFIGURATION - Continued

INSTRUMENT AND COMMUNICATION (Cont'd)		
S/V (MISSION) SECTION		52.0
2 KMC VOICE/TV XMTR.	6.0	
T/M XMTR-2 KMC	6.0	
2 KMC RECEIVER	5.0	
2 KMC DIRECTIONAL FILTER	5.0	
PWR SUPPLY	4.0	
ANTENNA (PARABOLA)	16.0	
ANTENNA (3)	10.0	
TOTAL INSTRUMENT AND COMMUNICATION		159.0
POWER SUPPLY SYSTEM		
R/V SECTION		357.0
BATTERIES	103.0	
FUEL CELLS	190.0	
REGULATOR (16)	64.0	
S/V (MISSION) SECTION		425.0
SOLAR CELLS AND COLLECTOR	425.0	
TOTAL POWER SUPPLY SYS.		782.0
NAVIGATION AND CONTROL SYSTEM		
R/V SECTION		190.0
RE-ENTRY FLIGHT CONTROL (FLAP ACTUATOR AND ROLL JETS)	75.0	
STABLE PLATFORM AND ELECTRONICS	40.0	
COMPUTER	50.0	
NAVIGATION AIDS	25.0	

TABLE III-3-VII

DETAIL WEIGHT BREAKDOWN
D-2 CONFIGURATION - Continued

NAVIGATION AND CONTROL SYSTEM (Cont'd)			
S/V (MISSION) SECTION			146.0
MANUAL NAVIGATION EQUIP.		25.0	
TRACKER PLATFORM AND ELECTRONICS		45.0	
RADAR ALTIMETER		50.0	
I.R. SENSOR AND ELECTRONICS (2)		26.0	
TOTAL NAVIGATION AND CONTROL SYSTEM			336.0
PROPULSION SYSTEM			
S/V (MISSION) SECTION			12225.0
ATTITUDE CONTROL SYS.		271.0	
TANKS, FUEL AND ETC.	(271.0)		
ABORT AND SEPARATION SYS.		2208.0	
SMALL SEPARATION ROCKETS (8)	(43.0)		
LARGE SEPARATION ROCKETS (4)	(335.0)		
ABORT ROCKETS (8)	(1830.0)		
PROPULSION SYS.		9746.0	
THRUST CHAMBER (4) (TANKS INCL'D)	(1461.0)		
FUEL, OXIDIZER AND PRESS GAS	(8285.0)		
TOTAL PROPULSION SYSTEM			12225.0
LIFE SUPPORT EQUIPMENT			
R/V SECTION			1489.0
CREW (3)		540.0	
ACCEL. SEATS AND RESTRAINT SYS. (3)		90.0	
SECONDARY PRESS SYS.		105.0	
EMERGENCY ENVIR. PACKS (3)		24.0	
WATER, CONTAINERS AND BLADDERS		68.0	
SURVIVAL EQUIPMENT		75.0	
INSTR. PANEL AND CONSOLE		25.0	
INSTR. AND CONTROLS		150.0	

TABLE III-3-VII

DETAIL WEIGHT BREAKDOWN
D-2 CONFIGURATION - Continued

LIFE SUPPORT EQUIPMENT (Cont'd)		
R/V SECTION (Cont'd)		
SENSING AND CONTROL	25.0	
CABIN COMMUNICATION	5.0	
MISC'L. FURNISHINGS	20.0	
FIRE CONTROL	15.0	
LIGHTING AND TRIM	5.0	
PERISCOPE	45.0	
HEAT EXCHANGER (INC'L.) WATER REMOV. (5.0*), WATER RECOV. EQUIP. (10.0*) AND PART. MATTER FILTER (5.0*)	40.0	
DILUENT SUPPLY	28.0	
O_2 SUPPLY (PRIMARY)	150.0	
CO_2 REMOV. (NORMAL) (INC'L.) CO_2 BACKUP (10*) AND N AND T REMOV. (10*)	79.0	
S/V (MISSION) SECTION		442.0
SPACE RADIATORS	35.0	
CREW STATION SEAT	5.0	
PERSONAL EQUIP.	30.0	
TOILET	15.0	
RECREATION EQUIP.	10.0	
LIGHTING AND TRIM	5.0	
GALLEY AND FOOD	183.0	
MISC'L. FURNISHINGS	10.0	
O_2 SUPPLY (SECONDARY)	50.0	
DILUENT SUPPLY	28.0	
FIRE CONTROL	15.0	
INSTR. AND CONTROLS (CONSOLE)	15.0	
URINE AND FECES RECOV. STORAGE	5.0	
URINE RECOVERY EQUIP.	27.0	
FOOD SERVICE EQUIP.	5.0	
HYGINE EQUIP.	4.0	
TOTAL LIFE SUPPORT EQUIPMENT		1931.0

TABLE III-3-VII

DETAIL WEIGHT BREAKDOWN
D-2 CONFIGURATION - Continued

SEARCH AND RECOVERY SYSTEM		
R/V SECTION		625.0
BEACON-ELEC	8.0	
ANTENNA	3.0	
CHAFF EJECTOR	8.0	
FLARE CLUSTER	9.0	
PWR. SUPPLY	15.0	
PROGRAMMER	6.0	
CHAFF	2.0	
LIGHT	2.0	
SO-FAR BOMB	4.0	
DYE MARKER	4.0	
HAND OPERATED DEVICES	10.0	
MAIN CHUTE (3)	130.0	
BRAKE CHUTE	30.0	
CHUTE-EQUIP.	40.0	
FLOTATION SYS.	150.0	
IMPACT EQUIP.	204.0	
TOTAL SEARCH AND RECOVERY		625.0
ELECTRICAL SYSTEM		
R/V SECTION		75.0
WIRING	35.0	
ELEC. EQUIP. (RELAY, CONN. GR. BR. AND ETC)	35.0	
INTER-STAGE CONN.	5.0	
S/V (MISSION) SECTION		210.0
WIRING	50.0	
ELEC. EQUIP. (RELAY, CONN. AND ETC)	140.0	
UMBILICAL CONN.	5.0	
INTER-STAGE CONN. (2)	10.0	
IN-FLIGHT CONN.	5.0	
TOTAL ELECTRICAL SYSTEM		285.0

TABLE III-3-VIII

WEIGHT SUMMARY - R-3 CONFIGURATION

Subsystem	Present Design Capability Weight	Predicted Design Capability Weight
Structure	4896	4440
Instruments and Communication	164	155
Power Supply	782	630
Navigation and Control	1373	1090
Propulsion (incl. abort)	9241	8790
Life Support	1890	1682
Search and Recovery	191	168
Electrical	433	382
Total	18970	17337

Therefore a weight reduction of 1633 pounds is predicted in the 1966 version.

TABLE III-3-IX

SUMMARY WEIGHT AND BALANCE - R-3 SPACECRAFT

	Weight	Arm	Moment
Recovery Vehicle	5783	(74.1)	428623
Structure	2797		241044
Instrument and Communication	112		4368
Power Supply	357		7140
Navigation and Control	756		55985
Life Support	1347		89758
Search and Recovery	191		20628
Electrical	223		9700
*Moments of Inertia for the Recovery Vehicle are:			
I_x (Roll) = 110 slug ft^2			
I_y (Pitch) = 2049 slug ft^2			
I_z (Yaw) = 2563 slug ft^2			
Space Vehicle	13187	(252.7)	3332176
Structure	2099		504006
Instrument and Communication	52		12335
Power Supply	425		142375
Navigation and Control	617		176250
Propulsion	9241		2332751
Life Support	210		44340
TOTAL VEHICLE	18970	(198.2)	3760799

TABLE III-3-X

DETAIL WEIGHT AND BALANCE R-3 CONFIGURATION

	Weight	Horizontal Arm	Horizontal Moment
Structure			
Recovery Vehicle	(2797)		(241044)
Aerodynamic Surfaces	(498)		(68830)
Elevons	(146)		(22338)
Structure	58	153	8874
Ablative Material	41	153	6273
Outer Wall Panels (Lower)	47	153	7191
Vertical Tail	(352)		(46492)
Structure	80	140	11200
Leading Edge	130	124	16120
Outer Wall Panels-Outer	53	141	7473
-Inner	39	141	5499
Finfold Structure and Mechanism	50	124	6200
Body	(2299)		(172214)
Primary Structure			
Cockpit	(681)		(58950)
Frames and Bulkheads	216	78	16848
Covering	222	85	18870
Longerons	90	58	5220
Crew Seat Attachment	12	68	816
Tie Rods	15	64	960
Elevon Attachment	12	138	1656
Abort Rocket Attachment	30	138	4140
Booster Attachment	12	135	1620
Parachute Attachment	8	113	904
Fin Fittings	12	118	1416
Fin Pylon	52	125	6500

TABLE III-3-X (Continued)

DETAIL WEIGHT AND BALANCE
R-3 CONFIGURATION

	Weight	Horizontal Arm	Moment
Secondary Structure	(426)		(25670)
Separation System	10	134	1340
Windshield	115	26	2990
Windshield Cowl	19	26	494
Windshield Cowl Jettison System	10	26	260
Hatch-Entrance	28	63	1764
Hatch-Entrance Rel. Mech.	10	63	630
Cockpit Floor	22	60	1320
Tunnel Pressure Door	21	134	2814
Parachute Container	16	113	1808
Equipment Supports	175	70	12250
Ablative Material	444	77	34188
Outer Wall Panels Incl. Insulation	(748)		(53406)
Body - Upper	274	63	17262
Body - Lower	384	66	25344
Fin - Pylon - Outer	63	120	7560
Fin Pylon - Inner	27	120	3240
Space Vehicle	(2099)		(504006)
Transition R/V to S/V	(245)		(38698)
Outer Fairing	49	160	7840
Box Section and Plate	30	140	4200
Bulkheads	7	149	1043
Rings	38	163	6194
Skin	82	165	13530
Tunnel	13	152	1976
Fittings	15	151	2265
Miscellaneous	11	150	1650

TABLE III-3-X (Continued)

DETAIL WEIGHT AND BALANCE
R-3 CONFIGURATION

	Weight	Horizontal Arm	Moment
Mission Module	(720)		(154272)
Outer Skin	240	205	49200
Forward Bulkhead	72	174	12528
Aft Bulkhead	231	240	55440
Forward Attachment Fitting	40	180	7200
Aft Attachment Fitting	63	228	14364
Equipment Supports	60	210	12600
Miscellaneous Standards	14	210	2940
Attachment Mission Module to Propulsion Module	(42)	228	(9576)
Propulsion Module	(988)		(269012)
Fairing	563	274	154262
Propulsion System Supports	425	270	114750
Attachment Propulsion Module To Booster	(104)	312	(32448)
Total Structure	4896		745050
Instrument and Communications			
Recovery Vehicle	(112)	39	(4368)
Transmitter	15		
Data Recorder	25		
PMC Multiplexer / Encoder / 51	40		
Transmitter	6		
Antenna	8		
Receiver Decoder	8		
Signal Conditioner	6		
Receiver	4		

TABLE III-3-X (Continued)

DETAIL WEIGHT AND BALANCE
R-3 CONFIGURATION

	Weight	Horizontal Arm	Horizontal Moment
Space Vehicle	(52)		(12335)
Power Amplifier	15	225	3375
Antenna Multiplexer	4	230	920
T/V Camera	17	200	3400
Antenna	16	290	4640
Total Instrument and Communication	164		16703
Power Supply System			
Recovery Vehicle	(357)		(7140)
Battery	103	20	2060
Fuel Cells	190	20	3800
Regulator	64	20	1280
Space Vehicle	(425)		(142375)
Solar Cells and Reflector	425	335	142375
Total Power Supply	782		149515
Navigation and Control	(756)		(55985)
Recovery Vehicle			
Orientation Controls			
Controller	(6)	58	(348)
Flight Control System	(47)	39	(1833)
Air Data System	(9)	20	(180)
Reaction Controls	(71)		(7946)
Nozzles and Valves	10	87	870
Pressure System	6	116	696
Propellant	30	116	3480
Propellant System Incl. - Tanks	25	116	2900

TABLE III-3-X (Continued)

DETAIL WEIGHT AND BALANCE
R-3 CONFIGURATION

	Weight	Horizontal Arm	Moment
Elevon Actuator	(45)	135	(6075)
Rudder Actuator	(35)	129	(4515)
Fin Fold Actuator	(48)	118	(5664)
Guidance	(190)		(10800)
Stable Platform	40	120	4800
Computer	50	42	2100
Radar Altimeter	50	39	1950
Navigation Aids	25	39	975
Miscellaneous	25	39	975
Hydraulics	(305)		(18624)
Motors (2)	130	22	2860
Pump (2)	32	13	416
Reservoir (2)	30	127	3810
Accumulator (2)	20	126	2520
Filters	8	126	1008
Valves	10	126	1260
Controls	3	90	270
Plumbing	30	90	2700
Fluid	32	90	2880
Miscellaneous	10	90	900
Space Vehicle	(617)		(176250)
Tracker Platform and Electronics	45	220	9900
I R Sensors	26	215	5590
Aux. Navigation Equipment	25	226	5650
Miscellaneous	14	215	3010
Attitude Control System	507	300	152100
Total Navigation and Control	1373		232235

TABLE III-3-X (Continued)

DETAIL WEIGHT AND BALANCE
R-3 CONFIGURATION

	Weight	Horizontal Arm	Moment
Propulsion			
Space Vehicle			
Abort Solid Propellant Chamber (6)	1129	126	142254
Attaching Rack for Abort Rockets	100	130	13000
Propulsion System Tanks	352	285	100320
Motor and Pump	555	280	155400
Instrumentation Pick-Ups	25	260	6500
Propellant System	122	280	34160
Pressurization System, Incl. Helium	189	283	53487
Propellant	6769	270	1827630
Total Propulsion System	9241		2332751
Life Support			
Recovery Vehicle	(1347)		(89758)
Crew	540	66	35640
Seats and Restraint System	90	70	6300
Cocoons (3)	30	70	2100
Survival Equipment	75	92	6900
Personal Equipment	30	88	2640
Console	25	69	1725
Lighting and Trim	5	70	350
Misc. Furnishings	25	88	2200
Cabin Communication	5	70	350
O_2 Liquid	112	69	7728
O_2 Container	38	69	2622
N_2 Liquid	22	38	836
N_2 Container	6	38	228
CO_2 Removal	79	66	5214

TABLE III-3-X (Continued)

DETAIL WEIGHT AND BALANCE
R-3 CONFIGURATION

	Weight	Horizontal Arm	Moment
Heat Exchanger	25	87	2175
Fire Control	15	70	1050
Sen. and Control	25	22	550
Urine and Feces Storage	5	88	440
Miscellaneous Pressure Suit (3)	45	88	3960
Instruments and Controls	150	45	6750
Space Vehicle	(543)		(120119)
Space Radiators	35	280	9800
Crew Station Seats	5	220	1100
Toilet	15	228	3420
Galley and Food (Incl. Water)	215	218	46870
Recreation Equipment	1	220	220
Lighting and Trim	5	190	950
Miscellaneous Furnishings	15	200	3000
O_2 Supply (Secondary)	50	227	11350
Diluent Supply	28	227	6356
Heat Exchanger (Secondary)	10	230	2300
Fire Control	15	200	3000
Water Recovery	4	220	880
Instruments and Controls	15	195	2925
Maint. Equip, and Misc.	40	210	8400
Water and Container	66	218	14388
Miscellaneous	24	215	5160
Total Life Support	1890		209877

TABLE III-3-X (Continued)

DETAIL WEIGHT AND BALANCE
R-3 CONFIGURATION

	Weight	Horizontal Arm	Moment
Search and Recovery			
Recovery Vehicle	(191)		(20628)
Emergency Abort Parachute			
Associated Equipment	61	108	6588
Main Chute	100	108	10800
Chute Equipment	30	108	3240
Total Search and Recovery	191		20628
Electrical			
Recovery Vehicle	(223)		(9700)
Inverters	90	23	2070
Protective Devices	4	25	100
Junction Boxes	15	25	375
Relays	15	25	375
Umbilical	6	70	420
Lights			
Controls	3	70	210
Wiring	70	65	4550
Separation	10	135	1350
Misc.	10	25	250
Space Vehicle	(210)		(44340)
Wiring	50	220	11000
Umbilical Connection	5	135	675
Inter-Stage Connection	10	135	1350
In-Flight Connection	5	135	675
Transformer	8	225	1800
AC and DC Buss	7	220	1540
Circuit Breakers and Relays	12	220	2640

TABLE III-3-X (Continued)

DETAIL WEIGHT AND BALANCE
R-3 CONFIGURATION

	Weight	Arm	Moment
Fuses and Regulators	3	220	660
Inverters and Junction Box	50	220	11000
Clamps and Supports	35	220	7700
Light, Recept, and Switch	10	200	2000
Misc.	15	220	3300
Total Electrical	433		54040

4.0 Structural Optimization

Preliminary studies indicated that for the selected configuration, D-2, aluminum honeycomb structure would be the best considering the environmental design conditions of the APOLLO Vehicle. The APOLLO spacecraft forward conical shell, designed for uniform external collapsing pressure, was investigated in a structural optimization study. This study considered several present state of the art materials; aluminum, steel and magnesium. Due to the inherent fabrication problems associated with magnesium construction it was eliminated as a structural material for the APOLLO spacecraft shell. Considering steel and aluminum, the basic theory, as shown on Figure III-4-1, that for materials with approximately the same ratio of modules of elasticity to density, the material with the lowest density would result in the lightest structure designed for stability, resulted in the choice of aluminum for the spacecraft outer shell.

Further study was pursued to determine the lightest type of aluminum construction. Figure III-4-2 indicates the comparison between semi-monocoque construction, thin skin and stabilizing frames, and honeycomb construction. As the figure denotes, the honeycomb construction is the lightest, in fact, approximately 1.1 pounds per square foot lighter than the skin and frame type of construction. Note that this study considered the splice and other support frames required for both types of construction.

Another consideration in the final selection of aluminum honeycomb construction was the efficient meteoroid protection it affords by providing effective multiple bumpers.

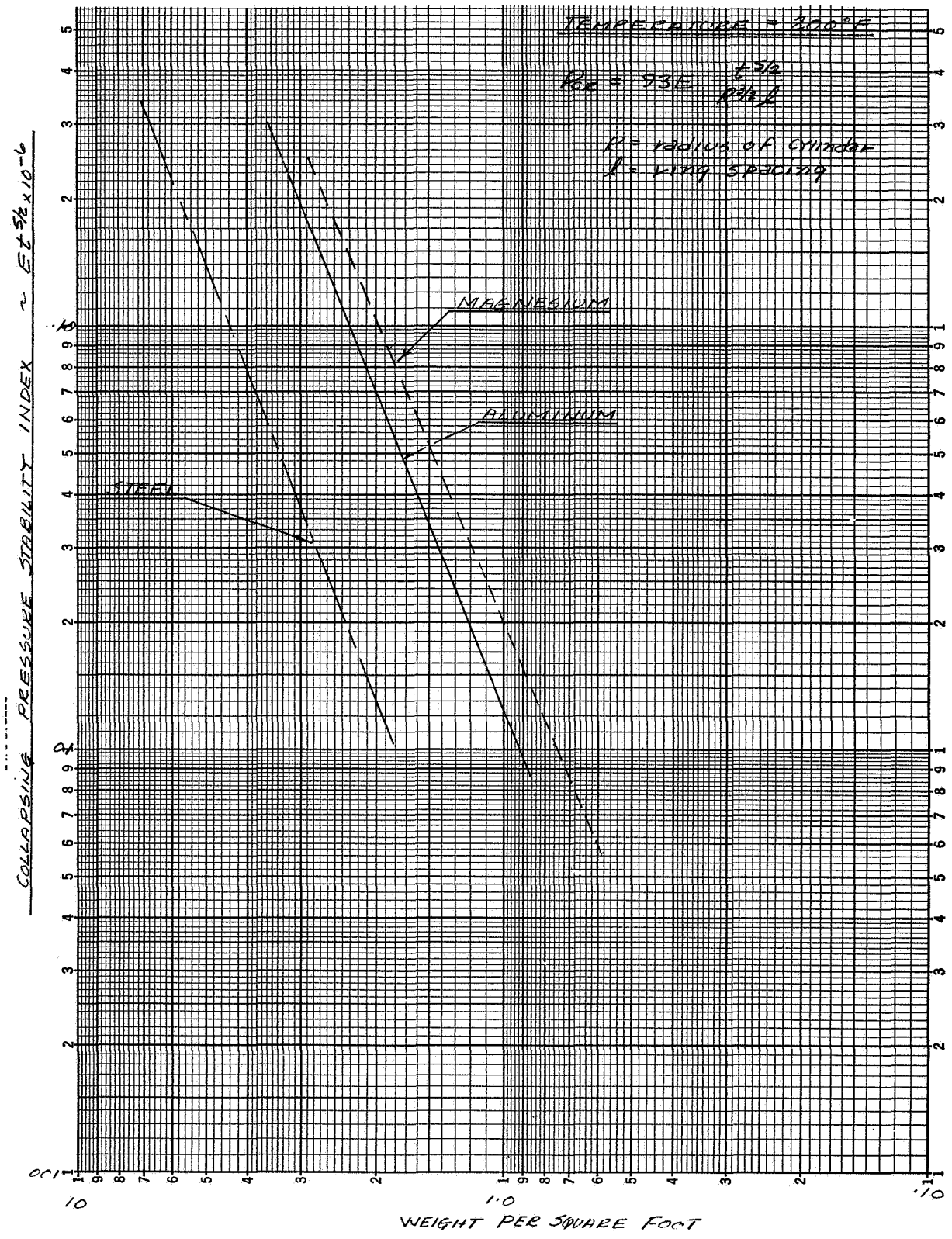

Figure III-4-1. Structural efficiency, external collapsing pressure loading

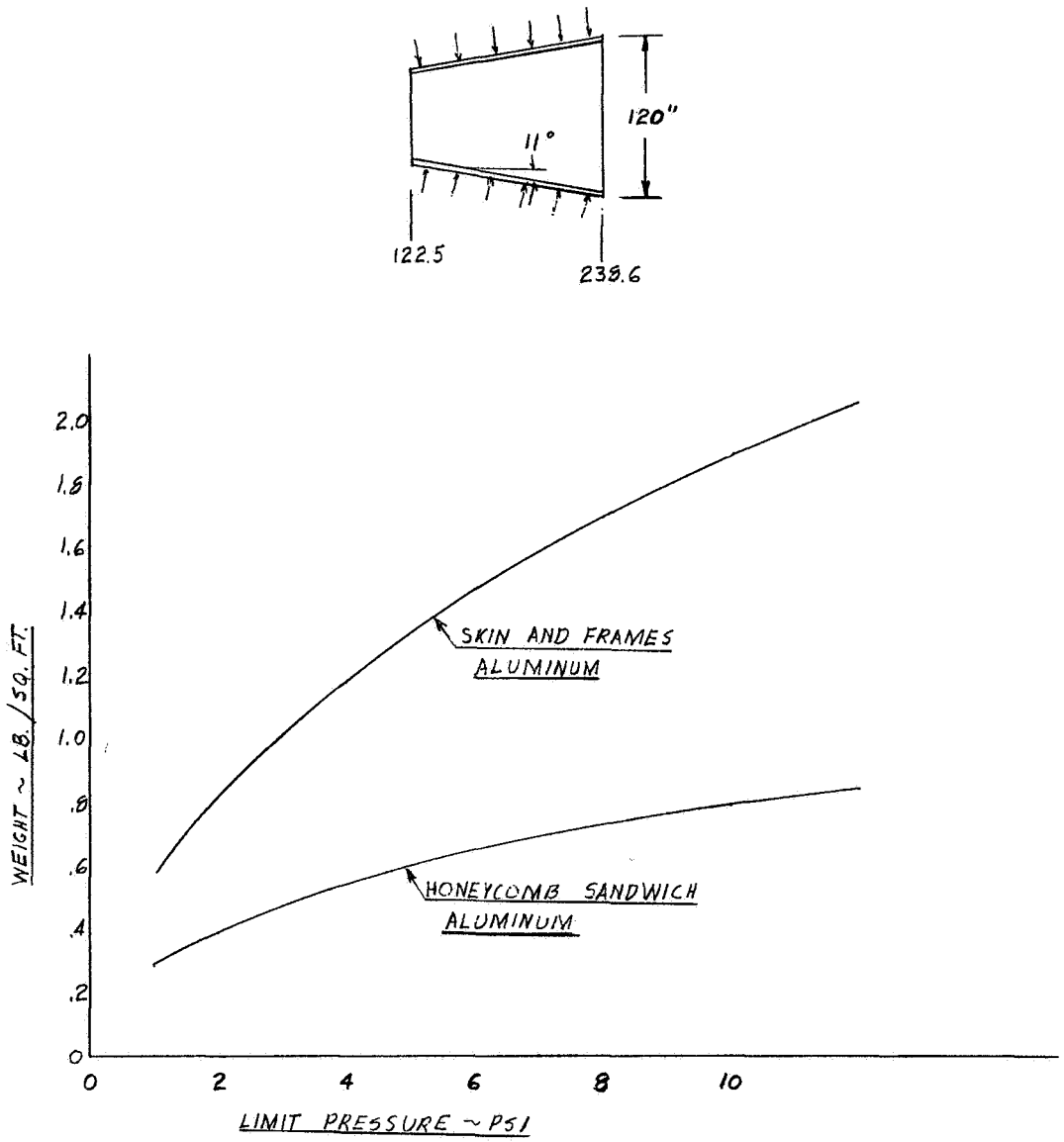

Figure III-4-2. Weight optimization, concial frustrum sta. 122.6 to 238.6, uniform external collapsing pressure

5.0 Meteoroid Impact Evaluation

The long flight times of the APOLLO vehicle in the lunar orbiting mission require that the design study thoroughly assess the damage potential of the environmental condition of the meteoroid population in space. Results of this study are then used in determining the protection which must be provided to insure a high probability of crew survival. The meteoroid population as estimated by various agencies is shown on Figure III-5-1.

The probabilities of meteoroid penetration of the APOLLO vehicle have been analyzed by two methods. The first method considered has been developed by M. Kornhauser of the General Electric Company, (Ref. 1), and assumes a meteoroid population equivalent to the Hughes maximum mass data. The second method, D. Beard, (Ref. 2), is based on an average meteoroid population. Results of these analyses illustrate the variations in damage predictions and the necessity of careful consideration of meteoroid damage in spacecraft design.

The results shown in Table III-5-I reflect the "bumper" effect of the spacecraft outer shell structure in protecting the internal components by shattering small meteoroids penetrating the shell. The Kornhauser method indicates the APOLLO spacecraft outer shell would be penetrated by meteoroids 21 times during a 14 day mission. The D-2 re-entry vehicle pressure cabin, protected by multiple bumpers (spacecraft outer shell and re-entry vehicle structure), would receive one penetration in 640 missions and the R-3 re-entry vehicle cabin would receive one penetration in 60 missions. Note that the multiple bumper effect provided by the D-2 arrangement gives higher resistance to penetration over the more exposed R-3 vehicle. For the D-2 vehicle the probability of penetration of the mission module is one penetration in 6 missions, and of the propulsion system is one penetration in 30 missions. Local bumpers (a good use for Beryllium) could further reduce meteoroid damage of these modules.

The more optimistic (but not necessarily more valid) method of Beard, gave 7 penetrations of the spacecraft outer shell and one penetration in 26,000 missions for the D-2 re-entry vehicle pressure cabin. Results of this method also indicate the mission

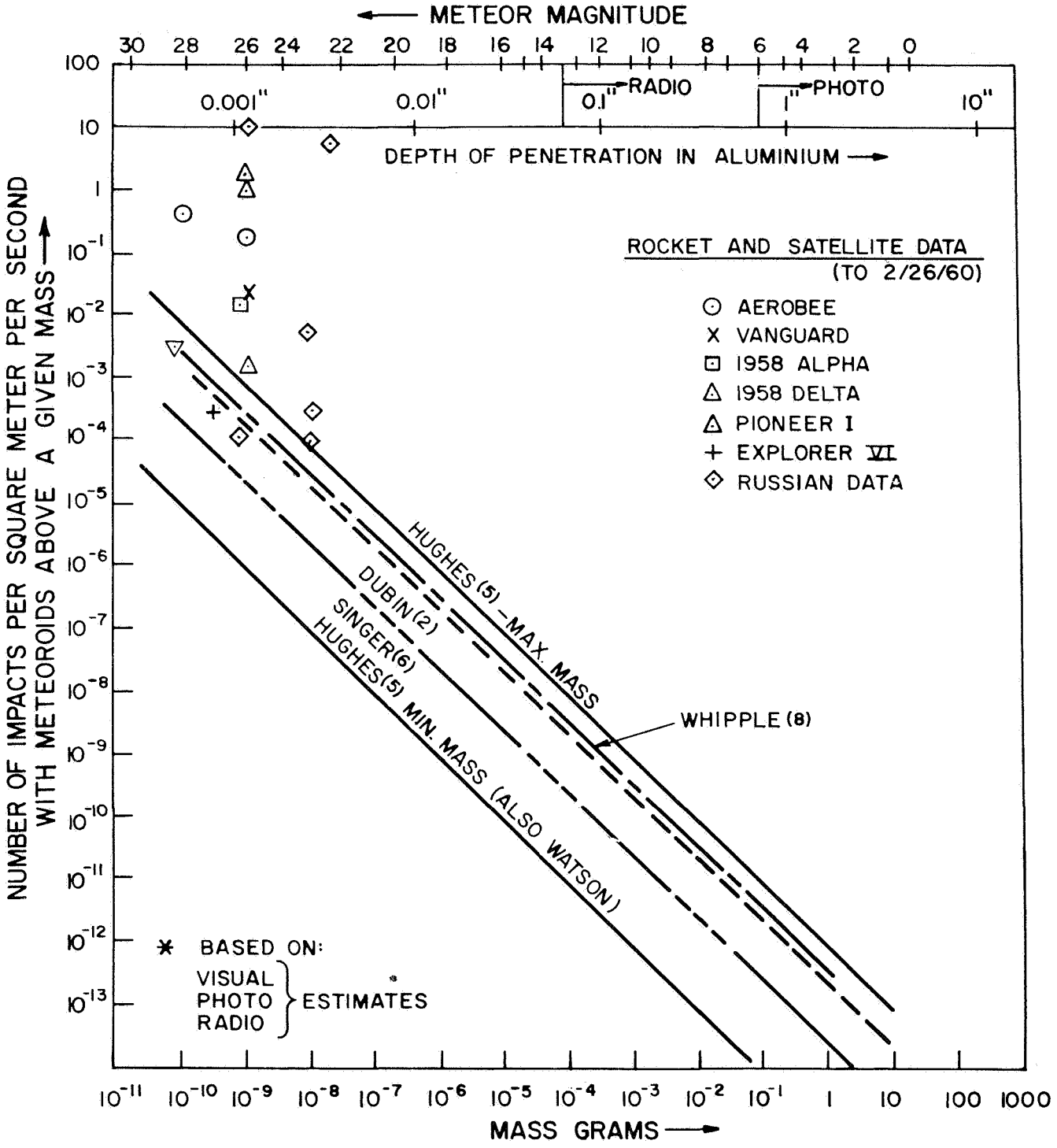

Figure III-5-1. Meteoroid population

CONFIDENTIAL

TABLE III-5-I

ANALYSIS OF METEOROID POPULATION

METHOD / VEHICLE AREA	KORNHAUSER (REF. 1)	BEARD (REF. 2)
SPACECRAFT OUTER SHELL	21	7
MISSION MODULE	1/6	1/50
PROPULSION SYSTEM	1/30	1/500
RE-ENTRY VEHICLE PRESSURE CABIN	1/640	1/26 000
	1/60	

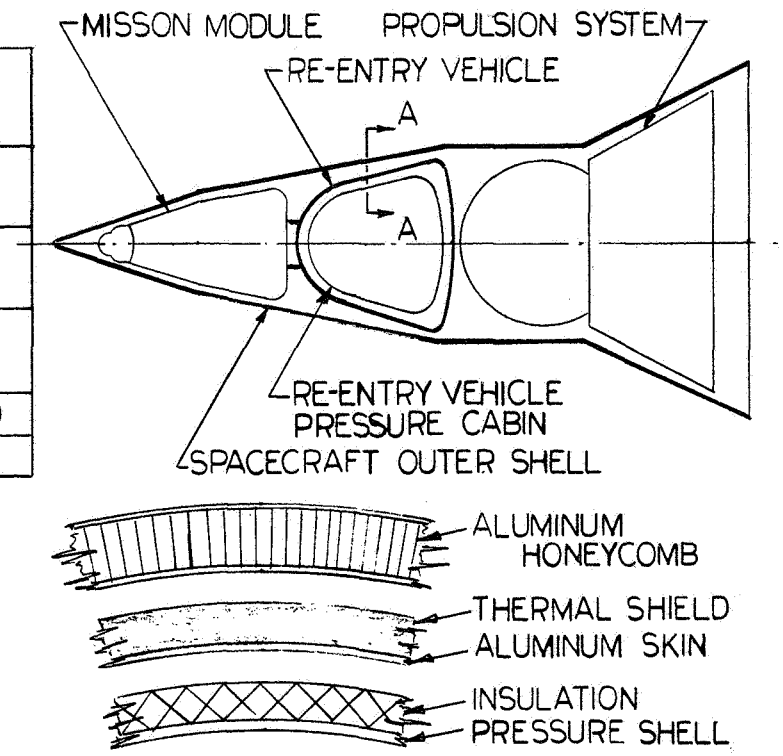

SECTION A-A

TYP. BUMPER PROTECTION FOR RE-ENTRY VEHICLE PRESSURE CABIN

CONFIDENTIAL

module and the propulsion system would receive one penetration in 50 missions and one penetration in 500 missions respectively.

It is recommended that the method of M. Kornhauser be specified for assessing the effects of meteoritic impact on the APOLLO Vehicle. This method, although seemingly conservative, appears justified for design pending a great deal of further flight test data and added experimental confirmation of theory.

Estimates of the penetration hole size for the D-2 re-entry vehicle pressure cabin is approximately one inch in diameter and serves to emphasize the necessity for access to the cabin inner surface for repair, if necessary.

These results have been based on a rational assessment of the effect of bumpers in alleviating meteoritic damage based on extensive tests conducted by the General Electric Company using a hypervelocity gun firing 1/4 inch steel and aluminum pellets at velocities of 17,000 feet per second. Tests of various structural materials and types of construction and a study of the analytical methods for determining meteoroid impact damage are constantly being conducted by the General Electric Company.

Since the number of penetrations for a specific spacecraft is a linear function of the mission duration, the shorter missions (circumlunar, - 5 to 7 days; highly eccentric orbit - 15 hours; etc.) will provide proportionately fewer penetrations per missions or proportionately more missions per penetration.

References:

1. Kornhauser, M., "Current Estimate of the Effect of Meteoroids on the Skin of a Satellite Vehicle", General Electric Missile and Space Vehicle Department, Advanced Space Vehicle Engineering Memo. No. 3, February 25, 1960.
2. Beard, D.B., "Meteoritic Impact", ARS Journal Volume 31, No. 1, Page 87, January, 1961.

6.0 Leakage and Seal Design

The problem of designing a spacecraft pressure cabin with requirements for an extremely low pressure leakage rate is recognized in the APOLLO study. Because of this requirement welded construction has been chosen for all pressure cabin structure. All mechanical penetrations; doors, electrical connections, etc. will require an extensive test program to develop positive sealing devices. Presently, at the General Electric Company, a research and development program is in progress to develop a reliable pressure door for use in spacecraft.

APOLLO vehicle drawings, included in this study report, reflect two considered methods for the design of pressure doors. (1) the use of inflatable tubes for sealing as on the access door, and (2) the use of a breech-lock type latching device with "O" ring seals as on the re-entry vehicle hatch. These designs are not necessarily the most optimum designs but reflect two suggested methods. Further tests, as outlined in the APOLLO Test Plan, and other research and development programs such as the existing program mentioned above will lead to the final, most reliable and optimum design for pressure doors and other required sealing systems to meet the design requirements of the APOLLO Vehicle. These tests will verify the door design and establish a finite leak rate for the design of the environmental control subsystem.

6.1 FRICTION/WELDING

The problem of metals in a space (vacuum) environment tending to adhere, producing a weld-like attachment has been considered in this design study for the APOLLO vehicle. The major effect of this problem will be evident in door latches, telescoping structure and other movable components. The present suggested solution is proper application of a dry film lubricant to all contact surfaces.

The magnitude of the friction/welding problem and necessary solutions required to meet the APOLLO Vehicle design specifications will be substantiated by extensive vacuum testing.

APPENDICES

A-A — Analytical Methods

The various technical methods to be used in guiding the correlation of the experimental data are discussed in the following sections. Some of the special problems areas for which advanced methods are already available are indicated as well as areas which will require further effort because of the present state of the art.

The contents of this section have been subdivided into the following topics for ease of discussion:

1) Body alone
2) Flow conditions about the body
3) Controls alone
4) Controls - Body Combinations
5) Low density considerations.

Items 1 through 4 are primarily concerned with methods for inviscid compressible flow. Item 5 is devoted mainly to viscous effects.

BODY ALONE:

There are basically only a few theoretical methods, with a high degree of utility, for determining the aerodynamic characteristics of bodies in inviscid continuum flows at hypersonic speeds. These include Newtonian theory, shock expansion theory and exact numerical flow field methods. There are several other techniques which are employed such as the blast wave analogy; however, these methods are only used for specific applications. Because of its utility in defining the entire shock layer the numerical flow field technique will be discussed first.

FLOW FIELDS:

Exact flow field methods for pointed cones and pointed bodies of revolution have been available for many years [40-42]. Only in recent years, however, have exact methods become available for the blunt body problem. The method of Gravalos, Edelfelt and and Emmons developed at GE-MSVD is in current use for design purposes. This method is applicable for bodies of revolution at zero angle of attack and for two dimensional bodies at angle of attack, in the supersonic flow of real gases in chemical equilibrium. The body shapes may include sharp corner expansions [43] or compressions, so called secondary shocks [44]. Hence the entire flow field including pressure distributions and shock shapes can be determined precisely for complex shapes such as sphere-cone-cylinder flares.

About fifty flow field solutions for real and ideal gases have been obtained for bodies of revolution. A list of the flow fields solutions which have been documented is presented in Ref. 45. As part of a continuing effort these flow field results are being summarized to determine general trends of related aerodynamic characteristics.

Flow field surface pressure distributions and associated thermodynamic and aerodynamic quantities have been used as inputs to a boundary layer-skin friction analysis to determine viscous drag coefficients on several types of bodies over a wide range of altitude and Mach number conditions. Ref. 46 presents a comparison of viscous and inviscid drag coefficients in terms of the ratio of C_{D_F/C_D}. Although these theroretical results are only qualitative because of certain engineering assumptions involved in the boundary layer-skin friction analysis, they are believed to be indicative of the significant magnitude of the viscous drag obtained by relatively blunt bodies at high altitudes.

GE-MSVD is currently programming for the 7090 computer an exact solution for the flow field about blunt bodies at angle of attack using a perturbation technique. This program is presently checked out and is available for determining the flow about bodies of revolution.

NEWTONIAN THEORY:

Newtonian theory is invaluable as a preliminary design tool. Pressure distributions, loads, and total aerodynamic characteristics for a large range of configuration variables at angle of attack can be readily determined. Because of its utility, several 7090 computer programs [1] have been developed at GE-MSVD to determine force and moment characteristics at angle of attack to 180 degrees. These programs have been used to obtain longitudinal force and moment coefficients at hypersonic speeds for such configurations as the D-2. This available computer program is also applicable to half-sphere cones, [14 or 15] elliptical cross section bodies and wing-body combinations.

LIMITATIONS OF AND CORRECTIONS TO NEWTONIAN THEORY:

In the course of many investigations by GE-MSVD there have arisen certain specific instances in which the limitations of the Newtonian theory have been clearly evidenced, even for preliminary design purposes. For example in the case of certain blunt nosed bodies, Newtonian theory has grossly overstimated the longitudinal stability at small angles of attack. Further analysis, using the Gravalos numerical flow fields at $\alpha = 0°$ gave more precise definition of the flow properties so that adjustments of the local dynamic pressure ratio within the shock layer can be made, yielding good agreement with experimental results.

FLOW CONDITIONS ABOUT THE BODY:

Zero Angle of Attack

In order to define the characteristics of controls or lifting surfaces mounted on hypersonic bodies it is necessary to define the non-uniform, shock layer flow fields about the body. For the particular case of bodies of revolution at zero angle of attack, this can best be done by the Gravalos flow field technique. To this end a number of the flow field solutions have been summarized [47] presenting correlations of pressure and entropy $S/_R$ across the shock layer for sphere cones over a cone angle range of 5 to 15 degrees, a Mach number range from 15 to 22 and a range of axial distances of 5 to 20 nose radii. From these flow properties, thermodynamic charts are used to determine profiles of local Mach number and dynamic pressure required to define the environment of controls.

ANGLE OF ATTACK

For angle of attack case, a perturbation method of the flow field technique has been programmed. Considerable progress has already been made for bodies of revolution and half cone bodies. The approach employs a type of tangent-cone theory. In this method, the flow field for the meridian plane of the subject body at angle of attack is computed as the flow field of symmetrical bodies of revolution at $\alpha = 0°$, whose major meridians coincide with the meridian of the subject body.

CONTROL ALONE:

Once again, flow field methods have been used to obtain accurate pressure distributions over two dimensional control profiles. Shock expansion theory has been used for rapid calculation of control characteristics. This method combined with Newtonian theory on blunt leading edges has resulted in good agreement with experimental findings.

Very little has been said about methods for predicting transonic characteristics of control surfaces, nor about the transonic characteristics of bodies. In general empirical techniques are employed at GE-MSVD to determine transonic and low supersonic aerodynamic characteristics.

CONTROL BODY COMBINATIONS:

In order to utilize the lift potential of non-winged bodies some means of trimming the vehicle at a desired angle of attack is necessary. Body upwash and sidewash are recognized as being important factors in determining the aerodynamic characteristics of bodies and controls. If this phenomenon is properly understood, the control size and weight can be minimized for a given design application. MSVD has developed a method for estimating the aerodynamic characteristics, including stability and control of non-winged lifting bodies with controls. A modified strip theory is employed which uses the flow field conditions just ahead of the control. The element contributions are integrated along the span to obtain general expressions for the control input to forces and moments. These control inputs are then added to body inputs and interference effects between control and body are added.

LOW DENSITY CONSIDERATIONS:

At high altitudes, or corresponding low Reynolds numbers, viscous effects will become important; that is skin friction drag and boundary layer induced pressures will become

appreciable. Recommended techniques for determining skin friction drag are available in a series of GE-MSVD reports by Nestler [48-52] for flat plates, bodies of revolution with and without pressure gradients and for slip flow. Those methods include heat transfer and mass transfer effects.

Induced pressures caused by boundary layer displacement of the local free stream flow will be determined by use of available boundary layer techniques. Dr. S.M. Scala of the MSVD Space Sciences Laboratory has contributed greatly to the field of hypersonic boundary layer. His methods are based on exact solutions to the stagnation point boundary layer problem. The continuation of this method downstream from the nose has been accomplished by use of a piece-wise application of the similarity concept. A recent published report on this method [53] presents aerodynamic forces on a sphere at angle of attack caused by skin friction.

In view of the unknowns existing in the very low density continuum region, a particular facet of the GE-MSVD engineering approach to this problem is of interest. In this approach, an attempt is being made to define the upper limit of the complex continuum flow regime, about which little is known, by defining the limit of free molecular flow for high altitude, hypersonic flight. Dr. Hurlbut of the University of California has been consulting with the GE-MSVD on this task. Simple free molecular flow methods for determining forces and moments over arbitrary convex shapes are being programmed for the 7090 computer. This program is very similar to the Newtonian program in approach. The molecular fluxes have been determined for a generalized (concave) control surface [54] assuming diffuse reflection. The summations necessary to provide aerodynamic forces and moments derived from these fluxes are now being programmed on the 7090 computer.

The question of appropriate values for the accommodation coefficients required by these analyses is under study in the GE-MSVD Space Sciences Laboratory, under the direction of Dr. S.M. Scala and Dr. H. Wachman and in consultation with Dr. Hurlbut. Contracted work is also under way at Princeton University to determine accommodation coefficients. The simultaneous efforts of these scientists is available for purposes of evaluating the free molecular techniques and accommodation coefficients employed in this portion of the analysis.

A-B — Experimental Aerodynamics — Related Experience, Present and Proposed Program

I. RELATED EXPERIENCE

Since ground-based facilities cannot simulate the environment throughout all trajectory conditions, combined results of various experimental facilities must be employed. Scaling laws and judicious extrapolations utilizing theory must be used for closer approximations of aerodynamic characteristics in the desired environment. Experimental data have been obtained for several re-entry configurations at very high altitudes in the low density wind tunnel at the University of California. Hypersonic high temperature environmental tests in the MSVD shock tunnel, the GE Research Laboratory and the AEDC Hot Shot Tunnels have been conducted at velocities up to Mach 28.

Dynamic stability of re-entry vehicles has been obtained in almost all ballistic range programs by measuring the motions of the vehicle and reducing the data to aerodynamic damping parameters. Correlation of the information from the ballistic ranges with that of wind tunnels has given an understanding of many of the more subtle problems, such as non-linear damping variations with angle of attack encountered in the dynamic behavior of re-entry vehicles.

During the past five years approximately 220 experimental programs have been conducted by MSVD in wind tunnels, shock tunnels, ballistic range, free flight facilities, drop test facilities and high temperature facilities supporting aerodynamic and thermodynamic design and evaluation of various vehicles. These experimental programs have been performed in support of problems associated with ballistic re-entry bodies, maneuvering re-entry bodies, orbital re-entry bodies, short range tactical weapons and recovery systems for ballistic and orbital re-entry bodies.

Experimental aerodynamic data have been obtained in support of Atlas, Thor and Titan nose cones, the Discoverer re-entry capsule, the NERV re-entry body, the LaCrosse missile, the RVX-1 and RVX-2 recoverable ballistic re-entry bodies and

the Mark 3C feasibility study. The latter study was concerned with an aerodynamic investigation of a maneuvering re-entry vehicle.

Aerodynamic characteristics, stability, pressures and heat transfer data have been obtained in various facilities (GE, Government, and private) for re-entry vehicles, sphere-cone-flare bodies, minimum heat transfer shapes, finned bodies, etc. MSVD experience in planning and conducting these expermental programs in the design and construction of the re-entry models and in the proper use of facilities in testing various configurations is directly applicable to the APOLLO study.

II. DESCRIPTION OF PRESENT TUNNEL TESTS:

To substantiate the aerodynamic prediction made for the selected APOLLO configuration in developing the estimated trimmed $(L/D)_{MAX}$ and static stability and control characteristics an experimental program was initiated in the GE-MSVD Shock Tunnel to obtain these aerodynamic parameter at M = 12.4 on the D-2 configuration at high angles of attack with flap deflections of 0 degrees and 90 degrees. Aerodynamic data from these tests is expected to become available on or about May 10, 1961.

An experimental aerodynamic program for the R-3 lenticular vehicle was agreed upon and initiated by NASA to obtain low speed data, applicable to the landing problems associated with this shape, in the Langley "Free Flight" Wind Tunnel. Information obtained in this facility will include measurements of longitudinal, lateral and directional stability parameters, control effectiveness and logitudinal and lateral dynamic damping parameters. Tests to obtain longitudinal and lateral static stability data will also be conducted at M = 3 and 6 in the Langley 20" Hypersonic Tunnel, if the low speed tests prove that the maximum (L/D) trimmed is great enough to consider the configuration feasible from the landing standpoint. Tests in the "Langley Free Flight" Tunnel are expected to start during the first part of May and the 20" tunnel tests are tentatively scheduled to begin in June, 1961.

III. PROPOSED AERODYNAMIC EXPERIMENTAL PROGRAM

Support for the aerodynamic design and performance of the APOLLO re-entry vehicle will depend on the results of numerous aerodynamic ground tests. This section presents a basic test program for the D-2 and R-3 configurations. Programs will be added in other facilities to obtain checks on the data throughout the Mach number and Reynolds number range.

This together with the detailed evaluations of the problem areas which will undoubtedly be uncovered by the proposed test programs will probably increase the scope of the programs appreciably.

The basic areas of the mission to be investigated by the test programs are:

1. Abort from pad
2. Abort from powered flight
3. Orbit
4. Re-entry
5. Landing
6. Booster Stability

A - Configuration

In order to insure successful abort either from the launching pad or powered flight, the configuration must be statically unstable in the backward attitude so that it will turn itself around prior to initiation of the recovery system. Extensive testing will be performed in the low Mach number range up through supersonic Mach numbers at angles of attack from 0 to 180 degrees. The recovery system itself (parachutes) will not be tested in wind tunnels other than exploratory tests to investigate problems areas because of their prohibitive sizes. In addition the BRL range will be utilized to determine the dynamic stability of the vehicle when attached to a non-rigid object by a non-rigid link. Although parachute scaling presents some problems the data obtained will provide an insight to the effects of the parachute on the dynamic stability.

The contribution of low density flow characteristics on the orbit decoy and initial re-entry stability will be determined utilizing low density wind tunnel tests. At present GE-MSVD is preparing to run tests on basic body configurations from the continuum flow regime through the transition region to the free molecular flow regime to obtain basic drag data. This technique will be used to obtain lift, drag and moment data for APOLLO configurations in their flow regimes.

In the hypersonic region the test program is designed to effectively define the static and dynamic stability parameters within the limits of the test facilities available.

The proposed aerodynamic experimental program in support of the D-2 vehicle design selected for the APOLLO mission, is outlined in Table IA.

B - Lenticular Configuration

The test program outlined for the lenticular configuration is also designed to investigate the basic areas of the mission profile. However, due to the inherent complexity of the configuration considerably more testing will be required to support a successful design effort. Most of the test programs will require extensive body buildup i.e., body alone, body plus elevon, etc., in order to obtain the cross coupling effects of the various control surfaces. This will be done throughout the Mach number, Reynolds number range to insure that the longitudinal and lateral-directional characteristics of the configuration within the specified limits. As before, the program outlined in Table IB is the basic test program. It is anticipated that many more experimental programs will be run to verify data, and investigate specific problems that arise. The interaction effects of the control surfaces will be investigated thoroughly and the results shown parametrically. It will be important to determine shock shapes and their effect on the flow field around the body plus control configuration and the interaction effects. Extensive flow-photo coverage at hypersonic and supersonic Mach numbers will be obtained.

CONFIDENTIAL

TABLE 1A

D-2 CONFIGURATION

TYPE OF TEST	DATA TO BE OBTAINED	FACILITY	MACH NO.	REYNOLDS NO. HIGH	REYNOLDS NO. LOW	ANGLE OF ATTACK
1- Hypersonic Center of Pressure	α vs time	MSVD 6" Shock Tun.	12		X	
2- Static Stability Transonic (flap effectiveness)	C_L, C_D, C_m C_{L_δ}, C_{m_δ}	Langley 8' Transonic	.25 - 1.2	X		0 - 180
3- Static Stability Supersonic (flap effectiveness)	C_L, C_D C_m C_{L_δ} C_{m_δ}	AEDC 16' PWT Supersonic	1.6 - 5	X		0 - 180
4- Dynamic Stability Transonic (with and without flaps)	$C_{m_q} + C_{m_{\dot{\alpha}}}$	Langley 8' Transonic	.25 - 1.2	X		through - trim
5- Dynamic Stability Supersonic (with and without flaps)	$C_{m_q} + C_{m_{\dot{\alpha}}}$	AEDC 16' PWT Supersonic	1.6 - 5	X		through - trim
6- Low Density Static Stability	C_L, C_D, C_m	Univ. of Cal.	5.8		X	0 - 180
7- Hypersonic Static Stability (flap effectiveness	C_L, C_D, C_m C_{L_δ}, C_{m_δ}	AEDC Hot Shot II	20		X	0 - 90

CONFIDENTIAL

CONFIDENTIAL

TABLE 1A

D-2 CONFIGURATION (Continued)

TYPE OF TEST	DATA TO BE OBTAINED	FACILITY	MACH NO.	REYNOLDS NO. HIGH	REYNOLDS NO. LOW	ANGLE OF ATTACK
8- Hypersonic Dynamic Stability (flap effectiveness)	$C_{m_q} + C_{m_{\dot{\alpha}}}$ C_{L_δ}, C_{m_δ}	Cornell Aero. Lab Shock Tunnel	12		X	0 - trim
9- Hypersonic Static Stability (flap effectiveness)	C_L, C_D, C_m C_{L_δ}, C_{m_δ}	AEDC Tunnel C or Langley 11" Hypersonic	10	X		0 - 30
			7 - 10		X	
10- Pressure Distributions Transonic (Body alone and flaps)	$C_P/C_{P_{MAX}}$	Langley 8' Transonic	.7 - 1.2	X		0 - 90
11- Pressure Distribution Supersonic	$C_P/C_{P_{MAX}}$	AEDC 16' PWT Supersonic	1.6 - 5	X		0 - 90
12- Pressure Distribution Hypersonic	$C_P/C_{P_{MAX}}$ Shadowgraphs	Langley 20" and Langley 11" Hypersonic	6 - 10		X	45 - 90
13- Pressure Distribution Hypersonic	$C_P/C_{P_{MAX}}$ Schelerens	AEDC Hot Shot II	17 - 20		X	45 - 90
14- Heat Transfer Body alone and Body + flaps	$\dot{q}$	Langley 20" and Langley 11" Hypersonic	6 - 10		X	45 - 90

CONFIDENTIAL

TABLE 1A

D-2 CONFIGURATION (Continued)

TYPE OF TEST	DATA TO BE OBTAINED	FACILITY	MACH NO.	REYNOLDS NO. HIGH	REYNOLDS NO. LOW	ANGLE OF ATTACK
15- Dynamic Damping w and w/o parachute	$C_{m_q} + C_{m_{\dot{\alpha}}}$	BRL	1.2	X		≈ 0
16- Parachute Characteristics	$C_D S$	Langley 20" Spin Tunnel	Low Subsonic		X	≈ 0
17- Hypersonic Static Stability	C_L, C_D, C_m	Ohio State	12.5		X	45 - 90
18- Supersonic Dynamic Damping and Sting Free Drag	$C_{m_q} + C_{m_{\dot{\alpha}}}$ C_D, C_{L_α} $C_{m_{\dot{\alpha}}}$	NOL	2 - 9	X		≈ 0
19- Static Stability Low Subsonic	C_L, C_D, C_m	Langley Full Scale Tunnel	.14	X		0 - 90
20- Static and Dynamic Low Speed Stab.	$C_{m_q} + C_{m_{\dot{\alpha}}}$ C_L, C_D, C_m	Langley Low Speed Free Flight	.10		X	0 - 90
21- Supersonic Heat Trans.	$\dot{q}$	Langley 4' x 4' Unitary	1.6 - 4.7	X		45 - 90

CONFIDENTIAL

CONFIDENTIAL

CONFIDENTIAL

TABLE 1A

D-2 CONFIGURATION (Continued)

TYPE OF TYPE	DATA TO BE OBTAINED	FACILITY	MACH NO.	REYNOLDS NO. HIGH	REYNOLDS NO. LOW	ANGLE OF ATTACK
22- Heat Transfer Hypersonic	$\dot{q}$	AEDC TUN.C	10	X		45 - 90
23- Heat Transfer Hypersonic	$\dot{q}$	MSVD 6" Shock Tun.	18		X	45 - 90
24- Booster Stability	C_N, C_A, C_m	Langley 16'	.5 - 1.3	X		0 - 20
		Langley 20"	6 - 10	X		
		Langley Full Scale	.14	X		

CONFIDENTIAL

CONFIDENTIAL

TABLE 1B

R-3 CONFIGURATION

TYPE OF TEST	DATA TO BE OBTAINED	FACILITY	MACH NO.	ANGLE OF ATTACK	REYNOLDS NO. RANGE HIGH	REYNOLDS NO. RANGE LOW
I-Longitudinal Characteristics (A) Body alone (B) Body and elevons (C) Body and elevons and fins (D) Elevon Pitch control (E) Ruddervon Pitch Control	C_L, C_D, C_m vs. α					
1- Subsonic		Langley FFWT	0-.10	0-40		X
2- Transonic-Subsonic		Langley 8' Tran.	25-1.2	0-40	X	
3- Supersonic		" 4 x 4 Unitary	1.6-4.7	0-90	X	
4- Hypersonic		AEDC Hot Shot II	17-21	45-90		X
5- Hypersonic		Lang. 11" Hyper.	7-10	45-90		X
6- Hypersonic		MSVD 6" Sho. Tun.	12	45-90		X
II-Lateral and Directional Characteristics (A) Body alone (B) Body and elevons (C) Body and elevons and fins (D) Lateral-Directional Control (E) Fin Roll Effectiveness (F) Ruddervon Lateral Control	C_Y, C_n, C_l vs α and β					
1- Subsonic		Langley FFWT	0-.10	0-40		X
2- Transonic		Lang. 8' Trans.	.25-1.2	0-40	X	
3- Supersonic		Lang. 4 x 4' Uni.	1.6-4.7	0-90	X	
4- Hypersonic		Lang. 11" Hyper.	7-10	45-90		X
5- Hypersonic		AEDC Hot Shot II	17-21	45-90		X
III-Dynamic Characteristics	$C_{m_q} + C_{m_{\dot{\alpha}}}$ $C_{n_r} + C_{n_{\dot{\beta}}}$					
1- Subsonic	C_{l_p}, C_{n_p}, C_{n_r}, C_{l_r}	Lang. FFWT	0-.10	through trim		X
2- Transonic		Lang. 8' Trans.	.25-1.2	"	X	
3- Supersonic		Lang. 4 x 4' Unit.	1.6-4.7	"	X	
4- Supersonic		Supersonic FF (Ames)	12-16	"		X
5- Hypersonic		Cornell Aero Lab.	12	through trim		
IV-Low Density Effects (Static Stability)	C_L, C_D, C_m	University of Cal.	6	0-90		X
V-Pressure Distribution and Flow Pictures	$C_P/C_{P_{MAX}}$					
1- Hypersonic		AEDC Hot Shot II	17-21	45-90		X
2- Hypersonic		Lang. 11" Hyper.	7-10	45-90		X
3- Supersonic		Lang. 4 x 4' Unit.	1.6-4.7	45-90	X	
4- Hypersonic		Ames 10" x 14" Hyper.	2.7-5.3	45-90		

CONFIDENTIAL

[redacted]

A-C — Pyrolytic Graphite

Pyrolytic graphite is a polycrystalline form of carbon having a high degree of orientation. It possesses no binder, has high purity and low (essentially zero) porosity. It includes a variety of materials differing in physical properties which are produced by vapor deposition of pure carbon onto a surface at high temperatures (3000 to 4000 F). The carbon atoms are arranged in sheets, similar to the layer planes in graphite crystals except they are stacked in a disordered arrangement. These sheets are keyed together by wrinkles or cups in the sheets and are oriented parallel to the surface of deposition.

As a result of this structure, it is the most anisotropic material yet discovered. Its properties exhibit strong directionality; those parallel to the surface are similar to metallic properties and those perpendicular to the surface resemble properties of non-metallics. This enables it to be used to replace refractory metals as well as conventional graphites in many areas of use. For example:

- Its high temperature tensile strength has been measured above 60,000 psi at 2750 C. No refractory metal can approach this strength at such high temperatures.
- Its room temperature strength in tensile and flexure is in the range of ceramics (10,000 to 30,000 psi). This enables it to be used where commercial graphites have been ruled out because of strength requirements.

Its applicability is further increased because of desirable combinations of its properties. The properties which have created the most interest are listed below.

- High strength at extremely high temperatures.
- Imperviousness to gases and liquids.
- Oxidation resistance.
- Thermal and electrical conductivity.
- High percent of theoretical density.

[redacted]

Because of certain important properties change with different manufacturing procedures, pyrolytic graphite may well develop into a family of materials offering a series of grades. At present, however, a single type having a density of 2.20 ±.02 gm/cm^3 is available.

DESIGN CONSIDERATIONS

Pyrolytic graphite is a coating which may be used as such, or it can be built up to sufficient thickness (up to 1/2 inch) to permit it to be free standing. It is not a material available in large blocks for machining. Because of this, the designer of parts should keep this aspect of "coating" in mind and take full advantage of its many desirable properties.

An advantage of pyrolytic graphite is that it is made to closely approximate the final shape, thus the necessity of machining is kept to a minimum.

Because of its high degree of preferred orientation of the crystals, pyrolytic graphite has a great difference in thermal expansion between the direction along the planes and the direction across the planes. This shows up on cooling from the deposition temperature; the thickness decreases 5 percent to 6 percent, and the length decreases only .3 percent to .6 percent.

The following considerations have been developed weighing both the problems and capabilities connected with manufacturing processes.

- Avoid sharp corners - use as large radii of curvature as possible, trying to maintain at least a 10-1 ratio of curvature to thickness.
- When using as a coating - use minimum possible thickness to improve adherence and to reduce residual stresses.
- Avoid exposing the edge planes after machining - to retain the good oxidation resistance of as-deposited surface.
- If machining is necessary, take light cuts to avoid tearing out individual layers. Otherwise, established procedures for machining or grinding commercial graphite should be used.
- When pyrolytic graphite is to be deposited on an internal surface of commercial graphite, a 10-1 to 40-1 ratio should be maintained of the thickness of the substrate to the pyrolytic to avoid breaking the conventional graphite.

Size possibilities are indicated by the fact that plates have been produced up to 17 inches wide by 30 inches long.

When free standing parts are needed, thick coatings can be accomplished on graphite or selected refractory materials. Within certain limits, this permits coating of many unusual shapes that can be fabricated from refractory metals.

Some free standing shapes that have been made at MSVD are:

- tubes
- rods
- plates
- flanges
- spheres
- hemispheres
- cones

Coatings have been made on refractory metals as springs, mesh and shapes.

A more comprehensive treatment of pyrolytic graphite may be found in the following publications:

(1) Diefendorf, R. J., "Preparation and Properties of Pyrolytic Graphite," GE Report No. 60-RL-2572 M, Nov. 1960.

(2) "Pyrolytic Graphite - Preliminary Engineering Data," (brochure), General Electric Metallurgical Products Dept., Specialty Alloys Section, 1960.

[redacted]

GENERAL
ELECTRIC

MISSILE AND SPACE VEHICLE DEPARTMENT
A DEPARTMENT OF THE DEFENSE ELECTRONICS DIVISION
3198 Chestnut Street, Philadelphia 4, Penna.

[redacted]